Springer Proceedings in Physics 167

Olena Fesenko
Leonid Yatsenko *Editors*

Nanoplasmonics, Nano-Optics, Nanocomposites, and Surface Studies

Selected Proceedings of the Second FP7 Conference and the Third International Summer School Nanotechnology: From Fundamental Research to Innovations, August 23–30, 2014, Yaremche-Lviv, Ukraine

Springer

Springer Proceedings in Physics

Volume 167

More information about this series at http://www.springer.com/series/361

Olena Fesenko • Leonid Yatsenko
Editors

Nanoplasmonics, Nano-Optics, Nanocomposites, and Surface Studies

Selected Proceedings of the Second FP7 Conference and the Third International Summer School Nanotechnology: From Fundamental Research to Innovations, August 23-30, 2014, Yaremche-Lviv, Ukraine

Springer

Editors
Olena Fesenko
Institute of Physics of NASU
Kiev, Ukraine

Leonid Yatsenko
Institute of Physics of NASU
Kiev, Ukraine

ISSN 0930-8989 ISSN 1867-4941 (electronic)
Springer Proceedings in Physics
ISBN 978-3-319-18542-2 ISBN 978-3-319-18543-9 (eBook)
DOI 10.1007/978-3-319-18543-9

Library of Congress Control Number: 2015944311

Springer Cham Heidelberg New York Dordrecht London

Printed on acid-free paper

Springer International Publishing AG Switzerland is part of Springer Science+Business Media (www.springer.com)

Preface

This book highlights the most recent advances in nanoscience from leading researchers in Ukraine, Europe, and beyond. It features contributions from participants of the Third International Summer School "Nanotechnology: From Fundamental Research to Innovations," held in Yaremche, Ukraine, on August 23–26, 2014 and of the Second International NANO-2014 Conference, held in Lviv, Ukraine, on August 27–30, 2014. These events took place within the framework of the European Commission FP7 project Nanotwinning and were organized jointly by the Institute of Physics of the National Academy of Sciences of Ukraine, University of Tartu (Estonia), University of Turin (Italy), and Pierre and Marie Curie University (France). Internationally recognized experts from a wide range of universities and research institutes share their knowledge and key results in the areas of nanocomposites and nanomaterials, nanostructured surfaces, microscopy of nano-objects, nano-optics, and nanophotonics, nanoplasmonics, nanochemistry, nanobiotechnology, and surface-enhanced spectroscopy.

The book is divided into four parts: Part I: *Nanocomposites and Nanostructures*; Part II: *Nanophotonics*; Part III: *Nanobiotechnology*; and Part IV: *Applications*.

Part I: Nanocomposites and Nanostructures

In Chap. 1 (Kovaleva), the authors discuss the deposition and characterization of Cr_3C_2–TaC–NiCr coating by multi-chamber detonation sprayer. Chapter 2 (Kizilova) focuses on biomimetic composites reinforced by branched nanofibers. The authors of Chap. 3 (Gab et al.) consider the kinetics of dispergation-coagulation processes of various metal nanofilms of 100 nm thickness, which are deposited onto oxide and nonoxide substrates and anneal in a wide range of temperatures. Chapter 4 (Korostil) focuses on the mechanisms of a pulsed laser impact on the magnetization configuration in ferrimagnetic multilayered magnetic nanostructures, specifically, tunneling magnetic junctions, taking into account laser-induced kinetic effects. Chapter 5

(Raczynski) presents the molecular dynamics of a thin mesogene layer covering a carbon nanotube. In Chap. 6 (Gburski), the dynamics of cholesterol molecules embedded in the high-density lipoprotein has been studied using computer simulation. A coating deposition method based on oxidizing polymerization of aniline derivatives directly on a substrate in the presence of Fe^{3+} ions under galvanostatic conditions is demonstrated in Chap. 7 (Vyshnevska). Chapter 8 (Martseniuk) presents the analysis of water nanostructure properties in natural water and the water medium of an alive organism. Chapter 9 (Karabanova) describes 3D artificial nanodiamonds containing nanocomposites based on hybrid polyurethane–poly polymer matrix. Chapter 10 (Gudyma) focuses on spin-crossover nanocrystals and the Ising model. In Chap. 11 (Ivanchenko), the authors present a study on the formulation and rheology of tape casting suspensions based on $BaTiO_3$ nanopowders. In Chap. 12 (Honcharov), the authors describe the computer program «RIO», which can calculate the distribution of implanted ions in various substrate materials, taking into account the diffusion of atoms and their emission from the surface. The one-dimensional superlattice (SL) based on a monolayer graphene with the Fermi velocity barriers is considered in Chap. 14 (Korol). Chapter 15 (Grabova) presents a two-level modeling colloidal structures method combining molecular dynamics and dissipative particle dynamics techniques. The authors of Chap. 16 (Bażela) report X-ray and neutron diffraction and magnetic measurements of polycrystalline bulk and nanosize $RMnO_3$ (R = Tb, Dy) compounds synthesized at temperatures of 800 and 850 °C. Chapter 17 (Tynkevich) focuses on temperature dependence of the band gap of CdTe–CdS core–shell quantum dots. A two-dimensional system of aggregated patchy particles with three attractive spots on the surface is studied by means of molecular dynamics in Chap. 18 (Chrzanowska).

Part II: Nanophotonics

In Chap. 19 (Dontsova), the advantages of using heterogeneous photocatalysis to remove organic substances from water are considered. In Chap. 20 (Rengevych), the potential of surface plasmon resonance-enhanced total internal reflection microscopy for visualization of microscopic particles is demonstrated using microscopic-sized silicon rods as a test object. The authors of Chap. 21 (Smokal) report the synthesis of side chain methacrylic polymers functionalized with styrylquinoline fragments. The classification of structural defects of synthetic opals by studying their surfaces using X-ray and optical microscopy is present in Chap. 22 (Yevchik). Chapter 23 (Varyshchuk) is devoted to the correlation processing of speckle pattern in multimode polymer optical fiber for deformation monitoring in the nanometer range. In Chap. 24 (Borovaya), some fundamentals of the structure and optical properties of semiconductor quantum dots (QDs) are discussed.

Part III: Nanobiotechnology

Chapter 25 (Raczynski) presents a computer simulation study of the molecular dynamics in homocysteine systems. The authors of Chap. 26 (Shcherbak) discuss the role of nanocomposites in technology for the cryopreservation of sperm boars. In Chap. 27 (Chegel), the authors present the first study on the influence of the dielectric permittivity of a substrate on the local electromagnetic field enhancement near a metal nanostructure, and, as a result, on the emission of organic dye molecules near its surface. The aim of Chap. 28 (Pavlovich) is to study the influence of gold nanoparticles (AuNPs) on the morphological and functional characteristics of human fibroblast cells before and after cryopreservation.

Part IV: Applications

Chapter 29 (Lebyedyeva) describes anodic alumina-based nanoporous coatings for sensory applications. Chapter 30 (Savchenko) focuses on new nanosized systems of polymer metal complexes based β-diketones and lanthanides for electroluminescent devices. Chapter 31 (Petrovska) discusses nanomaterials for ink-jet printed electronics. Chapter 32 (Nykyforchyn) describes the influence of hydrogen on the mechanical properties of steels with surface nanostructures. The authors of Chap. 33 (Kondratowicz) present a review of the chemical methods of synthesis of graphene oxide and its reduction in order to obtain the so-called reduced graphene oxide (rGO) whose properties are similar to those of pure graphene.

Kiev, Ukraine

Olena Fesenko
Leonid Yatsenko

Contents

Part IV Applications

Contributors

M.Y. Arseenko Belgorod State National Research University, Belgorod, Russia

I. Astrelin Faculty of Chemical Technology, National Technical University of Ukraine, "Kyiv Polytechnic Institute", Kiev, Ukraine

A.A. Avramenko Institute of Engineering Thermophysics, National Academy of Sciences of Ukraine, Kyiv, Ukraine

S. Baran M. Smoluchowski Institute of Physics, Jagiellonian University, Kraków, Poland

W. Bażela Institute of Physics, Cracov University of Technology, Kraków, Poland

G.V. Beketov V.E. Lashkaryov Institute of Semiconductor Physics of the National Academy of Sciences of Ukraine, Kyiv, Ukraine

V.M. Beresnev National Kharkov University, Kharkiv, Ukraine

A.S. Berezhnytska V.I. Vernadsky Institute of General and Inorganic Chemistry NASU, Kiev, Ukraine

Ya.B. Blume Department of Genomics and Molecular Biotechnology, Institute of Food Biotechnology and Genomics, National Academy of Sciences of Ukraine, Kiev, Ukraine

Ya. Bobitski Lviv Polytechnic National University, Lviv, Ukraine

Institute of Technology, University of Rzeszow, Rzeszow, Poland

M.N. Borovaya Department of Genomics and Molecular Biotechnology, Institute of Food Biotechnology and Genomics, National Academy of Sciences of Ukraine, Kiev, Ukraine

I. Brazhnyk Institute for Renewable Energy, Kyiv, Ukraine

O.M. Burlaka Department of Genomics and Molecular Biotechnology, Institute of Food Biotechnology and Genomics, National Academy of Sciences of Ukraine, Kiev, Ukraine

V.I. Chegel V.E. Lashkaryov Institute of Semiconductor Physics NAS of Ukraine, Kyiv, Ukraine

A.A. Cherny Institute of Chemical Technologies (Rubizhne) of the V.Dal' East-Ukrainian National University, Luhansk, Ukraine

A. Chrzanowska Institute of Physics, Cracow University of Technology, Kraków, Poland

A. Dawid Institute of Physics, University of Silesia, Katowice, Poland

M. Dergachov Oles Honchar Dnipropetrovsk National University, Dnipropetrovsk, Ukraine

A.A. Dolinsky Institute of Engineering Thermophysics, National Academy of Sciences of Ukraine, Kyiv, Ukraine

T. Dontsova Faculty of Chemical Technology, National Technical University of Ukraine, "Kyiv Polytechnic Institute", Kiev, Ukraine

I.O. Dulina Frant
sevich Institute for Problems of Materials Science of NASU, Kyiv, Ukraine

V. Dyakonov Institute of Physics PAS, Warsaw, Poland

P.M. Fochuk Department of Solid State Inorganic Chemistry and Nanomaterials, Yuriy Fedkovych Chernivtsi National University, Chernivtsi, Ukraine

I.I. Gab Frantsevich Institute for Problems of Materials Science of National Academy Sciences of Ukraine, Kyiv, Ukraine

N.P. Galagan O.O. Chuiko Institute of Surface Chemistry, National Academy of Science of Ukraine, Kiev, Ukraine

Z. Gburski Institute of Physics, University of Silesia, Katowice, Poland

O. Gorbatiuk Institute of Molecular Biology and Genetics, National Academy of Sciences of Ukraine, Kyiv, Ukraine

V. Gorelik Lebedev Physical Institute of the Russian Academy of Sciences, Moscow, Russia

T.L. Grabova Institute of Engineering Thermophysics, National Academy of Sciences of Ukraine, Kyiv, Ukraine

Iu. Gudyma Chernivtsi National University, Chernivtsi, Ukraine

V.V. Honcharov Institute of Chemical Technologies (Rubizhne) of the V.Dal' East-Ukrainian National University, Luhansk, Ukraine

A. Hoser Helmholtz-Zentrum Berlin für Materialen und Energie GmbH, Berlin, Germany

S.E. Ivanchenko Frantsevich Institute for Problems of Materials Science of NASU, Kyiv, Ukraine

I. Ivanenko Faculty of Chemical Technology, National Technical University of Ukraine, "Kyiv Polytechnic Institute", Kiev, Ukraine

V. Ivashko Chernivtsi National University, Chernivtsi, Ukraine

L.V. Karabanova Institute of Macromolecular Chemistry of National Academy of Sciences of Ukraine, Kiev, Ukraine

P. Karbowniczek Institute of Physics, Cracow University of Technology, Kraków, Poland

Yu.B. Khalavka Department of Solid State Inorganic Chemistry and Nanomaterials, Yuriy Fedkovych Chernivtsi National University, Chernivtsi, Ukraine

N. Kizilova ICM Warsaw University, Warsaw, Poland

Kharkov National University, Kharkov, Ukraine

N.Yu. Klymenko O.O. Chuiko Institute of Surface Chemistry, National Academy of Science of Ukraine, Kiev, Ukraine

A.Yu. Kolendo Macromolecular Chemistry Department, Taras Shevchenko National University of Kyiv, Kyiv, Ukraine

I. Kondratowicz Department of Solid State Physics, Faculty of Applied Physics and Mathematics, Gdansk University of Technology, Gdansk, Poland

A.M. Korol Laboratory on Quantum Theory in Linkoping, ISIR, Linkoping, Sweden

National University for Food Technologies, Kyiv, Ukraine

A.M. Korostil Institute of Magnetism NASU, Kiev, Ukraine

B.D. Kostyuk Frantsevich Institute for Problems of Materials Science of National Academy Sciences of Ukraine, Kyiv, Ukraine

B. Kotlyarchuk Pistryhach Institute for Applied Problems of Mechanics and Mathematics of NAS of Ukraine, Lviv, Ukraine

M.G. Kovaleva Belgorod State National Research University, Belgorod, Russia

S.I. Kovtun Biotechnology Laboratory, Institute of Animal Breeding and Genetics nd. a. M.V. Zubets, National Academy of Agrarian Science of Ukraine, Kiev, Ukraine

I.G. Kovzun Institute of Biocolloid Chemistry named after F.D. Ovcharenko, NAS of Ukraine, Kyiv, Ukraine

O. Kravchuk Lviv Polytechnic National University, Lviv, Ukraine

Department EFI, G.-S. Ohm University of Applied Sciences, Nuremberg, Germany

M.M. Krupa Institute of Magnetism NASU, Kiev, Ukraine

O.M. Krupka Macromolecular Chemistry Department, Taras Shevchenko National University of Kyiv, Kyiv, Ukraine

S. Kudrya Institute for Renewable Energy, Kyiv, Ukraine

J. Kurzyk Institute of Physics, Cracow University of Technology, Kraków, Poland

V. Kyryliv Karpenko Physico-Mechanical Institute of the NASU, Lviv, Ukraine

T. Lebyedyeva V.M. Glushkov Institute of Cybernetics, National Academy of Sciences of Ukraine, Kyiv, Ukraine

R. Lesyuk Pistryhach Institute for Applied Problems of Mechanics and Mathematics of NAS of Ukraine, Lviv, Ukraine

S.I. Litvynchuk National University for Food Technologies, Kyiv, Ukraine

A.W. Lloyd University of Brighton, Brighton, UK

A.M. Lopatynskyi V.E. Lashkaryov Institute of Semiconductor Physics NAS of Ukraine, Kyiv, Ukraine

E. Lunarska Institute of Physical Chemistry of PAN, Warsaw, Poland

V.K. Lytvyn V.E. Lashkaryov Institute of Semiconductor Physics NAS of Ukraine, Kyiv, Ukraine

O. Maksymiv Karpenko Physico-Mechanical Institute of the NASU, Lviv, Ukraine

A. Maksymov Chernivtsi National University, Chernivtsi, Ukraine

L.S. Martseniuk Institute of Nuclear Researches NAS Ukraine, Kiev, Ukraine

S.V. Maschenko Institute of Chemical Technologies (Rubizhne) of the V.Dal' East-Ukrainian National University, Luhansk, Ukraine

N.V. Medvid National University for Food Technologies, Kyiv, Ukraine

S.V. Mikhalovsky University of Brighton, Brighton, UK

A. Mishchenko V.I. Vernadsky Institute of General and Inorganic Chemistry NASU, Kiev, Ukraine

V. Moiseyenko Oles Honchar Dnipropetrovsk National University, Dnipropetrovsk, Ukraine

Y.V. Naidich Frantsevich Institute for Problems of Materials Science of National Academy Sciences of Ukraine, Kyiv, Ukraine

O.M. Naum V.E. Lashkaryov Institute of Semiconductor Physics NAS of Ukraine, Kyiv, Ukraine

E.M. Nikipelova Ukrainian Research Institute of Medical Rehabilitation and Balneology, Ministry of Health of Ukraine, Odessa, Ukraine

A.G. Nikulin Frantsevich Institute for Problems of Materials Science of NASU, Kyiv, Ukraine

H. Nykyforchyn Karpenko Physico-Mechanical Institute of the NASU, Lviv, Ukraine

V.A. Oleinik Institute of Biocolloid Chemistry named after F.D. Ovcharenko, NAS of Ukraine, Kyiv, Ukraine

O.S. Osypchuk Biotechnology Laboratory, Institute of Animal Breeding and Genetics nd. a. M.V. Zubets, National Academy of Agrarian Science of Ukraine, Kiev, Ukraine

M. Pabiszczak Institute of Physics, University of Silesia, Katowice, Poland

A.V. Panko Institute of Biocolloid Chemistry named after F.D. Ovcharenko, NAS of Ukraine, Kyiv, Ukraine

I.A. Pavlenko Belgorod State National Research University, Belgorod, Russia

E.V. Pavlovich Department for Cryobiology of Reproduction System, Institute for Problems of Cryobiology and Cryomedicine, National Academy of Sciences of Ukraine, Kharkiv, Ukraine

B. Penc M. Smoluchowski Institute of Physics, Jagiellonian University, Kraków, Poland

H. Petrowska Lviv Polytechnic National University, Lviv, Ukraine

V.A. Prokopenko Institute of Biocolloid Chemistry named after F.D. Ovcharenko, NAS of Ukraine, Kyiv, Ukraine

M.S. Prozorova Belgorod State National Research University, Belgorod, Russia

A. Rachkov Institute of Molecular Biology and Genetics, National Academy of Sciences of Ukraine, Kyiv, Ukraine

V. Raczyńska Institute of Physics, University of Silesia, Katowice, Poland

P. Raczyński Institute of Physics, University of Silesia, Katowice, Poland

O.V. Rengevych V.E. Lashkaryov Institute of Semiconductor Physics of the National Academy of Sciences of Ukraine, Kyiv, Ukraine

W. Sadowski Department of Solid State Physics, Faculty of Applied Physics and Mathematics, Gdansk University of Technology, Gdansk, Poland

I.A. Savchenko National Taras Shevchenko University of Kyiv, Kyiv, Ukraine

O.V. Shcherbak Biotechnology Laboratory, Institute of Animal Breeding and Genetics nd. a. M.V. Zubets, National Academy of Agrarian Science of Ukraine, Kiev, Ukraine

P. Shpylovyy V.M. Glushkov Institute of Cybernetics, National Academy of Sciences of Ukraine, Kyiv, Ukraine

V.V. Sirota Belgorod State National Research University, Belgorod, Russia

V.O. Smokal Macromolecular Chemistry Department, Taras Shevchenko National University of Kyiv, Kyiv, Ukraine

O. Spichak Oles Honchar Dnipropetrovsk National University, Dnipropetrovsk, Ukraine

T.V. Stetsyuk Frantsevich Institute for Problems of Materials Science of National Academy Sciences of Ukraine, Kyiv, Ukraine

A. Szytuła M. Smoluchowski Institute of Physics, Jagiellonian University, Kraków, Poland

O.O. Tynkevych Department of Solid State Inorganic Chemistry and Nanomaterials, Yuriy Fedkovych Chernivtsi National University, Chernivtsi, Ukraine

A.I. Tyrinov Institute of Engineering Thermophysics, National Academy of Sciences of Ukraine, Kyiv, Ukraine

Y.N. Tyurin Paton Electric Welding Institute, NANU, Kiev, Ukraine

Z.R. Ulberg Institute of Biocolloid Chemistry named after F.D. Ovcharenko, NAS of Ukraine, Kyiv, Ukraine

S.O. Umerova Frantsevich Institute for Problems of Materials Science of NASU, Kyiv, Ukraine

Yu.V. Ushenin V.E. Lashkaryov Institute of Semiconductor Physics of the National Academy of Sciences of Ukraine, Kyiv, Ukraine

V. Varyshchuk Lviv Polytechnic National University, Lviv, Ukraine

N.A. Volkova Department for Cryobiology of Reproduction System, Institute for Problems of Cryobiology and Cryomedicine, National Academy of Sciences of Ukraine, Kharkiv, Ukraine

I. Voitovich V.M. Glushkov Institute of Cybernetics, National Academy of Sciences of Ukraine, Kyiv, Ukraine

N.M. Vyhnan Department of Solid State Inorganic Chemistry and Nanomaterials, Yuriy Fedkovych Chernivtsi National University, Chernivtsi, Ukraine

Yu. Vyshnevska National Technical University of Ukraine "Kyiv Polytechnic Institute", Kyiv, Ukraine

A.I. Yemets Department of Genomics and Molecular Biotechnology, Institute of Food Biotechnology and Genomics, National Academy of Sciences of Ukraine, Kiev, Ukraine

A.V. Yevchik Oles Honchar Dnipropetrovsk National University, Dnipropetrovsk, Ukraine

A. Zarzycki H. Niewodniczański Institute of Nuclear Physics PAS, Kraków, Poland

V.A. Zazhigalov Institute for Sorption and Problems of Endoecology, National Academy of Sciences of Ukraine, Kyiv, Ukraine

K. Żelechowska Department of Solid State Physics, Faculty of Applied Physics and Mathematics, Gdansk University of Technology, Gdansk, Poland

Part I
Nanocomposites and Nanostructures

Chapter 1
Deposition and Characterization of Nanocomposition Cr_3C_2-TaC-NiCr Coating by Multi-Chamber Detonation Sprayer

M.G. Kovaleva, Y.N. Tyurin, V.M. Beresnev, M.S. Prozorova, M.Y. Arseenko, V.V. Sirota, and I.A. Pavlenko

1.1 Introduction

The coatings based on Cr_3C_2-NiCr have a good heat resistance (900 °C) and have sufficient wear resistance under conditions of dry friction in oxidizing environments. This type of coatings in most cases superior wear resistance of iron-based alloys, hard coatings based on chromium and tool steels [1]. However, these coatings are characterized by rather low resistance to hot corrosion and erosion. One way of solving this problem—adding tantalum carbide. Also the solution to this problem is to obtain ultrafine coating state, which leads to increased strength, increased ductility, and reduced coefficient of friction [2]. Also, it should be noted that the presence in the coating of chromium carbides and nickelides promotes diffusion flow restriction at the "metal substrate—coating", and provides an increase in the maximum operating temperature of the coating up to 1,250 °C, that has a value when applied to the thermally stressed turbine blades of gas turbine engines. The aim of this chapter is to investigate the microstructure and microhardness of Cr_3C_2-TaC-NiCr nanocomposition coating obtained on steel through a new method of powder acceleration which allows to achieve the powder velocity of 1,400 m/s.

M.G. Kovaleva (✉) • M.S. Prozorova • M.Y. Arseenko • V.V. Sirota • I.A. Pavlenko
Belgorod State National Research University, Pobedy 85, Belgorod 308015, Russia
e-mail: Kovaleva@bsu.edu.ru

Y.N. Tyurin
Paton Electric Welding Institute, NANU, Bozhenko 11, Kiev 03650, Ukraine
e-mail: ytyurin@i.com.ua

V.M. Beresnev
National Kharkov University, Svobody Sq. 4, Kharkiv, Ukraine

O. Fesenko, L. Yatsenko (eds.), *Nanoplasmonics, Nano-Optics, Nanocomposites, and Surface Studies*, Springer Proceedings in Physics 167,
DOI 10.1007/978-3-319-18543-9_1

1.2 Experimental Procedure

In this study, multi-chamber detonation sprayer (MCDS) (Fig. 1.1) [3, 4] with a barrel length of 300 mm was employed to deposit the nanocomposition Cr_3C_2-TaC-NiCr powder coating (100–125 μm thick) upon a steel A29 1044 (Fe-0.45C-0.18Si-0.6Mn) substrate. Flat specimens of a steel A29 1044 were sandblasted by alumina grits 25A F360 prior to spraying. Toshiba 50Cr_3C_2-20TaC-30NiCr powder (d(0.1): 24.70 μm, d(0.5): 41.11 μm, d(0.9): 60.704 μm) was used to deposit of a coating (Fig. 1.2). Coating was deposited with a frequency of 20 Hz of the snake. Speed of moving was 2,000 mm/min, distance from the sample—60 mm. A barrel with a throat diameter of 18 mm was adopted. The specimens were transversally cut by spark erosion, mechanically polished and prepared by standard metallographic methods of sample preparation—sectioning, mounting, and polishing [5]. The sample was

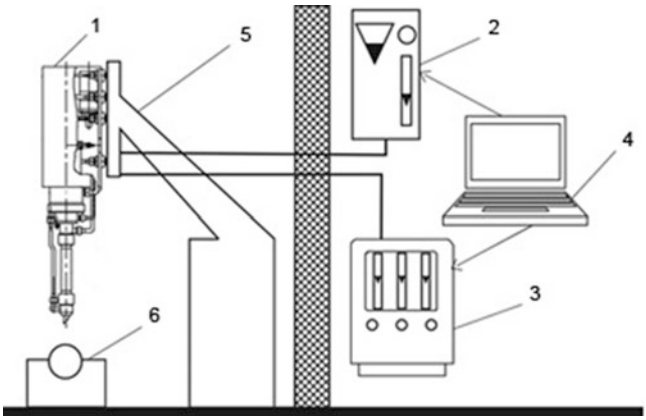

Fig. 1.1 Equipment for deposition of coatings: 1—device for spraying, 2—standard powder feeder with a feed rate of up to 3 kg/h, 3—a standard low-pressure (max. 0.3 MPa) gas panel for feeding oxygen, propane-butane, and air, 4—an automated control system for the technological process, 5—an automated manipulators for moving MCDS and 6—a specimen holder

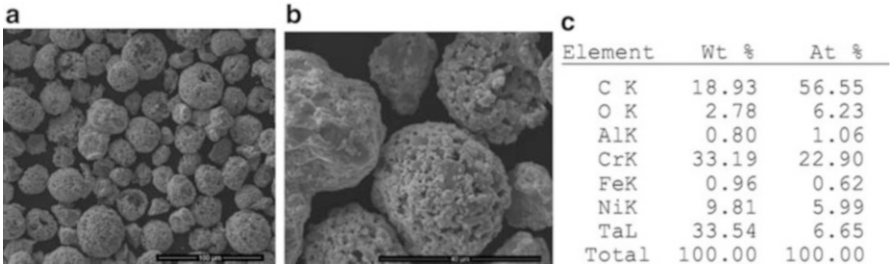

Fig. 1.2 SEM images of the microstructure (**a**, **b**) and elemental composition (**c**) of Cr_3C_2-TaC-NiCr powder

prepared by grinding with abrasive SiC paper (gradation 200, 500, 800, 1,000), followed by polishing with 1 μm diamond slurry according to the procedure recommended by Struers company for ceramic coatings.

The coating microstructures and phase compositions were characterized using SEM (Quanta 200 3D, Nova NanoSEM 450), OM (Olympus GX 51), and XRD techniques (X-ray powder diffractometer Rigaku Ultima IV). Porosity was determined by the metallographic method by using optical inverted microscope Olympus GX51 [6]. Measurement of the microhardness of samples was done with a microhardness tester DM–8B using a Vickers's indenter with load on of 0.3 N. Indentation was carried out on cross-sections of the samples of the coatings, the distance between the indents being 20 μm. In the average, ten tests were used as an indicator of the coating hardness.

The coating is formed through successive laying a set of deformed particles with different temperature, speed, and mass. The dense coating was formed through the intensive plastic deformation resulting from the impact of a particle moving with high velocity and the tamping effect on the source side of the following particles [7]. The interface between the coating and the substrate had no visible macro defects. Detonation spraying is associated with high temperatures and velocities of the moving powder particles with the result that large fractions of the powder are melted, and small are melted completely with the deposition of the appropriate alternating layers. The process of the detonation combustion in the MCDS allows getting increase in particles velocity [8].

1.3 Results

The nanocomposition coating shows a very dense microstructure consisting of well-flattened particles, which indicates that most of the powder particles were melted before deposition. The obtained coating consists of remelted splats "flattened powder particles," small amount of porosity and unmelted particles. The Cr_3C_2-TaC-NiCr nanocomposition coating consists of Cr_3C_2 with a orthorhombic lattice structure ($a = 5.53$ Å, $b = 11.45$ Å, $c = 2.83$ Å), $Al_{0.14}Ni_{0.86}$ with a cubic lattice structure ($a = 3.55$ Å), TaC with a cubic lattice structure ($a = 4.45$ Å), Fe_3C with a orthorhombic lattice structure ($a = 5.12$ Å, $b = 6.63$ Å, $c = 4.54$ Å), $Cr_{0.1}Ta_{0.9}C$ with a cubic lattice structure ($a = 4.46$ Å) phases.

It was established that MCDS has provided the conditions for formation of a dense nanocomposition layer (Fig. 1.3) with porosity below 2 % and microhardness of 800 ± 25 $HV_{0.3}$. The hardness variation along the coat thickness is not uniform which may be attributed to the phase composition of the coating and due to the size of the indentation marks produced at 300 g, the measurements performed in the vicinity of the substrate are increasingly affected by the latter.

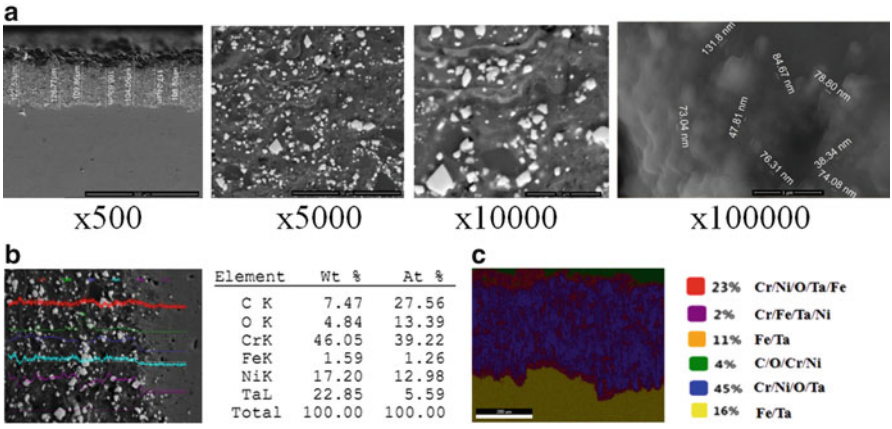

Fig. 1.3 SEM images of the microstructure (**a**), elemental composition (**b**), and SEM EDX element distribution maps (NanoSEM 450) (**c**) of Cr_3C_2-TaC-NiCr nanocomposition coating

Results of this work open up new prospects for further elaboration of new technologies to making protective Cr_3C_2-TaC-NiCr nanocomposition coating which can enhance properties of steel.

Acknowledgments This work was financially supported by the Ministry of Education and Science of the Russian Federation under project No 14.594.21.0010 (unique identifier is RFMEFI62114X0005). This study was performed by using equipment of the JRC "Diagnostics of structure and properties of nanomaterials" of the BelSU.

References

1. Mohanty M, Smith RW, Bonte MD, Celis JP, Lugscheider E (1996) Sliding wear behavior of thermally sprayed 75/25 Cr_3C_2/NiCr wear resistant coatings. Wear 198(1–2):251
2. Houdkova S, Zahálka F, Kašparová M, Berger L-M (2011) Comparative study of thermally sprayed coatings under different types of wear conditions for hard chromium replacement. Tribol Lett 43:139
3. Vasilik N et al (2012) Method for gas-dynamic detonating speedup of powders and device for its implementation. RU Patent 2506341
4. Kovaleva M, Yu T, Kolisnichenko O, Prozorova M, Arseenko M (2013) Properties of detonation nanostructured titanium-based coatings. J Therm Spray Technol 22(4):518
5. "Standard Methods of Preparing Metallographic specimens", E-3-86 (1986) Annual book of ASTM standards. Am Soc Metals 03.01:12
6. Moskal GJ (2007) The porosity assessment of thermal barrier coatings obtained by APS method. Achiev Mater Manuf Eng 20(1–2):483
7. Wang H-T, Li C-J, Yang G-J, Li C-X (2009) Effect of heat treatment on the microstructure and property of cold-sprayed nanostructured FeAl/Al_2O_3 intermetallic composite coating. Vacuum 83(1):146
8. Kovaleva M, Yu T, Vasilik N, Kolisnichenko O, Prozorova M, Arseenko M, Sirota V, Pavlenko I (2014) Effect of heat treatment on the microstructure and microhardness of detonation nanostructured Al_2O_3 coatings. J Therm Spray Technol 23:1199

Chapter 2
Biomimetic Composites Reinforced by Branched Nanofibers

N. Kizilova

2.1 Introduction

Biological organisms and their tissues possess optimal mechanical properties and exhibit maximal strength and durability at total lightweight design like bones, teeth, cartilage, respiratory airways, and blood vessels in animals; stems, trunks, and branches in high plants [1, 2]. Main principle of biological growth is connected with elongation of cells and extracellular reinforcing structures (trabecules in bones, sclerenchyma, and collenchyma in plants and others) according to principles of the stress tensor at given external load. When the external load varies changing the stress field, the reinforcing system is remodeled keeping the optimal density and orientation for new load conditions by active biological feedbacks. As a result, the uniform pattern of trabeculas in infant bones transform into clear body-specific orthogonal families of trabeculas, as well as tree trunks demonstrate straight or spiral grains depending on the permanent wind load [3]. The corresponding theoretical model of bone as adaptive material has been developed [4], but its practical implementation into the strategies of the in vivo growth control for tissue engineering purposes or into the smart materials with stress-dependent properties remains a challenge [5]. It is important that the principles of biological growth discovered in animals and plants are the same in spite of the phylogenetic development of plants and animals had been separated since early stages of evolution when both types of live matter were presented by single animal and single plant cells and did not possess any macroscopic transportation and reinforcing structures.

N. Kizilova (✉)
ICM Warsaw University, ul.Prosta, 69, Warsaw, Poland

Kharkov National University, Svobody sq., 4, Kharkov, Ukraine
e-mail: n.kizilova@gmail.com

O. Fesenko, L. Yatsenko (eds.), *Nanoplasmonics, Nano-Optics, Nanocomposites, and Surface Studies*, Springer Proceedings in Physics 167,
DOI 10.1007/978-3-319-18543-9_2

Most biological tissues are composite materials formed by layers with different properties, viscoelastic solid porous structures and fiber-reinforced materials with different structural patterns [1]. The composite structure of biomaterials provides their optimal mechanical performance for external mechanical load, fluid delivery to continually distributed live cells, heat, and mass exchange [6–9]. Mechanical load plays a very important role in growth and development of cells, tissues, and biological organisms of different families. Optimal reinforcement of bones is provided by the family of trabecules orthogonal to the loaded surface (i.e., elongated according to the directions of maximal compression), and the orthogonal family of trabecules is located according to the directions of maximal extension in the tissue. In that way, the trabecules effectively work against extension and compression loads, while the non-working substance is dissolved and deleted producing the lightweight design.

Similar layered structures composed according to the external load can be found in bone cartilage [1, 2]. Coordinated growth of skeletal muscles and bones is provided by extension of those bones and muscles which are in parallel connection. The bones, cartilage, ligaments, and other collagen structures possess piezoelectric properties, and electric fields generated in the loaded collagen fibers strongly influence growth direction and intensity [10, 11].

In human skin, the collagen fibers provide asymmetry in the skin distensibility depending on its natural loading. The collagen fibers in dermis and epidermis are oriented according to principles of stress tensor and provide maximal distensibility along the so-called Langer's lines and maximal rigidity along the orthogonal families [12]. The same orientation of fibers has been detected in the vascular cambium of trees [13]. Orientation of wood grains on the debarked surface of trunks and stems correspond to two families of fibers oriented according to the stress field. The outer layer of blood vessels (adventitia) is reinforced by two oppositely directed spiral families of collagen fibers [14]. It is important that the fibers in skin and other collagen tissues possess branching structure and are weaved in the textures of different density, anisotropy, and strength (Fig. 2.1).

The branching fibers have been found at the microscale in tendon [15], epithelium [16], myocardial, and many other tissues. In the myocardial tissues, the branchings are formed by myofibrils, not by collagen fibers. In that way, branching structures are proper to different types of cells and proteins. The branched nanostructures (Fig. 2.2) form cytoskeleton and serve for strength of animal cells and active intercellular transport by molecular motors [17].

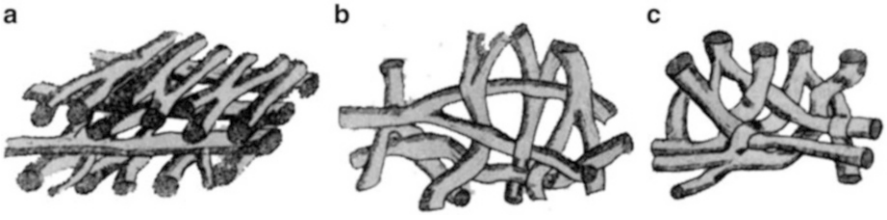

Fig. 2.1 Different patterns of branching collagen fibers in human skin (**a**), arterial wall of elastic (**b**) and muscle (**c**) types

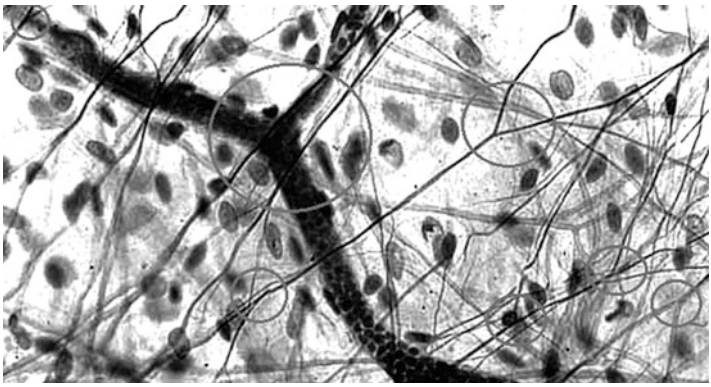

Fig. 2.2 Microscopic images of branching actin and tubulin structures

The rigid cell walls provided strength and stability of shoots, tree trunks, and branches are formed at strong influence of the body weight, mass distribution, and wind load. When a tree grows at a moderate wind load, the inner structure of the cell walls in the trunk is presented by radial rays, circumferential and vertical reinforcing structures located according the gravity field. When a dominated wind permanently acts on the tree crown which is naturally asymmetric in the north–south direction, it produces the moment of force and the trunk gradually possess spiral fibers instead of the straight vertical ones [3]. The tree branches also have natural asymmetry in the up and down vertical directions, and the moment of force acting on the smaller branches of branches produce the spiral patterns in them. The spiral reinforcement represents optimal solution for the lightweight design at twisting loads.

According to the Schwendener's theory, the shape of plants is based on the concept of maximum strength [18, 19]. The mechanical structure of plants is determined by their ability for gravity recognition. Positive gravitropism of shoots and negative gravitropism of roots are determined by sedimentation of statoliths in the gravity field and polar transport of the plant hormone auxin. Distribution of the small branches in the crown is determined by maximizing its effective leaf area [20]. Total leaf mass M_L is related to the diameter D of trunk as $M_L \sim D^2$ [21]. Therefore, the relations between different organs in plants are determined by mechanical (stress–strain) and hydraulic (water supply) factors.

Plant roots, stems and leaves, tree trunks, and branches are supplied by water and nutrients through complex conducting networks formed of long rigid tubes. In the young soft growing plant organs, the conducting systems also provide material reinforcement. The bifurcations of tree branches [22] was found obeying the Murray's law [23, 24]

$$d_0^3 = d_1^3 + d_2^3 \tag{2.1}$$

where d_0 and $d_{1,2}$ are diameters of the parent and daughter branches.

Equation (2.1) corresponds to optimal bifurcation of tubes that provides minimal total energy expenses for the viscous flow along the parent tube and into the

daughter ones with given diameters [23, 24]. Numerous measurements on arterial vasculatures revealed that the Murray's law is a blueprint for construction of arterial networks [25] and respiratory systems [26] in mammals, fluid trophic systems in molluscs, sponges, and other primitive animals [27]. The bifurcations of leaf veins also obey the Murray's law [7, 28, 29]. The venation system provides transport of water and nutrients to the leaf cells and geometry of the vein system corresponds to the optimal pipeline supplying the distributed system of consumers at minimal total hydrodynamic and metabolic energy expenses. The branchings in the pipeline exhibit optimal relations between their diameters (2.1) as well as optimal branching angles [25]:

$$\cos(\alpha_1) = \frac{\left(1+\xi^3\right)^{4/3} + 1 - \xi^4}{2\left(1+\xi^3\right)^{2/3}}, \quad \cos(\alpha_2) = \frac{\left(1+\xi^3\right)^{4/3} + \xi^4 - 1}{2\xi^2\left(1+\xi^3\right)^{2/3}} \tag{2.2}$$

where $\xi = \min\{d_{1,2}\}/\max\{d_{1,2}\}$ is the asymmetry coefficient.

It is interesting that the Murray's law (2.1) is the necessary condition of both the local branch optimality and global optimality of the pipeline when the Poiseuille flow is supposed in each pipe and the low Reynolds number regime allows neglecting the entrance length [30]. When the pipes have permeable walls and some liquid can percolate through the walls into the surrounding tissues, the optimization problem at $Re < 1$ and some geometric restrictions proper to the plant transportation systems ($d_j/L_j \ll 1$) has the same mathematical solution (2.1) [31]. In that way, similarity between the animal and plant long-range transport systems is based on similarity in the solutions of the corresponding optimization problems in spite of different physical nature of the flows. The mechanisms that could have led to evolutionary development of optimal arterial networks are connected with mechanosensory cells in endothelial layer of the blood vessels [32]. According to [23, 24] in the optimal tube, the volumetric rate $Q \sim d^3$ and the shear stress at the wall $\tau_w = \text{const}$ dependent on the fluid viscosity and metabolic rate. The mechanosensory cells can maintain $\tau_w = \text{const}$ and, therefore, provide gradual formation of the optimal tubes during biological growth and development. In the plant tissues, the optimal relationship can be maintained by the balance between the inflow in the tube and total outflow through its permeable wall because the latter depends on demands of the live cells supplied by this tube [33].

In the plant leaves, the soft photosynthesizing tissue is reinforced by a network of veins with rigid walls that serves to both fluid transport and mechanical strength. The branching tubes used for reinforcement and liquid delivery are proper to plant stems and leaf petioles (Fig. 2.3a), larger (Fig. 2.3b), and smallest (Fig. 2.3c) leaf veins. Some additional reinforcement is provided by rigid lignified insertions and mechanical elements, mostly shaped as T-beam and I-beam [34]. The blood vasculatures are also multi-objectively optimized for blood distribution and mechanical reinforcement of the soft matter of inner organs of animals like liver, spleen, kidneys, and others. The shapes of the organs can be easily restored from the branching structures

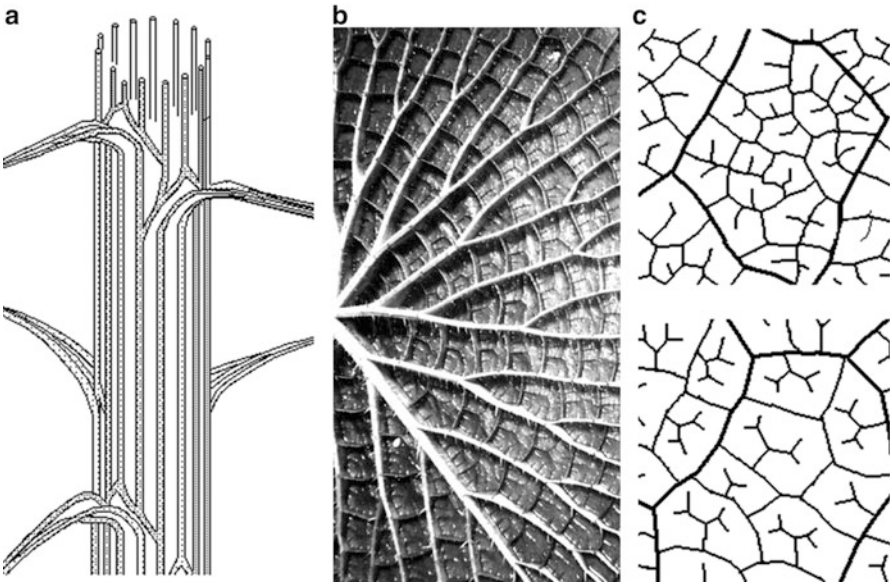

Fig. 2.3 Bifurcating patterns in the reinforcing/sap transportation systems in the stem and leaf petioles (**a**), the larger (**b**) and the smallest (**c**) veins of the leaf blade

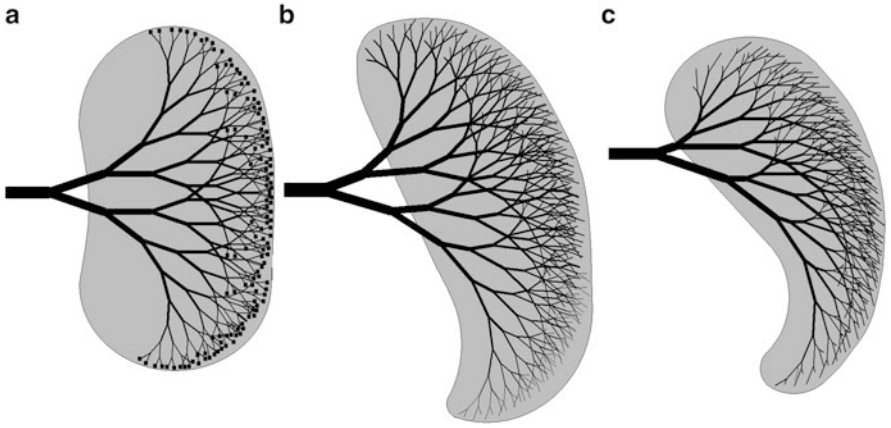

Fig. 2.4 The shapes and sizes of models of inner organs supplied by fractal binary trees with different asymmetric coefficients: $\xi = 0$ (**a**), $\xi = 0.8$ (**b**), $\xi = 0.6$ (**c**)

of their vascular beds. Several examples are presented in Fig. 2.4 for self-similar (fractal) systems.

It is interesting, exploitation of the prestressed fibers/tubes is also proper for both solid and soft tissues. The blood vessels are characterized by residual stresses; they become shorter and demonstrate positive open angles being excised from the tissue [1]. The skeletal bones are stretched by taut fascia and possess residual stress; so compression produced by body weight is partially compensated by initial stretch.

The principles of reinforcement are similar in the plant and animal tissues and based on minimal total energy expenses at a given body mass/volume and external load. The nature-inspired principles of reinforcement by micro- and nanofibers in cells, tissues, and organs can be used for elaboration of novel functional composite materials with optimal structural and transport properties, as well as in MEMS, fuel cells, micro heaters/coolers, and other advanced technological units. Since bifurcating fibers, nano- and microtubes are proper to live nature, their branching patterns deserve detailed consideration from the mechanical point of view.

Summarizing the above presented data on reinforcement in nature, one can conclude both plants and animals use the same main principles of mechanical construction of their tissues and organs, namely

- Reinforcement by relatively rigid fibers/tubes located according to the principles of the stress tensor at given external mechanical load
- The matrix material is viscoelastic/viscoplastic and serves for stress redistribution preventing crack generation or sticking crack propagation at fibers/tubes
- The embedded tubes serve for reinforcement of the material as well as for mass and heat transport purposes
- The branching fibers/tubes are commonly used at macro-, micro-, and nanoscales

2.2 Measurements and Data Analysis

The fresh cut leaves have been scanned at high resolution (1,200 dpi) and treated by special own-elaborated software (BioImage Analysis 4.1 [7]) allowing image contrasting, pattern recognition, skeletonization of the veins, and measurements of their lengths L_j, diameters d_j, branching angles $\alpha_{1,2}$, and influence domains $S_{1,2}$ (i.e., drainage areas) (Fig. 2.5) in separate bifurcations and trifurcations. In total ~1,500 images of leaf blades of different size, shape, and evolution age have been studied.

It was proved that the bifurcations obey the Murray's law (2.1) and optimal branching rules (2.2). Perfect linear dependence between the length and average diameter of the veins

$$L_j = kd_j \tag{2.3}$$

as well as the dependence between the length of the longest part along the main vein L_Σ and its drainage area

$$L_{\Sigma j} = bS_j^{1/2} \tag{2.4}$$

where k,b are constant coefficients that have been found on all the samples studied.

The dependencies $d_j(L_j)$ and $\sqrt{S_j}\left(L_{\Sigma j}\right)$ for one sample leaf blade are presented in Fig. 2.6a, b correspondingly. Since the shape of the influence domains vary

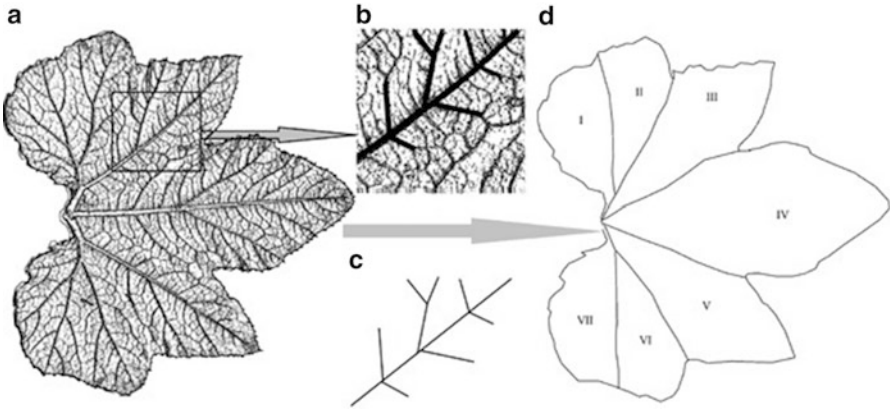

Fig. 2.5 The prepared image of the leaf blade (**a**), branching pattern (**b**), skeletonized system of veins (**c**) and influence domains of the main veins (**d**)

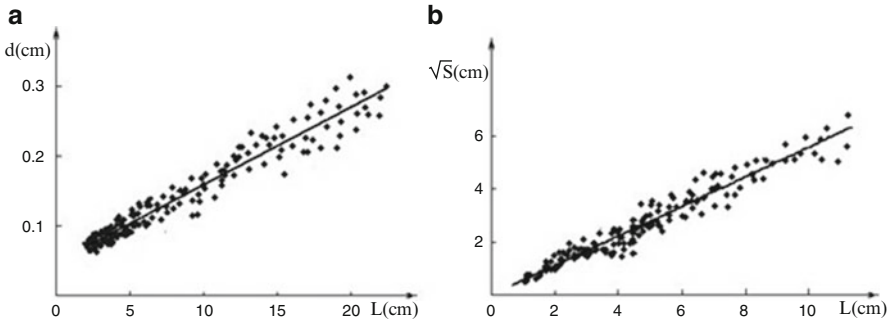

Fig. 2.6 $d_j(L_j)$ (**a**) and $\sqrt{S_j}(L_j)$ (**b**) distributions for a *Fragaria rusticana* leaf blade

significantly in the leaves of different shapes and sizes, the relationship (2.4) cannot be explained by geometrical similarity. Since the veins provide the plant sap delivery to the cells of the corresponding influence domain through the permeable wall of the vein, the uptake Q must be proportional to the volume of the cells $Q \sim V = h{\cdot}S$ where h is average thickness of the domain which is usually uniform and $h \ll \sqrt{S}$. The supplied amount of sap depends on the lateral permeable surface Σ of the vein $Q \sim \Sigma = 2\pi RL$. According to the measurement data, $L = k{\cdot}R$ and $\Sigma = 2k\pi R^2$. Combining the two dependencies one can obtain $S \sim R^2$ which is the obtained statistical relationship (2.3). In that way, the scaling law can explain the principle (2.4) of construction of the leaf venation network according to balance between the inflow of the sap into the main vein and its percolation through the porous wall and adsorption by live cells continuously distributed over the corresponding influence domain. The vein and its influence domain could be considered as a basic unit of functioning leaf, while the leaf is a set of interconnecting influence domains.

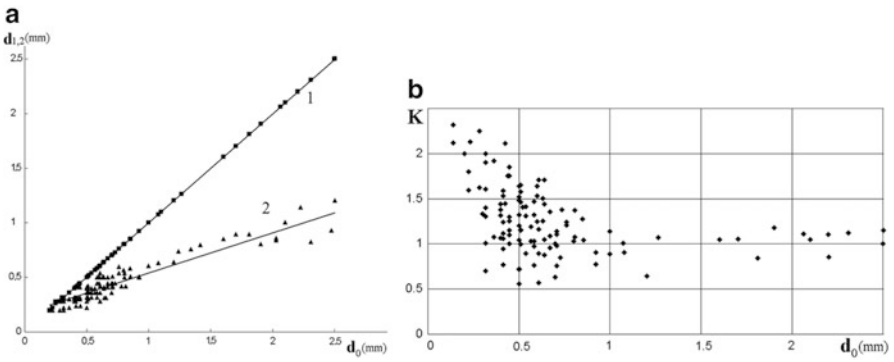

Fig. 2.7 Dependencies $d_0(d_2)$ (1) and $d_0(d_1)$ (2)—(**a**) and $K(d_0)$ (**b**) for *Cotinus obovatus* leaf blade

This plane unit is the plant analogy to the microcirculatory cell (Krogh cylinder) in animal tissues. The Krogh cylinder is composed by a segment of capillary vessel and the surrounding cells supplied by oxygen and nutrients through this capillary. The tissue can be modelled and as a set of compactly located interconnected cylinders [1].

The vein branchings are characterized by quite strict relations between the diameter d_0 of the parent vein and the diameters of the smaller d_1 and larger d_2 daughter veins (Fig. 2.7a). The diameter of the bigger daughter vein is determined by the parent vein ($d_2 = 0.9961\, d_0 + 0.0475$, $R^2 = 0.9993$), while the smaller daughter vein possesses more scatter around the linear dependence ($d_1 = 0.367\, d_0 + 1.7205$, $R^2 = 0.791$), though the scatter is very low comparing to typical ones for biological data. The branching ratio $K = \left(d_1^2 + d_2^2\right)/d_0^2$ describes hydraulic conditions for water pumping through bifurcations. When $K \approx 1$, the linear velocity of the flows in the parent and daughter veins remains almost the same; when $K > 1$ or $K < 1$ the linear velocity decreases or increases due to the volumetric flow conservation at the bifurcations. In all the studied leaf blades, the bifurcations of the larger veins have $K \approx 1$, while smaller bifurcations exhibited some scatter $0.5 < K < 2.5$ independently on the leaf size ($1 <$ length < 35 cm) and shape ($0.05 <$ width/length < 3) (Fig. 2.7b). The average values $\langle K \rangle \approx 1$; it seems the bifurcations with $K > 1$ and $K < 1$ are well-balanced producing the average effect of constant linear flow in both the larger and smaller veins. Similar distributions have been found in arterial bifurcations in humans and different animals [35, 36]. In that way, the subsystems of fluid delivering (with $K \approx 1$) and distributing (with $K > 1$ or $K < 1$) vessels have been distinguished in the fluid transportation networks in animals and plants.

Similar dependencies have been obtained for the branching angles (Fig. 2.8). The larger delivering veins supporting the leaf blade as reinforcing system possess almost optimal branching angles. The dependence $\alpha_{\text{rel}}(d_0)$ where $\alpha_{\text{rel}} = \alpha/\alpha_{\text{opt}}$, $\alpha = \alpha_1 + \alpha_2$ is the measured angle, and α_{opt} is computed from (2.2) using the value ξ measured for the bifurcation. The larger branches have $\alpha \approx \alpha_{\text{opt}}$

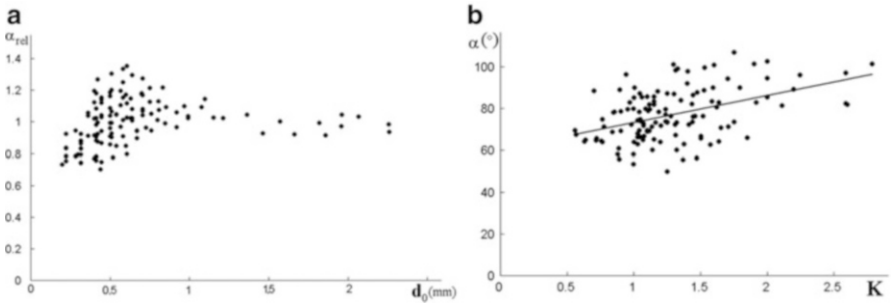

Fig. 2.8 Dependencies $\alpha_{rel}(d_0)$ (**a**) and $\alpha(K)$ (**b**) for the *Fragaria moschata* leaf blade

while the smaller bifurcations may possess either bigger or smaller branching angle in comparison to the optimal ones (Fig. 2.8a). The dependence $\alpha(K)$ exhibits significant scatter (Fig. 2.8b), but the tendency of increase in the branching angle with an increase in the branching ratio has been detected on all the studied leaf blades.

It means the bifurcations with $K > 1$ and, therefore with relatively thick daughter veins have bigger branching angles than the relatively thing bifurcations with $K < 1$, independently on their diameters and asymmetry coefficients. The bigger branching angles allow covering the wider leaf area and supply a bigger number of live cells, that is consistent with optimality for the fluid delivery. The dependence of the reinforcing properties of the bifurcations of tubes with different diameters and branching angles can be studied on the corresponding mechanical model.

2.3 Optimal Design of Loaded Bifurcations

Let us consider three bars of circular cross sections composed of a bifurcation OABC (Fig. 2.9). The lines OA, AB, and AC belong to the same plane, the coordinates of the points are O(0,0), A(x,0), B(a,b_1), and C(a,$-b_2$), the diameters and lengths of the bars are d_0, d_1, d_2 and L_0, L_1, L_2 correspondingly. The bar OA is rigidly clamped at the cross section $x = 0$, $y = 0$, the bars are loaded by point forces $\vec{F}_{1,2}$ located perpendicularly to the plane $0xy$ and applied in the points B,C (Fig. 2.9). Let us find out the branching design when at the given volume of the bifurcation

$$V = \frac{\pi}{4}\left(d_0^2 L_0 + d_1^2 L_1 + d_2^2 L_2\right) \tag{2.5}$$

the maximal stress σ_{max} in the bifurcation is restricted: $\sigma_{max} \leq \sigma^*$.

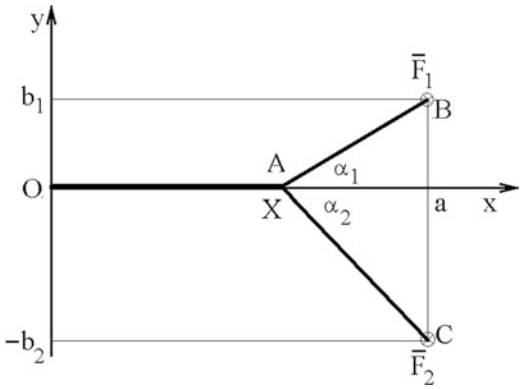

Fig. 2.9 Geometry of the bifurcation OA, AB, AC loaded by the forces $\vec{F}_{1,2}$ applied on the bifurcation in B,C perpendicularly to the plane $0xy$

The criterion (2.5) must be important for rigid branches of trees, bushes, and shoots [35], while for the leaf branches the total lateral surface

$$\Xi = \pi(d_0L_0 + d_1L_1 + d_2L_2) \tag{2.6}$$

provided the sap delivery to the distributed live cells can be more important [7].

Stress distribution is determined by the bending moment $M = \sigma J/h$, where J is the moment of inertia of the cross section with respect to its horizontal axis passed through the center of mass of the cross section, h is the distance to the axis (for the uniform circular bar, h is the radius of the cross section). Since the maximal bending moments are produced in the cross sections at maximal distance to the applied forces, for the three bars composing the bifurcations the maximal stresses will be reached at the section O of the first bar, and the section a of the second and third bars. Then, the restriction on the maximal stress will give the inequalities.

$$\begin{aligned} M_{1\max} &= F_1L_1 \le \frac{\pi}{32}\sigma^* d_1^3 \\ M_{2\max} &= F_2L_2 \le \frac{\pi}{32}\sigma^* d_2^3 \\ M_{0\max} &= (F_1 + F_2)a \le \frac{\pi}{32}\sigma^* d_0^3 \end{aligned} \tag{2.7}$$

According to (2.7), the minimal values of $M_{1\,\max}$, $M_{2\,\max}$, and $M_{0\,\max}$ will be given by minimal diameters, so we can come from (2.7) to the equalities

$$d_1 = \sqrt[3]{\frac{32F_{1,2}L_{1,2}}{\pi\sigma^*}}, \quad d_0 = \sqrt[3]{\frac{32(F_1 + F_2)a}{\pi\sigma^*}} \tag{2.8}$$

Since $L_{1,2} = \sqrt{(a - X)^2 + b_1^2}, L_0 = X$, substitution (2.8) in (2.5) and (2.6) gives the following optimization criteria in the dimensionless form

$$\Theta_{\mathrm{I,II}} = k_{\mathrm{I,II}}\left(f^{n_{\mathrm{I,II}}}\left((1-\chi)^2+\beta_1^2\right)^{m_{\mathrm{I,II}}} + \left((1-\chi)^2+\beta_2^2\right)^{m_{\mathrm{I,II}}} + \chi(f+1)^{n_{\mathrm{I,II}}}\right) \tag{2.9}$$

where $\chi = X/a$, $\beta_{1,2} = b_{1,2}/a$, $f = F_1/F_2$, $n_{\mathrm{I}} = 1/3$, $n_{\mathrm{II}} = 2/3$, $m_{\mathrm{I}} = 4/6$, $m_{\mathrm{II}} = 5/6$, $k_{\mathrm{I}} = \sqrt[3]{\frac{32\pi^2 a^4 F_2}{\sigma^*}}$, $k_{\mathrm{II}} = \sqrt[3]{\frac{16\pi a^5 F_2^2}{(\sigma^*)^2}}$, (I) and (II) correspond to the criteria (2.6) and (2.5) accordingly.

Optimal location X of the bifurcation for the given geometry (a, b_1, b_2) and mechanical load (F_1, F_2) can be found from the conditions

$$(\Theta_{\mathrm{I,II}})'_{\chi} = 0, \quad (\Theta_{\mathrm{I,II}})''_{\chi\chi} > 0 \tag{2.10}$$

The branching ratio K, the optimal Murray parameter $\mu = \left(d_1^3 + d_2^3\right)/d_0^3$ and the optimal bifurcation angles $\alpha_{1,2} = \frac{1-\chi}{\sqrt{(1-\chi)^2+\beta_1^2}}$ can be computed then and compared to the measured values presented in the previous chapter. Since the real load on the branching plant structures includes own body mass, the payload (leaf mass), the wind, rain and snow load, the force distribution $(\vec{F}_1, \vec{F}_2)$ must be insignificant and only the force asymmetry f might be important in connection of development the symmetric or quite asymmetric branches. Geometry of the bifurcation can also be described by relative parameters $(b_1 + b_2)/a \in \left]0, 2\right[$, $b_1/b_2 \in]0, 1\left[$.

2.4 Results and Discussions

Direct computations on (2.9), (2.10) at known $a, b_{1,2}, F_{1,2}$ give algebraic equation for determination the optimal location of the branching point $x = X$. Numerical computations have been carried out for the symmetric area $b_1 + b_2 = a$ and two non-symmetric areas $b_1 + b_2 = a/2$ and $b_1 + b_2 = 2a$. Three values of the force asymmetry f have been chosen: $f = 0; 2; 0.5$. Due to the symmetry, the values $\beta_1 = 0.1; 0.2; 0.3; 0.4; 05$ have been used. Location of the optimal bifurcation point A in dimensionless coordinate $\chi = \mathrm{X}/a$ at different area geometry and force distributions is presented in Fig. 2.10.

Location of the point A exhibit quite small variations $0.57 < \chi < 0.61$ for the symmetric area $b_1 + b_2 = a$, $0.61 < \chi < 0.71$ for the elongated area $b_1 + b_2 = a/2$, and $0.5 < \chi < 0.57$ for the widened area $b_1 + b_2 = 2a$. When the area is elongated, the main branch OA must be longer, while for the widened area is shorter, which is physical. The difference between the corresponding averaged values is $\pm 4.5\,\%$ only. For the symmetrical location of the main branch OA ($\beta_1 = 0.5$), the two non-symmetric force distributions $f = 2; 0.5$ give the same solution which is natural. The values computed for the symmetrical loaded branch

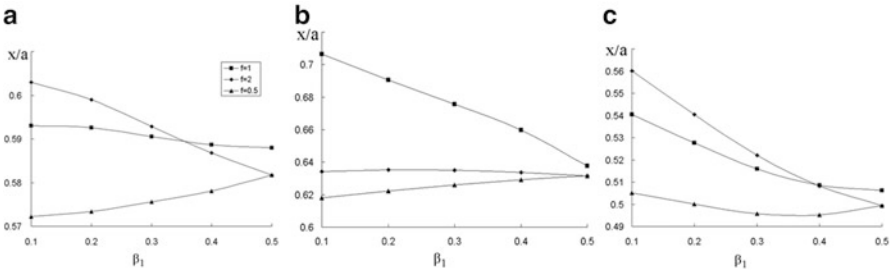

Fig. 2.10 Location of the optimal bifurcation point at different $\beta_1 \in [0.1; 0.5]$ at $b_1 + b_2 = a$ (**a**), $b_1 + b_2 = a/2$ (**b**), $b_1 + b_2 = 2a$ (**c**). *Square*, *rhomb,* and *triangle signs* correspond to the force asymmetries $f = 1$, $f = 2$, and $f = 0.5$ accordingly

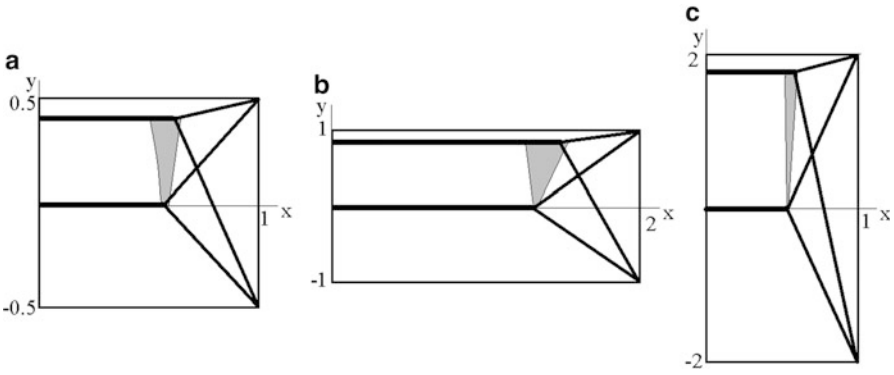

Fig. 2.11 Location of the bifurcation point on the area $x \in [0, a], b \in [-b_2, b_1]$ at different bifurcation asymmetry $\beta_1 \in [0.1, 0.5]$ and area geometry $b_1 + b_2 = a$ (**a**), $b_1 + b_2 = a/2$ (**b**), $b_1 + b_2 = 2a$ (**c**)

($f = 1, \beta_1 = 0.5$) correspond to the results obtained in [37]. The stability problem for the loaded branching structures composed of straight roads has been studied in [38]. The differences between the optimal location of the bifurcation point A at two non-symmetric loads ($f = 2;0.5$) are bigger for the asymmetric location of the main branch OA ($\beta_1 = 0.1$) and smaller for its symmetric location ($\beta_1 = 0.5$) (Fig. 2.10). It is obvious, the difference will increase for more asymmetric force distributions $f = 3;1/3;4;1/4;\ldots$. In some cases, the values X/a are close to the golden ratio $X/a \approx 0.6$. Geometries of the optimal branches are depicted in Fig. 2.11 for the most asymmetric ($\beta_1 = 0.1$) and symmetric ($\beta_1 = 0.5$) cases. Location of the bifurcation point A at different sets of the force asymmetry f and $0.1 < \beta_1 < 0.5$ are filled by gray color.

Since in the optimal branching the applied forces determine thicknesses of the beams or diameters of the cylindrical rods, the corresponding diameters can be computed from (2.7) at different model parameters. The asymmetry coefficient ξ, branching ratio K, and Murray's coefficient $\mu = \left(d_1^3 + d_2^3\right)/d_0^3$ can also be

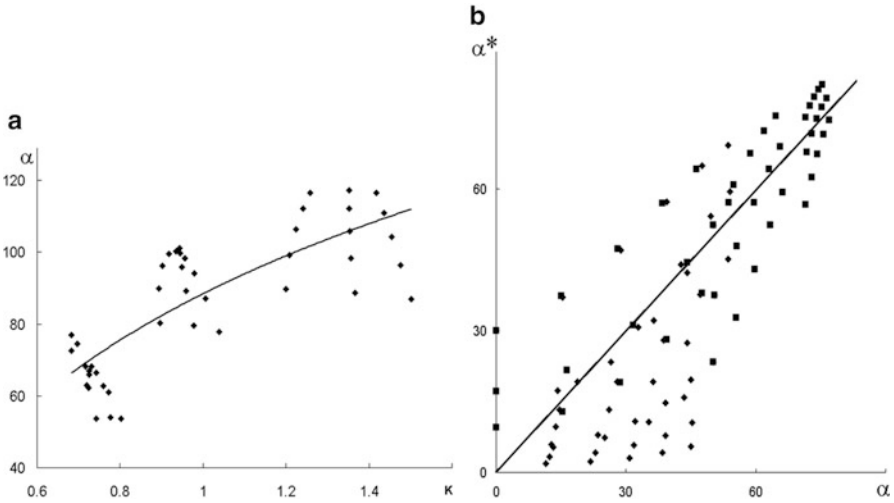

Fig. 2.12 Dependencies $\alpha(K)$ (**a**) and $\alpha^*(\alpha)$ (**b**). The *square* and *rhomb signs* in (**b**) correspond to the longer (AC) and shorter (AB) rods accordingly

computed. The branching ratio and Murray's coefficient describe rather transport properties of the bifurcation of the rigid tubes for the fluid flow than to the stress minimization. According to (2.1), when $\mu \sim 1$ the bifurcation is closer to the optimal one. The branching angles $\alpha_{1,2}$ can be computed from the calculated values χ for any given geometry (Fig. 2.9). The computed dependency $\alpha(K)$ where $\alpha = \alpha_1 + \alpha_2$ is presented in Fig. 2.12a. Three sets of data corresponded to different geometry of the area are clearly visible.

Inside each set the three sets correspondent to different force asymmetry are clearly separated only in the case $b_1 + b_2 = 2a$ with bigger branching angle α and branching coefficient K. There is quite good approximation of the general data $K = k_1 \exp(k_2 \alpha)$ ($R^2 = 0.688$) depicted in Fig. 2.12a by the solid line. The computed dependence is very close to those measured on the plant leaves (Fig. 2.8b).

If we compare the branching angle α optimal for the stress minimization in the structure and the branching angle α^* computed for the same diameters from (2.2) and optimal for the fluid delivery along the branch, we shall obtain quite good correlation between them (Fig. 2.12b). It means both optimal solutions are quite close to each other. Taking into account the computed influence of small deviations of location of the branching point A in the area which corresponds to $\pm 5\,\%$ additional energy lost [39], in nature the scatter of the data around the line $\alpha^* = \alpha$ (solid line in Fig. 2.12b) corresponds to rather small energy lost compensated by optimality to some other external conditions or internal properties.

The dependence $\mu(d_1/d_2)$ presented in Fig. 2.13a is similar to the measured dependencies $\mu(d_0)$ and $\mu(\xi)$ (Fig. 2.8a). The thicker the main branch, the closer the optimality coefficient to 1, while the small branches demonstrate bigger scatter around the optimal value. In the experimental data $0 < \xi < 1$, while in Fig. 2.13b

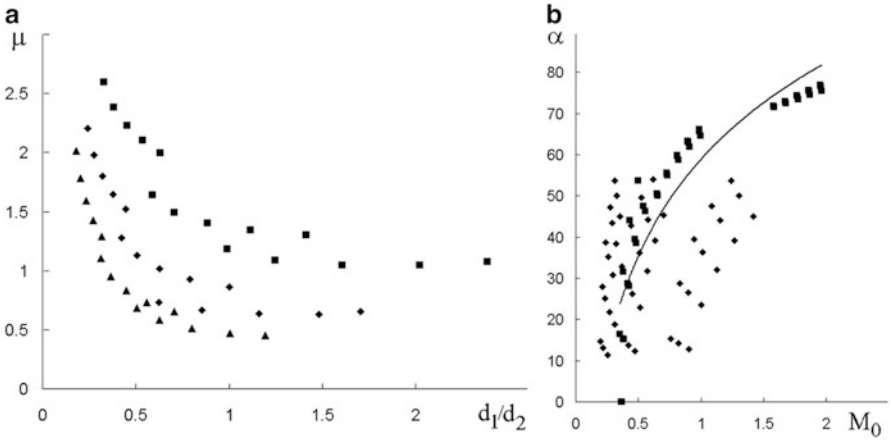

Fig. 2.13 Dependencies $\mu(d_1/d_2)$ (**a**) and $\alpha(M_0)$ (**b**) computed for the bifurcating beams

d_1/d_2 could be bigger than 1, because in the cases when the shorter rod is loaded by the bigger force, in the optimal case it is thicker than the less loaded longer branch. In this case, diameter ratios of the shorter and longer branches may give values $d_1/d_2 > 1$.

The quite strong dependence $\alpha_2 = \kappa_1 \ln(M_0) + \kappa_2$ ($R^2 = 0.864$) of the branching angle of the longer branch on the total bending moment M_0 appeared in the main rod has been found (Fig. 2.13b), while the shorter branch exhibits some noticeable scatter around the exponential averaged values (straight line in Fig. 2.13b) depending on the applied forces and initial branch asymmetry. The data measured on the vascular beds demonstrated the same dependence, as if the main daughter branch follows the diameter of the parent branch, while the smaller daughter branch has more freedom for branching and, therefore, the bigger scatter.

In that way, the computed configurations of the optimal bifurcating fibers experienced minimal internal stress at given asymmetric load can be used for reinforcement of the tissue-like engineered composites in the woven or layered (Fig. 2.1) patterns, as well as 3D structures reinforcing convex shells (containers, capsules, roofs, pavilions, panels, etc.).

The branched structures composed of nanotubes are perspective for optimal reinforcement of microscopic objects like artificial cells, tissue substitutes, MEMS units, fuel cells, and others. Modern technologies allow synthesis of carbon, metal, polymer, and other branched Y-shaped conjugations of nanotubes that can be used for simultaneous strengthening of the unit and delivery and distribution of macro- and nanofluids through them. The aerosol technique based on spray of a catalyst-precursor solution composed of metal salts in water directly into a furnace is a low-cost technology for obtaining Y-shape nanotubes and more complex branched structures of them [40]. The Y-shaped carbon nanotubes can be obtained by the arc discharge method [41] and used for the reinforcement and heat conductivity purposes. The Y-shape TiO_2 nanotubes have been obtained by multistep

sonoelectrochemical anodization method [42]. Being embedded into a viscoelastic matrix with needed thermomechanical or electromechanical properties, the structures form new composites reinforced by a branching network of tubes. Many microunits like liquid-based micro-coolers and heaters, fuel cells, artificial cells, molecular motors, lab on the chips need permanent delivery of the working substances, and taking away the products of reactions/decay, assimilates, and useful produced substances that can be fulfilled by the same elements which provide strengthening. It is a reasonable way for economy of the material and lightweight design of the micro- and nanosystems by double exploitation of the same system whose design provides optimality for both mechanical and transportation properties.

The diameters of the nanotubes in the manufactured Y-shape junctions are usually constant or uniform dependent on the material, and the branching angles are determined by the technological conditions and could be far from optimal ones in the above-discussed meaning. Recently, novel approaches for the controlled branching of the nanotubes by nucleation their lateral surface with a catalyst and, therefore, initiation of the branched growth [43]. This will allow manufacturing of the branched structures of nanotubes as reinforcing structures that provide multicriteria optimization of the mechanical, heat and flow conductivity properties of the corresponding composite materials.

2.5 Conclusions

Natural materials in tissues and organs of plants and animals are mostly presented by fiber-reinforced composites. The reinforcing fibers, from nano- to macroscales, are branched systems of tubes or rods that exhibited certain geometrical regularities between the diameters and branching angles at the bifurcations, diameters, and lengths in the general network. Statistical analysis of the measurement data obtained on the vascular beds of human and animals, as well as tree branches and leaf venation systems revealed the same regularities in their geometry. Solution of the optimization problem for the stationary fluid flow in rigid cylindrical tube when the total energy expenses for the viscous flow and metabolism are minimal gives the Murray's law. In that way, transportation networks in live nature are optimal pipelines provided minimal energy costs for transport and metabolism. Solution of similar optimization problem for the fluid percolation through the cylindrical tube with permeable wall at the assumption of the long thing tubes ($d/L \ll 1$) has the same form [31]. As it was shown in this chapter, the optimal rigid Y-shape rods fastened at the beginning of its parent rod and loaded by non-symmetric forces reveal the distributions between diameters, branching angles, and lengths that possess certain regularities similar to those obtained on the measured data.

Based on the theoretical results, the obtained regularities are proposed for fabrication of the branching structures of nano-/microtubes as reinforcing systems for the composite materials with optimal properties. Those materials will provide

multicriteria optimization of their mechanical (strengthening), heat and flow conductivity (transportation) properties. Due to similarity of the solutions of both the mechanical and transportation problems, significant economy of the materials and lightweight design could be reached, which is especially important for the micro heaters/coolers, microfluidic separators/homogenizators, fuel cells, artificial cells and tissues, microengines, and other MEMS units.

References

1. Fung YC (1981) Biomechanics: mechanical properties of living tissues. Springer, New York
2. Obraztsov IF (1989) Optimal biomechanical systems. Nauka, Moscow
3. Leelavanichkul S, Cherkaev A (2004) Why grain in tree's trunks spiral: mechanical perspective. Struct Multidisc Optim 28:127–135
4. Cowin SC (ed) (1989) Bone mechanics. CRC, Boca Raton
5. Kizilova N (2012) Mathematical modelling of biological growth and tissue engineering. In Bedzinski R, Petrtyl M (eds) Current trends in development of implantable tissue structures, Warsaw, pp 18–27
6. Bejan A (2000) Shape and structure: from engineering to nature. Cambridge University Press, Cambridge
7. Kizilova N (2004) Computational approach to optimal transport network construction in biomechanics. Lect Notes Comput Sci 3044:476–485
8. Kizilova N (2007) Optimal long-distance transport systems in nature: control and applications. PAMM 7:131–132
9. Hamadiche M, Kizilova N (2009) Advanced composite materials for elimination the flow-induced vibrations of plates and tubes. In: Karama M, Atanasiu C, Papanicolaou G, Horia G (eds) Structural analysis of advanced materials, Tarbes, pp 72–78
10. Fukada E, Yasuda I (1957) On the piezoelectric effect in bone. J Phys Soc Japan 12:1158–1162
11. Avdeev Yu A, Regirer SA (1985) Electromechanical properties of bone tissue. In: Modern problems of biomechanics, vol 2. Zinatne, Riga, pp 101–131
12. Langer K (1861) Zur Anatomie und Physiologie der Haut. Über die Spaltbarkeit der Cutis, Sitzungsbericht der Mathematisch-naturwissenschaftlichen Classe der Wiener Kaiserlichen Academie der Wissenschaften Abt., pp 44–54
13. Kramer EM (2002) A mathematical model of pattern formation in the vascular cambium of trees. J Theor Biol 216:147–159
14. Holzapfel GA, Gasser TC, Ogden RW (2006) A new constitutive framework for arterial wall mechanics and a comparative study of material models. J Elasticit 61:1–48
15. Birk DE, Southern JF, Zycband EI, Fallon JT, Trelstad RL (1989) Collagen fibril bundles: a branching assembly unit in tendon morphogenesis. Development 107:437–443
16. Brownfield DG, Venugopalan G, Lo A, Mori H, Tanner K, Fletcher DA, Bissell MJ (2013) Patterned collagen fibers orient branching mammary epithelium through distinct signaling modules. Curr Biol 23:703–709
17. Kizilova N (2011) Geometrical regularities and mechanical properties of branching actin structures. Nanobiophysics, Kharkov, pp 141–146
18. Schwendener S (1874) Das mechanische Prinzip in anatomische Bau der Monokotylen mit verleichenden Ausblicken auf die übringen Pfanzenklassen. Leipzig
19. Schwendener S (1878) Die mechanische theorie der blattstellungen. Leipzig
20. Honda H (1978) Tree branch angle: maximizing effective leaf area. Science 199:888–889
21. Niklas KJ, Spatz H-C (2004) Growth and hydraulic (not mechanical) constraints govern the scaling of tree height and mass. Proc Natl Acad Sci U S A 101:15661–15663

22. Zhi W, Zhao M, Yu Q-X (2001) Modeling of branching structures of plants. J Theor Biol 209:383–394
23. Murray CD (1926) The physiological principle of minimum work. I. The vascular system and the cost of blood volume. Proc Natl Acad Sci U S A 12:207–214
24. Murray CD (1926) The physiological principle of minimum work applied to the angle of branching of arteries. J Gen Physiol 9:835–841
25. Rosen R (1967) Optimality principles in biology. Plenum, New York
26. Weibel ER (1963) Morphometry of the human lung. Academic, New York
27. La Barbera M (1990) Principles of design of fluid transport systems in zoology. Science 1000:249–992
28. Kizilova N, Popova N (1999) Study on transportation systems of plant leaves. Probl Bionics 51:71–79
29. McCulloh KA, Sperry JS, Adler FR (2003) Water transport in plants obeys Murray's law. Nature 421:939–942
30. Chernousko FL (1977) Optimal structure of branching pipelines. Appl Mathem Mech 41:376–383
31. Kizilova N (2005) Hydraulic properties of branching pipelines with permeable walls. Intern J Fluid Mech Res 32:98–109
32. Zaragoza A, Márquez S, Saura M (2012) Endothelial mechanosensors of shear stress as regulators of atherogenesis. Curr Opin Lipidol 23:446–452
33. Kizilova N (2008) Common constructal principles in design of transportation networks in plants and animals. In: Bejan A, Grazzini G (eds) Shape and thermodynamics. Florence University Press, Florence, pp 1–12
34. Razdorsky VF (1955) Plant architectonics. Soviet Science, Moscow
35. Zamir M, Medeiros JA (1982) Arterial branching in man and monkey. J Gen Physiol 79:353–360
36. Zamir M (2005) The physics of coronary blood flow. Springer, New York
37. Chernousko FL (1979) Some optimal configurations of branching rods. Mech Solid Body 3:174–181
38. O'Reilly OM, Tresierras TN (2011) On the static equilibria of branched elastic rods. Int J Eng Sci 49:212–227
39. Kizilova N (2004) Optimization of branching pipelines on basis of design principles in Nature. In: Proceeding of the ECCM congress on computational methods in applied sciences, Finland, vol 1, pp 237–248
40. Heyning OT, Bernier P, Glerup M (2005) A low cost method for the direct synthesis of highly Y-branched nanotubes. Chem Phys Lett 409:43–47
41. Osvatha Z, Koosa AA, Horvatha ZE, Gyulaia J, Benitob AM, Martınezb MT, Maserb W, Biro LP (2003) STM observation of asymmetrical Y-branched carbon nanotubes and nano-knees produced by the arc discharge method. Mater Sci Eng 23:561–564
42. Mohapatra SK, Misra M, Mahajan VK, Raja KS (2008) Synthesis of Y-branched TiO2 nanotubes. Mater Lett 62:1772–1774
43. Gothard N, Daraio C, Gaillard J, Zidan R, Jin S, Rao AM (2004) Controlled growth of Y-junction nanotubes using Ti-doped vapor catalyst. Nano Lett 4:213–217

Chapter 3
Kinetics of Dispersion-Coagulation During Annealing of Metal Nanofilms Deposited onto the Surface of Non-metallic Materials

Y.V. Naidich, I.I. Gab, T.V. Stetsyuk, and B.D. Kostyuk

3.1 Introduction

To join different non-metallic materials, in particular, oxide and nonoxide ceramics, single crystals, and carbon-based materials, metallic coatings of different thicknesses deposited onto them are commonly used [1–5]. Thin metals films (within the nano thickness range) deposited onto non-metallic inorganic materials are of paramount importance for the processes of joining (soldering) of non-metals (ceramics, glass, single crystals, carbon materials, superhard materials). Metallization of such materials surfaces provides for their sufficient wetting by molten metals determining the very possibility of the soldered joint formation process, and also strength and other characteristics of such joints.

Thin films are widely used in various fields of science and technology. By their structure and properties, they may differ significantly from their massive counterparts. Preparation of films may be done by various methods, e.g., by chemical or electrolytic deposition from the solutions. In this chapter, we consider thin films obtained by condensation of molecular (atomic) material flow at a solid surface [6].

Since during pressure soldering or welding, parts to be joined must be heated up to a certain temperature, it is important to know the behavior of the thin metal films with heating. Previously, we have studied the thermodynamics of the conversion processes of morphology and structure of metal nanofilms deposited onto oxide and nonoxide non-metallic materials and annealed at various temperatures [7–12]

Y.V. Naidich • I.I. Gab (✉) • T.V. Stetsyuk • B.D. Kostyuk
Frantsevich Institute for Problems of Materials Science of National Academy Sciences of Ukraine, 3, Krzhyzhanovskogo st., Kyiv 03142, Ukraine
e-mail: igab@ukr.net

O. Fesenko, L. Yatsenko (eds.), *Nanoplasmonics, Nano-Optics, Nanocomposites, and Surface Studies*, Springer Proceedings in Physics 167,
DOI 10.1007/978-3-319-18543-9_3

and found differences in their behavior during annealing. Initially, even at high temperatures, solid metal nanofilms can remain intact or disintegrate into fragments–islets which are then converted into separate drop-shaped elements which height exceeds the initial thickness of the original film.

In this study, the kinetics, i.e., time evolution, of structural changes of the film proceeding from monolithic state to disintegration and further coagulation into individual droplets during annealing of several metals (Cu, Ag, Au, Nb, Hf) films deposited onto various oxide and non-oxide materials (alumina ceramics, quartz glass, sapphire, glassy carbon, silicon nitride) was investigated.

3.2 Materials and Experimental Methods

In this chapter, we have used electron-beam method [13] for deposition of silver, gold, cooper, niobium, and hafnium films ~100 nm thick onto the surface of the substrate made of quartz glass, alumina ceramic, technical sapphire, glassy carbon, and ceramics based on silicon nitride. The surface of non-metallic substrates were polished to a roughness of 0.01–0.02 mm and degreased with petrol and acetone. Oxide materials substrates were annealed in air at 1,000 °C for 1 h with subsequent annealing in vacuum at the same temperature for the same time; for glassy carbon and silicon nitride ceramic substrates, only the last step was applied. Non-metallic samples with deposited metal films, except for silver and gold films, were annealed in vacuum (2×10^{-3} Pa) at 900–1,600 °C for different times (2–20 min). Samples with gold and silver films were annealed in air at 400–1,100 °C; the exposition time was varied from 15 s up to 20 min. Annealed metal nanofilms were examined by optical, atomic force microscopy, and electron microscopy, as well as by the method of measuring of the electrical conductivity of the films which is the subject of several studies [14–18]. Taking into account the fact that many non-metallic ceramic materials are insulators with specific electrical resistivity ~$10^6 \div 10^{12}$ Ω·m, a convenient tool for such study is measuring of the electrical conductivity of metal films (non-metallic film substrate is not shunting the conductivity of the film).

Investigation of the films electrical conductivity was carried out for samples of alumina ceramics of $40 \times 10 \times 4$ mm size, which polished surface was coated with silver film 100 nm thick, and which ends were soldered by silver to platinum leads of a metering device (ohmmeter).

Photomicrographs obtained with scanning electron microscope were treated by planimetric method consisting in weighting of cutted out images of metal film fragments and droplets to determine the sample area occupied by these fragments depending on annealing temperature and time; after which, the data obtained were interpreted graphically.

3.3 Results and Discussion

After annealing, all non-metallic substrates show, at first, dispersion of metallic films up to their complete decomposition at high temperatures and long exposition times. In some cases after prolonged annealing, coagulation of films fragments was observed resulting in aggregation of smaller fragments ("droplets") into larger ones (this refers to solid "droplets" of metals since the annealing temperature was much lower than the metal melting point even taking into account the impact of "droplets" size onto the melting point). The most pronounced these processes become during annealing in air of the silver nanofilms deposited onto oxide materials (sapphire, quartz glass, alumina ceramic). The lowest temperature at which the coagulation of the silver films begins is 400 °C, and, at 600 °C, active droplets coagulation takes place already after 15 s of exposure and completes during the first min of annealing process (Figs. 3.1 and 3.2).

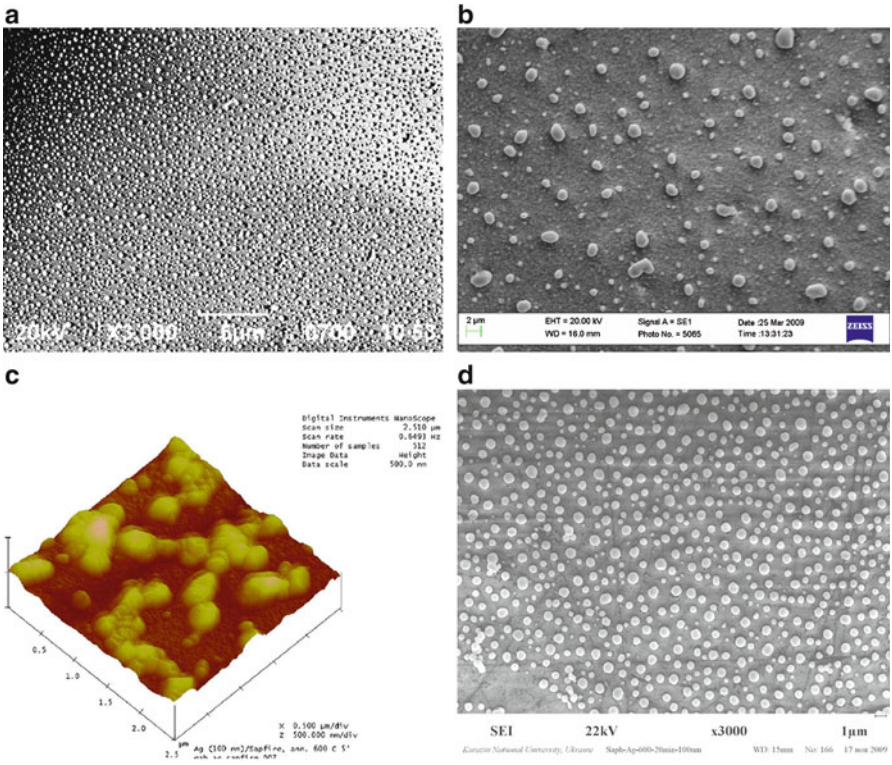

Fig. 3.1 Annealed under during various times in air silver film 100 nm thickness onto sapphire has been investigated using scanning microscopy (**a**, **b**, **d**) ×3,000 and atomic force microscopy (**c**): (**a**) 30 s ; (**b**, **c**) 5 min; (**d**) 20 min

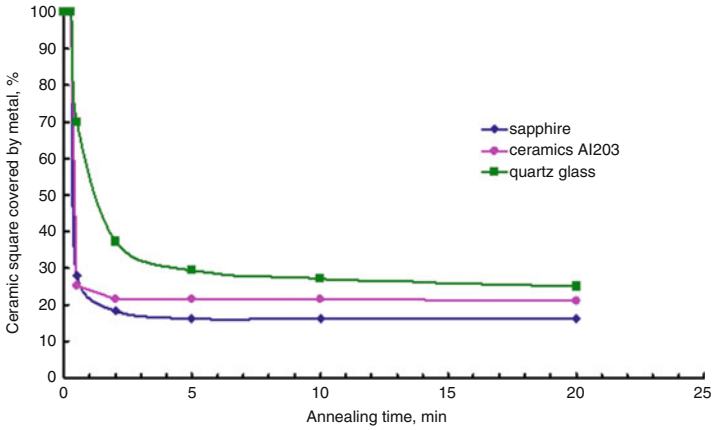

Fig. 3.2 Dependence of dispersion-coagulation processes from annealing time into silver films 100 mn thickness, deposited onto oxide materials and annealed under 600 °C in air

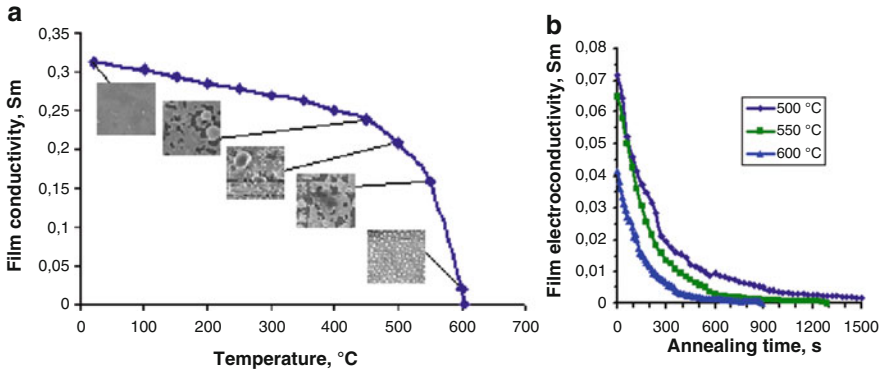

Fig. 3.3 Conductivity dependence of silver nanofilm 100 mn thickness deposited onto Al_2O_3: (**a**) from annealing temperature; (**b**) from annealing time at certain temperature

In this study, changes of the conductivity of silver nanofilm 100 nm thick deposited onto the alumina ceramic during annealing in air depending on the annealing temperature (Fig. 3.3a), and also the kinetics of the film conductivity changes at different temperatures (Fig. 3.3b), were investigated.

It should be noted that the rapid decrease of the ceramics area coated by film takes place in a few seconds or minutes of annealing (Fig. 3.2) which practically coincides with an equally sharp drop in conductivity of the film (Fig. 3.3b).

Copper and gold nanofilms coagulate intensively with annealing in vacuum only within the temperature range 900–1,000 °C for all investigated non-metal substrates (Figs. 3.4 and 3.5).

Niobium and hafnium nanofilms deposited onto oxide substrates begin to decompose during annealing in vacuum only at high temperatures (1,500 °C and higher)

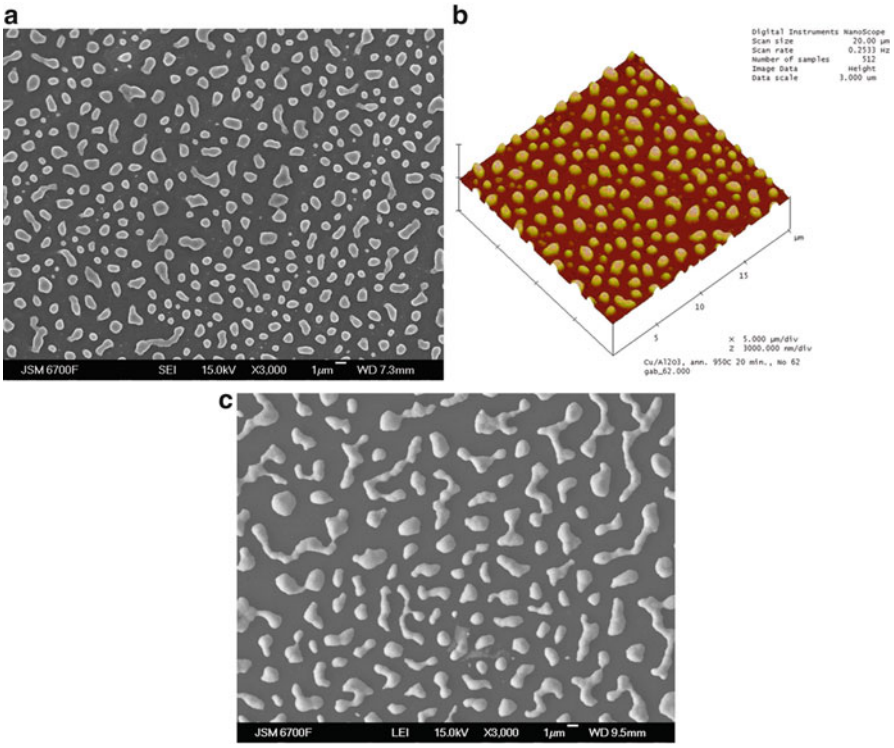

Fig. 3.4 Copper film 100 mn thickness deposited onto sapphire and annealed in vacuum has been investigated using scanning microscopy (**a**, **c**) ×3,000 and atomic force microscopy (**b**): (**a**, **b**) 950 °C, 20 min; (**c**) 1,000 °C, 5 min

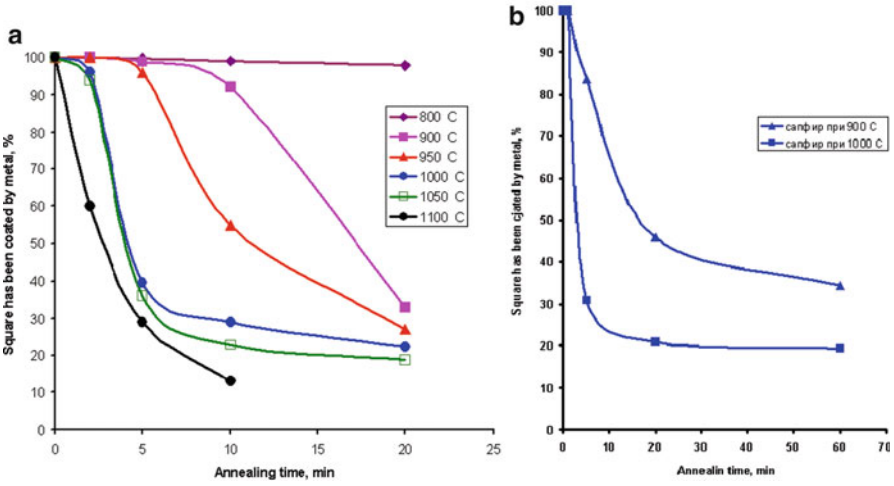

Fig. 3.5 Dependence of sapphire square coated by metallic film from annealing time under various temperature (800–1,100 °C): (**a**) copper; (**b**) aurum

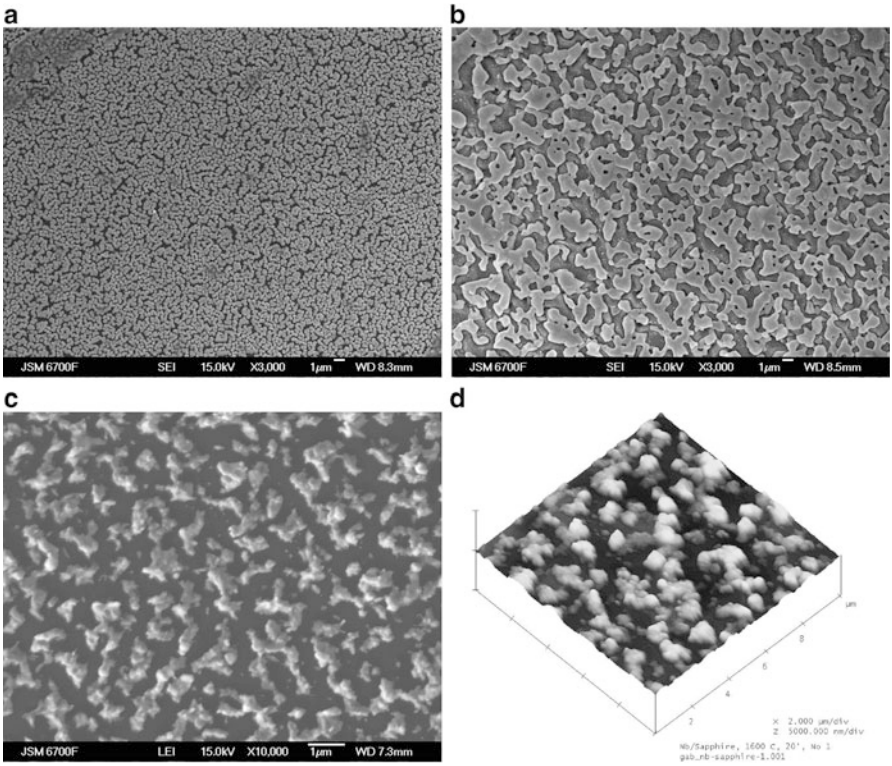

Fig. 3.6 Niobium film 100 mn thickness deposited onto sapphire and annealed in vacuum has been investigated using scanning microscopy (**a**–**c**) and atomic force microscopy (**d**): (**a**) 1,500 °C, 5 min, ×3,000; (**b**) 1,500 °C, 10 min, ×3,000; (**c**, **d**) 1,600 °C, 20 min, ×10,000

(Figs. 3.6 and 3.7). These films, deposited onto glassy carbon and silicon nitride ceramics surface, retain their continuity up to 1,200 °C; with further annealing temperature increase, structural changes are observed, apparently as a result of metals interaction with the substrates surfaces.

In this chapter, attention has been focused on the analysis of the thermodynamic and kinetic properties of the contact systems "metal film–non-metallic substrate." Results were treated mainly with respect to the adhesive interaction between the metal film and the non-metallic solid. If the metal adhesion to the non-metallic material W_A is less than the metal cohesion W_C, the continuous film state at the non-metallic surface is thermodynamically unstable. Similarly to the liquid metal, the film stability or instability is determined by the spreading coefficient (K_S) (by Harkins):

$$K_S = W_A - W_C \tag{3.1}$$

The film is stable if $K_S > 0$.

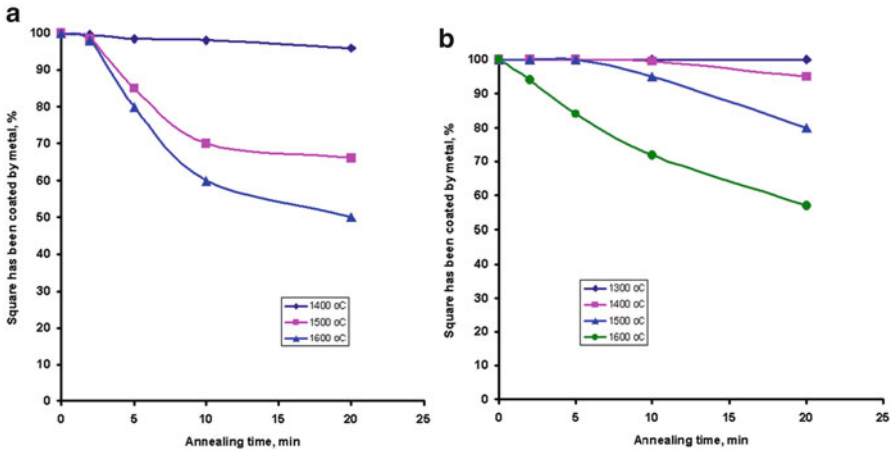

Fig. 3.7 Dependence of sapphire square coated by refractory metal film from annealing time under various temperature (1,400–1,600 °C): (**a**) niobium; (**b**) hafnium

Generally, metallic melts are characterized by high surface tension, and very high adhesion is required for the wettability of non-metal substrate by the molten metal to be good enough. Some metals, such as Cu, Ag, Au, and Ni, form a sufficiently large contact wetting angles (Θ) oxide materials.

In general, there may be the following cases: $\Theta = 0$, $K_S > 0$—continuous metal film at the solid surface is stable; $\Theta \neq 0$, the contact angle can be up to 90° and more—the film is unstable.

The work of the liquid metal adhesion can be written as follows:

$$W_A = \sigma_{lg}(1 + \cos\Theta) \tag{3.2}$$

where σ_{lg}—the value of the surface tension at the liquid–gas interface.

In turn, the work of cohesion can be written as follows:

$$W_A = 2\sigma_{lg} \tag{3.3}$$

On the basis of formulas (3.2) and (3.3), a formula for determining the spreading coefficient can be obtained as follows:

$$K_S = W_A - W_C = \sigma_{lg}(\cos\Theta - 1) \tag{3.4}$$

All of the above can be applied to metals in the solid state provided sufficient mobility of their atoms realizable at elevated temperature. During long-term exposure of contact system "non-metallic substrate–metal film," equilibrium state should be established finally (the term "solid wetting" should be used in this case). These considerations were discussed by us earlier [8, 10] to investigate the morphology of the films using electron microscopic techniques.

Possible cause of the initially sharp fall of the electrical conductivity of a thin metal film deposited onto the surface of non-metallic material during annealing can be explained as follows. During deposition (by electron-beam evaporation) of metal onto the cold solid surface, when the film thickness reaches 100 nm, polycrystalline grain structure of the film is observed (according to electron diffraction data).

During heating of such "film–substrate" contact system up to a certain temperature (below the melting point of the metal, even considering the influence of the size factor, i.e., melting point decrease of low-sized substance particles), a process of the metal film dispersing takes place. The reason is the non-equilibrium, unstable state of a continuous metal (copper, silver) film, i.e., $K_S < 0$ and contact angle is non-equal zero, or even more than 90°. Mechanism is proposed as follows: during heating, diffusion mobility of the metal atoms causes the formation of discontinuities in the film tending to the formation of separate thickened portions and, finally, of solid metal "droplets."

By analogy with the sintering of powders, in which the initial stage lies in a consolidation of individual sections uniting a group of particles and decompaction, loss of contacts between different groups, i.e., a zonal group isolation of particles, with which the porosity within the group [19] can be zero, and the intergroup porosity can be high. This leads to discontinuities between individual groups of particles. It should be noted that these processes occur in the solid phase (metal film), so the word "droplet" is within quotes. It is not necessary to believe that the film discontinuation takes place only when it is melting, as suggested in [18]. Besides, an important factor in the process of destroying the initial film integrity is a significant difference in thermal coefficients of linear expansion (TCLE) of metals and non-metals manifesting itself with heating. For example, TCLE of silver is $19.5 \times 10^{-6}\ ^{\circ}C^{-1}$, and of Al_2O_3 ceramics—$8 \times 10^{-6}\ ^{\circ}C^{-1}$.

Thus, it should be assumed that, in this chapter, true mechanism is proposed for changing the electrical conductivity of nanofilms during annealing up to the temperature at which the diffusion mobility of the metal atoms is quite high. It takes into account, besides the main adhesive-capillary-solid phase factor, the behavior of particles of the sintered body in powder-metallurgical processes (group isolation of multiple particles) and certain separation of particles groups from each other.

In practice, the very important fact is that niobium and hafnium nanofilms deposited onto oxide materials retain their integrity at temperatures up to 1,400 °C, which makes them suitable for the metallization of ceramics for subsequent soldering and usage at high temperatures (1,500 °C or higher).

3.4 Conclusions

It is found that the destruction behavior of all the studied films during annealing is almost the same and consisting in dispersion of initially continuous films into relatively large fragments of irregular shape with the subsequent decomposition

into smaller fragments and solid droplets growing upwards and acquiring more and more regular round shape, as it can be seen at the atomic force microscope images (Figs. 3.1 and 3.5).

Measurements of the conductivity changes during annealing of silver nanofilms have showed that the conductivity is practically in full accordance with the films dispersion degree and, thus, with the sample area value coated with metal.

The results obtained regarding dispersion and coagulation of metal nanofilms deposited onto metallic substrates are important for the development of processes of joining (soldering) of non-metallic materials with metals.

References

1. Elssner G, Diem W, Wallace J (1981) Materials of 17 University conference on ceramics, Berkeley, CA, 28 July–1 Aug 1980 (New York-London), p 629
2. Pan WX, Okamoto T, Ning XS (1994) Joining of Al-plasma-sprayed Si3N4 ceramics. J Mater Sci 29(6):1436
3. Dalgleish BJ, Tomsia AP, Nakashima K, Locatelli MR, Glaeser AM (1994) Low temperature routes to joining ceramics for high-temperature applications. Scr Metall Et Mater 31(8):1043
4. Hu MZ-C, Hunt RD, Payzant EA, Hubbard CR (1999) Nanocrystallization and phase transformation in monodispersed ultrafine zirconia particles from various homogeneous precipitation methods. J Am Ceram Soc 82(9):2313
5. Piticescu RR, Monty C, Taloi D, Motoc A, Axinte S (2001) Hydrothermal synthesis of zirconia nanomaterials. J Eur Ceram Soc 21(10–11):2057
6. Novikov VV (1972) Teoreticheskie osnovy mikroelektroniki. Vysshaya Shkola, Moskow (in Russian)
7. Yu Naydich V, Gab II, Kostyuk BD, Stetsyuk TV, Kurkova DI, Dukarov SV, Yu Kulikovskiy V, Onoprienko AA (2005) Adheziya Rasplavov i Paika Materialov (38):69 (in Ukrainian)
8. Yu Naydich V, Gab II, Kostyuk BD, Stetsyuk TV, Kurkova DI, Dukarov SV, Yu Kulikovskiy V, Onoprienko AA (2006) Nanostructurnoe Materialovedenie (1):31 (in Ukrainian)
9. Gab II, Kostyuk BD, Stetsyuk TV, Kurkova DI, Dukarov SV, Kryshtal AP, Litvin OS, Pasichnyy VV (2007) Adheziya Rasplavov i Paika Materialov (40):46 (in Ukrainian)
10. Yu Naydich V, II Gab, BD Kostyuk, TV Stetsyuk, DI Kurkova, SV Dukarov (2006) Tekhnika Mashinostroeniya 4:13 (in Russian)
11. Yu Naydich V, Gab II, Kostyuk BD, Stetsyuk TV, Kurkova DI, Dukarov SV (2007) Dopovidi Akademiyi Nauk (35):97 (in Ukrainian)
12. Yu Naydich V, Gab II, Kostyuk BD, Stetsyuk TV, Kurkova DI, Dukarov SV, Kryshtal AP, Litvin OS (2008) Nanosistemi, Nanomateriali, Nanotehnologii 6(4):1185 (in Ukrainian)
13. Metfessel S (1963) Tonkie Plenki, Ikh Izgotovlenie. Gosehnergoizdat, Moskow-Leningrad (in Russian)
14. Ryabtsev SV, Chuvenkova OA, Popov AE, Chernyshev FM, Ryabtseva NS, Domashevskaya EP (2012) Kondensirovannye Sredy i Mezhfaznye Granitsy 14(3):328 (in Russian)
15. Abramova GM, Kiselev NI, Patrin GS, Petrakovskiy, GA (1999) Fizika Tvyordogo Tela 41 (3):380 (in Russian)
16. Ju Bykov A, Karpukhin SD, Gazukina EI (2000) Metallovedenie i Termicheskaya Obrabotka Metallov (6):45 (in Russian)

17. Gavrilenko MA, Filatova NA, Burmeteva MS (2013) Izveatiya Tomskogo Politeknicheskogo Universiteta 322(3):42 (in Russian)
18. Gromov DG, Gavrilov SA, Redichev EN, Amosov RM (2007) Fizika Tvyordogo Tela 49(1):172 (in Russian)
19. Yu Balshin M, Kiparisov SS (1978) Osnovy Poroshkovoy Metallurgii. Metallurgiya: Moskow (in Russian)

Chapter 4
Magnetization in Nanostructures with Strong Spin–Orbit Interaction

A.M. Korostil and M.M. Krupa

4.1 Laser-Induced Remagnetization in Magnetic Nanostructures

4.1.1 Introduction

Today, features of the interaction of laser radiation with matter have searched out the wide application in several fields of science and technique. Specifically, corresponding effects effectively use in the magneto-optical spectroscopy with high spatial and time resolution and for controlling of magnetic states in nanostructures. The highly coherent laser radiation permits to study dynamic and kinetic processes with nanometer and femtosecond resolutions and to control the quantum transition of electron, spin and atomic subsystems in nanostructures. The laser-induced spin transition effects in magnetic nanostructures lie in the basis of work of tiny fast-speed elements for modern recording and readout magneto-optical systems.

The key role belongs to the effects connected with the laser-controlled spin manipulation including the spin-polarized electron transport in magnetic nanostructures that constitute the subject of the modern magnetism physics, spintronics, and microelectronics. The laser-induced magnetic transitions in magnetic nanostructures determine both by their spin and electron structure and by physical characteristics of laser radiation. Corresponding magnetic materials must possess by high enough values of magnetic anisotropy, magneto-optical susceptibility, and the spin polarization of conduction electrons. The laser radiation must be characterized by the high degree of polarization, a strong enough intensity and its pulse duration must correspond to short times of electron and spin relaxations.

A.M. Korostil (✉) • M.M. Krupa
Institute of Magnetism NASU, Kiev, Ukraine
e-mail: amand@rambler.ru

O. Fesenko, L. Yatsenko (eds.), *Nanoplasmonics, Nano-Optics, Nanocomposites, and Surface Studies*, Springer Proceedings in Physics 167,
DOI 10.1007/978-3-319-18543-9_4

Search magnetics with the high polarization degree connected with the known problem of efficient sources of the spin-polarized electron current providing the laser magnetic control. Magnetic nanostructures with the high spin polarization are seen as basic elements for devices, in which the laser excitation serves for the ultrafast magnetic control, including the control of the spin-polarized current. The practical realization such laser-controlled spin devices assume the development of techniques and design concepts of the mentioned spin control in solids.

The fast-speed directed laser magnetic impacts is realized via the laser-induced thermal demagnetization with subsequent bias by effective internal magnetic fields of different nature subject to the magnetic structure of materials and laser radiation characteristics. The effective internal magnetic bias fields can be related to the inverse magneto-optical Faraday effect (see [1–3]) and to the effects of the transient ferromagnetic-like state in combination with the relaxation of the exchange antiferromagnetic interaction under the pulsed laser-induced thermal demagnetization [4, 5]. In the first case, the bias magnetic field (H_{F}) arises only under circularly polarized laser irradiation. In the second case, the bias field (H_{TR}) is the internal transient field caused only by the different speeds of the laser-induced thermal demagnetization, and it is independent on the radiation polarization.

The effective bias field H_{F} corresponds to transition of electrons into the spin-flip perturbed ground state under the excitation by circularly polarized photons and the spin–orbital interaction [1]. Such process consists of the photon-induced electron transition with some photon frequency ω_1 into a virtual state with strong spin–orbital coupling and subsequent relaxation into the spin-flip perturbed state [2, 3]. The relaxation is accompanied by the coherent reemission of a photon with a frequency $\omega_2 = \omega_1 - \Omega_{\mathrm{m}}$, where Ω_{m} is a magnon frequency. The spin-flip time is determined by the energy of the spin–orbital interaction. For materials with a large magneto-optical susceptibility, the spin-flip duration can reach of 10 fs. The stimulating and re-emitted photons have identical circular polarizations that imply the conservation their angular momentums under the light-induced spin-flip. The laser magnetic impact via the effective bias field H_{F} occurs at a strong enough intensity of polarized pulsed radiation at some intervals of its pulse duration.

During the laser-induced thermal demagnetization, when one of ferrimagnetic sublattice becomes demagnetized, the field H_{TR}, coinciding with the magnetic field of the second again not demagnetized sublattice, realizes the magnetic bias of the first sublattice along its direction. Magnetic moments of both ferrimagnetic sublattices are parallel up to the complete demagnetization of the second sublattice that corresponds to a transient ferromagnetic-like state [4, 5]. Then, the field H_{TR} is determined by the relaxation of an antiferromagnetic exchange interaction that results in magnetic bias of the second ferrimagnetic sublattice antiparallel to its initial state. Such purely thermal laser-induced remagnetization of ferrimagnetic materials assumes large enough power short-time pulsed laser radiation with arbitrary polarization.

The indirect laser-induced magnetic impact can have the thermo-magnetic nature related to energy dissipation and the temperature dependence of magnetization and magnetic anisotropy constants. In this case, cooling time and heat limits the

laser impact speed and heat diffusion limits the laser impact localization. The indirect laser-induced magnetic impact can be realized via the laser-induced spin-polarized electron current [6, 7] caused by band-dependent kinetic properties of spin-polarized electrons under their momentum-selective interband laser excitations [8–11]. Then, the laser magnetic control is realized via the exchange interaction of the spin-polarized electron current with localized magnetic moments of a magnetic nanostructure. The laser-induced spin-polarized electron current belongs to the laser-induced kinetic effects (see [8]), which have a considerable role in the problem of laser-controlled particle transport in condensed matters (especially, in semiconducting and metallic nanostructures and gas mixtures).

Laser-induced kinetic effects, currents, and potential differences caused both by a photon momentum transfer (a photon pressure) and by the different mobility of ground and momentum-selective excited states of particles (electrons or atoms) underlie of the fast control of current states (including spin-polarized electron currents) and charge distribution in condensate systems. The momentum-selective laser impact causes the directed drift of particles with and against the direction of light propagation. The momentum of drift particles in some orders exceeds the photon momentum and therefore corresponding currents dominate. The character of the laser-induced excitations and the corresponding laser-induced drift (LID) of the particles are determined by their energy band spectra, which can have different dependence of interband transitions on a particle momentum (see [8]).

Such laser-induced electron kinetic effects occur in semiconductors with a two-dimensional structure of an electron subsystem (2DEG) [11–14], where the electron motion is quantum confined along one direction. The confinement achieves either by applying a magnetic field or by creation of quantum wells in semiconductor heterostructures. However, the LID in semiconductor due to smallness of the subband excitations occur at low temperatures that limits its practical application.

The mentioned kinetic effects can be realized through arbitrary interband transitions including those, which are excited by light in visible range and at room temperatures, in both semiconductors and metals (see [8]). The laser-induced electron transitions in metals occur between nonparallel conduction bands, since the edges of the conduction bands are typically located in different points of momentum space. However, the momentum-selective electron excitations provide by their concentration near to the gap in the band spectrum of electrons.

The laser-induced kinetic effects with respect to conduction magnetic materials can serve as the base for the laser-induced injection of spin-polarized electrons in magnetic nanostructures. The interaction of corresponding spin currents with the lattice spins in such nanostructure can be seen as the possible mechanism of the laser control of magnetic states of the mentioned heterogeneous nanostructures. The speed of corresponding magnetic switching is determined by the pulse duration of laser radiation and the rate of procession of lattice spin magnetic moments.

The feature of laser magnetic impact consists in possibility of the optical excitation of their spin system on a timescale faster than the characteristic time of the ferro- and antiferromagnetic exchange interactions that determines a nonadiabatic character of the spin dynamics. Accordingly, laser-induced spin-flip

processes and a magnetic reversal can occur with ultra-high speeds striving to a physical limit. Ferrimagnetic materials with the antiferromagnetic exchange interaction, which is the strongest interaction in magnetism, possess maximal speeds of the laser-induced remagnetization.

Namely in ferrimagnetic-based nanostructures the laser-induced effects provide the high-speed laser control by magnetic states, and particularly, remagnetization. Most strongly, the laser-induced effects are appeared in such rare-earth/transition metal-based nanostructures. Features of the laser-controlled magnetization and spin-polarized electron current in such nanostructures represent a great interest for high-speed writing and retrieving magnetically stored information.

Together with the laser-induced spin-polarized electron current, the laser-induced kinetic effect of the momentum-selective directed atomic drift results in magnetic changes via corresponding charge redistribution in irradiated materials. This is manifested via the change of magneto-optical properties of materials that also represents interest for the laser-controlled doping and impurity removal of magnetic materials.

The features and mechanisms of the laser-induced magnetization and remagnetization are considered below in ferrimagnetic-based single layers and multilayered nanostructures. The role of laser-induced spin-polarized currents in processes of the laser-induced remagnetization has investigated in tunnel magnetic junctions (TMJs). The laser control of the spin-polarized current in tunnel ferrimagnetic nanostructures via the pulsed laser-induced remagnetization is considered in the case TbFeCo-based compounds. In addition, we study the LID of impurities in semiconductors and its optical exhibitions.

Physical limits of remagnetization speed are one of the fundamental problems of magnetism physics, which has a crucial significance for creation of magnetic high-speed recording and readout systems of information [15–20]. Growth of attention to this problem is related to modern achievements of nanotechnologies, by possibilities of production of new magnetic nanostructures with predetermined physical properties, and development of the short-time pulsed laser radiation [21]. The prospect of the solution of this problem is related to the use of the impact of short-time laser impulses on the ferrimagnetic multilayered nanostructures, specifically, TMJs [22–25] that can lead to magnetic state variations and the remagnetization effect (see [19, 26]).

The laser-induced remagnetization of a ferrimagnetic nanolayer is characterized by its initial swift heating, thermal demagnetization of ferrimagnetic sublattices with different speeds, and by subsequent magnetic bias, which can cause both laser-induced electron excitations and nonequilibrium transitional magnetic states of ferrimagnetic sublattices [4, 26, 27].

The laser-induced electron excitation, occurring under circularly polarized laser radiation, results in the effective internal magnetic field H_F of the inverse magneto-optical Faraday effect and the effective internal magnetic field H_{sd} of the s–d exchange interaction of the spin-polarized current (laser-injected from a magnetic nanolayers) with the lattice magnetic moment of nanolayers. The intense laser-induced thermal demagnetization of ferrimagnetic sublattices can result in the

nonequilibrium transitional state with the parallel spin configuration of ferrimagnetic sublattice, which together with an interchange interaction relaxation can cause an internal magnetic field and the remagnetization effect [4, 5].

Such remagnetization can occur in the specific interval of relations between the laser pulse duration and laser-induced thermal demagnetization durations of ferrimagnetic materials [16]. The remagnetization dynamics of the ferrimagnetic nanolayers essentially depend on initial states and magnetic characteristics of ferromagnetic nanolayers. Therefore, our paper is devoted to study of features of the laser-induced remagnetization of ferrimagnetic nanostructure.

The structure of the presented paper is as follows. In Sect. 4.1.2, by a magneto-optical pump-probe method we investigate the laser-induced dynamics of the remagnetization and tunneling magnetoresistance effect in tunneling ferrimagnetic junctions on the basis rare-earth and transition metals TbCoFe with perpendicular magnetic anisotropy (PMA) [8–11]. The role of the laser-induced thermal demagnetization in the remagnetization under effective magnetic fields related to circularly polarized pulsed laser radiation is shown. In Sect. 4.1.3, it is studied the dependence of remagnetization dynamics on temperature behavior of an effective gyromagnetic ratio and a coercive magnetic field in ferrimagnetic junctions. Mechanisms of the laser-induced thermal remagnetization in ferrimagnetic layers with perpendicular and plane magnetic anisotropy via passing the nonequilibrium transitional magnetic state with parallel sublattice magnetizations are considered. Section 4.1.4 is devoted to the laser-induced kinetic effects, currents, and a potential difference in solids. A sequential approach to describe those kinetic effects is proposed. Influencing those kinetic effects on optical properties of semiconductors is considered.

4.1.2 Laser-Induced Remagnetization Under Effective Internal Magnetic Fields

The effect of the laser-induced remagnetization of thin magnetic materials represents the perspective and promising approach for increasing the physical limits of magnetic recording and information processing technologies. Based on the direct optical impact by laser pulses on magnetization, this approach represents the basis for the high-speed laser control of a magnetic reversal both uniform and nonuniform magnetic systems. The laser-induced magnetic transitions in the nonuniform multilayered magnetic junctions can also be the basis for controlling by a spin-polarized current and the tunnel magnetoresistance (TMR) in the TMJs.

The direct laser impact on the magnetization can be realized via the interaction with its circularly polarized photons with spin-polarized electrons of a magnetic medium. The Raman-like photon excitation of the electrons together with a spin–orbital interaction is accompanied by the spin-flip and remagnetization (see [1, 2]). That represents the quantum-mechanical mechanism of the inverse magneto-optical Faraday effect, which act on magnetic materials as the effective internal magnetic field (H_F). The magnitude of the effective magnetic field H_F is determined by the

magneto-optical susceptibility, which is in the direct dependence on the spin–orbital interaction. The pulsed laser irradiation causes heating and demagnetization that in combination with the laser-induced effective magnetic field can lead to variation of magnetic states and the remagnetization [3].

The indirect laser impact on magnetic states in nonuniform multilayered magnetic nanostructures can be realized via the laser-induced spin-polarized electron current between magnetic nanolayers [6, 7]. In this case, the remagnetization of the magnetic junction can be caused by the exchange *s–d* interaction of the laser-injected spin-polarized current with the localized magnetic moment of the injected layer of a magnetic junction. The effective internal magnetic field H_{sd} of that interaction constitutes from two components, $H_{sd} = H_s + H_{\text{inj}}$. The first component H_s is related to the *s–d* interaction of the transverse component (with respect to the magnetic moment of the injected layer) of the magnetic moment of the spin-polarized current. The second component H_{inj} is related to the *s–d* interaction of the laser-injected longitudinal spin component (with respect to the magnetic moment of the injected layer) which is characterized by a nonequilibrium distribution. The mentioned effective internal magnetic fields together with laser-induced thermal demagnetization result in the remagnetization, which is accompanied by a TMR effect.

The dynamics of the laser-induced magnetization is observed with the help of the magneto-optical pump and probe technique. In this technique, the one incident laser pulse stimulates magnetic switching and the second laser beam transmitted or reflected from the magnetic medium serves for image of the laser-induced magnetization. The magnetization image via transmitted or reflected laser beams is based on the magneto-optical Faraday effect or the Kerr effects, respectively (see [2, 19]). Corresponding magnetization dynamics can be described by the Landau–Lifshitz–Bloch (LLB) equation (see [19]) containing temperature-dependent parameters of longitudinal and transverse susceptibilities.

We have investigated the laser-induced remagnetization and TMR effect in magnetic tunnel junctions consisting of the two TbCoFe-based or the two CoFe-based amorphous ferrimagnetic nanolayers separated by the PrO-based isolating barrier nanolayers. The TbCoFe-based and FeCo-based ferrimagnetic layers are characterized by a perpendicular and single-axis planar magnetic anisotropy, respectively. Based on the magneto-optical measurements by the all-optic pump-probe technique, we have studied mechanisms and features of the remagnetization and TMF effects of the TMJs with intense polarized laser pulses.

Features of the Laser-Induced Remagnetization of Magnetic Nanostructures

The impact of pico- and femtosecond pulsed laser radiation on magnetic states and the conductance of the spin-polarized electron current was studied for the magnetic junctions $Al_2O_3/Tb_{22}Co_5Fe_{73}/Pr_6O_{11}/Tb_{19}Co_5Fe_{76}/Al_2O_3$ and $Al_2O_3/Co_{80}Fe_{20}/Pr_6O_{11}/Co_{30}Fe_{70}/Al_2O_3$ with the TbCoFe-based ferrimagnetic and the CoFe-based

ferromagnetic nanolayers (about 20 nm), respectively, separated by the PrO-based isolating barrier nanolayers (about 2–3 nm). The TbCoFe-based and CoFe-based layers are characterized by perpendicular (with respect to a magnetic layer) and single-axis planar magnetic anisotropy, respectively. In addition, the pulsed laser impact on a magnetization was studied for mentioned magnetic nanolayers singly.

The magnetic junctions were sprayed by a magnetron deposition technique on plates with sizes 10×14 mm and discs with the diameter 110 mm made of optical fused quartz with the thickness 1.2 mm. Thicknesses of magnetic nanolayers TbCoFe and CoFe constituted 20 nm. For the barrier nanolayer Pr_6O_{11} and the cover layer Al_2O_3 thickness constitute 2–3 nm and 40 nm, respectively. The magnetic junctions with a conductive surface $S = 20\mu^2$ are produced by a photolithography technique on the plates with sizes 10–14 mm. The edges of plates through which the current entered into the tunnel contacts TbCoFe and CoFe were covered by platinum. The contact zone and conductive magnetic strips also were protected by the Al_2O_3 cover with thickness near 40 nm.

The magnetic nanolayers $Tb_{22}Co_5Fe_{73}$ and $Co_{80}Fe_{20}$ have a high coercivity and the adjacent nanolayers $Tb_{19}Co_5Fe_{76}$ and $Co_{30}Fe_{70}$ have a low coercivity. The barrier layer represents a large-gap semiconductor similarly to the known [28–30] case of the MgO-based barrier in the magnetic junction Fe/MgO/Fe. The PrO-based barrier as well as the MgO-based barrier is characterized by a tunnel transparency, a large enough tunnel conductance and the TMR affect under external magnetic field [31]. Corresponding graphic data [31] are represented in Fig. 4.1.

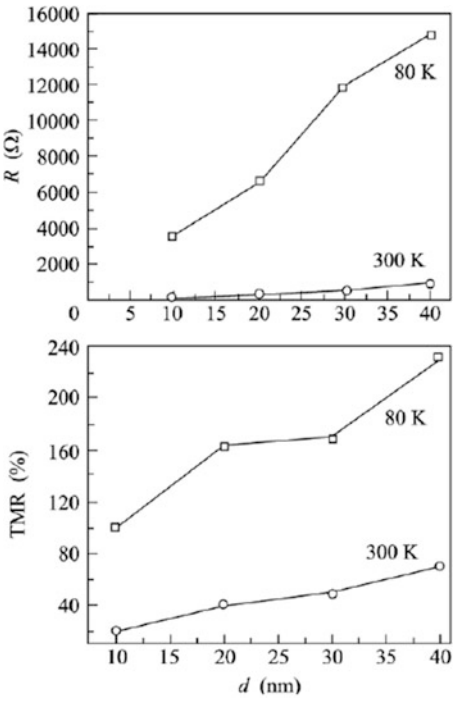

Fig. 4.1 (*Upper panel*) Tunnel resistance R and (*lower panel*) TMR effect of the $SiO_2/Tb_{19}Co_5Fe_{76}/Pr_6O_{11}/Tb_{22}Co_5Fe_{73}/SiO_2$ magnetic nanostructure versus the thickness of the Pr_6O_{11} barrier layer

The pulsed laser-induced remagnetization of magnetic nanolayers results in the pulsed change of the spin-polarized electron current through a TMJ. The laser-induced remagnetization of magnetic nanolayers results in the pulse change of the spin-polarized current through the TMJs.

This change relates to the dependence of the density of states of the spin-polarized electrons on the magnetic moment of a magnetic nanolayer. The tunnel current through considered magnetic nanostructures in the most general form is expressed via the tunneling probability (T) of the Bloch electrons from one magnetic nanolayer through the tunnel barrier nanolayer into an adjacent magnetic nanolayer [18, 19].

Thus, the current density of the spin-polarized electrons from a nanolayer with the chemical potential (μ_1) into the nanolayer with the chemical potential (μ_2) is described by the expression [29]

$$J_{\mu_1 \to \mu_2} = \frac{e}{(2\pi)^3} \int \mathrm{d}^3 \boldsymbol{k} v_z(\boldsymbol{k}) f(\mu_1) \sum_{\boldsymbol{k}'} T(\boldsymbol{k}, \boldsymbol{k}'), \tag{4.1}$$

where e is an electron charge, $v_z(\boldsymbol{k})$ is the velocity of electrons with the wave vector $\boldsymbol{k}$ along the axis z, perpendicular to the plane of the barrier nanolayer, $f(\mu_1)$ is the Fermi–Dirac distribution function, $T(\boldsymbol{k}, \boldsymbol{k}')$ is the tunneling probability of electrons with the change of the electron wave vector from $\boldsymbol{k}$ on $\boldsymbol{k}'$. Performing the integral over k_z yields

$$J_{\mu_1 \to \mu_2} = \frac{e}{(2\pi)^3} \sum_{k_{||}} \frac{1}{2\pi} \int \mathrm{d}^3 \boldsymbol{k}_z \frac{1}{\hbar} \frac{\partial \varepsilon}{\partial k_z} f(\mu_1) \sum_{\boldsymbol{k}'} T\left(\boldsymbol{k}, \boldsymbol{k}'\right), \tag{4.2}$$

where $\varepsilon = \varepsilon\left(\boldsymbol{k}'\right)$ is electron band spectrum.

Taking into account (4.2) the net tunnel current, which includes opposed tunnel currents between magnetic nanolayers, can be expressed as

$$I = \frac{e}{h} \int^{\mu_1} \mathrm{d}\varepsilon \sum_{k_{||} j} T\left(k_{||}, j\right), \tag{4.3}$$

where j is the number of the Bloch state for a given value of the transverse component $k_{||}$ of the electron wave vector. This results in the Landauer formula

$$G = \frac{e^2}{h} \sum_{k_{||} j} T\left(k_{||}, j\right), \tag{4.4}$$

which describes the conductance of the magnetic tunnel nanostructures subject to features of the electron transmission through the tunnel nanolayer.

Calculation of the tunneling probability assumes allowing for the quantum state structure of spin-polarized electrons in the magnetic nanolayers, the structure of decaying evanescent electron states in the tunnel barrier nanolayer PrO and near interfaces between them. In the considered TMJs, the barrier nanolayer is wide-band semiconductor, in which similarly to the case of the tunnel magnetic nanostructure Fe|Mg|Fe, the tunneling conductance is realized via the two tunneling channels corresponding majority and minority spin polarizations along and oppositely to the magnetic moment of a nanolayer. The existence of the electron Bloch states with the relatively high spin polarization in the magnetic nanolayers and their overlap with slowly decaying quantum states in the barrier cause the high enough tunneling conductance in the majority channel. In the minority channel, the relatively large tunneling conductance related to interfacial resonance states caused by quantum interference between the decaying states in the barrier layer that provides efficient tunneling the Bloch electrons through the barrier. The mentioned large electron spin polarization together with the effective tunneling results in the relatively large change of the spin-polarized current through the considered magnetic junctions at the change of the density states of the Bloch electrons in the magnetic layers corresponding to the change of their magnetic moments.

The explicit dependence of the spin-polarized current through the TMJ on the density of electron states, dependent on magnetic moments of the layers, follows from the formula (4.1). At given magnetizations of adjacent magnetic nanolayers of the magnetic junction, in the approximation of the mean tunneling probability T, the components of spin-polarized electron current are described by the expression [30]

$$I_{\sigma;m,m'} = \frac{4e\pi^2}{\hbar} T \int_{-\infty}^{+\infty} g_{1,\sigma}\left(\varepsilon - eV, \Sigma_1^m\right) g_{2,\sigma}\left(\varepsilon, \Sigma_2^{m'}\right) [f(\varepsilon - eV) - f(\varepsilon)] \mathrm{d}\varepsilon, \quad \sigma = (\uparrow, \downarrow), \tag{4.5}$$

where $g_{i,\sigma}\left(\varepsilon, \Sigma_i^m\right)$ $(i = 1, 2)$ is the density of electron states function in the ith magnetic nanolayer with the magnetization Σ_i^m, where the index m takes the values 1 and 2 if the electron spin is parallel and antiparallel to this magnetization, respectively. In addition, the function $f(\varepsilon)$ is the Fermi–Dirac distribution. The influence of the magnetization Σ_i^m adds up to the energy shift of the density of states function on the magnitude of the exchange interaction between the spin magnetic moments and the localized magnetic moment in nanolayers. As the density of states function depends on a magnetization direction that, as it is visible from (4.5), the spin-polarized electron current is dependent on the magnetization configuration of the magnetic nanolayers, which is determined by the relate directivity of these magnetizations.

At weak bias field and voltages (V), less than the width of energy band spectrum of the Bloch electrons, the expression for the tunneling spin-polarized current can be represented in the form

$$I_{\sigma;m,m'} = V\frac{4e^2\pi^2}{\hbar}T\int_{-\infty}^{+\infty} g_{1,\sigma}\left(\varepsilon,\Sigma_1^m\right)g_{2,\sigma}\left(\varepsilon,\Sigma_2^{m'}\right)\frac{\partial f(\varepsilon)}{\partial\varepsilon}\mathrm{d}\varepsilon. \tag{4.6}$$

Hence, at low temperatures, where the distribution function $f(\varepsilon)$ takes on the form of the Heaviside step function, the following formula can be obtained for the tunneling conductances in majority and minority channels:

$$G_{\sigma;m,m'} \approx \frac{4e^2\pi^2}{\hbar}g_{1,\sigma,\Sigma_1^m}g_{2,\sigma,\Sigma_2^{m'}}. \tag{4.7}$$

Here, density-of-states functions are taken at the Fermi energy ε_F, i.e., $g_{i,\sigma,\Sigma_i^m} = g_{i,\sigma,\Sigma}\left(\varepsilon_\mathrm{F},\Sigma_i^m\right)$. Due to (4.7) at low temperatures and voltages, the components of the tunneling conductance are determined by density-of-states functions of spin-polarized electrons at the Fermi energy in the magnetic layers.

At the parallel magnetization orientation of the adjacent magnetic nanolayers

$$G_\mathrm{P} = G_{\uparrow 1,1} + G_{\downarrow 11} \propto g_{1\uparrow,1,1}g_{2\uparrow,11} + g_{1\downarrow,11}g_{2\downarrow,11}. \tag{4.8}$$

At the antiparallel magnetization orientation $(\Sigma_1\big|\big|\Sigma_2)$

$$G_\mathrm{AP} = G_{\uparrow,1,2} + G_{\downarrow,1,2} \propto g_{1\uparrow,1}g_{2\uparrow,2} + g_{1\downarrow,2}g_{2\downarrow,1}. \tag{4.9}$$

Due to (4.8) and (4.9), the tunnel magneto-resistance effect (TMR), i.e., the relative change of the tunneling conductance under switching the magnetization configuration of the magnetic junction between parallel and antiparallel states is described by the expression

$$\mathrm{TMR} = \frac{G_\mathrm{P} - G_\mathrm{AP}}{G_\mathrm{AP}} = \frac{2P_1P_2}{1 - P_1P_2}, \quad P_i = \frac{g_{i\uparrow,1} - g_{i\downarrow,1}}{g_{i\uparrow,1}}, \tag{4.10}$$

where it is allowed for the relations $g_{i\uparrow,2} = g_{i\downarrow,1}$ and $g_{i\downarrow,2} = g_{i\uparrow,1}$. As it is visible from (4.10), TMR effect is connected by the direct dependence with spin polarizations P_i of magnetic nanolayers.

The Laser-Induced Picosecond Pulsed Remagnetization

The mechanisms of the impact of picosecond (about 80 ps) pulsed laser radiation on magnetic states and remagnetization of the magnetic junctions were studied by the magneto-optical pump-probe technique. The pump pulses of Nd-YAG laser radiation (with a central wavelength $\lambda_0 = 1.06\mu$) caused magnetic excitations. Probe pulses of the linearly polarized He–Ne laser radiation (with a central wavelength $\lambda_0 = 1.06\mu$) were used for imaging of the magnetization dynamics. The last was based on the polarization twisting in the magneto-optical Kerr and Faraday effects.

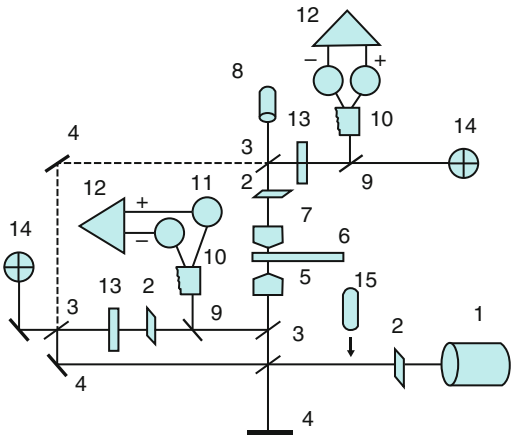

Fig. 4.2 The experimental setup for the optical investigation: the Nd-YAG laser *1*, polarizers *2*, interference mirrors *3*, the total reflecting mirrors *4*, the standard microscope objective *5*, the substrate with a magnetic film *6*, the special microscope objective *7*, the He–Ne laser *8*, semireflecting mirrors *9*, Senarmont prisms *10*, the sensing photo-diode *11*, differential amplifiers *12*, light filters *13*, photodiodes with four active area *14*, the Babinet compensator *15*

Features of the laser-induced magnetic dynamics were researched both via magneto-optical and by TMR effects.

The laser-induced magnetic dynamics under picosecond pulsed laser irradiation of the TMJs was studied by the all-optic pump-probe technique with the help of the experimental setup represented in Fig. 4.2.

The pump beam of the Nd-YAG laser 1 with Gaussian energy distribution in its cross section passed through the polarizer 2 and through the semimirror 3, and then it was directed by 100 % mirror 4 on the special microscope objective 5 with the numerical aperture 0.45. This microscope objective focused laser radiation on the researched film magnetic junction through the substrate 6. Polarized radiation of the He–Ne laser 8 with Gaussian energy distribution in its cross section was focused by the microscope objective 7 with the numerical aperture 0.5 on the surface of the magnetic junction from its opposite side.

The pump radiation of the Nd-YAG laser and the probe radiation of the He–Ne laser reflected from the nanolayers were directed by the interference mirrors 9 on the polarization Senarmont prisms 10. These radiations were split by these prisms on two beams and registered by the sensitive photodiode 11. The differential amplifiers 12 amplified the electric signals from the sensitive photodiode. Then, the double-beam oscilloscope registered these signals. The light filter 13 directed transmitted or reflected laser beams to the polarization Senarmont prism 10, which was used for registration of the radiation of He–Ne or Nd-YAG lasers. The polarization twisting of the reflected or the transmitted laser radiation was measured per differential signals from photodiodes 11.

Signals from the photodiode 14 came on the self-focusing microdrivers providing focusing the microscope objectives 5 and 7 on the magnetic junction surface. By reposition of a substrate with the magnetic junction, we could direct the beam of the

Nd-YAG laser on the film from the opposite side. The Babinet compensator 15 was used for research of the laser-induced magnetic switching in the magnetic junctions.

For enhancement of the time resolution in picosecond interval, the probe polarized beam of the He–Ne laser was formed by the system of 50 % mirrors 3 and 100 % mirrors 4. This beam with the controlled delay (with respect to the pump pulse) was focused on the researched area from the side of the pump laser pulses and opposite side. The polarization twisting of the reflected and transmitted probe laser beam was determined via changing of the signal amplitude, which was registered, by the sensing photodiodes and an oscilloscope.

The one-to-one correspondence between the polarization twisting of the probe radiation of the He–Ne laser and the laser-induced magnetization allowed to straightforwardly studying the magnetic dynamics of each nanolayers of the investigated magnetic junction $Al_2O_3/Tb_{22}Co_5Fe_{73}/Pr_6O_{11}/Tb_{19}Co_5Fe_{76}/Al_2O_3$. The impact of pulsed laser radiation on magnetic nanolayers $Tb_{22}Co_5$ Fe_{73} and $Tb_{19}Co_5Fe_{76}$ depends on physical characteristics of laser radiation including its intensity, polarization, pulse duration, and the magnetic structure of the magnetic junctions.

The measurement data concerning the time dynamics of the laser-induced magnetization in the magnetic junctions (with the help of the optical setup Fig. 4.2) under picoseconds pulsed laser radiation are represented in Fig. 4.3. In Fig. 4.3, the time evolution curves of photodiode signals for the reflected (the intensity I_R) and transmitted (the intensity I_T) probe laser pulses one-to-one image

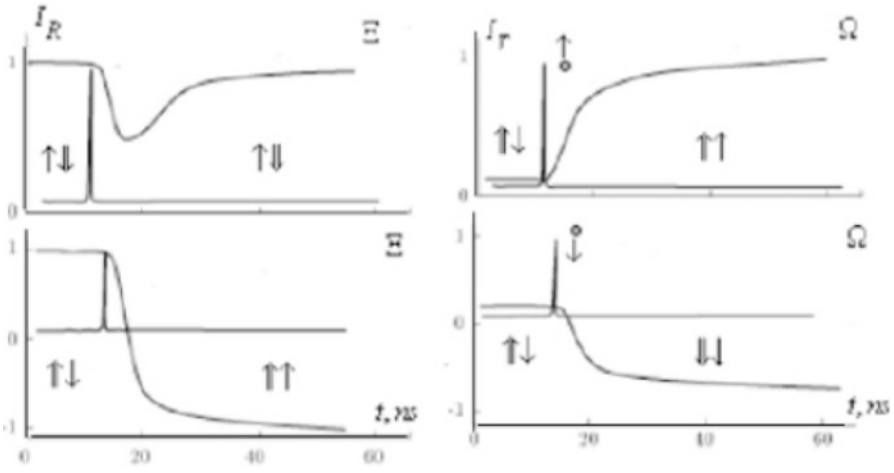

Fig. 4.3 The dynamics of the signals I_R and I_T of the He–Ne laser beams, reflected from the low-coercive magnetic layer $Tb_{19}Co_5Fe_{76}$ and transmitted through magnetic nanolayers, respectively, for the magnetic junction $Al_2O_3/Tb_{22}Co_5Fe_{73}/Pr_6O_{11}/Tb_{19}Co_5$ Fe_{76}/Al_2O_3 with different initial magnetization configuration under linearly (Ξ) and circularly (Ω) polarized picoseconds (time duration $\tau_i = 80\,\text{ps}$) pulsed radiation (*dot curves*) of the Nd-YAG laser with the intensity $I_i = 300\,\text{MW/cm}^2$ at temperature $T = 300\,\text{K}$. *Single* and *double arrows* denote magnetization directions of the low- and high-coercive nanolayers $Tb_{19}Co_5Fe_{76}$ and $Tb_{22}Co_5Fe_{73}$, respectively. The irradiated magnetic nanolayer is determined by the first *arrow* along the time axis. The *single arrow* with a *circle* denotes the direction of the effective magnetic field H_F, which is induced by circularly polarized laser pulses

the remagnetization of the magnetic nanolayers under picoseconds linearly and circularly polarized pump pulses of the Nd-YAG laser.

As it is visible from curves on the left in Fig. 4.3 (which corresponds to the linear polarization picosecond pump pulses), the laser-induced remagnetization occurs in the magnetic nanolayer adjoined to an irradiated magnetic nanolayer at the initial antiparallel magnetizations of magnetic nanolayers. Such magnetic reversal is caused by the effective internal magnetic field H_{sd} of the exchange interaction between the laser-induced spin-polarized electron current through the tunnel barrier and the lattice magnetization together with a laser-induced thermal demagnetization.

The strong enough intensity of the pump laser radiation and small enough its pulse duration constitute necessary conditions for the above-mentioned remagnetization. If the magnetic junction is irradiated by the linearly polarized laser pulses on the side of low-coercive nanolayer, the density of the spin-polarized current can be less than its threshold density and therefore the remagnetization not occurs as it represented on the top curve on the left in Fig. 4.3. At the irradiation on the side of the high-coercive nanolayer, the density of the spin-polarized current is increased, and it can exceed the threshold values of the remagnetization (the curve on the bottom is located in the left in Fig. 4.3).

Curves on the right side in Fig. 4.3 correspond to the circularly polarized pumping picosecond laser pulses. In this case, the laser-induced remagnetization of magnetic layers can be caused both by the effective internal magnetic field H_{sd} and the effective internal magnetic field H_{F} of the magneto-optical inverse Faraday effect together with the laser-induced thermal demagnetization. Usually, the threshold intensities of the pump laser radiation stimulating the remagnetization via the laser-induced effective magnetic fields H_{sd} and H_{F} are different.

Therefore, if such threshold intensity is less for the field H_{sd}, then the remagnetization via the laser-induced spin-polarized electron current passing from the high- to low-coercive magnetic nanolayer can amplify the remagnetization by the magnetic field H_{F}, as it is represented in the top curve on the right. If the above-mentioned circularly polarized laser pulses induce the internal magnetic field H_{F} directed toward the magnetization of high-coercive nanolayer, then the magnetic field H_{sd} vanishes and the remagnetization is completely determined by the magneto-optical inverse Faraday effect (bottom curve on the right in Fig. 4.3).

The laser-induced TMR effect was studied on the TbFeCo-based magnetic junction $Al_2O_3/Tb_{22}Co_5Fe_{73}/Pr_6O_{11}/Tb_{19}Co_5Fe_{76}/Al_2O_3$ and the CoFe-based magnetic junction $Al_2O_3/Co_{80}Fe_{20}/Pr_6O_{11}/Co_{30}Fe_{70}/Al_2O_3$. These junctions, as it was above denoted, are characterized by a large tunnel conductance and a TMR effect (which is determined by the relative resistance change under remagnetization).

In our opinion, similarly to the case of the MgO-based magnetic junctions, it is connected with a match between propagating electron–electron states in magnetic layers and evanescent states in the barrier layer near the Fermi level (see [28, 30]). That provides couple of an electron state from the TbCoFe into the PrO and out of the PrO into the TbCoFe. It is exhibited in the large TMR effect under external magnetic field, which for the TbCoFe-based magnetic junction reaches 70 % at 300 K and 240 % at 80 K [9]. Corresponding field dependences are represented in Fig. 4.4.

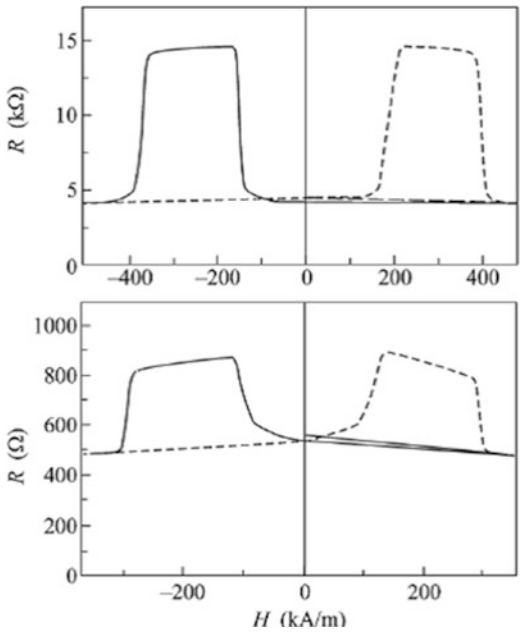

Fig. 4.4 Resistance of the $SiO_2/Tb_{19}Co_5Fe_{76}/Pr_6O_{11}/Tb_{22}Co_5Fe_{73}/SiO_2$ tunneling contact versus the applied magnetic field at $T = 80$ K (*upper panel*) and $T = 300$ K (*lower panel*)

The laser-induced remagnetization and TMR effect can be caused by the effective internal magnetic fields H_F of the inverse Faraday effect and H_{sd} of the exchange *s–d* interaction between the lattice spins and the spin current stimulated by the power enough polarized pulsed laser radiation [1, 6, 7, 19] together with the laser-induced demagnetization. The last precedes the mentioned magnetic switching. The laser-induced thermal magnetization should be sufficient for the remagnetization by the effective magnetic field. It assumes the suitable combinations of the laser pulse duration and intensity.

The TbCoFe-based and CoFe-based TMJ are characterized by the large enough magneto-optical susceptibility, a spin–orbital interaction, an electron spin polarization, and thermal susceptibility of their magnetic nanolayers that provide their laser-induced remagnetization.

For the TbCoFe-based magnetic junction possessing by a PMA, the essential role in the laser-induced magnetization belongs to the effective internal magnetic field H_F of the magneto-optical inverse Faraday effect, which is collinear to the magnetic anisotropy axis. The last can be amplified by the laser-induced effective magnetic field H_{sd}. The corresponding remagnetization results in resistance switching (the laser-induced magneto-resistance effect without an external magnetic field). In the case of the CoFe-based magnetic junction, possessing by a planar magnetic anisotropy axis, the impact of the laser-induced magnetic field H_F, perpendicular to this axis, vanish and the dominant role in the laser-induced magnetization can belong to the effective magnetic field H_{sd} related to the laser-induced spin-polarized electron current.

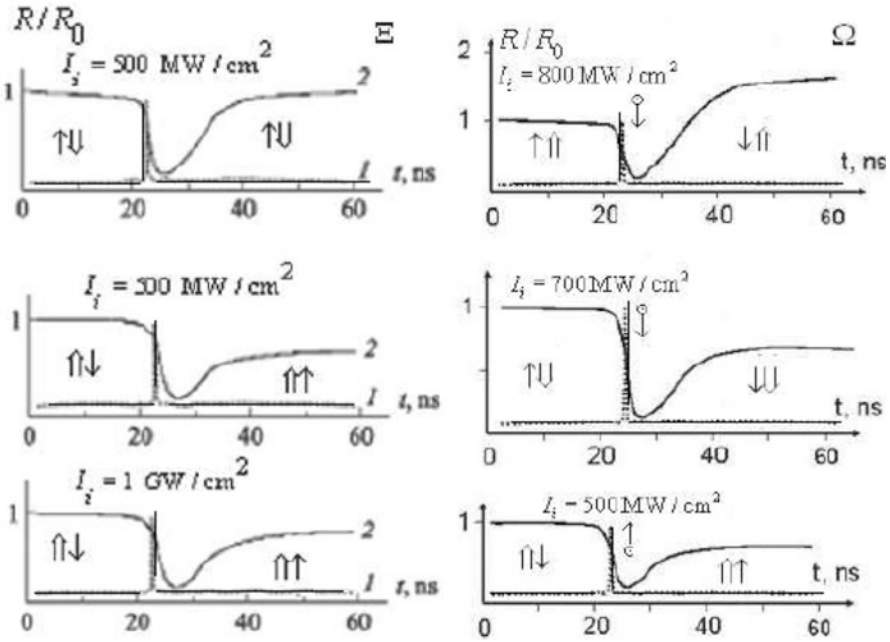

Fig. 4.5 The dynamics of the R/R_0 of the TMJ $Al_2O_3/Tb_{22}Co_5Fe_{73}/Pr_6O_{11}/Tb_{19}Co_5\ Fe_{76}/Al_2O_3$ (all curves except of the *bottom curve* on the *left*) and $Al_2O_3/Co_{80}Fe_{20}/Pr_6O_{11}/C_{30}Fe_{70}/Al_2O_3$ (the *bottom curve* on the *left*) with different magnetization configurations of magnetic nanolayers excited by linearly (denoted as Ξ on the *left*) and circularly (denoted as Ω on the *right*) polarized laser pulses (*dot curves*) with the duration $\tau_i = 80$ ps at different temperatures T and intensity I_i. Curves on the left and the *top curve* on the right correspond to the temperature $T = 80$ K and two *bottom curves* on the right correspond to temperature $T = 300$ K. *Single* and *double arrows* denote magnetization directions of the low- and high-coercive nanolayers $Tb_{19}Co_5\ Fe_{76}/Al_2O_3$, $Co_{80}Fe_{20}$ and $C_{30}Fe_{70}$, Co30Fe70, respectively. The irradiated nanolayers are determined by the first *arrow* along the temporary axis before the laser pulse. The *single arrow* with a *circle* denotes the direction of the effective magnetic field H_F, which is induced by the circularly polarized laser pulses

The above-mentioned laser-induced remagnetization and TMR effect experimentally was studied for the TbCoFe-based and CoFe-based TMJ with different initial magnetic configurations under linearly and circularly polarized picosecond laser pulses. Corresponding results are represented in Fig. 4.5. The remagnetization and resistance switching of the magnetic junctions with the line-polarized picoseconds laser pulses occur under the effect of the laser-induced thermal demagnetization and effective magnetic field H_{sd} in the magnetic nanolayer adjacent to an irradiated nanolayer. The laser radiation intensity and the induced field H_{sd} should be sufficient for the remagnetization. The field H_{sd} is directly dependent on the laser-induced spin-polarized current; therefore, its value is significantly larger at the laser irradiation of the high-coercive nanolayer than low-coercive nanolayer and can be insufficient for the magnetic switching.

In the case of the linearly polarized pulsed laser irradiation, the remagnetization and laser-induced TMR effect of the magnetic junctions occur only under the action of the laser-induced effective magnetic field H_{sd} and the laser-induced thermal demagnetization. Corresponding time dynamics of the resistance switching for the antiparallel initial magnetization configuration is represented by the curves on the left in Fig. 4.5. As it is visible from the top curve on the left, the laser irradiation of the low-coercive nanolayer $Tb_{19}Co_5Fe_{76}$ does not cause the remagnetization of the adjacent nanolayer and resistance switching, since the laser-induced spin-polarized electron current and the corresponding field H_{sd} are insufficient for the magnetic switching. However, the laser irradiation of the high-coercive nanolayers $Tb_{22}Co_5Fe_{73}$ and $Co_{80}Fe_{20}$ causes such remagnetization and resistance switching, since laser-induced spin-polarized electron current and the corresponding field H_{sd} became sufficient for the magnetic switching that is visible from two bottom curves on the left in Fig. 4.5.

For the circularly polarized picosecond pulsed laser irradiation, the remagnetization and laser-induced TMR effect of the magnetic junctions occur under the total action of the laser-induced effective magnetic fields H_F and H_{sd} together with the laser-induced thermal demagnetization. Corresponding time dynamics of the resistance switching for the different initial magnetization configurations is represented by the curves on the right in Fig. 4.5. As it is visible from the top curve on the right, at parallel initial magnetization configuration, the circularly polarized pulsed laser irradiation with the helicity, corresponding to the field H_F antiparallel to the initial magnetization of the irradiated low-coercive nanolayer $Tb_{19}Co_5Fe_{76}$ can cause its remagnetization and resistance switching. In this case, the field H_{sd} is absent.

In the case of antiparallel initial magnetization configuration, as it is visible from the middle curve on the right in Fig. 4.5, the circularly polarized pulsed laser irradiation with the helicity, corresponding to the field H_F antiparallel to the initial magnetization of the irradiated low-coercive nanolayer $Tb_{19}Co_5Fe_{76}$ can cause its remagnetization and resistance switching. The laser-induced spin-polarized current and efficient magnetic field H_{sd} are small with respective to the dominant field H_F.

For the antiparallel initial magnetization configuration, the circularly polarized pulsed laser irradiation with the helicity, corresponding to the field H_F parallel to the initial magnetization of the irradiated high-coercive nanolayer $Tb_{19}Co_5Fe_{76}$ can cause the remagnetization of the adjacent magnetic caused by both a sum of the magnetic fields H_F and H_{sd}. It results in the resistance switching, as it is visible from the bottom curve on the right in Fig. 4.3. In this case it is turned out that the laser-induced magnetic field H_{sd} gave an essential contribution in the remagnetization.

The Laser-Induced Femtosecond Pulsed Remagnetization

The laser-induced dynamics of the remagnetization of the magnetic junctions under femtosecond pulsed radiation is studied, similarly to the mentioned picosecond case, with the help of the pump-probe method, based on magneto-optical Kerr and

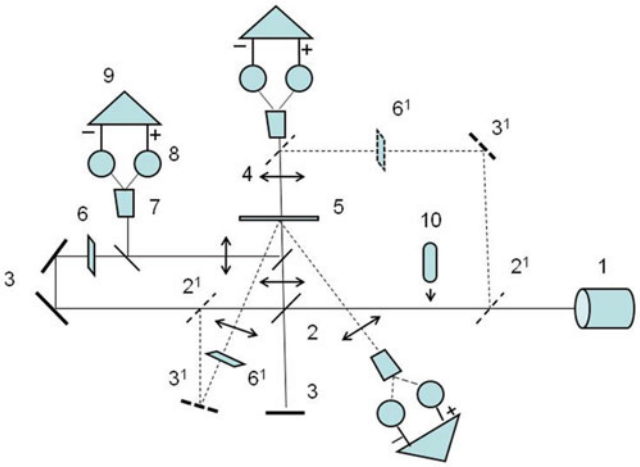

Fig. 4.6 The experimental scheme of researching: femtosecond laser *1*, 50 % mirror *2*, total reflection mirror *3*, long-focus lens *4*, the substrate with the magnetic nanostructure *5*, polarizer *6*, Senarmont prism *7*, photodiode *8*, differential amplifier *9*, Babinet compensator *10*

Faraday effects. The pump, i.e., the magnetic excitation was realized by the femtosecond pulses of the circularly polarized radiation of the Nd-YAG laser (with the pulse duration above $\tau_i \approx 130$ fs). Probing and controlling of the magnetization are realized with the help of pulses of linearly polarized radiation of the He–Ne laser. The scheme of corresponding magneto-optical researching is represented in Fig. 4.6

As it is visible in Fig. 4.6, femtosecond pulses of polarized radiation of the laser 1 are split by the mirror 2 on pump and probe pulses. The laser pulses, reflected from the mirror 3, were focused by the long-focus lens 4 on the substrate with the magnetic nanostructure 5. The probe laser pulses passed through a delay line, the polarizer 6, and were focused on a sample. By using the mirrors 2^1, 3^1, and polarizer 6^1, the laser pulses were directed on the investigated sample from its given side. The reflected probe laser pulses were split by the Senarmont prism 7 and were registered by the reading photodiode 8. The electric signals from the reading photodiode were amplified by the differential amplifier 9. Further, these signals were registered by the double-beam oscilloscope. For observation of magnetization switching by the pulses of circularly polarized laser radiation, the Babinet compensator 10 was used. The plane-of-polarization rotation of the laser radiation at reflection or transmission was measured with the help of the differential signals of the photodiodes 9.

The remagnetization dynamics of the magnetic nanolayers TbCoFe is determined by the features of the interaction of the femtosecond pulses of the circularly polarized laser with Tb and CoFe sublattices of ferrimagnetic material. The sufficiently distinction of magnetic moments of atoms Tb and Fe and the dominant interaction of the laser pulses with iron atoms are exhibited via the dependence of

the remagnetization dynamics on a ferrimagnetic composition. Increasing the concentration of Fe atoms possessing the strong laser-induced magnetization, and relative decreasing the concentration of Tb atoms possessing the strong spin-orbit coupling with the lattice restoring to intersublattice exchange interaction, lead to more fast laser-induced magnetization of the TbCoFe nanolayers.

The action of the femtosecond pulses of circularly polarized laser radiation on the magnetic nanolayers based on ferrimagnetic TbCoFe compounds is characterized by the initial thermal demagnetization of the magnetic sublattices Tb and FeCo, occurring with different rates, with sequent forming effective internal biasing fields of different nature. It can be the effective bias field H_{F} of the magneto-optical Faraday effect and also the mentioned transitional bias field H_{TR} which together with the relaxation of the intersublattice interaction causes the magnetic reversal of each of the magnetic sublattices of ferrimagnetic material. In the considered case, the effective bias field H_{F} plays a dominant role in the reversal process with respect to the bias field H_{TR} because off the influence of the spin–orbital interaction for Tb atoms on the relaxation of the intersublattice exchange interaction [16, 17]. Therefore, the bias field H_{TR}, arising as the result of the laser-induced thermal demagnetization of the magnetic sublattices Tb and CoFe, plays only the aiding role on the initial stage of the remagnetization under the bias field H_{F}. It is opposite to the case of the femtosecond laser-induced thermal remagnetization for similar GdCoFe-based ferrimagnetic nanolayers with rare-earth atoms Gd, possessing by the weak spin–orbit interaction [32].

The indirect magnetic impact of the femtosecond pulsed polarized laser radiation on the TMJ occurs via the laser-induced kinetic effect [8] of the spin-polarized electron current which transports magnetization from the irradiated magnetic nanolayer to the adjacent magnetic nanolayer through the barrier. The arising internal effective bias field H_{sd} of the exchange interaction between the spin-polarized current and the localized magnetic moment of the adjacent nanolayer gives itself contribution into the remagnetization. For the considered TMJs on the basis CoFe compounds, possessing by a planar magnetic anisotropy, the contribution of bias field H_{sd} in the remagnetization is dominant taking into account a single-sublattice ferromagnetic structure of these nanolayers.

In general, the total internal bias field, induced by the femtosecond pulsed circularly polarized laser radiation, can be represented as $H_{\mathrm{t}} = H_{\mathrm{F}} + H_{sd} + H_{\mathrm{TR}}$, where the contribution of each of component is dependent on a radiation polarization and magnetic structure of nanolayers. The first component H_{F} describing the effective bias field of the inverse magneto-optical Faraday effect corresponds to the circularly polarized laser radiation, and other components are independent on this polarization. The second component H_{sd}, related to a tunneling polarized current, is proper for tunnel magnetic nanostructures, the third component H_{TR} describing the transient bias field which is proper for ferrimagnetic materials.

The fast-speed remagnetization of the ferrimagnetic TbCoFe nanolayers under the femtosecond pulsed circularly polarized laser radiation can occur under the action of the two bias fields H_{F}, H_{TR}. In the ferromagnetic CoFe nanolayers with a

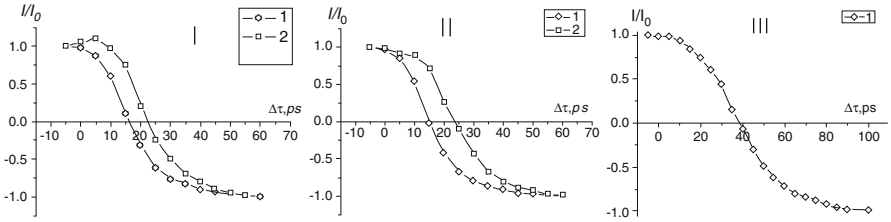

Fig. 4.7 The time dynamics of the laser-induced remagnetization under the high-power polarized laser pulses (I/I_0 denotes the signal value, which is proportional to the magnetization). (*I*) Probe laser pulses pass through the films $Al_2O_3/Tb_{19}Co_5Fe_{76}/Al_2O_3$ (1) and $Al_2O_3/Tb_{25}Co_5Fe_{70}/Al_2O_3$ (2) irradiated by circularly polarized pulses. (*II*) The probe laser pulses are reflected from the nanolayer $Tb_{19}Co_5Fe_{76}$ of the tunnel magnetic junction $Al_2O_3/Tb_{22}Co_5Fe_{73}\uparrow/Pr_6O_{11}/Tb_{19}Co_5Fe_{76}\downarrow/Al_2O_3$ irradiated from the side of the nanolayer $Tb_{22}Co_5Fe_{73}$ by circularly (1) and linearly (2) polarized laser pulses. (*III*) Probe pulses are reflected from the nanolayer $Co_{30}Fe_{70}$ of the tunnel magnetic junction $Al_2O_3/Co_{80}Fe_{20}\uparrow/Pr_6O_{11}/\downarrow Co_{30}Fe_{70}/Al_2O_3$ irradiated from the side of the nanolayer $Co_{80}Fe_{20}$ by circularly polarized laser pulses. *Arrows* denote directions of magnetic moments in nanolayers

plane magnetic anisotropy, the laser-induced remagnetization is possible only under the influence of the bias field H_{sd}.

The results of the magneto-optical measurements of the laser-induced remagnetization of the magnetic nanolayers and TMJs are represented in Fig. 4.7. As it is visible from the curves I in Fig. 4.7, the laser-induced remagnetization for the magnetic nanolayer $Tb_{19}Co_5Fe_{76}$ occurs faster than for the magnetic nanolayer $Tb_{25}Co_5Fe_{70}$ with the smaller contents of iron under the femtosecond pulsed circularly polarized laser radiation. It is conformed with the above-mentioned dominant interaction of the pulsed laser radiation with the iron sublattice in the ferrimagnetic nanolayers.

The curves II in Fig. 4.7 represent results of the study of the dependence of the laser-induced remagnetization by femtosecond pulses on the radiation polarization. The remagnetization of the weakly coercitive nanolayer $Tb_{19}Co_5Fe_{76}$ of the TMJ $Al_2O_3/Tb_{22}Co_5Fe_{73}\uparrow/Pr_6O_{11}/Tb_{19}Co_5Fe_{76}\downarrow/Al_2O_3$ irradiated from the side of the strongly coercitive nanolayer $Tb_{22}Co_5Fe_{73}$, as the circular polarization (the curve 1) occurs faster than at the linearly polarization (the curve 2). In the framework of the mentioned mechanism of the laser impact, at the circular polarization, the total effective bias field $H_F + H_{sd} + H_{TR}$ exceeds the effective bias field $H_{sd} + H_{TR}$ corresponding to the linear polarization.

The curves III in Fig. 4.7 show the role of the laser-induced spin-polarized current through the barrier nanolayer in the remagnetization magnetic nanolayers of TMJs. The laser-induced remagnetization of the weakly coercitive ferromagnetic nanolayer $Co_{30}Fe_{70}$ of the TMJ $Al_2O_3/Co_{80}Fe_{20}\uparrow/Pr_6O_{11}/\downarrow Co_{30}Fe_{70}/Al_2O_3$ with the plane magnetic anisotropy irradiated by femtosecond pulses from the side the strong coercitive magnetic nanolayer $Co_{80}Fe_{20}$ is mainly related to the effective bias field H_{sd}. In this case the effective bias field H_F of the inverse magneto-optic effect is relatively small and the main bias field H_{sd} corresponds to the exchange

interaction of spin-polarized current with the localized magnetic moment of the weakly coercitive nanolayer.

The laser-induced remagnetization and the change of the magnetization configuration of the magnetic nanolayers in the TMJs result in the changes of the spin-polarized current because of the corresponding change of the density of electron states in the magnetic nanolayers. Due to the above-mentioned formulae (4.5), the total spin-polarized electron current through the tunnel barrier in the approximation of the mean tunneling probability T is described by the expression

$$I_{m,m'} = \frac{4e\pi^2}{\hbar} T \int_{-\infty}^{+\infty} \sum_{\sigma} \int_{-\infty}^{+\infty} g_{1,\sigma}\left(\varepsilon - eV, \Sigma_1^m\right) g_{2,\sigma}\left(\varepsilon, \Sigma_2^{m'}\right) [f(\varepsilon - eV) - f(\varepsilon)] \mathrm{d}\varepsilon, \quad \sigma = (\uparrow, \downarrow), \tag{4.11}$$

where m and m' correspond to magnetization directions in the adjacent magnetic nanolayers of the TMJs, Σ_i^m is magnetization of the ith nanolayer with the mth direction, that determined by mechanisms of the laser-induced magnetization. Thus, the laser-induced pulsed change of the magnetization configuration (m, m') result in switching of the spin-polarized current via corresponding changes of the density of electron states $g_{1,\sigma}$ and $g_{2,\sigma}$ in nanolayers 1 and 2, respectively, i.e., the transition $I_{1,1} \rightarrow I_{1,2}$ occurs.

The results of the magneto-optical investigation of the dynamics of the spin-polarized current under the femtosecond pulses of the polarized laser radiation for the TMJs are represented in Fig. 4.8.

As it is visible from curves I and III in Fig. 4.8, the laser-induced remagnetization of the TMJ with antiparallel magnetization configuration, $Tb_{22}Co_5Fe_{73}\uparrow/Pr_6O_{11}/\downarrow Tb_{19}Co_5Fe_{76}$ into the state $Tb_{22}Co_5Fe_{73}\uparrow/Pr_6O_{11}/\uparrow Tb_{19}Co_5Fe_{76}$ with the parallel

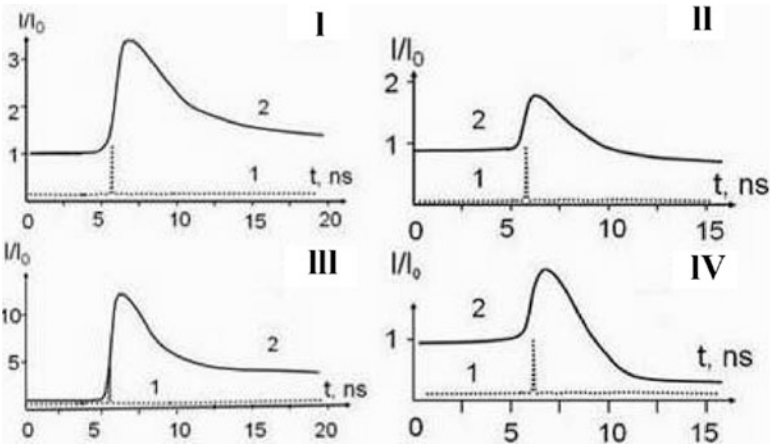

Fig. 4.8 The laser-induced dynamics of the spin-polarized current through tunnel magnetic junctions $Tb_{22}Co_5Fe_{73}\uparrow/Pr_6O_{11}/\downarrow Tb_{19}Co_5Fe_{76}$ (*I*, *III*) and $Co_{80}Fe_{20}\uparrow/Pr_6O_{11}/\uparrow Co_{30}Fe_{70}$ (*II*, *IV*) irradiated by the circularly polarized femtosecond laser pulses from the side of the layers $Tb_{22}Co_5Fe_{73}$ (*I*, *II*) and $Co_{80}Fe_{20}$ (*II*, *III*), respectively, at $T = 300$ K (*I*, *II*) and $T = 80$ K (*III*, *IV*)

magnetization configuration results in decrease of the spin-polarized current. Due to the circular polarization of the laser radiation and the ferrimagnetic structure of nanolayers, such switching is related to the laser-induced total effective bias field $H_F + H_{sd} + H_{TR}$. For the case of the TMJ $Co_{80}Fe_{20}\uparrow/Pr_6O_{11}/\uparrow Co_{30}Fe_{70}$ based on ferromagnetic nanolayers with the in-plane magnetic anisotropy, the laser-induced dynamics of the spin-polarized current is determined only by the effective bias field H_{sd} (curves II and IV in Fig. 4.8). In this case, the laser-induced remagnetization of the TMJ with the parallel magnetization configuration, $Co_{80}Fe_{20}\uparrow/Pr_6O_{11}/\uparrow Co_{30}Fe_{70}$ into the state $Co_{80}Fe_{20}\uparrow/Pr_6O_{11}/\downarrow Co_{30}Fe_{70}$ with the antiparallel magnetization configuration results in increase of the spin-polarized current.

The Description of the Laser-Induced Magnetic Dynamics

The laser-induced magnetization dynamics of the explored TMJ, including the temperature dependence of the magnetization magnitude, in the approximation of effective magnetic moments of nanolayers can be described by the macroscopic LLB equation [19, 33, 34]

$$\frac{\partial \mathbf{m}_i}{\partial t} = -\widetilde{\gamma}\left[\mathbf{m}_i \times \mathbf{H}^i_{\text{eff}}\right] + \frac{\widetilde{\gamma}\alpha_{||}}{m_i^2}\left[\mathbf{m}_i \cdot \left(\mathbf{H}^i_{\text{eff}} + \varsigma^i_{||}\right)\right]\mathbf{m}_i - \frac{\widetilde{\gamma}\alpha_{\perp}}{m_i^2}\left[\mathbf{m}_i \times \left[\mathbf{m}_i \times \left(\mathbf{H}^i_{\text{eff}} + \varsigma^i_{\perp}\right)\right]\right], \tag{4.12}$$

which was obtained in a mean-field approximation from the classical Fokker–Planck equation for individual spins interacting with a heat bath. In (4.12) $\widetilde{\gamma} = \gamma/\left(1+\lambda^2\right)$, where γ is the gyromagnetic ratio and λ is a microscopic parameter that characterizes the coupling of the individual atomistic spins with the heat bath. It is visible from (4.12) that a spin polarization m_i has no constant length and is temperature dependent. The coefficients $\alpha_{||}$ and $\alpha_{\perp}$ are dimensionless longitudinal and transverse damping parameters. Thermal fluctuations are included as an additional noise terms $\varsigma^i_l(t)$ with $l = \left(\perp, ||\right)$ and

$$\left\langle \varsigma^{i,\eta}_l \varsigma^{i,\mu}_l \right\rangle = \frac{2k_B T}{\widetilde{\gamma} M_s^0 \Delta^3}\delta_{\nu\eta}\delta_{ij}\delta(t) \tag{4.13}$$

where i, j denote lattice sites and η, μ denote the Cartesian components. Here, Δ^3 is the volume of the micromagnetic cell and M_s^0 is the value of the spontaneous magnetization at zero temperature. The damping parameters below and above the magnetic phase transition temperature T_M are described by the expressions $\alpha_{||} = 2T/(3T_M)$, $\alpha_{\perp} = \lambda(1 - T/T_M)$ and $\alpha_{\perp} = \alpha_{||} = 2\lambda T/(3T_M)$, respectively.

The effective magnetic field can be written as $H^i_{\text{eff}} = H_{\text{l-ind}} + H^i_{\text{a-ex}}$. Here, the first ingredient $H_{\text{l-ind}}$ is caused by the laser-induced electron excitations which includes both the effective internal magnetic field of the inverse magneto-optical Faraday effect (H_{F}) and the internal magnetic field (H_{sd}), generated by the *s–d* exchange interaction of laser-injected spin-polarized currents with localized spins of magnetic lattice in the spatially inhomogeneous magnetic junction. The second ingredient $H^i_{\text{a-ex}} = H + H^i_{\text{a}} + H^i_{\text{ex}}$ is given by

$$H^i_{\text{a-ex}} = \begin{cases} \dfrac{1}{2\widetilde{\xi}_{||}}\left(1 - \dfrac{m_i^2}{m_{\text{eq}}^2}\right)m_i, & T < T_{\text{M}}; \\ -\dfrac{1}{2\widetilde{\xi}_{||}}\left(1 + \dfrac{3T_m m_i^2}{5(T - T_{\text{M}})}\right)m_i, & T \geq T_{\text{M}}, \end{cases} \tag{4.14}$$

where the susceptibility $\widetilde{\xi}^l = \partial m_l / \partial H_l$. The anisotropy and exchange fields are given by

$$H^i_{\text{a}} = -\frac{\left(m^i_x e_x + m^i_y e_y\right)}{\widetilde{\xi}_{\perp}}$$

and

$$H^i_{\text{ex}} = -\frac{A}{m_e^2}\frac{2}{M_{\text{s}}^0 \Delta^2}\sum_{j \in \text{neigh}(i)}\left(m_j - m_i\right),$$

respectively.

Within the context of the LLB equation, field components parallel to the local magnetic moment can change the length of the magnetization vector. In the limit, $T \to 0$ the longitudinal damping parameter $\alpha_{||}$ vanishes and with $|m| = m_{\text{eq}}(0)$ the LLB, equation goes over to the usual Landau–Lifshitz–Gilbert (LLG) equation [35]. The temperature-dependent parameters in (4.12), i.e., longitudinal, transverse susceptibilities, and the temperature variation of the magnetization, $\chi_{||}(T), \chi_{\perp}(T)$, and $m_e(T)$ are determined using a Langevin dynamics combined with the LLG equation for each spin, i.e., by its stochastic modification [32]

$$\boldsymbol{S}_i = -\frac{\gamma}{(1+\lambda^2)\mu_s}[\boldsymbol{S}_i \times \boldsymbol{H}_i + \lambda \boldsymbol{S}_i \times \boldsymbol{S}_i + (\boldsymbol{S}_i \times \boldsymbol{H}_i)], \tag{4.15}$$

where the internal field $\cdot \boldsymbol{H}_i = \partial \boldsymbol{H} / \partial \boldsymbol{S}_i + \boldsymbol{\xi}_i(T)$. Thermal fluctuation of the mentioned parameters are included as an additional noise term in the internal field with $\langle \chi_i(t) \rangle = 0$ and $\left\langle \chi_i^k(t) \chi_j^l(t) \right\rangle = 2\delta_{ij}\delta_{kl}\lambda k_{\text{B}} T \mu_{\text{s}} / \gamma$.

The system (4.12) and (4.15) have solution for the magnetization $m(t)$, which at the temperatures close to the magnetic phase transition temperature T_{M} tends to

zero (that means a demagnetization process). Then at cooling, one tends to the magnitude with the sign opposite to initial value (that means the magnetic switching). The system (4.12) and (4.15) determine the conditions for parameters providing the magnetic switching. It turns out that the magnetic switching only occurs within a narrow range of parameters for the laser pulse. The realization of the magnetic switching assumes the suitable combinations of laser pulse duration and intensity.

The component H_{sd} of the effective magnetic field H_{eff} in (4.12) expresses via the *s–d*-exchange interaction U between the spin-polarized current and the lattice magnetization m as

$$H_{sd}(x,t) = -\frac{\delta U_{sd}}{\delta m(x,t)} = -\alpha \frac{\delta}{\delta m(x,t)} \int_0^L \mathrm{d}x' m_{\text{el}}\left(x',t\right) m\left(x',t\right) \tag{4.16}$$

where $m_{\text{el}}(x,t)$ is the magnetization of the laser-induced spin-polarized current and L is thick of a magnetic nanolayer of the TMJ. Since the magnetization $\boldsymbol{m}=\boldsymbol{m}(\boldsymbol{x},t)$ is connected with the magnetization flux density $\boldsymbol{J}$ by the continuity equation

$$\frac{\partial \mathbf{m}_{\text{el}}}{\partial t} + \frac{\partial \boldsymbol{J}}{\partial \boldsymbol{x}} + \gamma\alpha[\boldsymbol{m}_{\text{el}} \times \boldsymbol{m}] + \frac{\boldsymbol{m}_{\text{el}} - \overline{\boldsymbol{m}}_{\text{el}}}{\tau} = 0 \tag{4.17}$$

(where $\overline{\boldsymbol{m}}_{\text{el}}$ is an averaged magnetization, τ is a relaxation time with respect to a local equilibrium state), then the effective magnetic field $H_{sd} = H_{sd}(\boldsymbol{J})$, i.e., it depends on the magnitude of the laser-induced current and the intensity of laser pulses.

The continuity condition of the magnetization flux near the interface between continuity adjacent magnetic layers determines the boundary conditions for (4.17) that allows describing the magnetization dynamics under the laser-induced spin-polarized electron current. The continuity condition for the traverse components of the magnetization flux near interface between adjacent magnetic layers results in a transfer of torque moment from labile electrons to lattice moments. The corresponding transverse component ($H_{sd,\perp}$) of internal magnetic field H_{sd} can result in magnetic switching in a small region near the interface at excess of threshold intensity of laser pulses [5]. Such spin torque effect assumes spin dissipation.

At the same time, the continuity condition for the longitudinal components of the magnetization flux through the interface in (4.12) results in the longitudinal component $H_{sd,||}$ of the magnetic field H_{sd} caused by the nonequilibrium spin polarization of spin-polarized electrons of laser-injected through the interface into an adjacent magnetic layer. The magnetic field $H_{sd,\perp}$ (independent on the spin dissipation) results in the magnetization switching in bulk of the magnetic layer at a threshold magnitude of the laser intensity.

Thus, due to (4.12) the change of the effective magnetic field H_{eff} can result in the magnetization reorientation and switching. For the single magnetic nanolayer, the effective magnetic field is caused only by the effective field $H_{\text{i - ind}}$ related to the optic-magnetic excitations. For the tunneling magnetic junction, the laser-induced effective magnetic field $H_{\text{i - ind}}$ also includes magnetic field H_{sd} related to the laser-induced spin-polarized flux, playing the essential role in magnetization and switching processes. The last field is the sum $H_{sd} = H_{sd,\perp} + H_{sd,||}$, where the first and second terms are related to the transverse and longitudinal components of the spin flux, respectively.

The effective field $H_{sd,\perp}$ related to the exchange *s–d* interaction between the lattice magnetization and the transverse component of the laser-induced spin magnetic flux damping near the magnetic interface. The effective field corresponds to the scattering of spin-polarized electrons on localized magnetic ions accompanying by the action of the torque T on the magnetic lattice. Spin magnetic momentums of the spin-polarized current and the lattice are aligned on the distance l, i.e., the transverse component of the total magnetic flux is completely damped. This torque (corresponding to the continuity condition of the total magnetic flux) is determined via the spin electron polarization vector p_{cur} and magnetization vector m by the vector product

$$T = \sigma I[m \times m \times p_{cur}]/|m| \tag{4.18}$$

where σ is the constant depended on the efficiency of the scattering processes in the thin nanolayer, I is pro-proportional to the density of the laser-induced current of spin-polarized electrons. The increase of the laser-induced current density of spin-polarized electrons to some critical value (on the order 10^7 A/cm^2) causes the large enough torque for the magnetic switching near the junction interface.

The effective field $H_{sd||}$ is related to the longitudinal component of the total magnetic flux, consisting of laser-induced spin-polarized current and lattice magnetic components, which passes in the low-coercive layer on the spin diffusive depth (on the order 10 nm). This field generates by the exchange *s–d*-interaction between the nonequilibrium spin polarization and the lattice magnetization (that causes by the nonequilibrium distribution of the laser-induced electrons between spin subbands in the low-coercive magnetic layer) with the lattice magnetization. The field $H_{sd||}$ characterizes by the direct dependence on the density of the laser-induced spin-polarized electron current. It is always parallel in the magnetization of the strongly coercive magnetic layer. Therefore, the increasing of the current density to some critical value accompanies by the increasing of $H_{sd||}$ and magnetic switching if the magnetization directions of adjacent magnetic nanolayers are antiparallel.

4.1.3 Impact of Laser-Induced Heating on Remagnetization Dynamics

Features of the laser-induced thermal influence on a magnetization dynamics and remagnetization of ferrimagnetic layers can be caused by different temperature dependences of sublattice magnetizations and, accordingly, by different speeds of thermal demagnetizations of ferrimagnetic sublattices. The distinction of temperature behaviors of ferrimagnetic sublattices manifests in existence of magnetic and angular momentum compensation points, where temperature dependences of a sublattice magnetization and a sublattice angular momentum, respectively, intersect. The ferrimagnetic remagnetization determines by features of the temperature behavior of sublattice magnetization near the compensation points. Depending on their composition, ferrimagnetic can exhibit a magnetization compensation temperature T_M where the magnetizations of ferrimagnetic sublattices cancel each other, and similarly, an angular momentum compensation temperature T_A where the net angular momentum of the sublattices vanishes.

Substantially different timescales of the laser-induced thermal demagnetization of the ferrimagnetic sublattices result in emerging the effective bias magnetic field acting on the demagnetized sublattice on the side of again not demagnetized sublattice. It leads to the transient ferromagnetic state with parallel magnetizations of sublattice that together with the exchange interaction relaxation can cause a magnetization reversal of the sublattices.

The mentioned laser-induced thermal impact on the magnetization dynamics and the remagnetization of ferrimagnetic nanolayers observe in rare-earth-3*d* transition metal ferrimagnetic compounds (RE-TM). Such compounds, specifically, GdFeCo, are widely used materials for magneto-optical recording, and represent the suitable physical models for study the above-mentioned temperature-dependent magnetization in ferrimagnetic nanolayers.

Magnetization Dynamics Across Compensation Points

The dynamics of the laser-induced remagnetization of ferrimagnetic nanolayers substantially depends on the temperature magnetization behavior their sublattices [13, 14]. The remagnetization speed at transition across the magnetization compensation temperature T_M is in direct relation on a frequency and a magnetic precession damping. Considerable increase of these quantities in the framework of the modified Landau–Lifshitz model occurs at passage of the angular compensation temperature T_A.

The main regularities of the magnetization dynamics for ferrimagnetic nanolayers exhibit in the ferrimagnetic physical model based on rare-earth-3*d* (RE) transition metal (TM) ferrimagnetic composed of RE and TM sublattices with antiparallel magnetizations which can be represented by the ferrimagnetic

compound GdFeCo. The dynamics of the magnetization m_i ($i = \mathrm{RE}, \mathrm{TM}$) of this ferrimagnetic is described by the equation

$$\begin{gathered}\frac{\partial \boldsymbol{m}_i}{\partial t} = -\left|\gamma_i\right|\left[\boldsymbol{m}_i \times \boldsymbol{H}_i^{\mathrm{eff}}\right] + \frac{\alpha_i}{|m_i|}\left[\boldsymbol{m}_i \times \frac{\partial \boldsymbol{m}_i}{\partial t}\right], \\ \boldsymbol{H}_{i(j)}^{\mathrm{ex}} = -\chi_{\mathrm{ex}} \boldsymbol{m}_{(j)i}, \quad i, j = (\mathrm{RE}, \mathrm{TM})\end{gathered} \tag{4.19}$$

with gyromagnetic ratio and the Gilbert damping parameter given by $\left|\gamma_i\right| = g_i \mu_{\mathrm{B}}/\hbar$ and $\alpha_i = \left|\lambda_i\right|/\left|\gamma_i\right| m_i$, respectively. Here, λ_i is the Landau–Lifshitz damping parameter [26, 35]. The quantity χ_{ex} is a reversible magnetic susceptibility, coupling the magnetization of the sublattice RE (TM) with external magnetic field acting on the sublattice (TM) RE.

Solutions of the system (4.19) characterize by frequencies of ferromagnetic (ω_{FMR}) and exchange (ω_{ex}) resonances [23]

$$\omega_{\mathrm{FMR}} = \gamma_{\mathrm{eff}} H^{\mathrm{eff}}, \quad \omega_{\mathrm{ex}} = \chi_{\mathrm{ex}} \left|\gamma_{\mathrm{RE}}\right|\left|\gamma_{\mathrm{TM}}\right| A(T) \tag{4.20}$$

where an effective gyromagnetic ratio γ_{eff} is the function of temperature T and is determined via the sublattice magnetization as

$$\gamma_{\mathrm{eff}}(T) = \frac{m_{\mathrm{RE}}(T) - m_{\mathrm{TM}}(T)}{\frac{m_{\mathrm{RE}}(T)}{|\gamma_{\mathrm{RE}}|} - \frac{m_{\mathrm{TM}}(T)}{|\gamma_{\mathrm{TM}}|}} = \frac{M(T)}{A(T)} \tag{4.21}$$

Here, $m(T)$ and $A(T)$ are temperature dependent on the net magnetization and angular moment, A_0 is constant under the assumption of Landau–Lifshitz damping parameter being independent on temperature. At tending temperature T to the angular momentum compensation temperature T_{A} ($A(T) \to 0$), the effective gyromagnetic ratio (4.21) sharply increases. Similar increasing observes for the damping parameter of a magnetic precession

$$\alpha_{\mathrm{eff}}(T) = \frac{\frac{\lambda_{\mathrm{RE}}(T)}{\left|\gamma_{\mathrm{RE}}\right|^2} + \frac{\lambda_{\mathrm{TM}}(T)}{\left|\gamma_{\mathrm{TM}}\right|^2}}{\frac{m_{\mathrm{RE}}(T)}{|\gamma_{\mathrm{RE}}|} - \frac{m_{\mathrm{TM}}(T)}{|\gamma_{\mathrm{TM}}|}} = \frac{A_0}{A(T)} \tag{4.22}$$

Equations (4.21) and (4.22) indicate a divergence of both the precession frequency and Gilbert damping parameter of the FMR mode at the temperature T_{A}. Moreover, from the equation (4.21), one can be noticed that at the temperature T_{A}, the FMR frequency becomes zero. In contrast, the equation (4.20) indicates that the exchange resonance branch softens at the angular momentum compensation temperature T_{A}, where the FMR mode diverges.

The mentioned effects of increasing the ferromagnetic frequency and the damping parameter at decreasing the exchange resonant frequency represent the conditions for substantial increase of the remagnetization speed of ferrimagnetic

nanolayers under circularly polarized pulsed laser radiation. The damping of the exchange interaction resonant frequency accompanies by the interaction damping. This results in the acceleration of the magnetization reverse of these sublattices under the internal effective magnetic field of the inverse magneto-optical Faraday effect at passage the magnetization compensation temperature.

Character features of the impact of laser-induced pulsed heating on the dynamics and the remagnetization of a ferrimagnetic nanolayer also can observe under the linear polarized laser radiation in an external magnetic field at temperatures above the magnetization compensation point T_M. In this case, the ferrimagnetic magnetization m is directed along the effective magnetic field $H^{\text{eff}} = H_{\text{ex}} + H_a + H_s$, where H_a and H_s are a magneto-crystalline and a form anisotropy, respectively. The laser thermal pulses result in the change of the field H^{eff} that causes the magnetization precession round a changed equilibrium axis. The appropriate temperature behavior of the ferrimagnetic nanolayer based on compound $Gd_{22}Fe_{74.6}Co_{3.4}$ is represented in Fig. 4.9 [26].

The solutions of the equalization (4.24) for the magnetization dynamics are characterized by damping (as the result of an electron–phonon interaction) by magnetization vibrations which amplitudes are in a direct relation with the external magnetic field H_{ex}. It turns out that the ferrimagnetic sublattice TM gives a basic contribution to this magnetization. The expression for the square of frequency ω of the magnetization precession [36]

$$\omega^2 = \left(\frac{\gamma_{\text{eff}}}{\left(1+\alpha_{\text{eff}}^2\right)}\right)^2 \left(\left(H_{\text{ex}}\cos\theta_{\text{ex}} + \left|H_s + H_a\right|\right)^2 - \left(H_{\text{ex}}\sin\theta_{\text{ex}}\right)^2\right) \qquad (4.23)$$

(θ_{ex} is an angle between the external magnetic field and an easy magnetic anisotropy axis) allows to determine the internal magnetic field $H_a + H_s$ and also the effective gyromagnetic relation and damping parameter in the ferrimagnetic nanolayers.

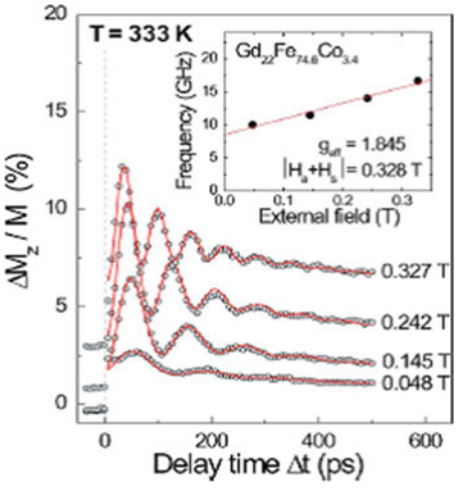

Fig. 4.9 Magnetization precession in GdFeCo as a function of the applied external field. *Inset* shows the field dependence of the precession frequency. Note that the sample temperature presented here includes the temperature increase induced by the pump heating

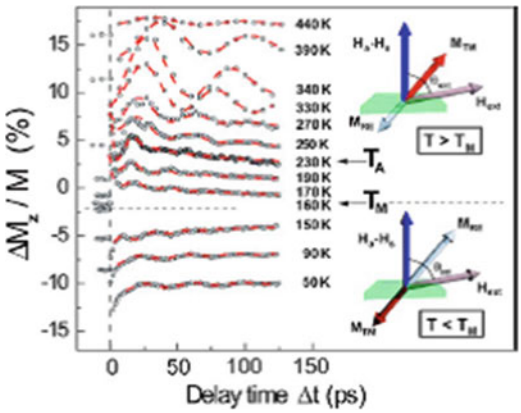

Fig. 4.10 Temperature dependence of coherent precession of the magnetizations in GdFeCo, measured at an external field $H_{ex} = 0.29T$. Around 160 K magnetic compensation T_M of the ferrimagnetic system occurs. The *inset* shows the alignment of the RE-TM system under an external applied field, below and above T_M

At initial temperatures below the magnetization compensation temperature T_M, a thermal relaxation after the pulsed laser heating can accompany by a transition of ferrimagnetic through the temperature T_M with reversing of magnetization of each sublattices RE and TM under the external magnetic field. Such the magnetization reversal is accompanied by phase changes of magnetic oscillations (Fig. 4.10) [26].

In the ferrimagnetic nanolayer GdFeCo at temperatures $T < T_M$, the magnetization m_{RE} of the sublattice RE (Gd) is larger than the magnetization m_{TE} of the sublattice TM (FeCo), and it is directed along the external magnetic field H_{ex}. At $T > T_M$, the magnetization $m_{TM} > m_{RE}$ and varies its direction along the external magnetic field H_{ex}, as it is visible in the inset of Fig. 4.10.

The magnetization reverse under the pulsed laser-induced heating and the external magnetic field are in direct relation on the frequency and the damping of the magnetization precession. It turns out [26, 27] that features of the temperature dependence of the magnetization procession frequencies near the angular momentum compensation temperature T_A determine their temperature behavior near magnetization compensation temperature T_M.

In the temperature interval $[T_A, T_M]$, the magnetization precession frequency determines by the total action of exchanging interaction between spins of each sublattices RE and TM, as it is visible in Fig. 4.11.

In the temperature interval $[T_A, T_M]$, it is observed the hybridization of the resonant frequencies ω_{FMR} and ω_{ex}, and the magnetization precession frequency at the magnetization compensation temperature T_M attains the significant value, constituting 40 GHz (Fig. 4.11a). The effective damping parameter at T_A takes the maximum value remaining large enough in closely approximating point T_M. Changing the composition of the ferrimagnetic (GdFeCo), it is possible to attain a necessary proximity between compensation points T_A and T_M, providing the rapid remagnetization of the ferrimagnetic nanolayer. For circularly polarized laser pulses, such remagnetization can occur without an external magnetic field under an effective internal magnetic field of the inverse magneto-optical Faraday effect.

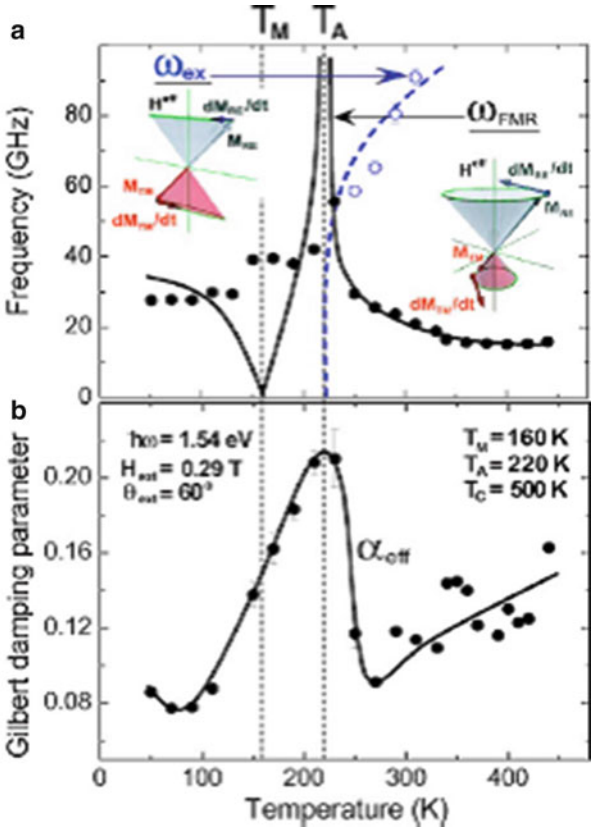

Fig. 4.11 (**a**) Temperature dependence of the magnetization precession frequencies ω_{FMR} and ω_{ex}. As temperature decreases from 310 K toward T_A, the exchange resonance mode ω_{ex} (*open circles*) softens and mix with the ordinary FMR resonance (*closed circles*). Since around 230 K both FMR and exchange modes have essentially the same frequency, the frequency indicated at 230 K may represent both the FMR and the exchange resonance modes. The *insets* show schematically the two modes. (**b**) Temperature dependence of the Gilbert damping parameter α_{eff}

The laser-induced heating above the angular momentum and magnetization compensation points results in the ultra-speed (subpicosecond) remagnetization of ferrimagnetic layers [27]. This is related to features of the magnetization dynamics of ferrimagnetic sublattices that are observed with the help of the magneto-optical pump-probe technique.

Thermal pumping is provided by pulsed laser irradiation and magnetic responses are imaged with the help of the magnet-optical Faraday effect via the polarization twisting of probing laser pulses. Then, the magnetization dynamics depends on the ratio between the applied magnetic field H_{ex} and the temperature-dependent coercive field $H_C(T)$ of the ferrimagnetic nanolayer.

Character features of magnetization dynamics of the ferrimagnetic nanolayers under laser thermal pulses of different power are observed for the amorphous ferrimagnetic $Gd_{22}Fe_{74.6}Co_{3.4}$ with the magnetization compensation temperature $T_M = 370$ and the angular momentum temperature $T_A = 420$ K (Fig. 4.12) [27].

The laser-induced pulsed heating the electron subsystem of ferrimagnetic continues by high-speed heating of its spin subsystem with subsequent cooling to an initial temperature that accompany by thermal changes of magnetizations $m_{RE}(T)$

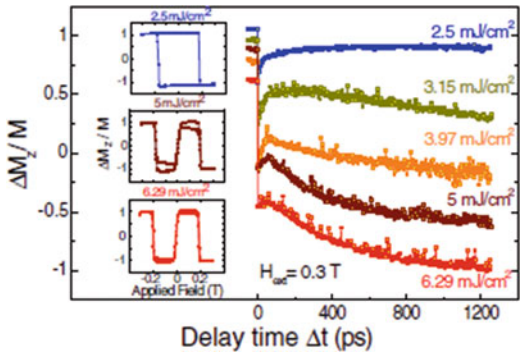

Fig. 4.12 The magnetization dynamics in the ferromagnetic $Gd_{22}Fe_{74.6}\,Co_{3.4}$ at a room temperature for different energies of the laser pumping [14]. Apt hysteresis loops are represented in the *inset*

and $m_{TM}(T)$ of the sublattices RE and TM of the ferrimagnetic GdFeCo. At enough laser radiation intensities, the mentioned heating can cause the magnetization reverse of the sublattice under an applied magnetic fields (which can be both an external field and the effective Faraday magnetic field) as it is visible in Fig. 4.12.

The mentioned magnetization reverse is related to the passage by opposite oriented magnetizations $m_{RE}(T)$ and $m_{TM}(T)$ across the magnetization compensation point T_M in which these magnetizations cancel each other. However, magnetization dynamics at a thermal relaxation can occur in a variety of ways in the dependence on the relation between the applied field H_{ex} and the temperature-dependent coercive field $H_C(T)$ in the temperature interval from the initial room temperature T_{room}, where $H_c(T_{room}) = H_c^{room}$ to the highest temperature T_{high}, where $H_c(T_{high}) = H_c^{high}$ is the condition of the ferrimagnetic remagnetization, as it is visible in Fig. 4.13.

Under the condition $H_{ex} > H_c^{room(high)}$, below the magnetization compensation temperature T_M the magnetization m_{RE} of the Gd sublattice is parallel to the magnetization $m_{TM}(T)$ of the FeCo sublattice. Under the impact of the laser-induced thermal pulse, a temperature increases above the point T_M and the magnetization $m_{TM}(T)$ becomes dominant and parallel to the applied magnetic field. After the pump laser, pulse at the temperatures above T_M the magnetization $m_{TM}(T)$ relaxes in the line its initial state. Subsequent cooling below the temperature T_M results in recovery the initial magnetization state of the ferrimagnetic nanolayer.

The magnetization dynamics is substantially different at $H_{ex} < H_c^{room}$ and $H_{ex} > H_c^{high}$, when the initial coercive field exceeds the applied magnetic field. In this case, the laser thermal pulse causes the remagnetization above the magnetization compensation point T_M, without return to the initial magnetization state under cooling system to the room temperature T_{room} (Fig. 4.13b(B)). This implies that at $H_{ex} < H_c^{room}$ after the remagnetization a thermal relaxation not changes the magnetization direction of the ferrimagnetic nanolayer.

The high remagnetization speed of the ferrimagnetic nanolayer under the laser-induced thermal pulses determine by the large effective gyromagnetic ratio γ_{eff} with a singularity at the angular momentum compensation temperature T_A of the

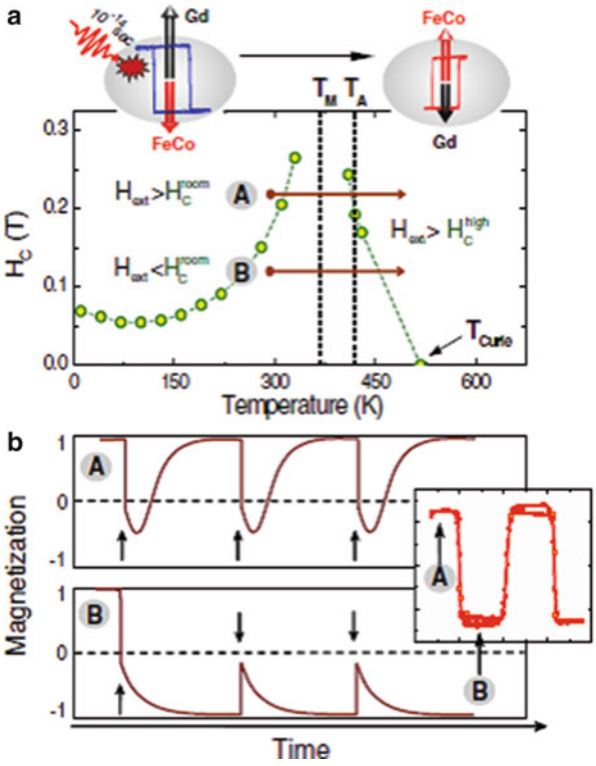

Fig. 4.13 (**a**) Temperature dependence of the effective coercive field H_C in the $Gd_{22}Fe_{74.6}$ $Co_{3.4}$ nanolayer. The *inset* shows schematically the ferrimagnetic system in an applied magnetic field below and above T_M. Depending on the strengths of the applied magnetic field, two different dynamic regimes can be distinguished: (*A*) for $H_{ex} > H_{room}$ and (*B*) for $H_{ex} < H_{room}$. (**b**) Qualitative description of the magnetization dynamics under pulsed laser irradiation

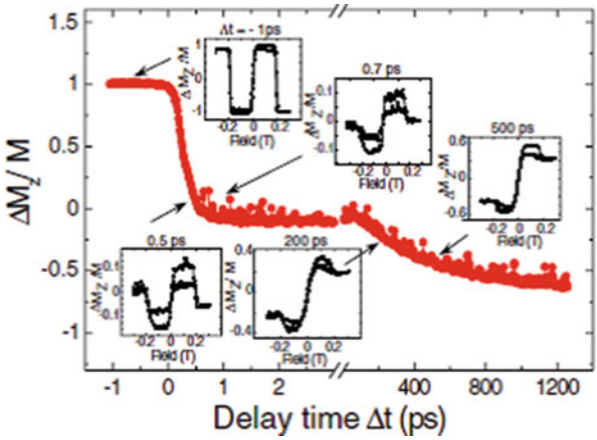

Fig. 4.14 Transient magnetization reversal dynamics measured for a pump fluence of 6.29 mJ/cm^2. *Insets* show hysteresis loops measured at distinct pump-probe delays. The loops demonstrate the magnetization reversal after about 700 fs

sublattices RE and TM. The magnetization dynamics for the ferrimagnetic $Gd_{22}Fe_{74.6}Co_{3.4}$ is characterized by the subpicosecond remagnetization, as it is visible in Fig. 4.14 representing results of the magneto-optical Faraday-based measurements [27].

The laser ultra-speed excitation of the magnetic moments of the atoms Fe in the sublattice FeCo occurs via conduction electrons. For the sublattice Gd, the 4*f* electrons give a main contribution in a magnetic atomic moment, whereas the contribution of 5*d*6*s* conduction electrons constitutes only 9 %. In this case, the ultra-speed laser excitation of the magnetic atomic moment occurs via 5*d* electrons, which characterized by the strong exchange interaction with the localized 5*d* electrons. The energy of this exchange couple corresponds to subpicosecond times, on which the mentioned remagnetization of the Gd sublattice.

The Fast Remagnetization Across Transient Ferromagnetic-Like State

The pulsed thermal impact of the layer radiation on the magnetization of the ferrimagnetic nanolayer occurs via the laser interaction with each of its sublattices. Therefore, in whole, the magnetization dynamics is determined by the magnetization dynamics of each of the ferrimagnetic sublattices. At the laser-induced excitation of the spin subsystem in timescales that correspond to an antiferromagnetic exchange interaction between sublattices (i.e., in the interval, 10–100 fs) the system is sometimes in a strong nonequilibrium magnetic with the disturbed equilibrium dynamic correlation between the sublattices. That implies the possibility of a disturbance of the equilibrium magnetization configuration at the magnetization relaxation of the ferrimagnetic system to an equilibrium state.

The lather-induced thermal demagnetization of each of the ferrimagnetic sublattices occurs over different periods. It is caused by pulsed laser heating transferring ferrimagnetic sublattices to the strongly nonequilibrium state with the disturbed exchange interactions. The first magnetic sublattice with the relatively greater demagnetization speed removes of the completely demagnetized state by the internal transient bias field H_{TR} of the second magnetic sublattice, with the relatively less demagnetization speed, that continues to the time point of the complete demagnetization of the second ferrimagnetic sublattice. In that time domain, magnetizations of both ferrimagnetic sublattices are parallel, i.e., the transient ferrimagnetic-like state realizes [15]. In the following time, the second magnetic sublattice removes from the demagnetized state by the transient bias field H_{TR}, of the relaxing antiferromagnetic exchange interaction, into the state with the antiparallel magnetization with respect to its initial state.

Such laser-induced remagnetization process can promote by the application of magnetic fields. For the linearly polarized pulsed laser radiation, the application of the external magnetic field H_{ex} assumes its time synchronization with the laser-induced thermal pulses. For the circularly polarized laser radiation, this problem avoids because the effective internal magnetic field H_F of the inverse magneto-optical Faraday effect is naturally synchronized with the laser-induced thermal pulses.

The above-mentioned laser-induced remagnetization observes in the ferrimagnetic nanolayer $Gd_{25}Fe_{65.6}Co_{9.4}$, as it is visible from measurement results of the

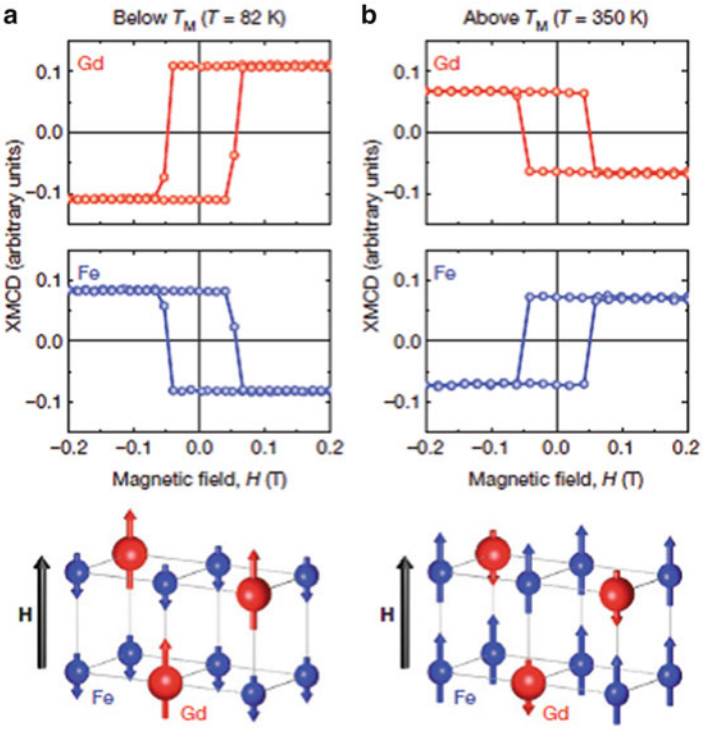

Fig. 4.15 Ferrimagnetic alignment of the Fe and Gd magnetic moments as measured by element-specific XMCD hysteresis. (**a**, **b**, *Top*) XMCD signals measured at the Fe and Gd absorption edges as a function of applied magnetic field below (**a**) and above (**b**) the magnetization compensation temperature (TM), demonstrating the ferrimagnetic alignment of the Fe and Gd magnetic moments. (**a**, **b**, *Bottom*) A generic ferrimagnet, showing the alignment of the magnetic moments of the constituent sublattices with respect to the external magnetic field, H

magnetization dynamics for m_{RE} and m_{TM}, based on the method of X-ray magnetic circular dichroism (XMCD), represented in Figs. 4.15 and 4.16 [4].

Under the action of the laser-induced thermal pulses temperature of the ferrimagnetic nanolayer passes across the magnetization compensation temperature T_{M}, the magnetizations of sublattices Gd and FeCo switch and a new magnetization configuration m_{RE} and m_{TM} becomes by the mirror image to their initial configuration (Fig. 4.15). Accordingly, hysteresis loops also pass in their mirror images, as it is visible in Fig. 4.15a. The magnetization dynamics of the ferrimagnetic sublattices characterize by different times of the laser-induced thermal demagnetization because of the distinct atomic structures of Gd and Fe sublattices. At the process of the laser-induced remagnetization, the thermal demagnetization of the sublattice RE (when $m_{\mathrm{RE}} = 0$) occurs at some time t_{RE} that is early than the time t_{TM} of the thermal demagnetization of the sublattice TM (when $m_{\mathrm{TM}} = 0$).

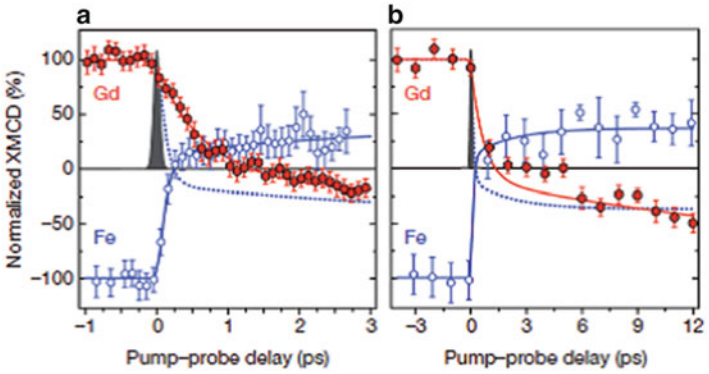

Fig. 4.16 Element-resolved dynamics of the Fe and Gd magnetic moments measured by time-resolved XMCD with femtosecond time-resolution

The time interval $t_{RE} \leq t \leq t_{TM}$ corresponds to the reverse of the magnetization m_{RE} into the transient ferromagnetic-like state with the magnetization, which is parallel to the magnetization m_{TM} of the sublattice TM. Such independent magnetization dynamics is related to the strong laser-induced perturbation of the exchange interaction between the ferrimagnetic sublattices.

Beginning from the time t_{TM} the relaxation of the antiferromagnetic exchange interaction between sublattices RE and TM results in the reverse of the magnetization m_{TM}, as it is visible in Fig. 4.16. Beginning with the time t_{TM} the relaxation of the antiferromagnetic exchange interaction between sublattices RE and TM results in the reverse of the magnetization m_{TM}.

The Laser-Induced Thermal Remagnetization of Ferrimagnetic Nanolayers

The magnetization dynamics of the ferrimagnetic under the laser-induced thermal pulses depends on the relation between the initial temperature T_{room} and the magnetization compensation temperature T_M. At $T_{room} < T_M$, the remagnetization includes the thermal demagnetization of the ferrimagnetic sublattices with subsequent transition of the magnetic state across the temperature T_M. Then, remagnetization activation assumes the presence of the applied magnetic field.

At $T_{room} < T_M$, the laser-induced thermal magnetization, dynamics retains the character properties of the passage across the transient ferromagnetic-like state and the relaxation of the antiferromagnetic exchange interaction between the ferrimagnetic sublattices. In the time interval $[t_1, t_2]$ between the time points t_1 and t_2 of the thermal demagnetization of the ferrimagnetic sublattices 1 and 2, the magnetic bias of the sublattice 1 occurs in the ferrimagnetic-like exchange field of the sublattice 2 that corresponds to the transient ferromagnetic-like state. In the time point t_2, the sublattice 2 undergoes of the effective magnetic bias of the antiferromagnetic

exchange interaction on the side of the sublattice 1 because of the relaxation of the antiferromagnetic exchange interaction between the sublattices. Thus, at the initial temperatures above the magnetization compensation temperature, the remagnetization of ferrimagnetic layer can occur only under the laser-induced thermal pulses without applied magnetic fields [17].

Such laser-induced thermal remagnetization mechanism is described an atomistic spin model [5]. Within this model, the energy of the spin system is described by the Hamiltonian

$$H = \sum_{i<j} J_{ij} \boldsymbol{S}_i \cdot \boldsymbol{S}_j + \kappa_{\mathrm{u}} \boldsymbol{S}_{j,z}^2, \tag{4.24}$$

where J_{ij} is the exchange energy between the nearest neighboring spins, $\boldsymbol{S}_i$ and $\boldsymbol{S}_j$ are unit vectors describing the spin directions for local sites i and the nearest neighbor sites j respectively, and κ_{u} is the uniaxial anisotropy constant. There are three distinct J_{ij} exchange interactions, arising from the ferromagnetic intrasublattice and antiferromagnetic intersublattice contributions.

The dynamics of each localized spin is described by the stochastic LLG equation of motion

$$\boldsymbol{S}_i = -\frac{\gamma}{(1+\lambda^2)\mu_{\mathrm{s}}} [\boldsymbol{S}_i \times \boldsymbol{H}_i + \lambda \boldsymbol{S}_i \times \boldsymbol{S}_i] \tag{4.25}$$

with internal field $\boldsymbol{H}_i = -\partial H / \partial \boldsymbol{S}_i + \varsigma_i(t)$, where thermal fluctuations are included as an addition noise term. Results of numerical computation magnetization dynamics for each sublattice of the model ferrimagnetic system are represented in Fig. 4.17.

As it is visible in Fig. 4.17, the remagnetization of the ferrimagnetic nanolayer accompanies every the laser-induced thermal pulse without applied magnetic fields. Turn out, that a field of 40 T is insufficient to prevent the remagnetization [5]. That argues about strong internal magnetic fields in ferrimagnetics.

The laser-induced thermal remagnetization of the ferrimagnetic $Gd_{24}Fe_{66.5}Co_{9.5}$ was observed with the help of the magneto-optical spectroscopy based on the Faraday effect and with the help of the photoemission electron microscope (PEFM) employing the XMCD. In the last case, the magnetization reverse for each of the sublattices observed [5].

Thus, purely lather-induced thermal remagnetization is possible for ferrimagnetic layers. Different speeds of the thermal demagnetization of the sublattices together with the relaxation of exchange interaction result in internal transient bias field causing the magnetization reversal. The mechanism does not require the presence of any other stimulus and occurs each time a laser pulse excites the magnetic sublattices of ferrimagnetic. Such laser-induced remagnetization occurs with starting temperature above and below the magnetization compensation temperature in GdFeCo continuous films and for microstructures with in-plane and out-plane magnetic anisotropy. The considered laser-induced thermal

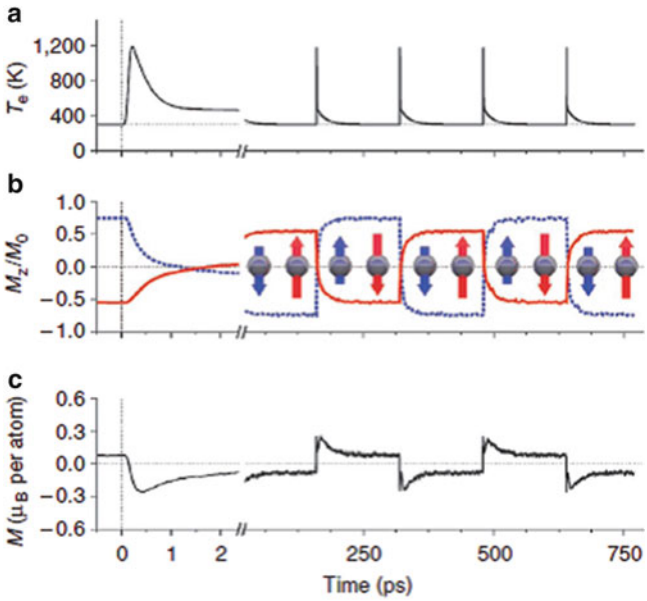

Fig. 4.17 Computed ultrafast thermally induced switching dynamics. (**a**) Evolution of the temperature of the electronic thermal bath during a sequence of five Gaussian pulses. (**b**) Computed time-resolved dynamics of the *z*-component of the magnetizations of Fe and Gd sublattices; Gd is represented by the *solid red line* and the Fe by the *dashed blue line*. The net magnetization is shown in (**c**). A spike in the temporal behavior of the total magnetization during the excitation is due to different dynamics of the magnetizations of the Fe and Gd sublattices

remagnetization may allow both higher recording densities and increased data rates, as the recording of a bit could be achieved on a timescale of picoseconds rather than the current nanoseconds.

4.1.4 The Laser-Induced Kinetic Effects

A Two-Band Model of the Laser-Induced Current of Particles

The laser-induced kinetic effects consist in the directed motion of particles caused by their momentum-selective excitation (via the Doppler Effect) and difference mobilities in ground and excited states (see [8–10]). The laser excitation on the laser frequency ω_0 occurs with particles whose velocity ($\mathbf{v}$) results in the Doppler-shifted frequency, $\omega = \omega_0 - (\mathbf{vq})$ ($\mathbf{q}$ is a photon wave vector) coinciding with the transition frequency $(E_2(\boldsymbol{k}) - E_1(\boldsymbol{k}))/\hbar$ between energy levels $E_1(\boldsymbol{k})$ and $E_2(\boldsymbol{k})$ of ground and excited quantum states ($\boldsymbol{k}$ is a particle wave vector, $\hbar$ is the Planck constant).

The momentum-selective excitation manifests itself via the selective excitation with respect to the motion with and against the laser beam. Subject to the laser

frequency ω_0, the excitation can occur with particles with velocities along and against the laser beam. If the laser frequency is less than the transition frequency, the excitation occurs at $(\mathbf{v}\cdot\mathbf{q})<0$ that corresponds to the opposing motion of particles and the laser beam. If the laser frequency is larger than the transition frequency, the excitation occurs at $(\mathbf{v}\cdot\mathbf{q})>0$ that corresponds to the parallel motion of particles and the laser beam.

The momentum-selective laser excitation can cause diffusive flows when the spatial distribution of the light intensity in solids is nonuniform. Similar to the LID such flows arise when the particle mobilities in the ground and excited states are different. Large diffusive flows of unexcited and excited particles can appear along and opposed to the intensity gradient, respectively. In many cases, the current due to LIDF may significantly exceed that to LID. The LIDF direction determines by the intensity gradient, which can be both parallel and normal to the laser beam. The LIDF effect is typically for metallic materials with the strongly light attenuation, which characterizes by light penetration of the order of few tens of nm.

The laser-induced kinetic effects realize both via the momentum-selective interband transitions of particles and via momentum-selective intra-particle quantum transitions. The mentioned laser-induced interband transitions occur with electrons and holes in metals, semiconductors (see [8]), and confinement semiconducting nanostructures with quantum wells or the Landau levels created by applying a magnetic field [10–14]. The mentioned momentum-selective intra-particle quantum transitions can occur with atoms and molecules in mixed gases [8, 34] resulting in the laser-induced currents.

Quantum states of the multiparticle system interacting with the laser radiation in the second quantization operators $\psi(\boldsymbol{x})$ in the binary interparticle approximation $w(\boldsymbol{x},\boldsymbol{y})$ are described by the full Hamiltonian

$$H(t)=\int \mathrm{d}\boldsymbol{x}\ \psi^{+}(\boldsymbol{x})h(\boldsymbol{x},t)\psi(\boldsymbol{x})+\frac{1}{2}\int \mathrm{d}\boldsymbol{x}\,\mathrm{d}\boldsymbol{y}\,w(\boldsymbol{x},\boldsymbol{y})\psi^{+}(\boldsymbol{x})\psi^{+}(\boldsymbol{y})\psi(\boldsymbol{x})\psi(\boldsymbol{y}) \quad (4.26)$$

with the one-body part

$$h(\boldsymbol{x},t)=-\frac{1}{2}\nabla^2-\sum_{j=1}^{N_0}w\left(\boldsymbol{x},\boldsymbol{x}_j\right)+u(\boldsymbol{x},t), \quad (4.27)$$

which contains both the background potential and the external potential $u(\boldsymbol{r},t)$ of a Fermi-particle in the laser field (a subscript j denotes a lattice cite). The laser-induced kinetics is described with the help of the nonequilibrium one-particle Green function $\hat{\boldsymbol{G}}$ satisfying the Kadanov–Baym quantum-kinetic equations (see [35, 36]), which for the assumed Fermi system can be represented in the matrix form

$$\left(\hat{\boldsymbol{L}}_0+\hat{\boldsymbol{L}}_1\right)\hat{\boldsymbol{G}}=\hat{\boldsymbol{I}},\quad \hat{\boldsymbol{L}}_0=\left\|L_{0,ij}(x,y)\right\|,\quad \hat{\boldsymbol{L}}_1=\left\|L_{1,ij}(x,y)\frac{\delta}{\delta\nu_j(y,t)}\right\|, \quad (4.28)$$

where $\nu_j(y,t)$ is the particle potential in the laser field. The matrix $\hat{\boldsymbol{L}}_0$ is the first order in the interaction w that corresponds to the Hartree–Fock approximation allowing for both the classical Hartree potential and the space-nonlocal exchange potential originating from the Pauli exclusion principle and antisymmetry of the wave functions. The matrix $\hat{\boldsymbol{L}}_1$ is differential matrix of the second and higher orders in w.

Due to the equality $\hat{\boldsymbol{L}}_1\left[\hat{\boldsymbol{G}}\hat{\boldsymbol{G}}^{-1}\right] = 0$, the (4.28) can be represented in the form

$$\left(\hat{\boldsymbol{L}}_0 + \hat{\boldsymbol{M}}\right)\hat{\boldsymbol{G}} = \hat{\boldsymbol{I}}\,, \tag{4.29}$$

with the self-energy matrix

$$\hat{\boldsymbol{M}} = -\hat{\boldsymbol{L}}_1\hat{\boldsymbol{G}}\left[\hat{\boldsymbol{L}}_0 + \hat{\boldsymbol{M}}\right], \tag{4.30}$$

where square brackets separate an expression on which the matrix operator $\hat{\boldsymbol{L}}_1$ effects. This matrix describes particle scattering both on a lattice and on itself.

In the considered two-band model system, with energies $E_i(\boldsymbol{k})$ in the ground $(i = 1)$ and excited $(i = 2)$ states, in which a particle (charge e) interacts with field $\boldsymbol{\varepsilon}$, the (4.29) in quasi-classical approximation can be reduced to the Boltzmann equations of the form [8]

$$\left(\frac{\partial}{\partial t} + \boldsymbol{v}_{i,\boldsymbol{k}} \cdot \nabla_{\boldsymbol{r}} + (e/\hbar)\boldsymbol{\varepsilon} \cdot \nabla_{\boldsymbol{k}} + \delta_{i,2}\Gamma_2\right) f_i(\boldsymbol{k})$$
$$= S_i(\boldsymbol{k}) + \delta_{i,2} I\sigma(\omega,\boldsymbol{k})(f_1(\boldsymbol{k}) - f_2(\boldsymbol{k})), \quad i = (1,2), \tag{4.31}$$

where $f_i(\boldsymbol{k})$ is the particle distribution function which depends on velocity $\boldsymbol{v}_{i,\boldsymbol{k}} = \hbar^{-1}\nabla_{\boldsymbol{k}}E_i(\boldsymbol{k})$, position vector $\boldsymbol{r}$, time t, and the collision integrals $S_i(\boldsymbol{k})$. In the band 2, this function depends on a light intensity I, an excitation cross section $\sigma(\omega,\boldsymbol{k})$, characterizing interband transitions, and the decay rate Γ_2 characterizing band to band $(2 \to 1)$ spontaneous relaxation and relaxation due to inelastic collisions. The collision integrals $S_i(\boldsymbol{k})$ determine by the dominant quasielastic collisions for which the collision-induced energy change is relatively small that corresponds to the condition of the large differences in the scattering rates of particles in the two bands. The quantity $\boldsymbol{\varepsilon}$ is the sum of the external laser field $\boldsymbol{\varepsilon}_0$ and the field $\boldsymbol{\varepsilon}_c = \nabla_{\boldsymbol{r}}\phi$ (ϕ is a laser-induced potential) due to the laser-induced nonuniform redistribution of charged particles inside the sample, i.e., $\boldsymbol{\varepsilon} = \boldsymbol{\varepsilon}_0 + \nabla_{\boldsymbol{r}}\phi$.

Assuming the small change of the particle distribution function $(f(\boldsymbol{k}) \approx f_1^0(\boldsymbol{k}))$, taking into account the momentum conservation low $\boldsymbol{v}_{1,\boldsymbol{k}}m_1 = \boldsymbol{v}_{2,\boldsymbol{k}}m_2$ and the relations

$$\int S_i(\boldsymbol{k})\boldsymbol{v}_{\boldsymbol{k}}\mathrm{d}\boldsymbol{k} = -\nu_i\boldsymbol{j}_i/e, \quad \boldsymbol{j}_i = e\int \boldsymbol{v}_{\boldsymbol{k}}(\boldsymbol{k})\mathrm{d}\boldsymbol{k}, \tag{4.32}$$

between the collision integrals $S_i(\boldsymbol{k})$ and the scattering rates ν_i, where $\boldsymbol{j}_i$ is the current density, one obtains the macroscopic momentum balance equation

$$\frac{\partial \boldsymbol{J}}{\partial t} + v_1 \sigma_c \cdot \nabla_{\boldsymbol{r}} \phi = \frac{\nu_1 m_1 - \nu_2 m_2}{m_1} \boldsymbol{j}_2 - \nu_1 \boldsymbol{J}, \quad \boldsymbol{J} = \boldsymbol{j}_1 + \boldsymbol{j}_2, \tag{4.33}$$

where the particle conductivity $\sigma_c = (1/3)\nu_1^{-1} e^2 \int v^2 \nabla_E f_0(k) \mathrm{d}\boldsymbol{k}$ potential difference ϕ is related to the nonequilibrium particle distribution. This equation describes the current, which is nonzero at the momentum-selective particle excitations ($\boldsymbol{j}_2 \neq 0$) and difference particle mobilities in the two bands ($\nu_1 m_1 = \nu_2 m_2$). Due to (4.33) steady-state currents in a closed and open circuits obey, respectively, relations

$$J = \frac{\nu_1 m_1 - \nu_2 m_2}{\nu_1 m_1} \boldsymbol{j}_2 \tag{4.34}$$

and

$$\boldsymbol{J}_{\mathrm{LID}} = \frac{\nu_1 m_1 - \nu_2 m_2}{\nu_1 m_1} \boldsymbol{j}_2 = \sigma_c \nabla_{\boldsymbol{r}} \phi_c. \tag{4.35}$$

In the last case, the LID current $J_{\mathrm{LID}} = ((\nu_1 m_1 - \nu_2 m_2)/\nu_1 m_1)\boldsymbol{j}_2$ is exactly compensated by the current $J_\phi = -\sigma_c \nabla_{\boldsymbol{r}} \phi_c$ caused by the electrostatic potential difference resulting from the laser-induced nonequilibrium distribution of particles in the sample.

Multiplying (4.31) at $i = 2$ by $\boldsymbol{v}_{\boldsymbol{k}}$ and integrating over $\boldsymbol{k}$, in the linear approximation one obtains the equation

$$(\Gamma_2 + \nu_2)\boldsymbol{j}_2 + \frac{1}{3} v^2 \nabla_{\boldsymbol{r}} \cdot N_2 = Ie \int \sigma\left(\omega', \boldsymbol{k}\right) \sigma(\omega, \boldsymbol{k}) f_1^0(\boldsymbol{k}), \quad N_2 = \int f_2(\boldsymbol{k}) \mathrm{d}\boldsymbol{k} \tag{4.36}$$

determining the current $\boldsymbol{j}_2$. Taking into account that the laser-induced particle concentration in the excited state, $N_2 = \eta I$ (η is a some constant), and substituting $\boldsymbol{j}_2$ from (4.34) into the expression (4.33), for the total current J result in the general expression $\boldsymbol{J} = \boldsymbol{J}_{\mathrm{LID}} + \boldsymbol{J}_{\mathrm{LIDF}}$, where the first term

$$\boldsymbol{J}_{\mathrm{LID}} = -\frac{\nu_1 m_1 - \nu_2 m_2}{\nu_1 m_1} \frac{Ie}{\Gamma_2 + \nu_2} \int \mathrm{d}\boldsymbol{k}\, \boldsymbol{v}_{\boldsymbol{k}} \sigma\left(\omega', \boldsymbol{k}\right) f_1^0(\boldsymbol{k}) \tag{4.37}$$

describes the laser-induced momentum-selective drift of particles, and the second term

$$\boldsymbol{J}_{\mathrm{LIDF}} = -\frac{\nu_1 m_1 - \nu_2 m_2}{\nu_1 m_1} eD_2 \eta \nabla_r I, \quad D_2 = \frac{1}{3}\frac{v_2^2}{\Gamma_2 + \nu_2}, \tag{4.38}$$

(D_2 is the diffusion coefficient for particles in the state 2) describes the laser-induced diffusive current caused by the nonuniform spatial distribution of the laser intensity and particle concentration gradients in states 1 and 2.

The collinearity of the LID current $\boldsymbol{J}_{\mathrm{LID}}$ with the light wave vector $\boldsymbol{q}$ implicitly contains in the excitation cross section $\sigma(\omega', \boldsymbol{k})$ with $\omega' = \omega - \boldsymbol{v_k q}$. The direction of the laser-induced diffusive current $\boldsymbol{J}_{\mathrm{LIDF}}$ determines by the gradient concentration so that these two currents mutually can be both parallel and antiparallel.

The excitation cross section is proportional to the pulse-frequency Fourier transform of the time correlation function of the photon-particle interaction operator $V(t)$ (see [8]), i.e.,

$$\sigma(\omega, \boldsymbol{k}) \propto \langle V(t)V(0)\rangle_{\omega,\boldsymbol{k}} \propto \mathrm{Im}\left[\left|V_{1,2}(\boldsymbol{k})\right|\left(E_1(\boldsymbol{k}) - E_2(\boldsymbol{k}) - \hbar\omega' - i\Gamma\right)^{-1}\right] \tag{4.39}$$

Within the two-band electron model with a homogeneous broadening ($E/\hbar \gg \Gamma \gg \boldsymbol{v_k q}$) in the second approximation in $\boldsymbol{v_k q}$

$$\sigma\left(\omega', \boldsymbol{k}\right) \approx \sigma(\omega, \boldsymbol{k}) - \boldsymbol{v_k q}\frac{\partial\sigma(\omega, \boldsymbol{k})}{\partial\omega}, \tag{4.40}$$

where with satisfactory accuracy it can be assumed that $\sigma(\omega, \boldsymbol{k}) = \delta(E_1(\boldsymbol{k}) - E_2(\boldsymbol{k}) - \hbar\omega)$. Thereafter, the transitions between two bands are restricted to the surface of constant interband energy: $\Sigma(\boldsymbol{k}) = E_2(\boldsymbol{k}) - E_1(\boldsymbol{k}) - \hbar\omega = 0$

Then, substitution (4.40) into (4.37) results in the general expression [8]

$$\boldsymbol{J}_{\mathrm{LID}} = -\chi\frac{\boldsymbol{q}}{q}\frac{\nu_1 m_1 - \nu_2 m_2}{\nu_1 m_1}(ev_0)\frac{qv_0}{\Gamma_2 + \nu_2}\frac{I}{\hbar c}\frac{\partial\zeta}{\partial\omega}, \quad \chi = \mathrm{sgn}(\boldsymbol{v_k}\cdot\boldsymbol{q}), \quad \zeta = \hbar c\int \mathrm{d}\boldsymbol{k}\,\sigma(\omega, \boldsymbol{k})f_1^0(\boldsymbol{k}) \tag{4.41}$$

describing the LID current directed with or against the laser beam in the dependence on the sign (+, −) of the particle velocity projection on the photon wave vector $\boldsymbol{q}$. Here, $v_0^2 = \int \mathrm{d}\boldsymbol{k}\,\boldsymbol{v}_{\boldsymbol{q}}^2\sigma\left(\omega', \boldsymbol{k}\right)f_1^0(\boldsymbol{k}) / \int \mathrm{d}\sigma(\omega, \boldsymbol{k})f_1^0(\boldsymbol{k})$ defines v_0 as characteristic velocity projection on the wave vector which lies on the surface $\Sigma(\boldsymbol{k}) = E_2(\boldsymbol{k}) - E_1(\boldsymbol{k}) - \hbar\omega = 0$. Features of the LID current depend on the particular form of the energy particle spectrum entering into the expression for the excitation cross section $\sigma(\omega, \boldsymbol{k})$.

Typical feature of LID electron currents in the two-band systems can be described in the finite-gap separable potential model (see [37]), for which the dispersion relations for the conduction bands have the form

$$E(\boldsymbol{k}) = \sum_{i=1}^{3} E(k_i), \quad E(k_i) = \frac{\hbar^2}{2mx_0^2}\wp\left(z(k_i)\right), \\ k_i = \varsigma(z_i) - \frac{\eta'}{\omega'} z_i, \quad z_i \in \left\{\left[\omega', \omega + \omega'\right], [\omega, 0]\right\}, \tag{4.42}$$

where a subscript i denotes ith component in the Cartesian coordinate system, $\wp(z) = \wp\left(z\middle|\omega, \omega'\right)$ is the Weierstrass function with real and imaginary periods ω and ω' ($\mathrm{Im}\,\omega' > 0$), respectively; $\varsigma(z)$ is the Weierstrass zeta function [38] which determines via the Weierstrass function by the relation $\wp(z) = -\varsigma'(z)$, in addition $\eta' = \varsigma(\omega')$, $\eta = \varsigma(\omega)$. The first permitted band of the spectrum is described by (1.16) in the variation interval $z_i \in \left[\omega', \omega + \omega'\right]$ that corresponds to the domain of the wave vector variation $k_i \in \left[0, \pi/2\middle|\omega'\middle|\right]$. The second permitted band of the spectrum is described by (4.42) in the domain of variation $z_i \in [\omega, 0]$ that corresponds to the domain of the wave vector variation $k_i \in \left[\pi/2\middle|\omega'\middle|, \infty\right]$. The gap in the band spectrum is equal to the difference $E\left(k_i(z)_{z=\varpi}\right) - E\left(k_i(z)_{z=\omega+\omega'}\right)$, i.e., it occurs in points $k_i \in \pi/2\middle|\omega'\middle|$ of the band spectrum.

Substitution (4.42) into the expression for the excitation cross section $\sigma(\omega, \boldsymbol{k})$ (4.39) permit to obtain the dependence of the LID current (4.41) on parameters of the band spectrum, specifically, on the parameters $\tau = \omega/\omega'$ characterizing the spectral gap for system with tetragonal symmetry. In the case of the near-free-electron approximation, the LID current in the two-band systems with arbitrary symmetry can consider within the two-orthogonalized-plane-wave approximation with dispersion relations (see [8])

$$E_{1,2}(\boldsymbol{k}) = \beta\left[(\boldsymbol{k} + \boldsymbol{G})^2 + k^2\right] \mp \left\{\beta^2\left[(\boldsymbol{k} + \boldsymbol{G})^2 + k^2\right]^2 + 4\left|V_{\mathrm{G}}\right|^2\right\}^{1/2}, \tag{4.43}$$

where $\beta = \left(\hbar^2/2m\right)$ and $\boldsymbol{G}$ is the reciprocal-lattice vector which generates the second band, and V_{G} is the Fourier component of the pseudopotential ($2V_{\mathrm{G}}$ is the energy gap). Then, substituting (4.43), the general expression (4.41) can be converted to the form

$$\boldsymbol{J}_{\mathrm{LID}} = \frac{\boldsymbol{q}}{q}\frac{\nu_1 m_1 - \nu_2 m_2}{\nu_1 m_1}(ev_0)\frac{qv_0}{\Gamma}\left[\frac{I\varsigma(\omega)}{(\Gamma_2 + \nu_2)}\right]L(\hbar\omega), \quad \zeta = \int \mathrm{d}\boldsymbol{k}\,\sigma(\omega, \boldsymbol{k}) f_1^0(\boldsymbol{k}), \tag{4.44}$$

where $\varsigma(\omega) \propto 1/\omega^4$. The function $L(\hbar\omega)$ determines the spectral dependence of the LID current, which characterizes by a peak-like dramatic dependence on the photon energy $\hbar\omega$ within a vicinity of the energy gap $2V_G$ and by a weak dependence outside of this vicinity. This function can take on both positive and negative values, suggesting that the LID current can be directed with or against the laser beam subject to signs plus or minus of the difference $\omega - V_G/\hbar$, respectively.

The laser-induced kinetic effects are valid for a range of materials including semimetals, semiconductors, insulators, and metals. The potential difference $\Delta\phi$ is proportional to the LID current and the sample resistivity R, i.e., $\Delta\phi \propto J_{LID}R$, where $R \sim 1/(N_0 e\mu)$, where N_0 and μ are the conduction electron concentration and the particle effective mobility, respectively. Since the LID current depends on the number of selectively excited particles that the potential difference can be different independently of the resistivity both in metals and semiconductors and isolators.

The laser-induced spin-polarized current, transporting spin magnetic moments in magnetic junctions leading to the magnetic switching, is related to the LID kinetic effect at the laser frequencies corresponding to the momentum-selective excitations with and interband transitions. If laser frequencies do not satisfy the mentioned conditions of the LID kinetic effect, the laser-induced spin-polarized currents can be caused by radiation pressure, which related to photon momentum transfer.

In an open circuit, these kinetic effects can be manifested via accumulation of particles on output or input, with respect to the laser beam, faces of a radiated sample. This result in changes of optical properties of the irradiated systems will be considered below.

Influence of Laser Irradiation on Optical Properties of Crystals

The laser-induced current in the semiconductor in an open circuit can lead to the high concentration of nonequilibrium electrons on its output surface, beside such obvious fact as the potential difference. It causes the significant change of the refractive index (n) in the area of the outgoing laser beam [39] that is given by

$$\Delta n_N(\omega) = -\frac{2\pi e^2}{n_0 m_e \omega^2} N^2 \tag{4.45}$$

where e, m_e, and N are a charge, effective mass, and the concentration of nonequilibrium conduction electrons, respectively; ω and n_0 are the frequency and the refractive index of the laser radiation.

The photon drag effect in two-photon absorption of laser radiation in undoped semiconductors with energy gap E_g higher than the laser photon energy $\hbar\omega < E_g < 2\hbar\omega$ causes a range of effects. The most interesting of these is the violation of total internal reflection (TIR) and high-speed scanning of a laser beam in the corner φ on the output of a semiconductor for high-power laser pulses (Fig. 4.18).

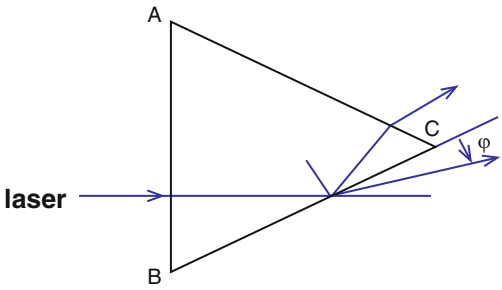

Fig. 4.18 Scheme of the violation of total internal reflection and scanning pulse laser beam from a ruby laser in CdS single crystal because of the photon drag effect

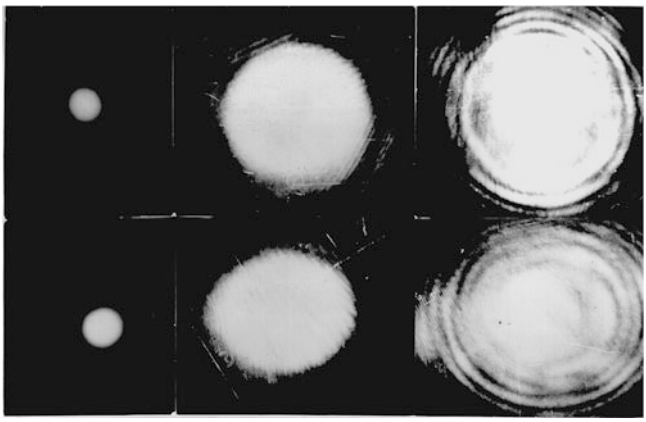

Fig. 4.19 Change of the cross-section of a Gaussian beam from a ruby laser (TEM_{00} $\tau_i = 15$ ns) after CdS crystal with defocusing for radiation with different polarizations: ($\overline{E} \perp \overline{C}$—*top*) and ($\overline{E} \| \overline{C}$—*bottom*) with increasing intensity: 1—$I = 10^5$ W/cm^2, 2—$I = 40$ MW/cm^2, 3—$I = 120$ MW/cm^2

According to our experimental data [40, 41] in single crystals of CdS and ZnSe, the scan angle for nanosecond and picosecond pulses reached 3°–7°.

In crystals with uniaxial anisotropy, the laser-induced kinetic effect leads to an elliptical defocusing of laser beams [41, 42] (Fig. 4.19). A significant decrease of the refractive index in the laser beam escape from a semiconductor due to the laser-induced kinetic effect also results in features in the destruction of the semiconductor [41]. Usually, the laser-induced destruction of transparent material starts with its output surface. This is caused by the difference of the interference conditions for laser radiation [43] on the input and output surfaces of the sample. Due to interferential, the intensity at the output surface I_1 is higher than the intensity at the input surface I_0. A significant decrease of the refractive index in the laser beam escape from a semiconductor due to the photon drag effect also results in features in the destruction of the semiconductor [41]. Usually, the laser-induced destruction of transparent material starts with its output surface. This is caused by the difference of the interference conditions for laser radiation [43] on the input and output surfaces

of the sample. Due to interferential, the intensity at the output surface I_1 is higher than the intensity at the input surface I_0

$$\frac{I_1}{I_0} = \frac{4n^2}{(n+1)^2}. \tag{4.46}$$

Our experimental researches have shown [41, 44] that the destruction of the semiconductors of the group A_2B_6 by nano- and picosecond laser pulses under the condition of two-photon absorption, when $h\nu < E_g < 2h\nu$ always destroyed only the input surface. When $E_g > 2h\nu$, then the output surface is destroyed.

Above-mentioned effects are nonequilibrium. They exist during action of the laser pulse and after its termination (except for surface destruction) relax rapidly. Besides, the spatial charge of nonequilibrium electrons on the output semiconductor surface causes an electrical potential. This potential can cause the LID of charged impurity atoms and native defects of the semiconducting crystal lattice [45, 46]. LID absorbing impurity atom is most easily observed in semiconductor crystals with very low absorption coefficient.

In semiconductors, the activation energy of motion of single impurity atoms is small enough (for the atom between lattice nodes $W_a = 0.1\,\text{eV}$ and for a vacancy $W_a = 0.2 - 0.4\,\text{eV}$), and their mobility μ_i strongly increase with increasing temperature T [47]

$$\mu_i = A \exp\left(-\frac{W_a}{kT}\right), \tag{4.47}$$

where k is the Boltzmann constant, A is a coefficient of proportionality.

To estimate the potential energy of electrostatic interaction of charged impurity atom with the field of the nonequilibrium spatial charge W_p, use the formula for the current density j, generated by the photon drag effect (see [41])

$$j = -e\alpha I \frac{n_0 \tau_p \gamma}{m_e c}. \tag{4.48}$$

Here, e and m_e are the charge and effective mass of an electron; c is the velocity of light; n_0 is the refractive index of the semiconductor; I, ω, and α are the intensity, frequency, and absorption coefficient of laser radiation. The quantity τ_p is averaged electron momentum relaxation time in the conduction band, γ is numerical factor less than unity, which defines the momentum transfer of photons by electrons.

For the case of two-photon absorption with the coefficient β, this formula can be written as

$$j = -e\beta I^2 \frac{n_0 \tau_p \gamma}{2 m_e c} \tag{4.49}$$

Hence, for the nonequilibrium electrons in the output of the laser beam, we obtain the expression

$$N_{\mathrm{p}} \approx \left(\alpha I \frac{n_0 \tau_{\mathrm{p}} \tau_{\mathrm{e}} \gamma}{m_{\mathrm{e}} c}\right)^{\frac{3}{2}} \tag{4.50}$$

The potential energy of electrostatic interaction of the charged impurity atom with the field of photon drag of electrons W_{p} can be written as

$$W_{\mathrm{p}} \approx \left(\alpha I \frac{n_0 \tau_{\mathrm{e}} \tau_{\mathrm{p}} \gamma}{m_{\mathrm{e}} c}\right)^{\frac{3}{2}} \frac{e^2 S_0 r_0}{\varepsilon r}, \quad W_{\mathrm{p}}^{'} \approx \left(\beta I^2 \frac{n_0 \tau_{\mathrm{p}} \tau_{\mathrm{e}} \gamma}{m_{\mathrm{e}} c}\right)^{\frac{3}{2}} \frac{e^2 S_0 r_0}{\varepsilon r} \tag{4.51}$$

where S is the sectional area of the laser beam; r_0 is thickness of the spatial localization of the electron charge; $r = (5 - 10) r_0$ is the distance between the charge of electrons and ionized impurity atom; ε is dielectric constant. For $I = 500\,\mathrm{W/cm^2}$, $a = 0.05\,\mathrm{cm^{-1}}$, $\beta = 0.01\,\mathrm{W^{-2}cm^2}$, $\tau_{\mathrm{e}} = 10^{-10}$ s and $\tau_{\mathrm{p}} = 10^{-11}$ s, we obtain for the energy of electrostatic interaction high enough values and $W_{\mathrm{p}} \approx 0.44\,\mathrm{eV}$.

Today has been established experimentally [48–50] that the penetration depth of the impurity atoms from the surface into the solid bulk far exceeds the amount caused by thermal diffusion. To explain the experimental facts, it is used to transport mechanisms related to shock and thermal waves caused by very rapid laser heating of the near-surface layer [49–52]. However, virtually the photon drag effect was ignored.

We have observed the impurity drift in the crystals CdS and ZnSe in the field of the powerful CO_2-laser [40, 45]. The CO_2-laser irradiation causes various changes in the spectra of low-temperature impurity luminescence on the input and the output surface of the crystals. On the input surface increases the amplitude of the radiation lines I_2 of bound excitons and decreases its half. In addition, there is a new broad luminescence emission band Q, which is associated with the glow on the complexes of defects. On the output surface almost disappears luminescence line I_1 associated with the first phonon replica of free-exciton line, as well as decreases the amplitude and greatly expanded the band luminescence of bound excitons I_2 (Fig. 4.20).

Besides, for some group of ZnSe single crystals with absorption coefficient of the CO_2-laser $\alpha = 0.05 - 0.01\,\mathrm{cm^{-1}}$, this results in the appearance of spots in the output surface, which consist of individual dark spots (Fig. 4.20). The contour spot coincides with the contour of the cross section of the laser beam on any surface of the crystal, and it contained a lot of carbon. Mass-spectrometric measurements showed that after irradiation of ZnSe by the CO_2-laser, the carbon concentration in the output surface is increased more than the order.

Low photon energy and intensity ($I \leq 500\,\mathrm{W/cm^2}$) radiation, virtually eliminate the process of direct generation of point defects by the CO_2-laser radiation in the crystal bulk. Crystal is being heated to the temperatures 100–160 °C. The generation of defects in the near-surface region should not result to large differences of input and output surfaces. The temperature difference between input and output

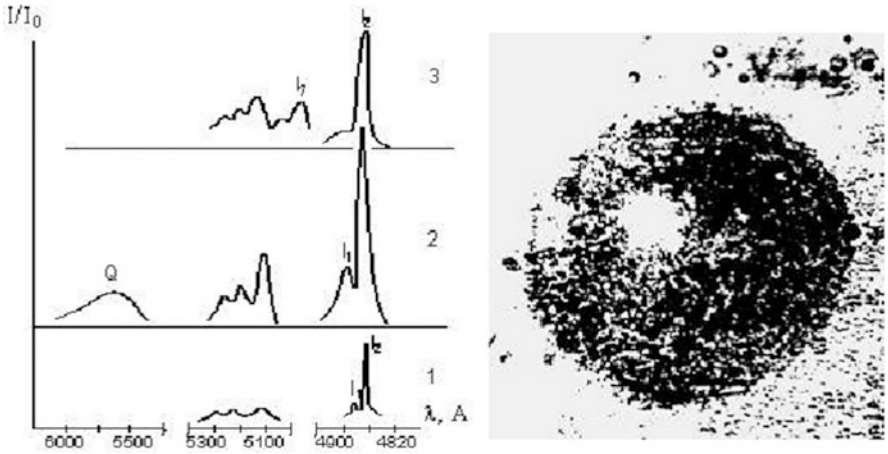

Fig. 4.20 Luminescent spectra of the CdS crystal at a temperature of 4.2 K and a photo of a *dark spot* on the output surface of ZnSe crystal after irradiation a continuous CO_2 laser with an intensity of 200 MW/cm^2. *1* initial spectrum, *2* and *3*—luminescence spectra after 10 min irradiation of CO_2 laser: *2*—spectrum of the input and the *3*—spectrum with the output of the crystal surface

surfaces during irradiation was less than a half degree. The obtained results give us reason to believe that photon drag of electrons under CO_2-laser radiation causes the drift of impurity carbon atoms ionized by laser radiation.

The described above results uniquely demonstrate that the laser-induced kinetic effects should play a significant role for doping of semiconductor crystals by laser radiation, especially for the case of thin semiconductor films. Thin nanofilms (with think $h < 100$ nm) almost uniformly are heated by laser radiation because the LID of impurity atoms caused by the temperature gradient is impossible. However, although for absorbing films on a transparent substrate, a thermal wave can cause the transfer of atoms from the film to the substrate. For multilayer nanofilms, the thermal wave can provide the atom transport from one layer to another in the direction of the substrate with magnetic impurities. Under heating the absorbing film by the short laser pulses to temperatures, much below than melting point the influence of the heat wave on the doping of the near-surface should be much smaller than the influence of the photon drag effect.

Our researches [53, 54] of the films dye-bismuth-dye and SiC–Bi–SiC, consisting of three sequentially deposited nanolayers with a thickness of individual layers 6–8 nm, showed that after irradiation of such a structure by the laser pulses bismuth atoms move along the laser beam. In these films, the layers of the semiconductor and the phthalocyanine dye are virtually transparent to laser light, and a layer of bismuth absorbs strongly. After the action of the single laser pulse, which causes no visible damage, there is an asymmetry in the distribution of bismuth atoms (Fig. 4.21).

The distribution of bismuth atoms in the output semiconductor surface or the dye was markedly different from the original. At the same time, the distribution of

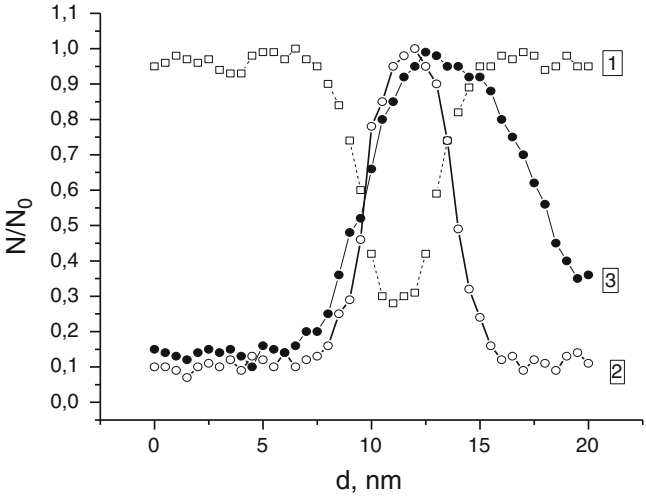

Fig. 4.21 Changes in the distribution of the concentration of bismuth in a three-layer film of phthalocyanine dye-bismuth-dye after the pulse irradiation ($\tau_i = 20$ ns) by the ruby laser: *1*—the carbon concentration, *2*—the concentration of bismuth prior to the irradiation, *3*—the bismuth concentration after irradiation

bismuth atoms in the input layer is changed very little. In order to eliminate the influence of the heat wave directed from the film to the substrate, we irradiated the film by nanosecond laser pulses from the film and the substrate. Changes in the distribution of bismuth atoms in these two cases are practically identical. The bismuth concentration in the output layer increases or one almost no change in the input layer of the semiconductor or dye.

Based on these results, it can be argued that a powerful laser pulses cause the drift of the bismuth atoms in the semiconductor layer or the dye. The reason for this drift is the electrostatic interaction of ionized atoms of bismuth with the field of nonequilibrium spatial charge of electrons, which is created in the output of the laser beam because of the photon drag effect. Possibility of electrostatic interaction of bismuth ions with the field of space charge of electrons generated by laser radiation is confirmed by photoelectric measurements.

To measure the electric field, which can occur in the investigated film structure, a thin transparent conductive film of indium oxide was sprayed on the film of a semiconductor or dye. The nanosecond pulsed laser irradiation of this structure causes a small potential difference (a few microvolts) that confirms the electron drift due to the photon drag effect.

The above-considered results of experimental studies show that the photon drag effect plays an important role in the doping of semiconductor materials and must be taken into account and be used for doping of semiconductor thin films. High-speed doping process, the small temperature heating, and rapid cooling of thin films using short laser pulses allows us to obtain a high homogeneity of doping thin-film materials. This must help for solving the problem of producing magnetic

semiconductors with high uniformity of impurity distribution. The laser doping technology for thin films assumes a further development, but already today, we can speak about its prospects.

4.2 Magnetization of Nanostructures with a Rashba Effect

The field-induced remagnetization in heterogeneous metal magnetic nanostructures can be realized both via laser-induced effective internal bias fields of the inverse magneto-optic Faraday effect, a spin-transfer torque (STT) effect, a nonequilibrium spin-injection effect, the effect of transient magnetic states caused by different temperature demagnetization rates of magnetic sublattices in combination with their exchange interaction relaxation and a spin–orbit interaction. The large enough spin–orbit interaction at broken spatial inverse symmetry in two-dimensional electron subsystems can result in the effective internal magnetic Rashba field [55] with spin splitting of energy band and polarized surface states of electrons (the Rashba effect).

In magnetic two-dimensional systems with an electron current such spin–orbit Rashba field in combination with *s*–*d*-exchange, interaction between spin-polarized conduction electrons and localized magnetic moments, can result in their remagnetization [56] (a current induced spin–orbit torque effect). This effect is realized both via the direct pulsed impact of an electric field and via the indirect impact of the pulsed laser-induced electron current. In two-dimensional magnetics the fast remagnetization can be directly exerted by electric field through the spin-orbit Rashba magnetic field together with the exchange interaction between spin-polarized electrons and localized spins. The important role in the laser-induced surface remagnetization can belong to the deformation of electron state distribution. The laser-induced remagnetization can be realized via the direct laser impact on the electron states distribution with subsequent change in a surface magnetic anisotropy.

The internal effective bias fields of the spin–orbit and exchange interactions can provide the high-speed remagnetization of magnetic nanostructures with reduced energy consumptions at room temperature. Therefore, the remagnetization opens new opportunities to integrate magnetic functionalities into electronic circuits and can be implicated in elements of magnetic data recording and read-out.

4.2.1 Features of the Influence of Spin–Orbit Interaction on Surface States

For infinite crystals, the electronic band structure is related to the motion of an electron in an effective periodic potential. For finite crystals, the boundary

conditions caused by the crystal surfaces result in the occurrence of discrete surfaces states. In the framework of the density functional theory, with an effective one-particle potential, the complex values of wave vector $\boldsymbol{k}$ correspond to the surface quantum states (real values of $\boldsymbol{k}$ correspond to infinite crystals). The energies of the surface states lie inside the region for real $\boldsymbol{k}$. Their wave functions damp in the direction of the vacuum and damp in an oscillatory way inside the crystal.

The spin–orbit interaction, that is the coupling of the orbital angular momentum and the electron spin, manifests itself via the electronic structure of solids in various ways including the magneto-crystalline anisotropy in magnetics. The last makes the origin of the magnetic dichroism in X-ray absorption, and Rashba effects in the two-dimensional systems with broken inversion symmetry. In two-dimensional condensed matter systems (heterostructures and surface states), the combination of atomic spin–orbit coupling and asymmetry of the one-particle potential in the direction perpendicular to the two-dimensional plane causes the Rashba momentum-dependent spin splitting of energy bands. This effect can drive a wide variety of novel physical phenomena even when it is a small correction to the band structure of the two-dimensional metallic states. One is probed by angle-resolved photoelectron spectroscopy (ARPES) [57–59].

The characteristic features of the Rashba spin–orbit effect, which can show up both in nonmagnetic and in magnetic heterostructures and surface states, are described in the standard model of an isotropic two-dimensional electron gas (2DEG). In this model, the effective magnetic Rashba field of the spin–orbit interaction arises in the rest frame of the moving electron and results in a Zeeman spin splitting. This field results in a unique spin topology of the electronic states both at interfaces of heterostructures and metal surfaces of at nonmagnetic and magnetic metal surfaces. The potential gradients for heterostructures and metal surfaces are determined by a band-banding and an image-potential barrier, respectively.

The relativistic spin–orbit interaction and corresponding features of quantum states, the energy band structure, and the spin polarization of electrons in an periodic electric field are naturally described by the Dirac equation for the four-component vector function (Ψ)

$$i\hbar\frac{\partial\Psi}{\partial t} = H_{\mathrm{D}}\Psi \tag{4.52}$$

with the Hamiltonian

$$H_{\mathrm{D}} = \boldsymbol{\alpha}\cdot\mathbf{p}c + \beta mc^2 + V. \tag{4.53}$$

Here $\boldsymbol{\alpha} = \|(i-j)\sigma\|$ $(i,j=(1,2))$, where σ is the Pauli vector-matrix; $\mathbf{p}$ is a momentum operator; c is a light speed; the second-order matrix $\beta = \left\|(-1)^i\delta_{ij}I\right\|$, $\left(I = \left\|\delta_{ij}\right\|\right)$; m is the electron mass; V is the operator of the electron-field

interaction; stationary states are described by the wave function of the form $\Psi = (\varphi, \chi)^T \exp(-i\varepsilon t/\hbar)$, where φ and χ are two-component vector-functions.

Then, stationary solving for (4.52) is reduced to solving the matrix equation

$$\begin{pmatrix} E' - V & -c\sigma\mathbf{p} \\ c\sigma\mathbf{p} & E' + 2mc^2 - V \end{pmatrix} \begin{pmatrix} \varphi \\ \chi \end{pmatrix} = 0, \tag{4.54}$$

$$E' = \varepsilon - mc^2. \tag{4.55}$$

Hence, in the second-order approximation in v/c (v is a particle speed) it follows that

$$\chi = \left(1 - \frac{E' - V}{2mc^2}\right) \frac{\sigma\mathbf{p}}{2mc} \varphi, \tag{4.56}$$

Then, eliminating the function χ from (4.54) together with a normalization condition for φ give the stationary equation $E'\varphi = H\varphi$ with the Hamiltonian

$$H = \frac{\mathbf{p}^2}{2m} + V(\boldsymbol{r}) + \frac{\hbar\sigma}{4m^2c^2}[(\operatorname{grad} V) \times \mathbf{p}] + \frac{\left[E' - V(r)\right]^2}{2mc^2} - \frac{\hbar^2}{8mc^2} \nabla^2 V(r), \tag{4.57}$$

where the third term represents the operator the spin–momentum interaction (H_{SO}) for the electron in the nonuniform electric potential $A_0 = V/e$ (e is the electron charge).

For the centrosymmetrical electric field, when $\operatorname{grad} V = \frac{\boldsymbol{r}}{r}\frac{\partial V}{\partial r}$, this interaction takes the form of the spin–orbit interaction, $H_{\mathrm{SO}} = \gamma_{\mathrm{SO}}(\boldsymbol{sL})$ with the parameter $\gamma_{\mathrm{SO}} = \frac{\hbar}{2m^2c^2}\frac{1}{r}\frac{\mathrm{d}V(r)}{\mathrm{d}r}$, where $\boldsymbol{s} = \frac{\hbar}{2}\sigma$ and $\boldsymbol{L}$ are spin and orbital moments, respectively. Taking into account the expression $\mu = \mu_{\mathrm{B}}\boldsymbol{s}$ for the spin magnetic moment, where $\mu_{\mathrm{B}} = e\hbar/(2mc)$ is the Born magneton, the spin–orbit operator H_{SO} can be rewritten in the form

$$H_{\mathrm{SO}} = (\boldsymbol{\mu} \cdot \boldsymbol{B}_{\mathrm{SO}}), \quad \boldsymbol{B}_{\mathrm{SO}} = \frac{1}{mc}[\boldsymbol{E} \times \boldsymbol{p}] \tag{4.58}$$

corresponding the interaction between the spin magnetic moment $\boldsymbol{\mu}$ and the effective magnetic field $\boldsymbol{B}_{\mathrm{SO}}$. This magnetic field, arising in the particle's frame, effectively couples the spin to the particle momentum, exciting the spin aligning along the field $\boldsymbol{B}_{\mathrm{SO}}$. The spin–orbit interaction can cause a spin polarization and the spin splitting in energy.

In the two-dimensional electron system of condensed matter with the broken symmetry, the spin–orbit interaction of the one-particle potential causes the effective magnetic field ($\boldsymbol{B}_{\mathrm{R}}$) (known as the Rashba effect) inducing the electron spin polarization and the momentum-dependent splitting in the electron band spectra. In general, the spin–orbit interaction parameter α_{R} in this case depends on physical

properties of the system. It usually exceeds the mentioned parameter α_{SO} in few orders.

In the two-dimensional free-electron condensed model, the electric potential A_0 in z-direction confines electrons to the surface. Then, from the general expression (4.53) the Hamiltonian of the system takes the form

$$H = \frac{\hbar^2}{2m}\left(\partial_x^2 + \partial_y^2\right) + \alpha_R\left(\sigma_x\partial_y - \sigma_y\partial_x\right), \tag{4.59}$$

where the first term is the operator of a free electron motion in the plane xy, the second term (denoted as H_{RSO}) is the Rashba spin–orbit interaction operator in the plane xy with the parameter $\alpha_R \sim \operatorname{grad} V = E$. Then, two-component wave functions of the stationary wave function $\Psi = (\varphi_1, \varphi_2)^T \exp i\left(\omega t + k_x x + k_y y\right)$ (k_x and k_y) are components of the planar wave vector $\boldsymbol{k}_{||}$ obeys the matrix equation

$$\begin{pmatrix} \varepsilon_k - E & -i\alpha_R k_- \\ i\alpha_R k_+ & \varepsilon_k - E \end{pmatrix}\begin{pmatrix} \varphi_1 \\ \varphi_2 \end{pmatrix} = 0, \quad k_\pm = k_x \pm ik_y. \tag{4.60}$$

Hence, from the existence condition of nonzero solutions we can obtain the expression

$$E_{1_2}(k) = \varepsilon_k \pm \alpha_R k = \frac{\hbar^2}{2m}\left(k \pm \frac{m\alpha_R}{\hbar^2}\right)^2 - \frac{m\alpha_R^2}{2\hbar^2}, \quad \varepsilon_k = \frac{\hbar^2 k^2}{2m}, \tag{4.61}$$

describing the splitting two-dimensional electron band spectrum. The last consists the two branches caused by spin splitting under the effective Rashba field $\boldsymbol{B}_{SO} = \frac{1}{mc}\left[\boldsymbol{E}_z \times \boldsymbol{p}_{||}\right]$ of the spin–orbit interaction.

It is returned out that spin polarizations of electrons with energies belonging to the different branches have opposite orientations. Indeed, the normalized spinor functions $(\varphi_1, \varphi_2)^T$ at the eigenvalues $E_1(k)$ and $E_2(k)$ is transformed to the spinor functions $(1, ik_+/k)^T/\sqrt{2}$ and $(ik_+/k, 1)^T/\sqrt{2}$, respectively. At $\boldsymbol{k}_{||}||0x$, these two spinor functions taking the form $(1, i)^T/\sqrt{2}$ and $(i, 1)^T/\sqrt{2}$ are eigenfunctions of the spin operator σ_y with the eigenvalues 1 and -1, respectively. That implies that spin moments of each from two band branches for considered nonmagnetic system are opposite and lie in the plane xy as is depicted in Fig. 4.22.

The above-mentioned nearly free electron (NFE) model is able to describe the nature of the splitting but it cannot give a correct quantitative result. The experimental splitting (e.g., in Au(111) [59]) is much larger than what is estimated by an NFE model. This small splitting is related to neglecting of the large gradient potential near of ionic cores. It has been shown, in the framework of the tight-binding model that is linearly dependent on the atomic spin–orbit splitting and the

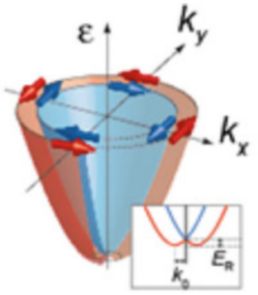

Fig. 4.22 The two Fermi sheets of nonmagnetic metal surface corresponding two spin polarizations (denoted by *arrows*) of conduction electrons under the Rashba spin–orbit splitting. Here, ε is an energy, k_0 is a splitting parameter; E_R is the spin–orbit energy. The sheets emerge from a "Dirac point" near the band bottom

surface potential. A large atomic spin–orbit interaction and a large gradient of the surface potential result in a large splitting of the surface state dispersion [60]. Since the electric field probed by the electron is strongest near the ion cores, a realistic description of the phenomenon should include atomic aspects. It is taken into account in a tight-binding model, where the spin–orbit splitting depends on the product of the surface-potential gradient times the atomic spin–orbit parameter [61]. For clean metal surfaces, the splitting depends not only on the atomic number Z, but also on the orbital character of the surface-state wave function, e.g., on the relative sizes of the p and s components in an sp surface state.

In the tight-binding model, the electrons that form the two-dimensional electron gas originate in all atomic s and p orbitals. The ingredients resulting in Rashba splitting are atomic spin–orbit interaction $\boldsymbol{H}_{\mathrm{SO}} = \Delta_{\mathrm{SO}}\boldsymbol{L} \otimes \sigma$, and an asymmetry potential in the direction perpendicular to the 2D surface ($V = E_0 z$). The main effect of the symmetry breaking potential is to open band gap Δ_g between the isotropic p_z and p_x p_y bands. In the tight-binding approximation, the hopping element from a p_z state at site i with spin σ to p_x or p_y state at site j with spin σ' is given by the expression $t^{x,y}_{i,\,j;\sigma\sigma'} = E_0\langle p_z, i;\ \sigma|z|p_{x,y}, j;\sigma'\rangle$. In the absence of a symmetry breaking, i.e., $V = 0$, the hopping element vanishes due to symmetry. If $V \neq 0$, then the hopping element is finite. The Rashba effect is the nonlinear effect, which is obtained in a second-order perturbation theory with the spin-flip quantum transition between $\langle p_z, i;\ \uparrow|$ and $\langle p_z, j;\ \downarrow|$ states via the transitional quantum state $\langle p_{x,y}, j;\ \sigma|$. It results in the Rashba parameters $\alpha_R \sim \Delta_{\mathrm{SO}}/\Delta_g$ that in two orders of magnitude larger than in the free-electron model.

In general, both mentioned models are mutually complementary and their description of the Rashba effect is in qualitative agreement with experimental data, specifically, with the experimental band structures obtained by ARPES (Fig. 4.23) [62].

It has been shown by ARPES that large Rashba splitting effect is observed at surfaces and interfaces of transition and rare-earth metals [63, 64] and in disordered

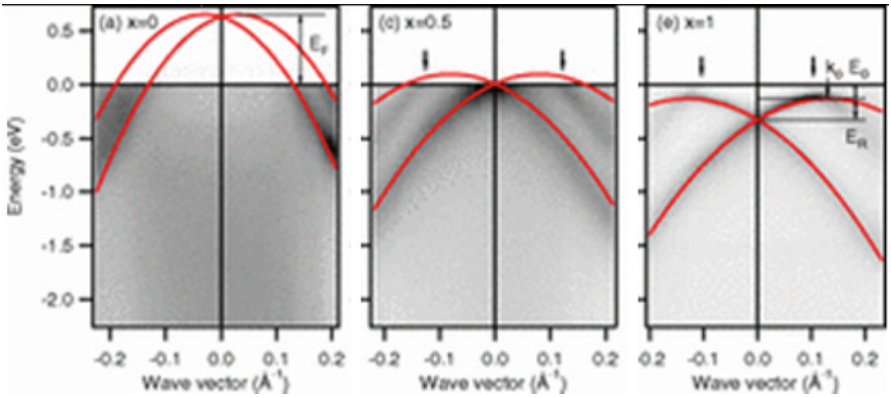

Fig. 4.23 Experimental band structures of $Bi_xPb_{1-x}Ag(111)$ surface alloys for x, obtained by angle-resolved photoelectron spectroscopy, where k_0 is the spin–orbit splitting and E_R is the Rashba energy

Au/Ag alloys [65]. Such large spin–orbit splitting is also peculiar for single-layer ordered metallic alloys formed by high-Z metals (Bi and Pb) at the Ag(111) surface [60]. In Bi/Ag (111), in particular, the wave vector separation $2k_0$ was found to be one order of magnitude larger than in Au(111), and much larger than typical values found in semiconductor heterostructures.

In realistic metal surfaces, such factors as impurities and the in-plane component of the potential can essentially influence on the Rashba effect and corresponding spin-splitting of the band spectrum. A potential gradient within the plane also effects causes on the spin–orbit interaction. The interplay of both contributions, in-plane and out-of-plane gradient potential, can manifest itself as an enhanced splitting in the anisotropic confinement plane and a nonzero spin polarization in z direction. These physics factors are taken into account in modern first principle calculation (see [66]) achieving quantitative agreement with the experimental data and providing insight of the physical origin of the Rashba splitting.

From the experimental and theoretical results, it follows that the spin–orbit splitting of the surface states generally is determined by the strong Coulomb potential of the nuclei, the perpendicular potential gradient, due to the surface-potential barrier, and the in-plane potential gradient, due to the surface geometry. The last one can be viewed as a crystal-field effect of the subsurface layers on the topmost layer. Both the perpendicular and the in-plane gradients break the symmetry of a freestanding surface layer. The strongest contribution is the atomic one. The other two are orders of magnitude less than the atomic contribution and approximately of the same strength. This hierarchy suggests the following scenario: for a sizable splitting, a strong atomic contribution is inevitable. An additional mechanism (the in-plane gradient) can increase the splitting. However, such mechanism can only “trigger” the effect. Without a strong atomic contribution, the splitting is small.

4.2.2 Current-Driven Spin Torque Induced by the Rashba Effect in a Ferromagnetic Layer

Methods to manipulate the magnetization of ferromagnets by means of local electric fields [67–69] or current-induced STT [70–72] allow the design of integrated spintronic devices with reduced dimensions and energy consumption compared with conventional magnetic field actuation [73, 74]. An alternative way to induce a spin torque using an electric current is based on intrinsic spin–orbit magnetic fields [75, 76]. In this case, strong magnetic fields can be induced in ferromagnetic metal films lacking structure inversion symmetry through the Rashba effect. Owing to the combination of spin–orbit and exchange interactions, an electric current flowing in the surface plane of a magnetic layer with asymmetric interfaces produces an effective transverse magnetic field of the order T per A/cm^2. Besides its fundamental significance, the high efficiency of this process makes it a realistic candidate for room-temperature spintronic applications.

Controlling the magnetization of nanodevices using local electric currents instead of externally applied magnetic fields opens a wide spectrum of opportunities to integrate magnetic functionalities into electronic circuits. In general, current-induced magnetization reversal requires the generation of a conduction electron spin density noncollinear with the local magnetic moments of a ferromagnet. This is achieved in multilayer structures such as spin valves and tunnel junctions by injecting spin-polarized electrons from a pinned ferromagnet into a "free" ferromagnetic layer through a nonmagnetic spacer, inducing the so-called STT effect (see [72]).

An alternative way to produce nonequilibrium polarization of the conduction electron spins is based on spin–orbit coupling in structures lacking inversion symmetry. Electrons moving in an asymmetric crystal-field potential experience a net electric field ($\boldsymbol{E}$), which, by transforming into a magnetic field in the electron's rest frame, effectively couples the spin to the electron's orbital motion. This effect is well known for semiconductors, where the occurrence of net spin polarization has been predicted [77, 78] and observed in electric currents flowing through nonmagnetic quantum wells as well as strained bulk compounds [79].

A Spin–Orbit Torque and Effective Internal Bias Fields

The mentioned current-induced spin–orbit effects detected in non-magnetic semiconductors [80] could be used in combination with [81] or be intrinsic to ferromagnets [82], providing a radically new mechanism for the manipulation of the magnetization in ferromagnetic systems. The effective magnetic Rashba field ($\boldsymbol{H}_{\mathrm{R}}$) (above-mentioned) produced by the spin–orbit interaction on the conduction electrons of a two-dimensional system characterized by structural inversion asymmetry (SIA). This field can be expressed in the form of the vector product $\boldsymbol{B}_{\mathrm{R}} = \alpha_{\mathrm{R}}[\boldsymbol{z} \times \langle \boldsymbol{k} \rangle]$, where $\boldsymbol{z}$ is a unit vector parallel to $\boldsymbol{E}$; $\langle \boldsymbol{k} \rangle$ is the average electron wave vector and α_{R} is a material parameter that depends on the strength of the

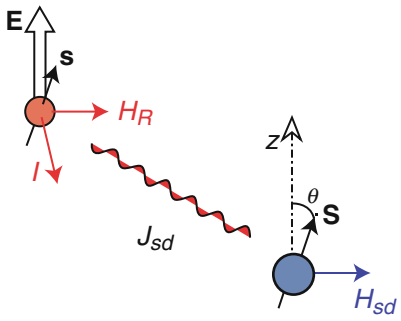

Fig. 4.24 Microscopic origin of the *s–d*-mediated Rashba field $\boldsymbol{H}_{\mathrm{R}}$ and experimental geometry. Conduction electrons moving perpendicular to $\boldsymbol{E}$ have their spin ($\boldsymbol{s}$) tilted by the Rashba magnetic field ($\boldsymbol{H}_{\mathrm{R}}$), exerting a torque on the localized moments ($\boldsymbol{S}$) through the exchange coupling (J_{sd}) and *s–d*-mediated Rashba field ($\boldsymbol{H}_{\mathrm{R}sd}$)

spin–orbit coupling. For zero current, $\boldsymbol{H}_{\mathrm{R}}$ cancels out as $\boldsymbol{k}$ and $-\boldsymbol{k}$ states are equally populated and $\langle \boldsymbol{k} \rangle = 0$. In the presence of a charge current, however, the electron distribution in $\boldsymbol{k}$-space becomes asymmetric, producing a net effective field and inducing a nonequilibrium spin density, perpendicular to the current direction.

In a ferromagnetic, the action of $\boldsymbol{H}_{\mathrm{R}}$ combines with the *s–d* exchange interaction that couples the conduction electron spin to the local magnetization ($\boldsymbol{M}$). Because of this interaction, a current passing through a uniformly magnetized ferromagnetic layer exerts an exchange-mediated effective field $\boldsymbol{H}_{\mathrm{R}sd}$ on $\boldsymbol{M}$ (Fig. 4.24), thereby producing a torque and eventually provoking the reversal of $\boldsymbol{M}$ [76].

A similar mechanism, albeit based on strain-induced Dresselhaus spin–orbit coupling [83] rather than the Rashba effect, has very recently been demonstrated in a p-type ferromagnetic semiconductor, $Ga0_{0.94}Mn_{0.06}As$, where the injection of 10^6 A/cm^2 produced an effective field of about 0.5 mT at $T = 40$ K (see [84, 85]). It should be noticed that a spin–orbit-induced torque is fundamentally different from STT, although its ultimate effects might be similar. Contrary to STT, there is no transfer of spin angular momentum from one ferromagnetic layer to another.

Rather, orbital angular momentum is transferred to the electron spins through the spin–orbit interaction intrinsic to the band structure of the ferromagnet. Thus, the application of a spin torque does not rely on two noncollinear, independently controlled ferromagnet electrodes and is realized in a single uniformly magnetized ferromagnetic layer. Moreover, the direction of the spin–orbit torque is changed by reversing the current, thereby enabling reversible control of the magnetization.

Although studies of the Rashba effect have traditionally focused on semiconducting materials, several groups have now reported evidence of Rashba-induced splitting of the surface states of both nonmagnetic [64, 86] and magnetic metals [56] using angle-resolved photoemission. Consequently, in a uniformly magnetized ferromagnetic metal layer with enhanced SIA can occur a current-induced spin–orbit torque in a uniformly magnetized ferromagnetic metal layer with enhanced SIA.

The current-induced spin–orbit torque in uniformly magnetized ferromagnetic metal layer with enhanced SIA was observed at room temperatures in the magnetic layered nanostructure $Pt/Co/AlO_x$ as it is represented in Fig. 4.25 [56].

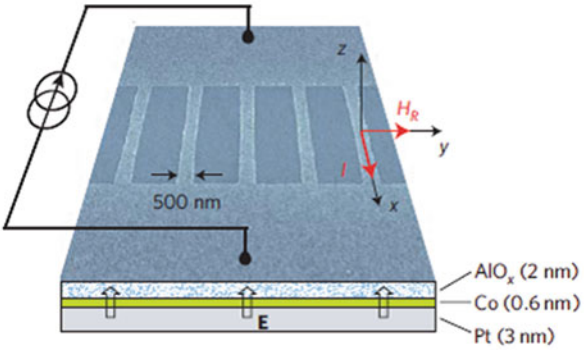

Fig. 4.25 Scanning electron micrograph detail of the magnetic nanostructure Pt/Co/AlO_x wire array and schematic vertical cross section of the layer. Arrows indicates the direction of the current (I), interfacial electric field ($\boldsymbol{E}||z$), and $\boldsymbol{H}_{\mathrm{R}}$. The sign of $\boldsymbol{E}$ is determined from the measured orientation of I and $\boldsymbol{H}_{\mathrm{R}sd}$ assuming positive polarization of the conduction electrons near the Fermi level

In the magnetic nanostructure depicted in Fig. 4.25, the SIA results from the presence of AlO_x and Pt on either side of the Co layer. The strong spin–orbit effects at metal surfaces are provided by the presence of heavy atoms and surface oxidation (see [85, 87]). The lasts have resulted in a strong out-of-plane electron potential gradient in Pt/Co/AlO_x. The Co layer is characterized by a strong perpendicular anisotropy, uniform monodomain state and a saturation magnetization close to the bulk ($M = 1.090\,\mathrm{kA/m}$) and is very stable. The out-of-plane uniaxial anisotropy field is $\mu_0 H_K = 0.92\,\mathrm{T}$. The effect of an electric current on M in the magnetic nanostructure Pt/Co/AlO_x occurs via the in-plane field $\boldsymbol{H}_{\mathrm{R}sd}||\boldsymbol{y}$ perpendicular to the wires.

Depending on the $H_{\mathrm{R}sd}/H_K$ ratio, the energy barrier for magnetization reversal will thus change from the initial symmetric shape typical for uniaxial anisotropy to a strongly asymmetric profile, lowering the barrier in one direction and raising it in the opposite one as the equilibrium magnetization direction gradually shifts from perpendicular to in-plane (Fig. 4.26) [56].

As be obviously from the plot in Fig. 4.26, similarly to an external magnetic field, the spin–orbit interaction reduces the energy barrier for magnetization reversal in the direction perpendicular to the current flow.

The current-driven spin torque induced by the Rashba effect and the magnetization reversal in ferromagnetic layer is observed for the investigated magnetic nanostructure Pt/Co/AlO_x with the help of the wide-field polar Kerr microscopy (Fig. 4.27) [56].

Starting from a fully saturated out-of-plane $\boldsymbol{M}$, single current pulses were injected into the wires (Fig. 4.25) until the nucleation of reversed magnetic domains was observed. This occurred as the wires evolved from the metastable monodomain state toward the macroscopically demagnetized ground state constituted by an equal mixture of up and down domains. The influence of $H_{\mathrm{R}sd}$ was regulated by an external in-plane field H_{ext} acting as a bias parallel or antiparallel to $\boldsymbol{y}$. The suppression of the field $H_{\mathrm{R}sd}$ by the opposite directed external field H_{ext} resulted in vanishing the current-driven magnetization effect. On the contrary, the enhancement of the field $H_{\mathrm{R}sd}$ by the parallel directed external field resulted in a rise and increasing of the current-driven magnetization effect.

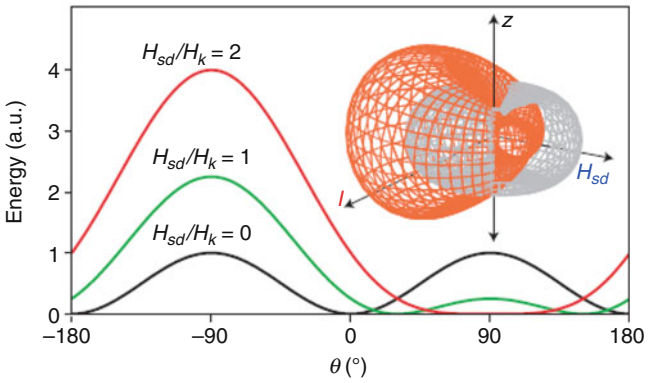

Fig. 4.26 The three-dimensional energy landscape in the presence (absence) of current is shown in *red* (*gray*). The plot shows the magnetization energy as a function of polar angle θ between ($\boldsymbol{M}$ and $\boldsymbol{z}$) for a magnetic layer with the uniaxial anisotropy easy axis parallel to $\boldsymbol{z}$ and current flow along $\boldsymbol{x}$. Both the equilibrium magnetization direction and barrier height depend on the ratio between the effective anisotropy field H_K and $H_{\mathrm{R}sd}$

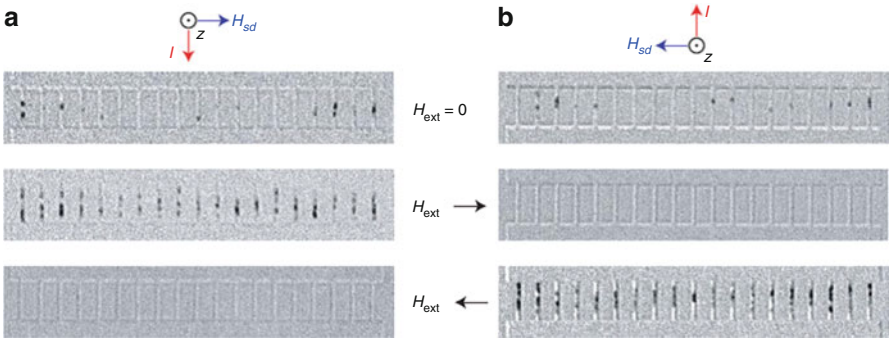

Fig. 4.27 Differential Kerr microscopy images recorded after current pulse injection. (**a**, **b**) Positive (**a**) and negative (**b**) current values with external field $H_{\mathrm{ext}} = 0, \pm 47.5\,\mathrm{mT}$ applied parallel to $\boldsymbol{y}$. The pulse amplitude is set to $7.8 \times 10^7\,\mathrm{A/cm^2}$ in all cases. Note that the topographic contrast in each image varies depending on the drift between pre-pulse and post-pulse images

For current density $j_e \sim 10^8\,\mathrm{A/cm^2}$ comparable to those required by STT device operation [88], extraordinary high effective spin–orbit-induced magnetic fields can attain values of the order of 1 T. If H_{Rsd} is set orthogonal to $\boldsymbol{M}$ by sending a current perpendicular to the easy magnetization axis, the energy barrier separating the two stable states is reduced. On the other hand, if H_K and $H_{\mathrm{R}sd}$ collinear, a favorable situation for achieving deterministic switching may be realized [64]. A major advantage of the Rashba torque mechanisms is that the thermal stability of the magnetization, determined by H_K, and spin-torque efficiency, determined by α_{R}, depend on the strength of the spin–orbit interaction.

Magnetization Dynamics Under Spin–Orbit and Exchange Interactions

The features of magnetization dynamics in magnetic metal nanostructure with structure inversion asymmetry and the spin–orbit-induced magnetic field $H_{\mathrm{R}sd}$ is described by the general form of the modified LLG equation [88]

$$\begin{aligned}\frac{\partial \boldsymbol{M}}{\partial t} &= \gamma_0[(\boldsymbol{H}_{\mathrm{eff}} + \boldsymbol{H}_{\mathrm{R}sd}) \times \boldsymbol{M}] + \frac{\alpha}{M_{\mathrm{S}}}\left(\boldsymbol{M} \times \frac{\partial \boldsymbol{M}}{\partial t}\right) \\ &\quad -\frac{\alpha}{(1+\beta^2)M_{\mathrm{S}}}(u \cdot \nabla)\boldsymbol{M} + \frac{\beta}{(1+\beta^2)M_{\mathrm{S}}^2}\boldsymbol{M} \times [(u \cdot \nabla)\boldsymbol{M}],\end{aligned} \tag{4.62}$$

where $\boldsymbol{M}$ is the local magnetization, γ_0 the gyromagnetic ratio, $\boldsymbol{H}_{\mathrm{eff}}$ the magnetic field including contributions from the external, anisotropic, and magnetostatic fields, α is the Gilbert damping parameter, and $\beta = \tau_{\mathrm{exs}}/\tau_{\mathrm{sf}}$ the ratio of the nonadiabatic to adiabatic spin torque, equal to the ratio of the exchange interaction and spin-flip relaxation times [89, 90]. Using the same parameter definitions as in the main text, one has

$$\boldsymbol{u} = \frac{g\mu_{\mathrm{B}}P}{2eM_{\mathrm{S}}}\boldsymbol{j}_e, \quad \boldsymbol{H}_{\mathrm{R}sd} = 2\frac{\alpha_{\mathrm{R}}m}{\hbar eM_{\mathrm{S}}}P(\boldsymbol{z} \times \boldsymbol{j}_e), \tag{4.63}$$

where P is a parameter that depends on the s–d coupling strength, which can be approximated by the degree of polarization of conduction electrons. From (4.62) it follows that the action of $\boldsymbol{H}_{\mathrm{R}sd}$ is analogous to that of an externally applied field, the sign of which depends on the current direction, but is independent on the local magnetization orientation.

As it is known from domain wall measurements [89], the injection of a current into a textured magnetic film produces two additional torque components, called the adiabatic and nonadiabatic spin torques [90, 91] corresponding, respectively, to the third and fourth terms in (4.62). Although these two torques exist independently of SIA, recent experiments revealed an enhancement of the nonadiabatic spin torque component in Pt/Co/AlO_x domain walls [92], which was attributed to the presence of SIA and related increase of the conduction electron spin-flip rate.

The field $\boldsymbol{H}_{\mathrm{R}sd}$ is orthogonal to both current and interface normal (see Fig. 4.24), i.e., is a hard axis field parallel to $\boldsymbol{y}$. It changes sign by reversing the current, is independent of the local magnetization direction, and is homogeneously distributed inside a magnetic nanolayer. The field-equivalent of the nonadiabatic spin torque ($\boldsymbol{H}_{\mathrm{NA}}$), on the other hand, acts as an easy axis field directed perpendicular to the layer. Unlike the Rashba field, $\boldsymbol{H}_{\mathrm{NA}}$ changes sign when the magnetic configuration is reversed and exists only inside a domain wall, vanishing in the case of uniform magnetization. It may be noted as well that the two fields and corresponding torques have opposite time reversal symmetries, with $\boldsymbol{H}_{\mathrm{R}sd}$ being odd (even) and $\boldsymbol{H}_{\mathrm{NA}}$ being even (odd) under reversal of both current and magnetization. The difference between these two types of torques reflects also on their magnitude and therefore on their efficacy: for the same current, $\boldsymbol{H}_{\mathrm{R}sd}$ is more than ten times greater compared to the field equivalent of the nonadiabatic spin torque component.

Comparing the different spin torque terms, it is evident that the presence of the Rashba effective field $\boldsymbol{H}_{\mathrm{R}sd}$ offers entirely new possibilities to control the magnetic behavior of nanostructures using an electric current, which are fully complementary and may be integrated with other forms of current-induced torques.

Thus, the current-driven spin torque induced by the Rashba effect in ferromagnetic metal nanolayers originates from the structural inversion asymmetry with *s–d* exchange, allowing for the transfer of angular momentum from the crystal lattice to the local spin magnetization. The value of the effective Rashba field acting on $\boldsymbol{M}$ is very large, making for one of the most efficient spin-torque effects. As this is a current-driven mechanism and layer structure is very similar to magnetic tunnel junctions, devices combining Rashba and STT effect can be designed. This opens a promising new avenue to manipulate the magnetization of spintronic devices by means of electric signals.

4.2.3 *Electric Field Control by Rashba Spin–Orbit Anisotropy*

The electric-induced magnetization via the Rashba effect in combination with *s–d* exchange interaction between conduction electrons and localized magnetic moments of magnetic nanostructures constitute the energy efficient, strong spatial localized, and rapid mechanism of the magnetization control in magnetic nanostructures. Such magnetization can constitute the basis of the effective electric-field magnetic control with the prospective of many technology important applications. A large enough surface electric field in nonmagnetic nanostructures gives rise to a Rashba spin–orbit coupling which leads to a spin-splitting of the conduction electrons. For magnetic nanostructures, this splitting is modified via the Dzyaloshinskii–Moriya mechanism resulting in changing of a magnetic anisotropy energy.

An Electric-Induced Magnetization Via Spin–Orbit Interaction

The possibility of controlling the magnetic anisotropy of thin ferromagnetic films using an electric field $\boldsymbol{E}$ is of great interest since it can potentially lead to magnetic random access memory (MRAM) devices which require less energy than spin-torque-transfer random access memory STT-MRAM [93–97]. Thin magnetic films with a PMA are important for applications [98, 99]. This interfacial internal electric field might be used to engineer such a PMA is also of great interest. Experiment [100, 101] has indeed shown that such a PMA might, in turn, be modified by an externally applied electric field. One can be caused both by the indirect electric-induced change of magnetic anisotropy via changes of the electronic contribution to magnetic anisotropy [101, 102] and the direct electric-induced changes of magnetic anisotropy via the Rashba effective field in combination with the exchange field.

The indirect electric-induced magnetization, in the terms of band theory, is related to the matrix elements of the spin–orbit interaction between empty states [103–105], a large contribution to which come from regions with different d-bands (almost) cross. The strong charge doping dependence of the magnetization in band theory is related to crossing d-bands near the Fermi surface, though it reduced to band splitting [106]. The direct electric-induced magnetization in the framework of the Rashba spin–orbit interaction [107] and the band Stoner magnetism is characterized by a very large magnetic anisotropy arising from the internal electric fields $\boldsymbol{E}_{\text{int}}$ which exist at, e.g., ferromagnetic/metal and ferromagnetic/oxide insulator interfaces but modified by the addition of an applied electric field $\boldsymbol{E}_{\text{ext}}$. There is a Rashba spin splitting of the band structure leading to a quadratic, E_{ext}^2, contribution to the magnetic anisotropy, contrasting with a linear in E_{ext} doping effect.

The magnetic states in the two-dimensional model with the direct electric-induced magnetization, based on the Rashba interaction and the band Stoner magnetization, is described by Hamiltonian [108]

$$H = \frac{p^2}{2m} - (J_0 S)\boldsymbol{m}\cdot\boldsymbol{\sigma} + \frac{\alpha_{\text{R}}}{\hbar}\left(\sigma_x p_y - \sigma_y p_x\right), \tag{4.64}$$

where p is the electron momentum operator, $\mathbf{m} = \boldsymbol{S}/S$ ($\boldsymbol{S}$ is the localized spin operator), $\boldsymbol{\sigma}$ is the Pauli matrices and $\alpha_{\text{R}} = e\eta_{\text{SO}}E$ is the Rashba parameter proportional to η_{SO}, which characterizes the spin–orbit coupling, and the magnitude E of the electric field $\boldsymbol{E} = E\mathbf{z}$, taken to be perpendicular to the plane of the system; $\boldsymbol{m}$ is perpendicular to $\boldsymbol{x}$ and makes an angle θ to the z-direction, as in Fig. 4.28 [108].

For the nonmagnetic two-dimensional electron system, corresponding to the surface metal nanolayer, e.g., the surface of Au, due to (4.64), the Rashba magnetic field $\boldsymbol{B}_{\text{R}}$ results in the spin-split band energy (Fig. 4.28)

$$\varepsilon_{k\sigma} = \frac{\hbar^2}{2m} - \left(k - \sigma k_0\right)^2 - E_{\text{R}}, \tag{4.65}$$

where the values of σ "+" and "−" correspond to minority and majority electrons, respectively; the momentum shift $k_0 = m\alpha_{\text{R}}/\hbar^2$, and

$$E_{\text{R}} = \frac{m\alpha_{\text{R}}^2}{2\hbar^2} = -\frac{1}{2}\left(\frac{e\eta_{\text{SO}}}{\hbar}\right)^2 mE_{\text{R}}^2. \tag{4.66}$$

For the surface state of Au, $E_{\text{R}} \approx 3.5\,\text{meV}$, exemplifying the energy scale. For the three-dimensional problem, there is no equivalent shift in k_z. In the nonmagnetic case ($J_0 = 0$), the Rashba magnetic field as defined as $g\mu_{\text{B}}\boldsymbol{B}_{\text{R}} = 2\alpha_{\text{R}}\left(-k_y\boldsymbol{x} + k_x\boldsymbol{y}\right)$, where g is the g-factor corresponding to the spin state $|s\rangle$ and μ_{B} is the Born magneton. There are two concentric Fermi surfaces. The energy splitting $2\alpha_{\text{R}}k = \Delta(k/k_{\text{F}})$, where Δ is the value for $k_{\text{F}} = \left(k_{\text{F}\uparrow} + k_{\text{F}\downarrow}\right)/2$, with $k_{\text{F}\uparrow,\downarrow}$ the Fermi wave number for the majority/minority band. For the surface state Au, $\Delta \approx 110$ meV while $E_{\text{F}} \approx 420\,\text{meV}$ giving $E_{\text{R}} \approx 3.5\,\text{meV}$.

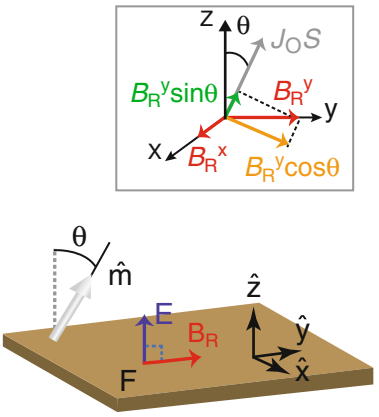

Fig. 4.28 The electric field $\boldsymbol{E}=E\boldsymbol{z}$ is perpendicular to the ferromagnet surface while the magnetic order vector direction $\boldsymbol{m}$ is defined by the angle θ relative to $\mathbf{z}$. Whatever the direction of $\boldsymbol{k}$, the Rashba magnetic field $\boldsymbol{B}_{\mathrm{R}}$ of direction $\boldsymbol{k} \times \boldsymbol{E}$ lies in the x–y plane

Field-Driven Magnetic Anisotropy in Magnetic Nanostructures

In the magnetic case, the magnetic order vector $\boldsymbol{m} = \cos\theta \boldsymbol{z} + \sin\theta \boldsymbol{y}$. The total Rashba field $\boldsymbol{B}_{\mathrm{R}sd}$ defining the axis of quantization,

$$g\mu_{\mathrm{B}}\boldsymbol{B}_{\mathrm{R}sd} = 2\left[(J_0S + \alpha_{\mathrm{R}}k_x \sin\theta) + \alpha_{\mathrm{R}}\left(-k_y\boldsymbol{x} + k_x \cos\theta(\boldsymbol{m} \times \boldsymbol{x})\right)\right], \tag{4.67}$$

due to (4.64), results in the nonsymmetrical spin-split energy band

$$\varepsilon_{k\sigma} = \frac{\hbar^2}{2m}\left[\left(k_x - \sigma k_0 \sin^2\theta\right)^2 + k_y^2\right] - E_{\mathrm{R}} \sin\theta - \sigma\left[(J_0S)^2 + \alpha_{\mathrm{R}}^2\left(k_x^2 \cos^2\theta + k_y^2\right)\right]^{1/2}. \tag{4.68}$$

The direction of the momentum shift depends upon $\sigma = \pm 1$, i.e., the majority/minority character of the band. These shifts also change sign with $\boldsymbol{m} \rightarrow -\boldsymbol{m}$ for a given σ. It is assumed, that $g\mu_{\mathrm{B}}B_{\mathrm{R}} < J_0S$, i.e., the Rashba magnetic field B_{R} is smaller than the exchange splitting. The second order in $g\mu_{\mathrm{B}}B_{\mathrm{R}}$, $g\mu_{\mathrm{B}}\boldsymbol{B}_{\mathrm{R}sd} = 2\left(JS + \alpha_{\mathrm{R}}k_x \sin\theta \boldsymbol{m}'\right)$, where $JS = \left[(J_0S)^2 + \alpha_{\mathrm{R}}^2\left(k_x^2 \cos^2\theta + k_y^2\right)\right]^{1/2} / J_0S$ and where $\boldsymbol{m}'$ differs from $\boldsymbol{m}$ by a small angle δ where $\tan\delta \approx \alpha_{\mathrm{R}}\left(k_x^2 \cos^2\theta + k_y^2\right)/J_0S$.

The contributions to the magnetic anisotropy are highlighted by contrasting the perpendicular and parallel orientations of magnetic order vector $\boldsymbol{m}$ to the plane. With $\boldsymbol{m}$ perpendicular to the plane, i.e., $\boldsymbol{m} = \boldsymbol{z}$ ($\theta = 0$), the exchange and Rashba fields are orthogonal and hence the net energy for a single electron (4.68) is

$$\varepsilon_{k\sigma} = \frac{\hbar^2}{2m}k^2 - \sigma\left[(J_0S)^2 + \left(\alpha_{\mathrm{R}}k^2\right)\right]^{1/2}. \tag{4.69}$$

The axis of quantization is tilted by $\delta(k) = \tan^{-1}(\alpha_{\mathrm{R}}k)/(J_0S)$ away from the z-axis as shown in Fig. 4.29b. The majority (minority) electrons gain (lose) an energy that

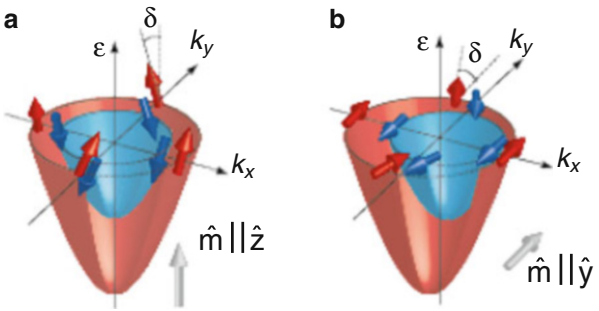

Fig. 4.29 Two Fermi sheets of conduction electrons created by the Rashba spin–orbit splitting in magnetic metals with different directions of the magnetization $\boldsymbol{m}$: (**a**) $\boldsymbol{m} \,||\, z$, (**b**) $\boldsymbol{m} \,||\, \mathbf{y}$

is even in E. This arises from the competition of the Rashba field, perpendicular to $\boldsymbol{m}$, with the exchange field. Such a competition generates a second order in E contribution to the magnetic anisotropy and is identified with the Dzyaloshinskii–Moriya (DM) mechanism [109, 110].

Now take $\boldsymbol{m}$ parallel to the y-axis, i.e., $\boldsymbol{m} = \boldsymbol{y}\,(\theta = \pi/2)$. The y-component of $\boldsymbol{B}_{\mathrm{R}}$ is parallel to the exchange field and is combined with the kinetic energy. The Fermi sea is shifted along the x-axis and lowered by E_{R} as shown in Fig. 4.29a. This energy gain corresponds to a pseudo-dipolar (PD) contribution to anisotropy energy, which favors an in-plane magnetization.

On the other hand, the x-component of $\boldsymbol{B}_{\mathrm{R}}$, which is perpendicular to $J_0 S\boldsymbol{m}$, gives rise to a correction to the effective exchange field. The direction of the moment tilts away from the y-axis in the direction perpendicular to the wave vector by $\delta(k_y) = \tan^{-1}\left(\alpha_{\mathrm{R}} k_y\right)/(J_0 S)$ as shown in Fig. 4.29b. The single particle energy, (4.68), is now,

$$\varepsilon_{k\sigma} = \frac{\hbar^2}{2m}\left[(k_x - \sigma k_0)^2 + k_y^2\right] - E_{\mathrm{R}} - \sigma\left[(J_0 S)^2 + \left(\alpha_{\mathrm{R}} k_y\right)^2\right]^{1/2}. \tag{4.70}$$

where the shift k_0 is the same as in (4.65) but only along the x-axis.

The effective exchange field in (4.70) is smaller than that in (4.68) due to the absence of a k_x^2 term. This indicates that the overall DM contribution favors a perpendicular m while the PD term favors an in-plane $\boldsymbol{m}$. This exchange field changes sign for the majority/minority spins, i.e., with σ. Assuming $(J_0 S)^2 > \left(\alpha_{\mathrm{R}} k_y\right)^2$ and retaining the θ-dependent terms up to the order of E^2 in (4.67), we obtained our principal result:

$$E_{\mathrm{an}} = E_{\mathrm{R}}\left[1 - \frac{2T}{J_0 S}\right]\cos^2\theta, \tag{4.71}$$

for the magnetic anisotropy energy, with

$$T = \frac{\hbar^2}{2m}\left(\langle k_x^2\rangle_{\uparrow} - \langle k_x^2\rangle_{\downarrow}\right), \tag{4.72}$$

where $\langle\rangle$ denotes an average over the Fermi sea (see methods). The Rashba spin–orbit interaction produces a uniaxial anisotropy energy, which, as in the Dzyaloshinskii–Moriya theory [83], comprises a direct second order in E easy

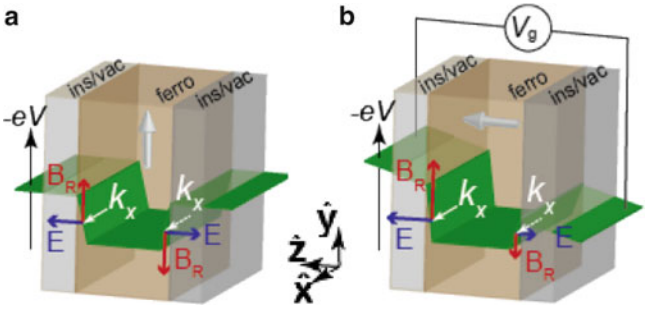

Fig. 4.30 (**a**) There is an electric field E in the surface region of a ferromagnet, however for a given wave vector $\boldsymbol{k}$, the Rashba field $\boldsymbol{B}_R$, proportional to $[\boldsymbol{k} \times \boldsymbol{E}]$, has an opposite sign at the two surfaces and the average field is zero. (**b**) With a finite external field this symmetry is broken and there is a net Rashba field acting upon the electrons

plane pseudo-dipolar interaction and indirect contribution proportional to E^2/J_0S. Clearly an E^2-dependent PMA results if $T > J_0S/2$, which is the case for real $3d$ ferromagnets.

The resulting anisotropy energy can be very large. Experiment [85] on conducting but nonmagnetic materials helps set the scale. In particular, the value of the scaling pre-factor E_R in (4.71) for the surface state of Au is ~3.5 meV or about 35 T in magnetic field units and very much larger than the typical ~1 T demagnetizing field. If the Au film is polarized by contact with an ultra-thin ferromagnet the second factor, $2T/J_0S$, in (4.70) for the field inside a Au surface layer can be quite large ~5 leading to a PMA and indeed ultra-thin Fe on Au does have such a PMA [111]. Ultra-thin ferromagnetic films in contact with, e.g., Pt, Pd, and Ta, also are found to have a PMA [68].

Schematically shown in Fig. 4.30a [108] is the potential seen by electrons in a freestanding ultra-thin ferromagnetic film. At the surface, the potential reaches the vacuum level within a few atomic spacings. This results in a finite large electric field $E \sim 10\,\mathrm{V/nm}$ at each surface but in opposite senses. Assuming an appreciable spin–orbit coupling in the interface region, this results, in turn, in a Rashba field $\boldsymbol{B}_R$, which also changes sign between the two surfaces for a given momentum. Thus for a perfectly symmetric film, the ferromagnetically polarized electrons see no average field $\boldsymbol{B}_R$. This symmetry can be broken by the application of an external electric field as shown in Fig. 4.30b [108].

The electric field is increased at one surface and decreased at the other doubling the net effect. In contrast, for this same symmetric situation, the surface charges are opposite and doping effects must cancel. Experimentally applied fields of 1 V/nm are relatively easy to achieve implying a ~10 % change in the surface anisotropy. Experiments [112] with a 1.5 nm $Fe_{80}B_{20}$ sandwiched between two MgO layers is perhaps closest to this situation although the thickness 1.5 and 2.5 nm of these layers are not equal.

Clearly the intrinsic Rashba field $\boldsymbol{B}_R$ is modified when the material adjacent to the ferromagnets (F), say Fe, are different. In many experiments an insulator I, often MgO, lies to one side and a normal metal (N), e.g., Au, Pt, or Pd, completes a tri-layer system. The potential, Fig. 4.30a, b, will increase in passing from Fe to

MgO but, depending on the effective work-functions, can either increase (Au), Fig. 4.30a, or decrease (Pt), Fig. 4.30b, at the FN interface. The latter case is particularly favorable since the intrinsic Rashba fields have the same sense and add. It is the case that both Pt and Pd N-layers can induce a PMA.

A large applied electric field E, the required asymmetry might be controlled in NFN tri-layers by varying in a systematic manner, at the mono-layer level, the thickness of one of the normal metal layers and by using metals with different spin–orbit couplings. In reality, the effect of the substrate transmitted to, and through, the bottom normal metal will simply an asymmetry even for large N-layer thickness. Indeed the PMA surface term for Au/Fe(110)/Au(111) structures does show a non-monotonic dependence on the top Au layer thickness. Experiments [113] for Fe layers on vicinal Ag (001) and Au(001) surfaces and which undergo a symmetry breaking (5×20) surface reconstruction manifest an in-plane surface term reflecting this broken symmetry and which is larger for Au, with its stronger spin–orbit coupling, than for Ag.

The Rashba magnetic field due to the internal electric field in the surface region of an ultra-thin ferromagnetic can make an important contribution to the PMA. Such surface fields might be modified by application of an applied electric field. Since the internal fields at two surfaces tend to cancel, an asymmetry between the surfaces is important. Different metal and insulator capping layers cause such an asymmetry.

References

1. Pershan PS, Ziel JP, Malmstrom LD (1966) Theoretical discussion of the inverse faraday effect, raman scattering, and related phenomena. Phys Rev 143:574–583
2. Kimel AV, Kirilyuk A, Hansteen F, Pisarev RV, Rasing T (2007) Nonthermal optical control of magnetism and ultrafast laser-induced spin dynamics in solids. J Phys Condens Matter 19:043201–043224
3. Hertel R (2009) For faster magnetic switching-destroy and rebuild. J Phys Condens Matter 2:73–76
4. Radu I, Vahaplar K, Stamm C, Kachel T, Pontius N, Durr HA, Ostler TA, Barker J, Evans RFL, Chantrell RW, Tsukamoto A, Itoh A, Kirilyuk A, Rasing T, Kimel AV (2011) Transient ferromagnetic-like state mediating ultrafast reversal of antiferromagnetically coupled spins. Nature 472:205–208
5. Ostler TA, Barker J, Evans RFL, Chantrell RW, Atxitia U, Chubykalo-Fesenko O, Moussaoui SE, Le Guyader L, Mengotti E, Heyderman LJ, Nolting F, Tsukamoto A, Itoh A, Afanasiev D, Ivanov BA, Kalashnikova AM, Vahaplar K, Mentink J, Kirilyuk A, Rasing T, Kimel AV (2012) Transient ferromagnetic-like state mediating ultrafast reversal of antiferromagnetically coupled spins. Nat Commun 3:1–6
6. Slonczewski JC (1996) Current-driven excitation of magnetic multilayers. J Magn Magn Mater 159:L1–L7
7. Gulyaev YV, Zil'berman PE, Epshtein EM, Elliott RJ (2005) Current-induced spin injection and a surface torque in a ferromagnetic metal junction. JETP 100:1005–1017
8. Shalaev VM, Douketis C, Stuckless JT, Moskovits M (1996) Light-induced kinetic effects in solids. Phys Rev B 53:11388–11402
9. Grinberg AA, Belorusets ED, Immanov EZ (1971) Theory of photo-electric and photomagnetic effects induced by light pressure. Fiz Tekh Poluprovodn 5:2010
10. Grinberg AA, Luryi S (1991) Comment on "Light-induced drift of quantum-confined semiconductor heterostructures". Phys Rev Lett 67:156
11. Luryi S (1987) Photon-drag effect in intersubband absorption by a two-dimensional electron gas. Phys Rev Lett 58:2263

12. Stockman MI, Pandey LN, George TF (1990) Light-induced drift of quantum-confined electrons in semiconductor heterostructures. Phys Rev Lett 65:3433–3441
13. Weick AD, Sigg H, Ploog K (1990) Observation of resonant photon drag in a two-dimensional electron gas. Phys Rev Lett 64:463–474
14. Skok EM, Shalagin AM (1980) Light-induced electron drift in semiconductors. JETP Lett 32:184–193
15. Gerrits T, Van den Berg HAM, Hohlfeld J, Bä L, Rasing T (2002) Ultra-fast precessional magnetization reversal by picosecond magnetic field pulses. Nature 418:509–512
16. Tudosa I, Stamm C, Kashuba AB, King F, Siegmann HC, Stöhr J, Ju G, Lu B, Weller D (2004) The ultimate speed of magnetic switching in granular recording media. Nat Phys 428:831–833
17. Devolder TA, Suzuki Y, Chappert C, Crozat P, Yagam K (2005) Distribution of the magnetization reversal duration in sub-ns spin-transport switching. J Appl Phys 98:053904–053911
18. Acremann Y, Strachan J, Chembrolu V, Andrews S, Tyliszczak T, Katine J, Carey M, Clemens B, Siegmann H, Stöh J (2006) Time-resolved imaging of spin transfer switching: beyond the macrospin concept. Phys Rev Lett 96:217202(1)–217202(4)
19. Vahaplar K, Kalashnikova AM, Kimel AV, Hinzke D, Nowak U, Chantrel R, Tsukamoto A, Itoh A, Kirilyuk A, Rasing T (2009) Ultrafast path for optical magnetization reversal via a strongly nonequilibrium state. Phys Rev Lett 103:117201(1)–117201(4)
20. Stöhr J, Siegmann HC (2006) Magnetism: from fundamentals to nanoscale dynamics. Springer, Berlin, p 223
21. Keller U (2003) Recent developments in compact ultrafast lasers. Nature 424:831–838
22. Krupa NN, Korostil AM (2012) On the laser-induced magnetoresistance effect in magnetic junctions. Int J Mod Phys B 26:20146(1)–20146(14)
23. Krupa NN (2012) Photo-driven spin transistor based on magnetic heterogeneous nanostructures. In: 5th international conference on nanoelectronic functional basis. Kharkov University Publishers, Kharkov, pp. 247–250
24. Bigot J-Y, Vomir M, Beaurepaire E (2009) Coherent ultrafast magnetism induced by femtosecond laser pulses. Nat Phys 5:513–519
25. Korostil AM (2012) A field-controlled current in nanojunctions. In: 5th international conference on nanoelectronic functional basis. Kharkov University Publishers, Kharkov, pp. 54–57
26. Stanciu CD, Kimel AV, Hansteen F, Tsukamoto A, Itoh A, Kirilyuk A, Rasing T (2006) Ultrafast spin dynamics across compensation points in ferrimagnetic GdFeCo: The role of angular momentum compensation. Phys Rev B 73:220402(1)–220402(4)
27. Stanciu CD, Hansteen F, Kimel AV, Tsukamoto A, Itoh A, Kirilyuk A, Rasing T (2007) Subpicosecond magnetization reversal across ferrimagnetic compensation points. Phys Rev Lett 99(21):217204(1)–217204(7)
28. Yuasa S, Djayaprawira DD (2007) Giant tunnel magnetoresistance in magnetic tunnel junctions with a crystalline MgO(001) barrier. J Phys D Appl Phys 40:R337–R354
29. Butler WH, Zhang X-G, Schulthess TC, MacLaren JM (2001) Spin-dependent tunneling conductance of Fe|MgO|Fe. Phys Rev B 63:054416(1)–054416(12)
30. Maekawa S, Takahashi S, Imamura H (2002) Theory of tunnel magnetoresistance. In: Maekawa S, Shinjo T (eds) Spin dependent transport in magnetic nanostructures. Taylor and Francis, New York, pp 143–236
31. Krupa NN (2008) Spin-dependent tunneling conductance in TbCoFe/Pr6 O11 /TbCoFe films. JETP 87:548–550
32. Khorsand AR, Savoini M, Kirilyuk A, Kimel AV et al (2013) Element-specific probing of ultrafast spin dynamics in multisublattice magnets with visible light. Phys Rev Lett 110:107205
33. Kazantseva N, Hinzke D, Nowak U, Chantrell RW, Atxitia U, Chubykalo-Fesenko O (2008) Towards multiscale modeling of magnetic materials: Simulations of FePt. Phys Rev B 77:184428–184428
34. Gel'muhanov FH, Shalagin AM (1979) Light-induced diffusion gases. JETF Lett 29:711–716
35. Myöhänen P, Stan A, Stefanucci G, van Leeuwen R (2009) Kadanoff-Baym approach to quantum transport through interacting nanoscale systems: From the transient to the steady-state regime. Phys Rev B 80:115107–115121

36. Danilelewicz F (1984) Quantum theory of nonequilibrium processes. Ann Phys 153:239–304
37. Baryakhtar VG, Belokolos ED, Korostil AM (1992) A new method for calculating the electron spectrum in solids. Application to high-temperature superconductors. Phys Status Solidi B 169:105–114
38. Bateman H, Erdely A (1955) Higher transcendental functions, vol 3. Mc Graw-Hill, New York
39. Cross M, Adams MJ (1974) Effects of doping and free carriers on the refrective index of direct-gap semiconductors. Opto-electronics 6:199
40. Krupa MM, Pogorily AM (1998) Changes in the structure and magnetic characteristic of nanofilms and control of spin current by short laser pulses. J Tech Phys 68:121
41. Krupa MM, Korostil AM, Skirta YB (2005) Drift of electrons and atoms in the laser radiation field and its influence on the optical properties of semiconductors. Radiophys Quantum Electron XLVIII:45
42. Krupa MM (2000) Selection of laser picosecond impulses and reduction of their duration by means of nonlinear lenses. Opt J 67:41
43. Boling NL, Dube G, Crisp MD (1973) Laser Induced Surface Damage. Appl Opt 12:650
44. Borsch AA, Brodyn MS, Krupa MM (1997) Electrodynamic linear responds of a superconductor film located at the surface of semiconductors. Quantum Electron 4:959
45. Bibik VA, Davydova NA, Kyyak BR, Krupa MM, Mysruchin LV (1984) TiO_2–Ta_2O_5 composite thin films deposited by radio frequency ion-beam sputtering. Solid State Phys 26:80
46. Placko SV (2002) Migration of point defects in compounds of A4 B6 in the field of laser wave. Phys Tech Semicod 36:666
47. Matare H (1971) Defect electronics in semiconductors. Wiley, New York
48. Pogorelov AE, Adeev VM (2001) Penetration of the alien atoms into aluminium at pulse laser effect. Met Phys Adv Tech 19:567
49. Zhuravlev AF, Pogorelov AE, Raboschapka KP (2001) On anomalous atomic diffusion under pulsed laser radiation. Metallophys New Technol 23:36
50. Kautek W, Rudolph P, Daminelli G, Kruuger J (2005) Ultrafast Laser Micro- and Nanostructuring. Appl Phys A 81(65)
51. Oane M, Morjan I, Medianu R (2004) Application of laser matter interaction for generation of small-sized materials. Opt Laser Technol 36:677
52. Xua B, Shenb Z, Nib X, Wanga J, Guanb J, Lub J (2006) Thermal and mechanical finite element modeling of laser-generated ultrasound in coating-substrate system. Opt Laser Technol 38:138
53. Krupa MM, Skirta YB (2006) Terahertz radiation with exciton transitions in CdS crystals. Radiophys Quantum Electron XLIX: 513
54. Krupa MM (2007) Photonic pressure and its influence on magnetic characteristics of multilayered tapes. J Tech Phys 77:93
55. Bychkov YA, Rashba EI (1984) Properties of a 2D electron gas with lifted spectral degeneracy. JETP Lett 39:78
56. Miron IM, Gaudin G, Auffret S, Rodmancq B, Schul A, Pizzini S, Vogel J, Gambardella P (2010) Current-driven spin torque induced by the Rashba effect in a ferromagnetic metal layer. Nat Mater 9:230
57. Reinert F, Nicolay G, Schmidt S, Ehm D, Hüfner S (2001) Direct measurements of the L-gap surface states on the (111) face of noble metals by photoelectron spectroscopy. Phys Rev B 63:115415
58. LaShell V, McDougall BA, Jensen E (1996) Spin Splitting of an Au(111) Surface State Band Observed with Angle Resolved Photoelectron Spectroscopy. Phys Rev Lett 77:3419
59. Nicolay G, Reinert F, Hüfner S, Blaha P (2001) Spin-orbit splitting of the L-gap surface state on Au(111) and Ag(111). Phys Rev B 65:033407
60. Cercellier H, Didiot C, Fagot-Revurat Y, Kierren B, Moreau L, Malterre D, Reinert F (2006) Interplay between structural, chemical, and spectroscopic properties of Ag/Au(111) epitaxial ultrathin films: A way to tune the Rashba coupling. Phys Rev B 73:195413
61. Petersen L, Hedegaard P (2000) A simple tight.-binding model spin-orbit splitting of sp-derived surface states. Surf Sci 459:49
62. Rotenberg E, Chung JW, Kevan SD (1999) Spin-Orbit Coupling Induced Surface Band Splitting in Li/W(110) and Li/Mo(110). Phys Rev Lett 82:4066

63. Hochstrasser M, Tobin JG, Rotenberg E, Kevan SD (2002) Spin-resolved photoemission of surface states of W(110)–(1×1)H. Phys Rev Lett 89:216802
64. Krupin O, Bihlmayer G, Starke K, Gorovikov S, Prieto JE, Döbrich K, Blügel S, Kaindl G (2005) Rashba effect at magnetic metal surfaces. Phys Rev B 71:201403(R)
65. Dedkov YS, Fonin M, Rüdiger U, Laubschat C (2008) Rashba Effect in the Graphene/Ni (111) System. Phys Rev Lett 100(107602)
66. Moreschini L, Bendounan A, Gierz I, Ast CR, Mirhosseini H, Höchst H, Kern K, Henk J, Ernst A, Ostanin S, Reinert F, Grioni M (2009) Spin-orbit coupling induced surface band splitting in Li/W(110) and Li/Mo(110). Phys Rev B 79:075424
67. Ohno H et al (2000) Electric-field control of ferromagnetism. Nature 408:944–946
68. Weisheit M et al (2007) Electric field-induced modification of magnetism in thin-film ferromagnets. Science 315:349–351
69. Chu Y-H et al (2008) Electric-field control of local ferromagnetism using a magnetoelectric multiferroic. Nat Mater 7:478–482
70. Myers EB, Ralph DC, Katine JA, Louie RN, Buhrman RA (1999) Current-induced switching of domains in magnetic multilayer devices. Science 285:867–870
71. Wegrowe J-E, Kelly D, Jaccard Y, Guittienne P, Ansermet J-P (1999) Current-induced magnetization reversal in magnetic nanowires. Europhys Lett 45:626–632
72. Ralph DC, Stiles MD (2008) Spin transfer torques. J Magn Magn Mater 320:1190–1216
73. Chappert C, Fert A, Nguyen Van Dau F (2007) The emergence of spin electronics in data storage. Nat Mater 6:813–823
74. Katine JA, Fullerton EE (2008) Device implications of spin-transfer torque. J Magn Magn Mater 320:1217–1226
75. Manchon A, Zhang S (2008) Theory of nonequilibrium intrinsic spin torque in a single nanomagnet. Phys Rev B 78:212405
76. Manchon A, Zhang S (2009) Theory of spin torque due to spin-orbit coupling. Phys Rev B 79:094422
77. Edelstein VM (1990) Spin polarization of conduction electrons induced by electric current in two-dimensional asymmetric electron systems. Solid State Commun 73:233–235
78. Inoue J, Bauer GEW, Molenkamp LW (2003) Diffuse transport and spin accumulation in a Rashba two-dimensional electron gas. Phys Rev B 67:033104
79. Kato YK, Myers RC, Gossard AC, Awschalom DD (2004) Current-induced spin polarization in strained semiconductors. Phys Rev Lett 93:176601
80. Awschalom D, Samarth N (2009) Trend: Spintronics without magnetism. Physics 2:50
81. Adagideli I, Bauer GEW, Halperin BI (2006) Detection of current-induced spins by ferromagnetic contacts. Phys Rev Lett 97:256601
82. Obata K, Tatara G (2008) Current-induced domain wall motion in Rashba spin-orbit system. Phys Rev B 77:214429
83. Cardona M, Christensen NE, Fasol G (1988) Relativistic band structure and spin-orbit splitting of zinc-blende-type semiconductors. Phys Rev B 38:1806
84. Chernyshov A et al (2009) Evidence for reversible control of magnetization in a ferromagnetic material by means of spin–orbit magnetic field. Nat Phys 5:656
85. Hoesch M, Muntwiler M, Petrov VN, Hengsberger M, Patthey L, Shi M, Falub M, Greber T, Osterwalder J (2004) Spin structure of the Shockley surface state on Au(111). Phys Rev B 69:241401
86. Henk J, Hoesch M, Osterwalder J, Ernst A, Bruno P (2004) Spin–orbit coupling in the L-gap surface states of Au(111): spin-resolved photoemission experiments and first-principles calculations. J Phys Condens Matter 16:7581
87. Gambardella P et al (2003) Giant magnetic anisotropy of single cobalt atoms and nanoparticles. Science 300:1130–1133
88. Miron IM, Gaudin G, Auffret S, Rodmacq B, Schuhl A, Pizzini S, Vogel J, Gambardella P (2013) Current-driven spin torque induced by the Rashba effect in a ferromagnetic metal layer. Nat Mater (Supplementary Information) 1
89. Beach GSD, Tsoi M, Erskine JL (2008) Current-induced domain wall motion. J Magn Magn Mater 320:1272

90. Zhang S, Li Z (2004) Roles of nonequilibrium conduction electrons on the magnetization dynamics of ferromagnets. Phys Rev Lett 93:127204
91. Thiaville A, Nakatani Y, Miltat J, Suzuki Y (2005) Micromagnetic understanding of current-driven domain wall motion in patterned. Europhys Lett 69:990
92. Miron IM, Zermatten P-J, Gaudin G, Auffret S, Rodmacq B, Schuhl A (2009) Domain wall spin torquemeter. Phys Rev Lett 102:137202
93. Eerenstein W, Mathur ND, Scott JF (2006) Multiferroic and magneto-electric materials. Nature 442:759–765
94. Chiba D, Yamanouchi M, Matsukura F, Ohno H (2003) Electrical Manipulation of Magnetization Reversal in a Ferromagnetic Semiconductor. Science 301:943–945
95. Chiba D, Sawicki M, Nishitani Y, Nakatani Y, Matsukura F, Ohno H (2008) Magnetization vector manipulation by electric fields. Nature 455:515–518
96. Stolichnov I, Riester SWE, Trodahl HJ, Setter N, Rushforth AW, Edmonds KW, Campion RP, Foxon CT, Gallagher BL, Jungwirth T (2008) Non-volatile ferroelectric control of ferromagnetism in (Ga,Mn)As. Nat Mater 7:464–467
97. Tsymbal EY (2012) Spintronics: Electric toggling of magnets. Nat Mater 11:12–13
98. Emori S, Bauer U, Ahn S-M, Martinez E, Beach GSD (2013) Current-driven dynamics of chiral ferromagnetic domain walls. Nat Mater 12:611
99. Ryu K-S, Thomas L, Yang S-H, Parkin S (2013) Chiral spin torque at magnetic domain walls. Nat Nanotechnol 8:527–533
100. Wang W-G, Li M, Hageman S, Chien CL (2012) Electric-field-assisted switching in magnetic tunnel junctions. Nat Mater 11:64–68
101. Maruyama T, Shiota Y, Nozaki T, Ohta K, Toda N, Mizuguchi M, Tulapurkar AA, Shinjo T, Shiraishi M, Mizukami S, Ando Y, Suzuki Y (2009) Large voltage-induced magnetic anisotropy change in a few atomic layers of iron. Nat Nanotechnol 4:158
102. Fowley C, Rode K, Oguz K, Kurt H, Coey JMD (2011) Electric field induced changes in the coercivity of a thin-film ferromagnet. J Phys D Appl Phys 44:305001
103. Kyuno K, Ha JG, Yamamoto R, Asano SJ (1996) First-principles calculation of the magnetic anisotropy energies of Ag/Fe(001) and Au/Fe(001). Phys Soc Jpn 65:1334–1339
104. Duan C-G, Jaswal SS, Tsymbal EY (2006) Predicted magnetoelectric effect in Fe/$BaTiO_3$ multilayers: ferroelectric control of magnetism. Phys Rev Lett 97:047201
105. Niranjan MK, Duan CG, Jaswal SS, Tsymbal EY (2010) Magneto-electric effect at the $SrRuO_3$/$BaTiO_3$ (001) interface: A first-principle study. Appl Phys Lett 96:222504
106. Nakamura K, Shimabukuro R, Fujiwara Y, Akiyama T, Ito T, Freeman A (2009) Giant modification of the magnetocrystalline anisotropy in transition-metal monolayers by an external electric field. J Phys Rev Lett 102:187201
107. Casella RC (1960) Toroidal energy surfaces in crystals with wurtzite symmetry. Phys Rev Lett 5:371
108. Barnes SE, Ieda J, Maekawa S (2014) Rashba spin-orbit anisotropy and the electric field control of magnetism. Sci Rep 7
109. Dzyaloshinskii IE (1958) A thermodynamic theory of "weak" ferromagnetism of antiferromagnetics. J Chem Solids 4:241
110. Moriya T (1960) Anisotropic superexchange interaction and weak ferromagnetism. Phys Rev 120:91
111. Chagpert C, Bruno P, Bartenlian B, Beauvillain P, Bounouh A, Megy R, Veillet P (1995) Magnetic anisotropy and interlayer exchange c~upling in Fe(110)/Art(11 1) ultrathin films. J Magn Magn Mater 148:165
112. Nozaki T, Yakushiji K, Tamaru S, Sekine M, Matsumoto R, Konoto M, Kubota H, Fukushima A, Yuasa S (2013) Voltage-induced magnetic anisotropy changes in an ultrathin FeB layer sandwiched between two MgO layers. Appl Phys Exp 6:073005
113. Leeb T, Brockmann M, Bensch F, Miethaner S, Bayreuther G (1999) In-plane magnetic anisotropies in Fe films on vicinal Ag(001) and Au(001) surfaces. J Appl Phys 85:4964

Chapter 5
Molecular Dynamics of Thin Mesogene Layer Covering Carbon Nanotube

P. Raczyński, V. Raczyńska, and Z. Gburski

5.1 Introduction

The phase of matter characterized by a considerable orientation order and some positional order is known as the liquid crystal phase (mesophase). The materials which exhibit these properties are called liquid crystals or mesogenes [1]. Liquid crystalline systems are still intensively studied because they exhibit very interesting properties. In the last decades, the scientists' attention was focused on the technical applications of liquid crystals, for example, liquid crystalline displays, optic filters, and memory devices [2–12]. Another objective was connected with biological systems, i.e., desire for fundamental understanding of membranes and nucleic acids [13].

The impact of carbon nanotube (CNT) on the liquid crystalline systems is presented in this chapter. In contrast to our recent works [14–19], 5CB, 6CB, 7CB, and 8CB mesogene molecules were taken into account. Studies have been carried out for a wide range of temperatures (from $T = 210$ to 360 K). The ultra-thin film, where the mesogene molecules form one or two layers surrounding the CNT, has been studied. As an example, snapshot of the systems with 7CB molecules and CNT is presented in Fig. 5.1.

All studies were performed using computer simulations technique, which is an useful tool for describing the structural and dynamical properties of various molecular systems [20–32], and it is the basis for subsequent experimental studies. In this chapter, we used MD technique for elucidating the differences in behavior of liquid crystals at various temperatures [4, 6, 8, 18, 33].

The structural and dynamical properties of systems studied show the differences between pure clusters and the clusters with the CNT. We show the

P. Raczyński (✉) • V. Raczyńska • Z. Gburski
Institute of Physics, University of Silesia, Uniwersytecka 4, Katowice 40-007, Poland
e-mail: przemyslaw.raczynski@us.edu.pl

O. Fesenko, L. Yatsenko (eds.), *Nanoplasmonics, Nano-Optics, Nanocomposites, and Surface Studies*, Springer Proceedings in Physics 167,
DOI 10.1007/978-3-319-18543-9_5

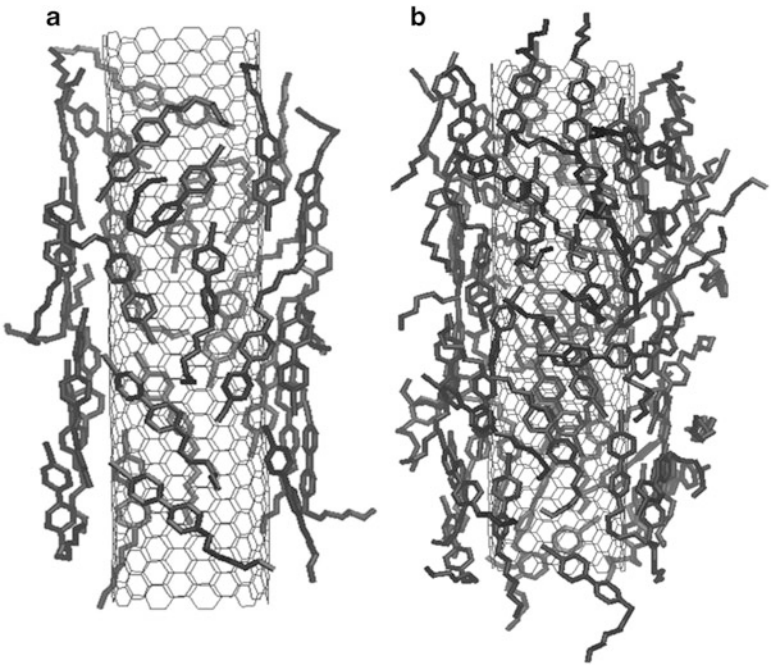

Fig. 5.1 The system composed of $n = 30$ (**a**) and $n = 65$ (**b**) 7CB molecules surrounding the carbon nanotube

distinctions in case of similar systems, but composed of different members of mCB family ($m = 5, 6, 7, 8$).

The physical properties presented in our research might be related to future endeavors of designing the new generations of display devices, spatial modulators, etc.

5.2 Computational Method

All simulations presented in this work were performed using NAMD 2.7 simulation code [34] and visualized with VMD 1.9.1 [35]. Interactions in studied systems were modeled with CHARMM-based potential [36].

The studied systems consist of $n = 30$ and $n = 65$ mesogene molecules of 5CB, 6CB, 7CB, or 8CB. All simulations were performed for four temperatures: $T = 210$ K, $T = 260$ K, $T = 310$ K, $T = 360$ K, with the applied simulation time step equal to $t = 0.5$ fs. The data were collected both for the pure clusters and for clusters surrounding the CNT.

All simulations were performed in NVT ensemble. The initial configurations of the systems were minimized for 1.5×10^6 simulation steps. The part of the simulations when the data were collected (after equilibration) takes 1×10^7 simulation steps.

Mesogene molecules from mCB family were described with model derived by Zannoni et al. [37]. This model successfully reproduces the liquid-crystal state of mesogenes [37] and was used to study the properties of mesogene layers and the anchoring effects [38]. The armchair (10, 10) CNT were described in the same way as reported in [39, 40].

5.3 Results

The first observable we would like to present is the mean square displacement $\left\langle \left| \Delta \vec{r}(t) \right|^2 \right\rangle$ of the center of mass of molecule. The mean square displacement is defined as

$$\left\langle \left| \Delta \vec{r}(t) \right|^2 \right\rangle = \left\langle \left| \vec{r}(t) - \vec{r}(0) \right|^2 \right\rangle \tag{5.1}$$

[41], where $\vec{r}$ is the position of the center of mass of a single molecule.

Figure 5.2 shows, as an example, the mean square displacement for the center of mass of 7CB in the pure cluster (Fig. 5.2a) and in the layer covering CNT (Fig. 5.2b).

In all studied mCB clusters, similar behavior is observed so for the clarity and curtness of presentation only plots for 7CB are shown. All conclusions given here are also true in the other samples. The $\left\langle \left| \Delta \vec{r}(t) \right|^2 \right\rangle$ plots show that the mobility of 7CB molecules increases with the heating of the clusters. The 7CB molecules

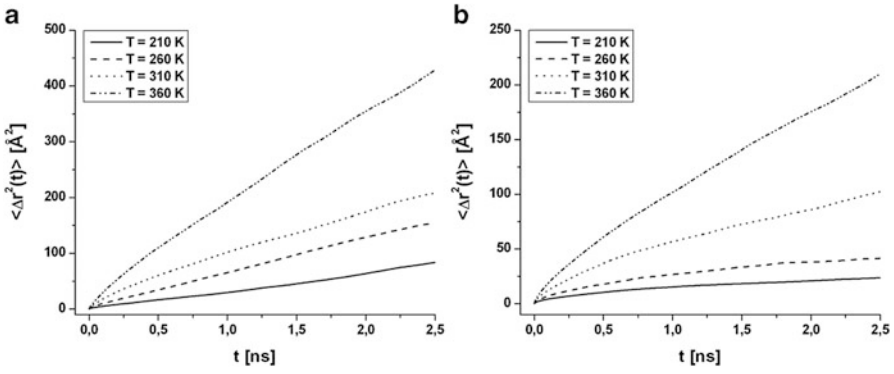

Fig. 5.2 The mean square displacement of the center of mass of 7CB molecules in the studied temperature range. (**a**) Pure cluster consists of $n = 65$ mesogene molecules. (**b**) Cluster $n = 65$ mesogene molecules with CNT

Table 5.1 The calculated values of D [Å^2/ps] for all studied systems

	5CB	6CB	7CB	8CB
The clusters without CNT composed of $n = 30$ mesogene molecules				
$T = 210$ K	1.02×10^{-2}	1.09×10^{-2}	1.06×10^{-2}	7.31×10^{-3}
$T = 260$ K	1.48×10^{-2}	1.26×10^{-2}	1.15×10^{-2}	1.1×10^{-2}
$T = 310$ K	2.6×10^{-2}	2.83×10^{-2}	2.04×10^{-2}	2.38×10^{-2}
$T = 360$ K	3.17×10^{-2}	3.25×10^{-2}	3.75×10^{-2}	3.25×10^{-2}
The clusters without CNT composed of $n = 65$ mesogene molecules				
$T = 210$ K	5.16×10^{-3}	5.29×10^{-3}	4.44×10^{-3}	4.79×10^{-3}
$T = 260$ K	1.27×10^{-2}	9.02×10^{-3}	1.03×10^{-2}	9.58×10^{-3}
$T = 310$ K	1.32×10^{-2}	1.74×10^{-2}	1.36×10^{-2}	1.36×10^{-2}
$T = 360$ K	2.85×10^{-2}	3.04×10^{-2}	2.77×10^{-2}	2.68×10^{-2}
The clusters with CNT composed of $n = 30$ mesogene molecules				
$T = 210$ K	6.18×10^{-3}	3.91×10^{-3}	1.9×10^{-3}	1.75×10^{-3}
$T = 260$ K	6.34×10^{-3}	9.48×10^{-3}	2.46×10^{-3}	5.99×10^{-3}
$T = 310$ K	1.13×10^{-2}	1.18×10^{-2}	8.9×10^{-3}	1.01×10^{-2}
$T = 360$ K	2.87×10^{-2}	1.95×10^{-2}	1.54×10^{-2}	2.05×10^{-2}
The clusters with CNT composed of $n = 65$ mesogene molecules				
$T = 210$ K	1.31×10^{-3}	1.67×10^{-3}	1.67×10^{-3}	2.07×10^{-3}
$T = 260$ K	4.1×10^{-3}	4.16×10^{-3}	3.74×10^{-3}	3.65×10^{-3}
$T = 310$ K	1.08×10^{-2}	1.07×10^{-2}	9.74×10^{-3}	8.4×10^{-3}
$T = 360$ K	2.33×10^{-2}	1.72×10^{-2}	1.62×10^{-2}	1.94×10^{-2}

surrounding CNT are not moving as easily as in the pure cluster and their mobility is lower.

To show the mobility of each studied system, we calculated the translational diffusion coefficient D. The mean square displacement is connected with the diffusion coefficient via Einstein relation [42]:

$$\left\langle \left| \Delta \vec{r}(t) \right|^2 \right\rangle \approx 6\mathrm{Dt} \tag{5.2}$$

The obtained values of D for all studied systems are presented in Table 5.1.

Some examples of D are also shown in Fig. 5.3.

Figure 5.3a shows the values of D for the pure 8CB clusters composed of $n = 30$ (squares) and $n = 65$ (triangles) molecules. The D values are always higher for smaller cluster, the mobility of molecules in $n = 65$ cluster is smaller. In the small cluster, relatively more molecules are located on the cluster surface and the cluster core, where molecules are surrounded by each other and they have a little volume to move, does not exist or it is very small.

In case of 8CB molecules surrounding CNT (Fig. 5.3b), the values of D are usually smaller for larger cluster. The free volume accessible to molecule in layer composed of smaller number of molecules is larger. In the layer consisted of larger

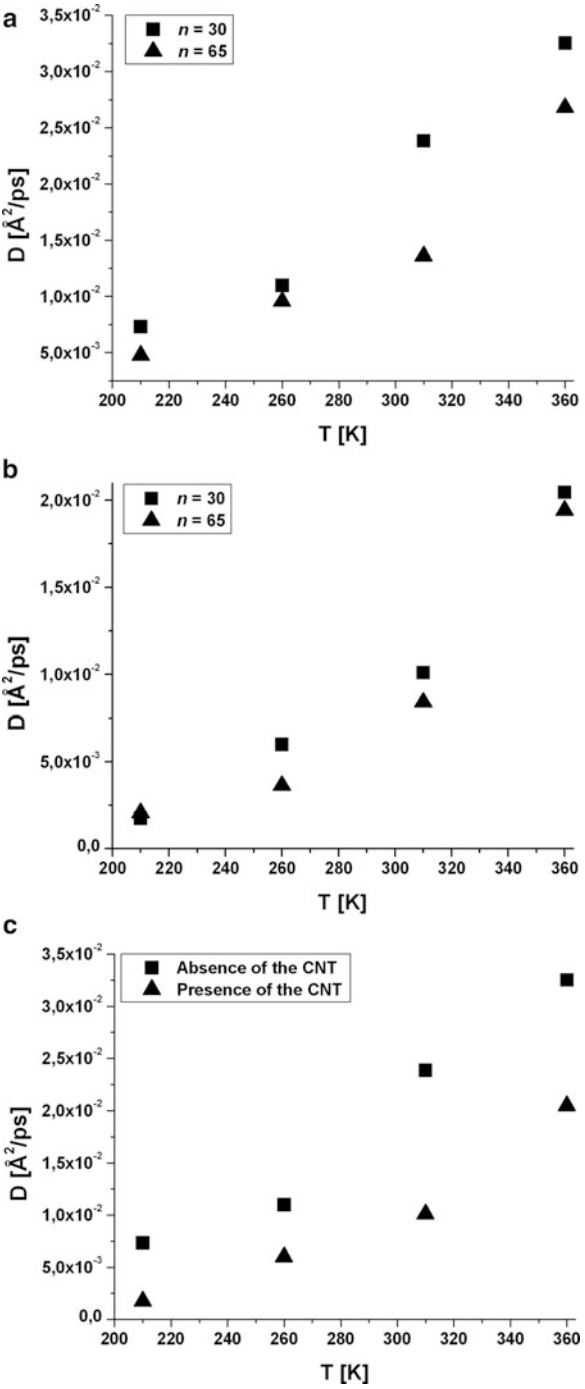

Fig. 5.3 The calculated values of D. (**a**) The comparison between pure 8CB smaller and bigger clusters. (**b**) The comparison between 8CB smaller and bigger clusters in the presence of the CNT. (**c**) The comparison between systems composed of $n = 30$ 8CB molecules

number ($n = 65$) of mesogene molecules the CNT surface is tightly covered by them what means smaller mobility. In case of 7CB and 8CB one can notice that the values of D are sometimes larger for larger layer, instead of 5CB and 6CB, where values of D are always smaller for larger layer. This can be explained by larger size of 7CB and 8CB. A few of these molecules in larger cluster formed the very loosely second layer around CNT (see Fig. 5.1b). It also explains, why for the 5CB and 6CB molecules slightly larger differences appearing in values of D, for bigger and smaller number of molecules covering CNT, comparing to 7CB and 8CB. These differences are more pronounced at lower temperatures studied, for example for 5CB molecules at 210 K and for 6CB at 260 K. Smaller 5CB and 6CB molecules in cluster $n = 30$ do not cover CNT's surface as tightly as larger 7CB and 8CB.

Figure 5.3c shows the comparison between the $n = 30$ systems with the absence and presence of the nanotube. The values of D are higher for the cluster without CNT, the molecules in the pure cluster exhibit greater mobility. The mCB molecules strictly adhere to the CNT surface, and the intermolecular interactions (van der Waals forces) are strong (physisorption).

In case of all studied systems, thermal activation of translational diffusion can be well described by Arrhenius law:

$$D = D_0 \exp\left(\frac{E_A}{k_B T}\right) \tag{5.3}$$

where k_B is the Boltzman constant and E_A is the activation energy. Fitting data with Arrhenius law allowed us to estimate the diffusion activation energy E_A (see Table 5.2). In case of clusters composed of $n = 30$ molecules (with and without CNT), the values of E_A are lower for the smaller 5CB and 6CB and higher for the 7CB and 8CB. In case of larger systems, particularly in the sample with CNT, the activation energy is the lowest for 8CB and the largest for 5CB. This inversion can be explained when one takes sizes of mCB. The larger size of 7CB and 8CB causes that more molecules move to the relatively loose second layer, they do not fall in CNT the nearest layer. In the second layer, the molecules have a larger free volume to move and their motion in that layer remind the motion in the pure cluster. When we took into account larger molecules from the mCB family, more molecules

Table 5.2 The calculated values of diffusion activation energy E_A [K] for all studied systems

	5CB	6CB	7CB	8CB
The clusters without CNT composed of n = 30 mesogene molecules				
Diffusion activation energy E_A [K]	596.75	603	619.32	781.81
The clusters without CNT composed of n = 65 mesogene molecules				
Diffusion activation energy E_A [K]	777.94	873.85	865.92	820.65
The clusters with CNT composed of $n = 30$ mesogene molecules				
Diffusion activation energy E_A [K]	719.78	770.22	1,101.58	1,201.31
The clusters with CNT composed of n = 65 mesogene molecules				
Diffusion activation energy E_A [K]	1,443.81	1,200.08	1,165.49	1,105.12

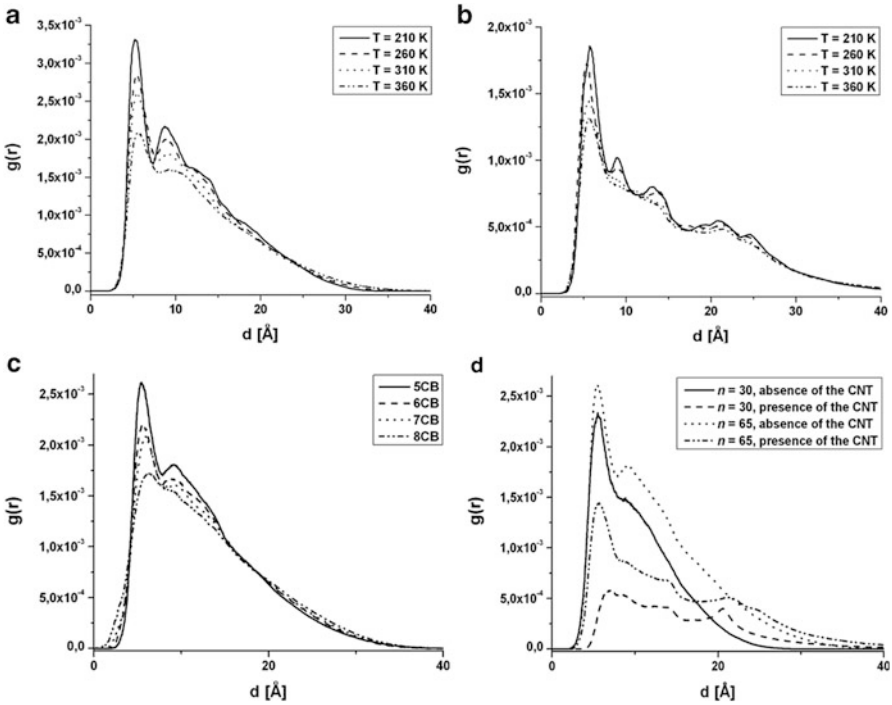

Fig. 5.4 The plots of radial distribution functions. (**a**) The temperature dependence of the $g(r)$ for the $n = 65$ 5CB molecules and with the absence of the CNT. (**b**) The temperature dependence of the $g(r)$ for the $n = 65$ 5CB molecules and with the presence of the CNT. (**c**) The $g(r)$ comparison of mCB family at $T = 310$ K for the system consists of $n = 65$ mesogene molecules (without CNT). (**d**) The comparison of $g(r)$ for various 5CB systems at $T = 310$ K

do not accommodate in the layer closest to CNT and their contribution to the movement can explain the decreasing E_A.

Figure 5.4 shows a few examples of the radial distribution functions $g(r)$.

Here, we placed only four $g(r)$ charts for the selected systems, temperatures. Remaining $g(r)$ functions for the other systems are very similar, therefore are not presented. In Fig. 5.4a, b, the temperature dependence for the systems with and without CNT is shown. At low temperature, clearly visible peaks are connected with the nearest ($d_1 \approx 5.2$ Å) and further neighbors ($d_2 \approx 9.1$ Å, $d_3 \approx 13.2$ Å). However, the peak corresponding to the third neighbors is visible only for the samples with CNT. Moreover, the fuzzy peak is visible about $d \approx 21$ Å for the systems with nanotube. This peak indicates the appearance of the neighbors on the opposite side of CNT (we used in simulations the nanotube of the diameter $d = 13$ Å).

In Fig. 5.4c, the comparison between 5CB, 6CB, 7CB, and 8CB molecules is shown. The values of $g(r)$ functions are lower for larger 7CB and 8CB molecules. These molecules have a lower number of neighbors. Moreover, the maximum of the peaks for 7CB and 8CB molecules are shifted towards greater distances and this

observation can also be explained when one takes into account the size of the mCB molecules. For example, the maximum of the first peak for 5CB molecule is at $d_1 \approx 5.5$ Å while for 8CB it appears at $d_1 \approx 6.4$ Å.

Figure 5.4d presents the comparison between systems with and without nanotubes. The lower values of the $g(r)$ function for the systems with CNT show that in these samples the mesogene molecules have a lower number of the neighbors.

To get deeper insight in structural properties of studied systems, especially into thermal disorder, we have also calculated the Lindemann index δ_L, defined as:

$$\delta_L = \frac{1}{n(n-1)} \sum_{i=1}^{n} \sum_{j=1,\, j\neq i}^{n} \sqrt{\frac{\left\langle r_{ij}^2 \right\rangle - \left\langle r_{ij} \right\rangle^2}{\left\langle r_{ij} \right\rangle}} \tag{5.4}$$

where n is the number of molecules, r_{ij} is the distance between ith and jth molecule, and $\langle\rangle$ denote the time average. Obtained data for all studied systems are presented in Table 5.3. In all studied systems, we did not observe any significant discontinuities in thermal characteristics of δ_L. This indicates that no phase transitions occurred in the studied temperature range [43–50]. Values of δ_L ($\delta_L \geq 0.1$) and lack of discontinuities indicate that investigated systems in studied

Table 5.3 The calculated values of δ_L

	5CB	6CB	7CB	8CB
The clusters without CNT composed of n = 30 mesogene molecules				
$T = 210$ K	0.17	0.15	0.17	0.14
$T = 260$ K	0.24	0.24	0.22	0.2
$T = 310$ K	0.31	0.29	0.3	0.28
$T = 360$ K	0.34	0.33	0.33	0.33
The clusters without CNT composed of n = 65 mesogene molecules				
$T = 210$ K	0.1	0.11	0.1	0.1
$T = 260$ K	0.19	0.19	0.17	0.16
$T = 310$ K	0.26	0.26	0.25	0.24
$T = 360$ K	0.32	0.31	0.31	0.29
The clusters with CNT composed of n = 30 mesogene molecules				
$T = 210$ K	0.13	0.13	0.1	0.09
$T = 260$ K	0.18	0.17	0.14	0.16
$T = 310$ K	0.21	0.21	0.21	0.21
$T = 360$ K	0.28	0.26	0.26	0.24
The clusters with CNT composed of n = 65 mesogene molecules				
$T = 210$ K	0.09	0.1	0.09	0.09
$T = 260$ K	0.13	0.14	0.12	0.12
$T = 310$ K	0.2	0.21	0.18	0.18
$T = 360$ K	0.26	0.24	0.23	0.23

temperature range are in liquid state. It should also be noted that for all mCB family members, the δ_L values for clusters in the presence of nanotube are smaller than for pure clusters. This observation is in good agreement with our previous findings for self-diffusion coefficient, where similar tendency was observed. Translational dynamics of mCB molecules is decelerated and thermally driven disorder is smaller in the presence of CNT. As one would expect, values of δ_L decrease with a number of molecules in cluster/layer.

5.4 Conclusions

We have performed a series of NVT simulations of mCB family of mesogene molecules forming thin layer around CNT. Obtained results suggest that the presence of nanotube has significant impact on translational dynamics of molecules. The strong interactions between mesogene molecules and nanotube surface lead to considerable deceleration of molecules movement.

This conclusion finds reflection in shape of mean square displacement curves and corresponding values of self-diffusion coefficients. As one could expect, the mobility of molecules decreases with the number of molecules forming cluster or layer, and decreases with the increase of molecular mass in mCB homologous series. We have been able to estimate the values of activation energies for translational diffusion for studied systems with CNTs and pure clusters. Calculated values confirm the observation that in the presence of CNT, mobility of mesogene molecules is reduced.

The obtained results might be interesting from the point of view of the design of new optical devices based on liquid crystals and carbon nanostructures.

References

1. Chandrasekhar S (1992) Liquid crystals. Cambridge University Press, Cambridge
2. Kuwajima S, Manabe A (2000) Computing the rotational viscosity of nematic liquid crystals by an atomistic molecular dynamics simulation. Chem Phys Lett 332:105–109. doi:10.1016/S0009-2614(00)01235-5
3. Chilaya G, Petriashvili G, Chanishvili A, Terenetskaya I, Kireeva N, Lisetski L (2005) Provitamin D-2 and provitamin D-3 photo transformations in cholesteric liquid crystal mixtures induced by UV radiation. Mol Cryst Liq Cryst 433:73–85. doi:10.1080/15421400590956243
4. Care CM, Cleaver DJ (2005) Computer simulation of liquid crystals. Rep Prog Phys 68:2665–2700. doi:10.1088/0034-4885/68/11/R04
5. Lisetski LN, Minenko SS, Zhukov AV, Shtifanyuk PP, Lebovka NI (2009) Dispersions of carbon nanotubes in cholesteric liquid crystals. Mol Cryst Liq Cryst 510:43–50. doi:10.1080/15421400903058056
6. McDonald AJ, Hanna S (2006) Atomistic simulation of a model liquid crystal. J Chem Phys 124:164906. doi:10.1063/1.2193154

7. Stassen H, Gburski Z (1994) Instantaneous normal-mode analysis of binary-liquid Ar-Kr mixtures. Chem Phys Lett 217:325–332. doi:10.1016/0009-2614(93)E1390-3
8. Berardi R, Costantini A, Muccioli L, Orlandi S, Zannoni C (2007) A computer simulation study of the formation of liquid crystal nanodroplets from a homogeneous solution. J Chem Phys 126:044905. doi:10.1063/1.2430710
9. Lisetski LN, Lebovka NI, Naydenov SV, Soskin MS (2011) Dispersions of multi-walled carbon nanotubes in liquid crystals: a physical picture of aggregation. J Mol Liq 164:143–147. doi:10.1016/j.molliq.2011.04.020
10. Dendzik Z, Kośmider M, Raczyński P, Piątek A (2007) Interaction induced absorption of rare gas mixtures physisorbed on nanotubes and fullerenes–computer simulation study. J Non-Cryst Solids 353:4586–4590
11. Bezrodna T, Chashechnikova I, Gavrilko T, Puchkovska G, Shaydyuk Y, Tolochko A, Baran J, Drozd M (2008) Structure formation and its influence on thermodynamic and optical properties of montmorillonite organoclay-5CB liquid crystal nanocomposites. Liq Cryst 35:265–274. doi:10.1080/02678290701830626
12. Bezrodna T, Chashechnikova I, Nesprava V, Puchkovska G, Shaydyuk Y, Boyko Y, Baran J, Drozd M (2010) Structure peculiarities and optical properties of nanocomposite: 5CB liquid crystal-CTAB-modified montmorillonite clay. Liq Cryst 37:263–270. doi:10.1080/02678290903511677
13. Komolkin A, Laaksonen A, Maliniak A (1994) Molecular-dynamics simulation of a nematic liquid-crystal. J Chem Phys 101:4103–4116. doi:10.1063/1.467460
14. Gwizdala W, Górny K, Gburski Z (2008) Molecular dynamics and dielectric loss in 4-cyano-4-n-pentylbiphenyl (5CB) mesogene film surrounding carbon nanotube—computer simulation. J Mol Struct 887:148–151. doi:10.1016/j.molstruc.2007.12.045
15. Dawid A, Gwizdala W (2009) Dynamical and structural properties of 4-cyano-4-n-pentylbiphenyl (5CB) molecules adsorbed on carbon nanotubes of different chiralities: computer simulation. J Non-Cryst Solids 355:1302–1306. doi:10.1016/j.jnoncrysol.2009.05.034
16. Dawid A, Gwizdala W (2010) The dynamics of 5cb mesogene molecules between graphite walls—an MD study. Rev Adv Mater Sci 23:37–41
17. Gwizdala W, Górny K, Gburski Z (2011) The dynamics of 4-cyano-4-n-pentylbiphenyl (5CB) mesogen molecules located between graphene layers–MD study. Spectrochim Acta A Mol Biomol Spectrosc. doi:10.1016/j.saa.2010.08.040
18. Dawid A, Gburski Z (2012) Molecular dynamics simulation study of the liquid crystal phase in small mesogene cluster (9CB)(20). Mater Sci-Pol 30:212–216. doi:10.2478/s13536-012-0024-1
19. Dawid A, Gburski Z (2007) Dielectric relaxation of 4-cyano-4-n-pentylbiphenyl (5CB) thin layer adsorbed on carbon nanotube—MD simulation. J Non-Cryst Solids 353:4339–4343. doi:10.1016/j.jnoncrysol.2007.02.072
20. Nakazaki N, Takao Y, Eriguchi K, Ono K (2014) Molecular dynamics simulations of silicon chloride ion incidence during Si etching in Cl-based plasmas. Jpn J Appl Phys 53:056201. doi:10.7567/JJAP.53.056201
21. Dawid A, Gburski Z (1997) Dynamical properties of the argon-krypton clusters: molecular dynamics calculations. J Mol Struct 410–411:507–511. doi:10.1016/S0022-2860(96)09512-9
22. Khan S, Singh JK (2014) Wetting transition of nanodroplets of water on textured surfaces: a molecular dynamics study. Mol Simul 40:458–468. doi:10.1080/08927022.2013.819578
23. Gburski Z, Zerda T (1980) Vibrational dephasing and intermolecular interactions in liquids. Acta Phys Pol A 57:447–454
24. Iguchi R, Kawamura T, Suzuki Y, Inoue M, Kangawa Y, Kakimoto K (2014) Molecular dynamics simulation of graphene growth by surface decomposition of 6H-SiC(0001) and (000(1)over-bar). Jpn J Appl Phys 53:065601. doi:10.7567/JJAP.53.065601
25. Kachel A, Gburski Z (1998) Chain formation in a model dipolar liquid: computer simulation study. J Phys Condens Matter 9:10095. doi:10.1088/0953-8984/9/46/007

26. Kosmider M, Dendzik Z, Palucha S, Gburski Z (2004) Computer simulation of argon cluster inside a single-walled carbon nanotube. J Mol Struct 704:197–201. doi:10.1016/j.molstruc.2004.02.050
27. Gao Y, Liu J, Shen J, Wu Y, Zhang L (2014) Influence of various nanoparticle shapes on the interfacial chain mobility: a molecular dynamics simulation. Phys Chem Chem Phys 16:21372–21382. doi:10.1039/c4cp03019b
28. Raczynski P, Dawid A, Pietek A, Gburski Z (2006) Reorientational dynamics of cholesterol molecules in thin film surrounded carbon nanotube: molecular dynamics simulations. J Mol Struct 792–793:216–220. doi:10.1016/j.molstruc.2006.01.064
29. Barker J, Fisher R, Watts R (1971) Liquid argon—Monte Carlo and molecular dynamics calculations. Mol Phys 21:657–673. doi:10.1080/00268977100101821
30. Grammatikopoulos P, Cassidy C, Singh V, Benelmekki M, Sowwan M (2014) Coalescence behaviour of amorphous and crystalline tantalum nanoparticles: a molecular dynamics study. J Mater Sci 49:3890–3897. doi:10.1007/s10853-013-7893-5
31. Honeycutt J, Andersen H (1987) Molecular-dynamics study of melting and freezing of small Lennard-Jones clusters. J Phys Chem 91:4950–4963. doi:10.1021/j100303a014
32. Gburski Z (1985) Convergence of memory functions for the vibrational dephasing process in liquids. Chem Phys Lett 115:236–240. doi:10.1016/0009-2614(85)80687-4
33. Fukunaga H, Takimoto J, Doi M (2004) Molecular dynamics simulation study on the phase behavior of the Gay-Berne model with a terminal dipole and a flexible tail. J Chem Phys 120:7792–7800. doi:10.1063/1.1687681
34. Phillips JC, Braun R, Wang W, Gumbart J, Tajkhorshid E, Villa E, Chipot C, Skeel RD, Kalé L, Schulten K (2005) Scalable molecular dynamics with NAMD. J Comput Chem 26:1781–1802. doi:10.1002/jcc.20289
35. Humphrey W, Dalke A, Schulten K (1996) VMD—visual molecular dynamics. J Mol Graph 14:33–38
36. MacKerell BD, Bellott D, Evanseck JD, Field MJ, Fischer S, Gao J, Guo H, Ha S, Joseph-McCarthy D, Kuchnir L, Kuczera K, Lau FTK, Mattos C, Michnick S, Ngo T, Nguyen DT, Prodhom B, Reiher WE, Roux B, Schlenkrich M, Smith JC, Stote R, Straub J, Watanabe M, Wiórkiewicz-Kuczera J, Yin D, Karplus M (1998) All-atom empirical potential for molecular modeling and dynamics studies of proteins. J Phys Chem B 102:3586–3616. doi:10.1021/jp973084f
37. Tiberio G, Muccioli L, Berardi R, Zannoni C (2009) Towards in silico liquid crystals. Realistic transition temperatures and physical properties for n-cyanobiphenyls via molecular dynamics simulations. ChemPhysChem 10:125–136. doi:10.1002/cphc.200800231
38. Pizzirusso A, Berardi R, Muccioli L, Ricci M, Zannoni C (2012) Predicting surface anchoring: molecular organization across a thin film of 5CB liquid crystal on silicon. Chem Sci 3:573–579. doi:10.1039/C1SC00696G
39. Alexiadis A, Kassinos S (2008) Molecular simulation of water in carbon nanotubes. Chem Rev 108:5014–5034. doi:10.1021/cr078140f
40. Gburski Z, Górny K, Raczynski P (2010) The impact of a carbon nanotube on the cholesterol domain localized on a protein surface. Solid State Commun 150:415–418. doi:10.1016/j.ssc.2009.12.005
41. Frenkel D, Smit B (2001) Understanding molecular simulation: from algorithms to applications, 2nd edn. Academic, San Diego
42. Rapaport DC (2004) The art of molecular dynamics simulation. Cambridge University Press, New York
43. Kosterlitz JM, Thouless DJ (1973) Ordering, metastability and phase-transitions in 2 dimensional systems. J Phys C-Solid State Phys 6:1181–1203. doi:10.1088/0022-3719/6/7/010
44. Dawid A, Gburski Z (2003) Interaction-induced light scattering in a fullerene surrounded by an ultrathin argon atmosphere: molecular dynamics simulation. Phys Rev A 68:065202. doi:10.1103/PhysRevA.68.065202

45. Piatek A, Dawid A, Gburski Z (2006) The existence of a plastic phase and a solid–liquid dynamical bistability region in small fullerene cluster $(C_{60})_7$: molecular dynamics simulation. J Phys Condens Matter 18:8471–8480. doi:10.1088/0953-8984/18/37/006
46. Wentzcovitch R (1991) Invariant molecular-dynamics approach to structural phase-transitions. Phys Rev B 44:2358–2361. doi:10.1103/PhysRevB.44.2358
47. Tycko R, Dabbagh G, Fleming R, Haddon R, Makhija A, Zahurak S (1991) Molecular-dynamics and the phase-transition in solid C60. Phys Rev Lett 67:1886–1889. doi:10.1103/PhysRevLett.67.1886
48. Dawid A, Dendzik Z, Gburski Z (2004) Molecular dynamics study of ultrathin argon layer covering fullerene molecule. J Mol Struct 704:173–176. doi:10.1016/j.molstruc.2004.01.065
49. Vicsek T, Czirok A, Benjacob E, Cohen I, Shochet O (1995) Novel type of phase-transition in a system of self-driven particles. Phys Rev Lett 75:1226–1229. doi:10.1103/PhysRevLett.75.1226
50. Raczynski P, Dawid A, Gburski Z (2005) Depolarized light scattering in small fullerene clusters—computer simulation. J Mol Struct 744:525–528. doi:10.1016/j.molstruc.2004.12.064

Chapter 6
Computer Simulation of Cholesterol Molecules Embedded in High-Density Lipoprotein

Z. Gburski, M. Pabiszczak, P. Raczyński, and V. Raczyńska

6.1 Introduction

Lipoproteins are particles composed of proteins and lipids which can circulate in the blood collecting lipids such as cholesterol or fatty acids. One of the major representative of lipoproteins is the high-density lipoprotein (HDL), commonly regarded as "good cholesterol" due to its ability to prevent atherosclerosis. By removing cholesterol from artery walls HDL contributes to the inhibition of major processes leading to atheromatous plaque formation—oxidation and inflammation of the endothelium and aggregation of blood platelets. Low levels of HDL have been implicated in the increased risk of coronary artery disease [1–11].

Production, transformation, and degradation of HDL particles are the key steps in the reverse cholesterol transport pathway contributing to the removal of cholesterol from tissues and protecting from atherosclerosis [12–14]. Apolipoprotein A-1 (apo A-1), the primary protein component of HDL produced in the liver and intestines, is secreted to the blood and initially forms a lipid-free particle. The efflux of lipids and cholesterol from peripheral tissues to these lipid-free HDL particles results in the formation of nascent discoidal HDL particles. The free cholesterol located on their surface is then esterified and migrates to their core causing the particles to change from discoidal to spherical. These spherical HDL continue to grow when additional cholesterol molecules aggregate on their surface and are subsequently esterified. The mature spherical HDL are eventually delivered

Z. Gburski (✉) • M. Pabiszczak • P. Raczyński • V. Raczyńska
Institute of Physics, University of Silesia, Uniwersytecka 4, Katowice 40-007, Poland
e-mail: zgburski@us.edu.pl

O. Fesenko, L. Yatsenko (eds.), *Nanoplasmonics, Nano-Optics, Nanocomposites, and Surface Studies*, Springer Proceedings in Physics 167,
DOI 10.1007/978-3-319-18543-9_6

to the liver, degraded and recycled, thus allowing for the removal of cholesterol from tissues. The properties of the discoidal HDL were successfully studied by means of computer simulations [15–17].

About 30 % of the blood cholesterol is carried by HDL, which conveys cholesterol in the blood stream [18, 19]. Although the cholesterol was intensively studied [6, 20–24], taking into account this important feature of HDL, it is necessary to possess, still poorly researched, detailed knowledge of the properties of cholesterols embedded inside HDL aggregate. Gaining this kind of knowledge is particularly demanding in view of a vigorous activity and search for the innovative cardiovascular therapies (molecular medicine). Motivated by this, we have made a series of computer simulations of the cholesterol cluster filling the interior of HDL. MD technique was successfully applied in many fields of research [25–42], not only to study the biological systems [43–48].

6.2 Materials and Methods

Molecular dynamics simulations were performed with NAMD 2.8 for IBM BlueGeneQ-MPI simulation code [49] and visualized with VMD [50, 51]. The studied system consisted of 180 cholesterol molecules placed inside the HDL aggregate (composed of 370 molecules of 1-palmitoyl-2-oleoyl-sn-glycero-3-phosphocholine). This system was simulated both with and without water environment. In case of the system with water, HDL aggregate was surrounded by 6×10^4 water molecules. Cholesterol molecules were modeled as described by Hénin and Chipot [52]. The 1-palmitoyl-2-oleoyl-sn-glycero-3-phosphocholine molecules (POPC) were modeled using CHARMM 27 forcefield [53]. Water was described with TIP3P, CHARMM adapted model [54, 55].

The average inner diameter of HDL was $d_i = 69$ Å and the average outside diameter was $d_o = 108$ Å.

The initial configuration of the system with water was obtained from the series of NPT simulations with the assumption of atmospheric pressure ($p = 1{,}013 \times 10^5$ Pa). In the case of the systems without water and the pure cholesterol cluster (without HDL and water), the initial configurations were obtained from the series of NVT simulations. After this initial step, all systems were equilibrated for 5×10^6 simulation steps in NVT ensemble at the temperature $T = 310$ K. The last part of our simulations was a production phase. During this process, each system was simulated in NVT ensemble for 3×10^7 simulation steps at the physiological temperature. In all our computer experiments, the simulation time step was 0.5 fs. The snapshot of the system with water at the end of the simulation run is shown in Fig. 6.1.

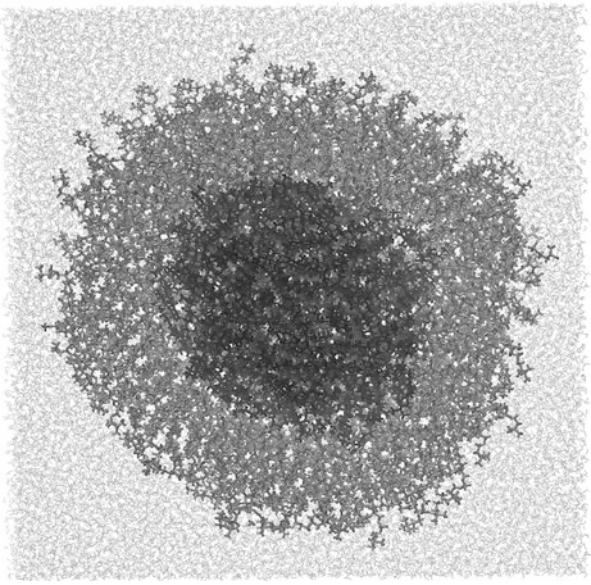

Fig. 6.1 The snapshot of HDL with cholesterols inside, surrounded by water. Water molecules are colored in *silver*, POPC molecules in *gray*, and the cholesterols in *black*

6.3 Results

The first observable we would like to discuss is the mean square displacement $\left\langle \left| \Delta \vec{r}(t) \right|^2 \right\rangle$ of the cholesterol molecule and its diffusion coefficient D. The mean square displacement is defined by

$$\left\langle \left| \Delta \vec{r}(t) \right|^2 \right\rangle = \left\langle \left| \vec{r}(t) - \vec{r}(0) \right|^2 \right\rangle \tag{6.1}$$

[56, 57], where $\vec{r}$ is the position of the center of mass of a single molecule.

The plots of $\left\langle \left| \Delta \vec{r}(t) \right|^2 \right\rangle$ of the cholesterol are presented in Fig. 6.2.

The mean square displacement is connected with diffusion coefficient via Einstein relation:

$$\left\langle \left| \Delta \vec{r}(t) \right|^2 \right\rangle \approx 6Dt \tag{6.2}$$

[56, 57], where D is the translational diffusion coefficient. The calculated values of D are: $D = 2.58 \times 10^{-4}$ Å^2/ps for the cholesterols embedded inside HDL (in the presence of water), $D = 2.15 \times 10^{-4}$ Å^2/ps for the cholesterols embedded inside HDL (without water), $D = 2.03 \times 10^{-3}$ Å^2/ps for the pure cholesterol cluster.

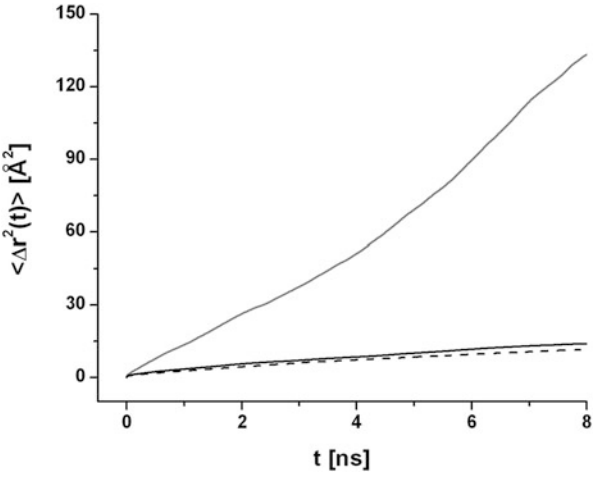

Fig. 6.2 The mean square displacement of the center of mass of cholesterol molecule. *Black dashed line* represents the system composed of cholesterols embedded inside HDL (without water), *black solid line* represents the same system surrounded by water, *gray solid line* represents pure cholesterol cluster. The same plot convention applies to Fig. 6.3

Both the mean square displacement and diffusion coefficient show that the motion of cholesterol molecules embedded in HDL aggregate is significantly slower than in the pure cholesterol cluster. Inside HDL, the cholesterol molecules are tightly packed and compressed by the surrounding POPC molecules, so they have limited free volume to move. The pure cluster is not constrained and the cholesterols can move more easily, especially these molecules which are located on the surface of the cluster. In case of the cholesterols inside HDL, the presence of water around the aggregate do not impact on the mobility of the cholesterol molecules, the motion of cholesterols inside HDL is similar in both cases.

We have estimated the values of the second rank order parameter S_2 defined as the highest eigenvalue of order tensor [58]:

$$Q_{\alpha\beta} = \frac{1}{N}\sum_{j=1}^{N}\left(\frac{3}{2}\hat{e}_{j\alpha}\hat{e}_{j\beta} - \frac{1}{2}\delta_{\alpha\beta}\right), \quad \alpha,\beta = x,y,z \tag{6.3}$$

where Q is a second rank tensor, $\hat{e}_j$ is a unit vector along the molecular long axis, and $\delta_{\alpha\beta}$ is the Kronecker delta. Diagonalization of this tensor gives three eigenvalues, and $\hat{n}$ is the eigenvector associated with the largest eigenvalue. The $\hat{n}$ vector is usually called the director of the sample. Value of S_2 is usually calculated as:

$$S_2 = \langle P_2(n \cdot e)\rangle = \langle P_2(\cos\theta)\rangle = \left\langle \frac{3}{2}\cos^2\theta - \frac{1}{2}\right\rangle \tag{6.4}$$

where P_2 is the second order Legendre polynomial, θ is the angle between a molecular axes and the director n, and $\langle\rangle$ denotes average over ensemble and time.

The obtained average values of S_2 are: $S_2 = 1.3 \times 10^{-1}$ for the cholesterols embedded inside HDL and with the presence of water , $S_2 = 1.73 \times 10^{-1}$ for the

cholesterols embedded inside HDL and without water, $S_2 = 8.22 \times 10^{-2}$ for the pure cholesterol cluster.

These low values of order parameter combined with low values of D suggest that cholesterol forms amorphous solid at the studied temperature.

To check that conclusion, we have also calculated the Lindemann index δ_L [59]:

$$\delta_L = \frac{2}{N(N-1)} \sum_{i<j}^{N} \frac{\left(\left\langle r_{ij}^2 \right\rangle - \left\langle r_{ij} \right\rangle^2 \right)^{1/2}}{\left\langle r_{ij} \right\rangle} \tag{6.5}$$

where r_{ij} is the distance between the center of mass of ith and jth molecules.

The calculated values of δ_L are: $\delta_L = 4.62 \times 10^{-2}$ for the cholesterols embedded inside the HDL and with the presence of water, $\delta_L = 3.88 \times 10^{-2}$ for the cholesterols embedded inside the HDL and without water, $\delta_L = 5.32 \times 10^{-2}$ for the pure cholesterol cluster. The values of δ_L confirm the conclusion that at $T = 310$ K cholesterol forms the amorphous solid.

The radial distribution function $g(r)$ of the center of mass of cholesterol is shown in Fig. 6.3.

In this figure only one evident peak is present, which indicates the distance d to the nearest neighbors, occurs about $d \approx 6.3$ Å. This peak is visible for all studied systems, and it is a little higher in case of pure cholesterol cluster. There are no more pronounced peaks on the $g(r)$ plots. This suggests that the cholesterol molecules both inside HDL and in the pure cluster are randomly arranged relative to each other, i.e., do not form any organized crystal-like structure [58, 60–66]. This observation is confirmed by the low values of the order parameter.

Another objective of our study was to examine the influence of water on the layer of the POPC molecules forming HDL aggregate. For this purpose, we would like to present the $\left\langle \left| \Delta \vec{r}(t) \right|^2 \right\rangle$ plots of the center of mass of the POPC molecule (Fig. 6.4).

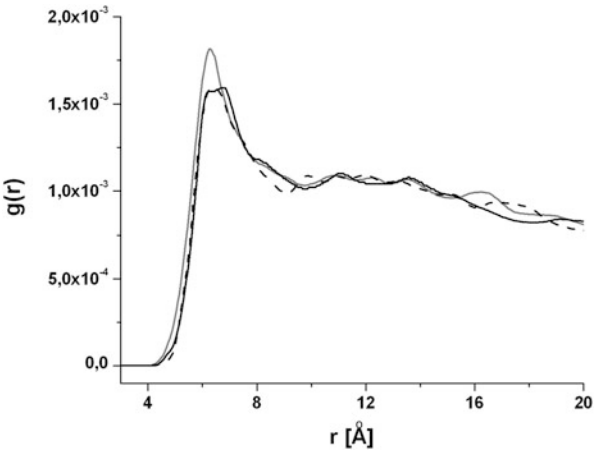

Fig. 6.3 The radial distribution function of the center of mass of cholesterol molecules

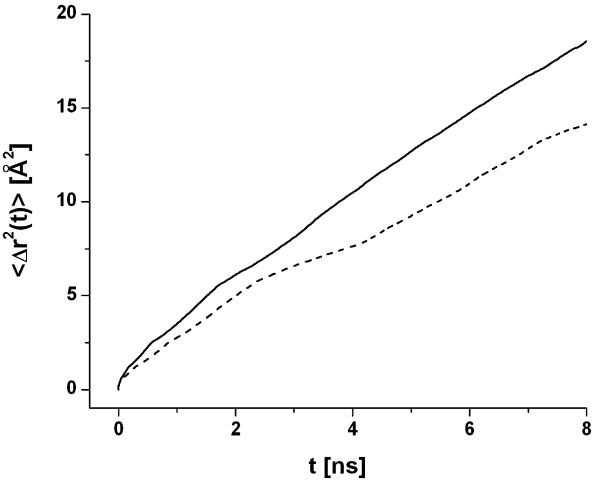

Fig. 6.4 The mean square displacement of the center of mass of POPC molecule. *Black solid line* represents the system with water, *black dashed* line represents the system composed of cholesterols embedded inside HDL (without water)

The translational diffusion coefficient associated with $\left\langle \left| \Delta \vec{r}(t) \right|^2 \right\rangle$ is equal $D = 3.53 \times 10^{-4}$ Å^2/ps for the system with water and $D = 2.97 \times 10^{-4}$ Å^2/ps for the system without it. The $\left\langle \left| \Delta \vec{r}(t) \right|^2 \right\rangle$ plots and values of D indicate the increased mobility of POPC molecules which form the surface of HDL aggregate. Water does not affect significantly POPC molecules of HDL aggregate because water molecules cannot penetrate the hydrophobic chains of the lipids.

The calculated values of Lindemann index is higher for the system with water ($\delta_L = 3.25 \times 10^{-2}$) compared to the case without water ($\delta_L = 2.31 \times 10^{-2}$). Obtained results confirm the conclusion of the moderate impact of water on the dynamics and structural properties of the POPC molecules.

6.4 Conclusions

The cholesterol molecules locate in the interior of HDL lipoprotein are tightly packed, they have a limited free volume to move. Their mobility is significantly slower than in the pure cluster, where the molecules can move freely. The low values of the diffusion coefficient, second rank order parameter, and Lindemann index suggest that the cholesterol forms the amorphous condensed phase at the studied temperature. The cholesterol molecules in all studied systems do not form any spatially ordered, crystal-like structure. With reference to the properties of POPC molecules in the outer layer of HDL, we conclude that water has moderate impact on their dynamics and structural peculiarity.

Our results of computer simulations will be of help when one would like to better understand the cholesterol dynamics inside HDL—the molecular aggregate playing important role in the context of coronary heart disease and atherosclerosis prevention.

Acknowledgment Calculations were performed at ICM University of Warsaw, Grant no. G53-6.

References

1. Fielding CJ (2007) High-density lipoproteins: from basic biology to clinical aspects. Wiley-VCH, Weinheim
2. Kontush A, Chapman MJ (2012) High-density lipoproteins structure, metabolism, function, and therapeutics. Wiley, Hoboken
3. Andersen CJ, Fernandez ML (2013) Dietary approaches to improving atheroprotective HDL functions. Food Funct 4:1304–1313. doi:10.1039/c3fo60207a
4. Balder J-W, Staels B, Kuivenhoven JA (2013) Pharmacological interventions in human HDL metabolism. Curr Opin Lipidol. doi:10.1097/MOL.0000000000000018
5. Holzer M, Trieb M, Konya V, Wadsack C, Heinemann A, Marsche G (2013) Aging affects high-density lipoprotein composition and function. Biochim Biophys Acta 1831:1442–1448. doi:10.1016/j.bbalip.2013.06.004
6. Lusis AJ (2000) Atherosclerosis. Nature 407:233–241. doi:10.1038/35025203
7. Miller G, Miller N (1975) Plasma-high-density-lipoprotein concentration and development of ischemic heart-disease. Lancet 1:16–19
8. Miller N, Thelle D, Forde O, Mjos O (1977) Tromso heart-study—high-density lipoprotein and coronary heart-disease—prospective case-control study. Lancet 1:965–968
9. Phillips MC (2013) Thematic review series: high density lipoprotein structure, function, and metabolism new insights into the determination of HDL structure by apolipoproteins. J Lipid Res 54:2034–2048. doi:10.1194/jlr.R034025
10. Riwanto M, Landmesser U (2013) High density lipoproteins and endothelial functions: mechanistic insights and alterations in cardiovascular disease. J Lipid Res. doi:10.1194/jlr.R037762
11. Zhang B, Kawachi E, Miura S, Uehara Y, Matsunaga A, Kuroki M, Saku K (2013) Therapeutic approaches to the regulation of metabolism of high-density lipoprotein—novel HDL-directed pharmacological intervention and exercise. Circ J 77:2651–2663. doi:10.1253/circj.CJ-12-1584
12. Fielding C, Fielding P (1995) Molecular physiology of reverse cholesterol transport. J Lipid Res 36:211–228
13. Nofer JR, Kehrel B, Fobker M, Levkau B, Assmann G, von Eckardstein A (2002) HDL and arteriosclerosis: beyond reverse cholesterol transport. Atherosclerosis 161:1–16. doi:10.1016/S0021-9150(01)00651-7
14. Lewis GF, Rader DJ (2005) New insights into the regulation of HDL metabolism and reverse cholesterol transport. Circ Res 96:1221–1232. doi:10.1161/01.RES.0000170946.56981.5c
15. Assmann G, Brewer H (1974) Molecular model of high-density lipoproteins. Proc Natl Acad Sci U S A 71:1534–1538. doi:10.1073/pnas.71.4.1534
16. Klon AE, Segrest JP, Harvey SC (2002) Molecular dynamics simulations on discoidal HDL particles suggest a mechanism for rotation in the apo A-I belt model. J Mol Biol 324:703–721. doi:10.1016/S0022-2836(02)01143-9

17. Shih AY, Arkhipov A, Freddolino PL, Schulten K (2006) Coarse grained protein—lipid model with application to lipoprotein particles. J Phys Chem B 110:3674–3684. doi:10.1021/jp0550816
18. Fox SI (2013) Human physiology. McGraw-Hill, New York
19. Preston RR, Wilson TE (2013) Physiology. Wolters Kluwer Health/Lippincott Williams & Wilkins, Philadelphia
20. Friedewa W, Fredrick D, Levy R (1972) Estimation of concentration of low-density lipoprotein cholesterol in plasma, without use of preparative ultracentrifuge. Clin Chem 18:499, 502
21. Casciola M, Bonhenry D, Liberti M, Apollonio F, Tarek M (2014) A molecular dynamic study of cholesterol rich lipid membranes: comparison of electroporation protocols. Bioelectrochemistry 100:11–17. doi:10.1016/j.bioelechem.2014.03.009
22. Róg T, Pasenkiewicz-Gierula M, Vattulainen I, Karttunen M (2009) Ordering effects of cholesterol and its analogues. Biochim Biophys Acta 1788:97–121. doi:10.1016/j.bbamem.2008.08.022
23. Raczynski P, Dawid A, Pietek A, Gburski Z (2006) Reorienatational dynamics of cholesterol molecules in thin film surrounded carbon nanotube: molecular dynamics simulations. J Mol Struct 792–793:216–220. doi:10.1016/j.molstruc.2006.01.064
24. Tong L-T, Zhong K, Liu L, Zhou X, Qiu J, Zhou S (2015) Effects of dietary hull-less barley beta-glucan on the cholesterol metabolism of hypercholesterolemic hamsters. Food Chem 169:344–349. doi:10.1016/j.foodchem.2014.07.157
25. Kachel A, Gburski Z (1998) Chain formation in a model dipolar liquid: computer simulation study. J Phys Condens Matter 9:10095. doi:10.1088/0953-8984/9/46/007
26. Kremer F (2002) Dielectric spectroscopy—yesterday, today and tomorrow. J Non-Cryst Solids 305:1–9. doi:10.1016/S0022-3093(02)01083-9
27. Dawid A, Gburski Z (2003) Interaction-induced light scattering in a fullerene surrounded by an ultrathin argon atmosphere: molecular dynamics simulation. Phys Rev A. doi:10.1103/PhysRevA.68.065202
28. Khan S, Singh JK (2014) Wetting transition of nanodroplets of water on textured surfaces: a molecular dynamics study. Mol Simul 40:458–468. doi:10.1080/08927022.2013.819578
29. Stassen H, Gburski Z (1994) Instantaneous normal-mode analysis of binary-liquid Ar-Kr mixtures. Chem Phys Lett 217:325–332. doi:10.1016/0009-2614(93)E1390-3
30. Rahman A, Stillinger FH (1971) Molecular dynamics study of liquid water. J Chem Phys 55:3336–3359. doi:10.1063/1.1676585
31. Gao Y, Liu J, Shen J, Wu Y, Zhang L (2014) Influence of various nanoparticle shapes on the interfacial chain mobility: a molecular dynamics simulation. Phys Chem Chem Phys 16:21372–21382. doi:10.1039/c4cp03019b
32. Kosmider M, Dendzik Z, Palucha S, Gburski Z (2004) Computer simulation of argon cluster inside a single-walled carbon nanotube. J Mol Struct 704:197–201. doi:10.1016/j.molstruc.2004.02.050
33. Ryckaert J, Bellemans A (1978) Molecular-dynamics of liquid alkanes. Faraday Discuss 66:95–106. doi:10.1039/dc9786600095
34. Gburski Z, Gray CG, Sullivan DE (1984) Lineshape in collision-induced absorption. Mori theory. Chem Phys Lett 106:55–59. doi:10.1016/0009-2614(84)87010-4
35. Honeycutt J, Andersen H (1987) Molecular-dynamics study of melting and freezing of small Lennard-Jones clusters. J Phys Chem 91:4950–4963. doi:10.1021/j100303a014
36. Dawid A, Gburski Z (2007) Dielectric relaxation of 4-cyano-4-n-pentylbiphenyl (5CB) thin layer adsorbed on carbon nanotube—MD simulation. J Non-Cryst Solids 353:4339–4343. doi:10.1016/j.jnoncrysol.2007.02.072
37. Yan K, Li X, Xu C, Lv Q, Ruan X (2014) Molecular dynamics simulation of the intercalation behaviors of methane hydrate in montmorillonite. J Mol Model 20:2311. doi:10.1007/s00894-014-2311-8

38. Raczynski P, Dawid A, Gburski Z (2005) Depolarized light scattering in small fullerene clusters—computer simulation. J Mol Struct 744:525–528. doi:10.1016/j.molstruc.2004.12.064
39. Martí J, Gordillo MC (2003) Structure and dynamics of liquid water adsorbed on the external walls of carbon nanotubes. J Chem Phys 119:12540. doi:10.1063/1.1625912
40. Gwizdala W, Górny K, Gburski Z (2008) Molecular dynamics and dielectric loss in 4-cyano-4-n-pentylbiphenyl (5CB) mesogene film surrounding carbon nanotube—computer simulation. J Mol Struct 887:148–151. doi:10.1016/j.molstruc.2007.12.045
41. Nakazaki N, Takao Y, Eriguchi K, Ono K (2014) Molecular dynamics simulations of silicon chloride ion incidence during Si etching in Cl-based plasmas. Jpn J Appl Phys 53:056201. doi:10.7567/JJAP.53.056201
42. Dawid A, Dendzik Z, Gburski Z (2004) Molecular dynamics study of ultrathin argon layer covering fullerene molecule. J Mol Struct 704:173–176. doi:10.1016/j.molstruc.2004.01.065
43. Isralewitz B, Gao M, Schulten K (2001) Steered molecular dynamics and mechanical functions of proteins. Curr Opin Struct Biol 11:224–230. doi:10.1016/S0959-440X(00)00194-9
44. Freddolino PL, Arkhipov AS, Larson SB, McPherson A, Schulten K (2006) Molecular dynamics simulations of the complete satellite tobacco mosaic virus. Structure 14:437–449. doi:10.1016/j.str.2005.11.014
45. Gburski Z, Górny K, Raczynski P (2010) The impact of a carbon nanotube on the cholesterol domain localized on a protein surface. Solid State Commun 150:415–418. doi:10.1016/j.ssc.2009.12.005
46. Heller H, Schaefer M, Schulten K (1993) Molecular-dynamics simulation of a bilayer of 200 lipids in the gel and. J Phys Chem 97:8343–8360. doi:10.1021/j100133a034
47. Lu H, Schulten K (1999) Steered molecular dynamics simulations of force-induced protein domain unfolding. Proteins-Struct Funct Genet 35:453–463. doi:10.1002/(SICI)1097-0134(19990601)35:4<453::AID-PROT9>3.0.CO;2-M
48. Raczynski P, Gorny K, Pabiszczak M, Gburski Z (2013) Nanoindentation of biomembrane by carbon nanotubes—MD simulation. Comput Mater Sci 70:13–18. doi:10.1016/j.commatsci.2012.12.031
49. Phillips JC, Braun R, Wang W, Gumbart J, Tajkhorshid E, Villa E, Chipot C, Skeel RD, Kalé L, Schulten K (2005) Scalable molecular dynamics with NAMD. J Comput Chem 26:1781–1802. doi:10.1002/jcc.20289
50. Humphrey W, Dalke A, Schulten K (1996) VMD—visual molecular dynamics. J Mol Graph 14:33–38
51. Price S (2011) Importing medicines: the VMD's special import and special treatment schemes. Vet Rec 168:445–446. doi:10.1136/vr.d2617
52. Henin J, Chipot C (2006) Hydrogen-bonding patterns of cholesterol in lipid membranes. Chem Phys Lett 425:329–335. doi:10.1016/j.cplett.2006.04.115
53. MacKerell AD, Bashford D, Bellott M, Dunbrack RL, Evanseck JD, Field MJ, Fischer S, Gao J, Guo H, Ha S, Joseph-McCarthy D, Kuchnir L, Kuczera K, Lau FTK, Mattos C, Michnick S, Ngo T, Nguyen DT, Prodhom B, Reiher WE, Roux B, Schlenkrich M, Smith JC, Stote R, Straub J, Watanabe M, Wiórkiewicz-Kuczera J, Yin D, Karplus M (1998) All-atom empirical potential for molecular modeling and dynamics studies of proteins. J Phys Chem B 102:3586–3616. doi:10.1021/jp973084f
54. Jorgensen WL, Chandrasekhar J, Madura JD, Impey RW, Klein ML (1983) Comparison of simple potential functions for simulating liquid water. J Chem Phys 79:926. doi:10.1063/1.445869
55. MacKerell AD Jr, Banavali N, Foloppe N (2000) Development and current status of the CHARMM force field for nucleic acids. Biopolymers 56:257–265. doi:10.1002/1097-0282(2000)56:4<257::AID-BIP10029>3.0.CO;2-W
56. Rapaport DC (2004) The art of molecular dynamics simulation. Cambridge University Press, Cambridge

57. Frenkel D, Smit B (2001) Understanding molecular simulation, second edition: from algorithms to applications, 2nd edn. Academic, San Diego
58. Luckhurst GR, Veracini CA (1994) The molecular dynamics of liquid crystals. Springer, New York
59. Jena P, Rao BK, Khanna SN (2013) Physics and chemistry of small clusters. Springer, New York
60. Chandrasekhar S (1992) Liquid crystals. Cambridge University Press, Cambridge
61. Wrischer M (1967) Electron microscope studies on crystal-like structures in plastid stroma. Planta 75:309–318. doi:10.1007/BF00387354
62. Piatek A, Dawid A, Gburski Z (2006) The existence of a plastic phase and a solid–liquid dynamical bistability region in small fullerene cluster $(C_{60})_7$: molecular dynamics simulation. J Phys Condens Matter 18:8471–8480. doi:10.1088/0953-8984/18/37/006
63. Adachi M, Murata Y, Takao J, Jiu JT, Sakamoto M, Wang FM (2004) Highly efficient dye-sensitized solar cells with a titania thin-film electrode composed of a network structure of single-crystal-like TiO2 nanowires made by the "oriented attachment" mechanism. J Am Chem Soc 126:14943–14949. doi:10.1021/ja048068s
64. Inagaki S, Guan S, Ohsuna T, Terasaki O (2002) An ordered mesoporous organosilica hybrid material with a crystal-like wall structure. Nature 416:304–307. doi:10.1038/416304a
65. Gburski Z, Zerda T (1980) Vibrational dephasing and intermolecular interactions in liquids. Acta Phys Pol A 57:447–454
66. Zhang LF, Bartels C, Yu YS, Shen HW, Eisenberg A (1997) Mesosized crystal-like structure of hexagonally packed hollow hoops by solution self-assembly of diblock copolymers. Phys Rev Lett 79:5034–5037. doi:10.1103/PhysRevLett.79.5034

Chapter 7
Design and Characterization of In Situ Synthesized Hybrid Polymeric Materials

Yu. Vyshnevska, I. Brazhnyk, and S. Kudrya

7.1 Introduction

Purposeful design of new nanostructured materials and functional coatings on their basis for photovoltaic and fuel cells, electrochemical and optical sensors, semiconducting and optoelectronic devices requires determination of the main regularities of influence of geometrical, morphological, and structural parameters on their physicochemical and functional properties.

A promising research area is the development of methods for obtaining hybrid materials and nanocomposites, which are based on the deposition of thin films of organic polymers on a substrate with preformed arrays of inorganic nanostructures or embedding the nanoscale objects into the polymeric matrix [1, 2]. Of particular interest are thin films of conducting polymers with incorporated palladium and silver nanoparticles as well as bimetallic core-shell objects [3].

At the same time, for designing and obtaining the materials with desired functional properties, the precise control of the polymers conductivity and the coating morphology are essential. The conductivity of polymeric films based on aniline derivatives is determined by the oxidation state of the polymer, structural irregularity, and the composition of the dopants, while the morphological and structural parameters of the coatings may be controlled by varying the deposition conditions.

Yu.Vyshnevska (✉)
National Technical University of Ukraine "Kyiv Polytechnic Institute",
37, Peremohy Ave, Kyiv 03056, Ukraine
e-mail: vishnevsk@ukr.net

I. Brazhnyk • S. Kudrya
Institute for Renewable Energy, 20A, Chervonogvardiyska str, Kyiv 03094, Ukraine

O. Fesenko, L. Yatsenko (eds.), *Nanoplasmonics, Nano-Optics, Nanocomposites, and Surface Studies*, Springer Proceedings in Physics 167,
DOI 10.1007/978-3-319-18543-9_7

7.2 Materials and Experimental Methods

The study of the morphology, structure, and mechanism of formation of coatings were carried out using SEM, AFM, as well as Raman and IR spectroscopy methods. Investigation of the mechanism of charge transfer, calculation of the energy parameters, and geometry optimization were carried out on a Hartree-Fock level with the 6-31G basis set using the NWChem 6.5 computational chemistry package [4]. Preparation of models, analysis, and visualization of the results were performed using the Avogadro modeling package [5]. Polarization measurements were carried out using a potentiostat PI-50.1 in potentiostatic and potentiodynamic (a scan rate of 1 mV/s) regimes in a three-electrode cell with separated cathodic and anodic compartments. Carbon steel 08 kp was used as the working electrode, platinum—as the counter-electrode and an Ag|AgCl|KCl(sat.) electrode—as the reference one. In this chapter, the potential values are given with respect to the normal hydrogen electrode potential. The study of the structure and determine the elemental composition of the obtained polymer coating was performed using the methods of infrared spectroscopy (instrument Avatar 370 FT-IR Thermo Nicolet) and Roentgen spectrometry.

7.3 Result and Discussion

One of the common methods for obtaining such coatings is based on electropolymerization of the aniline derivatives monomers under conditions of circular polarization (Fig. 7.1). In this case, control of thickness and morphology of the polymer film are performed by varying range and scan rate, as well as the number

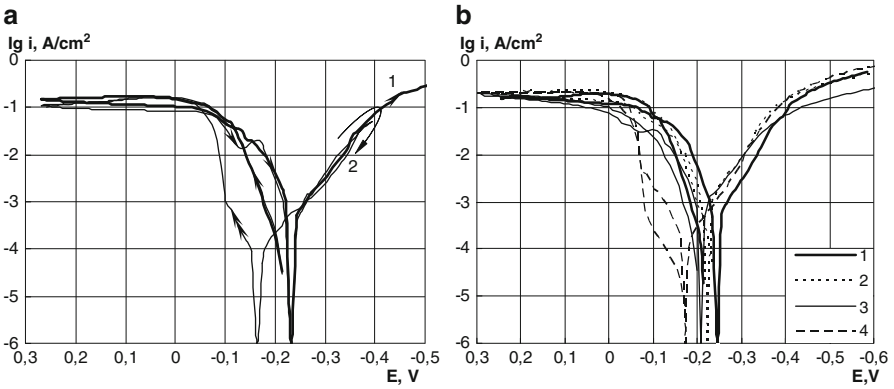

Fig. 7.1 Anode-cathodic polarization curves for steel electrode in (**a**) 1—0.5 M H_2SO_4; 2—0.5 M H_2SO_4 + 1 g/L DPA (circular polarization) (**b**) 1—0.5 M H_2SO_4; 2—0.5 M H_2SO_4 + 1 g/L DPA; 3—0.5 M H_2SO_4 + 1 g/L DPA + 2 g/L $Fe_2(SO_4)_3$; 4—0.5 M H_2SO_4 + 1 g/L DPA + 2 g/L $Fe_2(SO_4)_3$ + 2 g/L KI

of cycles of polarization. It was found that imposition of circular polarization in the presence of aniline, a marked decrease in the current density due to the formation of polymer films has been observed during the second scanning in the anodic region (Fig. 7.1, curve 2).

Among the advantages of in situ polymerization is the possibility of the controlled modification of electrodes of different nature, including precious metals and nanostructured carbon materials. In addition to using of circular polarization, the coatings formation may be achieved in result of in situ oxidizing polymerization of added monomers under stationary conditions in the presence of the catalyst.

The mechanism of the polymer film formation in such a system for the first time was proposed in [6]. It involves the oxidizing polymerization of DPA in the presence of Fe^{3+} ions and further deposition of PDPA on the metal surface:

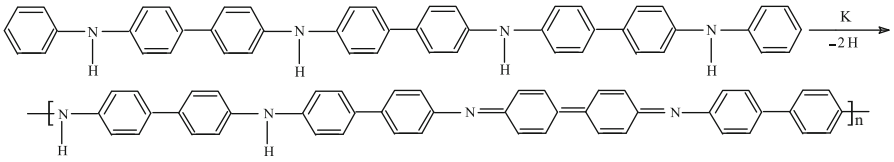

Taking into account significant influence of halide ions on the physical properties of polymeric materials based on aniline derivatives and given their prospect for the development of photovoltaic cells and organic semiconductor devices [1, 2], in present work the influence of Cl^-, Br^-, I^- ions on the polymerization process and properties of obtained coatings were estimated.

It was found, that addition of $Fe_2(SO_4)_3$ allows to initiate the polymerization of diphenylamine in stationary conditions (Fig. 7.2a, curve 2). It was shown that co-adding $Fe_2(SO_4)_3$ and KI (Fig. 7.2a, curve 3) can significantly increase the coating formation rate due to direct participation of the added Fe^{3+} ions and

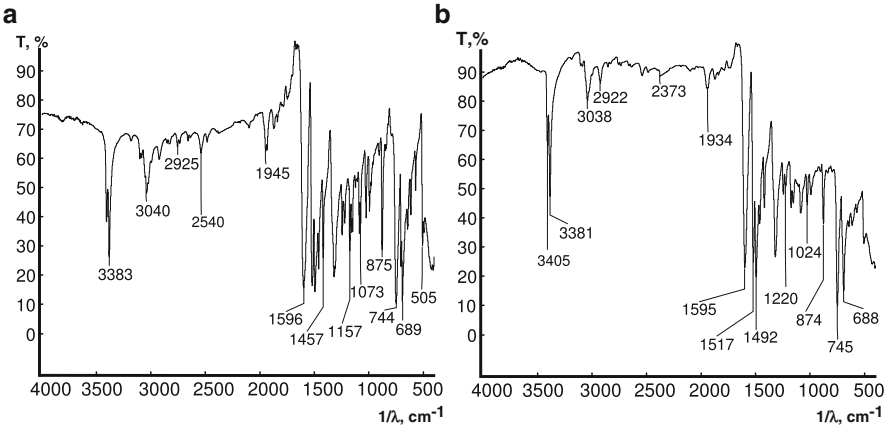

Fig. 7.2 Infra-red spectrum of DPA (**a**) and PDPA (**b**)

functioning of the redox system I^-/I^2 [6]. Investigation of influence of the halide ions on the kinetics of electrode processes and the dynamics of formation of polymer coatings in the presence of aniline derivatives shows that among Cl^-–Br^-–I^- the most significant effect on polymerization processes in such systems are demonstrated by I^- ions.

The reducing of anodic current density that occurs during the formation of polymer films based on aniline derivatives, also associated with the accumulation of iminoquinone fragments in macromolecules, resulting in a significant reduction in the electrical conductivity of the obtained coatings. In addition, the increase in the proportion of oxidized pernigraniline fragments accompanied by a reversible color change and corresponding shift of the maxima of absorption spectra, which agrees with [7]. It should also be noted that the addition of Fe^{3+} cations in the form of $Fe_2(SO_4)_3$ leads to increased concentrations of sulfate anions that in addition to increasing the rate of polymerization also facilitate a spontaneous doping of the polymers.

It was shown that in the presence of Fe^{3+} and I^- ions the multistage mechanism of the polymeric film formation is realized, where iodide ions acts as a mediator. Thus, KI can be treated as a dopant that allows to control the rate of polymerization as well as the electrical conductivity of the obtained coatings.

Depending on the polymerization conditions, environment pH, and anionic composition of the electrolyte, the various forms of polydiphenylamine can be obtained. For that reason, the actual structure of the polymers was determined using Fourier transform infrared spectroscopy (Fig. 7.2).

In the PDPA spectra at 3,381 cm^{-1} is observed intense absorption band corresponding to the valence vibrations of a bond $\nu_{N\text{-}H}$. The absorption peak at 784 cm^{-1} represents nonplanar deformation fluctuations $\delta_{N\text{-}H}$. Absorption band at 745 cm^{-1} corresponds to nonplanar deformation fluctuations $\delta_{C\text{-}H}$ of monosubstituted aromatic ring. Analysis of FTIR-spectrograms indicates the presence of a significant proportion of the original diphenylamine monomers in the film as well as the effects of self-doping with the sulfate anions that are present in the solution. Those present in coating diphenylamine molecules retain reactivity and in the case of a favorable conditions are prone to further polymerization that may be the basis for the self-healing mechanism of such coatings.

It should also be noted that obtained coating demonstrate the conductivity and color changes when immersed in acidic or alkaline solutions similar to the previously mentioned electrochromism phenomenon. Investigation of the charge transfer mechanism depending on the oxidation state was carried out using quantum-chemical calculations (Fig. 7.3). The total density (left) and HOMO orbital (right) plots shows the major electron density redistribution as a result of transition from protonated (a) to deprotonated (b) state of the polymer.

Despite the fact that conductivity may be fine tuned using protonation or doping, the exact contribution of polaron tunneling, phase irregularities, and the dopant composition to the physicochemical and functional properties in such a complex

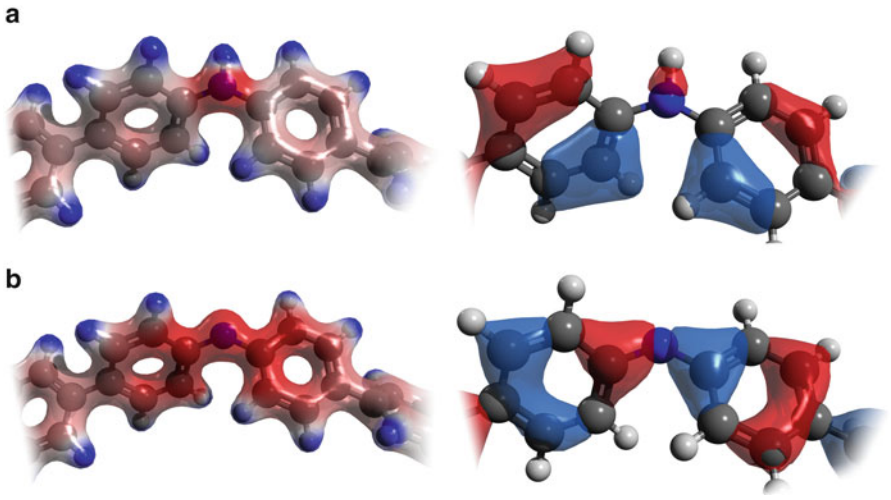

Fig. 7.3 Quantum-chemical calculation of the electronic structure of a protonated (**a**) and deprotonated (**b**) PDPA

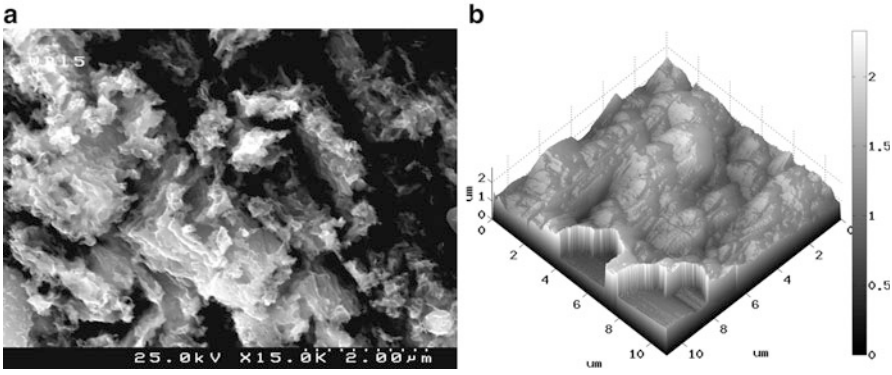

Fig. 7.4 SEM (**a**) and AFM (**b**) images of the film, which was formed in result of oxidizing polymerization of DPA

heterogeneous multicomponent system remains a subject of investigation. In the case considered, doping with I^- ions has a significant influence on the PDPA conductivity due to electron delocalization as a result of the redistribution of electron density.

The study of the morphology, topography, and thickness of the formed polymer coatings with using SEM and AFM indicates the formation of solid films characterized by large amplitude of roughness (Fig. 7.4).

Compared to electropolymerization, where control of thickness and morphology of the coating is performed by optimizing the number of the polarization cycles, given the charge Q expended on the electrochemical process [7], deposition involving catalyst allows control morphological and structural parameters of coatings by varying the concentration of added monomers, catalyst, mediator, and the exposure time. The proposed method of obtaining coatings by polymerization of added monomers involving catalyst in combination with the deposition as a result of electropolymerization as well as promising methods of forming coatings under sonochemical factors expands approaches to obtain coatings with a given range of physicochemical and functional properties.

7.4 Conclusions

The factors, which allow to initiate and maintain the reaction of diphenylamine polymerization in the steady-state conditions, were studied and the main kinetic regularities of this process with taking into account of electrolyte composition were determined.

The proposed method for formation of functional coatings based on in situ polymerization of added monomers, allows to control the morphologic and structural characteristics of layers with the variation of monomers, catalyst, mediator concentrations, and the exposure time, which give the possibility to obtain materials for diverse applications. In addition to fuel cells, printable electronics and electrochemical energy storage systems, such materials may be used for enhancing performance of the photovoltaic cells due to reduction of electron recombination. The proposed synthesis method including imposition of the catalyst and mediator dopants can be combined with various electrochemical and sonochemical techniques for the obtaining materials with desired functional properties.

References

1. Zhu S, Wei W, Chen X, Jiang M, Zhou Z (2012) Hybrid structure of polyaniline/ZnO nanograss and its application in dye-sensitized solar cell with performance improvement. J Solid State Chem 190:174
2. Li L, Raji AR, Fei H, Yang Y, Samuel EL, Tour JM (2013) Nanocomposite of polyaniline nanorods grown on graphene nanoribbons for highly capacitive pseudocapacitors. ACS Appl Mater Interfaces 5(14):6622
3. Thiagarajan S, Yang RF, Chen SM (2011) Palladium particles based nano films; electrochemical fabrication, characterization and applications. Int J Electrochem Sci 6:4537
4. Valiev M, Bylaska EJ, Govind N, Kowalski K, Straatsma TP, van Dam HJJ, Wang D, Nieplocha J, Apra E, Windus TL, de Jong WA (2010) NWChem: a comprehensive and scalable open-source solution for large scale molecular simulations. Comput Phys Commun 181:1477

5. Hanwell MD, Curtis DE, Lonie DC, Vandermeersch T, Zurek E, Hutchison GR (2012) Avogadro: an advanced semantic chemical editor, visualization, and analysis platform. J Cheminform 4:17
6. VishnevskaYuP (2006) 57th Annual meeting international society of electrochemistry, Edinburgh, 27 Aug–1 Sept 2006, p 116
7. Poliovyi DO (2009) Synthesis and optical properties of the conjugated polyarene thin layers. Thesis of Dissertation for Cand. Chem. Sci. Ivan Franko National University of Lviv, in Ukrainian, Lviv

Chapter 8
The Properties of Water Nanostructures in Nanosystems

L.S. Martseniuk

8.1 Introduction

The learning of properties of near-surface water layers of various materials, and also the water bounded by molecular structures of alive organisms, represents now enormous interest for developers of various devices of nano-bio-technologies and of others nano-devices. It is shown that water displays the big variety of properties in the near-surface layers having thickness of the order of few tens or hundreds of nanometers (nanowater), and the parameters of such water cardinally differ from the usual volumetric water [1–3].

The nanostructured water, adjoining to the surface of various hydrophobic materials, as a rule, modifies the properties, coordinating them with properties of the surface of material. At the same time water can substantially influence on the properties of these materials. One of the most interesting examples of such influence was the superconductivity induced by pure water in compounds $SrFe_2As_2$ and $FeTe_{0.8}S_{0.2}$ and by alcohol in $FeTe_{0.8}S_{0.2}$ [4–6].

Nanowater behaves in alive organisms most unusually. Water, adjoining to biostructures of alive organisms, actually forms with them a single unit and participates in all processes of cellular systems and all organisms as a whole, determining and synchronizing all the vital functions of an organism [7, 8]. Properties of water, in particular of water systems of an alive organism, mainly, present a riddle for researchers, despite of a high scientific and technical level of equipment of modern laboratories.

It may be connected with that fact that the traditional views on water structure as a homogeneous system, where the interaction between molecules is determined by the short-range forces formed by hydrogen bindings, are not correct enough.

L.S. Martseniuk (✉)
Institute of Nuclear Researches NAS Ukraine, Prospect Nauky 47, Kiev 03680, Ukraine
e-mail: prolisok77@yandex.ua

O. Fesenko, L. Yatsenko (eds.), *Nanoplasmonics, Nano-Optics, Nanocomposites, and Surface Studies*, Springer Proceedings in Physics 167,
DOI 10.1007/978-3-319-18543-9_8

For the adequate description of the phenomena in alive organisms, it is necessary to base on the modern theory of water structure, which agreed with the data received experimentally.

There is the opinion that until now the satisfactory theory of water is not created. However, the theory of condensation of water molecules in the liquid and solid state from the position of quantum electrodynamics, developed by a remarkable physicist J. Preparata [9], opened the new possibilities for understanding the behavior of water and for description of those properties which are not described with the help of the traditional views.

In the present work the theory of J. Preparata for the description of unusual behavior of water ***in nanostructures*** was basically used. This theory has shown the efficiency in the description of the properties of volumetric water and has received the experimental confirmation at researches of resonant interaction of a low intensive waves of the EHF-diapason with volumetric water and the water of alive organisms (SPE effect) [10], and in a number of other researches. Exactly experimental results, conducted by the method of SPE effect, confirmed the rightness of the theoretical predictions of J. Preparata that usual water represents the two-componential system.

One of the remarkable results, discovered directly at the research of resonance interaction spectra of electromagnetic radiation of the EHF-diapason with the water system, was the detection of a high degree of water coherence in nanostructures, especially in alive organisms. Good quality of resonant peaks for the water of alive organisms more than three times exceeded good quality of the corresponding peaks on the same frequencies, as in usual water [10].

In this work the properties of nanowater are analyzed as from the position of the theory of J. Preparata, which developed for volumetric water, with the use of theory of the superposition of quantum states and the interference transitions.

8.2 Near-Surface Nanowater

Properties of near-surface water in many respects are determined by properties of a surface of a material to which water contacts [1]. Explaining it is possible as follows [1].

The molecule of water is a dipole. If water adjoins to a surface on which there is a charge, it is possible to expect that dipoles will start to be oriented and attracted to a surface, forming a few layers near a surface. Owing to thermal fluctuations, these layers will form a few layers—no more than two–three layers, according to the traditional concept.

However at such treatment of the formation mechanism of near-surface layers, there are contradictions with really observable phenomena. It appears that near-surface water forms the layers occupying the much greater volume—sometimes and up to several hundreds of microns on thickness—depending on the properties of a material of a surface and such qualities of a surface, as water hydrophobic

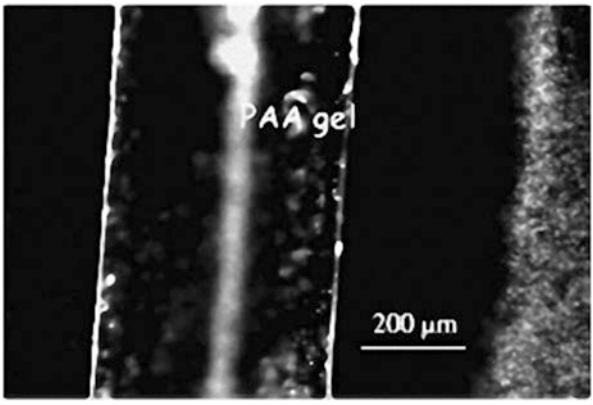

Fig. 8.1 Exclusion zones (*dark*) on either side of a polyacrylic acid gel [1]

property, degrees of structural order, and presence of surface charges and of some other factors (Fig. 8.1).

For visualization of a near-surface layer of water, G. Pollack has suggested to place in water the dyeing substances—suspensions with a diameter from 0.5 up to 2 μm. It was revealed that such substances do not remain inside a near-surface layer and a near-surface water is found out visually as undyed. Taking into account that a near-surface water pushes out from its own structure a micro-impurity of the most various nature, G. Pollack has designated this zone—*exclusion zone water* (EZ water) [1].

G. Pollack, investigating the properties of such water, noted that not only the great number of hydrophilic surfaces created a zone of exception. Generally, the charged hydrophilic surfaces also will create a zone of exception. Water, in this thick enough layer, differs from usual volumetric water practically, for all known parameters. We list the most essential differences.

1. EZ-вода is charged negatively (potential is achieved at 150 mV) in relation to contacting with it a volume water. Along conductor, which connects an electrode, placed in EZ water with an electrode, placed in volumetric water, passes a weak, but continuous electric current.
2. At illumination of EZ water by infrared radiation with $\lambda = 3{,}100$ nm, a magnitude of a current increases. At the same time, the thickness of a layer of EZ water grows also (the four multiples increasing in its thickness are observed).
3. Water protons concentrate on the border between EZ water and volumetric water. Thus, the water system in which the EZ water and volumetric water coexist represents a system with division of charges, something like the condenser in which a negative plate is displayed by EZ water and positive by volumetric water with a lot of protons—a radiant energy essentially increases the capacity of this "condenser."
4. EZ water absorbs ultraviolet radiation with a maximum at $\lambda = 270$ nm. At illumination of EZ water ultraviolet radiation with $\lambda = 270$ nm, it fluoresces.
5. Viscosity of EZ water is essentially higher than usual volumetric water. G. Pollack has selected three more properties of EZ water: its molecules—more coupled,

more stable and displaced as oriented. And it, in the opinion of G. Pollack, means that we have a liquid crystal; i.e., a situation when molecules are very well oriented in relation to each other.

Items 1–5 testify that electrons in EZ water are at much higher level of excitation than in usual water, i.e., it can be the donor of electrons.

G. Pollack did not see a possibility to explain all unusual properties observable by him in EZ water by means of traditional conceptions and specified on existence of a very distant orderings in water that is unexpected. If it is valid so then the most part of water in the universe is not the usual volumetric water which is described in textbooks, but is a liquid crystal.

8.3 Nanostructures in Volumetric Water and Water of Alive Organisms

It is considered that the surface of glass, as a material which has no ordered structure, does not change the internal architecture *of volumetric* water. It allows to investigate the properties of volumetric water, using as a material of a substrate—a glass plate or glass wares.

So, in a number of works [10, 11], it has been shown that usual water, depending on the character of its preparation and features of interaction with an environment, can show a huge variety of various properties, connected both with internal parameters and with the field characteristics stipulated by its internal organization. It is possible to judge about the presence in water of the structural formings from the data on researches by a crystal's optical method [11, 12], method of Kirlian's effect [12, 13], method of SPE effect, and others to techniques.

So in [12] the presence of lyotropy was experimentally confirmed in natural water by a crystal's optical method which was based on the realization of phase transitions of type solution (lyotropic structure)—solid phase, realized at evaporation of water drop, placed on a clean glass plate. As natural lyotropic crystals are first of all complex water solutions, always at crystallization (drying of the system at usual temperatures) the structure of a solid phase having optical anisotropy is formed. For natural potable water, the presence of such optical anisotropy in a solid phase (the deposit) is not only optical anisotropy but also a characteristic fractal structure [12].

Figure 8.2 shows the photo of a solid phase structure of the natural water from the work of [12]. Thus, it is shown that water can have a complex structure. If for pure distilled water or tap water such structure practically is not found out, natural water, according to researches [12], represents the liquid crystal with optical anisotropy (Fig. 8.2).

It is of interest to compare the given researches of the natural water which have been carried out in [12] with results by researches of a luminescence, carried out by a method of Kirlian's effect [13, 14]. This is important on the reason that from the photos, received by a method of Kirlian's effect, it is possible to judge about a

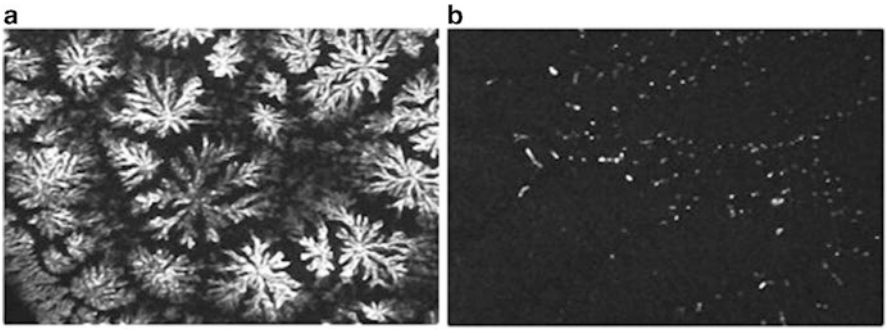

Fig. 8.2 The structure of potable water such as "Horianka" (**a**) and usual tap water (**b**) [12]

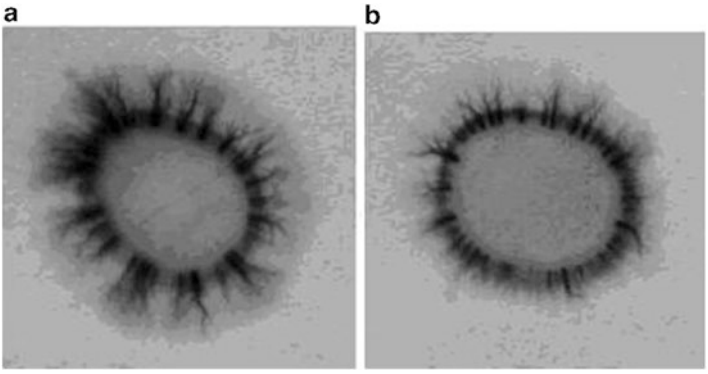

Fig. 8.3 The photo of natural water (**a**) and tap water (**b**) carried out by a method of Kirlian's effect [14]

presence in water of own field [13]. We shall note that the similar field is revealed by the same method and in an alive organism [14].

The photo of natural water and tap water, carried out by a method of Kirlian's effect, is shown on Fig. 8.3.

In Fig. 8.3, it is visible that the crown of luminescence around water drops has various characteristics for each type of researched liquid. The crown around of a drop of water from a natural source has a clear internal ring and wide external with uniform streamer formations (Fig. 8.3a). In a variant with tap water (Fig. 8.3b), a crown has smaller intensity of luminescence and short and more discharged streamers.

The offered method is characterized by a high degree of reproducibility of results. Hence, water is not a homogeneous structure; it has internal nanostructure elements and its own field characteristics. In addition, the field of tap water is less active than that of natural water. Presumably, it means that the power characteristics of tap water and natural water differ.

The results from the works of [12, 14] have allowed to confirm the existence of natural energetics of water and to prove an opportunity of definition of bioinformation properties of potable water.

Thus, *natural water* has memory, special energy, and a certain degree of stability to external influences [8, 11, 12, 14, 15]. It testifies to the presence in its composition of cluster structures which *can be in* the state *entangled* within itself.

Actually by the existence of cluster nanostructures which are in entangled state in homeopathic water preparations, the effect of steady homeopathic influence of these preparations on alive organisms are explained [16]. By its field characteristics, homeopathic liquids correlate with the properties of substance which were originally used for the preparation of these preparations. By a character of influence, they can differ essentially from the influence of the solutions containing the same substance in usual (not homeopathic) doses as it is shown in [16].

The liquids directly in contact with a material, which have a crystal structure, change the properties both in all volume and near to a surface. It allows to use the nanostructures of certain materials in medical aims and for diagnostics of living organisms [10, 17].

Numerous data about the change of the field characteristics of water, contacting with various materials, are found in [10]. It is important to note that the influence of a contacting surface is distributed to all volumes of water and not just on a small site of a near-surface layer. It means that water is not only the perceiving environment but also the compiler of the cumulative information about any influence on its structure on all volumes. Such features indicate on specific characteristics of water when each its elements gets the properties of all volume and mean that all elements of water are in reorganisation depending on a degree of interaction with a surface and are at the interaction with a surface and among themselves in correlated (entangled) state.

Just the same features of water, as the ability to reconstruct the field and structural characteristic (practically, without inertial) under action of external influence (external field), determine the possibility of water to participate **in all vital processes** of a living organism.

In an alive organism, the water is, basically, in the bounded state. Most if not all water in alive organisms is interfacial water. As a rule, in such structures the layers of water are also under influence of the strong field gradients existing, for example, in new membrane's areas of a cell. It can create delamination of water and makes the additional changes to properties of near-surface areas. Such water accepts partly, depending on the size of gradient, the characteristics of two-dimensional structures. As a direct studying of properties of the water bounded by structural elements of an alive organism is difficultly, very important to model and study the behavior of water **in objects** of the lifeless nature where it located by the similar way.

The discovery of SPE effect [10] has advanced essentially the area of researches on living organisms.

One of the remarkable results which have been received by authors [10] were the detection of the very strong similarity of resonant interaction spectra of mm waves with water and water medium of an alive organism (Fig. 8.4).

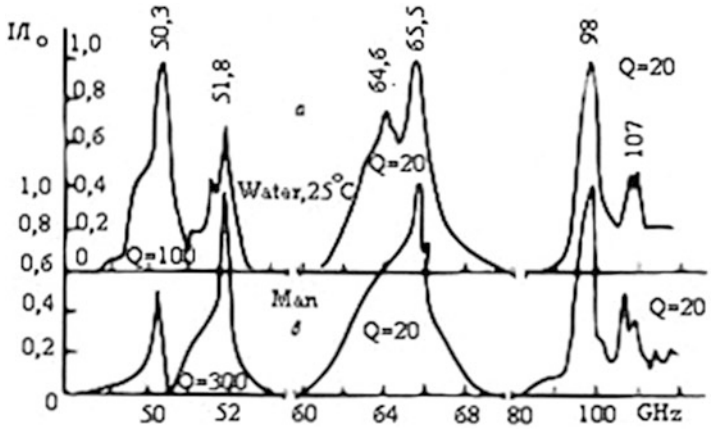

Fig. 8.4 Resonant spectra of electromagnetic wave interaction of the EHF range with water and the water medium of an alive organism (according to the works of [10])

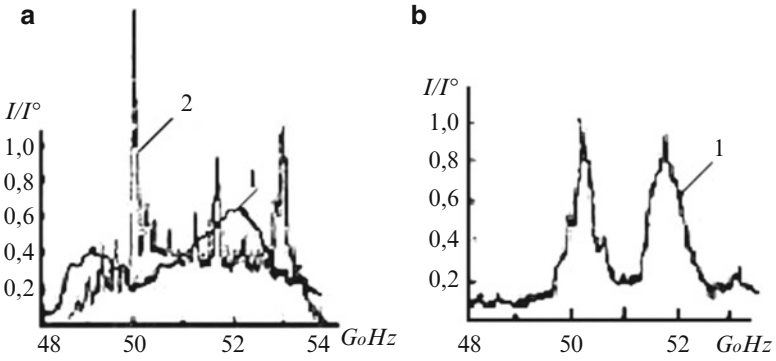

Fig. 8.5 Resonant spectra of fabrics of the patient before treatment (**a**) and at the end of treatment (**b**) [10]

Also it was revealed that the disease of an organism is accompanied by change of the properties of its water constituent, and the process of convalescence corresponds to returning of the properties of the water medium to an initial state, characteristic for a healthy organism (Fig. 8.5).

It indicates on the high degree of synchronization of the vital systems of the whole organisms that it is possible to explain that its structures, including the water cluster's formations, are in the entangled state. Pure maximally entangled state for water of alive organisms, as well as for the whole organism, cannot be realized, because an alive organism is an open system, interacting with an external environment and, hence, is not in a pure state.

A quantum theory of the entangled states is part of a modern quantum theory of the information in which the degree of entanglement directly connects with the quantum characteristics of system, by its quantum organization and correlation parameters of its elements.

The high degree of coherence, found at the research on the water medium of an alive organism, indicates a high degree of synchronization of the vital processes, occurring in the water environment; the existence of the single coordinating system of a living organism. These results of the work of [10] have confirmed the prediction of H. Frohlich about the existence of coherency in an alive organism; the results coincide with that of other authors investigating the phenomena of photosynthesis, a luminescence of living organisms [8, 18].

Long ago, still in [19], there was opinion about the existence of the single biological field of an alive organism, which determines the synchronism of the functioning of an organism. However the nature of this field unequivocally is not established till now. There was a supposition that it is formed by electromagnetic framework of organism, *functioning in a millimeter range* [20]. In the spectra of interaction of low-intensity radiations of a millimeter range with alive organisms [10], narrow peaks of very good quality are found out, which testify to the presence of water's own resonant frequencies and an alive organism in this range. However such theory does not explain all available facts of display of a single organizing structure which is associated with a biofield.

We suppose that a very substantial role in the organizations of synchronism of the functioning of a living matter played the entanglement which arises up as a result of a correlation interaction of its elements.

In [21] it was specified that "the entanglement is only the special quantum form of correlations, which, however, possesses a number of essential differences from classical correlations."

As an example of the entanglement, the authors [21] have taken the system, consisting of two particles with a one-half spin, which can accept only one of the two directions: "upward" or "downward." Such system is in a state with full spin, equal to zero (EPR state). This status is described by the formula

$$|\Psi_{\mathrm{EPR}}\rangle = \frac{1}{\sqrt{2}}\left(|\uparrow\rangle_1 \otimes |\downarrow\rangle_2 - |\downarrow\rangle_1 \otimes |\uparrow\rangle_2\right) \tag{8.1}$$

where $|\uparrow\rangle_1, |\downarrow\rangle_2$—wave functions of particles, one of which has a spin, directed upward, and other the spin, directed downward. The symbol $\otimes$ designates the operation of direct (tensor) product. At the change of spin direction of the first particle, the second particle also simultaneously must veer the spin direction, because the complete spin of the system is equal to zero.

Similar processes can take place for cellular nanostructures, contacting with the water medium of an organism through near-surface layers, both between separate cells and between organs. The given assumption can explain relative biological stability of alive organisms in relation to external influences.

In the spectra presented in Figs. 8.4 and 8.5, the resonant peaks which do not depend on the location of areas of fabrics, from which their registration was made, are shown. It means that the resonance frequencies are single for the whole organism; therefore, for the description of the state of an organism, it is possible to enter the certain wave function of Ω.

In that case a dynamics of disease of an organism can be descrabed mathematically as follows. The organism transfers to some superposition state under action of any influence (e.g., penetration of viruses) which can describe by some function X. The state which described by Ω is the superposition of equilibrium state with its own characteristic frequencies, described by function Ψ and a state described by function X.

$$\Omega = \alpha\Psi + \beta X \tag{8.2}$$

where α, β—some coefficients.

Some curve, described by a function $|\Omega|^2 = (\alpha\Psi + \beta X)^2$, is fixed; thus, experimentally, as a result another component is added in the spectra of a sick organism.

Apparently, narrow peaks of very good quality, in which a position does not coincide with the position of the basic resonant peaks and can correspond to the resonant frequencies not peculiar to a healthy organism corresponding to some factor of influence (e.g., to a virus), caused the disease.

If $|\beta| \to 0$, we have an equilibrium state of an organism; if $|\beta| \triangleright 0$, the organism leaves a state of equilibrium; the part of cells starts to function under the program, set by a virus, and in result the resonant status of an organism is violated. The partial decoherence of the equilibrium state of an organism occurs and a chaotic constituent begins to show up in the water spectra of an organism. Thus, in the spectra of the water environment of an organism, **three** components are shown: peaks of characteristic frequencies of an organism; spectra of some state, acting on a state of an organism and bringing it over to partial decoherence; and a chaotic component. Exactly these three components are found out in consideration of the spectra presented in Fig. 8.5 [10].

Whereas, as shown above, the spectra of the water component are fixed, here we deal exactly with the state of water system of an organism which as it was specified above exists in an organism as interfacial water. Certainly, these states of water of organism fully correspond to the state of an organism.

8.4 Some Statement of Water Molecule Condensation Theory, Shown in [9]

Water, in spite of its simple formula, is a very complex substance and behaves differently from other liquids, at diffusion of alien substances, at the dependence of density from temperature, and because of its many properties, including the nature of all its electric constants.

The theory of J. Preparata, created for the description of the phenomena in volumetric water, has enabled to explain well those phenomena which in principle could not be described by the traditional theories supposing of a homogeneous structure of usual water, as these phenomena directly testify about the insufficiency of such a single-component model.

It appeared also effective for the description of the phenomena in near-surface water.

Let's stop on some positions of this theory.

In accordance with [24], the state of the quantum system is determined as coherent if it is characterized by such a size as a phase. The quantum field is characterized by amplitude Ψ_0 in which square is proportional to number of quanta and a phase ϕ:

$$\psi = \psi_0 e^{i\varphi} = a\sqrt{N}e^{i\varphi} \tag{8.3}$$

In case of water system, N are a number of atoms in the selected volume.

Simplifying the description of forming process of coherence areas from the position of quantum electrodynamics, it is possible to do as follows [25]:

We will suppose that there is a certain ensemble from N molecules having two states—the **ground** and the excited states with the energy of excitation $E = \hbar\nu$ being approximately 12 eV.

The size of a molecule about 0.1 nm and the size of a virtual photon with length of a wave $\lambda = c/\nu$, which can make excitation with energy 12 eV, should be about 100.0 nm.

Therefore the linear size of region on which the excitations can be in 1,000 times more than a molecule. Let's assume that one virtual photon which is fluctuated from vacuum can excite an atom with probability P (according to a rating taken from the data at Lembov's shift value P about $10^{-4} \div 10^{-5}$). The excited molecule will be recombined through a certain time of recombination, returning back the photon in an environment which will be either absorbed by vacuum or will excite other molecule. The corresponding probability of these two events will depend on the density $n = N/\lambda^3$ of the molecules, present inside of volume λ^3.

When the density n will exceed threshold value n_{crit}, the photon can never return to vacuum and will pass from one molecule to another inside volume λ^3 under the condition of

$$P\lambda^3 n_{\text{crit}} = 1. \tag{8.4}$$

Thus, a vacuum gives a photon in a matter. This process will proceed until the great number of photons will not be captured and enough substantial field in this area does not appear.

The consequence of the formation of this field will be the occurrence of an attraction between molecules, to which short-range forces of intermolecular repulsion will counteract, and the formation of the common oscillation of all captured molecules inside all areas; for this reason, the specified area is named as coherent

domain (CD). In this process the molecules and photons lose the initial identity. Photons (as shown in these works) in the limited CD space acquire the imaginary mass; therefore, they cannot return back in a vacuum.

The areas designated as CD are surrounded with the molecules of usual "not coherent water." At a common temperature, in accordance with the estimations, made in [10, 24], the ratio describing a requirement of coexistence of both fractions, as in liquid helium, is carried out

$$F_c + F_{nc} = 1 \tag{8.5}$$

The equation (8.5) determines for every value of temperature the general amount of molecules, belonging to each phase; thus, each molecule passes through two phases continuously. It generates a "flickering" regime.

The reason of the existence of such regime, as well as for liquid helium, there are the temperature collisions. At room temperature, the total volume of such CD makes about 40 % from total volume of water. At temperature near zero, the total volume of CD makes the most part of the volume of water and at approximately 100 °C aspires to zero. Within the regions of CD, the property of water sharply differs from properties of noncoherent water: the viscosity of water medium and the decrement of vibrations are sharply reduced, and the fluidity of liquid is substantially increased.

The situation will change for near-surface water (so-called EZ water) and also in alive organisms where water closely contacts to surfaces of alive organisms (biomembranes, biomolecules). Appropriately to this case there will be a stabilization of the coherent state by virtue of attraction of water molecules to the wall, and a power barrier from the dividing effect of temperature collisions appears. In this case the coherent states can exist for a long time, and a formation of power whirlwinds in coherent domains is essential.

Just the same phenomena G. Pollack observed for, marking that for its formation, some forces of long-range action are responsible, and those molecules in it are in the excited state.

Let's note that a viscosity of near-surface water is essentially more than for usual water, and for the water bounded by molecular structures of an alive organism, viscosity, on the contrary, is reduced. In the effect explained in [24], in living organisms, the coherence is set not only within the regions of coherent domain but also between domains.

8.5 The Properties of One-Dimensional and Two-Dimensional Nanowater

For some systems consisting of the interaction between its own elements, the correlation relations between elements in the *classic* approach, it is possible to assimilate with some springs which link the separate elements of the system. The action on one of the elements will cause the change of the state of the other. However such changes do not occur instantly.

Fig. 8.6 The scheme of the water molecules linked among themselves by the hydrogen bindings [22]

Let's consider from a position of traditional performances the conductivity of water which, as is known, connects with the proton jump conduction [22].

The scheme of the arrangement of the water molecules linked among themselves in a chain through a system of a hydrogen binding is shown in Fig. 8.6 taken from [22].

The proton in such chain of water molecules can be in one of the two equivalent positions (corresponding to position of a proton in that or other quantum well), shared by a quantum barrier.

For overcoming this barrier a proton should receive the additional energy equal or large of the heights of a potential barrier, i.e., to pass in the excited state. However it can pass in another position due to tunneling.

In the common case of the random distribution of the potential, the transparency of barrier is determined from equation [25]

$$D = D_0 \exp\left(-\frac{2}{\hbar}\int_{x_1}^{x_2}\sqrt{2\mu(U(x)-E)}dx\right), \tag{8.6}$$

where E is the energy of proton and μ is the mass of proton.

The proton owing to tunneling periodically passes from one position to another, i.e., it periodically changes the position. At application of a potential, proton conductivity for volumetric water arises. This situation takes place for volumetric water.

However for near-surface waters of alive organisms, for water forming the single nano-layers or disposing in nano-systems, nanotubes, and capillaries, and in some other cases, additional effects related to quantum entanglement can arise. It is possible that exactly the quantum entanglement between the separate layers of water in compounds $SrFe_2As_2$ and $FeTe_{0.8}S_{0.2}$ is one of the factors of stimulation of superconductivity. In the case of entanglement between the molecules of water linked in chains via the hydrogen bindings, the change of a state of one molecule will instantly lead to change of a state of other molecules. Equation (8.1) describes the entangled state for two particles, but it is possible to describe the entanglement by analogical equalization in the system consisting of a great number of particles. If protons in any group of molecules appear in the excited state, sufficient for overcoming a quantum barrier sharing them, there will be the effects determined by not classical, but quantum laws.

In [26, 27], was specified that the energy, necessary in order that a proton passed to the delocalized state only of on 20 % below, than energy of hydrogen binding.

An interesting effect was found out by A. Kolesnikov with employees for water in carbon nanotubes at low temperatures [28, 29]. Water in nanotubes is not linked with the surface of nanotube by virtue of its hydrophobic state.

In the works of these researchers, it is specified that "The high momentum tail of the distribution, characteristic of the molecular covalent bond, is not present. . . .Our data reveal that the protons in the hydrogen bonds are coherently delocalized and that the low temperature phase is a qualitatively new phase of ice." "New water" did not freeze even at temperature, only on eight degrees distinguished from absolute zero.

The important assumption about the properties of nanotube waters was made by the author in [26, 27].

The author proceeded from that fact that in a coherent state the electrons of water molecules are in the excited state and, consequently, protons also should be excited. Quantum barriers do not hinder the motion of such protons (Fig. 8.6), and, in result, proton superconductivity is possible.

The author [26, 27] refers to the works of [30, 31] and informs that in these works the behavior of water in nanotube by diameter <5 nm was investigated. Authors [30, 31] discovered that the property of such water "was completely different from the more ordinary looking water confined in larger nanotubes." On the basis of experimental results of these works, the author [26, 27] asserts, "I suggested that the water confined in the small nanotubes, being far more ordered, ***could be superconducting*** because jump conduction could occur simultaneously down multiple chains of hydrogen-bonded water molecules" [32].

Proceeding from the assumption which has been put forward by the author in [26, 27], it is possible to assume also that in the layers of water diffused in compounds $SrFe_2As_2$ and $FeTe_{0.6}S_{0.2}$, protons also are in the excited state and hereupon can arise a delocalization of protons. It can be presented as follows.

The molecules of water diffused in compounds form the individual layers which settle down in parallel to the basic layers of compounds. As well as in volumetric water, the water molecules inside a layer can interact with the virtual photon that leaked out from vacuum [33]. In [24] the following is indicated: in the frame of quantum optics, it has been discovered that "a closely packed ensemble of atoms is able to leak out photons (namely to give rise to a non vanishing e.m.f.)."

The photon having length of a wave $\lambda = c/\nu$ corresponding to energy of transition of a water molecules to the excited state (approximately of 12 eV) can initiate the excitation of water molecules in region about 100 nm and can form the regions of coherency which can include of the many layers of diffused water. The same process causes the compression of crystalline grate of compounds $SrFe_2As_2$ and $FeTe_{0.6}S_{0.2}$, the phenomenon to which authors discover the effect of superconductivity stimulation and assign the reason of its origin.

With the reduction of temperature, the volumes of coherence regions, will increase, and at very low temperatures, the state of water may be similar to a one-dimensional chains of water and this state very differ from a state of usual ice. As well as for near-surface waters, the proton can appear delocalized; it means that it can be realized in conditions which, in opinion of the author [26], correspond to transition in a state of proton superconductivity of the waters. Consequently, if this supposition is correct, then water in the water layers of compounds $SrFe_2As_2$ and $FeTe_{0.8}S_{0.2}$ also can be in the superconducting state. Most likely, such transition in a

superconducting state of molecules of water coincides with the general transition of compounds $SrFe_2As_2$ and $FeTe_{0.8}S_{0.2}$ to a superconducting state.

However such assumption is necessary to confirm by the experimental researches similar by techniques of researches, carried out for nanotube waters.

8.6 Conclusions

Properties of nanowater essentially differ from properties of volumetric water. It concerns both to near-surface water and to interfacial water of living organisms.

Enormous roles in the formation of properties of volumetric water play the cluster nanostructures which determine its information and energetic characteristics. It is shown that the dynamics of convalescence of living organism is related to the normalization of the water system of an organism (determined by its nanostructure's complexes), as the inalienable constituent of organism, to convergence to an equilibrium state characterizing for a healthy state. The mathematical model of such process from a position of physics of the entangled states is offered.

The behavior of the water forming two-dimensional and one-dimensional systems is the most unusual. The settling of the water structures in cellular systems and micro capillaries of alive systems is supposed.

The two-dimensional properties of water in some approaching can be analogous to the properties of interfacial water of alive organism which, because of the influence of strong gradients of the existing field, for example, nearly of the cellular membranes, or of other reasons (such as the presence of admixtures), can obtain the stratification.

For the single layers of water, appearing because of water molecule diffusion in compounds $SrFe_2As_2$ and $FeTe_{0.8}S_{0.2}$, it was discovered by authors of [4–6] that such water can stimulate the origin of superconductivity in these compounds. Analogous to the works of [26, 27], which specified the possibility of realization of proton superconductivity for the nanotube water, the assumption for the first time is put forward in the present work—that the same phenomenon of proton superconductivity is possible for the water occupying the individual layers in compounds $SrFe_2As_2$ and $FeTe_{0.8}S_{0.2}$.

It is assumed that such transition is carried out at transition of these compounds to the superconductive state.

References

1. Pollack GH, Clegg J (2008) Unexpected linkage between unstirred layers, exclusion zones, and water. In: Pollack GH, Chin WC (eds) Phase transitions in cell biology. Springer Science & Business Media, Berlin, pp 143–152

2. Pollack GH (2010) Water, energy and life: fresh views from the water's edge. Int J Des Nat Ecodyn 5:27–29
3. Zheng JM, Chin WC, Khijniak E, Khijniak E, Pollack GH (2006) Surfaces and interfacial water: evidence that hydrophilic surfaces have long-range impact. Adv Coll Inter Sci 23:19–27
4. Hiramatsu H, Katase T, Kamiya T, Hirano M, Hosono H (2009) Water induced superconductivity in SrFe2As2. Phys Rev B 80:052501
5. Mizuguchi Y, Deguchi K, Tsuda S, Yamaguchi T, Takano Y (2010) Moisture-induced superconductivity in $FeTe_{0.8}S_{0.2}$. Phys Rev B 81:214510 [5 pages]
6. Deguchi K, Mizuguchi Y, Ozaki T, Tsuda S, Yamaguchi T, Takano Y (2011) Superconductivity in $FeTe_{1-x}S_x$ induced by alcohol. Supercond Sci Technol 24:arXiv:1008.0666
7. A.Sent-D'erd'I (1960) Bioenergetics. M., "Ph.-M.Literature". T.1, 155 p (in Russian)
8. Kurik MV, Martsenuyk LS (2012) The physical bases of the life. LAP LAMBERT Academic, Stuttgart, p 174
9. Preparata G (1995) QED coherence in condensed water. World Sci Singapore 236
10. Sinitsin NI, Petrosjan VI, Elkin VA et al (1999) The special role of system: "millimetric waves—the water environment in the nature". Biomed Radio Electron 1:3–21 (in Russian)
11. Krasnobryzhev VG, Kurik MV (2010) The quantum effects in a natural water. Quantum Magic 7(4):4132–4138 (in Russian)
12. Kurik MV About of the fractal of drinking-water. ("Living water"). Phys Conscious Life Cosmol Astrophys 1:45–48 (in Russian)
13. Korotkov KG (2007) Principles of analysis of GDV of bioelectrography. SPb.: "Reputation". 286 (in Russian)
14. Kurik MV, Lapitskiy VN, Pesotskaya LA (2010) Kirlianografiya of a drinking-water. Conscious Phys Real 15(12): 25–32 (in Russian)
15. Kurik MV (1991) Micellarity and fractal clusters of biological structures. News AN Ukraine. Ser Phys Sci 55(9):1798–1803 (in Russian)
16. Martsenyuk LS, Martsenyuk AS (2008) Questions of interaction of homoeopathic medicinal preparations and electromagnetic radiation of extremely high-frequency range with living organisms. Biomed Radio Electron 3:56–63 (in Russian)
17. Sinitsin NI, Elkin NA, Betskiy OV, Kislov VV (2009) The millimetric waves and nanostructure are the future of medicine and bioenergetics. Biomed Radio Electron (3):21–34 (in Russian)
18. Rieper E (2011) Quantum coherence in biological systems. Diplom Physikerin, Universit¨at Braunschweig, Germany. A thesis submitted for the degree of Philosophiæ Doctor (PhD). Centre for quantum technology, Germany, p 120
19. Gurvich AG (1944) Theory of the biological field. M. Soviet Science, p 156 (in Russian)
20. Sit'ko SP, Mkrtchyan LN (1994) Introduction to quantum medicine. K, "Pattern", p 146 (in Russian)
21. Bargatin IV, Grishanin BA, Zadkov VN (2001) The entangled quantum states of the atomic systems. Successes Phys Sci 171(6):625–647 (in Russian)
22. Antonchenko VJ, Davidov AS, Ильин VV (1991) Bases of water physics. Kiev, "Naykova dumka", p 672 (in Russian)
23. Emilio Del Giudice (2007) QED coherence in liquid water and the dynamics of the organization of water in living matter. INFN, Milano, Italy and IIB, Neuss, Germany. Second annual conference on the physics chemistry and biology of Water Mt. Snow, Vermont, 18–21 Oct 2007
24. Del Giudice E, Spinetti PR, Tedeschi A (2010) Water dynamics at the root of metamorphosis in living organisms. Water 2:566–586. www.mdpi.com/journal/water
25. Blokhintsev DI (1963) Bases of quantum mechanics. M. "Higher school". 619 (in Russian)
26. Ho MW (2012) Super-conducting liquid crystalline water aligned with collagen fibres in the fascia as acupuncture meridians of traditional Chinese medicine. Forum Immunopathol Dis Ther 3(3–4):221–236

27. Ho MW (2012) Superconducting quantum coherent water in nanospace confirmed. Sci Soc 55:48–51
28. Kolesnikov AI et al (2004) Neutron spectroscopy of water in carbon nanotubes. Phys Rev Lett 93:035503
29. Kolesnikov AI et al (2006) Anomalous behavior of proton zero point motion in water confined in carbon nanotubes. Phys Rev Lett 97:247801
30. Ye H, Naguib N, Gogotsi Y (2004) TEM study of water in carbon nanotubes. JEOL News 39:2–7
31. Naguib N, Ye H, Gogtsi Y, Yazicioglu AG, Megaridis CM, Yoshimura M (2004) Observation of water confined in nanometer channels of closed carbon nanotubes. NanoLett 4(22):37–43
32. Ho MW (2005) First sighting of structured water. Sci Soc 28:47–48.
33. Martseniuk LS, Martseniuk AS, Kyrik MV (2015) About some physical properties of water in nanosystems and the possible mechanism of superconductivity induction by water in compounds $SrFe_2As_2$ and $FeTe_{0.8}S_{0.2}$. Chapter 16, pp 187–206. In: Fesenko O, Yatsenko L (eds) Nanocomposites, nanophotonics, nanobiotechnology, and applications. Selected proceedings of the second FP7 conference and international summer school nanotechnology: from fundamental research to innovations, 25 Aug–1 Sept 2013, Bukovel, Ukraine, Springer, p 403

Chapter 9
3D Artificial Nanodiamonds Containing Nanocomposites Based on Hybrid Polyurethane-Poly(2-Hydroxyethyl Methacrylate) Polymer Matrix

L.V. Karabanova, A.W. Lloyd, and S.V. Mikhalovsky

9.1 Introduction

Polymer composites with small additives of nanofillers have attracted great attention over the last decade, both in industry and academia, since a considerable enhancement of mechanical, thermal, and other properties may be attained in the nanocomposites compared with those of virgin polymers. To date, the greatest number of studies has focused on polymer nanocomposites with two-dimensional (2D) nanoscale silicate layers [1, 2] and one-dimensional (1D) carbon nanotubes (CNTs) [3, 4]. The key to their enhanced efficiency is to achieve good dispersion, uniform spatial distribution, and alignment (for CNTs) of nanoparticles; however, the critical role of two more points is also usually emphasized, viz., (a) a high aspect (e.g., length-to-diameter for CNTs) ratio, typically of 10^3 or more, for a nanofiller, and (b) the necessity of chemical "functionalization" of nanofiller surface to provide its covalent coupling with a polymer matrix for improving interfacial properties and matrix performance. In addition, dispersion of nanoparticles may also be improved due to functionalization. The points (a) and (b) are typically considered as the prerequisites for attaining the highest performance of a polymer nanocomposite, by offering a low "percolation rheological threshold" (distinct effect of improved rheological behavior) at nanofiller content of less than 1 wt % [5, 6].

Among different nanocarbon structures used as polymer nanofillers (CNTs, carbon nanorods, fullerenes, ultra-dispersed artificial diamond (nanodiamonds,

L.V. Karabanova (✉)
Institute of Macromolecular Chemistry of National Academy of Sciences of Ukraine, Kharkov Road 48, Kiev 02660, Ukraine
e-mail: lyudmyla_karaban@ukr.net

A.W. Lloyd • S.V. Mikhalovsky
University of Brighton, Moulsecoomb Brighton, BN2 4GJ, UK
e-mail: a.w.lloyd@brighton.ac.uk; s.mikhalovsky@brighton.ac.uk

O. Fesenko, L. Yatsenko (eds.), *Nanoplasmonics, Nano-Optics, Nanocomposites, and Surface Studies*, Springer Proceedings in Physics 167,
DOI 10.1007/978-3-319-18543-9_9

NDs)), the latter have been available on a relatively large scale for last two decades and are also of interest. Synthesis and processing of 3D NDs have been described in refs. [6–9]. There are the examples of their successful applications in polymer nanocomposites as electronics materials, materials with protonic conductivity or enhanced thermal conductivity, in selective membranes, sensors, catalytic systems, nonlinear optical materials, and as an active filler increasing strength, wear, and heat-aging resistance of elastomers [6, 8–11].

In our previous work [12–14], dynamic-mechanical behavior, segmental motions, elastic and physico-mechanical properties have been studied in several polyurethane-poly(2-hydroxyethyl methacrylate) semi-interpenetrating polymer networks (PU-PHEMA semi-IPNs) over the temperature range −140 to 180 °C, by using combined DMA, laser-interferometric creep rate spectroscopy (CRS), and differential scanning calorimetry analysis. These systems had basically two-phase, nanoheterogeneous structure with incomplete phase separation and the pronounced dynamic heterogeneity within the extraordinarily broadened PHEMA and PU glass transitions, practically the united glass transition extending over the range from −60 to 160 °C, were observed in these semi-IPNs. Such dynamic behavior and, additionally, improved biocompatibility of PU-PHEMA semi-IPNs are of interest for developing improved biomedical, damping, or membrane materials based thereon.

In the present research we investigated, using thermodynamic and physico-mechanical approaches, the properties and their relation to nanostructure in the nanocomposites are based on the PU-PHEMA semi-IPNs filled with artificial 3D NDs.

9.2 Materials and Testing Methods

9.2.1 Materials

Neat PU and PHEMA, their semi-IPNs, and ND-containing nanocomposites based thereon were prepared as described elsewhere [14, 17]. PU network was initially obtained from the adduct of trimethylol propane, toluylene diisocyanate, and poly (oxypropylene)glycol (PPG) with $M_w = 2.000$ g mol^{-1}. The semi-IPNs with 17, 37, and 57 wt. % PHEMA were obtained by swelling PU network with 2-hydroxyethyl methacrylate (HEMA) and its subsequent photo-polymerization (the wavelength of UV light λ 340 nm).

For preparing the nanocomposites with PU, PHEMA, and semi-IPN matrices, the ultra-dispersed diamond powder (NDs) obtained by the shock-wave method (supplied by Alit Company, Ukraine), with the particle sizes of 2–100 nm and specific surface area of 220 m^2 g^{-1}, was used. NDs were introduced with the amounts of 0.25–20.00 wt. % into a polymer system at the stage of PU synthesis, or into HEMA in the case of preparing the nanocomposite based on neat PHEMA. NDs were dried for 48 h at 200 °C before using.

The prepared films with 1 mm thickness were post-cured for 2 h at 100 °C, and then were held for 36 h at 80 °C in vacuum 10^{-5} Pa.

9.2.2 Testing Methods

Vapor Sorption and Thermodynamic Calculations

The dichloromethane vapor sorption by semi-IPN samples and by nanocomposites samples was studied using a vacuum installation and a McBain balance [12]. The changes in partial free energy of dichloromethane by sorption (dissolution) were determined from the experimental data using (9.1)

$$\Delta\mu_1 = (1/M)RT \ \mathrm{In}(P/P_o), \tag{9.1}$$

where M is the molecular mass of dichloromethane and P/P_o is the relative vapor pressure. The value $\Delta\mu_1$ changes with solution concentration from 0 to $-\infty$.

To calculate the free energy of mixing of the polymer components with the solvent, the changes in partial free energy of the polymers (native polymers, semi-IPNs, nanocomposites) need to be determined. This requires the calculation of the difference between the polymer chemical potential in the solution of a given concentration and in pure polymer under the same conditions ($\Delta\mu_2$). $\Delta\mu_2$ for the polymer components were calculated using the Gibbs–Duhem equation:

$$\omega_1 d(\Delta\mu_1)/d\omega_1 + \omega_2 d(\Delta\mu_2)/d\omega_1 = 0, \tag{9.2}$$

where ω_1 and ω_2 are the weight fractions of a solvent and of a polymer. This can be rearranged to give (9.3)

$$\int d(\Delta\mu_2) = -\int (\omega_1/\omega_2) d(\Delta\mu_1). \tag{9.3}$$

Equation (9.3) allows the determination of $\Delta\mu_2$ for each polymer from the experimental data by integration over definite limits. The average free energy of mixing of solvent with the individual components, semi-IPNs of various compositions for the solutions of different concentration, was then estimated using (9.4) and using computational analysis.

$$\Delta g^m = \omega_1 \Delta\mu_1 + \omega_2 \Delta\mu_2. \tag{9.4}$$

Dynamic Mechanical Analysis

The dynamic mechanical analysis (DMA) measurements were carried out using a Dynamic Mechanical Thermal Analyzer Type DMA 2980 from TA Instruments

over the temperature range from 133 to 473 K and at fixed frequencies (5, 10, 15, 20, 30 Hz) with a heating rate of 3 K/min. The experiments were performed in the tension mode on rectangular specimens (35 mm × 5 mm × 1 mm). As poly (2-hydroxyethyl methacrylate) is a hydroscopic polymer, all samples were dried at 353 K for 48 h under vacuum before measurements. The samples were subsequently subjected to the following thermal cycle during DMA measurements: a first run from 293 up to 373 K, then second run from 133 up to 473 K. The second run was used for analysis of the results.

Creep Rate Spectroscopy

CRS, the high-resolution method of relaxation spectrometry and thermal analysis, developed at Ioffe Institute [15], was used here for analysis of the heterogeneity of segmental dynamics over the broad temperature regions of PU and PHEMA glass transitions in the studied semi-IPNs and nanocomposites based thereon. The CRS setups and the experimental technique have been described in detail elsewhere [15]. It consists in precisely measuring creep rates at a constant low stress as a function of temperature, using a laser interferometer based on the Doppler Effect. The time evolution of deformation is registered as a sequence of low-frequency beats in an interferogram whose beat frequency ν yields a creep rate

$$\dot{\varepsilon} = \frac{\lambda \nu}{2I_0}, \tag{9.5}$$

where $\lambda = 650$ nm is a laser wavelength, and I_0 is an initial length of the working part of a sample. The stress was chosen in the preliminary experiments as capable of inducing sufficient creep rates to be measured, while maintaining also a high spectral resolution, without smoothing and distortion of a spectral contour, and preventing a premature rupture of a sample.

Mechanical Testing

Mechanical properties of the neat PU and PHEMA, their semi-IPNs, and ND-containing nanocomposites were measured using a Series IX Automated Instron Materials Testing System. The samples were cut into micro dumb-bell shapes with gauge length of 20 mm, widths between 4 and 5 mm and sample thickness between 0.7 and 0.9 mm. Samples were processed at a continuous strain rate of 25 mm/min.

9.3 Results and Discussion

9.3.1 *Thermodynamic of Polymer–Filler Interactions in the Nanocomposites*

Figure 9.1 shows the sorption isotherms of dichloromethane vapor at 298 K by samples of polyurethane (1), poly (2-hydroxyethyl methacrylate) (2), polyurethane, containing artificial nanodiamonds (3, 5, 7), and poly (2-hydroxyethyl methacrylate), containing nanofiller (4, 6, 8). The sorption isotherm for PU (1) has the form characteristic of sorption isotherms polymers that are in viscoelastic state. For poly (2-hydroxyethyl methacrylate) (Fig. 9.1, curve 2) at $P/P_o < 0.6$ sorption is low, due to the dense packing of the macromolecules in the glassy state of this polymer [16, 17]. In the relative solvent vapor pressure $P/P_o > 0.6$, the transition of poly (2-hydroxyethyl methacrylate) from glassy state to the viscoelastic state takes place and an increase in vapor sorption dichloromethane could be observed.

With the introduction of nanodiamonds into the PU, the decrease of dichloromethane vapor sorption by filled samples occurs (Fig. 9.1, curves 3, 5, 7), which qualitatively indicates the formation of densely packed boundary layers in the filled PU's samples. But reducing dichloromethane vapor sorption by filled samples has nonmonotonic character: isotherm for PU containing 20 % of nanofiller runs higher than for PU with 5 and 10 % of nanofiller. It should be noted that during the formation of 3D polymer in the presence of nanofiller, except the densely

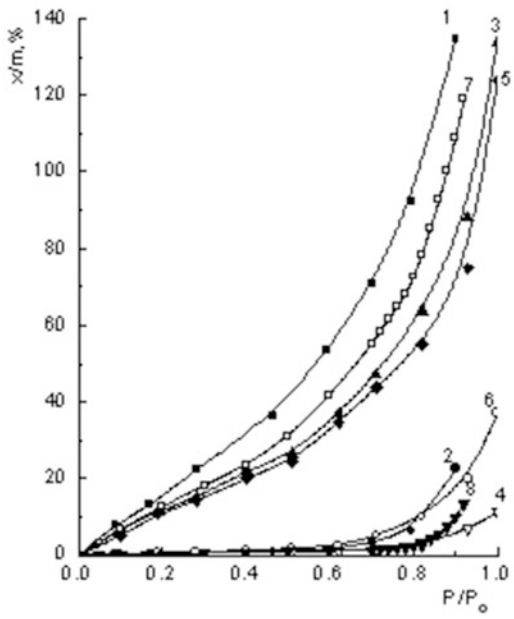

Fig. 9.1 Isotherms of dichloromethane vapor sorption at 298 K by samples of polyurethane (1), poly (2-hydroxyethyl methacrylate) (2), polyurethane, containing 5 % (3), 10 % (5), 20 % (7) of artificial nanodiamonds and poly (2-hydroxyethyl methacrylate), containing 5 % (4), 10 % (6), 20 % (8) of artificial nanodiamonds [23]

packed boundary layers, the appearance of a number of defects (reduction of the number of chemical junctions, "free" ends) could appear.

Moreover, as the amount of nanofiller within the network structure increases, the material becomes more defective [18]. This could explain the non-monotonic nature of dichloromethane vapor absorbed by the sample of filled PU.

For filled poly(2-hydroxyethyl methacrylate), the decrease of dichloromethane vapors sorption compared to unfilled polymer could also be observed, and the dependence of sorption has non-monotonic character with the amount of nanofiller (Fig. 9.1, curves 4, 6, 8). Sorption isotherms for poly(2-hydroxyethyl methacrylate) stand much lower than for polyurethane. This means that investigated polymers have significantly different sorption capacity, which allows calculation of the thermodynamic parameters for this pair of polymers [19].

Application of the thermodynamic methods and calculations based on the experimental data of vapor sorption of dichloromethane by nanocomposites samples allowed us to estimate a number of characteristics of the system, namely, the free energy of interaction of polymers with solid surfaces. In [19] for the thermodynamic parameters of the polymer–polymer interaction estimation, the approach based on the fundamental assumptions of independence of thermodynamics enthalpy and free energy of the system from the way of the process was used [19]. In [20, 21], this approach was applied to polymer–filler systems. Under this approach, we can calculate the parameters of interaction of polymer with a filler when parameters of the interaction of each of them and their mixtures with fluid are known. Based on sorption isotherms, the change of the partial free energy of dichloromethane $\Delta\mu_1$ was calculated using (9.1). The change in the partial free energy of individual polymer components, semi-IPNs and filled systems under sorption process $\Delta\mu_2$ was determined in accordance with the Gibbs–Duhem equation (9.2). Free energy of mixing of individual polymers and semi-IPNs with solvent Δg^{m} was determined in accordance with the (9.3).

Figure 9.2 shows calculated parameters Δg^{m} for individual polymers, semi-IPNs, and filled systems. All systems under investigation, polyurethane-dichloromethane, poly(2-hydroxyethyl methacrylate)-dichloromethane, semi-IPNs-dichloromethane, and filled systems-dichloromethane are thermodynamically stable ($d^2\Delta g^{\mathrm{m}}/dW_2^2 > 0$). The affinity of dichloromethane to polyurethane is higher (Fig. 9.2, curve 1) than to poly(2-hydroxyethyl methacrylate) (Fig. 9.2, curve 2). The affinity of dichloromethane to samples of filled polyurethane decreases with filler content (Fig. 9.2, curves 2, 4). For filled poly(2-hydroxyethyl methacrylate) is a non-monotonic dependence of dichloromethane affinity from amount of filler was found: affinity increases for nanocomposites containing 5 and 10 % of nanodiamonds (Fig. 9.2, curves 3, 5), but decreases with the introduction of 20 % of the filler.

For filled semi-IPNs, the same dependence of dichloromethane affinity to samples with increasing amount of filler is observed: dichloromethane affinity decreases with increasing filler content. Reduced affinity of dichloromethane to filled polymers and to semi-IPNs may indicate the formation of strong adhesion of polymers to the surface of filler and the formation of tightly packed boundary layers of polymers in the filled samples.

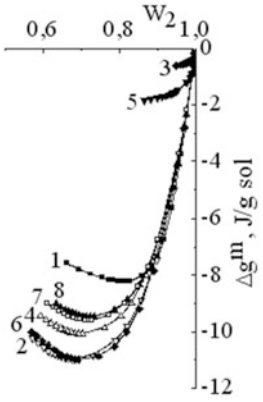

Fig. 9.2 Free energies of mixing of polymers and nanofiller with solvent dichloromethane Δg^{m}: nanodiamonds (1), polyurethane, containing 5 % of NDs (2), poly (2-hydroxyethyl methacrylate), containing 5 % of NDs (3), polyurethane, containing 10 % of NDs (4), poly (2-hydroxyethyl methacrylate), containing 10 % of NDs (5), semi-IPNs with 17 % PHEMA, containing 5 % of NDs (6), semi-IPNs with 17 % PHEMA, containing 10 % of NDs (7), semi-IPNs with 17 % PHEMA, containing 20 % of NDs (8) [23]

Based on the concentration dependence of the average free energy of mixing of the solvent with individual polymers PU, PHEMA, and with the nanocomposites, the values ΔG_1 and ΔG_{111} were obtained. ΔG_1 and ΔG_{111} are the free energies of interaction of polymers with lots of solvent. For $\Delta G^{*}_{\text{p-f}}$ calculation (free energy of polymer-filler interaction), the (9.6) was used.

$$\Delta G^{*}_{\text{p-f}} = \Delta G_1 + n\Delta G_{11} - \Delta G_{111}, \tag{9.6}$$

where ΔG_{11}—free energy of interaction of the filler with lots of solvent.

The results of $\Delta G^{*}_{\text{p-f}}$ calculation are shown in Fig. 9.3. As could be seen, the free energy of interaction of nanodiamonds with polyurethane (Fig. 9.3, curve 1) is negative for all investigated concentrations of filler. This indicates the thermodynamic stability of filled polyurethane samples, the high adhesion of polyurethane to this filler. But the value of free energy of interaction of nanodiamonds with polyurethane varies with the amount of filler. At high concentrations of filling (20 %), the value of the free energy of interaction decreases.

For poly(2-hydroxyethyl methacrylate), the free energy of interaction with nanodiamonds also has negative value for all concentrations of filler, but it is much lower than the value of free energy for polyurethane (Fig. 9.3, curve 2). This means that the affinity of nanodiamonds to polyurethane higher than to the poly(2-hydroxyethyl methacrylate). With introduction of the filler into the mixture of these two polymers, the overwhelming adsorption of polyurethane chains to the filler surface will take place and the formation of boundary layers with the prevailing amount of polyurethane in relation to the volume will occurs.

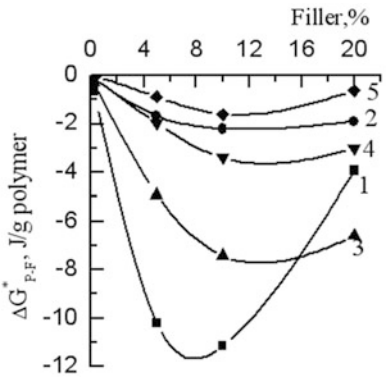

Fig. 9.3 Free energies of mixing of individual networks and semi-IPNs with artificial nanodiamonds: PU (1), PHEMA (2), semi-IPNs with 17 % PHEMA (3), with 28 % PHEMA (4), with 37 % PHEMA (5) [23]

For all filled semi-IPNs under investigation, the free energy of interaction with nanodiamonds has also a negative value (Fig. 9.3, curves 3–5). This indicates the thermodynamic stability of filled semi-IPN samples, the formation of strong adhesive contact of polyurethane-poly(2-hydroxyethyl methacrylate) mixture with the filler's surface.

Generally, the negative values of free energy of interaction of nanodiamonds with polymer components of the nanocomposites suggest that the nanodiamonds could be acting as a reinforcing filler for the investigated polymer systems.

9.3.2 Dynamic Mechanical Analysis Data of Nanocomposites

DMA data of unfilled semi-IPNs have revealed a pronounced change in the viscoelastic properties of semi-IPNs with different amounts of PHEMA in the samples. The semi-IPNs have two distinct maxima of tan δ related to the presence of two polymers in their glass transition temperature domains (Fig. 9.4). The tan δ maximum of PHEMA is shifted towards higher temperature and its amplitude increases with the increasing fraction of PHEMA (Fig. 9.4). These results confirm that the studied semi-IPNs are two-phase systems with incomplete phase separation and "frozen" non-equilibrium structure. The segregation degree α was calculated for semi-IPNs, and it was shown the values are varied from 0.22 to 0.35 depending on the amount of PHEMA [12]. This means that phase separation in the semi-IPNs was "frozen" in the initial stage by permanent entanglements of the chains.

The introduction of nanodiamonds in the semi-IPN samples result in essential changes in dynamic mechanical behavior of materials especially in the temperature range of PU glass transition (Fig. 9.5). The introduction just 0.25 % of filler into PU network lead to decreasing of amplitude of tan δ and broadening of glass transition domain of PU due to the formation of boundary layers of polymer on the surface of filler particles and, as a result, some restriction of polymer dynamics.

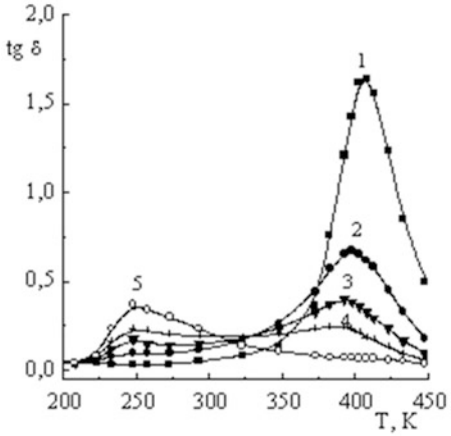

Fig. 9.4 Dynamic mechanical measurements of tan δ vs. temperature for unfilled semi-IPNs: PHEMA (1), semi-IPNs with 57 % PHEMA (2), with 32 % PHEMA (3), with 17 % PHEMA (4), PU (5)

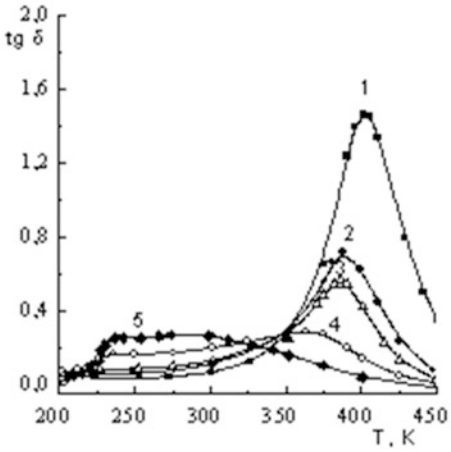

Fig. 9.5 Dynamic mechanical measurements of tan δ vs. temperature for semi-IPNs contained 0.25 % of nanodiamonds: semi-IPNs with 57 % PHEMA (2), with 37 % PHEMA (3), with 17 % PHEMA (4), PU (5)

The formation of PU in the presence of nanofiller particles could result also in separation of hard and soft segments of polymer as the two maxima could be observed in the glass transition temperature domains of filled polymer (Fig. 9.5, curve 5). For filled semi-IPNs. the superposition of two glass transition temperature domains of PU and PHEMA for small content of PHEMA and full suppression of segmental dynamic of PU for large amount of PHEMA were observed (Fig. 9.5, curves 2–4).

The essential changes of dynamic mechanical behavior of PU could be explained by preferential adsorption of PU chains on the nanodiamond particles surface during process of nanocomposites formation. This is correspondent with the thermodynamic affinity of the IPN's components to the nanofiller particles (Fig. 9.3).

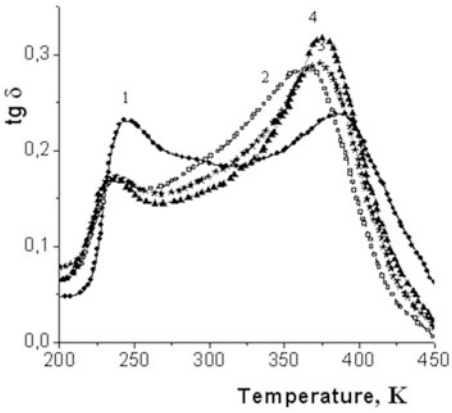

Fig. 9.6 Dynamic mechanical measurements of tan δ vs. temperature for semi-IPNs with 17 % PHEMA (1) and for nanocomposites based on semi-IPNs with 17 % PHEMA contained 0.25 % (2), 1 % (3) and 3 % (4) of nanodiamonds

In Fig. 9.6, the dynamic mechanical behavior of nanocomposites with different amount of nanodiamonds is presented. Temperature dependence of tan δ for unfilled semi-IPN containing 17 % PHEMA has two maxima in the range of glass transition domains of polyurethane and PHEMA (Fig. 9.6, curve 1). This indicates a two-phase structure of the investigated semi-IPNs. At the same time, the bridge between the two maxima is high enough. This means that two peaks overlap to some extent, and this is due to the microphase separation in the semi-IPN is not complete [12, 13, 17].

The introduction of nanodiamonds (Fig. 9.6, curves 2–4) leads to significant decrease in the intensity maximum in the glass transition temperature of polyurethane (223–273 K) and leads to the shift of the peak towards lower temperatures. This is consistent with results of investigation of nanocomposites, where the polyurethane was the matrix, and this is the evidence of inhibition of segmental motion of polyurethane in the nanocomposites where the matrix is a semi-IPN.

However, the impact of the introduction of the nanodiamonds to the maximum tan δ in the PHEMA glass transition temperature (348–423 K) has the opposite direction (Fig. 9.6, curves 2–4). It could be seen that the introduction of nanofiller leads to an increase in the intensity these maxima, their expansion, and shift towards low temperatures. This means that segmental motion of PHEMA in the nanocomposites is more free than in the unfilled semi-IPN. This effect of nanofiller is very different from the situation in filled PHEMA, where the introduction of nanodiamonds resulted in restriction of segmental motion.

Introduction of nanofiller into the multicomponent polymer matrix during process of polymers formation leads not only to the formation of surface layers of polymers on the nanoparticles, but also leads to the changes in the microphase separation of matrix's components [14, 17, 22]. In this case, obviously, deepening of microphase separation between the polyurethane and PHEMA in the presence of nanofiller during process of the nanocomposites formation will take place. However, preferential adsorption of PU chains on the surface of filler particles during process of nanocomposites formation resulted in inhibition of segmental motion of polyurethane and thawing segmental motion of PHEMA at lower temperatures (Fig. 9.6, curves 2–4).

9.3.3 Creep Rate Spectroscopy Investigation of Nanocomposites

The CRS investigation of nanocomposites produced the results consistent with DMA results [17, 22]. The maximal effect was observed for samples containing 0.25 % of filler. The separation of hard and soft segments is clearly observed for filled PU. Figure 9.7 shows the creep rate spectra obtained for neat PU network and ND-containing nanocomposites based thereon in the temperature region of PU glass transition. The pronounced dynamic heterogeneity in the glass transition of this PU network has already been displayed by CRS in the previous work [14]. As was shown, its CR spectrum, located between –60 and 50 °C, consists of four overlapping peaks, with the maxima at about –30(I), –10(II), +10(III), and +40 °C (IV). Peaks I–III were tentatively assigned to step-like unfreezing of a few segmental dynamics modes within five-segment PPG crosslinks ($M_w = 2.000$ g mol^{-1}), due to different positions of segments regarding PU network junctions and different hindering dynamics, respectively. Peak IV was assigned to unfreezing of network-junction motion. Figure 9.7 shows that the introduction of NDs particles results in some redistribution of the intensities of spectral peaks; nanofiller affects stronger lower-temperature peaks. Interestingly, below 0 °C the suppression effect was the largest at the minimal ND content in a nanocomposite.

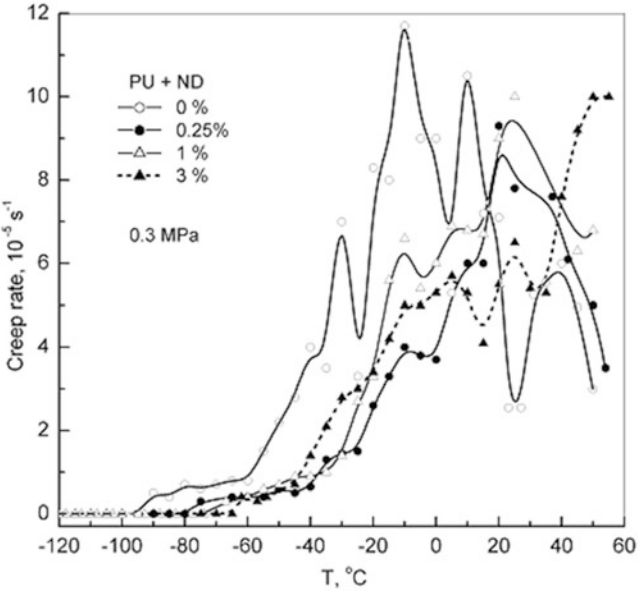

Fig. 9.7 Creep rate spectra obtained for neat PU network and ND-containing nanocomposites based thereon at tensile stress of 0.3 MPa in the temperature region of glass transition. ND weight contents are indicated [22]

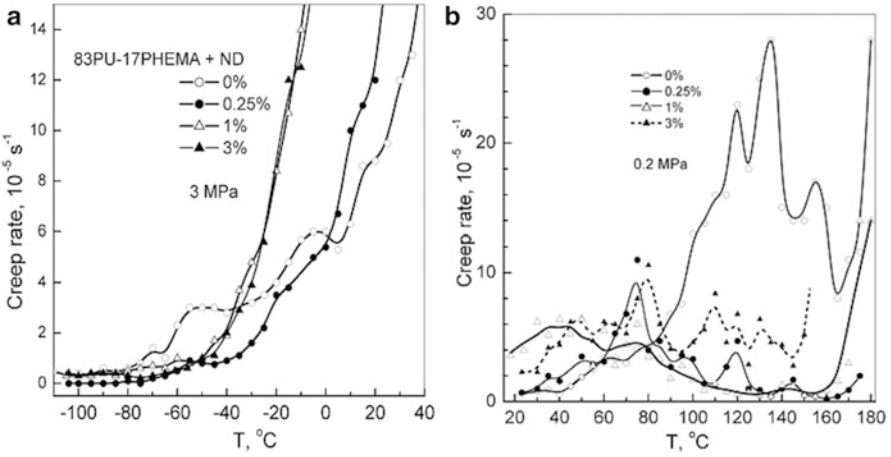

Fig. 9.8 (**a**, **b**) Creep rate spectra obtained for the 83PU-17PHEMA network and ND-containing nanocomposites based thereon in the temperature regions of PU glass transition, at tensile stress of 3 MPa (**a**), and of PHEMA glass transition, at tensile stress of 0.2 MPa (**b**). ND weight contents are indicated [22]

Figure 9.8a, b shows the CR spectra of the 83PU-17PHEMA-ND nanocomposites obtained over the temperature range covering both PU and PHEMA glass transitions. The introduction of 17 wt. % PHEMA into PU network, with the formation of hybrid semi-IPN, resulted in some suppression of segmental dynamics at low temperatures [14]. Therefore, the increased tensile stress of 3 MPa was used to register the distinct CR spectra of these compositions at −100 to 40 °C (Fig. 9.8a). On the whole, the complicated influence of the added NDs on glass transition dynamics in the 83PU-17PHEMA network is observed. Figure 9.8, a shows some suppression of dynamics by ND particles at the lowest temperatures of −80 to −40 °C but, contrarily, accelerated creep in nanocomposites with 1 or 3 % NDs starting from −30 °C. This effect of increased mobility (creep rates) in nanocomposites, compared to that in unfilled semi-IPN, is retained up to 50–80 °C (Fig. 9.8b).

Further, a single, very intense glass transition peak with $T_{max} = 90$ °C, observed in the CR spectrum of neat PHEMA, changed only slightly in the PHEMA-ND nanocomposite [17, 22].

At the same time, cardinal spectral changes in PHEMA glass transition were observed in the 83PU-17PHEMA-ND nanocomposites (Fig. 9.8b): the introduction of ND particles strongly changed the “relaxation picture” at elevated and high temperatures. The main effect here is a sharp suppression of PHEMA segmental dynamics (creep at low stress) over the range of 90–180 °C that corresponds to disappearance of high-temperature heat capacity anomaly in the DSC curve. The highest creep resistance at 150–180 °C is observed at the minimal ND content of 0.25 wt. % in the nanocomposite whereas, contrarily, the least effect of suppression of dynamics by nanofiller is registered at 3 wt. % NDs (Fig. 9.8b).

Again, the introduction of ND particles resulted also in the opposite effect of some accelerating segmental dynamics at 20–70 °C (Fig. 9.8b), i.e., increasing creep rates in the temperature region between the β- and α-transitions of PHEMA.

9.3.4 *Mechanical Testing of Nanocomposites*

Investigations of physico-mechanical properties of the nanocomposites have shown that the results are in good agreement with the calculations of thermodynamic parameters of polymer–fillers interactions. In Fig 9.9, the stress–strain curves for a series of samples containing the same amount of nanodiamonds (0.25 %), but different content of PHEMA in the matrixes are presented. Figure 9.10 presents the stress–strain curves for a series of samples having the same polymer matrix—semi-IPNs with PHEMA content of 28 %, but different amount of nanofiller.

It could be seen (Fig. 9.9) that for nanocomposites containing the same amount of nanofiller, stress at break naturally increases with the content of the second component of the semi-IPN—PHEMA. In this case, Young's modulus, which is proportional to the angle of initial part of curve's slope, increases dramatically for the sample containing 57 % of PHEMA. This may indicate a phase inversion of polymers constituent of matrix, or the formation of two-phase continuity of structure of two polymers constituent of matrix for semi-IPN containing 57 % of PHEMA.

In the study of the nanocomposites that have the same polymer matrix—semi-IPNs with PHEMA content of 28 %, but different amount of nanofiller (Fig. 9.10), it appears that all filled samples had higher stress at break and Young's modulus in comparison with unfilled samples (Fig. 9.10, curve 1). Thus, this result correlates with the data of thermodynamic calculations and suggests that artificial nanodiamonds could be a reinforcing nanofiller for investigated systems.

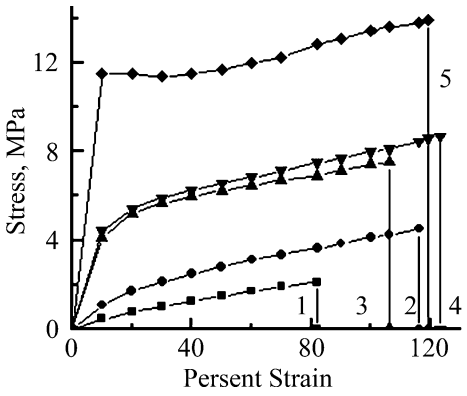

Fig. 9.9 Stress–strain curves for nanocomposites contained 0.25 % of NDs based on different matrixes: PU (1), PU/PHEMA semi-IPN with 17 % PHEMA (2), PU/PHEMA semi-IPN with 28 % PHEMA (3), PU/PHEMA semi-IPN with 37 % PHEMA (4), PU/PHEMA semi-IPN with 57 % PHEMA (5)

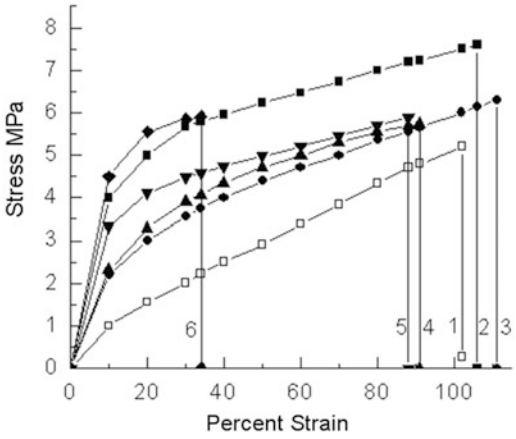

Fig. 9.10 Stress–strain curves for PU/PHEMA semi-IPN with 28 % PHEMA and with different amount of nanodiamonds: 0 % (1), 0.25 % (2), 1 % (3), 5 % (4), 10 % (5), 20 % (6) [24]

At the same time, it could be seen (Fig. 9.10) that the maximum of stress at break and maximum of Young's modulus characterize the nanocomposite with filler content of 0.25 % (Fig. 9.10, curve 2). With further increase of filler content (1–10 %), the relative decrease in stress at break is observed (Fig. 9.10, curves 3–5). This may indicate the formation of aggregates and clusters of nanofiller in the structure of nanocomposites with increasing nanofiller content, and as a result, the reduction of effective filler surface that interacts with components of the polymer matrix occurred [22].

At the maximum amount of artificial nanodiamonds (20 %), high Young's modulus observed, which is close to the value for the sample with minimal nanofiller content (0.25 %). But at the same time, the strain of this sample is dramatically reduced (Fig. 9.10, curve 6). This is connected with increasing nanofiller aggregation, the formation of continuous cluster of nanofiller, which prevents elongation of the nanocomposite's specimen with 20 % of artificial nanodiamonds [22].

9.4 Conclusion

The artificial nanodiamonds (NDs) with particle size of 2–50 nm (produced by high shock blow method) were used as nanofiller for composites based on multicomponent polymer matrix that consists of polyurethane and poly (2-hydroxyethyl methacrylate). The thermodynamic miscibility, dynamic mechanical, physical-mechanical properties, segmental motions, and morphology of composites have been investigated.

The vapor sorption by filled composites and by nanodiamonds was studied, and thermodynamic affinity of polymer components to the filler was estimated. The free energy of interaction between the polymer components and nanofiller was negative;

this means that NDs can be considered as the reinforcing nanofiller for the investigated polymer systems.

The mechanical properties of semi-IPN samples reflect the changes in structure with increasing amount of PHEMA in the systems. The stress at break changes from 3.5 to 24 MPa but strain at break has the extremum at 40 % of this polymer. Young's modulus increases from 13 up to 658 MPa with a fraction of PHEMA. The introduction of nanodiamonds into the semi-IPN samples resulted in the significant increase in stress at break and in Young's modulus. The maximal effects have been obtained for samples with 0.25 % of filler. The increasing amount of filler in the semi-IPN samples resulted in a relative decrease of reinforcing effect.

Segmental dynamics and elastic properties were studied by CRS method, network structure, and dispersion/spatial distribution of ND particles were studied by AFM/IRS techniques. The effects of double hybridization, the pronounced dynamic heterogeneity, the anomalous changes in PHEMA glass transition, sharp suppression of dynamics, and multifold enhancing elastic properties at only 0.25 wt % NDs were found. It is due to improved dispersion-/distribution of NDs, and the united glass transition, extending from –60 to 160 °C, and these effects are of interest for the biomedical and technical applications.

Acknowledgements The work was partly supported by FP7-PEOPLE-IRSES project 230790 COMPOSITUM. The project N 6.22.7.21 of the STSTP "Nanotechnology and Nanomaterials" of Ukraine (L.K.) is greatly acknowledged.

References

1. Ray SS, Okamoto M (2003) Polymer-layered silicate nanocomposites: a review from preparation to processing. Polym Sci 28:1539–1641
2. Alexandre M, Dubois P (2000) Polymer-layered silicate nanocomposites: preparation, properties and uses of a new class of materials. Mater Sci Eng 28:1–16
3. Moniruzzaman M, Winey KI (2006) Polymer nanocomposites containing carbon nanotubes. Macromolecules 39:5194–5205
4. Shaffer MSP, Sandler JKW, Advani S (2006) In processing and properties of nanocomposites. World Scientific, Singapore
5. Dolmatov VY (2001) Detonation synthesis ultradispersed diamonds: properties and applications. Russian Chem Rev 70:687–702
6. Gruen DM, Shenderova OA, Vul' AY (2005) Synthesis, properties and applications of ultrananocrystalline diamond. Springer, Amsterdam
7. Dolmatov VY, Shenderova OA, Gruen DM (2006) Ultrananocrystalline diamond: synthesis, properties and applications. William-Andrew, New York
8. Davidson JL, Kang WP, Gruen DM et al (2005) Synthesis, properties and applications of ultrananocrystalline diamond. Springer, Amsterdam
9. Shilov VV, Gomza YP, Shilova OA et al (2005) Synthesis, properties and applications of ultrananocrystal-line diamond. Springer, Amsterdam
10. Zhang H, Wang B, Li H et al (2003) Synthesis and characterization of nanocomposites of silicon dioxide and polyurethane and epoxy resin interpenetrating network. Polym Int 52 (9):1493–1497. doi:10.1002/pi.1247

11. Jeong HM, Lee SH (2003) Properties of waterborne polyurethane/PMMA/clay hybrid materials. J Macromol Sci Phys 42(6):1153–1167. doi:10.1081/MB-120024811
12. Karabanova LV, Boiteux G, Gain O et al (2004) Miscibility and thermal and dynamic mechanical behaviour of semi-interpenetrating polymer networks based on polyurethane and poly(hydroxyethyl methacrylate). Polym Int 53:2051–2058
13. Shilov VV, Karabanova LV, David L et al (2005) The structure peculiarities of the polyurethane/poly(hydroxyethyl methacrylate) semi-interpenetrating polymer networks. Polym J (Ukraine) 27:255–263
14. Karabanova LV, Sergeeva LM, Svyatyna AV et al (2007) Heterogeneity of glass transition dynamics in polyurethane-poly(2-hydroxyethyl methacrylate) semi-interpenetrating polymer networks. J Polym Sci B 45(8):963–975. doi:10.1002/polb.21108
15. Peschanskaya NN, Yakushev PN, Sinani AB et al (1994) New possibilities for study of deformation kinetics and relaxations using a laser interferometer. Thermochim Acta 238:429–437
16. Clark-Monks C, Ellis B (1973) Vapor sorption by filled/reinforced resins. I. General behavior and interpretation. J Polym Sci B 11(11):2089–2098. doi:10.1002/pol.1973.180111101
17. Bershtein VA, Karabanova LV, Sukhanova TE et al (2008) Peculiar dynamics and elastic properties of hybrid semi-interpenetrating polymer network—3-D diamond nanocomposites. Polymer 49:836–842
18. Karabanova LV, Gorbach LA, Skiba SI (1991) Thermodynamic investigations of interactions in filled interpenetrating polymer networks. Composit Polym Mater (Ukraine) 49:35–39
19. Tager AA (1972) Thermodynamic stability of polymer-solvent and polymer-polymer systems. Visokomol Soedin A 14(12):2690–2698
20. Bessonov YS, Tager AA, Yushkova SM et al (1978) Thermodynamic investigations of interactions in filled polyvinylchloride. Visokomol Soedin A 20(1):99–105
21. Kwei T (1965) Polymer-filler interaction thermodynamic calculations and a proposed model. J Polym Sci A 3(9):3229–3237. doi:10.1002/pol.1965.100030917
22. Karabanova LV, Bershtein VA, Sukhanova TE et al (2008) 3D diamond-containing nanocomposites based on hybrid polyurethane–poly(2-hydroxyethyl methacrylate) semi-IPNs: composition-nanostructure-segmental dynamics-elastic properties relationships. J Polym Sci B 46(16):1696–1712. doi:10.1002/polb.21506
23. Karabanova LV, Bondaruk OM (2012) Thermodynamic of polymer-filler interactions in the nanocomposites based on polyurethane-polyacrylate polymer matrix and artificial nanodiamonds. Ukrainian Chem J 78(7–8):116–123
24. Karabanova LV, Bershtein VA, Lloyd AW et al (2012) Nanocomposites based on multicomponent polymer matrix and artificial diamond nanofiller. In: Proceedings of 15th European conference on composite materials, Venice, Italy, 24–28 June 2012

Chapter 10
Spin-Crossover Nanocrystals and Ising Model

Iu. Gudyma, A. Maksymov, and V. Ivashko

10.1 Introduction

In the last decades become attractive the transition metal compounds as a new molecular magnetic materials able to slightly improve the existing characteristics of IT devices. The spin-crossover (SC) compounds belong to the family of bistable molecular magnetic complexes and are functional switching materials that can change their spin state under external physical perturbations (pressure, radiation, temperature, the actions of magnetic or electric fields). To these materials are attributed the coordination complexes with d^4–d^7 electronic configuration of transition metal ion situated in the center of ligand field with octahedral symmetry.

The action of ligand field split the d-level into two sublevels characterized by different repartition of d-electrons on them. The formed electronic configuration defines the spin state of the compounds. Typically, for spin-crossover compounds the electronic configuration of transition metal ions may have one of two stable states: high-spin (HS) or low-spin (LS) state. The setting of spin-state is related to the balance between the orbital energy, which is necessary for populating all the 3d sublevels, and the average energy of the Coulomb interaction between the electrons on the d-levels. As a result of an external perturbation the spin state of ion changes from paramagnetic LS to diamagnetic HS state [1–4].

The feature of SC lies in so-called spin transition that occurs within one bistable molecule and phase (cooperative) transitions that are the result of intermolecular interactions. These phenomena are related to the features of HS state of the

Iu. Gudyma (✉) • A. Maksymov • V. Ivashko
Chernivtsi National University, Kotsiubynsky Str., Nr. 2, Chernivtsi 58012, Ukraine
e-mail: yugudyma@gmail.com

O. Fesenko, L. Yatsenko (eds.), *Nanoplasmonics, Nano-Optics, Nanocomposites, and Surface Studies*, Springer Proceedings in Physics 167,
DOI 10.1007/978-3-319-18543-9_10

molecule that takes up more volume in space than LS one. Obviously, it should lead to elastic effects during conversion. For considering both magnetic and mechanical properties of materials we can use Ising-like model, which takes into account internal and external factors of compressibility. The microscopic Ising-like model for spin transition was suggested for the first time by Wajnflasz and Pick in papers [5, 6]. Some time ago this model was used for two-step spin-crossover of binuclear molecules [7, 8]. The microscopic Ising-like model was developed as two-level model with additional degeneracies implicitly accounting for intramolecular vibrations in paper [9]. These models reproduce the most equilibrium properties of SC materials, but the explanation of the nature of cooperativity requires to take into account the relation between the spin state and lattice degrees of freedom [10]. For the examination of equilibrium properties of SC solids authors [10] introduced an anharmonic Ising-like model developed in reference [11]. Based on this approach it is possible to describe the phase transition with two order parameters [12].

Klinduhov, Chernyshov, and Boukheddaden proposed a generalized version of the Ising-type Hamiltonian describing the spin-crossover SC solids, accounting for the tunneling effect, lattice phonons, and spin–phonon interactions [13]. It has been shown that under Lang-Firsov-type transformation, the model becomes isomorphic to an effective Ising-type Hamiltonian in which the "exchange" coupling between the spin operators originates from a multiphonon interaction, thus explaining the origin of the elastic interaction between the SC units.

The last achievements of chemical technologies make able to obtain the nanosized spincrossover materials through direct synthesis of coordination nanoparticles and nanopatterned thin films as were reported in [14–16]. Magnetic nanoparticles are of particular interest due to obvious applications for data storage into high density media. In addition, functionalized at room temperature magnetic nanoparticles can offer a wide variety of additional applications, specially for biological/medical usage. Protein detection, drug delivery, or tumor treatment are some other applications where magnetic nanoparticles can make a difference.

10.2 Ising-Like Thermodynamic Model of Spin-Crossover Compounds

10.2.1 Theoretical Considerations

The complexes of transition metals with the electronic configuration d^4–d^7 can have both high spin (HS) and low spin (LS) central ions. For example, the d^6 complexes of ferrous Fe^{2+} ion can have both ground states with total spin $S = 2$ (HS) and $S = 0$ (LS). In octahedral symmetry O_h only the HS and LS states are possible [17]. The five d-orbitals of bivalent iron ion are split into three t_{2g}- and two e_g-orbitals. The spin state is established by the balance between the orbital energy necessary to occupy all accessible $3d$ levels (measured by the size of crystal field Δ)

and the average energy of the Coulomb repulsion of the d-electrons. If these values are approximately equal, the difference between the energy minima of the corresponding HS and LS terms becomes comparable to the thermal energy. Under these conditions both states are populated and the system is bistable. In addition HS and LS states have different molecular volumes and this difference induces the HS–LS difference in inter-ion distances and generates both short and long range interactions [18–21]. It is noted that the free HS ferrous ion has the larger volume than the LS one. The spin conversion between the states in these compounds may be induced by a change of temperature, of pressure, of magnetic or electric fields or by light irradiation. The inter-conversion between the electronic spin states, that occurs in coordination compounds of $3d$ elements, is known as the spin-crossover transition [2–4, 22]. For example, the spin state of ferrous ion changes from diamagnetic ($S=0$, $^1A_1$) in the LS state, to paramagnetic ($S=2$,$^5T_2$) in the HS state. The possibility of conversion of the spin states through external stimuli opens the perspectives for switches and magnetic storage devices.

We consider thermodynamic model of spin-crossover compounds in the simplest way: when all deformations are homogeneous and isotropic and magnetic ions occupy lattice units of a cubic form, followed by their restriction to specific points of a regular space. The Hamiltonian of the model has the form:

$$H = -h\sum_i s_i - \sum_{\{i,\,j\}} J_{ij} s_i s_j + \frac{1}{2}K\xi^2 - P\xi, \tag{10.1}$$

here s_i is a fictitious classical spin which has two eigenvalues ± 1, corresponding to the LS and HS states, respectively ($i \neq j$). Variable $\xi = (a - a_0)/a_0$ is the change of relative inter-ion distance, a_0 is the average distance between neighboring spins at an equilibrium temperature T_{eq} and an atmospheric pressure, a is the average distance between neighboring spins at temperature T and external uniform pressure P. This Hamiltonian has often been proposed as phenomenological one and describes isotropic elastic media with classical spins. A simple phenomenological approach to the problem is the mean field approximation with the nearest-neighbor interactions in form $\sum_{j(j\neq i)} J_{ij} \approx zJ$ where z is the coordination (the number of nearest neighbors of a given molecule in the lattice).

In the present model the effects of ligand molecules on the transitions are taken into account mainly through the energy separation h between the $^1A_{1g}$ and $^5T_{2g}$ states. In the discrete level approach, for the isolated magnetic molecule, the uniform "magnetic field" h is generally the energy distance between the HS and the LS states

$$h = -(\Delta - k_B T \ln g), \tag{10.2}$$

where the parameter Δ is directly related to the crystal field of the site, $k_B T$ is the thermal energy, $g = g_H / g_L$ is the electrovibrational degeneracy ratio between the HS and LS states. A characteristic temperature for spin conversion T_{eq} is defined

by $k_B T_{\mathrm{eq}} \ln g = \Delta$, which corresponds to $\langle s \rangle = 0$. The HS fraction n_H of HS and LS complexes in the crystal is the natural order parameter of the LS $\leftrightarrow$ HS transition. Since $n_H + n_L = 1$ and $n_H - n_L = \langle s \rangle$, so that $n_H = \frac{1}{2}(1 + \langle s \rangle)$. Thus we can obtain $n_H = n_L = \frac{1}{2}$ for the equilibrium temperature T_{eq}.

The second term in the model (10.1) describes the intermolecular interactions of elastic origin through a phenomenological parameter accounting the ferromagnetic coupling ($J > 0$) between neighboring spins i and j. This is the simplest way to express the cooperativity between magnetic molecules [23–26]. In a first approach we thus merely took into account the existence of cooperativity without giving details of its origin.

The third term on the right in our Hamiltonian corresponds to the elastic energy of the crystal lattice, which is represented by harmonic potential between the nearest neighboring spin pairs, where K is the bulk modulus of the crystal lattice. The last term in (10.1) includes the effect of a constant external pressure. In this model, we have assumed that the relaxing diamagnetic state ($\langle s \rangle = 0$) at any temperature is unstrained, thus we neglect the thermal expansion.

So far, the effect of coupling between the fictitious spin and the strain has been neglected. This coupling gives rise to spontaneous strains in the process of ordering of the quasispins. The linear approximation of the exchange coupling dependence on lattice constant is motivated in such a way that only small deformations are considered. We will take into account the major origin of the coupling as the linear dependence of the exchange-like

$$J = J_0 + J_1 \xi, \tag{10.3}$$

where J_0 is the "exchange" function from the rigid-lattice value, J_1 is the first derivative of the exchange integral by strain. In this thermodynamic model, we also deal with the interactions between the magnetic ions which have a finite range (distance).

10.2.2 The Gibbs Free Energy

As is well known the free energy is that part of the internal energy of the system that can be converted into work. On the semi-macroscopic level of description neglecting fluctuations in the nearest-neighbor approach, the Hamiltonian (10.1) satisfies the conditions of the following equation:

$$H = NzJ + 4NzJn_H^2 - 4NzJn_H + \frac{1}{2}K\xi^2 - P\xi - (h + 4zJn_H - 2zJ)\sum_i s_i, \tag{10.4}$$

where N is the number of molecules. The partition function is defined as:

$$Z = \sum_{s_1=\pm 1} \sum_{s_2=\pm 1} \cdots \sum_{s_N=\pm 1} \exp\{-\beta[NzJ + 4NzJn_H^2 - 4NzJn_H + \frac{1}{2}K\xi^2 - P\xi]\}, \quad (10.5)$$

where β is the inversion heat energy. The Gibbs free energy is given by:

$$G = -k_B T \ln Z. \quad (10.6)$$

The Gibbs free energy per spin can be calculated by using the next equation:

$$g = \frac{G}{N} = zJ < s >^2 + K\xi^2 - p\xi - k_B T \ln[z(x)], \quad (10.7)$$

where $z(x) = 2\cosh(x)$ and $x = (2zJ\langle s\rangle + h)/k_B T$, $\langle s\rangle = 2n_H - 1$, $K = \frac{K}{N}$, $p = \frac{P}{N}$. In Fig. 10.1 are presented the results of the calculation of the Gibbs free energy per spin.

For the carried out calculations based on Eq. (10.7) we have used the following values of the system parameters: $\Delta = 1.000$, $K = 1.000$, $z = 4$, $k_B = 1$, $\xi = 0$, $J_0 = 100$, ln $g = 5$, $p = 0$. According to the resulting plots presented in Fig. 10.1 it is clearly seen that during the change of temperature the stable and metastable state are always realized for the fixed values of HS fraction of molecules, whereas unstable state varies. The asymmetry of free energy that is shown is the main reason of different properties for LS and HS states.

The minimizing of the free energy with respect to n_H and ξ leads to self-consistent equations:

$$n_H = \frac{1}{2}[1 + \tanh(x)], \quad (10.8)$$

$$\xi = \frac{1}{2K}(p - zJ_1\langle s\rangle^2). \quad (10.9)$$

The physical solutions of this set of coupled equations minimize the free energy and define the equilibrium properties of the system. Values n_H and ξ are its two coupled order parameters. Thus in the studies of spin-crossover transition, two

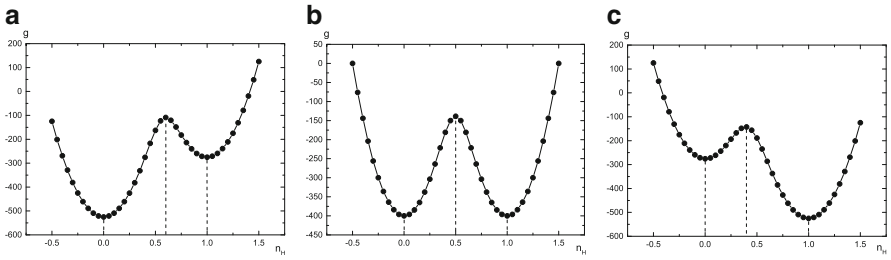

Fig. 10.1 The dependence of Gibbs free energy per spin on HS fraction of molecules below the equilibrium temperature ($T < T_{\text{eq}}, T = 175K$) (**a**), ($T = T_{eq} = 200K$) (**b**) and ($T > T_{\text{eq}}, T = 225K$) (**c**)

different quantities may serve as order parameters. Note that the lattice changes are reflected in the sum of strain caused by the magnetization and the applied external pressure. From high temperature expansion of the function in Eq. (10.8) we have the following T_c^0:

$$T_c^0 = \frac{2zJ_0}{k_B}. \tag{10.10}$$

Now, if the temperature T_c^0 is replaced by T_{eq}, the critical interaction parameter J_0^c may be defined as:

$$J_0^c = \frac{k_B T_{eq}}{2z}. \tag{10.11}$$

We will show next that the values T_{eq}, J_c^0 determine a critical point.

Due to the non-linear character of the functions n_H, ξ, Eqs. (10.8), (10.9) have to be solved numerically. The corresponding order parameters are plotted in Fig. 10.2 as the functions of T. Since the coordination number for 2D system is $z = 4$, we set the parameter $J_0^c = 25K$, which gives the realistic value of transition temperature $T_c^0 = 200K$. We will see that the system shows qualitatively different dynamic behavior of n_H and ξ. As is shown in Fig. 10.2, the equilibrium state of the system corresponds to the values $n_H = 0.5$ and $\xi = 0$. The thermal behavior of the dynamic order parameters characterizes the nature of phase

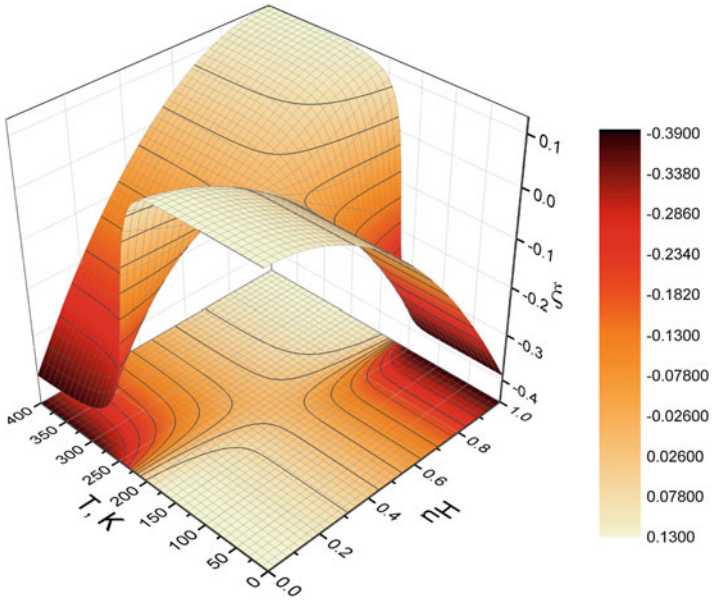

Fig. 10.2 The coupled dynamic parameters as functions of temperature. The result was obtained for the case when $J_0 = 25$, $J_1 > J_{1(\text{cr})} = 65$ where $J_{1(\text{cr})} = 64.5497$ and $p = 0$

transitions that may be discontinuous or continuous, depending on the choice of the values of J_0 and J_1.

The first-order phase transition results from zero coefficient at $\langle s\rangle^3$ in above expansion. Simultaneously the coefficient at $\langle s\rangle$ also should be zero. When $p = 0$ this criterion is as follows:

$$J_{1(cr)}^2 = \frac{4}{3}\frac{J_0^2 K}{k_B T_c}. \tag{10.12}$$

The expression represents the condition for a tricritical point on the second-order phase transition curve. For $J_1 > J_{1(\mathrm{cr})}$ the first-order phase transition is obtained. In the opposite case, the second-order phase transition occurs. Thus the order of the phase transition from diamagnetic to paramagnetic state is determined by $J_{1(\mathrm{cr})}$, the parameter which depends on β_c, the ferromagnetic exchange for nearest neighbors J_0, and the compressibility of the lattice.

10.2.3 The Behavior of Entropy

After substitution the solutions of Eqs. (10.8) and (10.9) for n_H and ξ into the expression (10.7) the thermodynamic potential is getting an equilibrium and may be used for calculating the thermodynamic parameters. For example, we obtain the entropy $S = -\partial g/\partial T$, taking into account the explicit dependence of Gibbs free energy on the temperature

$$S = k_B(ln[z(x)] + (lng - x)\langle s\rangle) - \frac{\partial K}{\partial T}\xi^2. \tag{10.13}$$

For further calculations we neglect the term related to temperature dependence of compression module. If we given the explicit form of the values T_c^0 (10.10) and $J_{1(\mathrm{cr})}$ (10.12), the transformed view for the variable x takes the form

$$x = \frac{1}{k_B T}\left(\left(k_B T_c^0 - \frac{zJ_1 p}{K}\right)\langle s\rangle + \frac{z^2 J_1^2\langle s\rangle^3}{K} + h\right). \tag{10.14}$$

We have shown that fluctuation of position of magnetic ion leads to additive term proportional to $\langle s\rangle^3$ and renormalize term proportional to $\langle s\rangle$.

In Fig. 10.3 we plot the entropy $S(T)$ for $p = 0$ and $J_1 = 0$ for different interaction parameter J_0. The curves describe the second-order transition obtained for $J_0 = 20K$ [line(1) (green online)] and the first-order transition obtained for $J_0 = 30K$ [line (3) (blue online)]. The line (2) (red online) calculated for $J_0^c = 25K$ demarcates the regions with first-order phase transition and second-order phase transition. For this boundary case the influence of the parameter J_1 on the entropy and HS fraction is investigated (see Fig. 10.4).

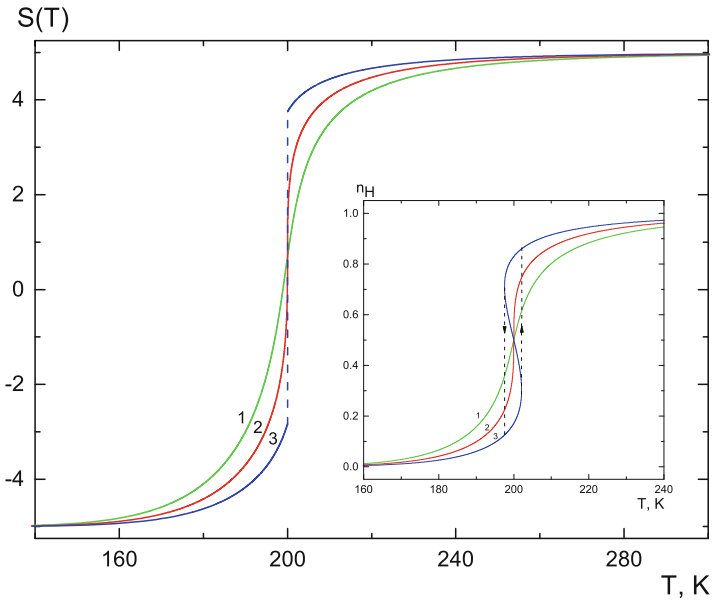

Fig. 10.3 The entropy $S(T)$ as a function of temperature T for various J_0. *Inset*: Computed HS fractions n_H corresponds to the entropy curves. The line 1 (*green online*) is for $J_0 = 20K$, the line 2 (*red online*) is for $J_0 = 25K$, and the line 3 (*blue online*) is for $J_0 = 30K$

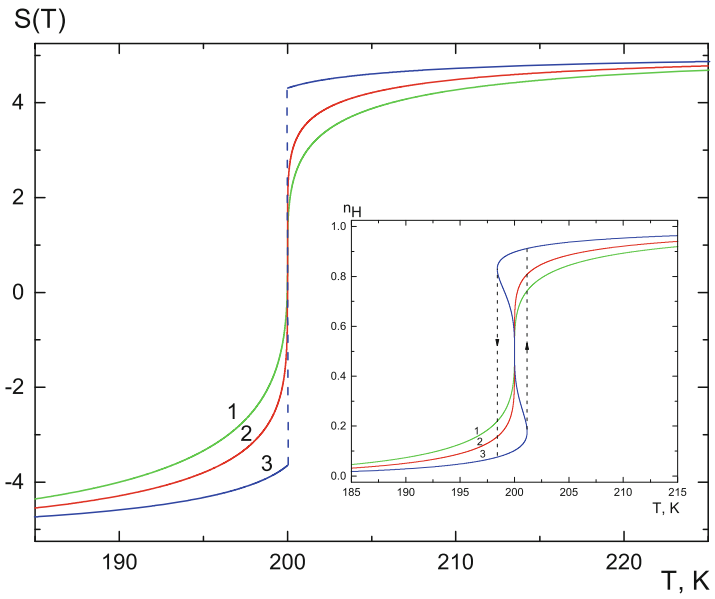

Fig. 10.4 The entropy $S(T)$ as a function of temperature T for $J_0 = 25K$ and $J_1 = 45K$ (curve 1—second-order transition), $J_1 = 64.5497K$ (curve 2—spinodal transition), $J_1 = 85K$ (curve 3—first-order transition). *Inset*: Computed HS fractions n_H corresponds to the entropy curves

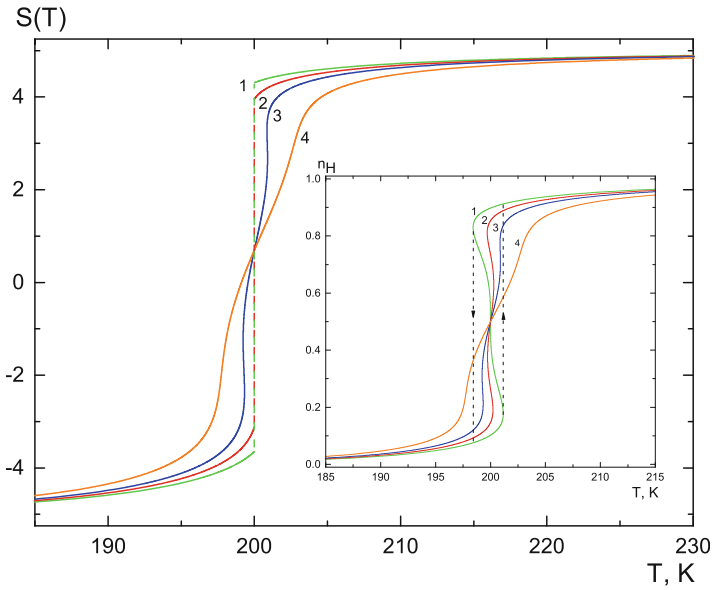

Fig. 10.5 The entropy $S(T)$ as a function of temperature T for $J_0 = 25K$, $J_1 = 85K$ and various applied pressures p. *Inset* Computed HS fractions n_H corresponds to the entropy curves

The respective behavior of HS fractions n_H during first-order and second-order phase transitions together with transition curves for spinodal boundary is presented in insets of Figs. 10.3 and 10.4. Figure 10.4 illustrates the effect of increasing the strain force on the transition curves for HS fraction and the entropy. As Fig. 10.4 shows the increasing of J_1 leads to a forthcoming of first-order phase transition.

To analyze the effect of applied pressure p, we have considered SC system for $J_0 = 25K$ and $J_1 = 85K$. The obtained results are reported in Fig. 10.5 and they undeniably exhibit the dependence of the entropy function and the thermal variation of the HS fraction on applied pressure. All functions in Fig. 10.5 are calculated for equivalent J_0 and J_1, while corresponding applied pressures are $p = 0K$, $25K$, $50K$, and $100K$ from (1) to (4), respectively. The sharp change in the difference of entropy, associated with the magnetic phase transition, is induced by pressure.

From (10.8) and (10.14) close to the magnetic phase transitions the following equation is obtained

$$A < s > + B < s >^3 + C < s >^5 = 0, \tag{10.15}$$

where

$$A = \frac{T - T_c}{T}, \tag{10.16}$$

$$B = A\frac{T_c}{T} + \frac{1}{3}\left(\frac{T_c}{T}\right)^3 - \frac{zJ_1 pT_c^0 T_c}{k_B K T^4} - \frac{z^2 J_1^2}{k_B K T}, \tag{10.17}$$

$$\begin{aligned} C= & \left[\left(\frac{T_c^0}{T}\right)^2 + \left(\frac{J_1 pz}{k_B K T}\right)^2\right] - \frac{4}{3}\left(\frac{T_c}{T}\right)^3 + \frac{2}{3}\left[\left(\frac{T_c^0}{T}\right)^4 + \left(\frac{J_1 pz}{k_B K T}\right)^4\right] \\ & - \frac{2}{15}\left(\frac{T_c}{T}\right)^5 - 2\frac{J_1 pT_c^0 z}{k_B K T^2}\left[1 + \frac{J_1 z}{p} - \frac{J_1^2 z^2}{k_B K T} + \frac{J_1^2 z^2}{k_B K T}\right] \\ & + 4\frac{J_1 pzT_c^0}{k_B K T^3}\left[T_c + \frac{J_1 pzT_c^0}{k_B K T}\right] - \frac{8}{3}\frac{J_1 pzT_c^0}{k_B K T^4}\left[(T_c^0)^2 + \left(\frac{J_1 pz}{k_B K}\right)^2\right] \\ & + \frac{2}{3}\frac{J_1 pzT_c^0}{k_B K T^5}(T_c) - \frac{4}{3}\left(\frac{J_1 pzT_c^0}{k_B K}\right)^2 \frac{T_c}{T^5} + \frac{J_1^2 z^2}{k_B K T}\left[1 + \left(\frac{T_c^0}{T}\right)^2 + \left(\frac{J_1 pz}{k_B K T}\right)^2\right]. \end{aligned} \tag{10.18}$$

The value of T_c depends on the pressure p according to (10.19). One observes that as the pressure is raised the critical temperature T_c is decreased.

$$T_c(p) = T_c^0 - \frac{zJ_1 p}{k_B K}. \tag{10.19}$$

For a given temperature T and intermolecular interaction J_0 the equilibrium values of n_H and ξ can also be directly obtained by calculating the Gibbs free energy (10.7) at all points in the $J_0 - T$ plane. We focus on the analysis of the main properties of the phase diagram obtained for $p = 0$ and $J_1 = 0$ in the mean-field approximation. In Fig. 10.6 we plotted numerically the phase diagram in a $J_0 - T$ plane. The solid line stands for the boundaries between monostable and bistable compositions. They correspond to the appearance of a secondary minimum in the free energy. Above this line the transition occurs with the coexistence of two states. By analogy with traditional equilibrium systems the metastable state corresponds to the local minimum of the free energy while the stable state corresponds to the global minimum. Accordingly, the change from the LS to the HS phases occurs below a critical point $(T_{\text{eq}}; J_0^c)$ with temperature rising. The critical point separates the second-order transition region from the first-order one. The vertical dashed line indicates the points of equivalent energy in both states. These are illustrated in the inset of Fig. 10.6.

The plots shown in the phase diagram are closely related to the transitions depicted in Figs. 10.3, 10.4, and 10.5. Below the critical point for value $J_0 < J_0^c$ transition occurs gradually, if it takes the values above J_0^c it is accompanied by hysteresis. The width of the hysteresis is determined by the temperature interval T, that may be defined by the intersection of horizontal straight line with the solid one shown in the figure. Noted that the nonzero p has caused only quantitative changes in comparison with the case for $p = 0$. The critical point has shifted to a smaller value of J_0 together with the solid line.

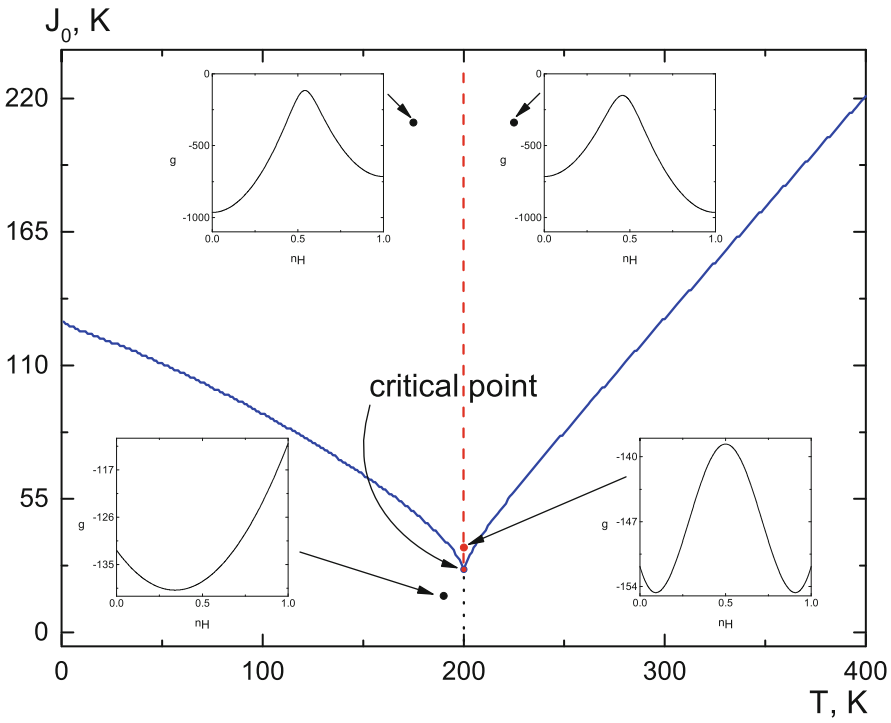

Fig. 10.6 Phase diagram for a spin transition system described by a Hamiltonian (10.1) for $p = 0$ and $J_1 = 0$

10.3 The Breathing Crystal Field Model

10.3.1 General Aspects

The interconversion of the spin states HS and LS can be determined by a change of an external variable such as temperature T or pressure p if the energy difference between the octahedral ligand field splitting energy Δ and the mean spin-pairing energy Π slightly differs from zero. Therefore the value of Δ is crucial to control the behavior of SC molecules. The SC compounds can be also switched from an LS to a HS state and vice versa under irradiation by visible light or magnetic field. Several physical theories, based on SC characteristic features, have been elaborated.

In the point charge model approximation of the ligand field theory [27]

$$\Delta = \frac{5}{3}\frac{Ze^2}{R^5}\langle r^4 \rangle, \tag{10.20}$$

where Ze is the charge (effective) of the ligand; R is the metal-ligand distance; $\langle r^4 \rangle$ is the mean fourth power radius of the d electron. One has to note that this relation

is valid only within an electrostatic model and for perfect octahedral symmetry. In a more rigorous approach, if we consider the value of a ligand field splitting energy in a small time interval, it is necessary to take into account its instantaneous and local fluctuations.

The parameters defining the ligand field splitting energy are not characterized by their precise meaning, but undergo spontaneous fluctuations, even in the thermodynamic equilibrium. It is obvious that it leads to the random deviation from the meaning value of the ligand field splitting energy. Since at the critical temperature the crystal field is zero, the introduction of fluctuations is relevant and important for the description of the evolution of systems around the thermal phase transition.

Fast and ultra-fast time-resolved diffraction provides direct experimental method of probing such structural dynamics, corresponding to atomic motion or changes of local structure in condensed matter [28–30]. The nature of these fluctuations may be very different but due to its randomness they may be described through addition of a stochastic term in the above expression for ligand field splitting energy. The physical basis of the corresponding variation of semi-empirical parameter Δ may take into account secondary effects as an asymmetric distortion of the molecular unit, thermal lattice dilatation inherent to crystal solids or the metal-ligand breathing mode. It may be also the result of structural disorder, such as disordered ligands or counter ions. These secondary effects are local and instantaneous and lead to the concept of breathing crystal field model developed in the next section.

The concept of breathing crystal field may be primarily applied to explain the behavior of breathing crystals characterized by changes in the metal-ligand bound length and corresponding alteration in the shape and volume of molecules leading to a change of the ligand field. Recent reports have shown [29, 31–34] that the breathing of spin-crossover materials must be taken into account in order to characterize their phase transition, but dynamic ligand field rearrangements can be hardly observed in solid state. In the same time, one agrees that nanoscale phenomena and spatiotemporal dynamics in cooperative SC systems will be the main driving forces of spin crossover research in the forthcoming years both from fundamental and applied scientific points of views [16]. In this work we restrict to Fe^{II} SC compounds for which the LS state is characterized by diamagnetic properties with total spin $S = 0$ and HS state by paramagnetic ones with total spin $S = 2$.

10.3.2 Mathematical Description

For describing the behavior of spin-crossover compounds at molecular level we use the microscopic Ising-like model, considering intermolecular interaction in the nearest neighbors approach with the following Hamiltonian:

$$H = -J\sum_{<ij>} s_i s_j - h_0 \sum_i s_i, \tag{10.21}$$

where s_i is the fictitious spin for each site i ($i = 1, 2, \ldots, N$) with the eigenvalues $\pm$ 1 which correspond to HS and LS states, respectively. The first term in the model (10.21) describes the intermolecular interactions of elastic origin through a phenomenological parameter accounting for the ferromagnetic coupling ($J > 0$) between neighboring spins i and j. This is the simplest way to express the cooperativity between magnetic molecules [23, 24]. In a first approach we thus merely take into account the existence of cooperativity without giving details of its origin. The second term characterizes the occurrence of intramolecular processes and describes the action of the crystal field on the spin-crossover site including the influence of the temperature:

$$h_0 = -(\Delta - k_B T \ln g), \tag{10.22}$$

where Δ is the energy gap between HS and LS states; T is the absolute temperature; k_B is the Boltzmann constant; $g = g_{\mathrm{HS}}/g_{\mathrm{LS}}$ is degeneracy of SC states. The additional term of the ligand field proportional to heat energy $k_B T$ is justified by the internal entropy effects. The Hamiltonian (10.21) is adapted from the Wajnflasz–Pick model for the short-range Ising-like two-level interacting systems, describing the main aspects of cooperative behavior of spin-crossover materials [6]. The model, successfully used for reproducing various aspects of the ordering processes in spin-crossover compounds, reflects the molecular origin of the spin-crossover phenomenon, and its dependence on intermolecular interactions [7, 35–39]. As mentioned in the microreview [40] the characteristic features of the Ising-like model (10.21), (10.22) include wide abstraction and generality, providing suitable standards referred to as starting points by other new and more refined approaches [11, 24, 41–44].

At microscopic level, an individual spin-crossover molecule is regarded as an isolated bistable unit. The interaction with the surrounding medium basically modulates the zero-point energy difference of the individual molecule and the change of the spin state—SC phenomenon—may occur at microscopic scale due to the coupling between the electronic and vibrational structures of the molecules [45]. In the zero-order mean field approximation the external field h_0 is regarded as identical for all molecules in the sample and for all times. This approach works well for highly symmetric systems, but local and instantaneous thermal fluctuations break their symmetry, creating deviations from zero-order approximation, which can be treated by using statistical fluctuations. This approach is based on the fact that the dynamics of the thermal switching span the microsecond time scale, while the molecular expansion takes place on nanosecond timescale [29].

It is obvious that the expressions (10.20), (10.22) in the present form describes the zero-order approximation of the mean-field theory. Therefore the model (10.21) must be improved for the case with "breathing" crystal field [26]. This means that the external site-dependent field h_i varies in time according to the relation $-h_i = -h_0 + \xi_i(t)$, which leads to the Hamiltonian of the next form:

$$H = -J\sum_{<ij>} s_i s_j + \sum_i [\Delta - k_B T \ln g + \xi_i(t)] s_i. \tag{10.23}$$

From the point of view of Ising model the stochastic process $\xi_i(t)$ reflects the external local random field statistically perturbed. From (10.23) it results that the role of stochastic term becomes significant especially for critical temperatures.

In the simplest case the fluctuations are uncorrelated and can be represented by a white Gaussian stochastic process. Without considering the local changes the statistical characteristics of fluctuations can be written as:

$$\begin{aligned} &\langle \xi(t) \rangle = 0, \\ &\langle \xi(t)\xi(t^{'}) \rangle = 2\varepsilon^2 \delta(t - t^{'}). \end{aligned} \tag{10.24}$$

Here ε is the strength of fluctuations (the spectral density of stochastic variable $\xi(t)$), t and $t^{'}$ are distinct times.

However the fluctuations cannot be theoretically uncorrelated and in a first approach, they can be described in terms of the Ornstein–Uhlenbeck (OU) process with an exponential correlation function

$$\langle \xi(t)\xi(t^{'}) \rangle = \frac{\varepsilon^2}{\tau} \exp\left(-\frac{|t - t^{'}|}{\tau} \right), \tag{10.25}$$

where τ is the autocorrelation time of the stochastic process $\xi(t)$, i.e. a measure of its memory in time, which is also related to the cut-off frequency characteristic to the Lorentzian power spectrum of OU noise:

$$S_\xi(\omega) = \frac{2\varepsilon^2}{\tau^2 \omega^2 + 1}. \tag{10.26}$$

If $\tau \to 0$, then the stochastic process becomes white. As it can be seen from Eqs. (10.25) and (10.26), for strong time correlations $\tau \to \infty$ the power spectrum of stochastic process becomes virtually negligibly. The stochastic differential equation which governs its evolutions is written:

$$\frac{d\xi(t)}{dt} = -\frac{\xi(t)}{\tau} + \frac{\varepsilon}{\tau}\eta(t), \tag{10.27}$$

where $\eta(t)$ is the independent white-noise source $\left[\langle \eta(t) \rangle = 0, \langle \eta(t)\eta(t^{'}) \rangle = 2\delta(t - t^{'})\right]$. The stationary OU process is frequently used as model of real noisy signal for which the values of $\xi(t)$ and $\xi(t^{'})$ are noticeably correlated at $\left|t - t^{'}\right| \sim \tau$.

Actually, the fluctuations which provoke the breathing crystal field vary in time and space. In addition, in the spin-crossover lattice the environmental field of each site is different. Therefore, the system is characterized by nonzero interactions, which means that the fluctuations of any individual site are affected by the fluctuation of all

other sites, i.e. the fluctuations are correlated in space. The system fluctuative environment may be described as a collection of harmonic oscillators [46]

$$\frac{\partial \xi_i}{\partial t} = \frac{C}{N}\sum_{j=1}^{N}(\xi_j - \xi_i) - \frac{\xi_i(t)}{\tau} + \frac{\varepsilon}{\tau}\eta_i(t). \tag{10.28}$$

Here C is the global coupling of random component. The noise $\eta_i(t)$ is Gaussian with zero mean, and correlation $< \eta_i(t)\eta_j(t') >= 2\delta_{ij}\delta(t-t')$, where δ_{ij} is the Kronecker delta symbol.

10.3.3 Simulation Technique

We consider the spin-crossover molecules situated on a discrete two-dimensional square lattice with side L between 10 and 120. The evolution of the system is described by the nearest neighbors Ising-like Hamiltonian (10.23) and was examined by Monte Carlo (MC) simulation according to Metropolis algorithm. The system was initialized with all spins up at a high enough temperature. Then we decrease slowly the temperature and put the system in contact with heat bath at every considered temperature T. We check then randomly the molecules and verify if they switch or not using the classical Monte Carlo probabilities.

The Metropolis spin-transition probability is written as follows:

$$P(s_i \rightarrow -s_i) = \min\left[1, \exp\left(-\frac{\Delta H\{s_i\}}{k_B T}\right)\right], \tag{10.29}$$

where $\Delta H\{s_i\}$ is the energy difference when a spin changes between s_i and $-s_i$

$$\Delta H\{s_i\} = 2Js_i\sum_j s_j - 2h_i s_i. \tag{10.30}$$

We use the unit $k_B = 1$ for the Boltzmann constant.

A Monte Carlo step (MCS) is completed when all molecules have been checked once in average. The sweeping rate is defined as the total number of MCS for every K. We repeat this procedure till a temperature where almost all molecules have switched to LS state, then we increase the temperature and proceed similarly till the starting temperature.

Two types of boundary conditions were considered: (1) periodic boundary conditions, where the nearest neighbors outside the lattice of the edge spins are the spins on the opposite edges of the lattice and (2) free edges. In the first case, we assume that we reach the behavior of infinite system, and therefore the surface effects are almost negligible.

The simulation is an ergodic Markov process with homogenous discrete time evolution.

The system behavior was examined through the magnetization per spin m, which is the statistical average of the Ising variable $\langle s \rangle = 1/L^2 \Sigma_i s_i$. It is directly related to the order parameter n_H, i.e. the HS fraction, since $m = 2n_H - 1$. To avoid the statistical fluctuation related with Monte Carlo procedure the final value of system magnetization for each temperature was obtained by thermodynamic average on the last quarter of MC steps assuming that the system has achieved the steady state. Colored fluctuations (random component in crystal field) were considered as numerical solutions of stochastic differential equations (10.24), (10.25) obtained from Milshtein algorithm [47, 48].

10.4 The Behavior of Breathing Spin-Crossover Nanocrystals

10.4.1 The Effects of System Size and Boundary Conditions

The behavior of a microscopic system, namely in the case of fluctuative dynamics, depends very much on the system size because spatio-temporal aspects are obviously strongly related to the size-reduction effects [16]. The size-dependent properties are important practical aspect in SC clusters and nanostructures. Recent developments in the synthesis and characterization of spin crossover (SC) nanoparticles [49–51] have opened the way for their applications in lithography, thin films and new detection methods adapted to nanometric scale [52]. Size effects in spin crossover nanoparticles have been already investigated in framework of the Husimi–Temperley model (or Weiss type model) in analytical manner [53, 54] but also using numerical approaches, related to Ising-like model [37], mechanoelastic model [55] or by considering the size dependent rigidity of nanoparticles [56]. In this subsection we discuss the influence of system size on bistable properties of spin-crossover system in microscopic approach by Ising-like Hamiltonian in the presence of fluctuations (10.23). The focus is done on the change of hysteresis loop with increasing the system size after the paper [57]. For our simulation, which are performed following [58], we chose the energy gap between the system states $\Delta = 1{,}000$ and the states degeneracy $g = 150$. The spin–spin interaction $J = 85$ is chosen so that it leads to appearance of deterministic hysteresis loop. These system parameters have been used for all the simulations in the chapter. The width of hysteresis loop of spin-crossover systems is characterized by two values of transition temperatures evaluated at $n_H = 0.5$: T_{up} and T_{down}. The estimation of hysteresis width $\Delta T = T_{\text{up}} - T_{\text{down}}$ for the system with white fluctuations with intensity $\varepsilon = 100$ and different boundary conditions is presented in Fig. 10.7. The calculations of each point were performed for $5,000$ MC steps. With increasing the system size the width of hysteresis loop monotonically decreases for

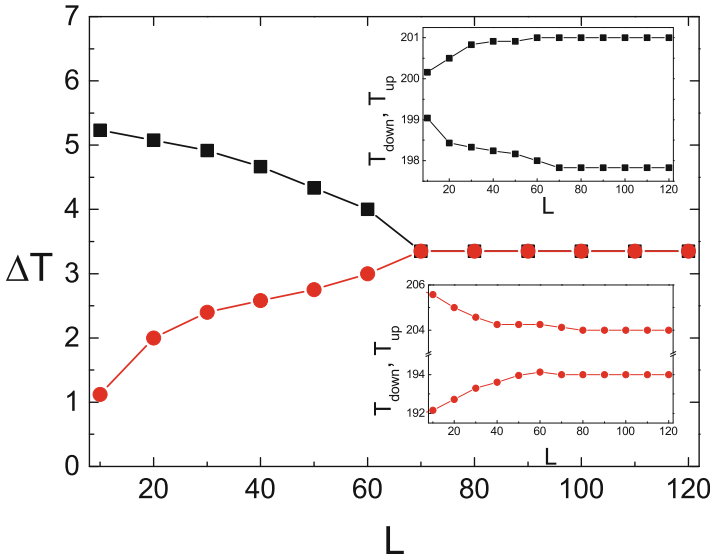

Fig. 10.7 The variation of the thermal hysteresis width as a function of the number of spins for a system with periodic boundary conditions (*black squares*) and with free boundary conditions (*red circles*) with the parameters $\Delta = 1,000$; $g = 150$; $J = 85$ and $\varepsilon = 100$

the system with periodic boundary and monotonically increases for the open boundary system. But in both cases from the lattices $L \geq 70$ the hysteresis width does not change, i.e. it reaches the saturation. As we can see from Fig. 10.7 the increasing of system size reduces the influence of fluctuations. We found that the intensity of fluctuations sets the width of hysteresis loop which shows evident dependence on system size for small system only. For the spin-crossover system with constant crystal field the hysteresis width tends to zero for all system size.

The evolution of transition temperatures T_{down} and T_{up} strongly differs for the systems with open and periodic boundary conditions. In the insets of Fig. 10.7 are shown the curves of T_{down} and T_{up} for systems with periodic boundary condition (top) and free boundary condition (bottom). In the first case the decreasing of hysteresis width is provoked by decreasing of T_{up} and increasing of T_{down}. The behavior of T_{up} and T_{down} for the second case is opposite: T_{up} increases and T_{down} decreases up to reach the saturation values of the system size, which takes place for both cases. Nevertheless in the thermodynamic limit we have obtained the same results which do not depend on the chosen boundary condition.

From a theoretical point of view, boundary condition effects in spin-crossover materials have been suggested to play a key role in cluster formation [59]. To compare the system behavior with periodic boundary condition and free boundary condition we have calculated the transition curves. The results for the fluctuationless system with side $L = 15$ are shown in Fig. 10.8. In the inset of Fig. 10.8 we present the transition curves for the system size 70×70. For small

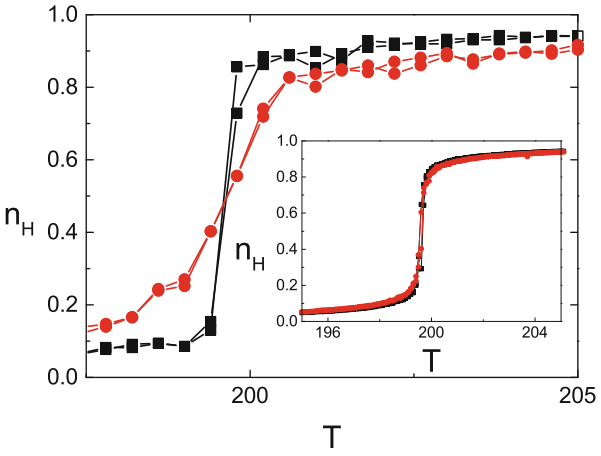

Fig. 10.8 The spin transition in the fluctuationless system for different boundary condition. The *symbols* are the same as in Fig. 10.7

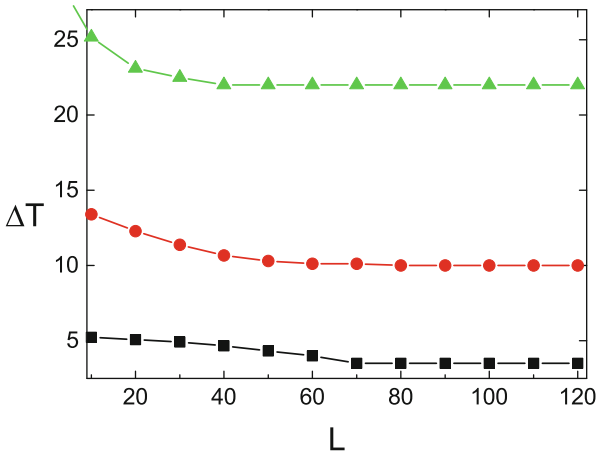

Fig. 10.9 The variation of the thermal hysteresis width for fixed values of fluctuation intensity: $\varepsilon = 100$ (*bottom curve*); $\varepsilon = 150$ (*central curve*); and $\varepsilon = 200$ (*top curve*). The other parameters are those from Fig. 10.7

systems with periodic boundary conditions the transition is steeper than those calculated for the free boundary systems, but for large system sizes this difference vanishes.

In addition to the above results we were interested to understand how the limits of finite-size regime depend on fluctuation intensity. For this purpose we calculated the dependencies of hysteresis width ΔT on lattice size $L \times L$ for fixed values of fluctuations intensity presented in Fig. 10.9. Here the curves marked by squares (black online), circles (red online), and triangles (green online) are obtained for the values of fluctuation intensity $\varepsilon = 100$, $\varepsilon = 150$, and $\varepsilon = 200$, respectively. As it can be seen for larger fluctuations intensity the dependence on system size disappears for smaller system.

10.4.2 Temperature Induced Hysteresis

We have subsequently examined the bistable behavior and the thermal phase transition of Ising-like spin-crossover model (10.23) both without random field action and for external random field with different statistical characteristics. The results are shown in Fig. 10.10. The calculations in this subsection were performed for 1,000 MC steps for the square system with $L = 70$ and periodic boundary conditions. According to the simulations carried out in previous subsection we chose the system size large enough so that the system could be considered as an infinite one. If the system cooperativity is higher than a threshold, the favorable conditions for the occurrence of hysteresis establish. The values of energy gap, states degeneracy, and spin–spin interaction chosen in previous subsection give the critical temperature about 200 K and are not related with specific compounds; however, similar parameters are frequently used for numerical simulations [35, 60]. The LS and HS steady states become ordered for the range of saturated values on the lower and upper parts of transition curves, respectively.

The transition curve marked by squares (black online) in Fig. 10.10a is calculated for the case without fluctuations. As we can see for the chosen spin–spin interaction J the hysteresis is almost unnoticeable. The hysteresis loop marked by circles (red online) corresponds to white fluctuations uncorrelated in space and time. The curves marked by triangles up (green online) and triangles down (blue online) describe the cases with space-uncorrelated colored fluctuation ($C = 0$) and with autocorrelation times $\tau = 2.5$ and $\tau = 5$, respectively. The case with correlated space–time fluctuations ($C = 0.5$ and $\tau = 5$) is presented by the curves marked by

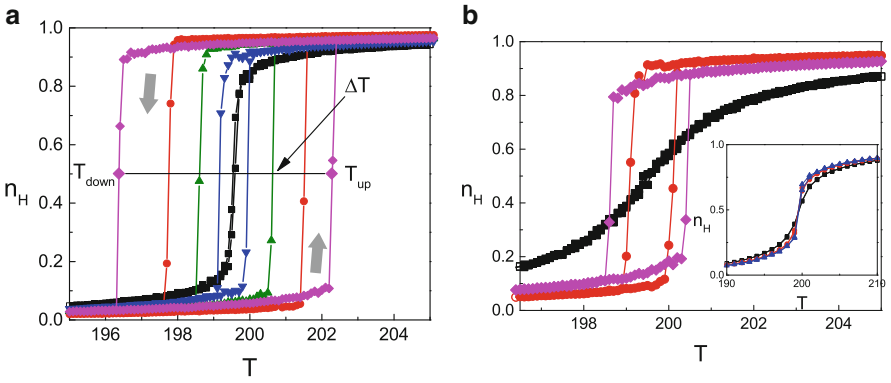

Fig. 10.10 The spin transition curves for different statistical characteristics of fluctuations for $J = 85$ (**a**) and $J = 70$ (**b**). The curve marked by *squares* (*black online*) corresponds to fluctuationless system; marked by *circles* (*red online*) corresponds to white uncorrelated fluctuations; marked by *triangles up* (*green online*) is for $C = 0$ and $\tau = 2.5$; marked by *triangles down* (*blue online*) is for $C = 0$ and $\tau = 5$; marked by *diamonds* (*pink online*) is for $C = 0.5$ and $\tau = 5$. Here the system size is 70×70. In the *inset* of (**b**) one presents the transition curves for fixed white noise intensities $\varepsilon = 100$ [*black* (*squared*) *line*)]; $\varepsilon = 115$ [*red* (*circled*) *line*], and $\varepsilon = 120$ [*blue* (*triangled*) *line*] for $J = 50$

diamonds (pink online). For the simulation of the transition curves in the case of a random field action represented in Fig. 10.10a we have used the same intensity of fluctuations $\varepsilon = 100$ and threshold spin–spin interaction $J = 85$ corresponds to a first-order phase transition regime. Noted that the thermal hysteresis width ΔT plotted in the Figs. 10.7, 10.9 we have determined as represented in Fig. 10.10a.

For a spin–spin interaction J lower than the above-mentioned threshold, a second-order phase transition is expected. However, the presence of fluctuations of crystal field dramatically changes the behavior of the spin-crossover system. The typical transition curves for an interaction J lower than threshold ($J = 70$), while keeping constant the other parameters, are shown in Fig. 10.10b for deterministic system and for a system with white and colored space–time correlated fluctuations (the markings are sustained as in Fig. 10.10a). As we can see the action of fluctuations promotes the occurrence of first-order phase transition and therefore the cooperativity threshold for the first-order phase transition shifts toward lower values. However, the critical transition temperature of the system for the second-order phase transition region does not change, as one can see in the inset of Fig. 10.10b where the transition curves for fixed values of white fluctuations intensity $\varepsilon = 100$ [black (squared) line)]; $\varepsilon = 115$ [red (circled) line]; and $\varepsilon = 120$ [blue (triangled) line] are presented.

Therefore, for the first-order phase transition the fluctuations of external field provoke the broadening of the hysteresis loop, and the hysteresis loop for the white Gaussian stochastic process envelops the ones for fluctuationless and space-uncorrelated colored fluctuations. With narrowing the spectrum of fluctuations the hysteresis loop is also narrower. The opposite behavior is observed with increasing the space coupling of OU random component (10.28). In other words, if the fluctuations are strongly space-correlated, the hysteresis loop width increases and finally it may become wider than for the case with white fluctuations. Moreover, for the space-correlated colored fluctuations the forward and reverse transitions do not reach the saturation as for white noise perturbed system.

Transition temperatures T_{up} and T_{down} are associated with the heating and cooling branches of the spin-crossover process and start from the low-temperature stable LS state and the high-temperature metastable HS state. In general, the competition between octahedral ligand field splitting energy Δ and energy of the molar entropy change $\Delta S = R\ln g$ determines which state (LS or HS) is the preferred one but the breathing of crystal field cardinally changes this situation. If Δ is larger than $k_B T \ln g$ (the strong ligand field), the ground is electronic configuration t_{2g}^6 associated with LS state, otherwise the $t_{2g}^4 e_g^2$ electronic configuration which corresponds to HS state of iron(II) spin-crossover system becomes ground. Our calculations show that the transition temperatures of the system strongly depend on the breathing crystal field.

For a more detailed pictorial view the ferromagnetic phase transition as transition from a non-magnetically ordered phase to a magnetically ordered we have built up the snapshots of states during the cooling process for all described types of hysteresis. The critical temperature of deterministic system was found from the

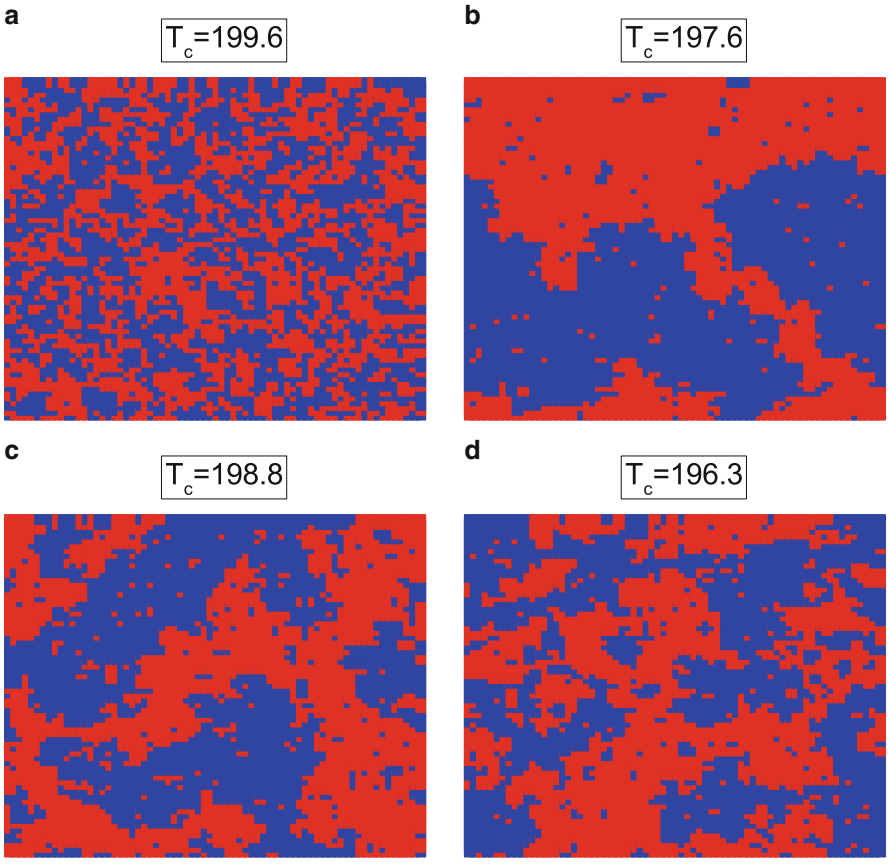

Fig. 10.11 The evolution of spin configuration in the system without fluctuations (**a**); with stochastic external field uncorrelated in time and space (**b**); with time correlated fluctuations (**c**) and with space–time correlated fluctuations (**d**)

Eq. (10.22) and is $T_c \simeq 199.6$. For all other cases the critical temperatures were found from numerical simulations as temperatures for which the fractions of LS and HS molecules are the same. In Fig. 10.11 we present the samples of the evolution of the spin configuration on the square lattice of 70×70 spins, for the system without fluctuations (a); with white uncorrelated fluctuations (b); with time correlated fluctuations (c) and with correlated space–time fluctuations (d) from starting configuration in which all the spins are aligned and have the value $\{s_i\} = 1$.

In Fig. 10.12 one shows the histograms describing the number of sites at a given value of fluctuating field for colored in time [left hatching (blue online)] and correlated space–time fluctuations [right hatching (red online)] relative to the distribution of the field with Gaussian white fluctuations (in the background, marked by dash line). The narrowing of distributions is a result of increasing of the autocorrelation time and corresponds to the distribution of OU stochastic

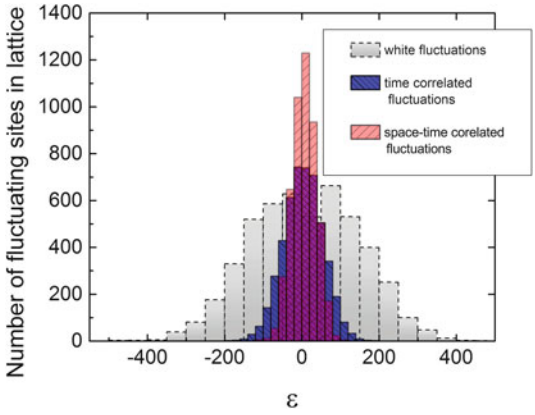

Fig. 10.12 The histograms of fluctuating crystal field plotted for the Gaussian white fluctuations, time correlated fluctuations for the $\tau = 5$ and space–time correlated fluctuation for the $\tau = 5$ and $C = 0.5$ (the corresponding markings are described in the text). Lattice size was 70×70

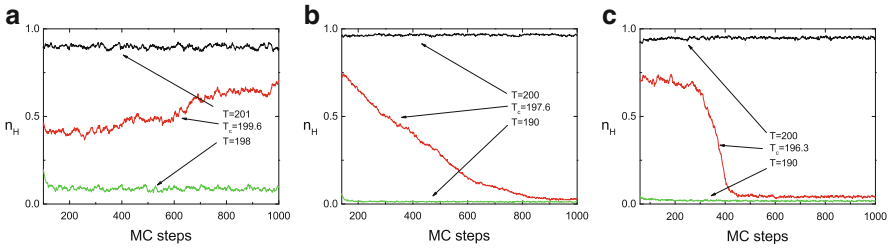

Fig. 10.13 The evolution of HS fractions of the system close to phase transition as a function of MC steps without fluctuations (**a**); with stochastic external field uncorrelated in time and space (**b**) and with space–time correlated fluctuations (**c**)

process. It must be noted that in the case of diffusive coupled OU processes (the space–time correlation of fluctuating centers) the stochastic process becomes non-Gaussian and non-Markovian [46].

For the system with white random field, with time correlated and colored in space and time random field with autocorrelation time $\tau = 5$ and global coupling $C = 0.5$ for the last case, the critical temperatures are $T_c = T_{\text{down}}(n_H = 1/2) \simeq 197.6$, $T_c = T_{\text{down}}(n_H = 1/2) \simeq 198.8$, and $T_c = T_{\text{down}}(n_H = 1/2) \simeq 196.3$, respectively. One notices the difference in the formation of domain of spins of the same sign near the critical temperature for the nonfluctuating external field and random field action. Indeed as are displayed in Fig. 10.11 the spin-crossover system at critical point may respond in different ways. As we can see from Fig. 10.13a the deterministic system evolves around the equilibrium value of order parameter $n_H = 1/2$. In the case with breathing crystal field the system evolves from LS to HS state. This evolution is gradual for the system with white uncorrelated fluctuations (Fig. 10.13b) and abrupt for the system with correlated space–time fluctuations (Fig. 10.13c). For all cases in Fig. 10.13 besides the Monte Carlo trajectories during cooling process for critical temperatures we show just the ones at temperatures before phase transition and just after phase transition.

To understand these results, one has to note that the system undergoes a weak first-order phase transition by formation of longer wavelength fluctuations as shown in Figs. 10.11b and 10.13b. At critical point, this is similar to a spinodal decomposition shown on snapshots. Mean field applied to magnetic ion vanishes and the system becomes similar to a classical Ising model with a second-order transition. For shorter wavelength fluctuations, this system has a discontinuous phase transition.

10.4.3 The Effect of Correlation of Fluctuations

Now we focus on the dependence of hysteresis loop on the main statistical characteristics of random field: the intensity of fluctuations, autocorrelation time, and global coupling representing the spatial relationship of fluctuating centers. In order to study the evolution of hysteresis width under the breathing of ligand field of various strength we realized a numerical experiment. An example of such simulation for lattice with $L = 70$ and periodic boundary condition is presented in Fig. 10.14. Here we have considered the space–time uncorrelated Gaussian noise with $\tau = 5$ and $C = 0.5$. All parameters for numerical simulation are the same as in previous subsections. As we can see the hysteresis loop width monotonically and slowly increases with increasing of fluctuation intensity. The monotonic dependence is also observed for the transition temperatures T_{down} and T_{up}. From the inset of Fig. 10.14 it can be seen that the transition temperature T_{down} undergoes a stronger influence of fluctuations than T_{up}. Thus the intensity of fluctuations leads to a broadening of the hysteresis loop due to increasing of T_{up} and decreasing T_{down} and displays evident dependence on the system size for small system only as previously shown.

While the above treatment is straightforward, there are reasons to consider the colored fluctuations with global coupled components which give more realistic

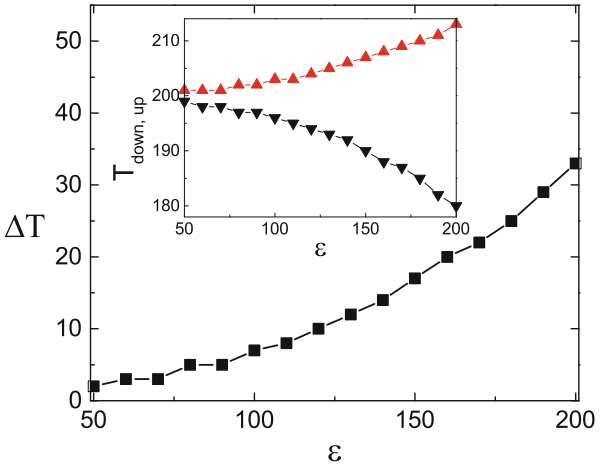

Fig. 10.14 The hysteresis width vs the intensity of fluctuations ($L = 70$)

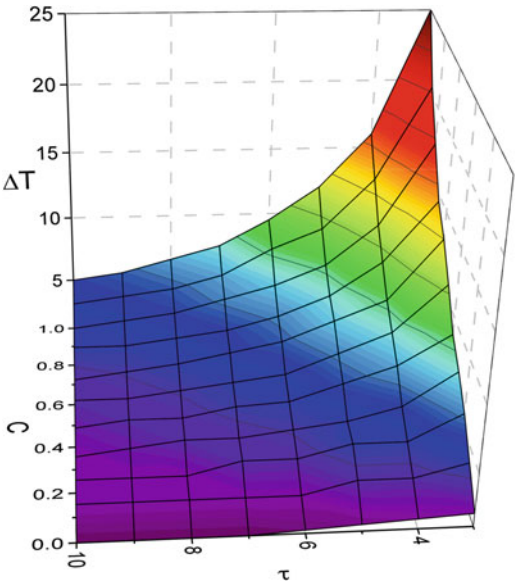

Fig. 10.15 The hysteresis width as a function of the autocorrelation time of fluctuations τ and the global coupling of random component of environment C. Lattice size was 70×70

descriptions of the interactions of SC system with environment. Figure 10.15 shows the variation of the hysteresis width as a function of fluctuations and coupling constant. The calculations in the Fig. 10.15 were carried out for a system under influence of fluctuations with intensity $\varepsilon = 100$ and lattice with side $L = 80$. It is worthwhile to note that the dependencies of the hysteresis width as a function of the autocorrelation time of fluctuations τ and the global coupling of random component of environment C are opposite. Contrary to C degree of fluctuations color τ leads to narrowing of ΔT. Such system behavior may be interpreted as a consequence of vanishing of total power spectrum of fluctuations with $\tau \to \infty$, which is clearly seen from Eqs. (10.25) and (10.26). The action of fluctuations is diminished and the system behavior becomes similar to the deterministic one, which partially can be seen from Fig. 10.11.

10.5 Conclusion

By taking into account the solid strain, we considered a simple Ising-like model with applied pressure. On the basis of this model we have obtained the free energy per spin-crossover molecule that makes possible to derive the state equations of the system. The thermodynamic functions show the transitions that may be divided into two basic types: (1) continuous high-spin $\rightleftharpoons$ low-spin transitions over a broad temperature range; (2) discontinuous high-spin $\rightleftharpoons$ low-spin transitions associated with a first-order phase transition at a definite temperature. The kind of phase transition in general depends on the magnitude of inter-ion interaction J_0. The obtained results show that increasing the strain component J_1 leads to the

forthcoming first-order phase transition. The obtained phase diagram gives a more complete description of diffusionless processes occurring in the spin-crossover system.

Also we have applied the concept of breathing crystal field to spin-crossover materials examined in the framework of Ising-like Hamiltonian. The essential feature of the model is the existence of an external (relative to magnetic ion) crystal field of random statistical nature.

By using Monte Carlo simulations we have computed transition curves for different external field: (1) without fluctuations; (2) with white fluctuations; (3) with colored fluctuations without space correlation; and (4) with fluctuations colored in time and space. The breathing of crystal field provokes the broadening of the hysteresis loop. Depending on statistical characteristics of fluctuations term the loop width shows different behavior. For the case with colored fluctuation the width of hysteresis loop increases with decreasing the color degree of fluctuation and increasing its global coupling. In the latter case the hysteresis width may be larger than the one obtained in the case of white fluctuations. The action of fluctuations decreases the threshold spin–spin interaction of the first-order phase transition.

The influence of the size effects on the hysteresis loops of spin-crossover system perturbed by fluctuations has been investigated. We have shown that the effects of fluctuations are more evident for small systems and the increasing of the system size reduces the influence of fluctuations until the saturation regime is not reached.

The study evolution of HS fractions close to phase transition under various realizations of the crystal field has also been provided. One may notice the abrupt evolution of the HS fractions for correlated space–time fluctuations.

It is important to note that the concepts proposed in this chapter may be also applied for other magnetic breathing crystals different from spin-crossover materials.

Acknowledgements The work of AIu is supported in part by the Ministry of Science and Education of Ukraine under grant No. 0113U003249.

References

1. Kahn O (1993) Molecular magnetism. VCH, New York
2. Gütlich P, Goodwin HA (eds) (2004) Spin crossover in transition metal compounds I-III. Springer, Berlin
3. Halcrow MA (ed) (2013) Spin-crossover materials: properties and applications. Wiley, Chichester
4. Gudyma Iu, Enachescu C, Maksymov A (2015) Kinetics of nonequilibrium transition in spin-crossover compounds. In: Fesenko O, Yatsenko L (eds) Nanocomposites, nanophotonics, nanobiotechnology, and applications. Springer, Cham, pp 375–401
5. Wajnflasz J (1970) Etude de la transition "Low Spin"-"High Spin" dans les complexes octaédriques d'ion de transition. Phys Status Solidi B 40:537–545
6. Wajnflasz J, Pick R (1971) Transitions "Low Spin"–"High Spin" dans les complexes de Fe^{2+}. J Phys Colloques 32:C1-91–C1-92

7. Bousseksou A, Nasser J, Linares J, Boukheddaden K, Varret F (1992) Ising-like model for the two-step spin-crossover. J Phys I 2:1381–1403
8. Bousseksou A, Varret F, Nasser J (1993) Ising-like model for the two-step spin-crossover of binuclear molecules. J Phys I 3:1463–1473
9. Bousseksou A, Constant-Macuado H, Varret F (1995) A simple Ising-like model for spin conversion including molecular vibration. J Phys I 5:747–760
10. Nicolazzi W, Pillet S, Lecomte C (2008) Two-variable anharmonic model for spin-crossover solids: a like-spin domains interpretation. Phys Rev B 78:174401
11. Nicolazzi W, Pillet S (2012) Structural aspects of the relaxation process in spin crossover solids: phase separation, mapping of lattice strain, and domain wall structure. Phys Rev B 85:094101
12. Gudyma Iu, Ivashko V, Linares J (2014) Diffusionless phase transition with two order parameters in spin-crossover solids. J Appl Phys 116:173509
13. Klinduhov N, Chernyshov D, Boukheddaden K (2010) Choice of dynamics for spin-crossover system. Phys Rev B 81:094408
14. Catala L, Volatron F, Brinzei D, Mallah T (2009) Functional coordination nanoparticles. Inorg Chem 48:3360–3370
15. Galán-Mascarós JR, Coronado E, Forment-Aliaga A, Monrabal-Capilla M, Pinilla-Cienfuegos E, Ceolin M (2010) Tuning size and thermal hysteresis in bistable spin crossover nanoparticles. Inorg Chem 49:5706–5714
16. Bousseksou A, Molnár G, Salmon L, Nicolazzi W (2011) Molecular spin crossover phenomenon: recent achievements and prospects. Chem Soc Rev 40:3313–3335
17. Tanabe Y, Sugano S (1954) On the absorption spectra of complex ions. I. J Phys Soc Jpn 9:753–766
18. Spiering H, Meissner E, Köppen H, Müller EW, Gütlich P (1982) The effect of the lattice expansion on high spin-low spin transitions. Chem Phys 68:65–71
19. Spiering H, Kohlhaas T, Romstedt H, Hauser A, Bruns-Yilmaz C, Kusz J, Gütlich P (1999) Correlations of the distribution of spin states in spin crossover compounds. Coord Chem Rev 190–192:629–647
20. Gütlich P, Garcia Y, Goodwin H (2000) Spin crossover phenomena in Fe(II) complexes. Coord Chem Rev 29:419–427
21. Real JA, Gaspar AB, Muñoz MC (2005) Thermal, pressure and light switchable spin-crossover materials. Dalton Trans 2005:2062–2079
22. Gaspar AB, Seredyuk M (2014) Iron catalysed nitrosation of olefins to oximes. Dalton Trans 43:38–41
23. Buron-Le Cointe M, Hébert J, Baldé C, Moisan N, Toupet L, Guionneau P, Létard JF, Freysz E, Cailleau H, Collet E (2012) Intermolecular control of thermoswitching and photoswitching phenomena in two spin-crossover polymorphs. Phys Rev B 85:064114
24. Nishino M, Miyashita S (2013) Effect of the short-range interaction on critical phenomena in elastic interaction systems. Phys Rev B 88:014108
25. Chiruta D, Jureschi C-M, Linares J, Garcia Y, Rotaru A (2014) Lattice architecture effect on the cooperativity of spin transition coordination polymers. J Appl Phys 115:053523
26. Gudyma I, Maksymov A, Enachescu C (2014) Phase transition in spin-crossover compounds in the breathing crystal field model. Phys Rev B 89:224412
27. Avram NM, Brik MG (2013) Optical properties of 3d-ions in crystals: spectroscopy and crystal field analysis. Springer, Berlin/Heidelberg
28. Chergui M, Zewail AH (2009) Electron and X-Ray methods of ultrafast structural dynamics: advances and applications. ChemPhysChem 10:28–43
29. Cailleau H, Lorenc M, Guérin M, Serrvol M, Collet E, Buron-Le Cointe M (2010) Structural dynamics of photoinduced molecular switching in the solid state. Acta Cryst A 66:189–197
30. Elsaesser T, Woerner M (2014) Perspective: structural dynamics in condensed matter mapped by femtosecond x-ray diffraction. J Chem Phys 66:020901

31. Ma H, Petersen JL, Young VG Jr, Yee GT, Jensen MP (2010) Solid-state spin crossover of Ni (II) in a bioinspired N_3S_2 ligand field. J Am Chem Soc 133:5644–5647
32. Chen L, Mowat JPS, Fairen-Jimenez D, Morrison CA, Thompson SP, Wright PA, Düren T (2013) Elucidating the breathing of the metal-organic framework MIL-53(Sc) with ab initio molecular dynamics simulations and in situ X-ray powder diffraction experiments. J Am Chem Soc 135:15763–15773
33. Guionneau P (2014) Crystallography and spin-crossover. A view of breathing materials. Dalton Trans 43:382–393
34. Sheveleva AM, Kolokolov DI, Gabrienko AA, Stepanov AG, Gromilov SA, Shundrina IK, Sagdeev RZ, Fedin MV, Bagryanskaya EG (2014) Structural dynamics in a "breathing" metal-organic framework studied by electron paramagnetic resonance of nitroxide spin probes. J Phys Chem Lett 5:20–24
35. Boukheddaden K, Shteto I, Hoô B, Varret F (2000) Dynamical model for spin-crossover solids. I. Relaxation effects in the mean-field approach. Phys Rev B 62:14796–14805
36. Miyashita S, Konishi Y, Nishino M, Tokoro H, Rikvold PA (2008) Realization of the mean-field, universality class in spin-crossover materials. Phys Rev B 77:014105
37. Muraoka A, Boukheddaden K, Linarès J, Varret F (2011) Two-dimensional Ising-like model with specific edge effects for spin-crossover nanoparticles: a Monte Carlo study. Phys Rev B 84:054119
38. Chiruta D, Linares J, Dahoo PR, Dimian M (2012) Analysis of long-range interaction effects on phase transitions in two-step spincrossover chains by using Ising-type systems and Monte Carlo entropic sampling technique. J Appl Phys 112:074906
39. Paez-Espejo M, Sy M, Varret F, Boukheddaden K (2014) Quantitative macroscopic treatment of the spatiotemporal properties of spin crossover solids based on a reaction diffusion equation. Phys Rev B 89:024306
40. Pavlik J, Boča R (2013) Established static models of spin crossover. Eur J Inorg Chem, 2013:697–709
41. Nakada T, Mori T, Miyashita S, Nishino M, Todo S, Nicolazzi W, Rikvold PA (2012) Critical temperature and correlation length of an elastic interaction model for spin-crossover materials. Phys Rev B 85:054408
42. Enachescu C, Nishino M, Miyashita S, Stoleriu L, Stancu A (2012) Monte Carlo Metropolis study of cluster evolution in spin-crossover solids within the framework of a mechanoelastic model. Phys Rev B 86:054114
43. Slimani A, Boukheddaden K, Varret F, Oubouchou H, Nishino M, Miyashita S (2013) Microscopic spin-distortion model for switchable molecular solids: spatiotemporal study of the deformation field and local stress at the thermal spin transition. Phys Rev B 87:014111
44. Nishino M, Nakada T, Enachescu C, Boukheddaden K, Miyashita S (2013) Crossover of the roughness exponent for interface growth in systems with long-range interactions due to lattice distortion. Phys Rev B 88:094303
45. Kambara T (1979) Theory of high-spin-low-spin transitions in transition metal compounds induced by the Jahn-Teller effect. J Chem Phys 70:4199
46. Gudyma AIu, Gudyma IuV (2010) Noise-induced collective regimes of complex system in contact with a random reservoir. Physica A 389:667–672
47. San Miguel M, Toral R (2000) Stochastic effects in physical systems. In: Tirapegui E, Martínez J, Tiemann R (eds) Instabilities and nonequilibrium structures VI. Kluwer Academic, Dordrecht, pp 35–130
48. Gudyma Iu, Maksymov A (2011) High spin metastable state relaxation of spin-crossover solids driven by white noise. J Phys Chem Solids 72:73–77
49. Volatron F, Catala L, Rivière E, Gloter A, Stéphan O, Mallah T (2008) Spin-crossover coordination nanoparticles. Inorg Chem 47:6584–6586
50. Martínez V, Boldog I, Gaspar AB, Ksenofontov V, Bhattacharjee A, Gütlich P, Real JA (2010) Spin crossover phenomenon in nanocrystals and nanoparticles of $[Fe(3\text{-}Fpy)_2M(CN)_4]$ (M^{II}=Ni, Pd, Pt) Two-dimensional coordination polymers. Chem Mater 22:4271–4281

51. Roubeau O (2012) Triazole-based one-dimensional spin-crossover coordination polymers. Chem Eur J 18:15230–15244
52. Shepherd HJ, Molnár G, Nicolazzi W, Salmon L, Bousseksou A (2013) Spin crossover at the nanometre scale. Eur J Inorg Chem 2013:653–661
53. Mori T, Miyashita S, Rikvold PA (2010) Asymptotic forms and scaling properties of the relaxation time near threshold points in spinodal-type dynamical phase transitions. Phys Rev E 81:011135
54. Gudyma Iu, Maksymov AI, Miyashita S (2011) Noise effects in a finite-size Ising-like model. Phys Rev E 84:031126
55. Stoleriu L, Chakraborty P, Hauser A. Stancu A, Enachescu C (2011) Thermal hysteresis in spin-crossover compounds studied within the mechanoelastic model and its potential application to nanoparticles. Phys Rev B 84:134102
56. Félix G, Nicolazzi W, Salmon L, Molnár G, Perrier M, Maurin G, Larionova J, Long J, Guari Y, Bousseksou A (2011) Enhanced cooperative interactions at the nanoscale in spin-crossover materials with a first-order phase transition. Phys Rev Lett 84:134102
57. Kawamoto T, Abe S (2005) Thermal hysteresis loop of the spin-state in nanoparticles of transition metal complexes: Monte Carlo simulations on an Ising-like model. Chem Commun 2005:3933–3935
58. Newman MEJ, Barkema GT (1999) Monte Carlo methods in statistical physics. Oxford University Press, Oxford
59. Miyashita S, Rikvold PA, Mori T, Konishi Y, Nishino M, Tokoro H (2009) Threshold phenomena under photoexcitation of spin-crossover materials with cooperativity due to elastic interactions. Phys Rev B 80:064414
60. Atitoaie A, Tanasa R, Enachescu C (2012) Size dependent thermal hysteresis in spin crossover nanoparticles reflected within a Monte Carlo based Ising-like model. J Mag Mag Mater 324:1596–1600

Chapter 11
Formulation and Rheology of Tape Casting Suspensions Based on $BaTiO_3$ Nanopowders

S.E. Ivanchenko, I.O. Dulina, S.O. Umerova, A.G. Nikulin, and A.V. Ragulya

11.1 Introduction

Reducing the size of microelectronic objects is always an important goal. Reducing the size and increasing of the capacity of multilayer ceramic capacitors can be achieved by reducing the thickness of its dielectric layers.

Tape casting is an important technology which obtains thin elastic films with high density, predetermined thickness, and a uniform distribution of powder in volume of the tape. By using a not complicated equipment, this high-performance and environmentally friendly technology obtains thin tapes from all materials in powder state [1].

The method is widely used as a basis for the manufacturing of all modern electronics and is constantly being upgraded.

Application of the nanoscale powders in this work causes significant differences in the nature of flow and viscosity of the suspension, due to their high specific surface and activity [2]. Therefore, for the preparation of a suspension, we cannot use the classic compound formulation, so it's necessary to create and explore new systems. Use of nanopowders will reduce the thickness and roughness of the tape as well as improve its mechanical properties.

This work investigated the effect of changing the type of the main components and their quantities on the properties of suspensions and casted tapes based on nanopowders.

S.E. Ivanchenko (✉) • I.O. Dulina • S.O. Umerova • A.G. Nikulin
Frantsevich Institute for Problems of Materials Science of NASU,
3, Krzhyzhanovsky Street, Kyiv 03142, Ukraine
e-mail: sergonische@ukr.net

A.V. Ragulya
Institute for Problems in Materials Science of NASU, Ukraine

O. Fesenko, L. Yatsenko (eds.), *Nanoplasmonics, Nano-Optics, Nanocomposites, and Surface Studies*, Springer Proceedings in Physics 167,
DOI 10.1007/978-3-319-18543-9_11

The suspension for tape casting consists of the following components: solid phase in powder form which determinates the main features and sphere of application of the film, the polymer solution which will form a matrix which is uniformly distributed in the solid phase, plasticizer which will provide the required flexibility and elasticity to the polymer matrix, and solvent required for the preparation of the polymer and plasticizer solutions, which is also used for wet milling of the powder. In addition to these basic components, additional components are used to help improve the stability of the system, to obtain specific properties, and so on [3].

11.2 Materials and Methods

As solid phase used $BaTiO_3$ powder of our own production with mean particle size of 20–25 nm, ethanol, butanol, and the azeotropic mixture of low polar solvents were used as the solvents. Polyvinyl butyral with molecular weights from 40,000 to 75,000 was used as a polymer binder and dibutyl phthalate as a plasticizer. Preparation of polymer and binder solutions was carried out by dissolving polymer and plasticizer in chosen solvents.

Milling of powder and preparation of suspensions were carried out using a planetary mill Pulverisette 6. Rheological properties of suspensions of powder $BaTiO_3$ were determined by using a rotation rheometer "Rheotest RN4.1." Films of $BaTiO_3$ suspensions were formed on casting machine TTC-1200. Measuring of thickness and topography of the samples was carried out on an optical profilometer Micron-alpha. Investigation of the microstructure of casted $BaTiO_3$ films was carried out on metallographic microscope XJL-17AT.

11.3 Results and Discussion

First, change of rheological properties at different stages of preparation of suspensions was carried out in order to identify the role of the effect of individual components in changing the nature of the flow and to obtain further suspensions. The main goal is to obtain suspension with predefined nature of the flow.

Firstly, the nature of the polymer solution flow was investigated, and then plasticizer was added and another study was conducted. These curves were compared with a final $BaTiO_3$ suspension, based on the same polymer solution and plasticizer (Fig. 11.1).

Reduction of the viscosity after adding the plasticizer can be explained by the fact that the addition of weakly polar substances such as dibutyl phthalate leads to better dispersion of the polymer in the solvent which likely corresponds to the molecular plasticization process [4]. Solutions 1 and 2 show the thixotropic nature of flow, indicating the presence of structure-polymer networks.

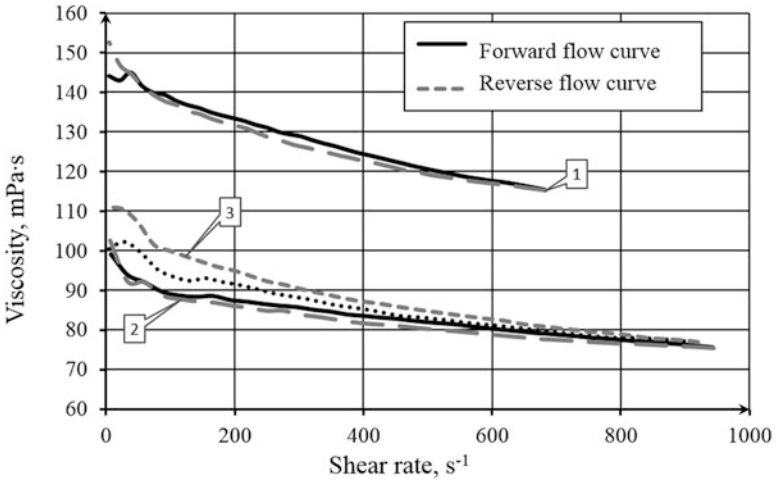

Fig. 11.1 Dependence of viscosity from shear rate for different systems. 1, polymer solution; 2, polymer solution with 15 % of plasticizer; 3, suspension with $BaTiO_3$ powder and 15 % of plasticizer

Adding a powder to the system causes thickening of the suspension. Also the thixotropic nature of the flow changes to rheopexy (due to the formation of random bounds after the destruction of the structure and the high activity of particles of nanopowder).

In order to optimize the process of the preparation of suspensions, the influence of changing the order of addition of the components on rheological properties was studied.

In suspension TCS-23, dispersed powder was initially added to a solution of polymer and then plasticizer solution. In TCS-24 suspension, the order of adding the components was changed. First, dispersed powder was added to a plasticizer solution and second a polymer solution. The obtained rheological curves show that changing the order of addition of components in TCS-24 reduced the viscosity of the system and changed the nature of the flow curve from pseudoplastic-rheopexy to pseudoplastic-thixotropic (Fig. 11.2). The formation of a regular spatial pattern and better passing of plasticizing process can explain this system's behavior.

Thixotropy increases the viscosity of the suspension in the absence of mechanical stress. During the time when there is no mechanical strain on the suspension, the forces of short-range order start forming polymer networks. Polymer chains form weak links all over the suspension creating a grid. The current grid has no long-range order, such as in the crystal matrix, and is more similar to a short-range order of the glass mesh [5]. The phenomenon of increase in viscosity with time used in the casting of thick films of low viscous systems. In addition, thixotropy can enhance the stability of the system due to the increase in viscosity and sedimentation stability during the storage of the suspension.

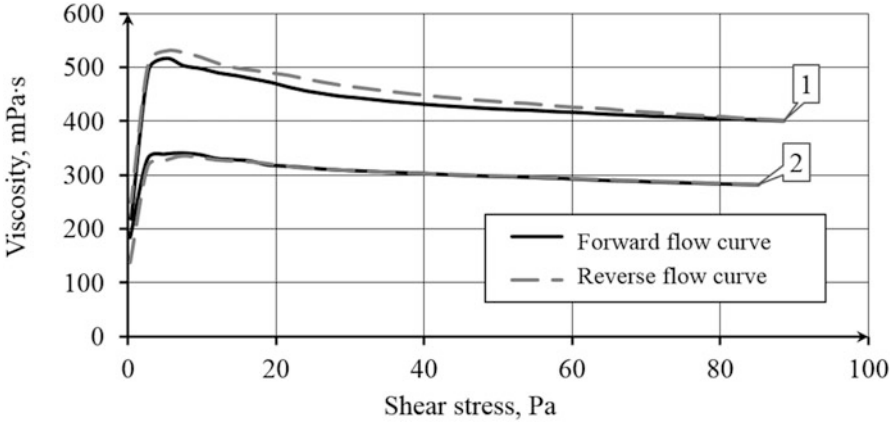

Fig. 11.2 The dependence of viscosity from shear stress for suspensions with different order of addition of the components during preparation. 1, TCS-23; 2, TCS-24

11.4 The Influence of the Quantity of Polymer in the Suspension on Its Rheological Properties

The quantity of polymer in the suspension greatly affects the viscosity but has a little effect on the nature of the flow. Suspension with low polymer content shows a weak rheopexy (Fig. 11.3). Rheopexy fluid remains liquid at the beginning of mixing and becomes more viscous due to stirring.

Also a decrease in threshold of shearing stress is observed. Obviously, it happens due to the fact that the quantity of particles in the powder in the presence of high polymer content is not enough for leveling of the polymer chain [6–8].

In addition, there is a dependence of the viscosity of the suspension on film thickness (Table 11.1).

11.5 The Influence of the Amount of Powder on the Rheological Properties of Suspensions

Powder determines the initial properties of the films and has the greatest influence on the microstructure, density, and dielectric constant [9, 10]. Increasing the amount of powder into the system considerably increases the viscosity and strongly modifies the nature of flow of the current suspension (Figs. 11.4 and 11.5).

The appearance of rheopexy can be explained by high concentration of solid phase in the suspension and formation of random bounds after the destruction of the structure. Powder particles collide and rub against each other. High effective surface of particles will increase this phenomenon (Table 11.2).

There is also a natural increase in thickness of the obtained films.

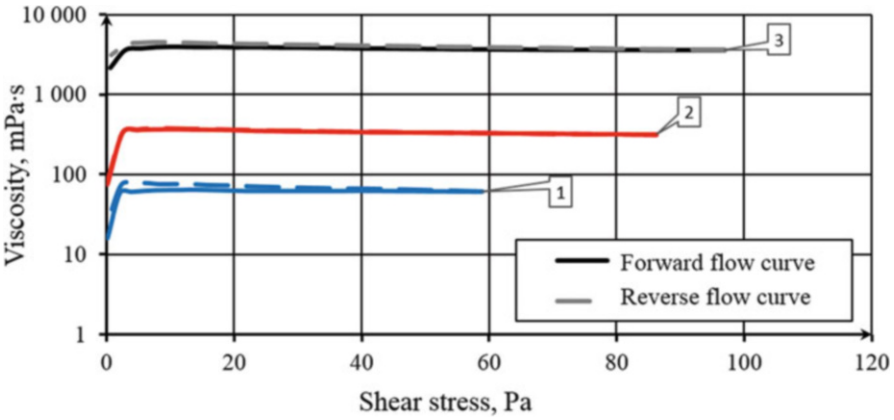

Fig. 11.3 Dependence of viscosity from shear stress for suspensions with different amount of polymer. 1, TCS-20 (5 % of polymer); 2, TCS-14 (10 % of polymer); 3, TCS-19 (20 % of polymer)

Table 11.1 The dependence of tape thickness of the polymer amount in the suspension

System name	Amount of polymer in solution, wt%	*h*, mcm	Ra, nm
TCS-19	20	5	45
TCS-14	10	3	49
TCS-20	5	1.5	38

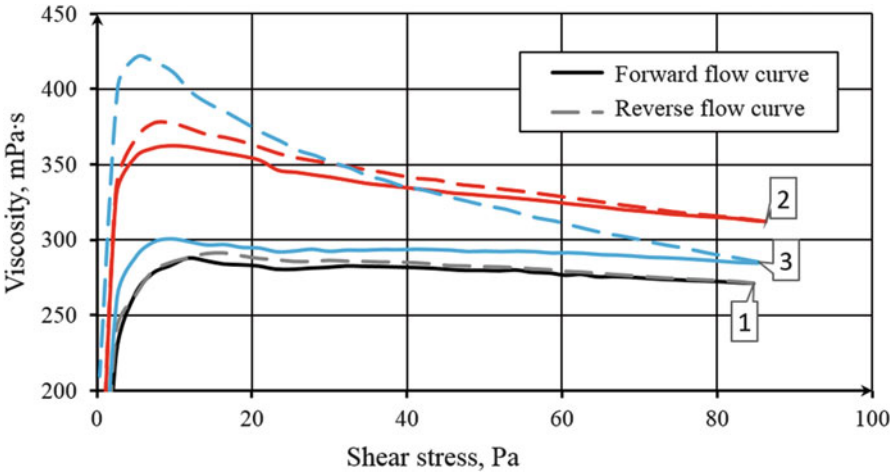

Fig. 11.4 Dependence of viscosity from shear stress for suspensions with different content of powder. 1, TCS-17 (15 wt% of powder); 2, TCS 14 (30 wt% of powder); 3, TCS-22 (37.5 wt% of powder)

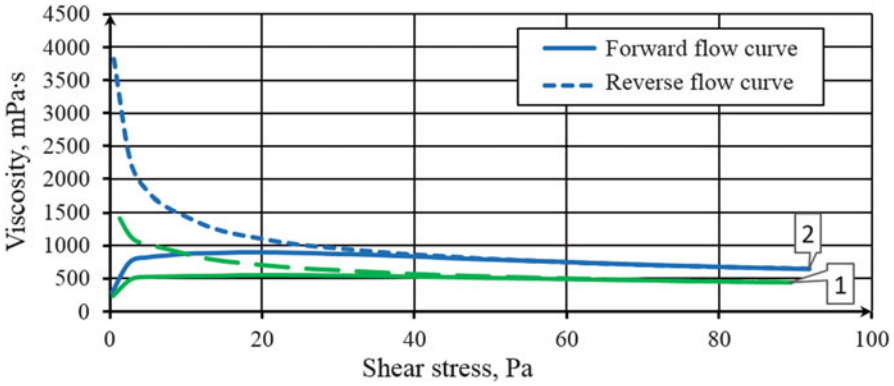

Fig. 11.5 Dependence of viscosity from shear stress for suspensions with different amount of powder. 1, TCS-21 (45 wt% of powder); 2, TCS 18 (60 weight of powder)

Table 11.2 The dependence of tape thickness from the amount of powder in suspension

System name	Powder amount, wt%	*h*, mcm	Ra, nm
TCS-17	15	2	52
TCS-14	30	3	49
TCS-18	60	3.5	40

Table 11.3 Effect of powder amount in the system on the maximum structural tensile strength

System name	Amount of powder, wt%	Structural tensile strength, Pa
TCS-17	15	84.75
TCS-14	30	86.30
TCS-18	60	91.79

The increase of maximum shear stress along with increasing of powder content in the system has been observed (Table 11.3). This happens due to a change in spatial orientation (stretching) of the polymer chains resulting from the change of electronic potential caused by the attachment of polymer molecules to the powder particles. In this state, the polymer chain resists shear that corresponds to an increase of the threshold of structural tensile strength.

Also noticeable is that, under small shear stresses, suspensions exhibit the dilatancy nature of flow. However, with increasing shear stress, the nature of the flow goes into pseudoplastic. With decreasing amount of powder in a system transition point, dilatancy-pseudoplastic gradually shifted toward lower shear stresses.

Tensile strength increases with increasing amount of powder in the system.

11.6 The Influence of the Amount of Plasticizer on the Rheological Properties of Suspensions

Plasticizer reduces the strength of intermolecular bonds between polymer chains (Fig. 11.6). Plasticizer molecules between polymer chains prevent leveling of chains circuit and reduce the van der Waals force between them [11]. This leads to softening of the polymer matrix, resulting from the decrease in viscosity of the suspension. Also the addition of plasticizer lowers the strength of the polymer networks that can be seen from reducing the threshold of structural tensile strength with increasing percentage of plasticizer in the suspension.

Effect of changes of solvent type on the rheological properties of suspensions.

Follows dependence between thickness and viscosity. Systems with lower viscosity can produce tapes with low roughness (Table 11.4).

From these dependencies, changing the solvent can affect the viscosity of the system (Fig. 11.7). Lower viscosity is achieved through better dispersion of the particles in the suspension and better dissolution of the polymer. However, in systems with low viscosity, a decrease in structural tensile strength can be explained by twisting the polymer chains.

Also, notice that azeotropic solvent mixtures containing ethanol exhibit a small degree of rheopexy.

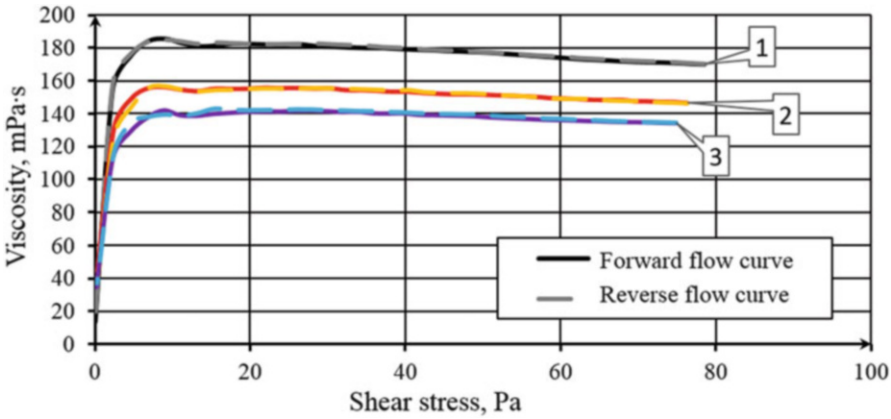

Fig. 11.6 Dependence of viscosity from shear stress for suspension TCS-15 (butanol based). 1, 10 % of plasticizer; 2, 15 % of plasticizer; 3, 20 % of plasticizer

Table 11.4 Effect of changing solvent type on the surface profile and thickness of the tape

System name	Solvent	*h*, mcm	Ra, nm	Rz, nm
TCS-14	Menthone/EtOh—40/60	3.5	57–86	123–317
TCS-15	Butanol	3	45–93	128–210
TCS-16	MEK/EtOH—66/34	2	37–63	168–317

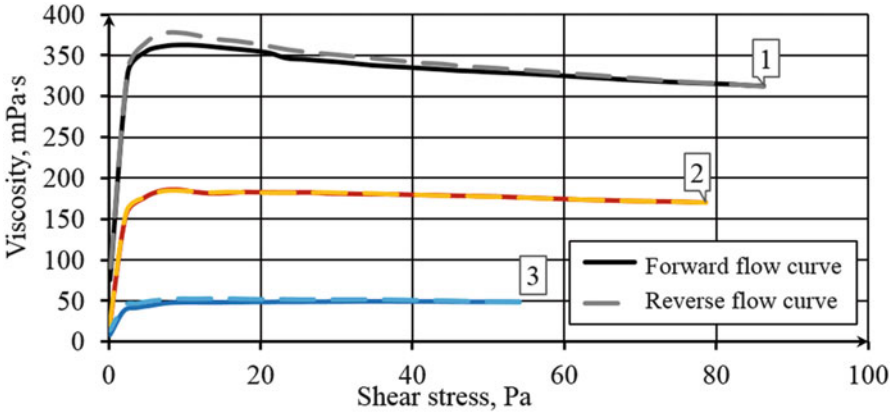

Fig. 11.7 Dependence of viscosity from shear stress for suspensions based on different solvents. 1, TCS-14 (menthone/ethanol); 2, TCS-15 (butanol); 3, TCS-16 (MEK)

11.7 Investigation of the Surface Profile of the Obtained Tapes

Investigation of the surface profile obtained from suspensions using low polar (TCS-2) and polar (TCS-5) solvent showed that replacement of a polar solvent in the composition of suspension with low polar solvent gives tape surface less roughness. In our opinion, this is due to the fact that organic binders and plasticizers are used in the composition of suspensions; on the one hand, there is a low polar substance, and on the other, the polarity of the surface-modified barium titanate powder causes accession of binder and plasticizer molecules by its polar groups and nonpolar extracted into solution. The formation of such nonpolar particles in the suspension causes its splitting from polar solvent, resulting in the formation of "islands" of solid-phase particles coated with a layer of organic bounds on tape surface.

It should be noted that based on the results of optical profilometry (Figs. 11.8 and 11.9), this behavior of the solid-phase particles in the suspension does not change the average thickness of the film.

11.8 Conclusions

Suspensions for tape casting based on barium titanate nanopowder characterized mainly pseudoplastic—rheopexy nature of the flow. The mount of polymer in the suspension greatly affects the viscosity but has little effect on the nature of the flow. The change in viscosity affects the thickness of the obtained films. Increasing the

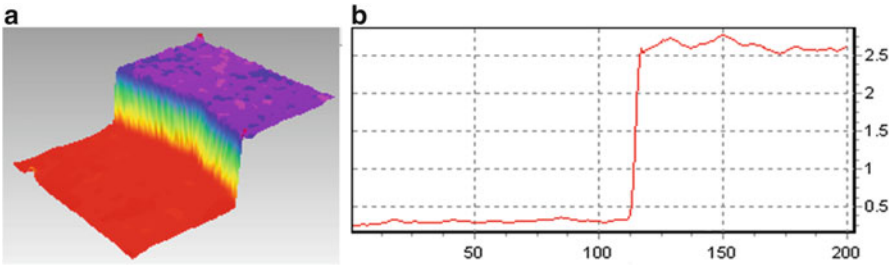

Fig. 11.8 3D and 2D surface profile of raw barium titanate tape obtained from suspension TCS-2 (with low polar solvent). (**a**) 3D profile; (**b**) 2D profile

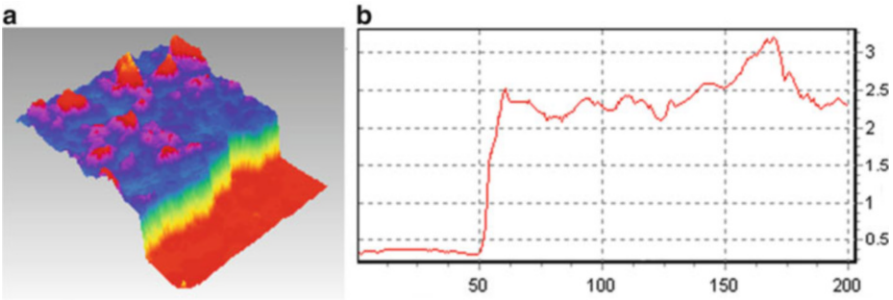

Fig. 11.9 3D and 2D surface profile of raw barium titanate tape obtained from suspension TCS-5 (with polar solvent). (**a**) 3D profile; (**b**) 2D profile

amount of powder in the system leads to increased viscosity and the appearance of rheopexy due to the formation of random bounds after the destruction of the structure. Structural tensile strength of the system increases with increasing amount of powder. Adding plasticizer enhances the rheological characteristics of solutions without changing the nature of flow curve and reduces the viscosity of the system by passing the molecular mechanism of plasticization. Changing the solvent tape can affect the viscosity of the system, the nature of the flow curve, and the surface roughness. Lower viscosity is achieved through better dispersion of the particles in the suspension. Replacing a polar solvent in the composition of suspension with low polar solvent gives tape surface less roughness.

References

1. Mistler RE, Twiname ER (2000) Tape casting: theory and practice. The American Ceramic Society, Westerville
2. Liu G, Zhang D, Button TW (2010) Preparation of concentrated barium titanate suspensions incorporating nano-sized powders. J Eur Ceram Soc 30:171–176
3. Shanefield DJ (1995) Organic additives and ceramic processing. Kluwer, Boston, p 118

4. Kim D-H, Lim K-Y, Paik U, Jung Y-G (2004) Effects of chemical structure and molecular weight of plasticizer on physical properties of green tape in BaTiO3/PVB system. J Eur Ceram Soc 24(5):733–738
5. Rahaman MN (2003) Ceramic processing and sintering. Taylor & Francis, New York, p 875
6. Cutler RA, Kleinlein B (2009) Effect of the hydroxyl content and molecular weight of polyvinyl butyral on tape properties. J Eur Ceram Soc 29(15):3211–3218
7. Yoon D-H, Lee BI (2004) Processing of barium titanate tapes with different binders for MLCC applications—part I: optimization using design of experiments. J Eur Ceram Soc 24 (5):739–752
8. Yoon D-H, Lee BI (2004) Processing of barium titanate tapes with different binders for MLCC applications—part II: comparison of the properties. J Eur Ceram Soc 24(5):753–761
9. Mikeska KP, Cannon WR (1988) Non-aqueous dispersion properties of pure barium titanate for tape casting. Colloids Surf 29:305–321
10. Chu L, Prakash K, Tsai MT, Lin IN (2008) Dispersion of nano-sized BaTiO3 powders in nonaqueous for MLCC. J Eur Ceram Soc 28(6):1205–1212
11. Tok AIY, Boey FYC, Khor KA (1999) Tape casting of high dielectric ceramic composite substrates for microelectronics application. J Mater Process Technol 89–90:508–512

Chapter 12
Nanodimension Layers on Stainless Steel Surface Synthesized by Ionic Implantation and Their Simulation

A.A. Cherny, S.V. Maschenko, V.V. Honcharov, and V.A. Zazhigalov

12.1 Introduction

Ionic implantation has proven to be excellent as a technology for synthesis and modification of semiconductors in the production of the integrated circuits [1–5]. In the last decades, the high-energy methods of impact on the substance were also used for the synthesis of materials with enhanced mechanical the properties [6–16]. Special attention is paid to the issue of the influence of ionic doping on optical, tribological, electric, and chemical properties. Studying the structure, element composition, and valence state of the surface layer opens possibilities for the application of ionic implantation in chemical technology, catalysis, and medicine [17–22]. But the available publications relating to the research of the surface properties are insufficient for the objective estimation of the prospects of implants on the basis of materials, i.e., stainless steels, which are widespread due to their mechanical, physicochemical, and other characteristics. The main reasons for this are the complex composition of the substrate (because steel is an alloy of several components), the dependence on the plasma-forming agent, and the complexity of technology. In general, ionic doping includes a series of processes: ionic implantation, sputtering, deposition, radioactive swelling, and point defect formation. Ionic implantation is also accompanied by chemical reactions, desorption, interfusion of atoms, channeling, and diffusion. Some effects take place on the substrate's surface; other ones in a volume.

A.A. Cherny • S.V. Maschenko • V.V. Honcharov (✉)
Institute of Chemical Technologies (Rubizhne) of the V.Dal' East-Ukrainian National University, 31, Lenin Street, Rubizhne, Luhansk Region 93009, Ukraine
e-mail: gonchvit@rambler.ru

V.A. Zazhigalov
Institute for Sorption and Problems of Endoecology, National Academy of Sciences of Ukraine, 13, Naumov Street, Kyiv 03164, Ukraine

O. Fesenko, L. Yatsenko (eds.), *Nanoplasmonics, Nano-Optics, Nanocomposites, and Surface Studies*, Springer Proceedings in Physics 167,
DOI 10.1007/978-3-319-18543-9_12

During the bombing of solids by ions, effects contributing to their inhibition or scattering arise. They are classified as follows [7, 8]:

- Inelastic collisions with bound electrons of the inhibitory substance (in such collisions, energy loss occurs due to excitation of atoms or molecules)
- Inelastic collisions with nuclei (they produce bremsstrahlung, excitation of the nucleus, or nuclear reactions)
- Elastic collisions with bound electrons
- Elastic collisions with nuclei or atoms (part of the kinetic energy is transferred to the target atoms)
- Cherenkov radiation (it is excited by the particles, which move in a medium at a velocity greater than the phase velocity of light)

During ionic implantation, particles move at a velocity less than the phase velocity of light; therefore, there is no Cherenkov radiation. During braking of particles, inelastic collisions with nuclei and elastic collisions with electrons do not play such a large role as compared to inelastic collisions with electrons (electronic braking) and elastic collisions with nuclei (nuclear braking). Therefore, it is expedient to examine these two mechanisms only. Which effect will dominate depends on the energy and mass of speed-up particles and mass and sequence number of atoms of the substance.

The complications described do not allow to explain fully and to forecast exactly the modification of the superficial properties of materials during ionic implantation. The most authoritative physical models and methodologies of calculations of implants are given in works [1, 2, 7, 10, 15, 23–28]. Obviously, now, there exists no model which would take into account all the processes taking place during ionic implantation full enough. That is why the studying, design, and prognostication of results of implantation of ions in stainless steel have a scientific value and prospects of practical application.

12.2 The Process Model

The depth of penetration of the implanted ions in a substance is characterized by their range. The trajectory of separate ions in a crystal is similar to the polygonal lines, in which every rectilinear section and complete length of which differ from each other. All aggregate of ranges of separate ions are grouped according to the law of normal distribution of the random variable with the value of the average of the total range R and a standard deviation of ΔR. Of practical importance is the average normal range of R_p—the projection of the trajectory of the average total range in the direction of the initial ion velocity and its standard deviation ΔR_p.

Many models, in particular the model of Lindhard-Scharff-Schiott (LSchSh) [1, 23, 24], are based on the following suppositions:

- A target is considered to be amorphous, that is, the cases of the correlated successive collisions are eliminated from the consideration.
- In the process, a potential, calculated on the basis of the statistical model of atoms by Thomas-Fermi, is used, taking into account electrostatic cooperation between electrons only.
- Energy, passed to the target atoms in the process of collisions, is much less than the kinetic energy of ion.
- The basic mechanisms of braking particles in the processed substance are the inelastic collisions with electrons (electronic braking) and elastic collisions with nuclei (nuclear braking). Both mechanisms are considered to be independent in the processes of braking.
- Energy fluctuations conditioned in the process of braking only in cooperation with nuclei are taken into account.
- Describing cooperation of an ion with the atoms of the substrate, the classic approach of binary collisions is used.

The distribution profiles of the concentration of the implanted ions are determined by the character of distribution of average normal ranges on the depth of the irradiated layer. The ion beam, getting in a substance, tests casual collisions with atoms, and distribution of ranges is described by the law of distribution of the random variable. In this case, the profile of the implanted atoms is described by the Gaussian curve [1, 23].

When implantation the accelerated ions into the substrate at an angle to the normal the maximum of concentration is shifted toward the surface. In this case, both longitudinal standard deviation ΔR_p and root mean square transverse deviation ΔR_p contribute to the value of the standard deviation ΔR. The mode of implantation is in the range 1 keV–10 MeV, and the mode of sputtering surface −100 keV, and in the case where it is necessary to get an implanted layer at a depth corresponding to the lowest energy and avoid the sputtering process, it is possible to use an inclined implantation and higher energy values.

Dispersion is an insignificant process—a process in which atoms in a solid, lying close to the surface, get energy from an ion which is sufficient to escape into the environment (vacuum). This phenomenon can be attributed to the formation of defects in a subsurface layer during ionic implantation.

Depending on the density of collision cascades, there are three types of spray processes: a simple ejection of atoms, a linear cascade mode, a peak of displacements mode.

According to estimations and experiments, the top limit of implanted impurity, resulting from the spray surface during implantation, is limited to 20–50 % of atoms, which is quite sufficient to produce alloys and control the surface properties. In fact, it corresponds to the range of doses 10^{17}–10^{18} ion/sm^2. In practice, the dose of irradiation, as a rule, ranges from 10^{15} to 10^{18} ion/sm^2 [9]. At doses less than 10^{15} ion/sm^2, improving the performance of products is insignificant [12, 14]. Upon increasing the dose of implantation higher than 10^{18} ion/sm^2, improving the performance of products is substantially slowed, and different undesirable effects

begin to show up, for example, radiation swelling [8, 25], which results in destruction of the superficial layer of the processed material.

A very important effect that often accompanies ionic implantation is diffusion. It is necessary to distinguish a few types of diffusion. The most known one is thermal diffusion which can appear during realization of the necessary annealing or the process of implantation, if a semiconductor standard is strongly heated due to the distinguished power of bunch. Numerous vacancies, which even at a relatively subzero temperature can cause diffusion during implantation because many atoms of alloying elements are diffused on vacancies, appear under ionic bombardment. Interstitial diffusion can also play a noticeable role, because a part of the implanted atoms is stopped in a grate in non-nodal positions and before being captured they can rapidly diffuse along the interstices [1, 3, 24, 27]. The process of diffusion influences the distribution of admixture; however, the depth of maximal concentration remains unchanged.

12.3 The Experimental Part

The synthesis of standards was carried out in an implanter, the main components of which are a vacuum chamber, implanter (ion source), system providing vacuum (vacuum pump, vacuum unit), control unit, and measuring devices. Material processing was carried out by the next scheme. Plasma-forming gas (nitrogen) is supplied into the implanter where it is ionized in an electromagnetic field and is directed to a target made of the desired metal (in this work, we used titanium, molybdenum, and aluminum). Ions of metal, knocked out from a target, form a stream under the electric potential (to 50 kV) and bombard the stainless steel substrate. Thus, as a result of processing, we've got such standards: SS (stainless steel) and Me/SS (Me-Al, Mo, Ti). The mode of operations was chosen so that the dose of doping of standards was 5×10^{17} ion/sm^2.

The software used for the implementation of the models, taking into account the effects of the above, is a computer module "RIO," developed by the authors. In this software, according to the user's choice (by the models of Yudin and LSchSh), the calculation of distribution of the implanted ions can be carried out for materials of simple and difficult composition and homogeneous and multilayered structures. The simulation simultaneously takes into account:

- Oblique implantation
- Process of dispersion and radioactive swelling
- Process of diffusion
- Doping process into multilayered structures

The results of the calculations executed by the program were compared to data taken from the program SRIM-2012 [29], the calculations of which are based on a quantum-mechanical model, and also to data taken from the classic simplified model by Lindhard-Scharff-Schiott [23].

Optical pictures to simulate the surface were obtained using a microscope MIM-7 equipped with a digital camera Kodak EasyShare C1013.

Processing of the obtained photomicrographs and neural network modeling were executed by means of the software "Gwyddion" [30, 31].

12.4 Results and Discussion

The target effect of ion implantation is the introduction of particles in the subsurface layer. Therefore, we compared the ions' ranges in the material using different models (Table 12.1). Because, as mentioned above, the publications relating to investigations of implants based on stainless steel are not numerous, we gave the data for silicon substrates to compare the results presented.

The data in Table 12.1 show that the models by Yudin and by LSchSh in the program "RIO" have sufficient convergence both with the program "SRIM-2012" and with the classical model LSchSh in a wide range of energies. And for the steel substrate at energies up to 50 keV (operating range), the estimated depth of penetration of the ions for all models is less than 100 nm. Hence, it can be concluded that ionic implantation is a nanodimension steel modification technology. This conclusion confirmed the results of scanning electron microscopy [30], according to which the thickness of the modified layer with the aluminum implant is about 100 nm.

During ionic implantation, there occurs not only introduction of particles in the subsurface layer but also erosion and deposition of the film. Largely, the nature of what is happening depends on the angle at which the ion current falls on the specimen surface. Calculations performed by the application "RIO" (Fig. 12.1) for Ti/SS showed that under the deflection angles of the ion flux from the normal not more than 50°, a film is formed (depositing the particles), and at the angle more than 60° of etching, ejection substrate particles take place.

Thus, using the possibilities of the program "RIO," it is possible to determine the descriptions of geometry and the profile of the surface of standards after processing.

Using surface micrographs, 3D modeling, and calculation of texture parameters by the software "Gwyddion" [31], surface profiles of the initial samples were received. The surface profile of the untreated sample and Ti/SS after the simulation using the program "RIO" is shown in Fig. 12.2. To calculate, the length of the profile in 100 μm was taken.

Figure 12.2 shows the behavior of the surface profile of the sample after ionic processing. For quantitative comparison of the profiles, roughness Ra was selected.

Analysis of the micrographs by the program "Gwyddion" showed that for real samples with a similar mode of implantation, an increase of roughness is from 152 to 163 nm.

According to the calculations of the simulated profile, roughness during ionic implantation increased from 152 to 165 nm, which is in excellent agreement with the experimental data.

Table 12.1 The comparison of results for normal ranges and dispersions of normal ranges

	Program "RIO"											
	Model by Yudin				Model by LSchSh				Program "SRIM-2012"		Model by LSchSh [23]	
	a_{TF}		a_F		a_{TF}		a_F					
Standard, ion energy	R_p	ΔR_p	R_p	ΔR_p	R_p	ΔR_p	R_p	ΔR_p	R_p	ΔR_p	R_p	ΔR_p
B/Si, 20 keV	55.6	20.3	64.8	23.7	67.1	24.5	66.2	24.2	77.1	37.9	78.4	32.1
B/Si, 100 keV	252	92.2	306	112	241	88	236	86	318	88.6	398	93.9
Sb/Si, 20 keV	17.9	5.7	21.1	6.7	9.7	3.1	9.7	3.1	18.0	5.5	14	2.4
Sb/Si, 100 keV	44.1	14.1	51.6	16.4	46.0	14.7	46.0	14.7	54.0	13.8	45.7	7.4
N/SS, 20 keV	17.9	5.6	21.0	6.9	20.7	6.8	20.4	6.7	23	12.8	–	–
N/SS, 100 keV	72.5	23.8	85.8	28.2	74.2	24.4	72.3	23.7	109.4	44.6	–	–
Ti/SS, 20 keV	8.8	3.6	10.5	4.3	8.6	3.5	8.6	3.5	9.4	3.9	–	–
Ti/SS, 100 keV	26.5	10.8	31.1	12.6	38.4	15.6	38.3	15.6	38.6	13.2	–	–
Mo/SS, 20 keV	7.4	2.9	8.8	3.5	4.5	1.8	4.5	1.8	7.0	2.4	–	–
Mo/SS, 100 keV	18.6	7.3	22.0	8.6	21.3	8.4	21.3	8.4	22.7	6.7	–	–
Al/SS, 20 keV	11.6	4.4	13.7	5.3	14.0	5.4	13.9	5.3	14.1	7.0	–	–
Al/SS, 100 keV	41.5	15.9	48.6	18.6	57.5	22.0	56.8	21.8	69.6	27.6	–	–

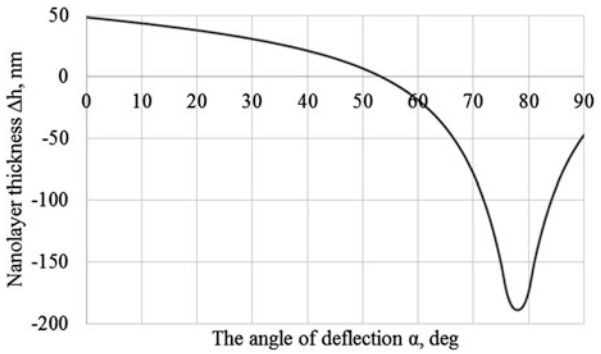

Fig. 12.1 Dependence of increase of layer on the angle of slope of stream of ions to the normal

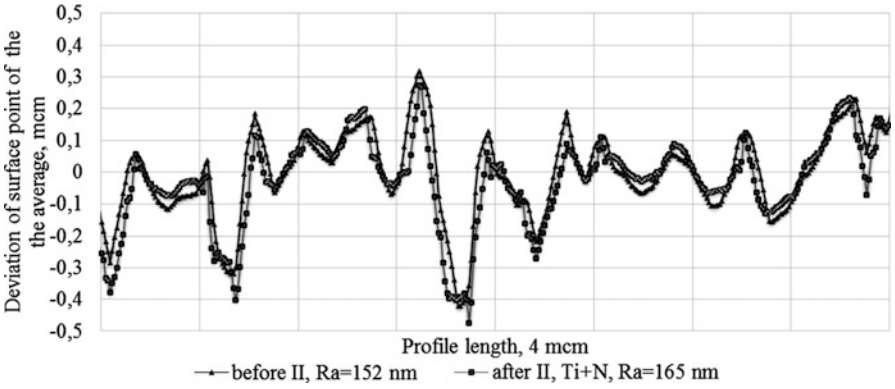

Fig. 12.2 Profiles of surface texture of standards before and after ionic implantation (II)

Despite these results, the profiles obtained provide little information because practical interest is in the surface characteristics of a sample, such as roughness K_{Ra}.

Important parameter of the surface geometry for different heat exchangers, catalytic, optical and other devices is roughness coefficient K_{Ra}, which is determined by the ratio of the real surface area to the projective one. To find the roughness coefficient, it is not enough to have one of the transverse profiles; you need to have all the geometry of the surface, which is a simulation of a complex process.

Initially, we tested the hypothesis that the roughness coefficient is dependent on the relative length of the profile. To check it, we took 250 random profiles and calculated the roughness coefficients. Based on the data, we calculated the dependence with the magnitude squared $R^2 = 0.87$ (Fig. 12.3).

In parallel with the development of the model based on deposition and etching, the variant of surface modeling using neural networks was considered. The program "Gwyddion" allows us to make such prediction.

Neural network is a modeling method, which can reproduce extremely complex relationships through learning by examples. The modeling process is to train the

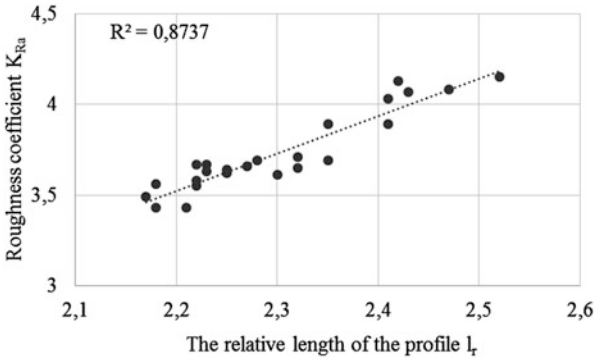

Fig. 12.3 Dependence of coefficient of roughness on relative length of profile

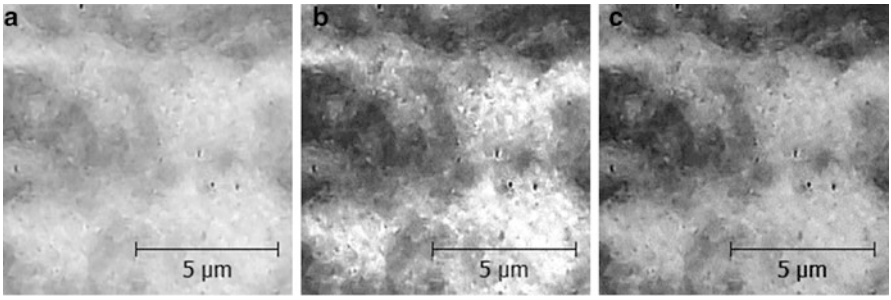

Fig. 12.4 Micrographs of the surface of standards, 10×10 μm: (**a**) SS; (**b**) Ti/SS; (**c**) Ti/SS, modeled by neural network

network by data set (model and the corresponding signal) and to use these "knowledge" by the network to the model with an unknown signal.

In this work, neural network training was performed on the basis of photographs of the surface area before implantation (model) and after implantation (signal). Then, using the method of neural networks to the untreated surface photograph, we got a simulation—a surface picture, as it should be after the implantation process.

In operation, neural network was trained on the basis of microphotographs (10×10 μm), obtained by the microscope MIM-7 (Fig. 12.4).

The similarity of profiles (Fig. 12.5) and values of K_{Ra} (Table 12.2) shows that the neural network reliably reproduces the ratio of the height of peaks and cavities of the surface.

Despite the ability to predict a number of parameters, the simulation using neural networks has several disadvantages. Firstly, for full learning, it is necessary to use large amounts of pairs "model-signal," which makes this method practically unusable if there are no initial experimental data. Secondly, the number of steps of training and the number of hidden nodes should also be sufficient which, coupled with high-resolution photos, makes the learning process long. Thirdly, a neural network training and its application are possible only under the conditions where

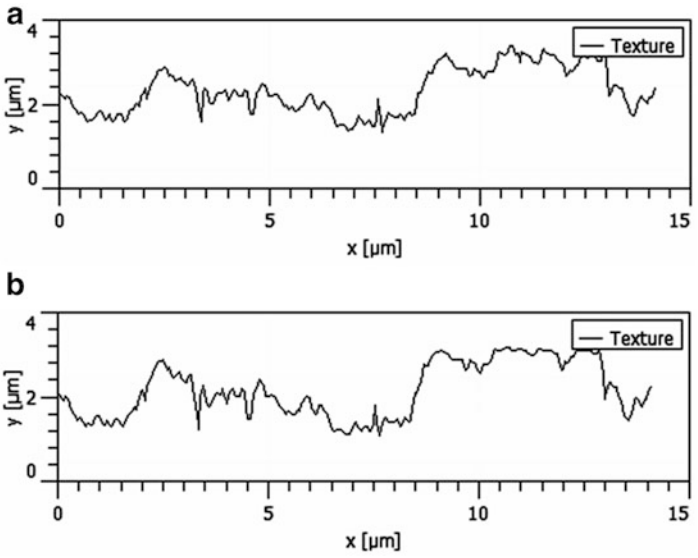

Fig. 12.5 Profiles of standards: (**a**) Ti/SS; (**b**) Ti/SS, modeled by neural network

Table 12.2 Coefficient of roughness of standards

Sample		K_{Ra}
Initial steel	Original, "Gwyddion"	3.72
Ti/SS	Original, "Gwyddion"	4.14
	Model based on neural network, "Gwyddion"	3.93
	Model based on the profile, "RIO"	3.95

the substrate, the implantable material, and the mode of implantation (doping dose, etc.) are identical, and the difference lies in the geometry of the surface, i.e., two different implanted ions require two neural models.

12.5 Conclusions

This research has shown that, despite the complexity of the process of ionic implantation, it is quite possible to be predicted by the models underlying the program "RIO." This software allows you to predict the concentration profiles and the penetration depth of the target and related ions in terms of their implantation, diffusion, and deposition in the form of a film. These opportunities offer the promise of an accurate selection of the operating mode setting without first conducting experiments.

Accumulated experimental results increase the level of learning and, therefore, the accuracy of the simulation results with the help of neural networks. Combining computer software and neural network modeling, it is possible to predict not only the results of ionic implantation but also the textural characteristics of the samples, which allows you to control the mechanical, physical, chemical, optical, and other properties of the implants. Taking into account the unbounded localization of reduced modeling, its application covers the macro- and microelement base of catalytic heat-exchanging devices, precision and tribological pairs of products with special requirements for strength and durability, etc.

References

1. Bobyl' AV, Karmanenko SF (2005) Fiziko-khimicheskiye osnovy tekhnologii poluprovodnikov. Puchkovyye i plazmennyye protsessy v planarnoy tekhnologii: Ucheb. posobiye. Izd-vo Politekhn. un-ta, Sankt-Peterburg
2. Brouday I, Merrey D (1985) Fizicheskiye osnovy mikrotekhnologii: Per. s angl. Mir, Moskva
3. Kurnosov AI, Yudin VV (1979) Tekhnologiya proizvodstva poluprovodni-kovykh priborov i integral'nykh mikroskhem: ucheb. Posobiye. Vyssh. shk, Moskva
4. Bernd S, Klaus W (2012) Materials processing. In: Schmidt B, Wetzig K (eds) Ion beams in materials processing and analysis. Springer, Vienna, pp 117–251
5. Dearnaley G (1975) Ion implantation in metals. In: Ziegler JF (ed) New uses of Ion accelerators. Springer, New York, pp 283–322
6. Gott YV, Yavlinskiy YN (1973) Vzaimodeystviye medlennykh chastits s veshchestvom i diagnostika plazmy. Atomizdat, Moskva
7. Khirvonen DK (1985) Ionnaya implantatsiya. Metallurgiya, Moskva
8. Zelenskiy VF, Neklyudov IM, Chernyayeva TP (1988) Radiatsionnyye defekty i raspukhaniye metallov. Naukova dumka, Kiyev
9. Pogrebnyak AD, Remnev GY, Chistyakov SA et al (1999) Modifikatsiya svoystv metallov pod deystviyem ionnykh puchkov. Izv VUZov Fizika 1:52–65
10. Rissel H, Ruge I (1983) Ionnaya implantatsiya. Nauka Glavnaya redaktsiya fiziko-matematicheskoy literatury, Moskva
11. Kosterin KV (1995) Raspyleniye tverdykh tel ionnoy bombardirovkoy: adatomnyye mekhanizmy i vozmozhnaya rol' fononov. Fizika i khimiya obrabotki materialov 3:43–48
12. Bobrovskiy SM (1998) Povysheniye ekspluatatsionnykh svoystv rezhushchego instrumenta metodom ionnoy implantatsii. Dissertation, Tol'yatti
13. Belyy AV, Dogodeyko VG, Makushok YM et al (1989) Progressivnyye metody izgotovleniya metallorezhushchego instrumenta. BELNIITI, Minsk
14. Inzartsev YuV (2002) Povysheniye ekspluatatsionnykh kharakteristik instrumenta metodom ionnoy implantatsii azota. Dissertation, Tul'skiy Gosudarstvennyy Universitet
15. Boyko VI, Kadlubovich BY, Shamanin IV (1991) Vliyaniye defektnosti struktury metallov na profil' rasperdeleniya vnedrennykh ionov. Fizika i khimiya obrabotki materialov 3:56–61
16. Val'dner VO, Kvyadras VP (1987) Vliyaniye nikoenergeticheskoy implantatsii na mekhanicheskiye svoystva splavov titana i zheleza. Fizika i khimiya obrabotki materialov 2:18–24
17. Kalin BA (2001) Radiatsionno-puchkovyye tekhnologii obrabotki konstruktsionnykh materialov. Fizika i khimiya obrabotki materialov 4:5–16
18. Tyumentsev AN, Korotaev AD, Bugaev SP (1994) Structural—phase transformations in metal alloys during high-dose ionic implantation. Russ Phys J 37(5):452–461

19. June KT, Jeong-Gil K, Ho-Young L et al (2014) Modification of optical and mechanical surface properties of sputter-deposited aluminum thin films through ion implantation. Int J Precis Eng Manuf 15(5):889–894
20. Popok VN, Stepanov AL, Odzhaev VB (2005) Synthesis of silver nanoparticles by the ion implantation method and investigation of their optical properties. J Appl Spectros 72 (5):229–234
21. Bertoti I (2012) Nitrogen modified metal oxide surfaces. Catal Today 181:95–101
22. Rautray TR, Narayanan R, Kim K (2011) Ion implantation of titanium based biomaterials. Progr Mater Sci 56:1137–1177
23. Nikonenko VA (2001) Matematicheskoye modelirovaniye tekhnologicheskikh protsessov: modelirovaniye v srede MathCAD, Praktikum. MISiS, Moskva
24. Lindhard J, Scharff M (1961) Energy dissipation by ions in the keV region. Phys Rev 124:128–130
25. Kishinevskiy LM (1962) Secheniye neuprugikh atomnykh stolknoveniy. Izv AN SSSR, Ser fiz 26(11):1410–1414
26. Bubert H (1986) Monte Carlo simulation of ion implantation into solids as a tool for the characterization of surface analytical reference materials. Microchimica Acta 90 (5–6):387–406
27. Antonetti P, Antoniadisa D, Dattona R et al (eds) (1988) MOP-SBIS, Modelirovaniye elementov i tekhnologicheskikh protsessov. Radio i svyaz', Moskva
28. Nevolin VN, Fominski VY, Gnedovets AG et al (2007) Peculiarities of pulsed ion implantation from a laser plasma containing multiply charged ions. Tech Phys 52(11):1475–1482
29. Particle interactions with matter (2008) Web-site of James F. Ziegler. http://www.srim.org/SRIM/SRIMLEGL.htm. Accessed 20 Oct 2014
30. Chernyy AA, Mashchenko SV, Goncharov VV et al (2014) Nizko-temperaturnaya nanomodifikatsiya poverkhnosti nerzhaveyushchey stali ionnymi puchkami. Khimiya, fizika ta tekhnologiya poverkhni 5(2):190–196
31. Gwyddion (2004) Free SPM (AFM, SNOM/NSOM, STM, MFM, ...) data analysis software. http://gwyddion.net/. Accessed 20 Oct 2014

Chapter 13
Transport Properties of the Dirac-Weyl Electrons Through the Graphene-Based Superlattice Modulated by the Fermi Velocity Barriers

A.M. Korol, N.V. Medvid, and S.I. Litvynchuk

13.1 Introduction

Graphene and the graphene-based structures draw the attention of researchers in recent years. It is explained by the unique physical properties of graphene and also by good prospects of its use in nanoelectronics (see, e.g., [1, 2]). It is convenient to operate the Dirac-Weyl fermions in graphene by means of the external electric and magnetic fields, and a lot of publications are devoted to the corresponding problem for this reason. Recently, one more way of controlling the electronic properties of the graphene structures, namely, by means of the spatial change of the Fermi velocity, was offered [3–9]. Some ways of fabrication of structures in which the Fermi velocity of quasiparticles is spatially dependent value were approved. This achievement opens new opportunities for receiving nanoelectronic devices with desirable transport properties.

It is known that the solution of this problem can be promoted in no small measure by use of the superlattices. This explains the emergence of a lot of publications in which the charge carriers' behavior in graphene superlattices of various types is investigated; these SL include the strictly periodic, the disordered, and the quasiperiodic ones and SL with barriers of various nature—electrostatic, magnetic, and Fermi velocity barriers. (As the last, we understand the areas of graphene where quasiparticles have different Fermi velocity, smaller or bigger than that in the pristine graphene.) The authors of the papers cited above considered the low-energy ranges and focused mainly on the analysis of the dependence of the

A.M. Korol (✉)
Laboratory on Quantum Theory in Linkoping, ISIR, P.O. Box 8017, Linkoping 580, Sweden

National University for Food Technologies, 68, Volodymyrska Street, Kyiv, Ukraine
e-mail: korolam@ukr.net

N.V. Medvid • S.I. Litvynchuk
National University for Food Technologies, 68, Volodymyrska Street, Kyiv, Ukraine

O. Fesenko, L. Yatsenko (eds.), *Nanoplasmonics, Nano-Optics, Nanocomposites, and Surface Studies*, Springer Proceedings in Physics 167,
DOI 10.1007/978-3-319-18543-9_13

quasi-electron transmission rates and conductance on the angle of incidence of charge carriers on a lattice. In this work, we study the features of the transmission spectra of the Dirac-Weyl fermions through a SL with Fermi velocity barriers in a wide energy range, taking into consideration the action of the external electric field.

13.2 Model and Formulae

Consider the one-dimensional graphene superlattice in which regions with various values of the Fermi velocity are located along the $0x$ axis. The areas for which the Fermi velocity is equal to that as in a pristine graphene $\boldsymbol{\upsilon}_{\mathrm{w}} = \boldsymbol{\upsilon}_0$ are replaced in turn by regions where the Fermi velocity υ is bigger or smaller than υ_0.

We also assume that the external electrostatic potential can act on the barrier areas. Thus, this paper deals with the SL with barriers of dual nature. The key quantity that affects the transport properties of the system considered is the transmission coefficient T of the quasi-electrons through the SL.

To calculate it, we turn to the massless Dirac-Weyl-type equation which takes into consideration that the Fermi velocity is dependent on a spatial coordinate $\vec{r}$, i.e., $\vec{v} = \vec{v}\left(\vec{r}\right)$, so the quasiparticles submit to the following equation:

$$-i\hbar\vec{\sigma}\cdot\nabla\left[\sqrt{\vec{v}\left(\vec{r}\right)}\varphi\left(\vec{r}\right)\right]\sqrt{\vec{v}\left(\vec{r}\right)} = E\varphi\left(\vec{r}\right) \tag{13.1}$$

where $\vec{\sigma} = \left(\sigma_x, \sigma_y\right)$ the Pauli two-dimensional matrix, $\varphi\left(\vec{r}\right) = \left[\varphi_{\mathrm{A}}\left(\vec{r}\right), \varphi_{\mathrm{B}}\left(\vec{r}\right)\right]^{\mathrm{T}}$ the two-component spinor, and T the transposing symbol. Introducing an auxiliary spinor $\Phi\left(\vec{r}\right) = \sqrt{\vec{v}\left(\vec{r}\right)}\varphi\left(\vec{r}\right)$, one can rewrite equation (13.1) as follows:

$$-i\hbar\vec{v}\left(\vec{r}\right)\vec{\sigma}\cdot\nabla\Phi\left(\vec{r}\right) = E\Phi\left(\vec{r}\right) \tag{13.2}$$

Assume that the external potential consists of the periodically repeating rectangular velocity barriers along the axis $0x$ and the potential is constant in each jth barrier. In this case, using the translational invariance of the solution over the $0y$ axis, it is possible to receive from equation (13.2)

$$\frac{d^2\Phi_{\mathrm{A,B}}}{dx^2} + \left(k_j^2 - k_y^2\right)\Phi_{\mathrm{A,B}} = 0, \tag{13.3}$$

where indices A and B relate to the graphene sublattices A and B, respectively, $k_j = Ev_j$, and measurement units $\hbar = \upsilon_0 = 1$ are accepted. If we represent the

solution for eigenfunctions in the form of the plane waves moving in the direct and opposite direction along an axis Ox, we derive

$$\Phi(x) = \left[a_j e^{iq_j x} \begin{pmatrix} 1 \\ g_j^+ \end{pmatrix} + b_j e^{-iq_j x} \begin{pmatrix} 1 \\ g_j^- \end{pmatrix} \right] \tag{13.4}$$

where $q_j = \sqrt{k_j^2 - k_y^2}$ for $k_j^2 > k_y^2$ and $q_j = \mathrm{i}\sqrt{k_y^2 - k_j^2}$ otherwise and $g_j^{\pm} = \frac{\pm q_j + \mathrm{i}k_y}{Ev_j}$, the top line in (13.4) pertains to sublattice A and the lower one to sublattice B.

Meaning that the Fermi velocity depends only on coordinate x, i.e., $v\left(\vec{r}\right) = v(x)$, it is possible to receive the boundary matching condition from the continuity equation for the current density as follows:

$$\sqrt{v_b}\Phi\left(x_{bw}^-\right) = \sqrt{v_w}\Phi\left(x_{bw}^+\right) \tag{13.5}$$

where indices b and w relate to a barrier and a quantum well, respectively, and x_{bw} is the coordinate of the barrier-well interface. The coefficient of transmission of quasi-electrons through the superlattice T(E) is evaluated by means of a transfer matrix method. Energy ranges, for which the coefficient of electron transmission through the lattice is close to unity, form the allowed bands, while band gaps correspond to values $T \ll 1$. Since the specified procedure of obtaining the value of T(E) was described in literature repeatedly, we have the opportunity to proceed with analyzing the results obtained.

13.3 Results and Discussion

As is well known, in practice, you can create sections of graphene with the values of the Fermi velocity v less ($\zeta = v/v_0 < 1$) or larger than v_0 ($\zeta > 1$). Normally, these two cases are considered separately. But first, we want to draw attention to one feature of the transmission spectra common for both cases $\zeta < 1, \zeta > 1$, which at the same time distinguishes spectra for the SL with the velocity barriers from those of other graphene superlattices. The thing is that the spectra of the SL with the velocity barriers reveal the property of periodicity over the entire range of energy. Figure 13.1a shows the dependence of log $T(E)$ for the SL modulated with the velocity barriers for the following parameters: $\zeta = 2$, the barrier width $b = 0.5$, and the quantum well width $w = 2$.

Periodic dependence of the energy spectra is explained by the fact that the velocity barriers are dependent on energy [3]. If we make an analogy between tunneling of quasiparticles in electrostatic barrier and tunneling through a velocity barrier, for the potential of the last, it is necessary to write down

$$U(E) = E - E/v_{\mathrm{F}} \tag{13.6}$$

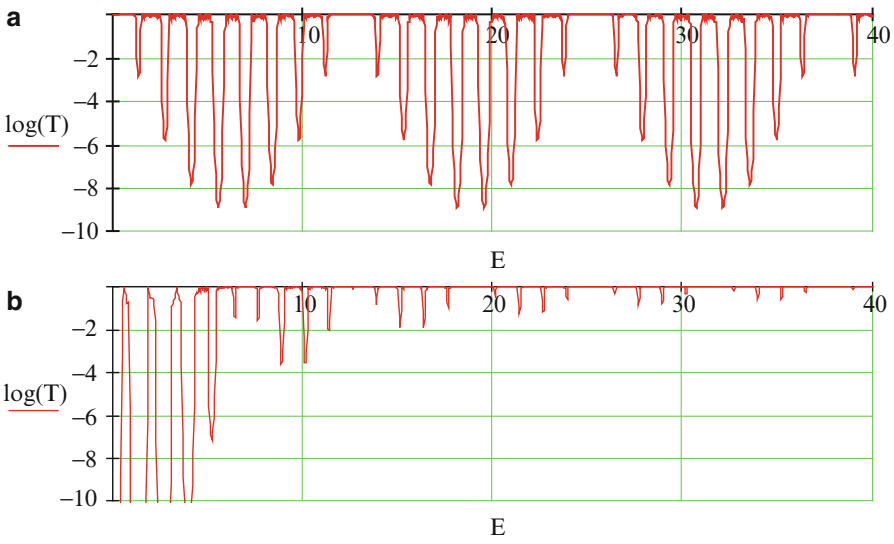

Fig. 13.1 Transmission spectra for two different kinds of superlattices: (**a**) SL modulated with velocity barriers, (**b**) SL modulated with the gap

In other words, expressions for the transmission coefficient T in the specified cases coincide if the condition (13.6) is satisfied. This formula explains the fact that spectra of dependence of T(E) for SL with the velocity barriers are periodic over all energy scale.

Also for comparison, Fig. 13.1b shows the dependence of $\log T$(E) for the SL, composed of portions of gap and gapless graphene which alternately succeed each other. The parameters are 1, the gap width $\Delta = 1$, $b = 0.5$, and $w = 2$. (Calculation is made on the basis of our previous works: [10, 11].) We see that the structure of the second spectrum is also repeated periodically on the energy axis (this fact hasn't been noted in the literature yet), but in this case, the band gaps become narrower with the energy increasing, so that the transmission coefficient T approaches asymptotically to unity. Note that the shrinking of gaps occurs very rapidly. Parameters for the spectra in Fig. 13.1 are chosen so as to show that their structure for the graphene SL of different nature may be identical.

We now turn to a brief analysis of the spectra for the SL with the velocity barriers for the case $\zeta < 1$. There are gaps in the spectra when ζ differs from unity, i.e., when the velocity barriers are present. Their width depends, naturally, on the difference in the values of v and v_0 (v–$v_0 = \Delta v$): when Δv differs a little from zero, narrow gaps are observed and they widen with Δv increasing. We emphasize that the occurrence of gaps takes place at the value of $k_y = 0$, i.e., at normal incidence of the quasi-electrons on a lattice—unlike the case of the SL with the electrostatic barriers. And the electrons with $k_y = 0$ make the main contribution to the conductance in accordance with the known Landauer-Buttiker formula. Interestingly, the increase of Δv not only leads to gap expansion but also to increase of their number

in a certain energy range. In general, the spectra corresponding to $\zeta < 1$ demonstrate a set of narrow forbidden and allowed energy bands.

Turn next to the case of $\zeta > 1$. The first step is to answer the question of whether the velocity barriers are effective sufficiently. Here, we mean that since this paper deals with a finite number of periods, it is obvious that, for the practical use of forbidden bands in the transmission spectra, it is necessary that not only their presence but also values of T must be sufficiently small for the corresponding energy gaps (specially in the transistor-type devices). Calculations show that for the double-barrier structure ($N = 2$) with the value of $\zeta = 1.5$, minimum value $T_{\min}$ is approximately equal to 0.5; for the SL with $N = 10$, we have $T_{\min} \approx 10^{-4}$; if $\zeta = 2$, then $T_{\min} \approx 0.1$ for $N = 2$, while for $N = 10, T_{\min} \approx 10^{-9}$ (all figures are obtained for typical values of b and w). Thus, it is clear that the velocity barriers are sufficiently effective in the case of practically used parameters of the SL studied.

As well as for $\zeta < 1$, there are gaps in the spectra if $\zeta > 1$, the width of which increases with increasing ζ. Generally, the spectra also are irregular, but for some sets of the parameter values, they are regular and symmetrical with respect to a certain point on the energy axis. Thus, there is a large variety of shapes of the spectra, i.e., of the configurations of the forbidden and allowed bands. The width of the gaps may be considerably larger than in the case of $\zeta < 1$. Spectra of regular shape may serve as the specific electrical filters for the charge carriers. On the other hand, they are convenient for analysis, so we pay special attention to them (several such spectra are shown in Fig. 13.1b). Periods of these spectra can be equal to several units as well as to several tens of units of energy used in the system of units adopted in this paper. Note that the coefficient T is equal to unity at low energies for arbitrary values of the SL parameters, i.e., the effect of Klein tunneling is observed for the SL modulated by the Fermi velocity barriers.

Behavior of charge carriers in graphene structures can be conveniently controlled by an external electrostatic potential, so it is natural to consider its effect on the motion of the Dirac-Weyl fermions in a given problem. Suppose that there is the external potential U in the SL areas for which $\zeta \neq 1$. Its effect on the transmission spectra of quasi-electrons is illustrated in Fig. 13.2, which shows the spectra for several values of U, $U = 0$ (Fig. 13.2a), $U = 2$ (Fig. 13.2b), and $U = 4.5$ (Fig. 13.2c), and the other parameters, $\zeta = 2$, $b = 1$, and $w = 0.5$. We see that with the "inclusion" of the potential U, additional gaps appear whose width increases with U increasing. At the same time, the restriction of the initial gaps (i.e., those which are derived from the velocity barriers) takes place. This confirms the observation done in the paper [8] for simple models that the "switching" of the potential U can in principle lead to the broadening or narrowing of the allowed bands of energies. Note also that the displacement of gaps on the energy axis under the influence of the potential U is observed.

The spectra analyzed reveal the periodic nature of their dependence on the value of U. For example, the spectrum for a value of $U \approx 1.5$ repeats its shape when $U \approx 7.5$; so the spectra period is approximately equal to 6 in the adopted system of units of measurement.

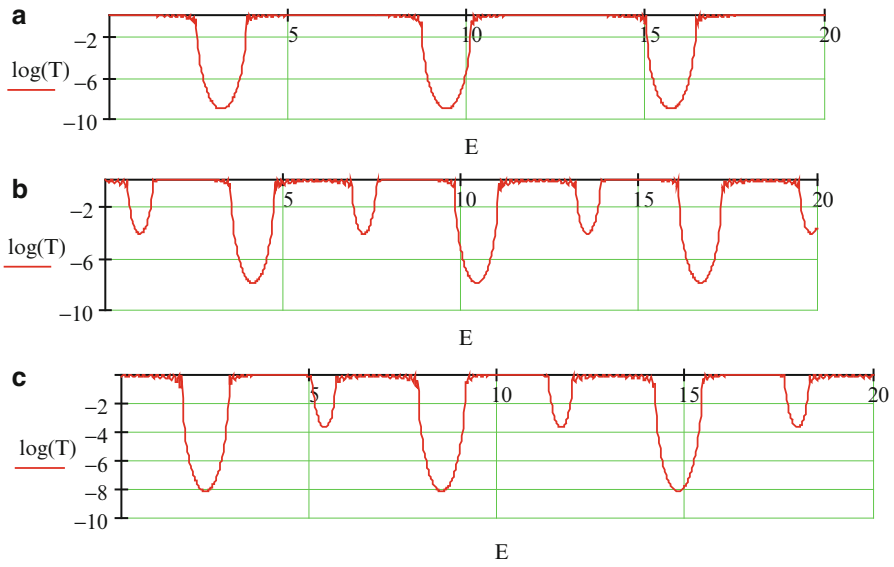

Fig. 13.2 Transmission spectra for various values of the electrostatic potential $U = 0, 2, 4.5$ for **a**, **b**, **c** respectively

13.4 Conclusion

We show that a set of the forbidden bands in the transmission spectra of the Dirac-Weyl quasi-electrons emerges due to Fermi velocity barriers of the graphene superlattice investigated. The magnitude of the transmission rates is strongly affected by small changes in the SL parameter values; it depends also on the external electrostatic potential essentially.

Spectra demonstrate the rich variety of configurations (patterns) of the allowed and forbidden bands' location, and, for some special parameter values, they expose the regular character, symmetrical with respect to a certain point.

Additional possibility for controlling the transmission spectra of quasi-electrons through the superlattice considered (with the velocity barriers) is the use of an external electrostatic potential of different values in different barriers.

Varying the parameters of the system considered, it is possible to change the spectra flexibly; so the results of this work may be useful for applications in the graphene-based electronics.

References

1. Geim AK, Novoselov KS (2007) The rise of graphene. Nat Mater 6:183
2. Castro Neto AN, Guinea F, Peres NMR, Novoselov KS, Geim AK (2009) The electronic properties of graphene. Rev Mod Phys 81:109

3. Raoux A, Polini M, Asgari R, Hamilton AR, Fasio R, MacDonald AH (2010) Velocity-modulation control of electron-wave propagation in graphene. Phys Rev B 81:073407, arXiv:0912.2608v1 [cond-mat.mes-holl]
4. Concha A, Tešanović Z (2010) Effect of a velocity barrier on the ballistic transport of Dirac fermions. Phys Rev B 82:033413
5. Krstajic PM, Vasilopoulos P (2011) Ballistic transport through graphene nanostructures of velocity and potential barriers. J Phys Condens Matter 23:000000(8pp)
6. Liu L, Li Y-X, Liu J (2012) Transport properties of Dirac electrons in graphene based double velocity-barrier structures in electric and magnetic fields. Phys Lett A 376:3342–3350
7. Wang Y, Liu Y, Wang B (2013) Resonant tunneling and enhanced Goos-Hänchen shift in graphene double velocity barrier structure. Physica E 53:186–192
8. Sun L, Fang C, Liang T (2013) Novel transport properties in monolayer graphene with velocity modulation. Chin Phys Lett 30(4):047201
9. Yuan JH, Zhang JJ, Zeng QJ, Zhang JP, Cheng Z (2011) Tunneling of Dirac fermions in graphene through a velocity barrier with modulated by magnetic fields. Physica B 406:4214–4220
10. Korol AN, Isai VN (2013) Energy spectrum of the graphene-based Fibonacci superlattice. Phys solid state 55:2596–2601
11. Korol AN (2014) Transmission spectra of electrons through the Thue-Morse graphene superlattice. Low Temp Phys 40:324–329

Chapter 14
Study of the Dynamics of Formation of Spatial Nanostructures

A.A. Dolinsky, A.A. Avramenko, A.I. Tyrinov, and T.L. Grabova

Nomenclature

b_0	Equilibrium values of the valence lengths
$\mathbf{e}_{ij}$	Unit vector directed from particle j to particle i
F	Forces acting on a particle
$K_\mathrm{b}, K_\vartheta, K_\Phi$	Respective force constants
m	Particle mass
q	Partial charge of particle
r	Distance between the particles
r_c	Clipping radius at which $\omega = 0$
U	Potential energy
x, v	Position and velocity of a particle, respectively
γ	Coefficient of dissipative forces
δ	Scale factor of random forces
θ	Random variable with average value is 0 and values between 0 and 1
κ	Torsion barrier multiplicity
π	Scale factor of conservative forces
χ	Phase shift
ω	Weight function, which depends on the distance between the particles
ϑ_0	Equilibrium values of angles
ϑ	Current values of angles
ε^*	Well depth

A.A. Dolinsky • A.A. Avramenko • A.I. Tyrinov • T.L. Grabova (✉)
Institute of Engineering Thermophysics, National Academy of Sciences of Ukraine,
2a, Zhelyabov Street, Kyiv 03680, Ukraine
e-mail: htplab@ukr.net

O. Fesenko, L. Yatsenko (eds.), *Nanoplasmonics, Nano-Optics, Nanocomposites, and Surface Studies*, Springer Proceedings in Physics 167,
DOI 10.1007/978-3-319-18543-9_14

ε_0	Medium permittivity
σ_{ij}	Distance at which the interaction energy becomes equal to zero

Superscripts

n	Time step

Subscript

C–C, C–S	Colloid–colloid and colloid–liquid, respectively
i, j	Numbers of particles

14.1 Introduction

The application of discrete pulse input of energy (DPIE) thermal technologies is promising for the formation of biological entities, organic and inorganic sorbents, gel and paste systems, and other colloidal-disperse systems used in various branches of industry [1, 2]. The formation of colloidal aggregates, clustering of micelles, and nanoparticles play an important role in the creation of new materials, biological entities with unique thermal physical, physicochemical, and functional properties. Important aspect that affects the properties of colloidal systems is their stability [3]. The complexity of the evaluation of experimental samples of colloidal structures is the requirements to use expensive equipment based on optical methods (ultramicroscopy, nephelometry, turbidimetry). Different methods for the numerical simulation of nano (1...100 nm) and mesoscale (100 nm...100 μm) processes are used for the study of structure formation in the colloid systems.

The results of numerical simulation of heterogeneous media, based on the Molecular Dynamics (MD) method and Dissipative Particle Dynamics (DPD) method, are in [4–7]. There is aggregation of colloidal particles (CP) in various structures as a result of colloidal interaction. Numerical simulation allows us to observe the generation of the spherical and rod-shaped micelles and their formation in stable structures.

The difference between spatial and time scales of the components of the investigated medium is the main problem in the modeling of colloid structure formation. For example, the water molecule has a diameter of about 0.3 nm in the water colloidal solution with particle size of 10 nm. Consequently, the difference in spatial scale is significant. It is very significant for time scales due to the difference in the particles velocity (water molecules and colloid particles).

DPD method is particularly suited to simulate the liquid behavior considering a liquid dispersion medium in colloidal systems, not as a set of molecules, and as a set

of liquid droplets (soft particles), comparable in size to the colloidal particles. This allows to equal system scales while maintaining the accuracy of the results. However, the drawback of the DPD method is the absence of attracting forces, the presence of which makes for colloidal structures to be self-organized. In contrast to the DPD method, used for mesoscale calculations, MD method is based on the Lennard-Jones potential and, therefore, takes into account the forces of repulsion and attraction between simulated particles. MD method is used for simulation phenomena on the atomic scale. However, there are the results of simulation meso- and even macroscale phenomena on the basis of MD method in [8]. Scaling MD method allowed to obtain good results in the calculation of granular flows [9].

These results show that MD method with Lennard-Jones potential to describe the interactions between colloidal particles and liquid is more preferable to use. Due to it, there is the opportunity to simulate the attracting forces between the liquid and colloidal particles. It is possibly easy to control the interaction by changing of Lennard-Jones well depth, taking into account that both the colloid–colloid and colloid–liquid particle interactions are represented by a single formula. This approach makes it possible to calculate self-organization of the micelles and their aggregation.

A two-level simulation method of colloidal structures combining MD and DPD methods is considered in this paper.

14.1.1 Mathematical Model

According to the MD method, molecule is treated as a system of particles that interact with each other with a given interaction potential. In mechanics the state of N system particles at the time t is uniquely determined by the vector coordinates $x = \{x_i(t)\}$ and velocities $\{v_i(t)\}$ of the particles. The state of the system at any time t is described by $3N$ Newton's equations

$$m_i \frac{d^2 x_i}{dt^2} = F_i(x), \quad i = 1, 2, \ldots, 3N, \tag{14.1}$$

$$F_i(x) = -\frac{\partial U(x)}{\partial x_i}, \tag{14.2}$$

$U(x)$—potential energy, which depends on the relative positions of all atoms, is electromagnetic, and usually given as a sum of contributions—valence (covalent) and nonvalence interaction:

$$U = U_\mathrm{b} + U_\vartheta + U_\phi + U_\omega + U_\mathrm{LJ} + U_\mathrm{el}, \tag{14.3}$$

where interaction modes: U_b is chemical bonds; U_ϑ is valence angles; U_ϕ is torsion angles; U_ω is plain groups; U_LJ is van der Waals interactions; and U_el is electrostatic bonds.

Valence interaction occurs between the atoms of one molecule during the formation of the chemical bond and is described by potential

$$U_{\mathrm{b}} = \frac{1}{2}\sum_{b} K_{\mathrm{b}}(r - b_0)^2, \tag{14.4}$$

where the summation is over all the chemical bonds.

Valence angles form potential described by the equation:

$$U_{\vartheta} = \frac{1}{2}\sum_{\vartheta} K_{\vartheta}(\vartheta - \vartheta_0)^2. \tag{14.5}$$

Energy of torsion interactions (rotation of atomic groups around single chemical bonds) and potentials appropriate to plane groups are given as the same view of potential:

$$U_{\phi} = \sum_{\phi} K_{\phi}[\cos(\kappa\phi - \chi) + 1]. \tag{14.6}$$

Van der Waals and electrostatic interactions are nonvalent interactions. Van der Waals interactions between the atoms are described by Lennard-Jones potentials:

$$U_{\mathrm{LJ}} = 4\sum_{i,\,j} \varepsilon^{*}\left(\left(\frac{\sigma_{ij}}{r_{ij}}\right)^{12} - \left(\frac{\sigma_{ij}}{r_{ij}}\right)^{6}\right). \tag{14.7}$$

These forces include orientation forces arising between the molecules, which are permanent dipoles; inductive attraction forces formed between the permanent and induced dipoles; and dispersion forces arising between the instant and induced dipoles. Van der Waals forces are the main reason of the colloidal structure formation and aggregate stability according to DLFO theory (Deriagin, Landau, Fairway, and Overbeck).

Electrostatic interactions are defined by Coolon potential:

$$U_{\mathrm{el}} = \sum_{i,\,j} \frac{q_i q_j}{4\varepsilon_0 r_{ij}}. \tag{14.8}$$

Partial charges on the atoms are not multiples of the electron charge because of the atoms of certain elements, which tend to draw to itself the electron pair of the covalent bond stronger than the atoms of the other elements. ε_0 is medium permittivity.

The DPD method is preferable to use to simulate the behavior of the fluid particles. This method takes into account three types of interaction forces: conservative $\mathbf{F}_{\mathrm{C}}$, dissipative $\mathbf{F}_{\mathrm{D}}$, and stochastic $\mathbf{F}_{\mathrm{C}}$:

$$\begin{aligned}\mathbf{F}_{\mathrm{C}} &= \pi\omega\left(r_{ij}\right)\mathbf{e}_{ij},\\ \mathbf{F}_{\mathrm{D}} &= \gamma m\omega\left(r_{ij}\right)\left(\xi_{ij}\cdot\mathbf{e}_{ij}\right)\mathbf{e}_{ij},\\ \mathbf{F}_{\mathrm{R}} &= \frac{\delta\theta_{ij}}{\sqrt{\Delta t}}\omega\left(r_{ij}\right)\mathbf{e}_{ij},\end{aligned} \tag{14.9}$$

where the expressions (equations) for the dissipative and stochastic forces are related through the fluctuation–dissipation theorem.

It is necessary to use the combination of techniques MD and DPD methods for the calculation of colloid–colloid, colloid–fluid, and fluid–fluid particle interactions as mentioned above. Consequently, two-level mathematical model is convenient to use to describe the colloidal interactions of particle pair. In this model, the interaction forces between the fluid–fluid particles are calculated using DPD method (14.10), since this method most describes the behavior of the fluid medium. To calculate the interactions between the colloid–colloid and colloid–fluid particles, the attractive forces must be considered, since they are responsible for the processes of structure formation. Therefore, the MD method is the most suitable for the calculation (14.3). Since van der Waals forces play the main role in colloidal interactions, the two-level model can be written as [5]

$$F_{ij}^{n}=\begin{cases}\pi_{ij}\omega_1\left(r_{ij}^{n}\right)-\gamma_{ij}m_i\omega_2\left(r_{ij}^{n}\right)\left(\mathbf{v}_{ij}^{n}\cdot\mathbf{e}_{ij}^{n}\right)+\dfrac{\delta_{ij}\theta_{ij}}{\sqrt{\Delta t}}\omega_1\left(r_{ij}^{n}\right), & \text{if } i \text{ and } j \text{ dispercion medium}\\ \dfrac{24\varepsilon_{ij}}{r_{ij}^{n}}\left[\left(\dfrac{\sigma_{ij}}{r_{ij}^{n}}\right)^{6}-2\left(\dfrac{\sigma_{ij}}{r_{ij}^{n}}\right)^{12}\right], & \text{if } i \text{ and } j \text{ colloid}\end{cases} \tag{14.10}$$

and $F_{ij}^{n}=0$ for $r_{ij}>r_c$, where

$$\begin{aligned}&\mathbf{v}_{ij}^{n}=\mathbf{v}_{i}^{n}-\mathbf{v}_{j}^{n},\quad \omega_1\left(r_{ij}^{n}\right)=\frac{3}{\pi r_{\mathrm{c}}^{2}n}\left(1-\frac{r_{ij}^{n}}{r_{\mathrm{c}}}\right),\\ &\omega_2\left(r_{ij}^{n}\right)=\frac{6}{\pi r_{\mathrm{c}}^{2}n}\left(1-\frac{r_{ij}^{n}}{r_{\mathrm{c}}}\right)^{2},\quad \mathbf{e}_{ij}^{n}=\frac{\mathbf{r}_{i}^{n}-\mathbf{r}_{j}^{n}}{r_{ij}^{n}},\quad r_{ij}^{n}=\sqrt{\left(\mathbf{r}_{i}^{n}-\mathbf{r}_{j}^{n}\right)^{2}},\end{aligned} \tag{14.11}$$

where the second formula in (14.10) is obtained from (14.7).

14.1.2 Realization Features of the Two-Level Model

Modeling is performed in dimensionless form since the actual size of the system and the time steps are very small. The initial data becomes dimensionless according to the following scales: the clipping radius of colloid particles is assumed as a linear scale; the colloid particle mass is assumed as the unit of mass, and the time scale is assumed the time of distance of colloid particle equal to its clipping radius. The energies made dimensionless by value of Lennard-Jones potential scaling interactions as colloidal particles with each other and with the fluid droplets. The maximum value of the attractive forces of Lennard-Jones potential is equal to the absolute value of a conservative force in DPD interaction. Thus, the parameters of the interaction of colloid–colloid and colloid–fluid particles will have the same value. Scale factor of the conservative forces responsible for compressible fluid has to be chosen so that the system of fluid particles behaves like a fluid in the mesoscale range. In this case, its value is chosen such that the fluid considered has the compressibility of water. The particle density is chosen such that the number of particles in the clipping radius is approximately equal to 20 [10].

The system integration of equations (14.10) was carried out in a comprehensive way [11]. The "leap-frog" method was used to calculate positions of the particles, and the Adams-Bashforth method was used for the determination of their velocities. The algorithm has a procedure for the conversion of the particle velocities every 10 time steps for system thermostatic control. It is assumed that the colloid particles are uniformly distributed over the computational area at initial time.

14.1.3 Simulation Results

Numerical studies of the colloidal system dynamics have been carried out on the basis of two-level mathematical model described above. The concentration of colloidal particles was 20 %. The calculations were performed on a rectangular lattice with periodic boundary conditions (if the particle leaved the computational area through one of the boundaries, then it came back through the opposite boundary). Several options with different values of the interaction potentials of colloidal particles with each other and with the fluid particles were modeled. Calculations were made before the system energy balancing, to the point where the free energy of the system reached a minimum value.

The configuration of particles after the calculation of the interaction potential ratio $\varepsilon_{C-C}/\varepsilon_{C-S} = 1.1/0.9$ is shown in Fig. 14.1. With this, the values of the potentials are formed mainly by spherical micelles. This is due to the mutual repulsion of the particles, which occurs when the values of the potential interactions ε_{C-C} (colloid–colloid) are greater than 1. At the same time, there is the mutual attraction of the particles (hydrophilic colloid particles) if the values of potential interactions ε_{C-S} (colloid–solvent) are less than 1. In this case, formed spherical micelles, which

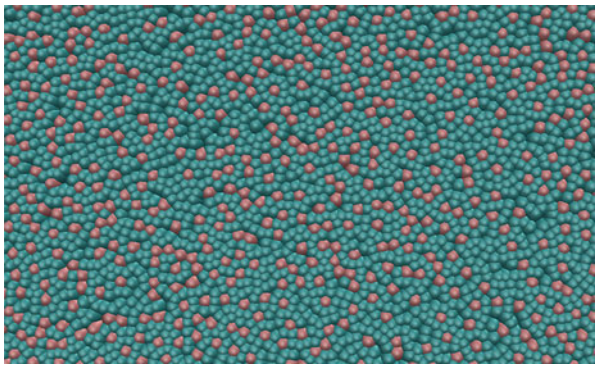

Fig. 14.1 Spherical micelles, formed from single colloid particles (*orange*) are surrounded by fluid particles (*turquoise*)

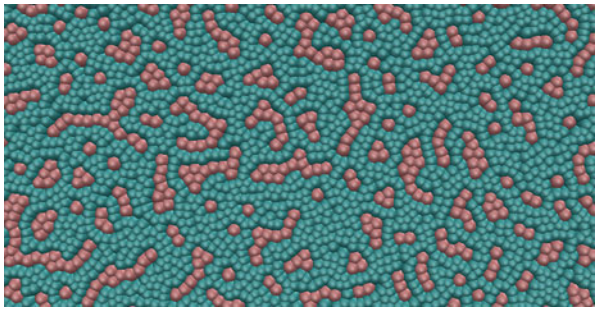

Fig. 14.2 Rod-shaped micelles

are single hydrophilic colloid particles (orange), are surrounded by fluid particles (turquoise).

The inverse options were further investigated. The ratio of the potential interactions $\varepsilon_{C-C}/\varepsilon_{C-S}$ was less than 1. In this case, the attraction forces between the particles are predominant, and the colloid particles are hydrophobic.

The spatial configuration of the particles of the researched system for potentials $\varepsilon_{C-C}/\varepsilon_{C-S} = 0.9/1.3$ is shown in Fig. 14.2. In this form, rod-shaped micelles consisting of colloidal particle chains (orange) are surrounded by fluid particles (turquoise). Such structures are formed due to the predominance of the attraction forces between the non-wetted particles.

The worm-shaped micelles are formed at an intermediate stage with a further increase in the attractive forces between colloidal particles and simultaneous increase of their hydrophobicity (potential interactions $\varepsilon_{C-C}/\varepsilon_{C-S} = 0.8/1.4$) that over time (in the equilibrium state) are transformed into globular structure. These simulated particle configurations are shown in Figs. 14.3 and 14.4, respectively.

The results of numerical calculations based on the two-level model of colloidal interactions with the experimentally determined structure of the colloidal system are compared to verify the proposed method. Aerosil A-175® (Ukraine manufactured) nonporous silica (SiO_2) with specific surface area (175 m^2/g) and spherical particles with a size of 10. . .40 nm is taken as a model hydrophilic colloid particles. Water is taken as a model fluid. The choice of such model system is

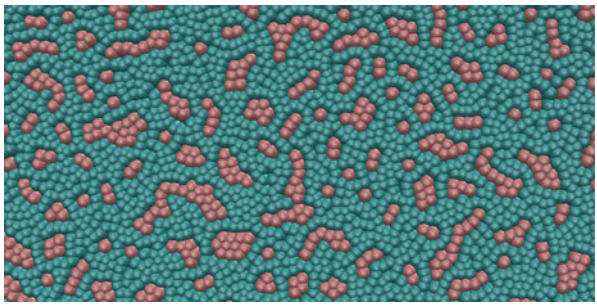

Fig. 14.3 Configurations worm-shaped structures in the intermediate stage of formation

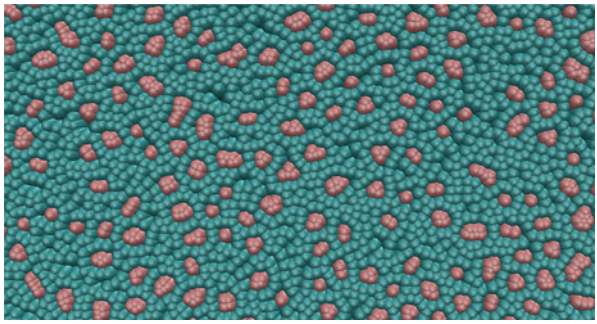

Fig. 14.4 The globular structure of the colloidal particles

dictated by the wide practical use: sorbents, fine forms, gels, paint protection, and other structured systems.

The researched system is obtained by a single passage through the disk-cylinder apparatus AP-3000, by realizing the DPIE principle [2]. The frequency of the generated pulses reaches 3.5 kHz, the shear rate—up to 200×10^3 s^{-1}, the average circumferential speed = 17 m/s in AP-3000 apparatus with 4 stator–rotor pair.

The model system microstructure (see Fig. 14.5a), which after treatment has been in static conditions before the end of structure formation process, was studied using an optical method microscope Zeiss Axio Imager Z1. The configuration of the particles, obtained by numerical simulation is shown in Fig. 14.5b. It can be seen that the experimental and theoretical structures that contain clearly distinguishable globular structure of colloidal particles are quite good correlated. This correlation makes it possible to use the proposed model for the analysis of processes of colloidal structure formation.

14.2 Conclusions

The colloidal structure form and its hydrophobic or hydrophilic nature depends on the interaction parameter ratio $\varepsilon_{CP-CP}/\varepsilon_{CP-SP}$ of colloidal particles (CP) and solvent (SP).

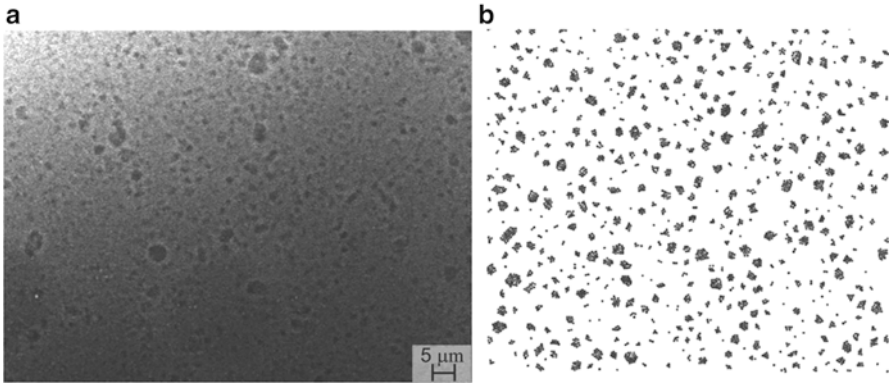

Fig. 14.5 Globular structures in the "Aerosil A-175®—Water" system: (**a**) photo of structure (640 times larger scale), (**b**) calculated configuration of particles

Spherical micelles are dominant in case of prevailing repulsive forces between the hydrophilic colloidal particles ($\varepsilon_{CP-CP} > 1$; $\varepsilon_{CP-SP} < 1$) in the resulting structure.

Rod-shaped micelles consist of the linear arrangement colloidal particles surrounded by fluid particles. They are formed when the hydrophobic colloid particles are attracted to each other ($\varepsilon_{CP-CP} < 1$; $\varepsilon_{CP-SP} > 1$). Worm-shaped structures are formed with further increase in the attraction forces and further-globular.

Two-level method quite well describes the processes of colloidal structure formation that follows from the comparison of the experimental and theoretical results.

The proposed method is appropriate for prediction and assessment of the properties of functional colloidal systems.

References

1. Dolinsky AA, Basok BI, Nakorchevsky AI (2001) Effervescing adiabatic flows. Theory, experiment, technology use. Naukova dumka, Kiev, p 207
2. Dolinsky AA, Grabov LN, Grabova TL (2012) DPIE method in innovative technologies and heat-mass exchange equipment. Ind Heat Eng 34(3):18–30
3. Witharana S, Chen H, Ding Y (2011) Stability of nanofluids in quiescent and shear flow fields. Nanoscale Res Lett 6:231–236
4. Dzwinel W, Yuen LA, Boryczko K (2002) Mesoscopic dynamics of colloids simulated with dissipative particle dynamics and fluid particle model. J Mol Model 8:33–43
5. Dzwinel W, Yuen LA (2000) A two-level, discrete particle approach for large-scale simulation of colloidal aggregates. Int J Mod Phys C 11(5):1037–1061
6. Dzwinel W, Yuen LA, Boryczko K (2006) Dridging diverse physical scales with the discrete-particle paradigm in modeling colloidal dynamics with mesoscopic features. Chem Eng Sci 61:2169–2185
7. Dzwinel W, Yuen DA (2000) A two-level, discrete-particle approach for simulating ordered colloidal structures. J Colloid Interface Sci 225:179–190

8. Dzwinel W, Alda W, Kitowski J, Moscinski J, Wcislo R, Yuen D (1995) Macro-scale simulation using molecular dynamics method. Mol Simul 15:343–360
9. Herrmann J (1999) The importance of computer simulations of granular flow. Comput Sci Eng 1:72–73
10. Espanol P, Serrano M (1999) Dynamical regimes in the dissipative particle dynamics model. Phys Rev E Stat Phys Plasmas Fluids Relat Interdiscip Topics 59:6340
11. Dzwinel W, Yuen LA (2000) Matching macroscopic properties of binary fluids to the interactions of dissipative particle dynamics. Int J Mod Phys C 11(1):1–25

Chapter 15
Colloid-Chemical and Nanochemical Processes in Peloids on Basis of Ferrous Clay Minerals

I.G. Kovzun, Z.R. Ulberg, A.V. Panko, V.A. Prokopenko, V.A. Oleinik, and E.M. Nikipelova

15.1 Introduction

Clay-contained peloids (medical muds which role in medical and spa practice is growing permanently) are recent or geologically young organo-mineral fine-dispersed sediments of basins. They are forming as a result of biocolloidal decomposition of flora and fauna with microorganisms and simultaneous micro- and nanostructured reconstruction of inorganic peloid basis as a result of complex biocolloidal (colloid-chemical and biochemical) processes [1–4]. Peloids contain fine- and nanodispersed clay minerals, carbonates, feldspars, quarts, opal, diatomite, microorganisms and microalgae, bioactive organic substances, sulphur and other compounds [3–7]. Medical muds have different properties such as chemical, mineralogical and microbiological composition. Nevertheless, they have almost the same multifunctional physiological and therapeutic influence on living organism. They are wide world used as ingredients of therapeutic and cosmetic compositions. Thus increasing practical use of peloids results in their reserve depletion and decreasing of quality. This problem can be solved as by finding new deposits of medical muds so as by doing systematic physicochemical, colloid-chemical, biocolloidal and medical investigations of peloids from already known and new deposits. Latter should be done for designing scientific basis of making new high effective peloid compositions and its rational use in balneological and medical spheres.

I.G. Kovzun • Z.R. Ulberg • A.V. Panko (✉) • V.A. Prokopenko • V.A. Oleinik
Institute of Biocolloid Chemistry named after F.D. Ovcharenko, NAS of Ukraine,
42, Ak. Vernadskogo Blvd., Kyiv 03680, Ukraine
e-mail: wiz@list.ru

E.M. Nikipelova
Ukrainian Research Institute of Medical Rehabilitation and Balneology, Ministry of Health of Ukraine, 6, Lermontovskiy Lane, Odessa 65014, Ukraine

O. Fesenko, L. Yatsenko (eds.), *Nanoplasmonics, Nano-Optics, Nanocomposites, and Surface Studies*, Springer Proceedings in Physics 167,
DOI 10.1007/978-3-319-18543-9_15

One of the promising ways to solve this global problem is doping of nanodispersed inorganic additives of clays, sorbents and salts into peloids along with complex investigations of influence of such additives on them [3–11]. Recent colloid-chemical and biochemical investigations of peloids with nanoadditives goes in Institute of biocolloid chemistry of National Academy of Sciences of Ukraine in cooperation with Ukrainian Research Institute of Medical Rehabilitation and Balneology (microbiological and physiological researches, valuation of biological activity and anti-inflammatory action of medical muds). These researches involve as long-developed Ukrainian peloids (widespread at the Black Sea and Azov Sea health-resort zone) so as new developed deep-sea (over 2 km) bottom sediments of the Black Sea. It was deduced that bottom sediments of the Black Sea which definitely contain in other seas and oceans (because of common mechanism of pelagic sediment forming) have unique medical properties [4]. However, influence of nanosized additives on occurring in peloids colloid-chemical and nanochemical processes was almost absent. And this was the reason for conducting presented investigations.

15.2 Experimental

The Black Sea deepwater peloid (UA) specimen was taken as an object of colloid-chemical and balneological researches. It was prepared according to recommendations [2, 3]. Analysis of microscopic images of peloid samples (Fig. 15.1) showed that there are particles from 0.1 to 5–10 μm in them. Mineral component of peloids is clay minerals, carbonate decomposition of microorganisms' products (Fig. 15.1a), sulphide formations (central part of Fig. 15.1b) and rests of protozoa crustaceans (Fig. 15.1c). Figure 15.1d shows microphotography of peloid composition with addition of chemically precipitated nano- and microparticles of calcium carbonate. And in Fig. 15.1e there is shown a peloid composition containing nano- and microparticles of calcium carbonate obtained by power-dispersion of initial composition.

Microscopic images were captured on electron microscope PEMU (SELMI, Ukraine) in light field mode. Morphology and chemical composition of specimens were made on scanning electron microscope JSM6490 LV (JEOL, Japan) (3 nm maximum resolution) with INCA ENERGY-450 ("Oxford", England) energy dispersive analysis system. XRD analysis was made on DRON-UM1 (UA) with filtrated CuK_{α} emission and reading rate 1°/min at room temperature. Decryption of XRD data were made using ASTM catalogue. Rheological data were obtained with rotary viscometer Rheotest-2 (Germany), connected with PC [4].

Chemical composition spectral investigation of different parts of peloid on microscopic images have shown the presence of carbonates, oxides of aluminium, silicon, iron and sulphides in broad concentration interval (Table 15.1). Microelemental peloid composition, wt%: 0.015 Mn; 0.003 Ni; 0.0003 Co; 0.03 Ti; 0.008 V; 0.006 Cr; 0.0003 Mo; 0.0006 Nb; 0.02 Zr; 0.005 Cu; 0.002 Pb;

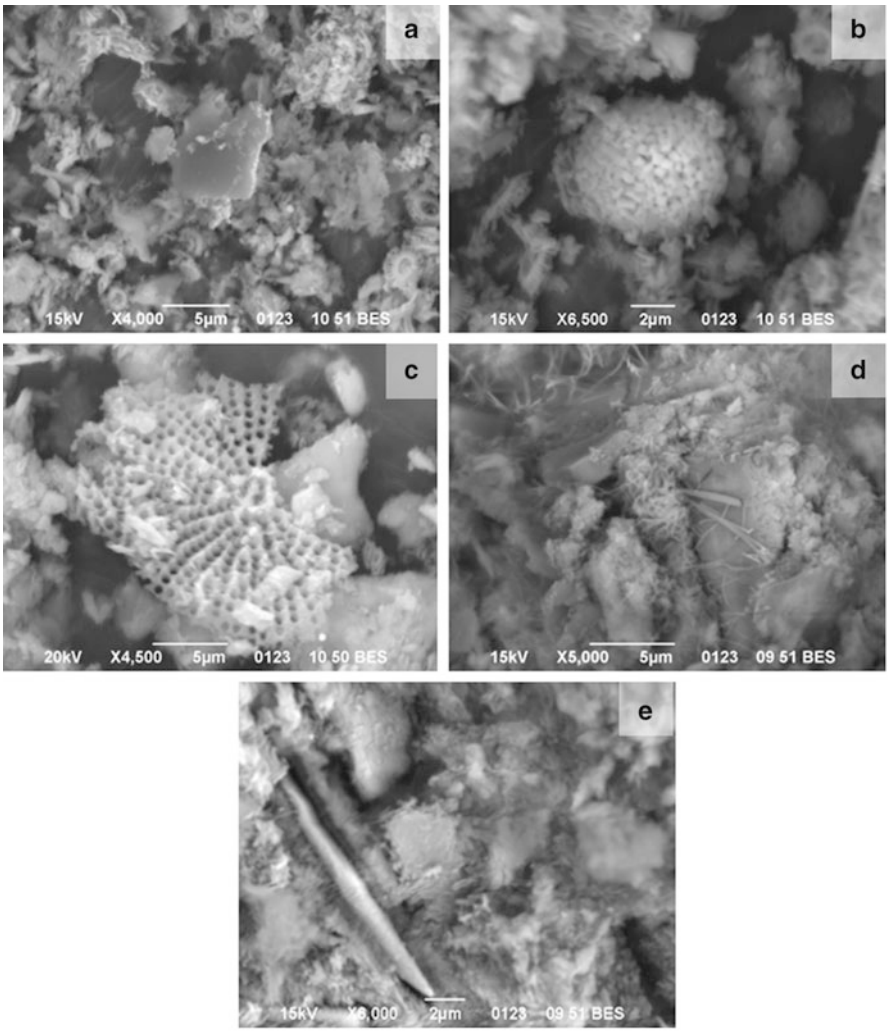

Fig. 15.1 SEM images of peloid samples (**a**–**e**—description is in text)

0.0001 Ag; 0.0001 Bi; 0.006 Zn; 0.0004 Sn; 0.0008 Ga; 0.0003 Be; 0.002 Sc; 0.02 Ce; 0.01 La; 0.003 Y; 0.08 P; 0.005 Li; 0.02 Ba.

Average chemical composition of used peloid, wt%: 54.57 SiO_2; 11.35 Al_2O_3; 5.54 Fe_2O_3; 8.87 CaO; 1.80 MgO; 0.04 MnO; 1.19 Na_2O; 1.86 K_2O; 14.71 LOI (loss on ignition).

On the whole, the investigation of peloids with physicochemical methods [4] showed their full correspondence with medical and spa standards and requirements by its colloid-chemical properties and composition.

Table 15.1 Energy dispersive analysis of peloid specimen in different parts of microscopic image

	Element concentration in different parts of microscopic images, wt%										
Element	1	2	3	4	5	6	7	8	9	10	11
C	19.95	3.95	12.26	21.15	48.80	4.99	17.13	7.60	12.21	12.19	9.23
O	15.04	60.29	61.23	40.66	37.87	60.00	57.71	45.96	57.00	58.76	60.36
Na	–	0.29	2.15	0.36	0.17	1.95	0.65	0.30	0.43	1.29	6.25
Mg	–	0.35	–	0.85	0.29	0.55	0.63	0.23	1.37	1.38	–
Al	–	12.76	4.36	8.37	3.31	8.11	4.26	2.88	6.72	6.27	5.81
Si	0.86	15.29	14.88	15.82	4.68	17.00	15.46	39.13	13.21	13.30	17.51
S	34.82	–	–	–	0.13	–	–	0.39	–	–	–
Cl	–	–	0.24	–	–	–	0.35	–	0.55	0.43	–
K	–	4.52	1.93	5.86	1.33	0.28	0.95	0.99	1.29	2.04	–
Ca	1.36	1.87	2.39	5.36	2.94	5.93	1.48	1.77	2.92	2.38	0.83
Fe	27.01	0.68	0.57	1.58	0.49	1.19	1.37	0.74	4.28	1.96	–
Br	0.95	–	–	–	–	–	–	–	–	–	–
Total	100	100	100	100	100	100	100	100	100	100	100

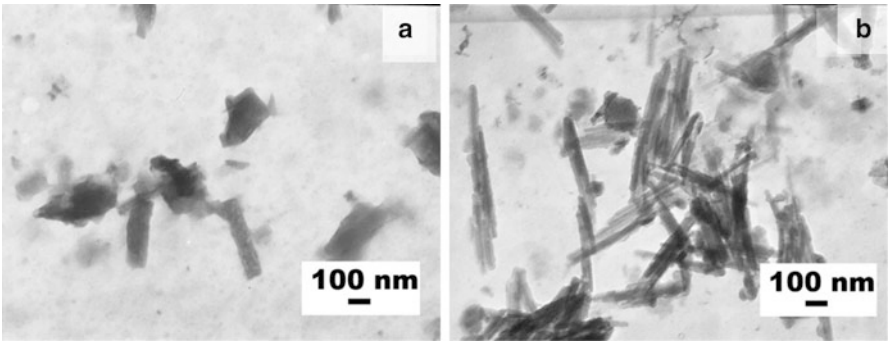

Fig. 15.2 Microphotographs of Cherkassy bentonite (Ukraine) components: montmorillonite (**a**), attapulgite (**b**)

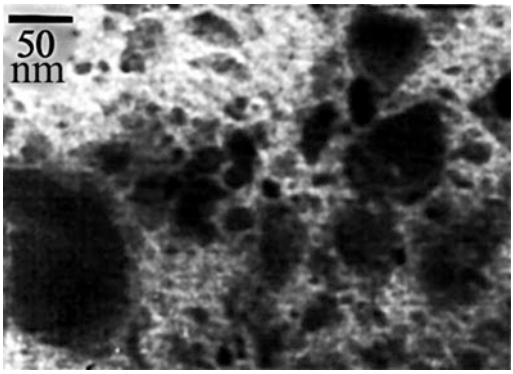

Fig. 15.3 Micrograph of nanoparticles of burnt at 600 °C bentonite with organic precursor

Natural iron-contained bentonite clay (Daschukovka section of Cherkassy deposit, UA) and iron-contained saponite were used as nanoadditives to peloid. They were ultrasonic treated to obtain micro- and nanoparticles (Fig. 15.2) to add them into peloid. Chemical composition of bentonite, wt%: 53.61 SiO_2; 14.02 Al_2O_3; 7.63 Fe_2O_3; 0.96 CaO; 4.43 MgO; 0.39 Na_2O; 0.31 K_2O; 18.61 LOI. Chemical composition of saponite, wt%: 46.73 SiO_2; 5.12 Al_2O_3; 2.76 Fe_2O_3; 23.21 FeO; 3.87 CaO; 11.43 MgO; 0.24 Na_2O; 0.26 K_2O; 13.67 LOI. Bentonite was exposed to thermodestruction at 600 °C (Figs. 15.3 and 15.4) by method [11]. Nanosized calcium carbonate which was used as an additive to peloids was prepared by chemical precipitation according to method [12]. Received particle size was within 20–100 nm (Figs. 15.3, 15.4 and 15.5). Physiological tests of peloid compositions with nanomaterials (Fig. 15.1) were made according to recommendations [13]—testing of composition influence on different systems of healthy animal (white Wistar rats) organism. Hereat, peloid and peloid composition influence on central nervous system (CNS) and liver were tested by making thiopental probe (0.75 mg of sodium thiopental on 100 g of body mass). Falling asleep time (minutes after barbiturate injection) was taken into account, it characterizes the

Fig. 15.4 Micrograph of calcium carbonate nanoparticles

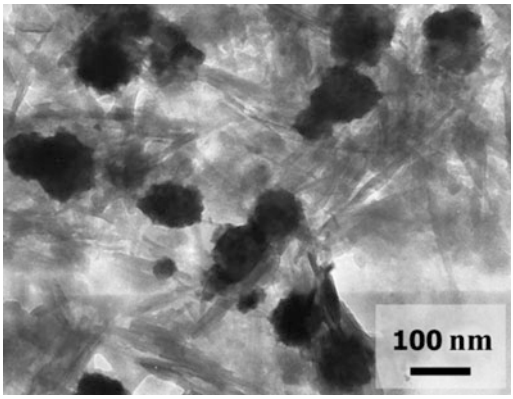

Fig. 15.5 Micrograph of polymineral clay with calcium carbonate additive

influence of compositions on CNS. On the other hand, medication sleep duration characterizes antitoxic liver ability. Urine formation (uropoiesis) indexes were determined too.

Composition components were transported into animal organism on special stand by immersion of rat tails into tested suspensions on 2 h at 40 ± 1 °C temperature.

15.3 Results and Discussion

Data given in Fig. 15.6 shows skin-resorptive influence of natural bentonites on functional liver state of lab animals. Addition of 5 or 10 % of bentonite into peloid almost has no influence on medication sleep during metabolic probe with barbiturates. This assumes [13] that such compositions have no negative influence on central nervous system (CNS) and liver. Increasing of bentonite concentration up to 15 % or addition of 5 % of saponite clay into peloid composition decreases metabolic processes in liver. Latter indicates by increasing of animal's metabolic

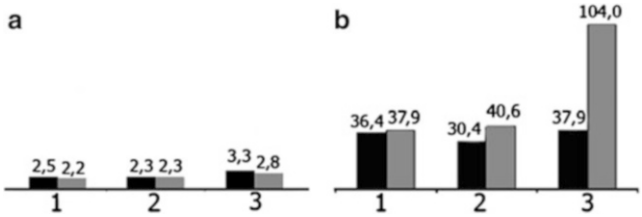

Fig. 15.6 Time of falling asleep (**a**, min) and sleep duration (**b**, min) of laboratory animals with addition of 5 % (1), 10 % (2) and 15 % (3) of natural clay into peloid. *Black bar*—check test, *Grey bar*—experiment

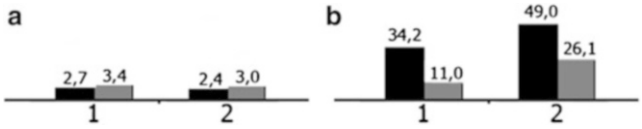

Fig. 15.7 Influence of addition of bentonite burnt at 600 °C on falling asleep time (**a**, min) and medication sleep duration (**b**, min) of lab animals. 1 and 2: 5 % and 10 % of bentonite correspondingly. *Black bar*—control test, *Grey bar*—experiment

sleep during thiopental test. At the same time, functional state of CNS remains on almost the same level.

Testing of functional state of conventional animals' kidneys under skin-resorptive influence of peloids with nanoadditives showed that functions of kidneys remain almost the same with addition of 5 % of bentonite clay. Increase of clay additive up to 10 % leads to negative effects, which exhibit in decreasing of primary urine filtration in nephron glomerulus. This causes decreasing of diurnal diuresis in 1.5 times, diurnal urine excretion in 1.2 times and creatinine in 1.6 times.

Addition of 5 % of saponite clay into peloids stimulates mutually exclusive processes of uropoiesis (urine formation): primary urine filtration and urine readsorption. At the same time, we can see no changes in diurnal diuresis, increase of creatinine excretion in 1.5 times and chlorides in 1.3 times. Daily chloride excretion and reaction of daily urine remains without changes.

Investigation of thermodestructed at 600 °C bentonitic clay influence on biological activity of peloids showed (Fig. 15.7) that addition of 5 and 10 % into peloid changes this index notably. But its influence on CNS remains without changes, and antitoxic liver ability increases. Latter confirms by decreasing of medication sleep in three times for 5 % of bentonite and in 1.9 times for 10 % of bentonite.

Rat uropoiesis improves (Fig. 15.8) with addition of 10 % of burnt bentonite into peloid. Increase of daily diuresis is determined by the growth of primary urine rate and fixed water readsorption in tubular kidney structure.

Addition of 5, 10 and 15 % of chemically precipitated calcium carbonate (Fig. 15.9) showed that functional state of CNS is stable but antitoxic liver ability increases in 2–3 times. Addition of 5 and 10 % of calcium carbonate doesn't change kidney functional state while skin-resorptive use. Adding of 15 % of $CaCO_3$ leads

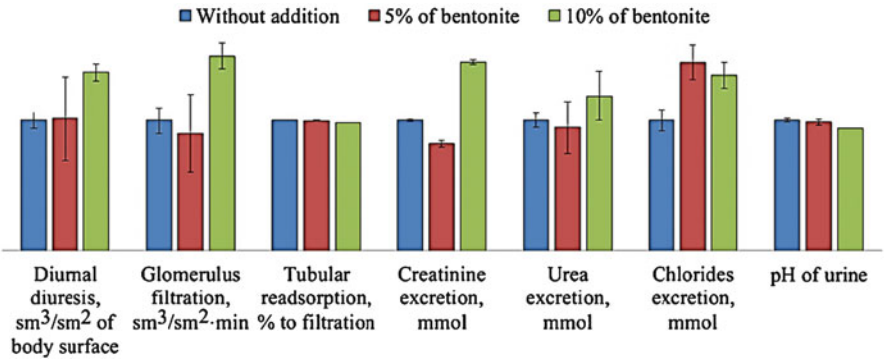

Fig. 15.8 Skin-resorptive influence of peloids with 5 % (1) and 10 % (2) of bentonite (burnt at 600 °C) additive on kidney functional state of Wistar white rats

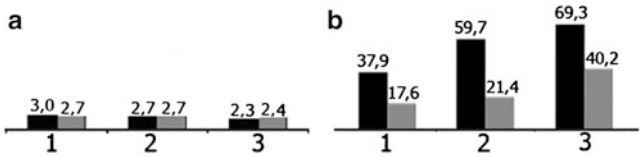

Fig. 15.9 Influence of calcite nanoparticles on duration of falling asleep (**a**, min) and medication sleep (**b**, min) of tested animals. 1, 2, 3—5, 10, 15 % of calcite correspondingly. *Black bar*—control test, *Grey bar*—experiment

to increasing of primary urine rate in nephron glomerulus in 1.5 times with decreasing volume of readsorbed water in tubular kidney structure. And besides, excrete kidney function is being intensified. It indicates by increasing of creatinine excretion in 1.5 times and urea in 1.12 times. Chlorides are being excreted from rat organism more actively as well.

However, mentioned results were received for peloid compositions with artificially added calcium carbonate suspension with nanoparticles. According to [14], their role being decreased with time. It happens because of ageing of clay-carbonate compositions in quiescent state due to isothermal distillation process. On the other hand, same literature [14] shows that in opened dissipative systems (mixing conditions) occurs nanochemical dispersion of carbonate microparticles with formation of nanoparticles in condition of availability of dissolved NaCl and CO_2 from air goes. Latter could be shown by next scheme:

Nanochemical recondensation in laminar-flow conditions (peloid application) (State 1)

$$\underset{\text{dispersed phase (state 1)}}{Ca(Mg,Fe)CO_3} + H_2O + \underset{\text{air}}{CO_2} \xrightleftharpoons{NaCl} \underset{\text{intermediate bicarbonates}}{Ca(Mg,Fe)(HCO_3)_2} \rightleftarrows \underset{\text{superdispersed phase (state 2)}}{Ca(Mg,Fe)CO_3 + H_2CO_3}$$

Mechanochemical superdispersion in turbulent-flow conditions of peloid preparation (State 2)

Table 15.2 Dependence of clay-carbonate suspension effective viscosity from mixing duration

Duration of mixing	Viscosity of 50 % peloid suspension, Pa·s	
	Power-dispersion mixing state	Quiescent state
0 min	0.83	15.50
10 min	5.30	14.30
1 h	10.20	10.10
10 h	15.70	8.90
3 month	–	2.30

According to the scheme, it is possible to disperse carbonate microparticles from native salt peloids up to nanoparticles using intensive mixing by nanochemical dispersion mechanism and further recondensation described in [14]. And indeed, rheological investigation of model composition (90 % of montmorillonite clay and 10 % of microsized calcium carbonate) prepared according to recommendations [14] showed material changing of peloid suspension indexes after its intensive mixing. Thus, according to Table 15.2, effective viscosity of 50 % clay-carbonate aqueous suspension increases in conditions of long-term mixing, and it decreases in quiescent state. This indicates that the process goes according to the scheme.

Testing of real peloid suspensions after their mixing for 10 h showed that their biological activity (within mistake limits) corresponds to data for artificially prepared peloid compositions (Fig. 15.9).

Thus, the results undoubtedly indicate that mixing leads to realization of nanochemical dispersion mechanism of carbonate microparticles and that it goes under influence of mechanochemical processes [2, 15]. And that in turn influences on colloid-chemical properties and biological activity of peloids.

Additional investigations of biological activity and anti-inflammatory action of peloids with nanoadditives on intact animals and in conditions of ovalbumin arthritis modelling showed that preventive course of medical mud applications leads to significant effect. Latter is considered in improvement of metabolic and immunity indexes under inflammation and by increasing of glucocorticoid background in organism.

15.4 Conclusions

Analysis of experimental results indicates that addition of nature bentonites and saponites into peloids almost has no effect on biological activity of medical mud. Also it is stated that peloid bioactivity increases with up to 15 % concentration of burnt bentonites and calcite.

Thus, these results show that increasing of bentonite or calcium carbonate nanoparticles concentration increases biological activity of peloids. This evidently occurs due to raised sorption and ion-exchange ability of calcite and burnt (and rehydrated while making suspensions) bentonite nanoparticles [4, 11, 16, 17].

At the same time, nanoparticle formation process is being suppressed in natural bentonite in peloids with calcite admixture by mechanism described in [14]. And this in turn does not improve biological activity.

Completed investigations and literature data about colloid-chemical and nanochemical transformations of clay-carbonate structures [2, 14] allowed to make a conclusion: the presence of nanoparticles in clay-carbonate peloids (which contain salt media (brine) and have a contact with CO_2 of the air) can lead to considerable effect on colloid-chemical properties of peloid compositions and their biological activity. The connection between nanochemical transformations, colloid-chemical properties, and biological activity of peloid compositions in terms of mixing state (application on skin or mixing—thermodynamically isolated or opened dissipative system, respectively) was established. That confirms conclusions received earlier [2, 14] for other clay-carbonate colloid systems. However, such connection is quite complex and the role of clay minerals in biocolloid properties changing is still not clear enough. So this needs further investigations.

References

1. Gomes C, Carretero MI, Pozo M et al (2013) Peloids and pelotherapy: historical evolution, classification and glossary. Appl Clay Sci 75–76:28–38
2. Kovzun IG, Pertsov NV (2010) Colloid-chemical processes of contact self-organization in alkaline silicate composites and their relation to formation of nanosized surface structures (chapter 19). In: Starov VM (ed) Nanoscience. Colloidal and interfacial aspects. CRC Press, London, pp 523–568
3. Loboda MV, Babov KD, Zolotariova TA, Nikipelova EM (2006) Lechebnie griazi ukrainy (Therapeutic muds of Ukraine). Kuprijanova, Kyiv
4. Nikipelova EM (2011) Colloid-chemical properties of sludge peloid systems and main principles of their regulation. Dissertation, Institute of biocolloid chemistry named after F. D. Ovcharenko, NAS of Ukraine
5. Gamiz E, Martin-Garcia JM, Fernandez-Gonzalez MV, Delgado G, Delgado R (2009) Influence of water type and maturation time on the properties of kaolinite–saponite peloids. Appl Clay Sci 46:117–123
6. Gomes C, Silva J (2007) Minerals and clay minerals in medical geology. Appl Clay Sci 36:4–21
7. Kikouama JR, Konan KL, Katty A, Bonnet JP, Baldé L, Yagoubi N (2009) Physicochemical characterization of edible clays and release of trace elements. Appl Clay Sci 43:135–141
8. Legido JL, Medina C, Mourelle ML, Carretero MI, Pozo M (2007) Comparative study of the cooling rates of bentonite, sepiolite and common clays for their use in pelotherapy. Appl Clay Sci 36:148–160
9. Williams L, Haydel S, Giese R, Eberl D (2008) Chemical and mineralogical characteristics of French green clays used for healing. Clays Clay Miner 56:437–452
10. Okada M, Furuzono T (2012) Hydroxylapatite nanoparticles: fabrication methods and medical applications. Sci Technol Adv Mater 13:064103. doi:10.1088/1468-6996/13/6/064103
11. Panko AV, Kovzun IG, Ulberg ZR, Protsenko IT, Zubkova VA (2009) Ispolzovanie nanoporistyih glin v kachestve sorbentov dlya udaleniya ftalatov iz vodnyih sred (Application of nanoporous clays as sorbents for phtalate removal from aqueous media). Mater Sci Nanostruct 2:93–102

12. Kowzun IG, Prozenko IT, Owtscharenko FD (1986) Energieeinspazzung bei der Verarbeitung von Rohstoffen zu keramischen Schlickern. Sprechsaal 119(11):1019–1022
13. Speranskij SV (1980) Simple method to determine hepatogenic and neurogenic effects in toxicological test. Hygiene Sanitation 7:62–65
14. Kovzun IG, Kovalenko IM, Protsenko IT (2005) Influence of sodium chloride, carbonates and iron hydroxides on the viscosity of aqueous suspensions of clay minerals. Colloid J 67 (1):27–31
15. Oleinyk VA, Pan'ko AV, Ilyashov MO, Kovzun IG, Protsenko IT (2011) Enrichment of iron ores with Use of nanomaterials based on the alkaline silicates. Metallofizika I Noveishie Tekhnologii 33:587–594
16. Kovzun IG, Protsenko IT (1994) Hydrophilicity of disperse carbon-silicate compositions and carbonaceous materials. Colloid J 56(6):712–716
17. Kovzun IG, Protsenko IT (1994) The effect of alkaline solutions on spontaneous hydration-induced dispersion of natural, dehydrated and carbon-containing silicates. Colloid J 56 (6):794–799

Chapter 16
Magnetic and Neutron Diffraction Studies of Magnetic Properties of the Nanoparticle $RMnO_3$ (R = Tb, Dy) Manganites

W. Bażela, S. Baran, V. Dyakonov, A. Hoser, B. Penc, A. Zarzycki, and A. Szytuła

16.1 Introduction

Physical properties of manganites were shown to depend on both doping and the grain size [1, 2]. Usually, the nanocrystalline samples exhibit properties which are different from those of the bulk material. An important factor is increasing surface-to-volume ratio for the grains as the particle size is reduced to the nanoscale. As a result, the small size effect and the surface effect perturb the properties of nanoparticle samples. In these samples, the magnetic behavior is additionally modified by the interparticle interactions which can be both of the exchange and

W. Bażela (✉)
Institute of Physics, Cracow University of Technology,
Podchorążych 1, Kraków 30-084, Poland
e-mail: wbazela@pk.edu.pl

S. Baran • B. Penc • A. Szytuła
M. Smoluchowski Institute of Physics, Jagiellonian University,
Łojasiewicza 11, Kraków 30-348, Poland
e-mail: stanislaw.baran@uj.edu.pl; boguslaw.penc@uj.edu.pl; andrzej.szytula@uj.edu.pl

V. Dyakonov
Institute of Physics PAS, Al. Lotników 32/46, Warszawa 02-68, Poland
e-mail: dyakon@ifpan.edu.pl

A. Hoser
Helmholtz-Zentrum Berlin für Materialen und Energie GmbH,
Hahn-Meitner Platz 1, Berlin 14-109, Germany
e-mail: hoser@helmholtz-berlin.de

A. Zarzycki
H. Niewodniczański Institute of Nuclear Physics PAS, Radzikowskiego 152,
Kraków 31-342, Poland
e-mail: Arkadiusz.Zarzycki@ifj.edu.pl

O. Fesenko, L. Yatsenko (eds.), *Nanoplasmonics, Nano-Optics, Nanocomposites, and Surface Studies*, Springer Proceedings in Physics 167,
DOI 10.1007/978-3-319-18543-9_16

magnetostatic origins. The main motivation for these studies was to obtain the data concerning the evolution of magnetic properties as a function of grain size.

In the last years, the $RMnO_3$ compounds have attracted a lot of attention due to strong coupling between ferroelectricity and magnetism [3].

Magnetic measurements of $TbMnO_3$ indicate that this compound is antiferromagnet in which Tb^{3+} and Mn^{3+} moments order below 7 K and 41 K, respectively. Neutron diffraction data indicate sine-modulated magnetic structure in both sublattices. In Mn site the change of magnetic ordering at 27 K is observed [4].

In $DyMnO_3$ below 6.5 K, the Dy magnetic moments order in a commensurate structure with the propagation vector $\mathbf{k} = (½, 0, 0)$, while the Mn moments form incommensurate structure below 39 K. At $T_t = 18$ K, the change in the magnetic structure of the Mn sublattice is observed. Below T_t this ordering is collinear, while above T_t it is sine modulated [5].

In this work the results of X-ray and neutron diffraction and magnetometric measurements of the nano and bulk $RMnO_3$ (R = Tb, Dy) samples are discussed. The obtained data are analyzed from the point of view of grain-size value.

16.2 Experimental and Results

The investigated nanoparticle $RMnO_3$ compounds where R = Tb and Dy were obtained by a sol–gel technique described in Ref. [6]. The obtained products were annealed at temperatures of 800 and 850 °C. Polycrystalline bulk samples as references ones were synthesized at 1,170 °C in air for 20 h and then slowly were cooled down to room temperature.

The quality of the products was checked by X-ray powder diffraction at room temperature using a Philips PW-3710 X'PERT diffractometer with CuK_α radiation. The obtained data were analyzed with the Rietveld-type refinement FullProf program [7]. For all the samples, the following *dc* magnetic measurements using a commercial MPMS SQUID magnetometer have been carried out: magnetic susceptibility measurements in magnetic field of 1 kOe over a temperature range of 2–300 K (from these data the effective magnetic moment μ_{eff} and the paramagnetic Curie temperature θ_p were obtained) and magnetization measurements in magnetic fields up to 50 kOe and at temperatures down to 2 K (in order to get the value of the pseudo-saturated magnetic moment and character of the magnetization curve).

The ac magnetic susceptibility, $\chi_{ac} = \chi' + i\chi''$, where χ' and χ'' are the real and imaginary components, respectively, was measured versus temperature and frequency between 100 Hz and 5 kHz in a magnetic field equal to 2 Oe with the use of PPMS.

The neutron diffractograms were obtained at different temperatures using the E6 diffractometer at BERII reactor (Helmholtz-Zentrum Berlin). The incident neutron wavelength was 2.44 Å. The data were analyzed using the Rietveld-type program FullProf [7].

The X-ray diffraction data indicate that all the samples studied are homogenous single phase and have orthorhombic crystal structure described by the space group P*nma*. In this structure the atoms occupy the following sites: *R* and *O*1 in 4c site: (*x*, *y*, ¼), *O*2 in 8l site: (*x*, *y*, *z*) and Mn in 4b site: (½, 0, 0). All the fitted structural parameters, lattice constants and positional x_i, y_i, and z_i parameters, are listed in Table 16.1. The obtained data indicate that the crystal structure parameters of the nanosamples are slightly less than the values for bulk materials.

In the next step, the grain sizes were determined using the Scherrer relation $d = \lambda/\beta \cos\theta_B$, where d is the grain size, $\lambda = 0.154178$ nm the X-rays wavelength, θ_B the corresponding angle of Bragg diffraction, and β the difference between half-widths of the Bragg reflex of the nanopowder and the standard sample (Si powder with the size 10 μm). The grains sizes were calculated using the experimental X-ray data and the following relations [8]:

1. $d_1 = \beta - \beta_0$, where β is the half-widths of the Bragg reflex of the investigated sample and β_0 the similar value for the standard sample of Si powder.

Table 16.1 Structural parameters of $TbMnO_3$ and $DyMnO_3$ at room temperature derived from X-ray diffraction data (S_1, polycrystalline sample, S_2 and S_3, the nanocrystalline samples annealed at 800 °C and 850 °C, respectively); Δ1, difference between the volume of nano and bulk samples; Δ2, difference of volume between Dy and Tb samples

$TbMnO_3$				$DyMnO_3$			
Samples	S_1	S_2 (800)	S_3 (850)	Samples	S_1	S_2	S_3
a (Å)	5.8456 (1)	5.8191 (1)	5.8152 (2)	*a* (Å)	5.8385 (2)	5.8334 (1)	5.8306 (1)
b (Å)	7.4040 (2)	7.4092920	7.4104 (2)	*b* (Å)	7.3792 (2)	7.3794 (2)	7.3806 (1)
c (Å)	5.2995 (1)	5.2862 (1)	5.2847 (2)	*c* (Å)	5.2789 (1)	5.2742 (1)	5.2738 (1)
V (Å^3)	229.37 (1)	227.914 (14)	227.733 (23)	*V* (Å^3)	227.433 (19)	227.04 (1)	226.95 (1)
R x	0.0806 (2)	0.0806 (2)	0.0805 (2)	R x	0.0819 (2)	0.0820 (1)	0.0822 (1)
Y	−0.0140 (5)	−0.0167 (2)	−0.0154 (3)	*y*	−0.0139 (4)	−0.0156 (2)	−0.0185 (2)
O1 x	0.469 (2)	0.465 (1)	0.467 (2)	O1 x	0.473 (2)	0.462 (2)	0.463 (1)
y	0.101 (2)	0.104 (1)	0.107 (2)	*y*	0.102 (3)	0.104 (2)	0.105 (1)
O2 x	0.329 (2)	0.315 (1)	0.311 (2)	O2 x	0.324 (2)	0.327 (1)	0.323 (1)
y	0.053 (1)	0.050 (1)	0.052 (1)	*y*	0.049 (1)	0.054 (1)	0.052 (1)
z	0.705 (2)	0.695 (1)	0.703 (2)	*z*	0.705 (2)	0.699 (1)	0.704 (1)
R_{Bragg} (%)	6.6	9.2	8.6	R_{Bragg} (%)	8.1	6.6	6.6
R_{prof} (%)	7.3	11.1	9.7	R_{prof} (%)	10.0	9.3	6.3
Δ1 (Å^3)		−1.456	−1.637	Δ1 (Å^3)		−0.393	−0.483
Δ2 (Å^3)				Δ2 (Å^3)	−1.937	−0.874	−0.783

2. $d_2 = \sqrt{\beta^2 - \beta_0^2}$.

3. $d_3 = \sqrt{(\beta - \beta_0)\sqrt{\beta^2 - \beta_0^2}}$.

The grain-size values d_i ($i = 1, 2, 3$) determined from these relations are listed in Table 16.2. Presented data indicate that the grain size increases with increasing annealing temperature.

The temperature dependences of reciprocal magnetic susceptibility and *dc* magnetic susceptibility for all the samples are shown in Fig. 16.1. The inset shows the low-temperature data.

The reciprocal magnetic susceptibility of all the compounds indicates breakdown near 40 K which is connected with magnetic ordering in the Mn sublattice. Above and below this temperature, $\chi(T)^{-1}$ fulfils the Curie–Weiss law. The $\chi(T)$ data are analyzed using relation $C/(T - \theta_p)$ at high temperature and $\chi_0 + C/(T - \theta_p)$ at low one, where χ_0 is the independent term equal to 2×10^{-2} emu/molOe for $TbMnO_3$ and $2–6 \times 10^{-3}$ emu/molOe for $DyMnO_3$ samples and C the Curie constant. The fitted values of the paramagnetic Curie temperature θ_p and effective magnetic moments μ_{eff} are listed in Table 16.3. In both temperature regions, the paramagnetic Curie temperatures are negative which indicate the antiferromagnetic interactions. Comparison of the paramagnetic Curie temperatures determined from the high temperature data

Table 16.2 Values of the grain size in (nm) of nanopowder of $TbMnO_3$ and $DyMnO_3$ prepared at temperature 800 °C (S_2) and 850 °C (S_3)

	d_1 (nm)	d_2 (nm)	d_3 (nm)	$\langle d \rangle$ (nm)
$TbMnO_3$				
S_2	28.0	22.8	25.3	25.4
S_3	35.8	29.4	33.3	32.8
$DyMnO_3$				
S_2	31.6	25.2	28.2	28.3
S_3	57.2	40.0	47.8	48.3

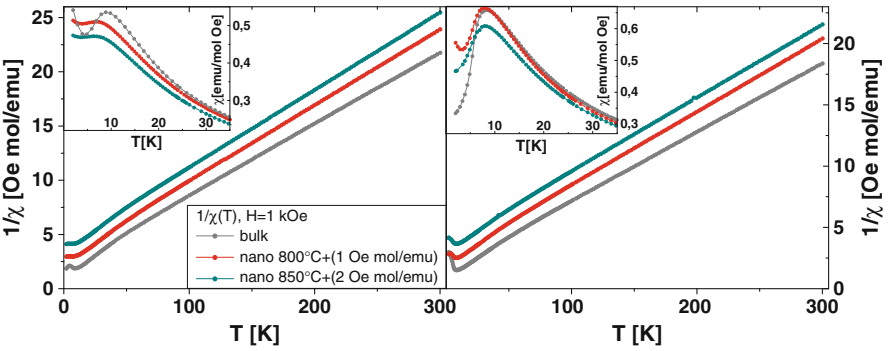

Fig. 16.1 Temperature dependences of the reciprocal magnetic susceptibility of polycrystalline bulk and nanosize of (**a**) $TbMnO_3$ and (**b**) $DyMnO_3$ samples. *Inset* shows the low-temperature part of magnetic susceptibility. The data for S_2 (*filled square*) and S_3 (*filled triangle*) coincide in the broad temperature region

Table 16.3 Magnetic data for $DyMnO_3$ and $TbMnO_3$

Name		High temperature		Low temperature		μ (μ_B) at 2 K	H (kOe) at 2 K
		θ_p (K)	μ_{eff} (μ_B)	θ_p (K)	μ_{eff} (μ_B)		
$DyMnO_3$	S_1	−27.33 (4)	12.36 (1)	−10.2 (1)	10.96 (4)	4.8	14.1
	S_2	−24.95 (5)	11.90 (1)	−9.7 (2)	10.53 (5)	4.5	14.2
	S_3	−26.90 (6)	11.97 (1)	−11.1 (2)	10.71 (6)	4.4	14.8
$TbMnO_3$	S_1	−30.79 (11)	11.413 (3)	−6.5 (1)	9.49 (3)	4.15	17.6
	S_2	−27.93 (6)	11.084 (2)	−8.9 (1)	9.42 (3)	3.7	17.6
	S_3	−28.29 (3)	10.954 (1)	−10.7 (3)	9.41 (8)	3.5	17.6

with those determined from the low-temperature data indicates that the magnetic interaction in Mn sublattice is dominant.

For the bulk samples, in low-temperature region, the effective magnetic moments are close to values for free R^{3+} ion equal to 9.72 μ_B (R = Tb) and 10.65 μ_B (R = Dy), while in high temperature region, they are close to values calculated from the relation $\mu_{eff} = \sqrt{\left(\mu_{eff}^{R}\right)^2 + \left(\mu_{eff}^{Mn}\right)^2}$ for free R^{3+} and Mn^{3+} (4.9 μ_B) ions equal to 10.88 μ_B for $TbMnO_3$ and 11.72 μ_B for $DyMnO_3$.

For the nanosamples, the values of both the paramagnetic Curie temperature and the effective magnetic moments decrease slightly with decreasing grain sizes.

At low temperatures, the maximum of temperature dependences of magnetic susceptibility indicate magnetic ordering in rare earth sublattice. The maximum temperature decreases for $TbMnO_3$ nanosamples and does not change for $DyMnO_3$ ones. The magnetization isotherms measured at 2 K show a metamagnetic transition in a magnetic field equal to 17.6 kOe for $TbMnO_3$ and 14.5 kOe for $DyMnO_3$. For all the samples, magnetization is not saturated in the magnetic field up to 50 kOe. The magnetic moment values at $T = 2$ K and $H = 50$ kOe are less than the values for free R^{3+} ion equal to 9.0 μ_B for R = Tb and 10.0 μ_B for R = Dy. The values obtained for the nanosamples are less than these for bulk material. Reduction of the moment is larger in $TbMnO_3$ samples. The hysteresis loop at 2 K in low magnetic field shows the difference in the coercivity field equal to 350–500 Oe for $TbMnO_3$ samples and 160 Oe for the $DyMnO_3$ samples. This result indicates the large number defects in $TbMnO_3$ compounds.

Temperature dependences of the ac susceptibility real component (Fig. 16.2) show the broad maximum at 8 K for nano-$TbMnO_3$ and 9.0 K and 9.5 K for nano and bulk $DyMnO_3$, respectively. The imaginary component χ'' does not give anomalies at critical temperatures corresponding to magnetic ordering in the Mn and R sublattices. This shows that in the magnetic ordering, the ferromagnetic component is absent. For all the samples, below 5 K, the strong increase of χ'' component probably connected with change of magnetic structure is observed. Presented data do not exhibit the anomaly near 40 K connected with ordering of the magnetic moment in the Mn sublattice.

The neutron diffraction patterns for the samples annealed at 850 °C are shown in Fig. 16.3. For both samples, the data obtained at 50 K confirm the crystal structure

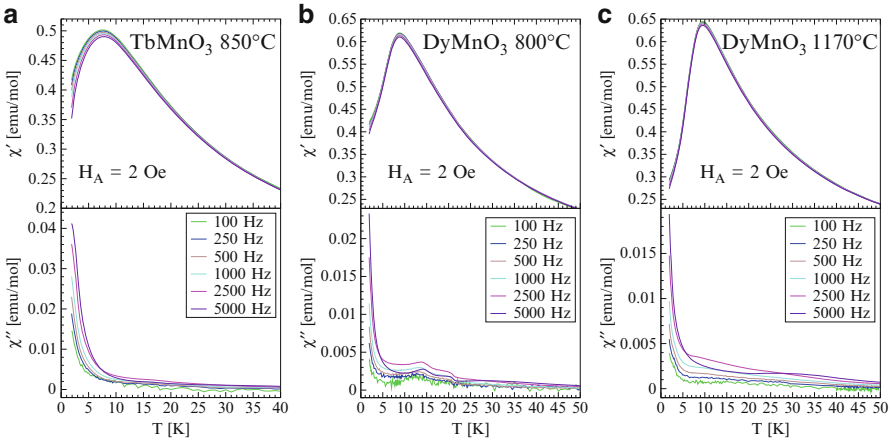

Fig. 16.2 Temperature dependences of the real χ' and imaginary χ'' component of the ac magnetic susceptibility of (**a**) nano-$TbMnO_3$, (**b**) nano-$DyMnO_3$, and (**c**) bulk $DyMnO_3$ measured in magnetic field of $H_A = 2$ Oe at frequencies varied between 100 Hz and 5 kHz

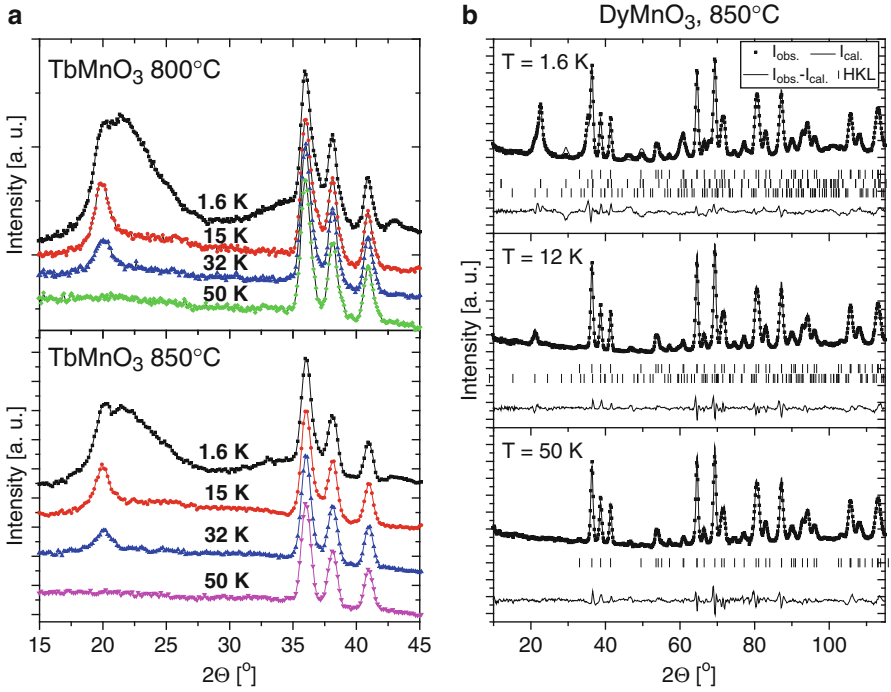

Fig. 16.3 Neutron diffraction patterns for (**a**) $TbMnO_3$ and (**b**) $DyMnO_3$ obtained at different temperatures

Table 16.4 Parameters of the magnetic structure for nano-800 (S_2) and nano-850 (S_3) samples of $RMnO_3$ (R = Tb, Dy)

	$TbMnO_3$				$DyMnO_3$	
	nano-800 (S_2)		nano-850 (S_3)		nano-850 (S_3)	
T [K]	μ_{Mn} (μ_B)	k_x	μ_{Mn} (μ_B)	k_x	μ_{Mn} (μ_B)	k_x
32	1.60 (12)	0.326 (4)	1.35 (15)	0.326 (5)	3.24 (14)	0.360 (1)
15	2.29 (8)	0.312 (2)	2.08 (10)	0.315 (2)	3.74 (12)	0.370 (2)
1.6	2.94 (2)	0.321 (2)	3.03 (4)	0.328 (2)	4.24 (11)	0.376 (4)
	3.68 (11)	0.443 (5)	4.43 (7)	0.451 (3)	8.71 (18)	0.501 (12)

[a]Data for *R* sublattice

determined from the X-ray data. The data at $T = 15$ K for $TbMnO_3$ and 12 K for $DyMnO_3$ confirm the antiferromagnetic ordering in the Mn sublattice described by the A_x mode [9]. The Mn magnetic moments parallel to the *a*-axis form the modulated magnetic structure with the propagation vector $\mathbf{k} = (k_x, 0, 0)$.

At $T = 1.6$ K, the additional peaks corresponding to the magnetic ordering in rare earth sublattice are observed. The magnetic order is described by the propagation vector $\mathbf{k} = (k_x,0,0)$ with the k_x values which differ from the values for the Mn sublattice. In $TbMnO_3$ the magnetic ordering of Tb moments is noncollinear and is described by the F_yA_z mode [9], while in $DyMnO_3$, the magnetic ordering of Dy moments is collinear and is described by the A_x mode. The magnetic ordering in Mn sublattice in both compounds and Tb moments in $TbMnO_3$ is incommensurate with respect to the crystal structure, while in Dy sublattice, it is commensurate. The shape of these peaks is different, namely, it is broad for $TbMnO_3$ and narrow for $DyMnO_3$. The magnetic ordering parameters are summarized in Table 16.4.

16.3 Discussion

Presented in the work data indicate that the investigated nanosamples $RMnO_3$ (R = Tb, Dy) have the orthorhombic crystal structure which is similar to that for bulk materials. The structural parameters indicate the small influence of the grain size on atomic ordering. The grain-size values determined from X-ray data are shown to be less than 100 nm.

The nanosamples are characterized by the lesser values of the unit cell volumes (see values Δ1 in Table 16.1). The difference is larger for the Tb samples. The volume values are smaller for the Dy samples that are connected with the lanthanide contraction.

The grain-size values determined for the Tb and Dy samples are close to each other.

The effective magnetic moments values suggest the localization of the magnetic moments on the Mn and R (Tb, Dy) elements ordered at different temperatures.

Magnetic and neutron diffraction data indicate that all the samples have antiferromagnetic ordering. Negative values of the paramagnetic Curie temperature confirm the antiferromagnetic interactions.

The macroscopic magnetic data do not give the large difference in magnetic properties of two series (see Table 16.3).

Presented in the work, the neutron diffraction data indicate the different character of influence of the rare earth element on the properties of nanosamples including magnetic ordering.

For nano-$DyMnO_3$, a small change of the magnetic ordering character in the Dy sublattice is observed [10]. In contrary, in the $TbMnO_3$ nanosamples, the neutron diffraction data suggest the cluster-like character of the magnetic ordering in the Tb sublattice [11].

This result is surprising taking into consideration similar macroscopic magnetic properties and similar magnetic ordering described by sine-modulated structure. The magnetic ordering in the rare earth sublattices is different: noncollinear in $TbMnO_3$ and collinear in $DyMnO_3$. Second difference is connected with the rare earth magnetic moment values, namely, 3.68 (11) μ_B and 4.43 (7) μ_B in $TbMnO_3$ and 8.71 (18) μ_B in $DyMnO_3$ which are 40.9 and 49.2 % of the value for free Tb^{3+} ion (9 μ_B) and 87.1 % of the value for free Dy^{3+} ion (10 μ_B). The large decrease of the observed Tb magnetic moment is probably a result of a strong influence of the crystal electric field or the existence of nonmagnetic layer on the grain surface.

The large values of χ_0 and coercive field indicate large number of the atomic defects in $TbMnO_3$ samples which play an important role in magnetic interactions.

Acknowledgments The research was carried out with the equipment purchased thanks to the financial support of the European Regional Development Fund in the framework of the Polish Innovation Economy Operational Program (contract no. POIG.02.01.00-12-023/08).

References

1. Balcells LI, Fontcuberta J, Martinez B, Obradors X (1998) High-field magnetoresistance at interface in manganese perovskite. Phys Rev B 58, R14697. doi:10.1103/Phys. Rev. B 58.R
2. Dyakonov V, Bażela W, Duraj R, Dul M, Kravchenko Z, Zubov E, Dyakonov K, Baran S, Szytuła A, Szymczak H (2013) Grain size effect on magnetic properties of $REMnO_3$ (RE=Pr, Nd). Low Temp Phys 39:452. doi:10.1063/1.3691530
3. López-Quintela MA, Hueso LE, Rivas J, Rivadulla F (2003) Intergranular magnetoresistance in nanomanganites. Nanotechnology 14:212. doi:10.1088/0957-4484/14/20322
4. Quezel S, Tcheo F, Mignot-Rossat J, Queze G, Roudaut E (1977) Magnetic structure of the perovskite-like compound $TbMnO_3$. Physica B+C 86–88:916
5. Feyerherm R, Dudzik E, Aliouane N, Argyriou DN (2006) Commensurate Dy magnetic ordering associated with incommensurate lattice distortion in multiferroic $DyMnO_3$. Phys Rev B 73, R180401. doi:10.1103/Phys. Rev. B. 73.180401
6. Dyakonov V, Szytuła A, Baran S, Kravchenko Z, Zubov E, Iessenchuk O, Bażela W, Dul M, Zarzycki A, Szymczak M (2010) Magnetic properties of the nanocrystalline $DyMnO_3$ compound. Acta Phys Polon A 117:607

7. Rodriguez-Carvajal J (1993) Recent advanced in magnetic structure determination by neutron powder diffraction. Physica B 192:55. doi:10.1016/0921-4526(93)90108-1
8. Cullity BD (1978) Elements of X-ray diffraction. Addison-Wesley, Reading
9. Bertaut EF (1963) Representation analysis of magnetic structures. In: Rado GT, Shul H (eds) Magnetism, vol III. Academic, New York, p 149
10. Szytuła A, Penc B, Dyakonov V, Baran S, Hoser A (2014) Neutron diffraction studies of nanoparticle $DyMnO_3$ compound. Acta Phys Polon A 125:65
11. Bażela W, Dul M, Dyakonov V, Gondek Ł, Hoser A, Hoffmann J-U, Penc B, Szytula A, Kravchenko Z, Nosalev I, Zarzycki A (2012) Influence of the grain size on the magnetic properties of $TbMnO_3$. Acta Phys Polon A 121:785

Chapter 17
Temperature Dependence of the Bandgap of CdTe/CdS Core–Shell Quantum Dots

O.O. Tynkevych, N.M. Vyhnan, P.M. Fochuk, and Yu. B. Khalavka

17.1 Introduction

Quantum dots or semiconductor nanocrystals exhibit the so-called quantum confinement effect when synthesized with a crystallite size below to Bohr exciton radius of the bulk material. The QDs are characterized by the physical and chemical properties which significantly differ from their individual molecules or bulk forms [1]. The quantum confinement effect gives rise to unique size-dependent electro-optical properties, which are important for their potential use in lasers, solid-state lighting, solar cells, and biomedical fields [2–7]. While optical absorption measurements yield information on the QD size and the relative energy level configurations, they do not allow the determination of absolute energy levels positioned with respect to a standard potential. These values are vital for completing our understanding of the confinement effect in QDs. The most common method for the determination of the size-dependent conduction and valence band edge shift in quantum confined systems to date is cyclic voltammetry (CV) [8].

Studies on the temperature dependence of QDs optical and electrochemical properties are important for their potential application because the desired device should emit in the visible spectral range at room temperature.

Previous works by Poznyak et al. [9], Haram et al. [10], and Jasieniak et al. [8] investigate the band edge size-dependent electrochemical behavior of CdTe, CdS, CdSe, PbS, and PbSe nanocrystals by means of cyclic voltammetry [8–11]. Kucur et al. [12] investigated the surface defect state energy levels in the bandgap of CdSe nanocrystals and their behavior under excited conditions due to blue-light

O.O. Tynkevych (✉) • N.M. Vyhnan • P.M. Fochuk • Yu.B. Khalavka
Department of Solid State Inorganic Chemistry and Nanomaterials, Yuriy Fedkovych Chernivtsi National University, 2, Kotsiubynsky Street, Chernivtsi 58012, Ukraine
e-mail: o.tynkevych@gmail.com; y.khalavka@chnu.edu.ua

O. Fesenko, L. Yatsenko (eds.), *Nanoplasmonics, Nano-Optics, Nanocomposites, and Surface Studies*, Springer Proceedings in Physics 167,
DOI 10.1007/978-3-319-18543-9_17

irradiation [12]. On the other hand, the temperature dependence of the bandgap energy in different QDs by using photoluminescence (PL) and absorption (Ab) techniques was studied by other groups [13–17]. In this report, we present the results of optical and electrochemical investigations of bandgap structure and its temperature dependence behavior for CdTe/CdS QDs.

17.2 Experimental

17.2.1 Synthesis of CdTe/CdS QDs

The thioglycolic acid-stabilized CdTe/CdS nanocrystals were synthesized at room temperature in alkali aqueous solution by the reaction of $CdBr_2$ or $CdSO_4$ and H_2Te. The H_2Te was produced by the electrochemical reduction of tellurium on the tellurium cathode. The oxygen was removed from the system by bubbling argon through it for 10–15 min. In the next step, the temperature was raised to 100 °C for growth of CdTe/CdS QDs of the required size. Samples with an average size of 2.3–3.8 nm have been produced this way.

For our studies, two series of samples were synthesized. The first series of samples was prepared by varying the time of H_2Te passing through the solution. The second series of samples was synthesized with different heat treatment times, which allowed us to obtain a wide range of QDs sizes in both cases.

17.2.2 Material Characterization

Photoluminescence (PL) spectra were excited by the solid-state diode laser (405 nm) and recorded by the Ocean Optics USB-4000 spectrophotometer. The electrochemical measurements were performed using Reference 3000 Potentiostat/Galvanostat. A three-electrode system with platinum or glassy carbon counter electrodes, an Ag/AgCl reference electrode, and the flat platinum electrode as the working electrode was used for the CV measurements. The cyclic voltammograms were obtained by scanning the potentials from −2 to 2 V at scan rates of 10, 20, 50, 100, and 200 mV/s. Measurements were carried out in the range starting from room temperature up to 55 °C. The size of the particle was determined using spectroscopic data, namely, absorption peak maxima according to [18].

17.3 Results and Discussion

17.3.1 Optical Characterization of the CdTe/CdS QDs

The optical properties of the prepared CdTe/CdS QDs were characterized spectroscopically. Figure 17.1 shows absorption (a) and photoluminescence (b) spectra of

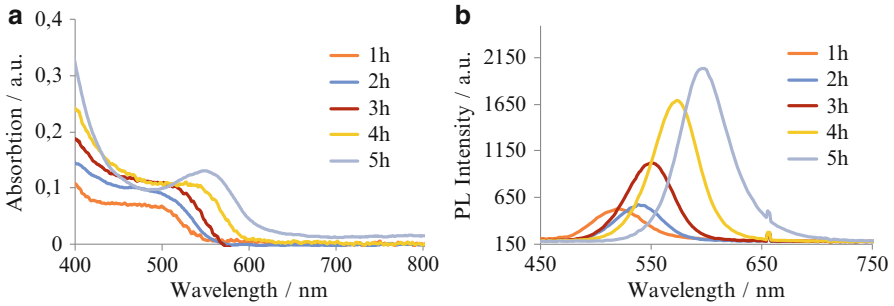

Fig. 17.1 Absorption (**a**) and PL (**b**) spectra of thioglycolic acid-capped CdTe/CdS QDs of different sizes (time of ripening at 100 °C is shown in the legend)

Table 17.1 Band structure parameters of thiol-capped CdTe/CdS QDs of different sizes obtained from spectroscopy and cyclic voltammetry

QDs diameter, nm	Abs peak, nm	Eg (opt), eV	Peak C (Ered), V	Peak A (Eox), V	Conduction band edge vs. vacuum	Valence band edge vs. vacuum	Eg (CV), eV
First series of samples							
3.8	640	1.94	−0.33	1.60	−3.91	−5.86	1.93
3.3	593	2.09	−0.46	1.51	−3.78	−5.75	1.97
3.0	569	2.18	−1.02	1.09	−3.22	−5.33	2.11
2.6	523	2.37	−1.03	1.07	−3.21	−5.31	2.10
2.5	519	2.39	−1.18	0.92	−3.06	−5.16	2.10
2.4	512	2.42	−1.32	0.90	−2.92	−5.14	2.22
2.3	504	2.46	−1.57	0.89	−2.67	−5.13	2.46
Second series of samples							
2.3	499	2.48	−1.38	0.82	−2.86	−5.06	2.20
2.4	503	2.35	−1.34	0.82	−2.90	−5.06	2.16
2.5	519	2.39	−1.38	0.84	−2.86	−5.08	2.22
2.7	541	2.28	−1.33	0.77	−2.91	−5.01	2.10
2.8	558	2.25	−1.32	0.83	−2.92	−5.07	2.15

the thiol-capped CdTe/CdS QDs in colloidal solutions which were chosen for the investigation of the temperature dependence of the electrochemical bandgap variations. Aliquots of CdTe NCs of different sizes were taken from the crude solution at different heat treatment times. When prolonging the refluxing time, the growth of the CdTe NCs can be clearly seen by the "red" shift of absorption and PL spectra.

The characteristic absorption and PL peaks for two series of samples were observed in the range of 499–653 nm. The average particle sizes and optical bandgap (Eg_{opt}) for all the samples were obtained from the absorption peak maxima and are listed in Table 17.1.

17.3.2 Electrochemical Characterization of the CdTe/CdS QD Band Structure

Cyclic voltammetry (CV) is the most widely used electrochemical technique, is used for the characterization of redox systems, and is often the first experiment performed in an electroanalytical study. It can provide rapid information about the number of redox states of the electroactive species, as well as qualitative information about the stability of these oxidation states and the electron transfer kinetics [19].

A cyclic voltammetry method was applied to determine band structure of the particles, for instance, the bandgap (Eg), conduction band edge, and valence band edge as a function of quantum dot size. In case of nanoparticles, the lowest energy level available to accept electrons (bottom of the conduction band) corresponds to the reduction potential, and highest level from which electrons can be taken away (top of the valence band) is related to oxidation potential. On typical CV (Fig. 17.2), cathodic and anodic peaks at −0.330 V (marked as C) and 1.605 V (marked as A), respectively, are observed.

The potential difference of 1.935 V between C and A is in accordance with the optical bandgap of 1.940 eV. CV for different samples shows the presence of similar cathodic and anodic peaks that correspond to the electrochemical activity of CdTe QDs.

As the bandgap (Eg_{opt}) is a function of particle size, the electrochemically determined bandgap (Eg_{CV}) should also increase with decreasing particle size. It was found that distance between the oxidation and reduction peaks increases with decreasing QDs sizes. This difference can be used to estimate electrochemical bandgap, energy of conduction band edge, and valence band edge levels of QDs. The results of optical and electrochemical calculations are presented in Table 17.1.

It should be noted that the CV bandgap energy (Eg_{CV}) is 0.1–0.3 eV lower than the optical Eg_{opt} in most cases (Fig. 17.3). This difference decreases for larger

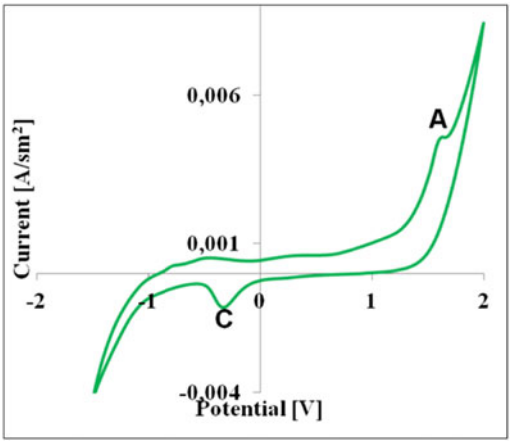

Fig. 17.2 A typical cyclic voltammogram recorder for CdTe/CdS core–shell QDs colloidal solution ($d = 3.8$ nm). The scan rate was 100 mV/s

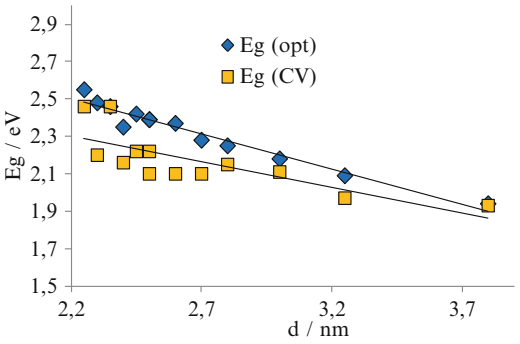

Fig. 17.3 Comparison of the optical (Eg (opt)) and electrochemical (Eg (CV)) bandgaps for varied sizes of CdTe/CdS core–shell QDs

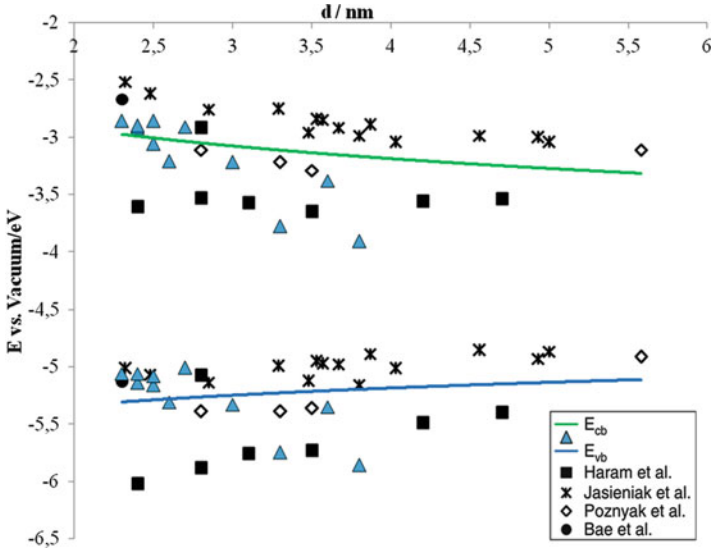

Fig. 17.4 Plot of valence (*blue line*) and conduction (*green line*) band edge positions for CdTe/CdS QDs, obtained as a function of size from the respective anodic (A) and cathodic (C) peaks (*blue triangles*)

particles due to the less impact of surface states and vanishes when the particle size reaches 3.8 nm.

Like the authors of [9], we also expected to observe oxidation at more positive potentials and reduction at more negative potentials for smaller QDs, since the top of the valence band usually shifts toward lower energies and the bottom of the conduction band rises to higher energies with decreasing particle size. In our case, the oxidation peak A shifts to the negative direction with decreasing QD size too. A reason for these disagreements may be related to the oxidation of surface defects forming surface states in the bandgap that act as electrically active local trap states.

In Fig. 17.4, we plotted our experimental data in comparison to the similar data of other authors [8, 9, 11, 20] that were performed by cyclic voltammetry. A good

correlation in the trend of the data between these studies and our own is observed. However, the magnitude of the values does show some variation, due to slight surface chemistry differences between samples.

It is important to note that we have observed the appearance of an additional oxidation peak in the cyclic voltammograms at 1.8 V (not shown) described in [9] for samples with heat treatment time over 4 h. This may indicate the additional oxidation process that may be caused by the presence of a CdS shell of a certain thickness.

To understand the electron transfer reactions, the effects of scan rates on peak current were studied. CV of CdTe QDs aqueous colloidal solutions obtained at 10, 20, 50, 100, and 200 mV/s scan rates showed similar features of oxidation/reduction waves (Fig. 17.5). The inset shows a plot of anodic and cathodic peaks current values relative to square root of the scan rates. The solid lines indicate the corresponding linear regression the data fitted in the Randles-Sevcik equation [21], suggesting that the electron transfer is limited by diffusion. Slopes for cathodic peaks are shallower than for anodic peaks due to differences in the kinetics of reduction and oxidation reactions.

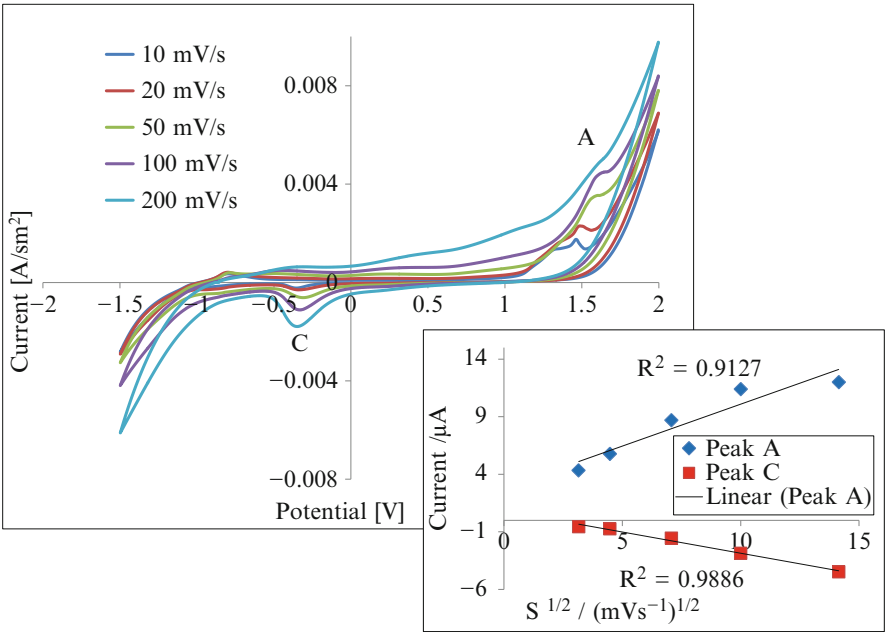

Fig. 17.5 Scan rate dependence of the CV response for CdTe/CdS QD at a Pt electrode. *Inset*: plots of cathodic (C) and anodic (A) peak current values relative to $S^{1/2}$ calculated from scan rate-dependent CV

17.3.3 Temperature-Dependent Bandgap Variation in CdTe/CdS QDs

A cyclic voltammetry method can also be applied to determine the temperature-dependent bandgap variations of CdTe/CdS QDs. While incubating CdTe/CdS QDs colloidal solutions at different temperatures from 293 to 328 K, we observed a symmetrical shift of the oxidation and redaction peaks (Fig. 17.6a). As seen in Fig. 17.6b, this shift was linearly dependent on temperature. The estimated energy bandgap tends to decrease as the temperature increased. A reason for such behavior may be the increase of interatomic spacing when the amplitude of the atomic vibrations increases due to the increased thermal energy and as a result of enhanced quantum confinement [16, 18].

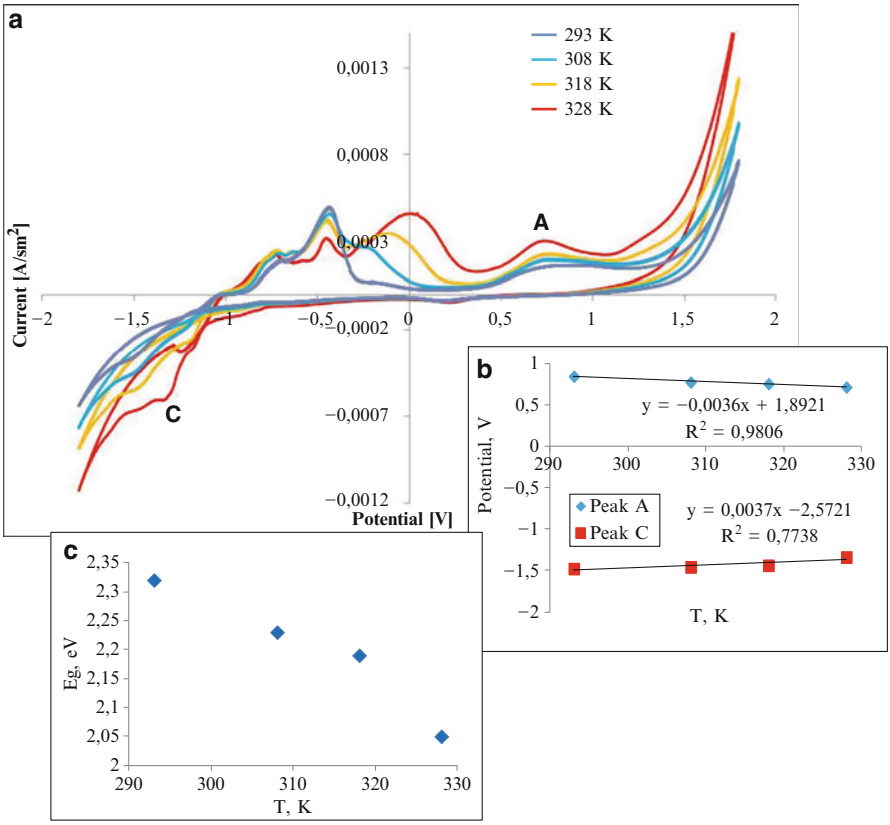

Fig. 17.6 (**a**) CV of CdTe/CdS QDs colloidal solution at different temperatures ($d = 2.5$ nm). The scan rate was 100 mV/s; (**b**) plots of anodic and cathodic peak potential vs. temperature; (**c**) the temperature dependence of the Eg. (CV) energy

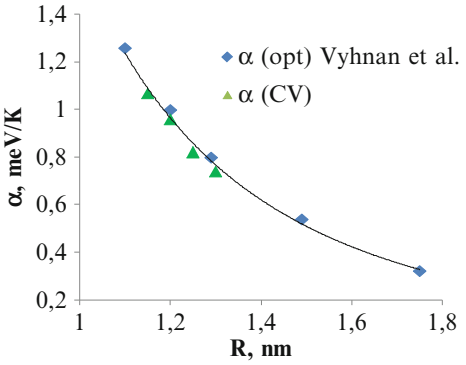

Fig. 17.7 The size dependence of the temperature sensitivity of CdTe/CdS core–shell QDs

A relation for the variation of the energy gap with temperature in semiconductors described by the Varshni equation [22]:

$$E_g = E_0 - \alpha \frac{T^2}{T + \theta} \tag{17.1}$$

where E_0 is the energy gap at 0 K, θ is the Debye temperature (for bulk CdTe $\theta = 160$ K), and α is the temperature sensitivity.

As previously shown [14], the shift of PL band of the QDs with temperature is almost the same as that of the temperature-dependent bandgap decrease of the bulk material. Therefore, the Varshni equation can be used to describe the temperature dependence of the energy gap of QDs. We noticed that similar to optical bandgap (Eg_{opt}), electrochemical (Eg_{CV}) bandgap of QDs demonstrates the same trend, so the temperature sensitivity of QDs of a certain size can be determined from the slope of the linear regression approximation plotted in the coordinates Eg vs. $\alpha T^2/(T + \theta)$. In this case, the temperature coefficient α will describe the change in the PL energy when the temperature is changed by 1 K, and E_0 is the PL energy at 0 K [23].

While investigating the temperature dependence of the electrochemical bandgap energy, we noticed that the temperature coefficient decreases with the increasing radius of the QDs (Fig. 17.7) as we reported before.

The fact that the temperature coefficients (determined from optical and electrochemical measurements) are similar means that they have the same origin and provide valuable information to design desired multishell structures and photocatalysts.

17.4 Conclusions

We used optical and electrochemical studies to refine positions of energy levels in CdTe quantum dots. It was found that the difference between the oxidation and reduction peaks on CV correlates well with the optically determined bandgap of QD sizes. We observed that heating of CdTe/CdS QDs decreases bandgap energy as the

result of decreased quantum confinement. Bandgap (Eg) diagrams for different particle sizes were plotted on the base of the obtained results.

Acknowledgments We thank the research team of Jagiellonian University in Cracow (Poland), Department of Physical Chemistry and Electrochemistry, Faculty of Chemistry.

This publication is based on the work supported by a grant from the US Civilian Research and Development Foundation (CRDF Global) (UKC2-7071-CH–12), State Agency on Science, Innovation and Informatization of Ukraine (M/85-2014).

References

1. Ortega-López M, Rosendo E, Ortega-Avilés M, Sánchez-Reséndiz V, Hernández-Hernández A, Meléndez-Lira M, Matsumoto-Kuwabara Y, Espinoza-Riva AM, Pérez-Guzmán MA (2012) Synthesis of CdTe quantum dots in aqueous solution and their optical and structural characterization. Sci Adv Mater 4(5–6):604–608
2. Kamat PV (2008) Quantum dot solar cells. Semiconductor nanocrystals as light harvesters. J Phys Chem 112(48):18737–18753
3. Bang JH, Kamat PV (2009) Quantum dot sensitized solar cells. A tale of two semiconductor nanocrystals: CdSe and CdTe. ACS Nano 3(6):1467–1476
4. Hetsch F, Xu X, Wang H, Kershaw SV, Rogach AL (2011) Semiconductor nanocrystal quantum dots as solar cell components and photosensitizers: material, charge transfer, and separation aspects of some device topologies. J Phys Chem Lett 2(15):1879–1887
5. Tsao JY, Brener I, Kelley DF, Ken Lyo S (2013) Quantum dot based solid-state lighting with electric field tunable chromaticity. J Disp Tech 9(6):419–426
6. So MK, Xu C, Loening AM, Gambhir SS, Rao J (2006) Self-illuminating quantum dot conjugates for in vivo imaging. Nat Biotechnol 24(3):339–343
7. Xing Y, Rao J (2008) Quantum dot bioconjugates for in vitro diagnostics & in vivo imaging. Cancer Biomark 4(6):307–319
8. Jasieniak J, Califano M, Watkins SE (2011) Size-dependent valence and conduction band-edge energies of semiconductor nanocrystals. ACS Nano 5(7):5888–5902
9. Poznyak SK, Osipovich NP, Shavel A, Talapin DV, Gao M, Eychmüller A, Gaponik N (2005) Size-dependent electrochemical behavior of thiol-capped CdTe nanocrystals in aqueous solution. J Phys Chem B 109(3):1094–1100
10. Haram SK, Quinn BM, Bard AJ (2001) Electrochemistry of CdS nanoparticles: a correlation between optical and electrochemical band gaps. J Am Chem Soc 123(36):8860–8861
11. Haram SK, Kshirsagar A, Gujarathi YD, Ingole PP, Nene OA, Markad GB, Nanavati SP (2011) Quantum confinement in CdTe quantum dots: investigation through cyclic voltammetry supported by density functional theory (DFT). J Phys Chem C 115(14):6243–6249
12. Kucur E, Riegler J, Urban GA, Nann T (2003) Determination of quantum confinement in CdSe nanocrystals by cyclic voltammetry. J Chem Phys 119(4):2333–2337
13. Yeo I, Song JD, Lee J (2011) Temperature-dependent energy band gap variation in self-organized InAs quantum dots. Appl Phys Lett 99(15):151909
14. Chi TTK, Thuy UTD, Liem NQ, Nam MH, Thanh DX (2008) Temperature-dependent photoluminescence and absorption of CdSe quantum dots embedded in PMMA. J Korean Phys Soc 52(5):1510–1513
15. Dey P, Paul J, Bylsma J, Karaiskaj D, Luther JM, Beard MC, Romero AH (2013) Origin of the temperature dependence of the band gap of PbS and PbSe quantum dots. Solid State Commun 165:49–54
16. Morello G, Giorgi MD, Kudera S, Manna L, Cingolani R, Anni M (2007) Temperature and size dependence of nonradiative relaxation and exciton-phonon coupling in colloidal CdTe quantum dots. J Phys Chem 111:5846–5849

17. Wang HL, Ning D, Feng SL (2000) Temperature dependence of the optical properties of InAs/GaAs self-organized quantum dots with bimodal size distribution. J Cryst growth 209 (4):630–636
18. Rogach AL, Franzl T, Klar TA, Feldmann J, Gaponik N, Lesnyak V, Shavel A, Eychmüller A, Rakovich YP, Donegan JF (2007) Aqueous synthesis of thiol-capped CdTe nanocrystals: state-of-the-art. J Phys Chem C 111(40):14628–14637
19. Sobrova P, Ryvolova M, Hubalek J, Adam V, Kizek R (2013) Voltammetry as a tool for characterization of CdTe quantum dots. Int J Mol Sci 14(7):13497–13510
20. Bae Y, Myung N, Bard AJ (2004) Electrochemistry and electrogenerated chemiluminescence of CdTe nanoparticles. Nano Lett 4(6):1153–1161
21. Pletcher D, Greff R, Peat R, Peter LM, Robinson J (2001) Instrumental methods in electrochemistry. Elsevier, Burlington
22. Varshni YP (1967) Temperature dependence of the energy gap in semiconductors. Physica 34 (1):149–154
23. Vyhnan N, Khalavka Y (2013) Size-dependent temperature sensitivity of photoluminescence peak position of CdTe quantum dots. Luminescence 29(7):952–954

Chapter 18
Dynamical Properties of Two-Dimensional Aggregates in Patchy Particle Systems

A. Chrzanowska, J. Kurzyk, and P. Karbowniczek

18.1 Introduction

Over the last decades, there has been an enormous interest in studying properties of the systems composed from the patchy particles—particles which are covered discontinuously with spots interacting differently than the other parts of the surface. This interest is spurred by two major reasons: (a) such systems can be used as model systems that can be studied in a very detailed way as well by the theories as by the simulations [1–3] (b) recent advances in producing patchy colloids, especially DNA-guided colloids [4–7]. The efforts are also directed onto the possible applications for photonic band gap structures, functional materials or studies on directed self-assemblies.

Major part of the computer investigations on patchy particle systems is done by the use of the Monte Carlo methods and is focused on obtaining static properties like phase diagrams or clusters statistics. Yet molecular dynamics techniques still offer more possibilities allowing for better understanding of physical mechanisms governing these systems [8–10].

In this paper MD results for a two-dimensional system of aggregated particles have been presented for two chosen stages of clustering.

A. Chrzanowska (✉) • J. Kurzyk • P. Karbowniczek
Institute of Physics, Cracow University of Technology, ul. Podchorążych 1,
30-084 Kraków, Poland
e-mail: achrzano@usk.pk.edu.pl

O. Fesenko, L. Yatsenko (eds.), *Nanoplasmonics, Nano-Optics, Nanocomposites, and Surface Studies*, Springer Proceedings in Physics 167,
DOI 10.1007/978-3-319-18543-9_18

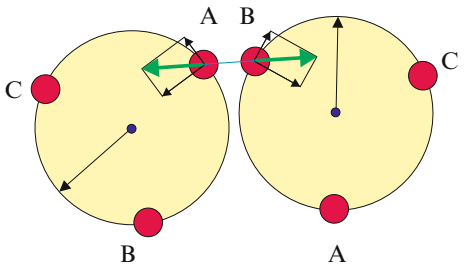

Fig. 18.1 Geometry of interaction

18.2 The System

In our simulations we considered 986 spheres of the diameter 1 with three attractive patches. The interactions between patches were modeled by an attractive square well potential of the depth $u = 0.5$. The temperature considered is equal to $T = 0.1$. Geometry of the interaction between two particles is given in Fig. 18.1. Such localization of specific surface interactions is in accordance with a more general rule that each site is involved at most in *one* bonded interaction. In contrast to the Kern Frenkel model [11], the interactions are off-center (the spots are interacting, not the centers of the particles) exerting torques on the bodies each time the particle reaches the edge of the well of the interaction potential of the patch. Such a choice of the interaction model is therefore realistic.

When the particles are close to each other in such a way that the patches interact via the square well potential and have energies below the value characterizing the potential well the particles form a bond. As a consequence of minimizing the interaction energy the whole set of patchy particles will attain a certain clustered state, in which the size and structure of the aggregates depend as well on the density as on temperature of the system. The system reminds of a polymer, yet the bonds are not very stable, thus one observes continuous process of bonds creations and their unbonding with an average of bonds being at constant level. This interplay introduces completely new features to the dynamical picture of the system. Another crucial factor influencing dynamical properties is the structure of the aggregates. In next section typical features of these properties will be presented.

18.3 Molecular Dynamics Results

The starting configurations have been obtained with the help of the Monte Carlo simulations. Then the molecular dynamics has been applied to the systems for two chosen densities that lead to different stages of aggregation, $\rho = 0.1$ (case A) and $\rho = 0.3$ (case B), see Fig. 18.2. In the case B one practically deals with a single big cluster that spans over the whole studied volume. In the case A several smaller clusters are being observed. To perform MD simulation each particle must obtain a

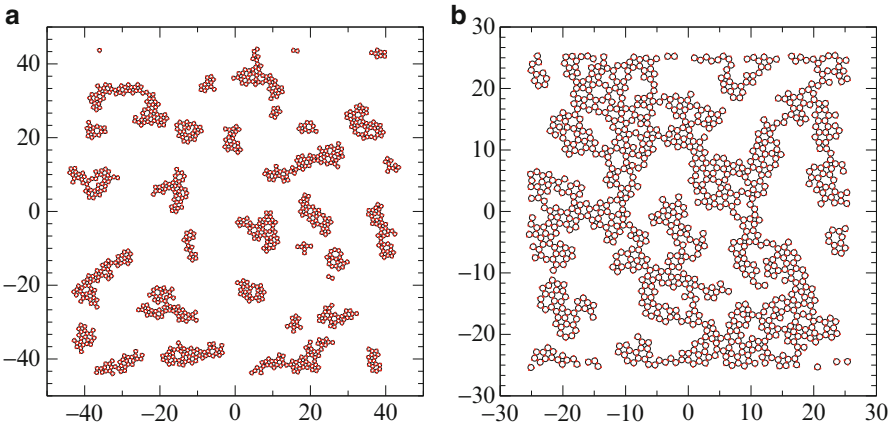

Fig. 18.2 Configurations of patchy particles at the density (**a**) $\rho = 0.1$ and (**b**) $\rho = 0.3$

certain value of linear and angular velocity. These values have been chosen randomly from the Maxwellian distribution adjusted to the assumed system temperature, here for $kT = 0.1$. Molecular dynamics is performed by resolving subsequent dynamical events of collisions between hard parts of the spheres and collisions at the edges of the square well potential (event driven molecular dynamics). The last one requires analysis of all possible interactions of the patches. As a consequence, the particle may freely move or be captured in the potential well forming a bond. When two particles are within the range of the potential action they can still freely move until the hard collision with the main sphere or with the edge of the potential well takes place. If the energy is smaller than the potential depth, then the particle bounces until it may get a new portion of energy from the third companion interaction, then one deals with an unbonding. Thus bonding and unbonding processes are connected with the transport of energy within the aggregate and must depend on its structure.

In Fig. 18.3 the autocorrelations of the total value of the particles velocity are shown for two different stages of aggregations. The presented profiles exhibit regular features. One can distinguish three different parts: (a) a quick decrease of the ACF-V value till a level of 40 % (b) a pronounced minimum occurring after a quick drop of the ACF-V value (c) a very slow decrease of the whole profile showing that the velocity correlations are very long lasting. For a denser system with a larger degree of aggregation the autocorrelation drops to a lower value than for a less dense system, yet the slopes of the slow decay for two cases studied seem to be very similar. Larger aggregates are less capable to preserve the information about the particles velocity.

A minimum after the fast decay is caused by particle's rattling within the potential well. A similar single minimum structure occurs in simply liquids, for instance, in liquid argon [12], but the argon minimum attains negative values. Here, in the case of patchy particles aggregates strong correlations still exist having a long

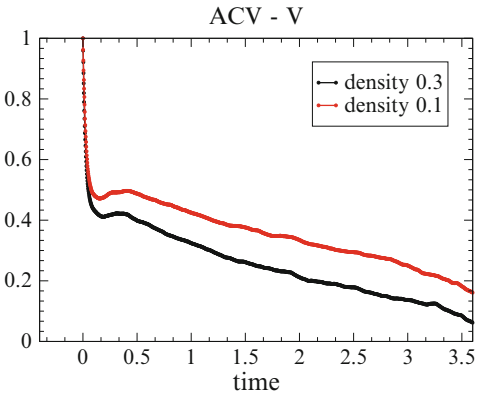

Fig. 18.3 Autocorrelation function of the total linear velocity obtained for the configurations at two different densities

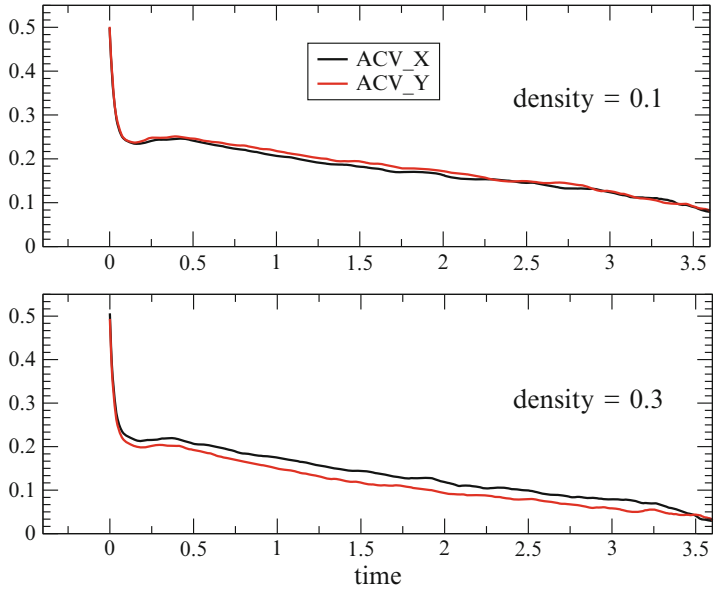

Fig. 18.4 Autocorrelation functions obtained for the X and Y components of the total velocity

lasting character. Because of this, one may regard the occurrence of the minimum as the feature related to the bonding process itself and not to the size of the aggregates or their presence (in the case of argon the bonds are stable and there are no aggregates). The time scope needed to drop ACF-V to the null level is about four times larger than the ballistic regime time [see the figure for the mean square displacement (MSD)]. This regime is recognized as determined by the aggregates presence.

Profiles presented in Fig. 18.4 suggest possible influence of the structure on the distribution autocorrelations. In the lower panel for a denser system with larger

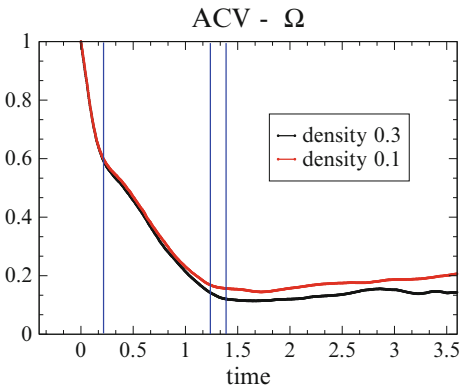

Fig. 18.5 Angular velocity autocorrelation function

aggregates one observes a noticeable departure of ACF-VX from ACF-VY. This effect is connected with a particular configuration considered (Fig. 18.2b) which, as a system, is rather small and, in this particular case, exhibits a certain degree of structural anisotropy—the voids are dominated by elongated shapes in Y direction. This feature, the relation between elongated in one direction aggregates and velocity correlations, requires however more detailed studies.

In Fig. 18.5 the angular velocity autocorrelations (ACF-OM) are presented. One can distinguish here also three characteristic regimes: a regime of fast decay (till about 1,800 collisions or 2 collisions per particle), a regime with linear dependence on time which lasts till about 11,600 collisions (or 12 collisions per particle), an uneven profile where the angular ACF still remains at the level of several percent. The first regime of quick decay seems to be identical for both studied configurations. It is a very interesting observation that this regimes end at the level of the minimum present in the velocity ACF-V, which, at the same time, becomes an onset of the next regime.

Also in the second regime the characteristics are very similar, yet the curves are distinguishable with ACF-OM for denser system having slightly smaller values than smaller aggregates system (the vertical lines are the eye guides for the borders of these regimes). This difference becomes more pronounced in the third regime which suggests an existence of a constant level of ACF-OM of several percent, (within the range of the simulation time). This feature is an interesting and novel quality, hence more work is still needed on its time persistence. The linear regime is also interpreted as related to the molecular mechanism of the bond exchange [8].

During the simulations also the MSD has been monitored. In both cases of different states of aggregation one observes only two typical regimes. In the first regime MSD is very well described by a quadratic function of time with departures occurring only at the small number of initial collisions (presented in Fig. 18.6). Then MSD becomes linear as is typical for the fluid and liquid cases. Figure 18.6 presents MSD profiles for the studied values of the density for the time interval where the process is of the ballistic type. The simulation data, besides the narrow regime of the initial time, fit very well to the square function of time. The type of the departure for small times is given in Fig. 18.7.

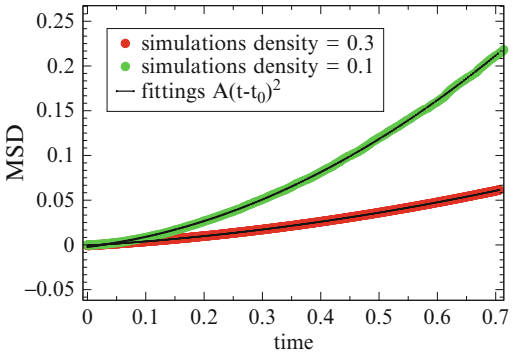

Fig. 18.6 Mean square displacement

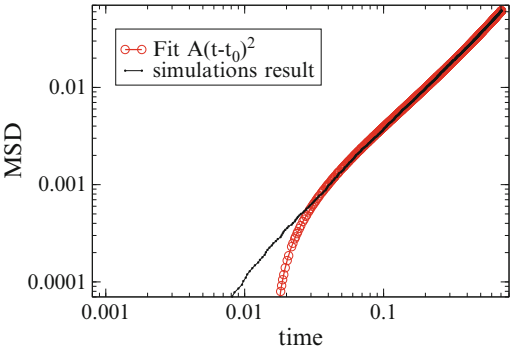

Fig. 18.7 Departure of MSD from quadratic function for short times

References

1. Bianchi E, Largo J, Tartaglia P, Zaccarelli E, Sciortino F (2006) Phase diagram of patchy colloids: towards empty liquids. Phys Rev Lett 97:168301–168304
2. Sciortino F, Bianchi E, Douglas JF, Tartaglia P (2007) Self-assembly of patchy particles into polymer chains: a parameter-free comparison between Wertheim theory and Monte Carlo simulation. J Chem Phys 126:4903
3. Liu H, Kumar SK, Sciortino F (2007) Vapor-liquid coexistence of patchy models: relevance to protein phase behavior. J Chem Phys 127:084902
4. Park SY et al (2008) DNA-programmable nanoparticle crystallization. Nature 451:553–556
5. Nykypanchuk D, Maye MM, van der Lelie D, Gang O (2008) DNA-guided crystallization of colloidal nanoparticles. Nature 451:549–552.
6. Mirkin CA, Letsinger RL, Mucic RC, Storhoff JJ (1996) A DNA-based method for rationally assembling nanoparticles into macroscopic materials. Nature 382:607–609
7. Alivisatos AP, Johnsson KP, Peng X, Wilson TE, Loweth CJ, Bruchez MP, Schultz PG (1996) Organization of nanocrystal molecules using DNA. Nature 382:609–611
8. Smallenburg F, Leibler L, Sciortino F (2013) Patchy particle model for vitrimers. Phys Rev Lett 111:188002
9. Dias CS, Araújo NAM, Telo da Gama MM (2013) Non-equilibrium adsorption of 2AnB patchy colloids on substrates. Soft Matter 9:5616
10. Dias CS, Araújo NAM, Telo da Gama MM (2013) Nonequilibrium growth of patchy-colloid networks on substrates. Phys Rev E 87:032308

11. Kern N, Frenkel D (2003) Fluid-fluid coexistence in colloidal systems with short-ranged strongly directional attraction. J Chem Phys 118(21):9882–9889
12. Rahman A, Stillinger FH (1971) Molecular dynamics study of liquid water. J Chem Phys 55:3336–3359

Part II
Nanophotonics

Chapter 19
Synthesis and Characterization of Titanium (IV) Oxide from Various Precursors

T. Dontsova, I. Ivanenko, and I. Astrelin

19.1 General

19.1.1 Introduction

In the last decade, the photocatalytic processes attract growing interest due to their wide industrial application in a variety of applications: the photocatalytic decomposition of harmful organic compounds both in solution and in the gas phase, the transformation of solar energy into chemical and electrical energy, the creation of sensors and nanophotonics devices, the organic synthesis, etc. Often, photocatalytic reaction can proceed at room or lower temperature by the action of visible light, which allows using the solar energy for useful processes [1].

Decomposition of organic pollutants in air and water due to the photocatalytic reactions attributed to high-end technologies of environmental protection [1–3]. Photocatalytic processes or so-called activated oxidation processes (AOP), which are used in wastewater treatment, refer to the methods of deep oxidation and are highly effective in the case of the removal of organic pollutants that cannot be decomposed by biological methods. These processes include various combinations of homogeneous and heterogeneous photocatalysis, and other methods (see Fig. 19.1) are able to generate a strong oxidizer—the hydroxyl radical ($OH^{\bullet}$). The hydroxyl radical has a high potential and can oxidize a great amount of organic pollutants.

Heterogeneous photocatalysis is the most environmentally friendly and economical technology due to its use of nontoxic catalyst-based semiconductor materials. It is becoming more widely used in various water treatment processes. The reasons for

T. Dontsova (✉) • I. Ivanenko • I. Astrelin
Faculty of Chemical Technology, National Technical University of Ukraine, "Kyiv Polytechnic Institute", 37 Prospect Peremogy, Kiev 03056, Ukraine
e-mail: dontsova@ua.fm; irinaivanenko@hotmail.com; i.m.astrelin@xtf.kpi.ua

O. Fesenko, L. Yatsenko (eds.), *Nanoplasmonics, Nano-Optics, Nanocomposites, and Surface Studies*, Springer Proceedings in Physics 167,
DOI 10.1007/978-3-319-18543-9_19

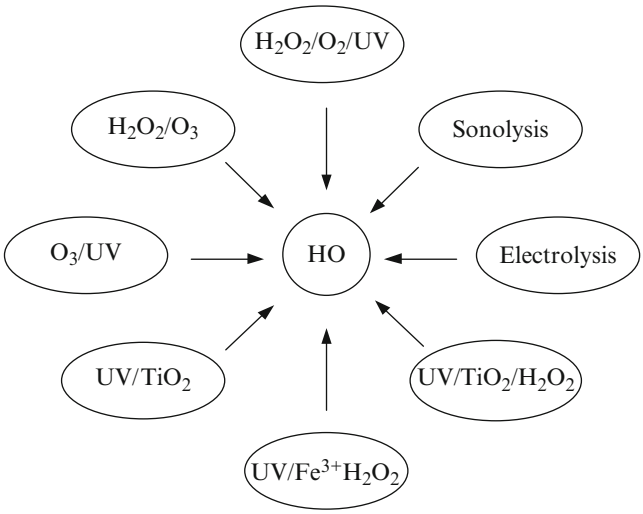

Fig. 19.1 Basic activated oxidation processes (AOP) [2]

this are the possibility of oxidation of organic compounds with a sufficient degree of mineralization at low temperatures and the substantial reduction of energy consumption in the transition through the use of sunshine.

A great variety of photocatalysts proposed and synthesized currently, which accelerate the different reactions of synthesis and decomposition under light irradiation. Most semiconductor materials used as photocatalytic substance are metal oxides ZnO, SnO_2, Fe_2O_3, CdO, WO_3, In_2O_3, and TiO_2. Such materials have been successfully used for water and air purification from organic pollutants as well as to kill the bacteria [4].

Titanium (IV) oxide is the most popular photocatalyst. The prospects of the practical application are associated with its high photocatalytic activity (it allows to implement a number of physical and chemical oxidative type processes [5]), as well as chemical stability, low cost, and nontoxicity. However, the photocatalysis with titanium oxide (IV) has a number of significant drawbacks. The bandgap of titanium (IV) oxide is 3.0–3.2 eV, the light absorption by them is in the UV region of the spectrum, and therefore the efficiency of this photocatalyst by visible light is small. Also, there is a slight quantum yield of photoconversion that is associated with a high degree of recombination of carriers, low specific surface area, and adsorption ability of TiO_2 catalysts.

Consequently, the increasing photocatalytic activity and quantum yield of catalysts based on titanium (IV) oxide (especially in the visible light range) are an actual task of modern photocatalysis.

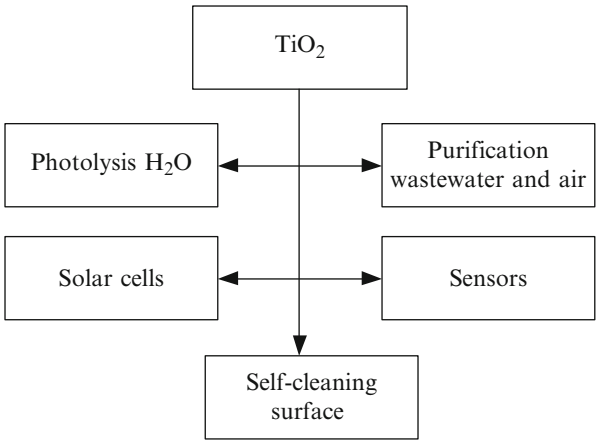

Fig. 19.2 Scheme practical use of TiO_2

19.1.2 Use of Titanium (IV) Oxide

There are a variety of application materials based on titanium (IV) oxide: pigments, catalysts and photocatalysts, fillers, and cosmetic and food additives. Titanium (IV) oxide is becoming increasingly used in the special purpose (see Fig. 19.2). Especially interesting is its use in photocatalytic sterilization for medical and food industries as well as its use in solving environmental problems.

Lately the combination of titanium oxide with ultraviolet radiation is one of the best disinfection technologies, because this technology does not form dangerous (carcinogenic, mutagenic, bad smelling) compounds unlike others [6].

19.1.3 Methods of Obtaining Titanium (IV) Oxide

The lower the crystallite size and the higher the degree of crystallinity and porosity, the more the photoactivity of the catalyst. To achieve these characteristics, different methods and techniques in the photocatalysts synthesis have been used [7–11] and in this sense have had some successes.

Today metal oxides can be prepared with different morphologies, mainly nanoparticles, nanotubes, nanowires, nanorods, and mesoporous structure [7]. For this purpose, we use the synthesis from liquid phase (hydrolysis of metal salts [8], hydrothermal and solvothermal methods [9], sol–gel technology [10]) and the synthesis from gas phase (chemical vapor deposition (CVD) [11]) and some specific methods (electrodeposition and sonochemical and microwave methods). All these methods can be successfully used for the synthesis of photocatalysts with specified physicochemical characteristics.

19.1.4 Mechanism of Photocatalysis on the Surface of Titanium (IV) Oxide

TiO_2 naturally exists in three polymorphic modifications: anatase, rutile, and brookite [12]. Usually in photocatalysis, rutile and anatase modifications are used that have tetragonal crystal structures which are composed of octahedrons TiO_6 that differ by distortion of each octahedron and octahedral chains (see Fig. 19.3). Each Ti^{4+} ion in the octahedron is surrounded by six ions O^{2-}. The difference in the lattice structure of anatase and rutile causes their different densities and electronic band structures. Therefore, light absorption of anatase and rutile occurs at a wavelength of 388 and 413 nm, respectively.

Formation of photoactive TiO_2 surface includes the appearance of holes in the valence band (h^+_{vb}) and electrons in the conduction band (e^-_{cb}) due to the absorption of the photon energy. The conduction band must be equal to or greater than the width of the bandgap ($h\nu \geq E_{gb}$) semiconductor (bandgap of TiO_2 is for rutile, 3.0 eV; for anatase, 3.2 eV) [13]. Holes contribute to the formation of hydroxyl radicals and oxidation of organic compounds, and electrons promote the superoxide radicals and the decomposition and oxidation reactions [14].

Hydroxyl and superoxide radicals characterized the photocatalytic activity of TiO_2 and formed by the reaction [15]:

$$TiO_2 + h\upsilon \rightarrow TiO_2(e^-CB + h^+VB), \tag{19.1}$$

$$TiO_2(e^-CB + h^+VB) \rightarrow TiO_2(\text{recombination}), \tag{19.2}$$

$$TiO_2(h^+VB) + OH^- \rightarrow TiO_2 + OH^{\cdot}, \tag{19.3}$$

$$TiO_2(e^-CB) + O_2 \rightarrow TiO_2 + O_2^{\cdot}, \tag{19.4}$$

where CB is the conduction band and VB is the valence band.

Furthermore, formed hydroxyl and superoxide radicals react with organic pollutants, and their oxidation occurs. The general scheme of the photocatalytic degradation of organic pollutants can be represented as [15]:

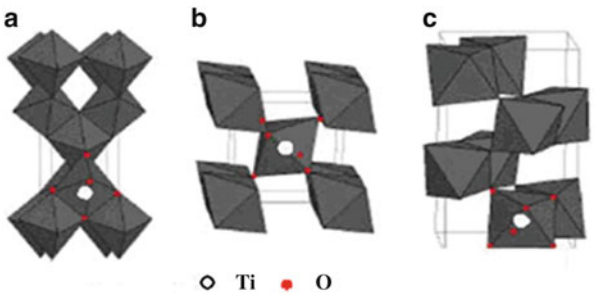

Fig. 19.3 Crystallographic form TiO_2: (**a**) anatase, (**b**) rutile, and (**c**) brookite [12]

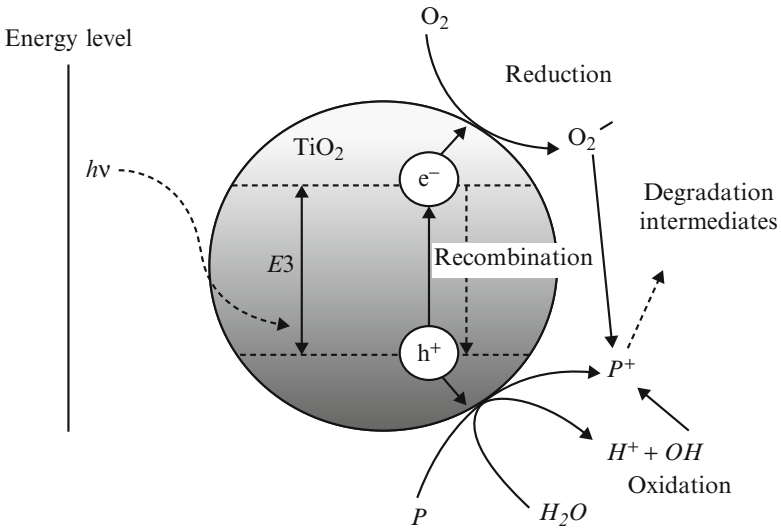

Fig. 19.4 Schematic representation of the photoactivation mechanism and photocatalysis on the TiO_2 surface [16]: *P* pollutants, E_{gb} the width of bandgap

$$\text{Organic pollutants (P)} \overset{TiO_2/h\nu}{\rightarrow} \text{intermediates} \rightarrow CO_2 + H_2O. \tag{19.5}$$

Schematically, the mechanism of photoactivation of TiO_2 particles by ultraviolet is shown in Fig. 19.4.

Thus, the photocatalytic oxidation of organic pollutants occurs in the following steps [15]:

1. Transfer of organic pollutant mass from liquid phase to the TiO_2 surface
2. Adsorption of organic pollutants on the photoactivated TiO_2 surface (surface activation by photon energy takes place with the first step simultaneously)
3. Photocatalytic reactions on the TiO_2 surface
4. Desorption of products (including intermediate) from the TiO_2 surface
5. Transfer of product mass in the liquid medium

According to the present mechanism, it is obvious that for effective photocatalytic process, in general, TiO_2 must have a high specific surface area (in order to increase the efficiency of adsorption of organic compounds) and a small particle size (to reduce the recombination of electron–hole pairs).

Using nanoscale of metal oxide particles leads to significant improvement of their properties such as photo- and electroconductivity and catalytic reactivity and more. Metal oxide nanoparticles as photocatalysts have obvious advantages compared with microparticles due to high probability of exit charges on their surface. Due to the fact that the depth of UV penetration light into TiO_2 particles (~100 nm) is limited, in the case of microparticles, it is active only on external surface [16]. Figure 19.5 shows the diagram absorption of light quanta of TiO_2 micro- and

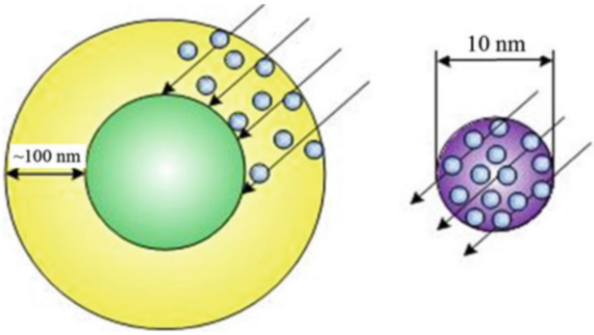

Fig. 19.5 The absorption of light quanta in micro- and nanoparticles [16]

nanoparticles. Reducing the particle size photocatalyst to nanoscale promotes the absorption of all the light volume of particles.

Creation of catalyst based on titanium (IV) oxide with smaller bandgap, which would work in the visible range, is a very important scientific and practical task. To solve this problem, modification of titanium oxide (IV) or obtaining its nanocomposites is proposed [17–20].

Application of metal and nonmetal dopants in semiconductor surface significantly alters the physical and chemical properties, thus changing the photocatalytic properties. Creating composites (including heterostructures) based on two semiconductors presents promising direction for increasing the photocatalytic process efficiency through better charge distribution and range expansion of existing light [21].

It is necessary to obtain titanium (IV) oxide in a highly dispersed state with maximum surface area and less bandgap to develop effective technology of photocatalytic purification with using TiO_2.

TiO_2 nanopowders are synthesized most widely and successfully by sol–gel technology, which allows to obtain high purity nanoparticles at relatively low temperatures with a uniform particle size distribution [22–26].

Purpose of the present work is to study the effect of precursors and modifiers in sol–gel synthesis on the structure, morphology, and photocatalytic activity of nanosized titanium (IV) oxide.

19.2 Experimental

19.2.1 Obtaining of Titanium (IV) Oxide Samples

TiO_2 samples were obtained with the use of a precursor 15 % solution of titanium (III) chloride in chloride acid as follows (Fig. 19.6). Initial solution of titanium chloride (III) was diluted with distilled water at pH 0.8 and left 168 h for hydrolysis, which took place slowly. First, turbidity and opalescence became visible only after 72 h. Next, on the basis of this solution, five samples were prepared. The conditions of synthesis are summarized in Table 19.1. Separation of solid phase in the

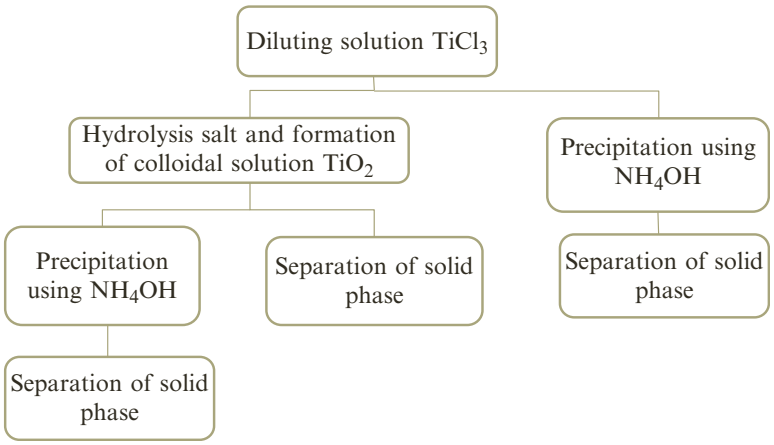

Fig. 19.6 Scheme of synthesis of TiO_2 particles from $TiCl_3$

Table 19.1 Conditions for the synthesis of TiO_2 samples

Sample	Precursor	Solvent	T_{hydr}, h	Precipitator	Modifier	$T_{synthesis}$, °C
1	$TiCl_3$ in chloride acid	Water	168	–	–	20
2				NH_4OH to pH 9.4		
3			0			
4			168	–	K_2SO_4 (molar ratio (Ti^{3+}): (SO_4^{2-}) = 1:2)	
5					KF (molar ratio (Ti^{3+}): (F^-) = 1:2)	
6	$TiCl_4$	Water	72	–	–	60
7					CdS (0.5 % mas.)	
8					CdS (2 % mas.)	
9					CdS (4 % mas.)	
10					CdS (7 % mas.)	
11		Water–isopropyl			–	
12					CdS (0.5 % mas.)	
13					CdS (2 % mas.)	
14					CdS (4 % mas.)	
15					CdS (7 % mas.)	
16		Water–isobutyl			–	
17					CdS (0.5 % mas.)	
18					CdS (2 % mas.)	
19					CdS (4 % mas.)	
20					CdS (7 % mas.)	

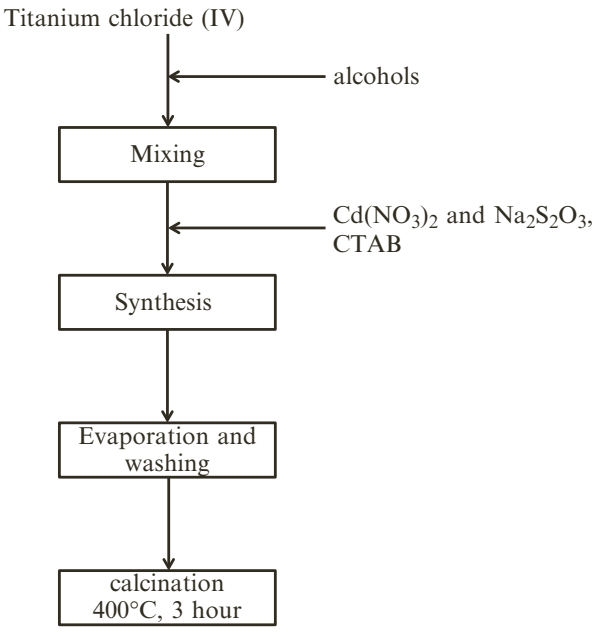

Fig. 19.7 Scheme of synthesis of TiO_2 particles from $TiCl_4$

suspensions obtained by hydrolysis and/or precipitation was performed by centrifuging with intermediate decantation. Further, precipitates were dried at room temperature and triturated in an agate mortar. The syntheses of samples 4 and 5 were carried out in the presence of ions SO_4^{2-} by adding a calculated amount of K_2SO_4 in a molar ratio $(Ti^{3+}):(SO_4^{2-}) = 1:2$ and fluoride ions by the addition of KF from ratio $(Ti^{3+}):(F^-) = 1:2$.

Synthesis of TiO_2 using precursor titanium (IV) chloride was carried out as follows (Fig. 19.7). Cooled titanium (IV) chloride under stirring was slowly inputted into alcohol or cold distilled water (0 °C) with the addition of cetyltrimethylammonium bromide (CTAB) in an amount of 1 g. Next, the solution was stirred for 30 min and allowed to age at 60 °C for 72 h. The resulting precipitates were collected by centrifugation, and after they were dried and calcined at 400 °C for 3 h to remove residual CTAB. Thereafter, samples were triturated in an agate mortar. Thus, the five samples were obtained, which differed in the number of dopant CdS (see Table 19.1) used for the preparation of aqueous solutions of sodium (I) thiosulfate and cadmium (II) nitrate.

19.2.2 X-Ray Analysis

X-ray analysis of the samples was carried out on a diffractometer Rigaku Ultima IV in copper Cu K_α radiation ($\lambda = 0.154184$ nm) at the rate of 0.02°/s, voltage of

40 kV, and amperage of 40 mA. X-ray diffraction analysis was carried out using the instrument software.

The particle size was determined by transmission electron microscope PEM 125 K with an accelerating voltage of 80 kV.

Structural-sorption characteristics of the samples were explored by low-temperature nitrogen adsorption–desorption on the Quantachrome® ASiQwin™ device at −195.6 °C. The specific surface area (S_{sp}, m_2/g) and the allocation of pore radius were calculated by the software of the device according to the method of density functional theory (density functional theory, DFT method).

The photocatalytic activity of synthesized samples was evaluated by the ability to decolorize model solutions of methylene blue dyes (cationic) and Congo red and methylene orange (anionic type) under ultraviolet radiation with a wavelength of 368 nm at room temperature.

Synthesis of titanium (IV) oxide from titanium (III) precursor was carried out as follows. As is known from the literature [21, 22], the transition of Ti (III) to Ti (IV) occurs due to hydrolysis:

$$4TiCl_3 + O_2 + 2H_2O = 4TiOCl_2 + 4HCl. \quad (19.6)$$

Further, TiO_2 was formed by the hydrolysis of titanium (IV) oxychloride:

$$TiOCl_2 + H_2O = TiO_2 + 2HCl, \quad (19.7)$$

and the effect of the precipitator:

$$TiOCl_2 + 2NH_4OH = TiO(OH)_2 + 2NH_4Cl, \quad (19.8)$$

$$TiO(OH)_2 = TiO_2 + H_2O. \quad (19.9)$$

Synthesis of titanium (IV) oxide from titanium (IV) chloride was carried out according to the reaction:

$$TiCl_4 + 2H_2O = TiO_2 + 4HCl. \quad (19.10)$$

CdS dopant in this case was formed according to the reaction:

$$Cd(NO_3)_2 + Na_2S_2O_3 + H_2O = CdS + 2NaNO_3 + H_2SO_4. \quad (19.11)$$

Figure 19.8 shows diffraction patterns of the obtained samples, which were automatically analyzed by the software package PDXL using databases ICDD/PDF-2, COD, and files JCPDS.

Accordingly, for cards 00-001-0562 (anatase TiO_2, base ICDD/PDF-2), 03-065-0190 (rutile TiO_2, base ICDD/PDF-2), №29-1360 (brookite TiO_2, Files JCPDS), and 00-041-1049 (CdS, base ICDD/PDF-2), the samples were identified as follows.

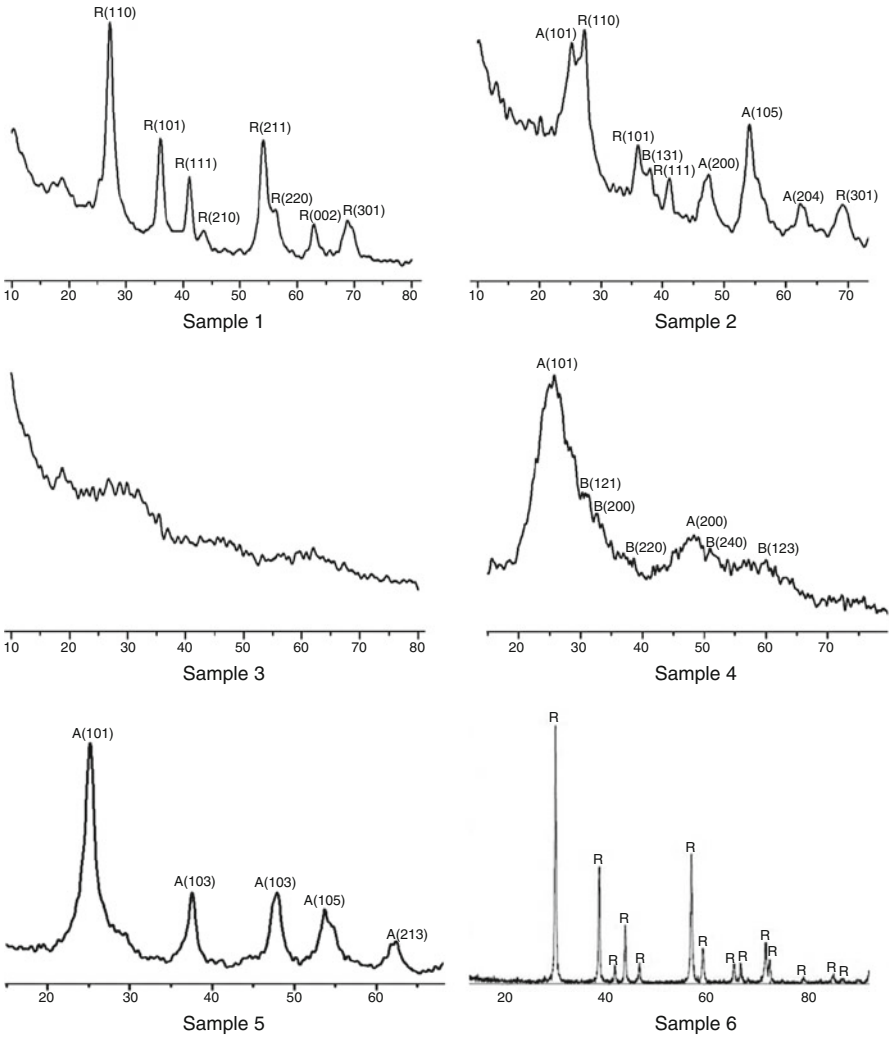

Fig. 19.8 X-ray analysis of synthesized titanium (IV) oxide samples 1–6

Hydrolysis of $TiCl_3$ solution in the absence of any precipitator or modifier contributes to the formation of pure rutile phase (Fig. 19.8, sample 1).

Using NH_4OH as a precipitator after hydrolysis of this solution creates conditions for forming almost equal amounts of rutile and anatase (Fig. 19.8, sample 2).

Crystal phase does not form if hydrolysis stage is absent. Sample 3 synthesized by precipitation method without hydrolysis turned out to be X-ray amorphous.

Addition of K_2SO_4 modifier during synthesis creates conditions for crystallization mixture of anatase and brookite (Fig. 19.8, sample 4). Pure anatase phase was

formed as a result of synthesis without a precipitator but with modifier KF (Fig. 19.8, sample 5).

If $TiCl_4$ solution was used without a modifier or with a small amount (CdS 0.5 % mass) in an aqueous medium, it would form a pure rutile modification of TiO_2 (Fig. 19.8 sample 5 and Fig. 19.9 sample 6). Further, increasing CdS amount causes crystallization of both phases of TiO_2—anatase and rutile (Fig. 19.9, samples 7–9). While the amount of modifier increases, the content of anatase also increases. It should also be noted that CdS phase is detected only in samples 9 and 10 (Fig. 19.9, samples 8 and 9).

In samples obtained in aqueous–alcoholic medium, rutile phase (Fig. 19.9, samples 16) and rutile–anatase modification (Figs. 19.9 and 19.10, samples 11–15, 17–20) were identified. Using $TiCl_3$ as precursor allows to get samples with different phase compositions and using $TiCl_4$ with rutile and anatase–rutile modifications.

Table 19.2 shows the calculated crystallite size and specific surface areas for the TiO_2 samples. It can be seen that values of specific surface area are a variety.

19.2.3 Microscopy

Represented TEM images of samples 1–5, 9, 14, and 19 (Fig. 19.11) indicate different morphologies and structures of obtained TiO_2 particles. TEM images of samples 6–8, 10–13, 15–18, and 20 are identical with samples 9, 14, and 19.

On Fig. 19.11a, b, we can see that globular formations of sample 1 mostly consist of small crystal-like particles, which is proved by semitransparency and gray color. Globules themselves are about 100–250 nm. They are surrounded by rod-shaped separated TiO_2 particles about 15 nm wide and 50 nm long.

Aggregates of sample 2 (Fig. 19.9c, d) formed by crystalline TiO_2 with rods are 20–30 nm wide and 50 nm long.

TEM image of sample 3 shows globules associated with bigger agglomerates of amorphous titanium (IV) oxide with an average size of 800–1,000 nm. Crystal phase starts to form at the edge of these structures (Fig. 19.11e). Average size of sample 3 globules ranges between 250 and 500 nm. Amorphous composition of conglomerates is also confirmed by X-ray analysis of this sample.

Particles of sample 4 (Fig. 19.11f) have a shape of a sphere with an average size of about 1 μm.

Aggregates of almost spherical-shaped particles may be seen at the image of sample 5 (Fig. 19.12a, b). Average size is from 30 to 70 nm. Each TiO_2 aggregate is surrounded by shell, probably hydrate, because desiccation of this sample was held at room temperature.

Samples 6–10 (Fig. 19.12c–f) have clearly limited edges of crystal of almost spherical-shaped separated particles that differ only in size.

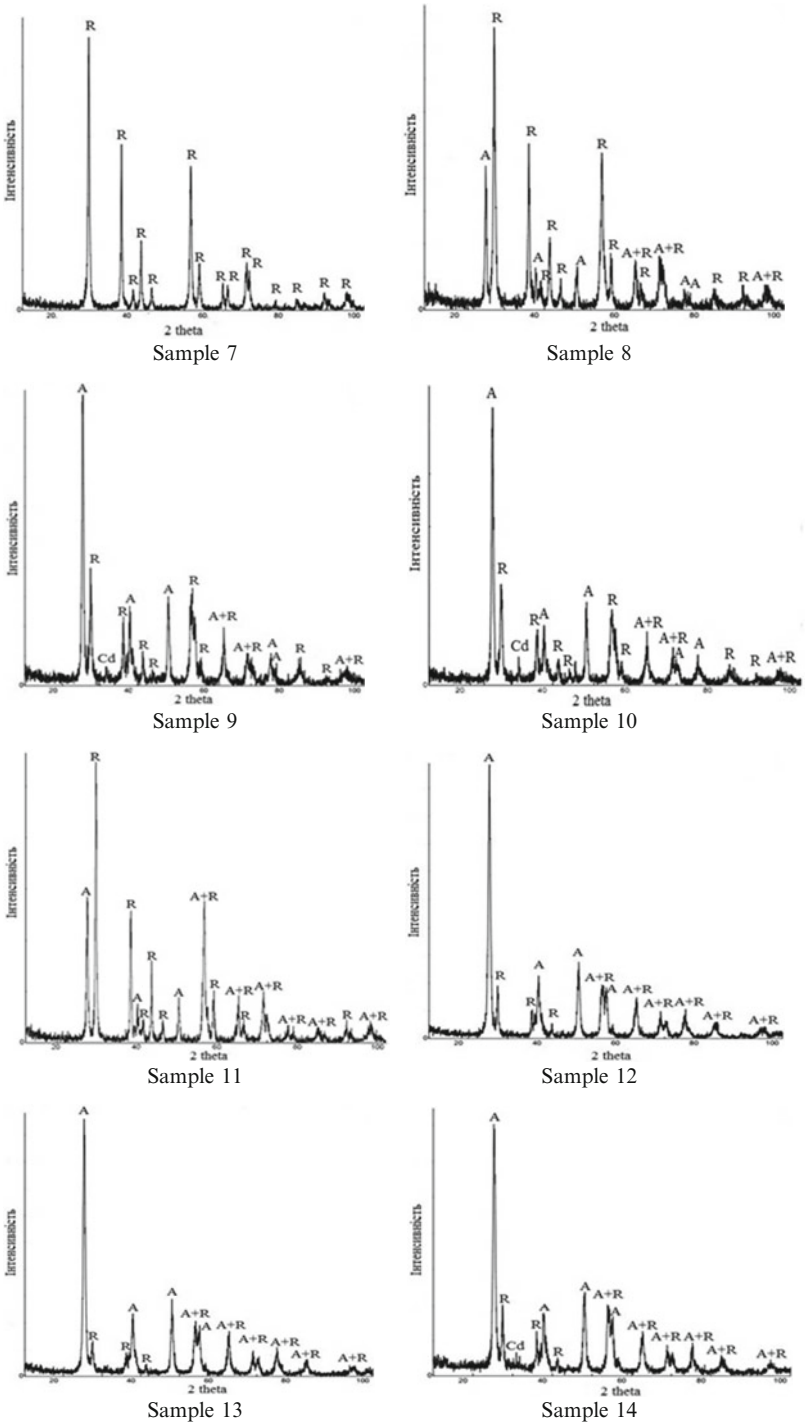

Fig. 19.9 X-ray analysis of synthesized titanium (IV) oxide samples 7–14

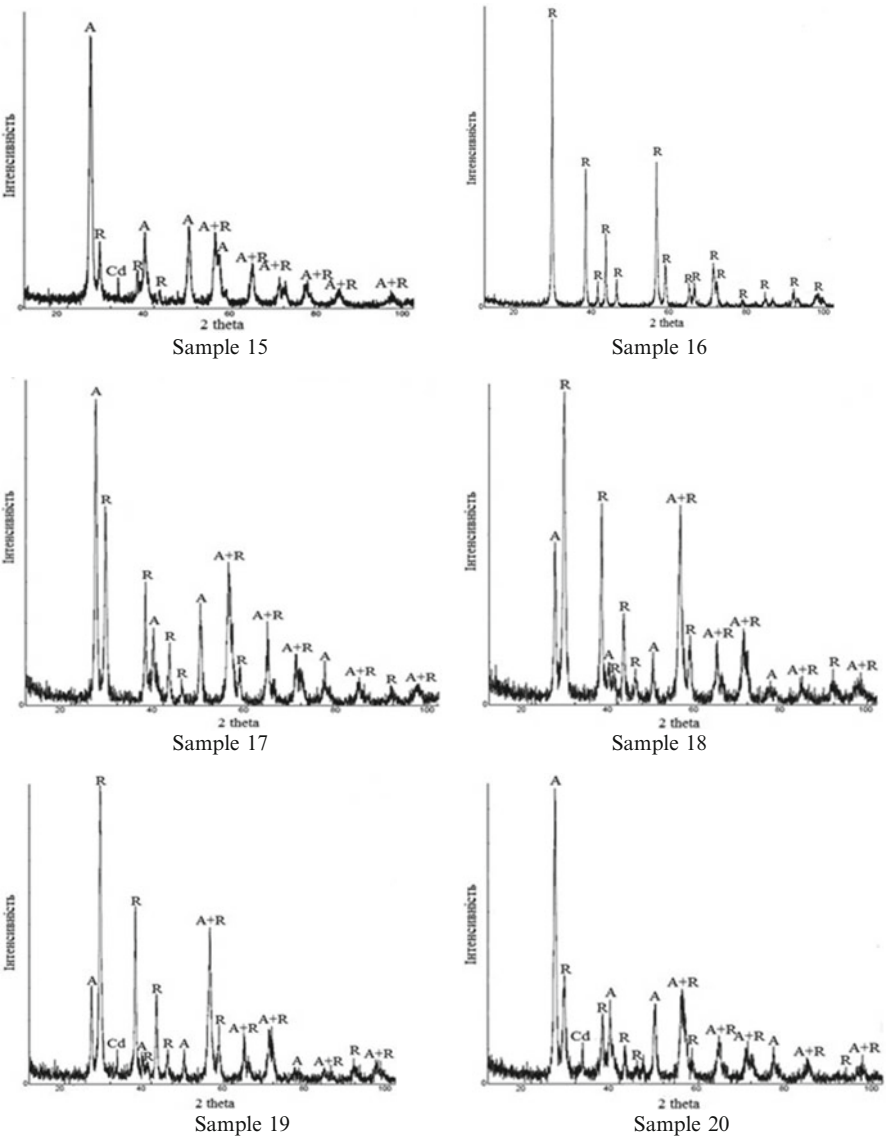

Fig. 19.10 X-ray analysis of synthesized titanium (IV) oxide samples 15–20

19.2.4 Photocatalytic Properties

Only sample 1 among five synthesized samples of TiO_2 (from $TiCl_3$ precursor) was photocatalytically active against Congo red (representative of anionic dyes). Degree of discoloration for this sample reached 100 %. Samples 2 and 3 did not

Table 19.2 Characteristics of synthesized TiO_2 samples

Sample	Phase composition, %	Crystallites size, nm	S_{sp}, m_2/g
1	Rutile 100	6.2	270
2	Anatase 50, rutile 50	6.3	270
3	Amorphous	–	430
4	Anatase 40, brookite 60	1.2	5
5	Anatase 100	6.0	355
6	Rutile 100	23.0	9
7	Rutile 100	14.9	37
8	Anatase 26, rutile 74	14.6	45
9	Anatase 56, rutile 42, CdS 2	13.1	67
10	Anatase 63, rutile 35,CdS 3	13.5	60
11	Anatase 36, rutile 64	10.5	16
12	Anatase 70, rutile 30	8.3	55
13	Anatase 72, rutile 28	8.0	70
14	Anatase 64, rutile 32, CdS 2	10.2	63
15	Anatase 64, rutile 33,CdS 3	10.9	61
16	Rutile 100	21.0	13
17	Anatase 52, rutile 48	13.3	27
18	Anatase 37, rutile 63	10.9	41
19	Anatase 32, rutile 66, CdS 2	10.2	70
20	Anatase 56, rutile 41,CdS 3	13.0	63

absorb Congo red solution, and samples 4 and 5 changed the color of this dye from red to blue.

TiO_2 powders behave differently against methylene blue (representative of cationic dyes). It is represented by a diagram on Fig. 19.13.

Sample 1 showed favorable results in its ability to discolor methylene blue: the maximum fixed conversion rate did not exceed 13.5 %.

Sample 2, in contrast, showed high activity toward methylene blue ($X = 88.5$ %) but does not exhibit photocatalytic activity to the Congo red at all.

Sample 3 is very similar to sample 2 in their ability to remove dyes; it discolors methylene blue by almost 91 % and is absolutely not active against Congo red.

Sample 4 does not discolor the methylene blue and Congo red. Moreover, Congo red upon contact with a sample 4 changes its color from red to blue. Low photocatalytic activity of sample 4 is due to low specific surface area, as well as the isolation of crystals of the titanium oxide (IV) by sulfur-containing particles which aggregated and formed the globules with round shape and with size of about 1 μm, which resonates with the opinion of the authors [22].

The degree of discoloration of the methylene blue solution by sample 5 is 17 %, while the discoloration of the Congo red solution on it does not occur at all.

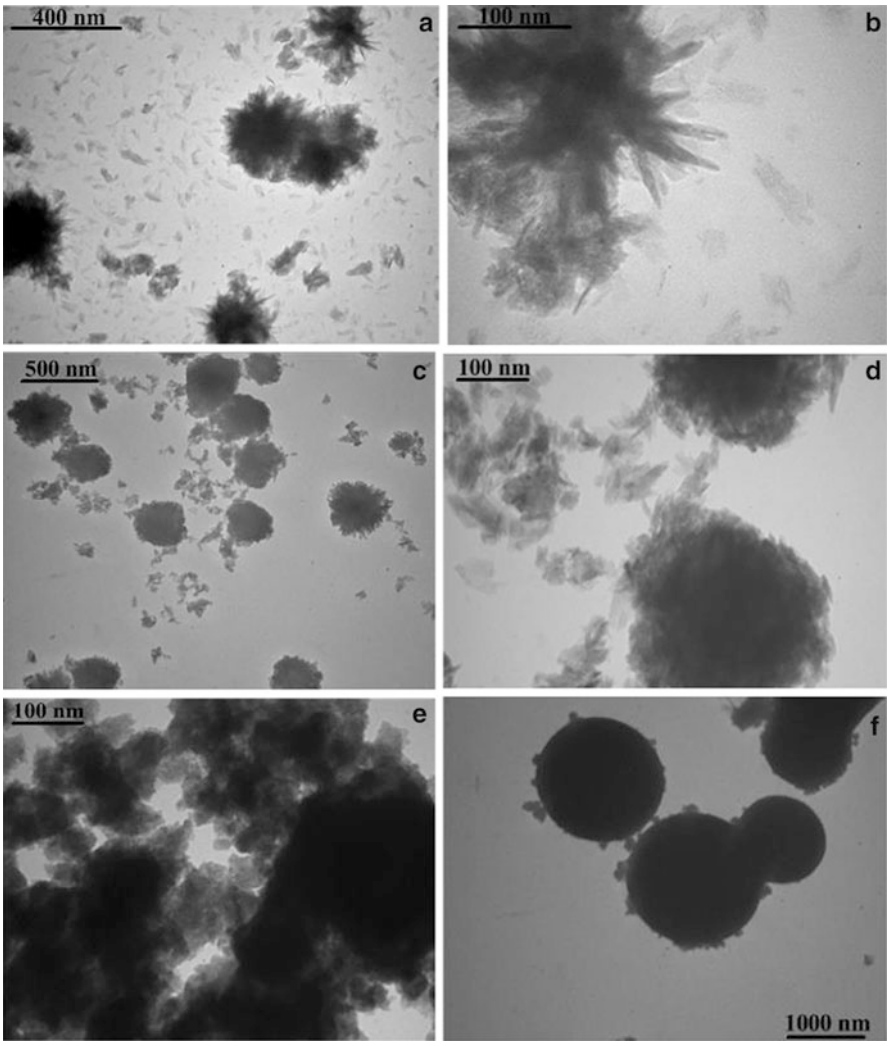

Fig. 19.11 TEM images of synthesized samples of titanium oxide (IV): (**a**, **b**) sample 1, (**c**, **d**) sample 2, (**e**) sample 3, and (**f**) sample 4

The photocatalytic activity of synthesized titanium (IV) nanostructures was compared with the reference photocatalyst Degussa P25, which is a decolorized solution of methylene blue by 60 % and Congo red by 83 %.

Figure 19.14 shows data on the photocatalytic activity of samples 6–10 (obtained from precursor $TiCl_4$) in solution of methylene orange (anionic dye) and methylene blue.

As the diagram shows, this series of samples is most active catalysts for cationic dye type, and its activity increases with the increase of dopant amounts.

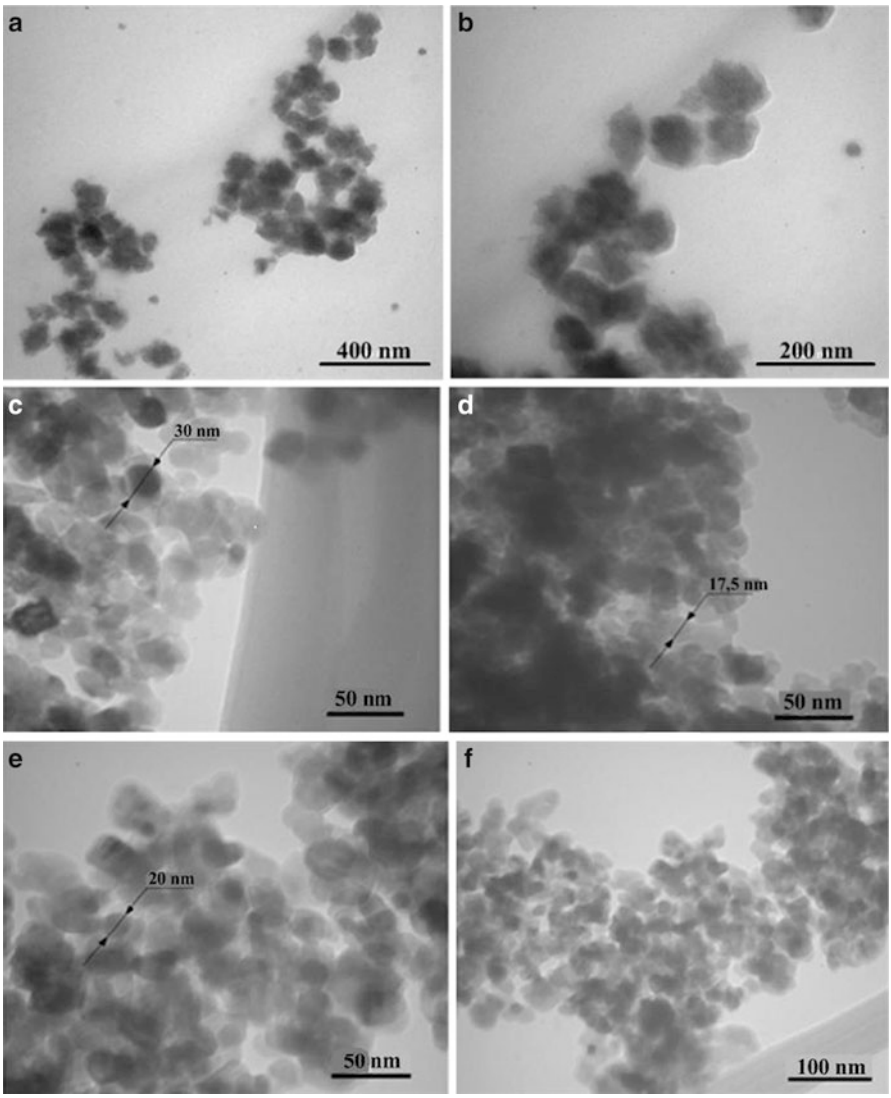

Fig. 19.12 TEM images of synthesized samples of titanium oxide (IV) (**a**, **b**) sample 5, (**c**) sample 9, (**d**) sample 14, and (**e**, **f**) sample 19

Samples 6–10 are also active to the anionic dye and improve with the increase of dopant amounts too. Samples 11–20 in photocatalytic experiments have shown themselves similarly.

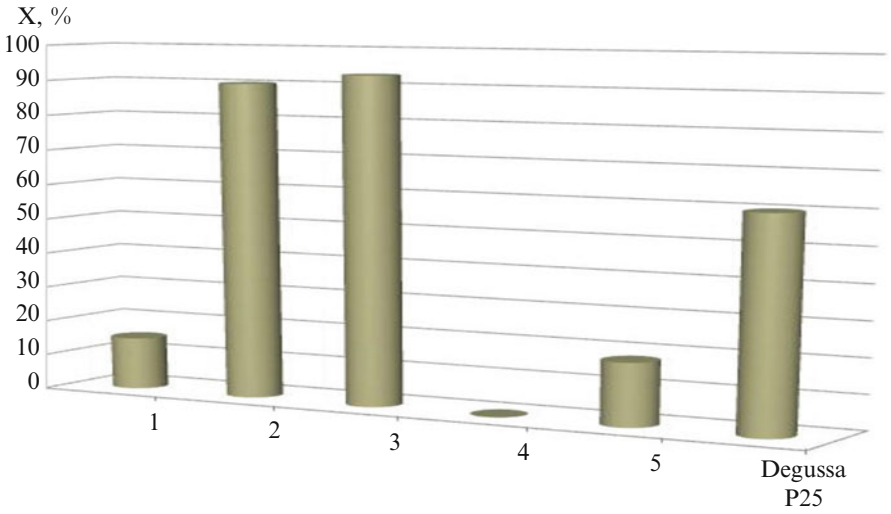

Fig. 19.13 Photocatalytic activity (X, %) of synthesized samples 1–5 toward methylene blue

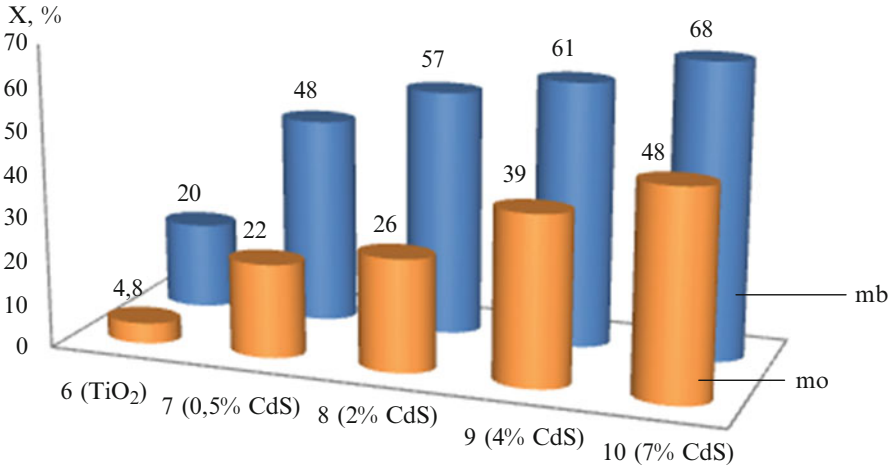

Fig. 19.14 The photocatalytic activity (X, %) of synthesized samples 6–10 toward methylene *blue* and methylene *orange*

19.3 Conclusions

Thus, this study considered the benefits of using heterogeneous photocatalyst titanium (IV) oxide and photocatalysis mechanism on their surface. The perspectives of oxidative method for the removal of organic pollutants from the water are proven. The ways of increasing the photocatalytic activity of the photocatalyst titanium (IV) oxide by modifying methods are proposed.

The two series of samples from different precursors TiO_2 with and without modifiers are synthesized. It is shown that the use of different precursors and/or modifiers allows to get a variety of photocatalysts properties, the phase composition and structural-sorption characteristics ($S_{sp} = 5–430\ m^2/g$).

It was established that the obtained samples exhibit a high activity against anionic dyes (up to 100 %) and the dye of cationic type (90 %). At the same time, the represented low-temperature methods of synthesis of TiO_2 are technologically and economically feasible. It was revealed that the individual sample that obtained titanium (IV) oxide exhibits the activity even higher than commercial products.

Acknowledgment The authors would like to thank the Faculty of Physical Engineering of National Technical University of Ukraine "KPI" for their support in conducting this research.

References

1. Nazeeruddin MK, Gratzel MJ (2001) Photocatalysis. Photochem Photobiol A Chem 145:252–257
2. Vinu R, Madras G (2010) Environmental remediation by photocatalysis. J Indian Inst Sci 90 (2):189–230
3. Ollis DF, Al-Ekabi H (eds) (1993) Photocatalytic purification and treatment of water and air. Elsevier, Amsterdam
4. Herrmann JM (2005) Heterogeneous photocatalysis: state of the art and present applications. Top Catal 34(1–4):49–65
5. Nozik AJ (2002) Photoelectrolysis of water using semiconducting TiO_2 crystals. Nature 36 (11):2703–2710
6. Prasad G, Chandra Babu KS, Srivastava O (2007) Photocatalysis on TiO_2. Int J Hydrogen Energy 148:172–177
7. Melghit K, Al-Rabaniah S (2006) Photodegradation of Congo red under sunlight catalyzed by nanorod rutile TiO_2. J Photochem Photobiol A Chem 184(3):331–334
8. Mahshid S, Sasani GM, Askari M et al (2006) Synthesis of TiO_2 nanoparticles by hydrolysis and peptization of titanium isopropoxide solution. Semicond Phys Quantum Electron Optoelectron 9(2):65–68
9. Dong SK, Seung-Yeop K (2007) The hydrothermal synthesis of mesoporous TiO_2 with high crystallinity, thermal stability, large surface area, and enhanced photocatalytic activity. Appl Catal A Gene 323:110–118
10. Pusit P, Sukon P (2009) Titanium dioxide powder prepared by a sol-gel method. J Ceram Process Res 10(2):167–170

11. Besserguenev VG, Pereira RJF, Mateus MC et al (2003) TiO_2 thin film synthesis from complex precursors by CVD, its physical and photocatalytic properties. Int J photoenergy 5:99–105
12. Li JG, Ishigaki T, Sun X (2007) Anatase, brookite, and rutile nanocrystals via redox reactions conditions: phase-selective synthesis and physicochemical properties. J Phys Chem 111:72–79
13. Wyckoff RW (1963) Crystal structure. Wiley, New York
14. Thompson TL, Yates JT (2006) Surface science studies of the photoactivation of TiO_2. New Photochem Processes Chem Rev 106:4428–4453
15. Park JY, Lee C, Jung KW et al (2009) Structure related photocatalytic properties of TiO_2. Bull Korean Chem Soc 30(2):402–404
16. Zhu J, Zäch M (2009) Nanostructured materials for photocatalytic hydrogen production. Curr Opin Colloid Interface Sci 14(2):260–269
17. Ahmed S, Rasul MG, Martens WN (2011) Advances in heterogeneous photocatalytic degradation of phenols and dyes in wastewater: a review. Water Air Soil Pollut 215(4):3–31
18. Diebold U (2003) The surface science of titanium dioxide. Sur Sci Rep 48:53–229
19. Xiaobo C, Mao S (2006) Titanium dioxide: synthesis, properties, modifications, and applications. Chem Rev 111(7):2656–2672
20. Bakardjieva S (2005) Photoactivity of anatase–rutile TiO_2 nanocrystalline mixtures obtained by heat treatment of homogeneously precipitated anatase. Appl Catal B 58:193–202
21. Kudo A (2003) Photocatalyst materials for water splitting. Catal Surv Asia 7(1):31–38
22. Ahmad A, Awan GH, Aziz S (2009) Synthesis and applications of TiO_2 nanoparticles. Pak Eng 283:3107–3116
23. Chen X, Mao SS (2007) Titanium dioxide nanomaterials: synthesis, properties, modifications, and applications. Chem Rev 107:2891–2959
24. Hafizah N, Sopyan I (2009) Nanosized TiO_2 photocatalyst powder via sol-gel method: effect of hydrolysis degree on powder properties. Int J Photoen 78:40–48
25. Pookmanee P, Phanichphant S (2009) Titanium dioxide powder prepared by a sol-gel method. J Ceram Process Res 2:167–170
26. Inaba R, Fukahori T, Hamamoto M et al (2006) Synthesis of nanosized TiO_2 particles in reverse micelle systems and their photocatalytic activity for degradation of toluene in gas phase. J Mol Catal A Chem 260:247–254

Chapter 20
Silicon Submicron Rods Imaging by Surface Plasmon Resonance

O.V. Rengevych, G.V. Beketov, and Yu.V. Ushenin

20.1 Introduction

Nanoparticle technology plays an important role in providing opportunities and possibilities for the development of new generation of sensing tools. Characterization of nanoparticles and accessing the nanoparticle-based devices requires development of experimental techniques capable of revealing the nanoscale objects. Though methods utilizing the scanning probe principle (STM, AFM, NSOM, etc.) offer unravelling spatial resolution, in many cases optical techniques are preferable. In particular, this concerns applications, which exploit phenomena related to or involving interaction of visible light with the nanoparticles, like localized surface plasmon resonance (LSPR) [1–3].

Resolution of conventional far-field optical microscopy is limited to roughly half the wavelength due to diffraction. However, during last decades a great progress has been achieved in development of imaging methods capable of attaining a resolution beyond the diffraction limit. One of particularly fruitful approaches was based on the use of an evanescent wave which appears as a side effect of total internal reflection. Existence of the evanescent wave is a consequence of boundary condition of continuity for the tangential components of **E** and **H** fields, following from Maxwell's theory [4]. In the contexts of optics, evanescent waves occur at the boundary between two media with different optical constants, when the incident wave comes from the medium having higher optical density. Since at the angle of incidence which exceeds the critical angle no travelling transmitted wave can exist, the electromagnetic field behind the boundary exhibits exponential decay

O.V. Rengevych (✉) • G.V. Beketov • Yu.V. Ushenin
V.E. Lashkaryov Institute of Semiconductor Physics of the National Academy of Sciences of Ukraine, 45 Prospekt Nauki, 03028 Kyiv, Ukraine
e-mail: rengev@isp.kiev.ua; gbeketov@isp.kiev.ua; ushyury@mail.ru

O. Fesenko, L. Yatsenko (eds.), *Nanoplasmonics, Nano-Optics, Nanocomposites, and Surface Studies*, Springer Proceedings in Physics 167,
DOI 10.1007/978-3-319-18543-9_20

without absorption as a function of the distance from the boundary. For this reason, it can be considered as a near-field wave.

Similarly to the propagating wave, the evanescent waves can experience scattering from near- and subwavelength objects. This effect has been employed for demonstration of existence of the evanescent light [5]. Practical applications of evanescent waves in microscopy essentially rely upon sharp dependence of their intensity on the distance, thus providing enhanced vertical resolution. Evanescent-wave microscopy, or total internal reflection microscopy (TIRM), has been employed in the fields of biology and chemistry since the 1970s. The TIRM technique has long been used in cell biology studies. With this technique, cells on a glass substrate are illuminated by the evanescent field, created at the cell/glass interface through a total internal reflection, and the scattered light produces image of the surface in the optical microscope. TIRM appeared to be very suitable for measurements of chemical kinetics and surface diffusion, molecular conformation of adsorbates, cell development during culturing, visualization of cell structures and dynamics, and single molecule visualization and spectroscopy [6].

In physics, this technique allowed for real-time monitoring the separation distance between the colloidal particles and the plain surface. Distance dependence of scattered light intensity when the particles are illuminated by an evanescent wave provides a sensitive, nonintrusive, and instantaneous measure of the gap between the particle and the surface. Reported sensitivity of this method to the vertical position of the particle is sufficient to detect ~1 nm shift [7].

However, the most impressive achievements were obtained due to fluorescence-enhanced TIRM, referred to as TIRF [8–11]. This method is based on a highly localized evanescent-wave excitation of fluorescent dyes. With recently discovered biocompatible fluorescent markers, green fluorescent protein (GFP) and its cyan, yellow, and red derivatives (CFP/YFP/DsRFP), TIRF provides tools for exploring the biochemical processes in living cells at a molecular level. Further enhancement of this technique, the stimulated emission depletion (STED) microscopy [12], provides superior axial sectioning capabilities with the potential to reduce photo-bleaching and photo-damage in live cell imaging.

The aim of the present study is to explore potentialities of the other enhancement of TIRM technique, based on the phenomenon of surface plasmon resonance (SPR). Surface plasmon is a confined mode of coupled electromagnetic waves and oscillations of free electron gas propagating along the boundary between the metal and the dielectric. The electromagnetic field of a surface plasmon decays exponentially into both media, thus providing a possibility to realize a visualization method similar to conventional TIRM. On the other hand, SPR phenomenon underlies the operating principle of optical sensors, which at present has grown to a principal tool for characterizing and quantifying biomolecular interactions and detection of biological species related to medical diagnostics, environmental monitoring, and many other fields. This allows the SPR-enhanced TIRM to inherit the major advantages of SPR biosensors: capability of label-free real-time operation and high specificity to the biological nature of species to be detected. At the same time, this method has

also a potentiality to attain much higher sensitivity compared to standard SPR biosensors due to possibility of implementation of counting instead of analogous principle of measurements.

20.2 Background

It has become common to use term *surface plasmons* as a synonym for surface polarization waves. Actually, the concept of surface plasmon was first introduced by Ritchie [13] to explain discrete electron energy loss spectra in thin films and refers to quanta of plasma wave field. For the purpose of theoretical description of SPR as a linear optical effect, exhaustive background is provided by classic Maxwell theory. In this theory, electromagnetic excitations propagating at the interface between the two media and evanescently confined in the perpendicular direction appear when dielectric constants of these media have opposite sign [14]. This condition holds true for metals with high conductivity brought into contact with dielectrics. In classic theory, the optical response of metals is described by the Drude model, where electrons are considered as a free electron gas:

$$\varepsilon_{\mathrm{D}}(\omega) = 1 - \frac{\omega_{\mathrm{p}}^2}{\omega^2 + i\gamma\omega} \tag{20.1}$$

where ω_{p} is the plasma frequency, and γ is a damping factor due to electron–electron and electron–phonon collisions [15]. Averaged real and imaginary parts of dielectric constant of gold at $\lambda = 0.65$ μm are, respectively, -13.0 and $i{\cdot}1.3$ [16]. Neglecting the small imaginary part, gold can be considered as a medium with negative dielectric constant. Surface plasmons can also be observed at surfaces of Ag, Cu, In, and Al. Nevertheless, the nonzero imaginary part results in plasmon decay when propagating along the interface. In the newly emerged discipline of plasmonics, much efforts are directed toward engineering of new lossless materials with negative dielectric constant for plasmonic waveguides, circuits and devices [17]. The simplest example is the system which consists of two dielectrics or dielectric and semiconductor, in which dielectric constant can possess negative value due to the presence of resonant states, provided that the dipole strength and oscillator density are high enough. More elaborated approaches include use of superstructures, quantum dots, and metamaterials [18–20], but till now these new developments have not found yet substantial application in SPR sensors.

Real plasmon-supporting structure used in SPR sensors consists of thin metal film deposited onto transparent dielectric substrate, usually glass plate. For gold, optimal thickness of metal film is about 50 nm. With this thickness, the metal film is semitransparent, that allows for optical excitation of surface plasmons. Dispersion relation for surface plasmon shows that its propagation constant, k_{p}, exceeds that of the travelling electromagnetic wave [16]. The excitatory light wave will couple to a

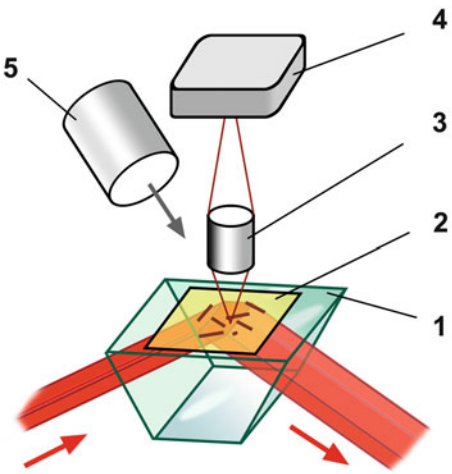

Fig. 20.1 Experimental setup. *1*—ATR prism, *2*—semitransparent Au film ~50 nm thick, *3*—microscope lens, *4*—CCD-camera, *5*—external source of directional light

surface plasmon at a metal-dielectric interface if the component of its wavevector which is parallel to the interface, $k_{||}$, matches the propagation constant of the surface plasmon. In context of SPR sensors, the most commonly used technique for optical excitation of surface plasmons utilizes prism couplers. In the Kretschmann configuration, tangential components of wavevectors characterizing propagation of surface plasmon and the incident light are matched by using the attenuated total reflection (ATR) prism (Fig. 20.1). In this configuration, exact match is achieved at a certain angle of incidence, referred to as a resonant angle, φ_{res}. Excitation of surface plasmons manifests itself as a dip in the angular dependence of reflected light intensity [16].

Application of SPR in sensor instruments relies upon dependence of the resonant angle on changes of refractive index in a thin volume adjacent to the metal surface. In biosensors, this change can be caused by adsorption or selective binding of biomolecules, the angular shift of the resonance being the measure of the amount of adsorbed species. This principle can also be used in studying physical adsorption, electrochemical processes, corrosion, oxidation, and in other fields. Since SPR can be described in terms of classic theory, the angular dependence of refraction can be calculated on the base of well-known theoretical approaches, in particular, using Abeles matrix method for layered structures [21]. Response of the SPR sensor to formation of external layers on the gold surface can be evaluated by numerical simulation. Computation using software described in [22] shows that 1 nm thick surface layer with $n = 1.42$ changes the resonant angle from 66.40 to 66.52 angular degrees when the measurements are carried out in water environment. For this estimation, optical constants of Au, prism glass, and water were assumed to be, respectively, $N^* = 0.18 - i \cdot 3.0$, $n_{pr} = 1.615$, $n_{wt} = 1.332$, and light wavelength, $\lambda = 0.65$ μm. This sensitivity is sufficient for biological applications, since, for example, IgG antibodies are large molecules, having a molecular weight of approximately 150 kDa. The minimal distance between the two hapten binding sites of rabbit immunoglobulin G molecules in solution was deduced around 8 nm from studying singlet-singlet energy transfer [23].

To achieve higher sensitivity, necessary for characterization of smaller adsorbed molecules, various extensions of standard SPR sensor are actively studied. Among them worth mentioning phase-sensitive SPR sensors [24], bandgap-assisted surface-plasmon sensors [25], and sensors utilizing plasmonic nanohole arrays [26].

Biological applications of SPR are based on high specificity of biomolecular interactions, or molecular recognition, which plays a fundamental role in virtually all biochemical processes in living organisms. Experimental exploration of these interactions with SPR biosensors requires immobilization of one counterpart of the interacting pair at the surface of the plasmon-supporting metal (normally Au), while another one is dissolved in the liquid probe. When the solution is brought in contact with the sensor surface, selective binding between these species can be monitored by measurement of the resonance angle shift [27]. To date, plentiful immobilization techniques have been developed, and further investigations in this area are in progress [28].

It should be emphasized that specific biomolecular interactions, especially interactions of antigen-antibody type, can be used for detection of whole pathogen cells due to specific binding of immobilized antibodies to their target biomolecules (usually proteins or glycoproteins) expressed in the cell membranes [30–32]. Nevertheless, the operation principle of the standard SPR sensor has considerable drawback when applied for pathogen detection. It assumes that distance between adsorbed or specifically bound particles at the metal surface is at least of the order of the surface plasmon wavelength or smaller. This is a condition for non-disturbed and, consequently, nonradiative propagation of surface plasmons. In other words, only the integral response to specific binding can be measured using this principle that impose intrinsic limitation on its sensitivity. Implementation of SPR-enhanced TIRM method for pathogens detection has the potentiality to counting of single bacterial cells or complete viral particles, thus attaining the absolute sensitivity for revealing pathogenic microorganisms and viruses.

20.3 Experimental Results and Discussion

Feasibility of SPR-enhanced TIRM was investigated using VLS-grown silicon rods as a test object. The reason for this choice was that their geometric shape can easily be recognized, and high index of refraction ($n = 3.865$) along with relatively low optical absorption ($k = 0.015$) for $\lambda = 0.65$ μm are conducive to strong optical scattering. The rods were grown by VLS process in a closed volume using the chemical gas-conveying reaction with Au nanodroplets as a catalyst [32]. The as-grown Si filiform crystals (FC) formed entangled clots in the ampoule volume. To avoid mechanical destruction, the tangles of Si-rods were disengaged by stirring in ethanol until a homogeneous suspension is formed. Ethanol was found to be the most suitable solvent, producing a stable enough suspension without addition of surfactants. The Si-rods were then separated by size using sedimentation method. Experiments were performed with Si-rods distinguishable by the optical microscope. Plasmon-supporting sensor chips were prepared by thermal evaporation of

Au onto F1 glass substrates $20 \times 20 \times 1$ mm in size with a Cr adhesive sublayer. Optimal thickness of Au film for efficient excitation of SPR is ~50 nm. Si-rods were deposited onto the Au surface of the sensor chips from the ethanol suspension. Special measures were taken to avoid conglutination of Si-rods during deposition and form uniformly dispersed sediment.

Microscopic images of Si-rods deposited onto Au layer were obtained using custom-built experimental setup based on the SPR biosensor model Plasmon-6 (ISP NASU, Ukraine). The optical layout of the setup is shown in the Fig. 20.1. The Kretchmann configuration was used for optical excitation of SPR with the 3 mW GaInP/AlGaInP semiconductor laser diode ($\lambda = 650$ nm) as a light source, and a total internal reflection (TIR) prism as a coupler. The laser radiation was focused into 5×1 mm spot. Measurements were carried out in air environment with TIR prism made from K8 (BK7) optical glass. The setup was also equipped with movable source of directed light to obtain images of Si-rods by standard light microscopy. Specific features of images retrieved using SPR-enhanced TIRM and the light microscopy were compared for different orientations of the external light source and the substrate.

For K8 glass prism ($n = 1.5141$ at $\lambda = 0.65$ μm) and Au thickness 45 nm, the calculated value of the resonant angle, φ_{res}, is 43.368°. For calculation, the optical constants of Au were assumed to be $0.2 + i \cdot 3.8$. Precise positioning of the prism at the resonant angle was made under control of both the intensity of the reflected beam and the visual brightness of the specimen surface. The presence of Si-rods at the Au/air interface results in breaking the momentum conservation for surface plasmons thus letting the electromagnetic waves to be emitted into the external medium (air). The scattered light was focused by the objective lens onto the solid-state imaging device, and the images were acquired using standard software. All the images were obtained using the objective lens with numerical aperture 0.11.

Typical images of Si-rods are shown in Fig. 20.2. In the SPR-enhanced TIRM image (Fig. 20.2a), the Si-rods look like bright touches on a dark background. Ideally, at the resonance angle no radiation should be transmitted into the air

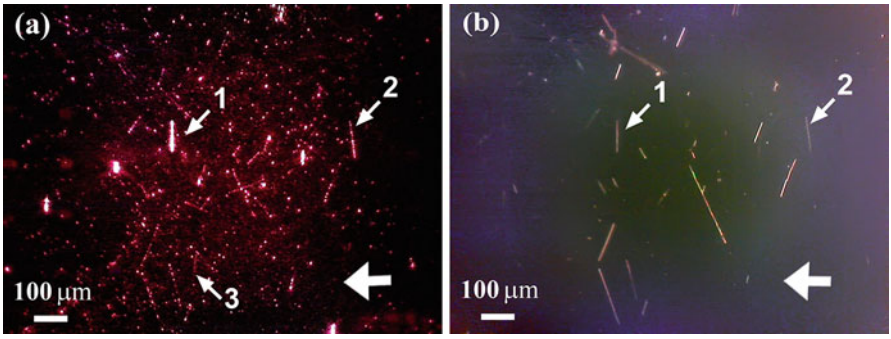

Fig. 20.2 Images of Si-rods in the SPR-enhanced TIRM (**a**), image of the same area obtained using standard light microscope under directional illumination (**b**). Correspondent details are indicated with *numbered arrows*. There is no visible counterpart for the rod 3 under directional light. *Bold arrows* indicate the illumination direction

through the Au layer. Nevertheless, numerous luminous spots and faintly glowing nebulas can also be observed in the background. This radiation was attributed to initially existing surface defects resulted from contamination or imperfect technology and/or deposition of nanoparticles still remaining in the suspension. In this image, drastic difference stands out in scattering intensity between the rods oriented in a direction perpendicular to the direction of SPs propagation, and the other randomly oriented rods.

The image in Fig. 20.2b was obtained using standard light microscope under directional illumination. It is evident that correspondence between these two images is incomplete. Besides the orientation dependence of scattering intensity in SPR-enhanced TIRM, another reason for this may originate from dependence of brightness on illumination direction. Under conditions of directional illumination, strong dependence of visibility for long, thin objects on the direction and polarization of the incident light was also observed in regular light microscopy [34]. Theoretical analysis of this effect shows that intensity of light scattering by infinite homogeneous cylinders is a function of illumination angle, polarization of the incident light, and the observation angle [35]. Though this analysis is not directly applicable to the scattering of light by the particle interacting with the evanescent field, dependence of intensity on the observation angle can be conjectured also for this case. An important point is that image in Fig. 20.2a contains much more details than the image in Fig. 20.2b. This fact demonstrates high efficiency of SPR-enhanced TIRM, which is probably due to field enhancement under SPR conditions [16].

Angular dependence of visibility on the illumination direction is demonstrated in Fig. 20.3, where Si-rods were deposited on the chemomechanically polished monocrystalline Si wafer. This substrate does not support surface plasmons that exclude their possible influence on the obtained images.

To ascertain that scattering of evanescent light is also orientation dependent, images of the same Si-rod acquired at different angular orientations were compared (Fig. 20.4). It is clearly seen that for the Si-rod the angular deviation of only

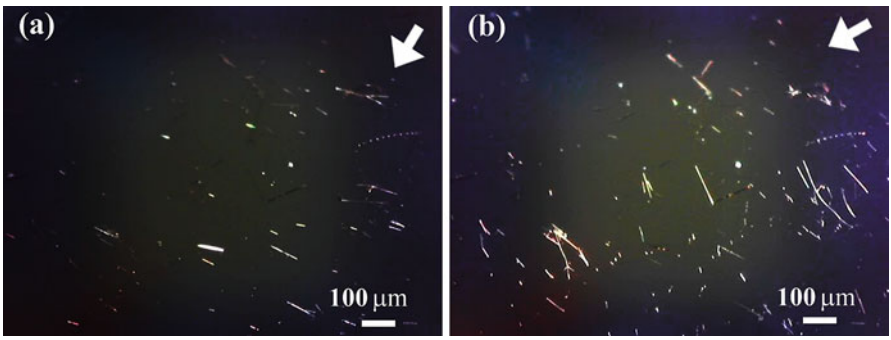

Fig. 20.3 Angular dependence of visibility on the illumination direction (*bold arrows* in frames (a), (b) indicate different illumination directions). Si-rods are deposited on the chemomechanically polished monocrystalline Si wafer

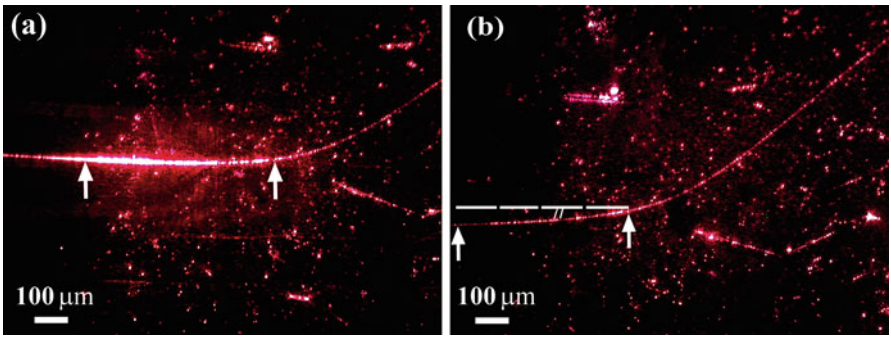

Fig. 20.4 Images of the same Si-rods acquired at different angular orientations. The bent filiform crystal shows nonuniform brightness as different parts have different tilt against the plasmon propagation direction. Substrate in the frame (**b**) was turned against the frame (**a**) by ~5°. Correspondent points in the images as well as illumination direction are indicated by *arrows*

5° causes drastic drop of light scattering intensity, while brightness of dot-like scatterers remains practically unchanged.

In principle, brightness of Si-rods in SPR-enhanced TIRM images can be influenced not only by angular dependence of the scattering intensity, but also by other factors. In particular, in case of evanescent field, the intensity of scattered light is dependent on the distance between the scattering particle and the surface [7]. Nevertheless, this does not rule out the existence of other physical effects influencing the visible brightness of the rods in dependence of their orientation. Thus, considering the rod as a limiting case of a thin strip of transparent material at the Au surface, it could be surmised that the total internal reflection also contributes to this effect. It is evident that a wide strip oriented along the direction of SPs propagation, will not transfer light into the external medium when its angle of incidence exceeds the critical one. Unfortunately, this possibility could not be explored with the experimental setup used in this study, and will be the subject of further research.

The proposed SPR-assisted visualization of small particles by light scattering may appear a promising concept for development of fast, sensitive, label-free, and real-time method for detection of pathogenic microorganisms and viruses. Several drawbacks revealed in this study can be obviated by several improvements. First, background produced by imperfections of the starting gold film which affects the quality of the image can be removed by computer processing of the images taken before and after measurements (Fig. 20.5). In this picture, brightness of the rods is relatively weak because of nonoptimal orientation, but brightness of the point-like objects is excellent. Though supposed practical applications of this method scarcely will include imaging of extended objects, orientation dependence of their visibility can also be removed by using rotation of the plasmon exciting light beam around the vertical axis in conjunction with the hemispherical or conical ATR prism. To reduce influence of the angular dependence of the scattered light, objective lens with larger numerical aperture, which collects light in a wider angular range, is to be used. These improvements are subject of further studies.

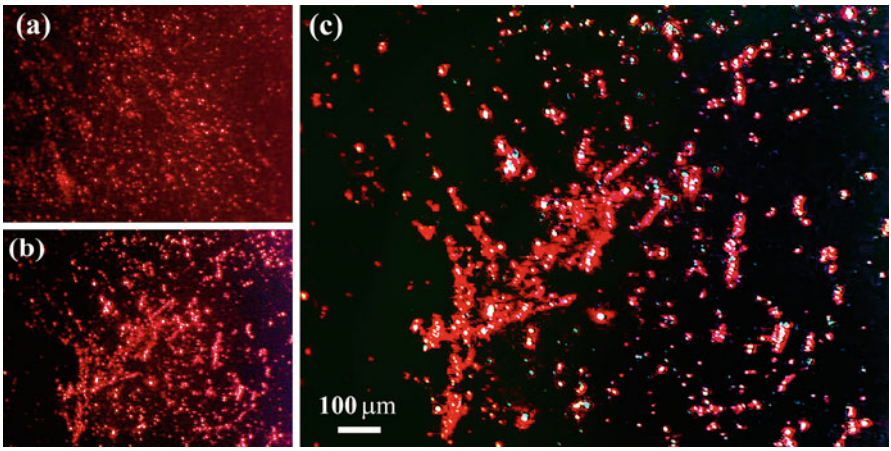

Fig. 20.5 Background SPR-enhanced TIRM image of the starting gold plated substrate (**a**); the same place with the deposited Si-rods (**b**); the result of the background subtraction (**c**)

The proposed technique can also readily be combined with fluorescence microscopy and, possibly, with surface-enhanced Raman scattering, providing additional information about the objects under study.

20.4 Conclusions

Advantages of the novel method, the SPR-enhanced TIRM, for imaging of microscopic particles immobilized at the surface of the plasmon-supporting film have been demonstrated. Usage of microscopic silicon rods as a test object allowed for clear distinguishing their images from extraneous defects usually present at the surface.

Pronounced difference in scattering intensity between the rods oriented in a direction perpendicular to the direction of SPs propagation, and the other randomly oriented rods has been observed. Experimental evidence was obtained that this behavior can be partially attributed to angular dependence of scattering intensity on the observation angle. Other possible mechanisms of this dependence are discussed. The ways of overcoming several drawbacks revealed in this study are proposed.

This study was aimed at development of a novel type of SPR-based technique relied upon direct count of biological species of interest (bacteria, viruses, large biomolecular complexes), rather then measuring the integral effect of specific binding exploited in current SPR-based biosensors.

The search for innovative principles of nanodiagnostic assays for detection of infectious pathogens is an active area of investigation. It is expected that the proposed method could find applications in biochemistry, biomedicine, food safety inspection, and environmental monitoring, especially for fast detection and identification of trace amounts of pathogens in the natural water resources.

Acknowledgments The authors would like to extend their most sincere appreciation to Prof. A. Klimovskaya for providing the VLS-grown silicon rods for this study.

This work was partially supported by Swiss National Science Foundation through SCOPES Joint Research Project IZ73Z0_152661 "Manufacturing of Biosensors Aided by Plasma Polymerization."

References

1. Sagle LB, Ruvuna LK, Ruemmele JA et al (2011) Advances in localized surface plasmon resonance spectroscopy biosensing. Nanomedicine 6(8):1447–1462
2. Wang F, Ron Shen Y (2006) General properties of local plasmons in metal nanostructures. Phys Rev Lett 97:206806
3. Zeng S, Yong K-T, Roy I et al (2011) A review on functionalized gold nanoparticles for biosensing applications. Plasmonics 6(3):491–506
4. Born M, Wolf E (1975) Principles of optics, 5th edn. Pergamon, London
5. Papathanassoglou DA, Vohnsen B (2003) Direct visualization of evanescent optical waves. Am J Phys 71(7):670–677
6. Guasto JF, Huang P, Breuer KS (2008) Evanescent wave microscopy. In: Li D (ed) Encyclopedia of microfluidics and nanofluidics. Springer, New York, pp 638–645
7. Prieve DC (1999) Measurement of colloidal forces with TIRM. Adv Colloid Interface Sci 82 (1–3):93–125
8. Axelrod D (1990) Total internal reflection fluorescence microscopy. In: Grinstein S, Foskett JK (eds) Modern non-invasive techniques in cell biology, Cell biology series. Wiley-Liss, New York, pp 93–127
9. Axelrod D, Hellen EH, Fulbright RM (1992) Total internal reflection fluorescence. In: Lakowicz J (ed) Fluorescence spectroscopy: principles and applications, vol 3, Biochemical applications. Plenum, New York, pp 289–343
10. Schneckenburger H (2005) Total internal reflection fluorescence microscopy: technical innovations and novel applications. Curr Opin Biotechnol 16(1):13–18
11. Knight AE (2014) Single-molecule fluorescence imaging by total internal reflection fluorescence microscopy (IUPAC Technical Report). Pure Appl Chem 86(8):1303–1320
12. Farahani JN, Schibler MJ, Bentolila LA (2010) Stimulated emission depletion (STED) microscopy: from theory to practice. In: Méndez-Vilas A, Díaz J (eds) Microscopy: science, technology, applications and education, vol 2. FORMATEX, Spain, pp 1539–1547
13. Ritchie RH (1957) Plasma losses by fast electrons in thin films. Phys Rev A 106:874–881
14. Yariv A, Yeh P (1984) Optical waves in crystals. Wiley, New York
15. Kittel C (1996) Introduction to solid state physics. Wiley, New York
16. Raether H (1988) Surface plasmons on smooth and rough surfaces and on gratings. Springer tracts in modern physics, vol 111. Springer, Berlin
17. Maier SA (2007) Plasmonics: fundamentals and applications. Springer, New York
18. Fu Y, Thylen L, Agren H (2008) A lossless negative dielectric constant from quantum dot exciton polaritons. Nano Lett 8(5):1551–1555
19. Ginzburg P, Orenstein M (2008) Metal-free quantum-based metamaterial for surface plasmon polariton guiding with amplification. J Appl Phys 104:063513
20. Withayachumnankul W, Abbott D (2009) Metamaterials in the Terahertz Regime. IEEE Photonics J 1(2):99–118
21. Abelès F (1950) Recherches sur la propagation des ondes électromagnétiques sinusoidales dans les milieux stratifiés. Application aux couche minces. Ann Phys 5:596–640

22. Beketov GV, Shirshov YM, Shynkarenko OV, Chegel VI (1998) Surface plasmon resonance spectroscopy: prospects of superstrate refractive index variation for separate extraction of molecular layer parameters. Sens Actuators B 48(1–3):432–438
23. Werner TC, Bunting JR, Cathou RE (1972) The shape of the immunoglobulin molecules in solution. Proc Natl Acad Sci U S A 69(4):795–799
24. Ye G, Yang W, Jiang L, He S (2014) Surface plasmon resonance phase-sensitive imaging (SPR-PI) sensor based on a novel prism phase modulator. Prog Electromagn Res 145:309–318
25. Benahmed AJ, Ho C-M (2007) Bandgap-assisted surface-plasmon sensing. Appl Opt 46 (16):3369–3375
26. Lesuffleur A, Im H, Lindquist NC, Lim KS, Oh S-H (2008) Plasmonic nanohole arrays for real-time multiplex biosensing. Proc SPIE 7035:703504–703510
27. De Mol NJ, Fisher MJE (eds) (2010) Surface plasmon resonance: methods and protocols. Methods in Molecular Biology, vol 627. Humana Press
28. Tanious FA, Nguyen B, Wilson WD (2008) Biosensor-surface plasmon resonance methods for quantitative analysis of biomolecular interactions. In: Correia J, Detrich III HW (eds), Biophysical tools for biologists: in vitro techniques, vol 1. Academic, Elsevier, pp 53–77
29. Fratamico PM, Strobaugh TP, Medina MB et al (1998) Detection of Escherichia coli O157:H7 using a surface plasmon resonance biosensor. Biotechnol Tech 12(7):571–576
30. Leonard P, Hearty S, Quinn J et al (2004) A generic approach for the detection of whole Listeria monocytogenes cells in contaminated samples using surface plasmon resonance. Biosens Bioelectron 19(10):1331–1335
31. Waswa JW, Debroy C, Irudayaraj J (2006) Rapid detection of Salmonella enteritidis and Escherichia coli using surface plasmon resonance biosensor. J Food Process Eng 29 (4):373–385
32. Barlen B, Mazumdar SD, Lezrich O et al (2007) Detection of *Salmonella* by surface plasmon resonance. Sensors 7:1427–1446
33. Choi H-J (2012) Vapor–liquid–solid growth of semiconductor nanowires. In: Yi G-C (ed) Semiconductor nanostructures for optoelectronic devices. Springer, Berlin, pp 1–36
34. Arimoto R, Murray JM (1996) Orientation-dependent visibility of long thin objects in polarization-based microscopy. Biophys J 70(6):2969–2980
35. Bohren CF, Huffman DR (1998) Angular dependence of scattering. In: Absorption and scattering of light by small particles. Wiley, New York, pp 321–429

Chapter 21
Synthesis of Photoactive Styrylquinoline Containing Polymers

V.O. Smokal, O.M. Krupka, and A.Yu. Kolendo

21.1 Introduction

In recent years, the development of modern technologies enables one to create polymer materials with a number of properties which would be impossible to realize in a single polymer. Therefore, we focus on development of a new type of methylmethacrylic-based polymers with styrylquinoline moiety.

Families of styrylquinolines are interesting due to their photochemical and photophysical properties [1]. On the other hand, to an increasing extend, technical processes based on the interaction of light with polymers have become important for various applications [2–4]. The photochromic transformations are always accompanied by changes in physical properties. There are changes in dipole moment and in the geometrical structure at the molecular level, etc. [5, 6]. Light-induced transformations from one structure to another have been studied with many organic compounds.

Moreover, 2-styrylquinoline and 4-styrylquinoline undergoes reversible *trans–cis* photoisomerization [7, 8] have been used for designing molecular logic gates [9]. The principles of design of various molecular photoswitches and logical devices [10–12], in particular, those based on the photoisomerization reaction of diarylethylenes [13, 14] have been actively investigated in recent years. The presence of additional functional groups in molecules of diarylethylenes, for example, crown ether groups [15], makes it possible to control the photochemical properties of diarylethylenes by the action on these groups. In styrylquinolines, the role of such a functional group is played by the endocyclic nitrogen atom,

V.O. Smokal (✉) • O.M. Krupka • A.Yu. Kolendo
Macromolecular Chemistry Department, Taras Shevchenko National University of Kyiv, Volodymyrs'ka Str., 60, Kyiv 01033, Ukraine
e-mail: vitaliismokal@gmail.com

O. Fesenko, L. Yatsenko (eds.), *Nanoplasmonics, Nano-Optics, Nanocomposites, and Surface Studies*, Springer Proceedings in Physics 167,
DOI 10.1007/978-3-319-18543-9_21

protonation of which changes the quantum yield of the *trans–cis* photoisomerization reaction [7].

Therefore, such chromophore systems offer a unique opportunity for applications involving photo-induced isomerization.

21.2 Experimental

21.2.1 Materials

2-(4-Hydroxystyryl)quinoline (p1a): 5 g of quinaldine was added to a solution of benzoyl chloride 0.98 g in 1 mL dimethylformamide (DMF). The reagents have been mixed during 20 min at room temperature after that 0.85 g of 4-hydroxybenzaldehyde were added to a solution. The reaction mixture was heated for 12 h on a steam bath at 80–90 °C and then poured into water. The resultant solid product was collected, washed with cold ethanol, hot water, ethanol, and then small amount of hexane and then dried to afford compound as yellow solid, yield 40 %. ^{1}H NMR spectrum, (400 MHz, DMSO-d_6), δ, ppm: 6.8 d (2H, Ar-*H*), 7.17 d (1H, –C*H*=CH–), 7.44–7.53 m (3H, Ar-*H*), 7.66–7.72 m (3H, –CH=C*H*–, Ar-*H*, pyridine-*H*), 7.81 d (1H, Ar-*H*), 7.92 d (1H, Ar-*H*), 8.19 d (1H, pyridine-*H*), 9.57 br. s (1H, OH).

Styrylquinoline containing compound (m1a), (p1b) was synthesized analogously to p1a as described previously.

2-(3-Hydroxystyryl)quinoline (m1a): yield 45 %. ^{1}H NMR spectrum, (400 MHz, DMSO-d_6), δ, ppm: 6.7 d (1H, Ar-*H*), 7.0–7.13 m (2H, Ar-*H*), 7.22 d (1H, –C*H*=CH–), 7.36 d (1H, Ar-*H*), 7.53 d (1H, –CH=C*H*–) 7.7–7.74 m (2H, Ar-*H*), 7.8 d (1H, pyridine-*H*), 7.9 d (1H, Ar-*H*), 8.0 d (1H, Ar-*H*), 8.3 d (1H, pyridine-*H*), 9.5 br. s (1H, OH).

2-(4-Hydroxystyryl)-6-methoxyquinoline (p1b): yield 40 %. ^{1}H NMR spectrum, (400 MHz, DMSO-d_6), δ, ppm: 3.9 s (3H, –OCH_3), 6.77 d (2H, Ar-*H*), 7.12 d (1H, –C*H*=CH–), 7.18 s (1H, Ar-*H*), 7.3 d (1H, Ar-*H*), 7.44 d (2H, Ar-*H*) 7.56–7.65 m (2H, –CH=C*H*–, pyridine-*H*), 7.81 d (1H, Ar-*H*), 8.0 d (1H, pyridine-*H*), 10.25 br. s (1H, O*H*).

2-(4-Methacryloxystyryl)quinoline (p2a): 2-(4-Hydroxystyryl)quinoline 2 g was dissolved in 3.25 mL of methacrylic anhydride. The reaction mixture was heated for 4 h at 80 °C and then poured into water. The light yellow powder was collected by filtration. The product was recrystallized from EtOH, yield: 80 %. ^{1}H NMR spectrum, (400 MHz, DMSO-d_6), δ, ppm: 2.05 s, (1H, –CH_3), 5.85 s, (1H, CH_2=), 6.31 (s, 1H, CH_2=), 7.17 d (2H, Ar-*H*) 7.42 d (1H, –C*H*=CH–), 7.51 t (1H, Ar-*H*), 7.69–7.83 m (7H, –CH=C*H*–, Ar-*H*, pyridine-*H*), 7.98 d (1H, Ar-*H*), 8.25 d (1H, pyridine-*H*).

2-(3-Methacryloxystyryl)quinoline (m2a) obtained as described for 2-(4-Methacryloxystyryl)quinoline. The yellow powder was collected by filtration.

The product was recrystallized from EtOH, yield: 70 %. ^{1}H NMR spectrum, (400 MHz, DMSO-d_6), δ, ppm: 2.06 (s, 1H, –CH_3), 5.85 (s, 1H, CH_2=), 6.33 (s, 1H, CH_2=), 7.07 d (1H, Ar-*H*), 7.43–7.56 m (5H, Ar-*H*,–C*H*=CH–, –CH=C*H*–), 7.7 t, (1H, Ar-*H*), 7.78–7.8 m (3H, pyridine-*H*, Ar-*H*), 7.9 d (1H, Ar-*H*), 8.26 d (1H, pyridine-*H*).

2-(4-Methacryloxystyryl)-6-methoxyquinoline (p2b) obtained as described for 2-(4-methacryloxystyryl)quinoline. The beige powder was collected by filtration. The product was recrystallized from EtOH, yield: 80 %. ^{1}H NMR spectrum, (400 MHz, DMSO-d_6), δ, ppm: 2.05 (s, 1H, –CH_3), 3.93 (s, 1H, –OCH_3), 5.85 (s, 1H, CH_2=), 6.32 (s, 1H, CH_2=), 7.16 d (2H, Ar-*H*), 7.24 s (1H, Ar-*H*), 7.32–7.38 m (2H, –C*H*=CH–, Ar-*H*), 7.71–7.74 m (4H, –CH=C*H*–, Ar-*H*, pyridine-*H*), 7.86 d (1H, Ar-*H*), 8.16 d (1H, pyridine-*H*).

21.2.2 Polymers

Polymers with styrylquinoline fragments were synthesized by free radical polymerization in DMF. The polymerization was carried out in 10 wt% DMF solution monomers and MMA with initial mole ratios 1:3. The polymerization was conducted using azobisisobutyronitrile (AIBN) as a free radical initiator (1 wt% of monomer) at 80 °C 35 h in argon atmosphere. Previously, initial mixture was degassed with repeated freeze-pump-taw cycles.

The polymerization was stopped by pouring the reaction mixture into methanol. This procedure was repeated several times to ensure the removal of unreacted methacrylic monomers and finally the polymers dried under vacuum at 50 °C overnight. The copolymerization ratios in the corresponding polymers were calculated based on the integrated peak areas of ^{1}H NMR spectra in DMSO-d_6. The polymerization ability of the new styrylquinoline containing monomers was investigated kinetically for radical copolymerization using the dilatometric method. The process was conducted in 10 % DMF solution at 80 °C contractions were measured by KM-6 cathetometer. The resulting viscous solution was added dropwise into methanol to precipitate polymeric material. Polymers were purified from ethanol.

The conversion rates were controlled gravimetrically. The conversion rate during the copolymerization processes of p2a with MMA was 60 % in 240 min, m2a with MMA was 57 % in 260 min, p2b with MMA was 55 % in 260 min. The structures of all copolymers are approximately the same in all cases as the structure of the initial mixture 1:3.

21.3 Results and Discussion

The common structure of synthesized quinaldine containing compounds is represented in Fig. 21.1.

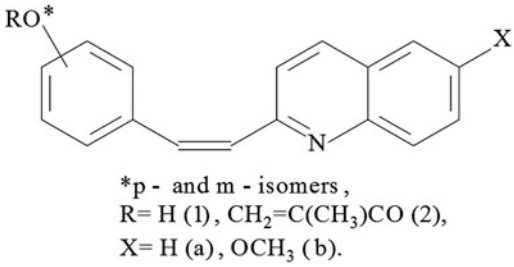

Fig. 21.1 The chemical structure of synthesized styrylquinolines

The initial hydroxystyryl derivatives were obtained by condensation of 4- and 3-hydroxybenzaldehyde with quinaldine and 6-methoxyquinoline in DMF solution with benzoyl chloride. Methacrylic monomers with quinaldine fragments were obtained by acylation adapting procedure.

Methacryloyl chloride is reacted with the suitable hydroxy derivative of p1a, m1a, p1b in the presence of triethylamine. The polymers were synthesized by radical polymerization using AIBN as radical initiator. The kinetic characteristics of polymerization process were investigated for new monomers with styrylquinoline fragment. The kinetics of the polymerization for p2a, m2a, p2b were investigated during radical copolymerization with MMA using the dilatometric method.

The spectral properties of substituted styrylquinolines have been studied in relation to the problem of intramolecular charge transfer [16–18]. The photochemical properties were studied previously for some substituted styrylquinolines and their quaternized salts [19].

It is well known that as most of diarylethylenes, 2-styrylquinoline isomerizes reversibly by adiabatic mechanism [8], so it is impossible to convert completely one isomer into another photochemically. Under irradiation, the photostationary state can be reached, and concentrations *trans*- and *cis*-isomers in the mixture depend of the irradiation wavelength [9]. The absorption spectra m1a during UV irradiation in ethanol are represented in Fig. 21.2. In the spectrum of absorption, the ethanol solutions of m1a have intensive long-wave band with a molar absorption coefficient on the order $2.72 \times 10^4\ M^{-1}\ cm^{-1}$ with approximate maximum of 340–345 nm and absorption band with its maximum about 282 nm ($2.5 \times 10^4\ M^{-1}\ cm^{-1}$). During the m1a solution irradiation process was observed decrease of absorption intensity at 340 and 282 nm with isosbestic point at 376 nm. The presence of isosbestic points prompting the total invariability of the running processes.

The spectral changes observed by the irradiation of polymers with styrylquinoline fragments using the light source with a wavelength 365 nm in solution of 1,2,2-trichlorethane and solid state are shown in Figs. 21.3, 21.4, 21.5, and 21.6, respectively. The initial spectra in Figs. 21.3–21.6 belong to the *trans*-isomers, and the final spectra belong to the photostationary states PS_{365} consisting of a mixture of *trans*- and *cis*-isomers. The photostationary states were stable upon further irradiation for all compounds under study.

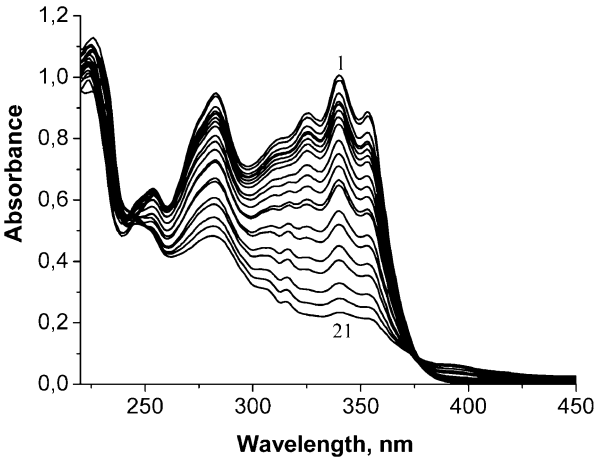

Fig. 21.2 Changes in the absorption spectra of m1a in ethanol ($C = 1.2 \times 10^{-5}$ mol L^{-1}) before—1 and after 3,180 s of irradiation—21 with light at a wavelength of 365 nm at room temperature

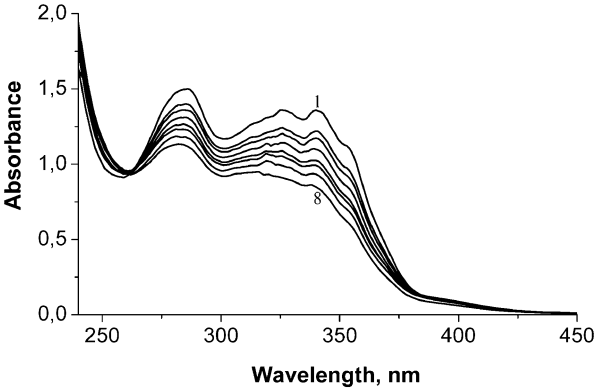

Fig. 21.3 Absorption spectra of copolymer based on p2a and MMA (1:3) in 1,2,2-trichlorethane before—1 and after 1,680 s of irradiation—8 with light at a wavelength of 365 nm at room temperature

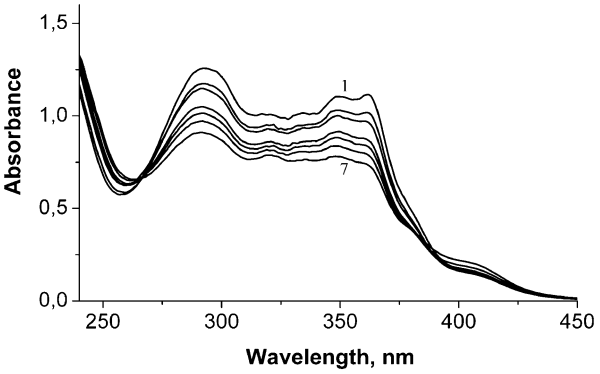

Fig. 21.4 Absorption spectra of copolymer based on p2b and MMA (1:3) in 1,2,2-trichlorethane before—1 and after 1,440 s of irradiation—7 with light at a wavelength of 365 nm at room temperature

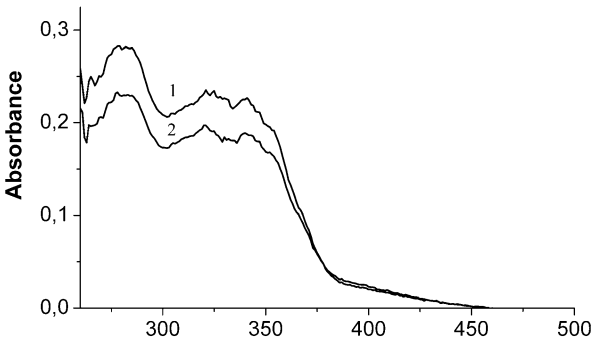

Fig. 21.5 Absorption spectra of copolymer based on p2a and MMA (1:3) in thin solid film before—1 and after 1,800 s of irradiation—2 with light at a wavelength of 365 nm at room temperature

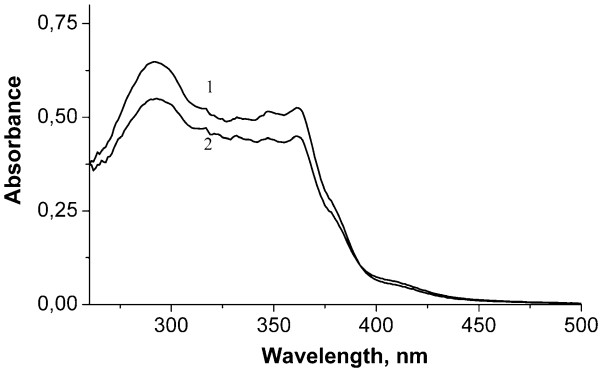

Fig. 21.6 Absorption spectra of copolymer based on p2b and MMA (1:3) in thin solid film before—1 and after 1,800 s of irradiation—2 with light at a wavelength of 365 nm at room temperature

21.4 Concluding Remarks

The polymers with MMA with styrylquinoline fragments were obtained. The polymerization ability of the new monomers was investigated kinetically for radical copolymerization using the dilatometric method. It was found that optical activity of styrylquinoline fragments is maintained in the polymers thereby photochemical properties of new polymers with styrylquinoline fragments will be according to the properties of styrylquinoline compounds. The styrylquinoline polymers have been characterized as compound with non-repeatable *trans-cis* isomerization process. These polymers can prove to be important candidate for optical signal processing and information storage.

References

1. Budyka M, Potashova N, Gavrishova T et al (2009) Solvent-driven adiabatic trans-to-cis photoisomerization of 4-styrylquinoline. J Photochem Photobiol A 203:100–104

2. Smokal V, Derkowska B, Czaplicki R et al (2009) Nonlinear optical properties of thiazolidinone derivatives. Opt Mater 31:554–557
3. Nikonorova N, Yakimansky A, Smirnov N et al (2007) Dielectric relaxation in copolymethacrylates containing side-chain nonlinear optical chromophores. Polymer 48:556–563
4. Hong Park K, Tae Lim J, Song S et al (1999) Nonlinear optical polymers with novel benzoxazole chromophores: IV. Synthesis of maleimide–styrene and maleimide–methacrylate copolymers. React Funct Polym 40:169–175
5. Shin E, Stackowa R, Foote C (2002) Excited state properties of some 1-(9-anthryl)-2-naphthylethene and 1-(9-anthryl)-2-quinolylethene derivatives. Phys Chem Chem Phys 4:5088–5095
6. Yamaki S, Nakagawa M, Morino S et al (2001) Photochemical behavior and the ability to control liquid crystal alignment of polymethacrylates with styrylpyridine side chains. Macromol Chem Phys 202:325–334
7. Lipunova G, Nosova E, Trashakhova T et al (2011) Azinylarylethenes: synthesis and photophysical and photochemical properties. Russ Chem Rev 80:1115–1133
8. Budyka M, Potashova N, Gavrishova T et al (2008) Photoisomerization of 2–styrylquinoline in neutral and protonated forms. High Energy Chem 42:446–453
9. Budyka M, Potashova N, Gavrishova T et al (2009) Reconfigurable molecular logic gate operating in polymer film. J Mater Chem 19:7721–7724
10. Balzani V, Credi A, Venturi M (2003) Molecular logic circuits. Chem Phys Chem 4:49–59
11. De Silva A, McClenaghan N (2004) Molecular-scale logic gates. Chem Eur J 10:574–586
12. Gust D, Moore T, Moore A (2006) Molecular switches controlled by light. Chem Commun 11:1169–1178
13. Sugimoto H, Kimura T, Inoue S (1999) An alternative supramolecular approach based on *E*-*Z*-photoisomerization of a stilbene-type pyridine ligand leads to photomodulation of axial ligation in aluminum porphyrins and hence catalytic activity in the copolymerization of carbon dioxide and ethylene oxide. J Am Chem Soc 121:2325–2326
14. Lewis J, Perutz R, Moore J (2000) Proton-controlled photoisomerization: rhenium (I) tricarbonyl bipyridine linked to amine or azacrown ether groups by a styryl pyridine bridging ligand. Chem Commun 19:1865–1866
15. Alfimov M, Fedorova O, Gromov S (2003) Photoswitchable molecular receptors. J Photochem Photobiol A 158:183–198
16. Wang S, Ho T (1997) Protonation dependent electron transfer in 2-styrylquinolines. Chem Phys Lett 268:434–438
17. Wang S, Ho T (2000) Substituent effects on intramolecular charge-transfer behaviour of styrylheterocycles. Photochem Photobiol A 135:119–126
18. Wang S, Lee C, Ho T (2002) Excited state proton transfer and steric effect on the hydrogen bonding interaction of the styrylquinoline system. Photochem Photobiol A 151:21–26
19. Gorner H (1987) Photoinduced electron transfer vs. trans–cis photoisomerization of quaternary salts of 4 substituted 4′-azastilbenes (R = CN, H, CH3, and OCH_3) and their quinolinium analogues. J Phys Chem 91:1887–1894

Chapter 22
The Effects of Disorder on the Optical Spectra of Synthetic Opals

V. Moiseyenko, A.V. Yevchik, M. Dergachov, O. Spichak, and V. Gorelik

22.1 Introduction

One way of enlarging element base of nanophotonic devices, integrated optics, and sensorics is the use of templates based on synthetic opals (SO's) with active fillers [1–3]. Opal-like structures composed of globules of SiO_2, TiO_2, polystyrene, or polymethylmethacrylate are considered as a promising material for photonic crystals (PC) fabrication [4]. In PC, we may observe optical Bragg's diffraction, as the result of which light waves within certain frequency range are completely reflected at some angles. This frequency range corresponds to the photonic band-gap where the density of optical states (DOS) is zero in a case of an ideal periodic structure.

Currently, special attention is paid to the creation of artificial defects in PC whose appearance and concentration can be controlled [5, 6]. The presence of single defects in such structures leads to the appearance of local photonic states and consequently to the nonzero values of DOS in the photonic band-gap, like in semiconductors. The number of local photonic states increases with the increase of defects amount up to complete disappearance of band-gap [7]. From the applied point of view, regular structures with single defects can be used for channeling light in optical waveguides, splitters, and multiplexers [8–10]. In structures with a certain disorder degree, the effect of photon localization predicted earlier [11, 12] should be expected.

The structure of initial SO's composed of SiO_2 globules and air in interglobular space is not completely regular and includes various types of defects [13, 14].

V. Moiseyenko • A.V. Yevchik (✉) • M. Dergachov • O. Spichak
Oles Honchar Dnipropetrovsk National University, Dnipropetrovsk, Ukraine
e-mail: vnmois@yandex.ua; AV.Yevchik@gmail.com; dergachov-mp@yandex.ru; lexkunzim@gmail.com

V. Gorelik
Lebedev Physical Institute of the Russian Academy of Sciences, Moscow, Russia
e-mail: gorelik@sci.lebedev.ru

O. Fesenko, L. Yatsenko (eds.), *Nanoplasmonics, Nano-Optics, Nanocomposites, and Surface Studies*, Springer Proceedings in Physics 167,
DOI 10.1007/978-3-319-18543-9_22

Owing to that the light channeling can be disturbed. At the high concentration of uncontrolled defects, SO are interested in studying random-lasing effects [15]. Thus, there is a necessity to establish objective criteria to identify the applicability of SO in one of the mentioned research directions.

The aim of this work is to study both theoretically and experimentally the effects of structural defects on the optical properties of globular PC based on SO.

22.2 Fabrication and Characterization of Synthetic Opal Samples

Bulk SO samples were grown by natural sedimentation of SiO_2 globules suspension. Film SO were grown by deposition of globules on the vertical substrate and by spraying suspension to the substrate. Synthesis of silica globules was performed by the modified Stöber method [16]. According to that, the silica particles were produced by hydrolysis of the ether of tetraethyl orthosilicate (TEOS) in ethanol. Ammonia was used as a catalyst. The precipitate after drying on air was annealed at 125 °C for a 1 h, and then at 750 °C for 2 h. Dimensions of obtained bulk samples were about $1.0 \times 1.0 \times 0.2$ cm^3.

Characterization of initial opals was performed by analyzing the surface structure with the use of X-Ray Microanalyzer JEO JXA 8200 and by measuring transmission and reflection spectra within a visible spectral range.

The experiments on the diffraction were carried out by using the semiconductor lasers at $\lambda = 407$ nm and $\lambda = 635$ nm, and diode pumped solid-state laser at $\lambda = 532$ nm. The SO films with a thickness of 2–3 μm were used in these experiments. Optical scheme of the experiment was implemented in transmission geometry. Focused laser radiation pathed through film along $\langle 111 \rangle$ direction.

Opal structure is a face-centered cubic lattice formed by hexagonal close packed layers of monodisperse globules. Globule diameter D and distance d between the planes (111) are determined by peak position λ_0 in the Bragg reflection spectra or minimum position in transmission spectra using Bragg's law

$$\lambda_0(\theta) = 2d\sqrt{\varepsilon_{\text{eff}} - \sin^2\theta} \tag{22.1}$$

where θ is the angle of incidence of the light beam upon the system of $\{111\}$ planes, $D = d\sqrt{3/2}$, and ε_{eff} is the effective dielectric permittivity. The last one is determined by the total contribution of the dielectric permittivities ε_i of substances in SO pores, according to their volume fraction f_i ($\varepsilon_{\text{eff}} = 0.74 \cdot \varepsilon_{SiO_2} + \sum_i f_i \cdot \varepsilon_i$, $\sum_i f = 0.26$). The globules diameter and interplanar distance for the different samples were in ranges $D = 250$–270 nm, $d = 200$–220 nm.

Initial SO samples have band-gap only in certain spatial directions, the so-called stop-band. The spectral width and position of photonic stop-band were determined by position λ_0 and half-width $\Delta\lambda$ of Bragg reflection band. For the initial SO samples, it corresponds to the 53–620 nm spectral range along $\langle 111 \rangle$ direction.

22.2.1 The Classification of Defects Types in Fabricated Samples

The first characterization problem of SO was to perform the microscopic analysis of the sample structure and to classify defects. All observed defects by the size and volume fraction may be divided into macroscopic and microscopic defects. Macroscopic defects include violations of the SO regular structure with the size significant larger than the wavelength of light and can be observed with an optical microscope, even under a small magnification. Such defects are cracks (Fig. 22.1a), relief surface (Fig. 22.1a, b), pits (Fig. 22.1b), regions with different brightness of iridescence (Fig. 22.1b, c). These regions can be represented as the domains (Fig. 22.1c) with different orientations relative to each other and to the surface plane of the sample. All these defects lead to the fact that the growth (111) plane of the whole sample do not coincide with the corresponding planes of individual domains.

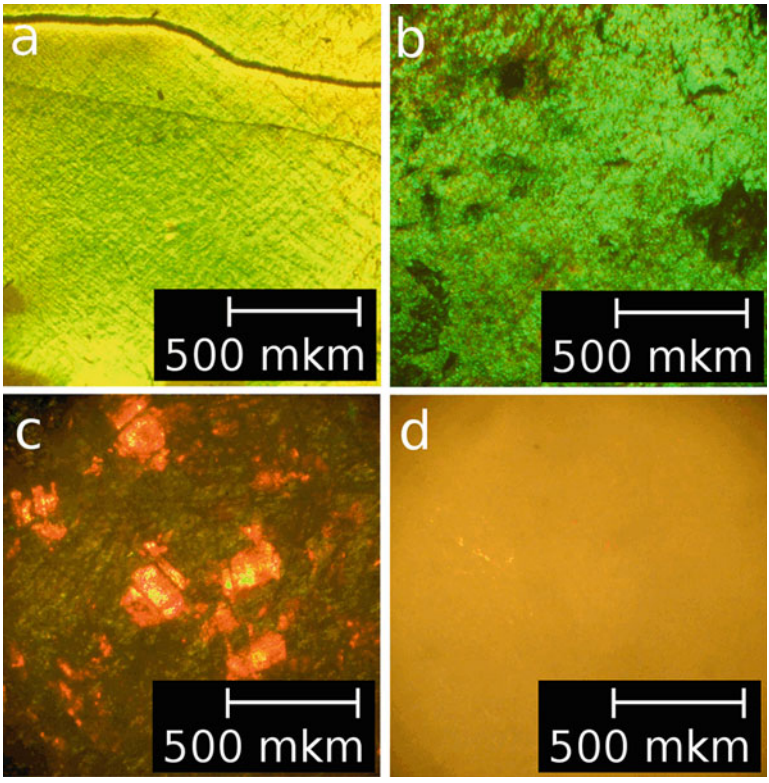

Fig. 22.1 Photos of SO surface with different types of macroscopic defects made with an optical microscope under the ×40 magnification, (**a**) sample with cracks; (**b**) sample with relief surface and pits; (**c**) sample with domains; (**d**) photonic glass

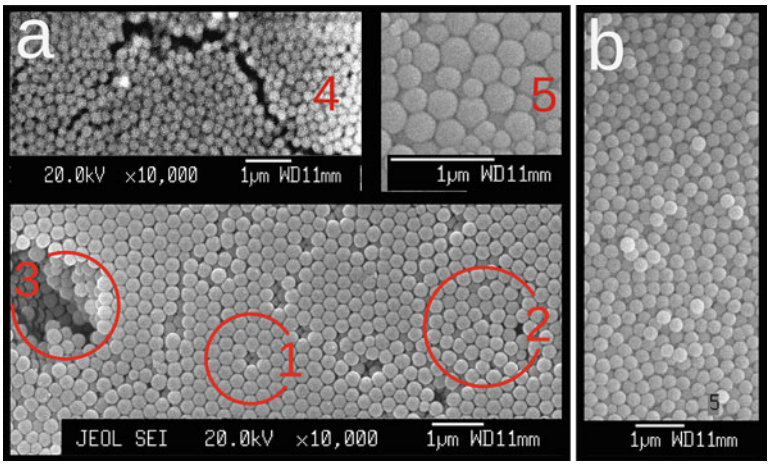

Fig. 22.2 Photomicrographs of the SO surface made by X-Ray Microanalyzer JEO JXA 8200, (**a**) photonic crystals with different types of the structure defects: vacancy (1), local disorder (2), pit (3), cracks (4), different size of globules (5); (**b**) completely disordered structure (photonic glass) with an absence of local and long-range structural order

The sample surface (Fig. 22.1d) without any iridescence is an example of photonic glass which has no both local and long-range order in the arrangement of globules.

Microscopic defects include violations in size compared to the lattice parameter of SO. These violations consist of vacancies (label 1 in Fig. 22.2a) and local disorder at distances from a few to several hundred lattice parameters (label 2 in Fig. 22.2a). Three-dimensional defects are expressed as micro pits and cracks (labels 3 and 4 in Fig. 22.2a). These types of defects are transitional to the macroscopic defects. Several hundreds of such defects combined together can be form macroscopic defects described above. Label 5 shows defects arising from presence of globules with different diameters. A photomicrograph of the surface with a complete absence of local and long-range order is shown in Fig 22.2b.

Defectiveness of structure is easy to see in diffraction patterns of film opals.

Diffraction patterns registered from the different points of the sample have a significant redistribution of the reflex intensity (Fig. 22.3b, c), blurring the reflexes and diffuse background (Fig. 22.3a, b). The last two effects may indicate to the presence of microscopic defects and structure disordering. Pattern with the six reflexes preserves symmetry C_6, despite the blurring, and shows the relative integrity of hexagonal layers. A number of reflexes less than six indicates the presence of cracks, channels, pits while number more than six is due to the presence of binary structures [13] (several differently oriented domains take part in diffraction process).

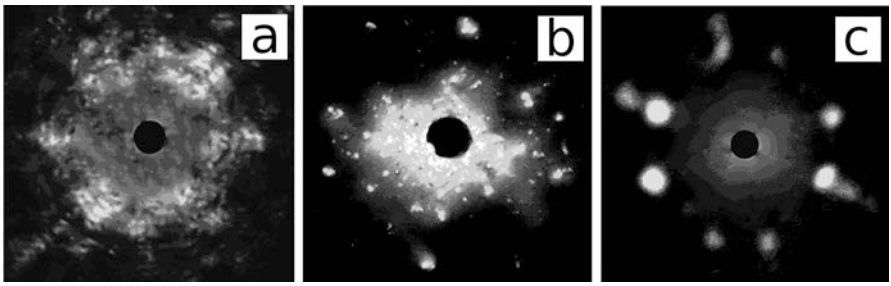

Fig. 22.3 Diffraction patterns of film opals with different types of defects, (**a**) blurring of reflexes; (**b**) less than six reflexes; (**c**) more than six reflexes

22.2.2 The Relative Ordering Parameter of Samples Structure: Characteristics of Optical Spectra for Samples with the Different Degree of Defectiveness

Investigation of structural defects and their effect on the optical properties of SO requires an introduction of a quantitative parameter, describing the degree of sample structure ordering.

Suppose that regions with iridescence in the sample volume are distributed uniformly, and their number coincides with the number of regions, corresponding to the non-defective structure. Then, the relative amount of ordered regions on the surface should correspond to the relative amount of ordered regions throughout the investigated volume. The relative ordering parameter is expressed as the ratio of the total area of the regions with irisdescence S_{iris} to the overall area of the sample surface S_{overall} as follows

$$\eta_{\text{order}} = \frac{S_{\text{iris}}}{S_{\text{overall}}} \tag{22.2}$$

In order to correctly estimate the S_{iris} and S_{overall} values, the photographs of samples were subjected to software processing. Photographs were discolored so that the amount of whitened regions coincided with the number of iridescence regions. Then, the parameter η_{order} is expressed as the number of whitened pixels per the total number of pixels

$$\eta_{\text{order}} = \frac{n_{\text{white}}}{n_{\text{overall}}} \tag{22.3}$$

The results of the software processing for samples with different numbers of defects and appropriate values of the relative ordering parameter obtained by (22.3) are shown in Fig. 22.4.

For each sample, the Bragg reflection spectra were measured, and the relation between the reflection band half-width $\Delta\lambda$ and η_{order} was found (Fig. 22.4).

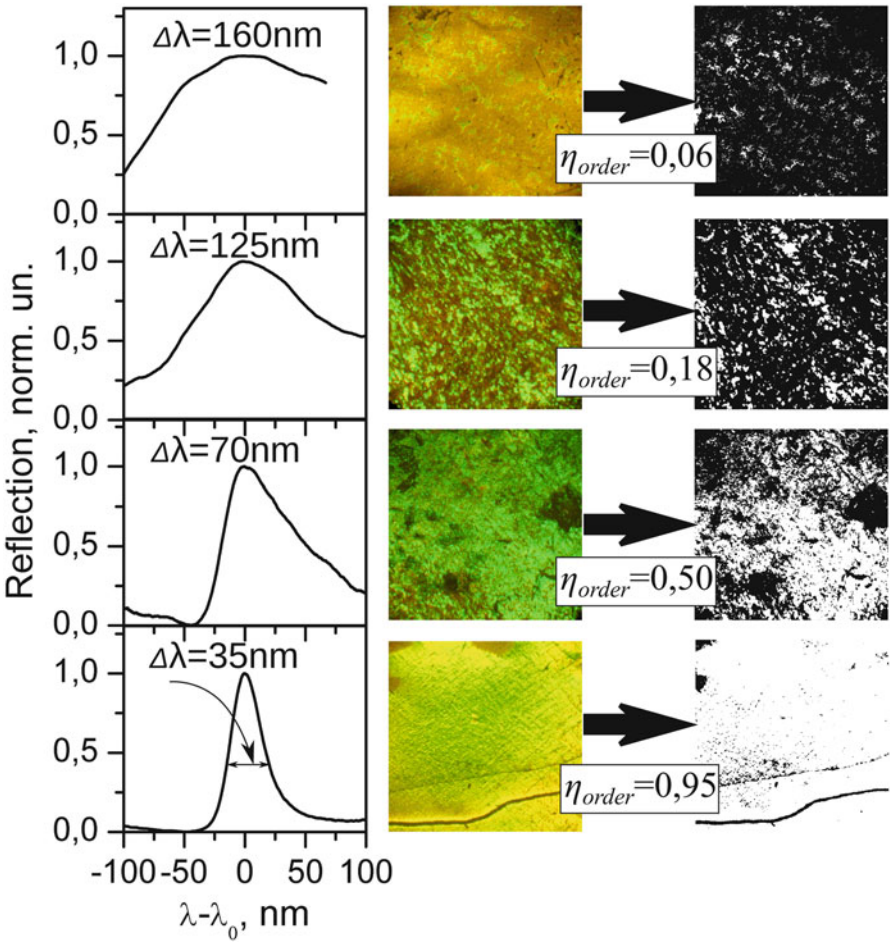

Fig. 22.4 *Left*—reflection spectra of SO surfaces with different η_{order}, *right*—software processing of samples surface photographs with the corresponding η_{order}

22.3 The Model of 1D Periodic Defective Structure

The model of 1D periodic structure with defects, typical for SO's was developed in order to calculate the effect of the structural defects on the optical spectra of opals. Simulation of reflection spectra $R(\lambda)$ was performed by transfer-matrix method [17], while the simulation of DOS(λ) spectra was done by the plane wave expansion method [18–20]. The analytical expressions for DOS and reflection or transmission spectra include the structure period d. In our model the value of d were randomly changed.

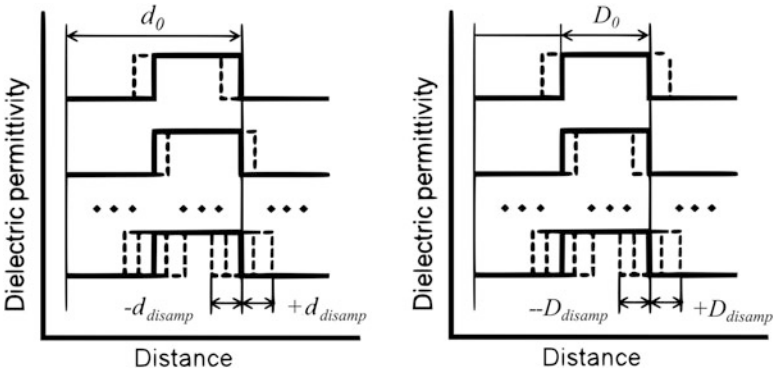

Fig. 22.5 Determination of the d_{disamp} and D_{disamp}

The value of the maximum disorder amplitude (maximum amplitude of deviation of structural element from its correct position) was introduced as a quantitative evaluation of the disorder degree d_{disamp} (Fig. 22.5). The maximum deviation amplitude of globules diameter from the values corresponding to the maximum value of the distribution function of globule diameter, represented as D_{disamp}.

Simulation was carried out using the mathematical package GNU Octave. DOS(λ) and $R(\lambda)$ simulation was performed by sequential iteration of wavelength λ in the range from 350 to 650 nm. For each iteration step, the structure period was determined by the expression $d = d_0 \pm \Delta \cdot d_{\text{disamp}}$, where d_0 was the period of regular structure, Δ took random values within the range from –1 to +1. The globule diameter was expressed in a similar way as $D = D_0 \pm \Delta \cdot D_{\text{disamp}}$, where D_0 was the most probable globule diameter, Δ took the same values as within the case of a period structure. For more accurate calculations, one thousand iteration cycles were performed with a subsequent averaging of the obtained spectra. Combination of cycles with $d = d_0$ ($D = D_0$) and cycles with $d = d_0 \pm \Delta \cdot d_{\text{disamp}}$ ($D = D_0 \pm \Delta \cdot D_{\text{disamp}}$) allowed to introduce the relative ordering parameter in this model. The relative ordering parameter η_{order} was expressed as the ratio of the cycles amount that define regular structure Cn_{order} to total cycles amount Cn_{overall}

$$\eta_{\text{order}} = \frac{Cn_{\text{order}}}{Cn_{\text{overall}}}$$

In order to adapt the model to real samples the d_{disamp}, D_{disamp}, and η_{order} values were assigned by analyzing the photomicrographs.

22.3.1 Reflection Spectra: Simulation and Experiment

Simulation of reflection spectra were performed for multilayer structure with a couple of layers with n_1, n_2, d and D, consistently alternating. The case of normal incidence of light was considered. The disorder effect was taken into account by

assigning d and D the values in accordance with the above mentioned expressions. Reflection spectrum was defined as $R = \left|\frac{a}{b}\right|^2$ where $\left(\frac{a}{b}\right) = \begin{pmatrix} n_0 & -1 \\ n_0 & 1 \end{pmatrix} \cdot M_{12}^N \cdot \begin{pmatrix} 1 \\ n_{\text{fin}} \end{pmatrix}$, n_0 was the refraction index of medium from which the light comes to multilayer structure and n_{fin} was the refraction index of the medium in which the light comes from multilayer structure, N was the number of pairs of layers. The product of matrices describing the propagation of light in a pair of layers was

$$M_{12} = \begin{pmatrix} \cos(\delta_1) & \frac{1}{n_1} i \sin(\delta_1) \\ i n_1 \sin(\delta_1) & \cos(\delta_1) \end{pmatrix} \cdot \begin{pmatrix} \cos(\delta_2) & \frac{1}{n_2} i \sin(\delta_2) \\ i n_2 \sin(\delta_2) & \cos(\delta_2) \end{pmatrix}$$

where $\delta_1 = \frac{2\pi}{\lambda} n_1 d$ and $\delta_2 = \frac{2\pi}{\lambda} n_2 D$.

The dependences of the relative half-width of reflection band via the value η_{order} for calculated and measured reflection spectra are presented in Fig. 22.6. The difference between curve 1, calculated by the described procedure, and experimental curve 3 is probably caused by neglecting the multiple elastic scattering processes in the considered model.

In order to improve the model, the reflection spectrum of photonic glass was measured at the normal incidence of light. Since the constructive interference is absent in this structure, the only processes, that form the spectral response in opals (with eliminating absorption and inelastic scattering), are the elastic scattering processes. The right part of Fig. 22.6 shows the reflection spectrum of the photonic glass. The dashed line shows the fitted function of this spectrum.

The product of this function and simulated reflection spectra brings the model close to real conditions. Figure 22.7 shows comparison of reflection spectra, simulated with taking into account of the scattering effect, and experimental reflection spectra (at the normal incidence of light) for the appropriate η_{order}. Curve 2 on Fig. 22.6 shows the dependence of $\Delta\lambda/\lambda_0$ on the η_{order} with respect to

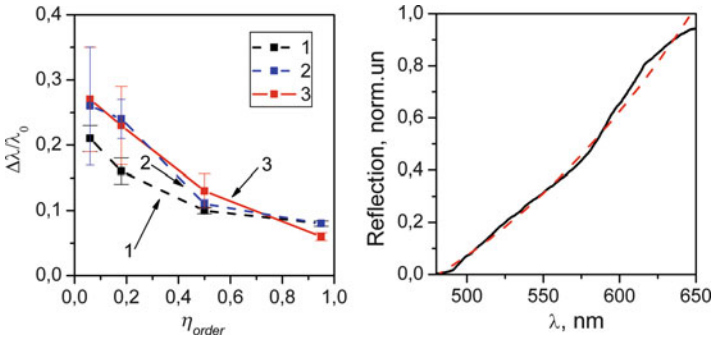

Fig. 22.6 *Left*—the dependence of the relative half-width of Bragg reflection band on coefficient η_{order}: calculated dependence (1), calculated dependence taking into account the elastic multiple scattering (2), experimental dependence (3); *right*—the normal reflection spectrum of the photonic glass (*solid line*) and a fitted curve of this spectrum (*dashed line*)

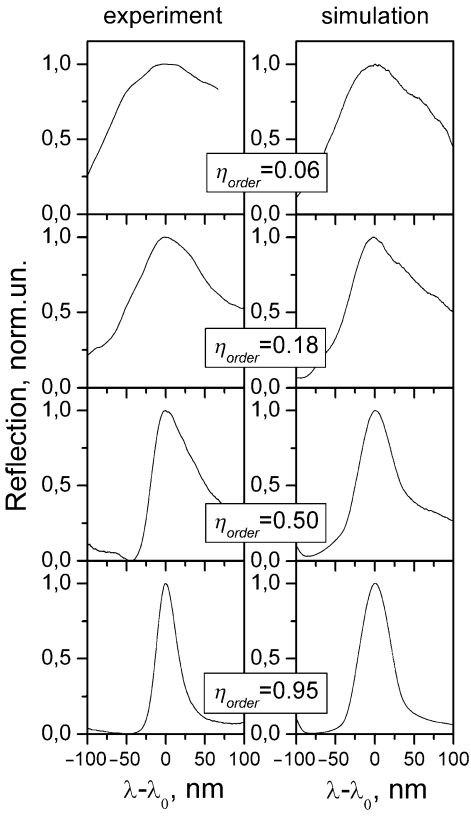

Fig. 22.7 *Right*—measured normal reflection spectra of the sample surface with different value of η_{order}, *left*—the simulated reflection spectra for one-dimensional layered structure with the corresponding η_{order}

the effect of scattering. As can be seen from Fig. 22.6, the experimental and simulated curves demonstrate a good agreement.

Thus, together with Bragg's diffraction, the effect of multiple elastic scattering should be taken into account for describing optical response of SO, too.

22.3.2 *The Influence of Disorder on Density of Optical States Spectra*

As well known, the function of the DOS in PC has singularities at the edges of the photonic band-gap as a result of structure regularity. The DOS function play an important role in optical processes. This is why it is necessary to investigate the influence of structure defects on its behavior.

Analytical expression of DOS as a function of light frequency ω, for one-dimensional structures is obtained on the basis of the plane wave expansion method as follows

$$g(\omega) = \frac{1}{\pi^2}\left\{\frac{\pi}{d} \pm \left[\frac{\omega^2}{c^2}\varepsilon_0 + \frac{\pi^2}{d^2} \pm \frac{\omega}{c}\left(\frac{4}{3}\frac{\omega^2}{c^2}\varepsilon_1^2 + \varepsilon_0\left(\frac{2\pi}{d}\right)^2\right)^{1/2}\right]^{1/2}\right\}^2$$
$$\times \left\{\pm\frac{1}{2}\left(\frac{\omega^2}{c^2}\varepsilon_0 + \frac{\pi^2}{d^2} \pm \frac{\omega}{c}\varepsilon_\omega\right)^{-1/2}\left[\frac{2\omega\varepsilon_0}{c} \pm \left(\varepsilon_\omega + \frac{4}{3}\frac{\omega^2}{c^2}\varepsilon_1^2\frac{1}{\varepsilon_\omega}\right)\right]\right\},$$

where c is a light velocity, $\varepsilon_\omega = \sqrt{\frac{4}{3}\frac{\omega^2}{c^2}\varepsilon_1^2 + \varepsilon_0\left(\frac{2\pi}{d}\right)^2}$, ε_0 and ε_1 are the Fourier coefficients determined as $\varepsilon_m = (\varepsilon_s - \varepsilon_p)\frac{D}{d}\left[\frac{\sin\left(m\frac{\pi D}{d}\right)}{m\frac{\pi D}{d}}\right]$, ε_s and ε_p are the dielectric permittivities of globules and pores, respectively.

Consideration of the disorder effect was carried out over values d and D as described above in the model. DOS was plotted as a dependence of the wavelength λ.

Figure 22.8 shows the changes in DOS with the increase of d_{disamp} and D_{disamp}. It can be seen that very small deviations of the proper structure 203 period and globules diameter (d_{disamp}, $D_{disamp} = 6$ nm is not more than 2–3 % of the values of $d = 200 \div 220$ nm and $D = 250 \div 270$ nm) results in filling of states in the middle of the band gap until its complete filling. Owing to the microscopic defects, real SO always have a deviation of structure period at least a few percent, and the deviation from the normal globules diameter is at least 5 %. Thus, it suggests that we have studied samples where optical states within the photonic stop-band are completely filled.

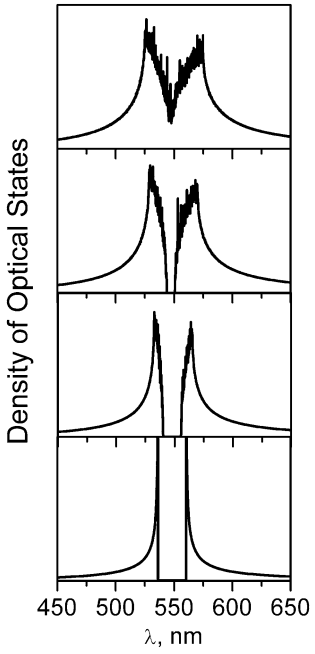

Fig. 22.8 The evolution of the DOS spectrum with a gradual increase of values d_{disamp} and D_{disamp} (from bottom to the up: d_{disamp}, $D_{disamp} = 0; 2; 4; 6$ nm)

22.4 The Influence of Disorder on the Fluorescence and Raman Spectra

Two basic mechanisms of the radiation amplification can be expected in SO. The first one is due to Bragg's diffraction of the short-wave radiation on the system of {111} planes at larger angles with the following escaping of radiation along ⟨111⟩ direction [1]. The second one, determined by multiple scattering of the exciting photons by the structural defects, results in increasing the mean time of photon residence in the opal volume, and consequently, their accumulation. At a significant amount of structural defects the closed paths both of source and the emitted photons can arise, and it may lead to the conditions for the occurrence of lasing effect [15].

22.4.1 Fluorescence Spectra of Opal-R6G Samples

The fluorescence spectra of rhodamine 6G (R6G) embedded in opals with different ordering degree (signed as SO1, SO2, and SO3) were measured in the "reflection" geometry under absolutely identical conditions. The concentration of R6G molecules in the infiltrated solution for all samples was the same. Initial samples before the infiltration have been characterized to determine the relative of half-width $\Delta\lambda/\lambda_0$ of the Bragg reflection band. The relative ordering parameter η_{order} of initial opals was defined by the value of $\Delta\lambda/\lambda_0$ obtained from the measured normal reflection spectra through experimental dependence depicted in Fig. 22.6.

The value I_{SO}/I_0 given in Table 22.1 is the ratio between integral fluorescence intensities of R6G in SO (I_{SO}) and in an ethanol solution in optical cell (I_0). This value is the criterion that indicates an amplification of the spontaneous emission intensity in SO.

Thus, the fluorescence spectra show an increase of integral intensity of fluorescence with the increase of the number of structural defects inside opals. The increase in fluorescence intensity correlates with the increase of the relative ordering parameter η_{order} and, consequently, an increase of the number of slowed exciting photons with diffusive transfer.

Table 22.1 The dependence of relative integral intensity on relative ordering parameter

	η_{order}	I_{SO}/I_0
SO1	0.95	2
SO2	0.70	3
SO3	0.00	6

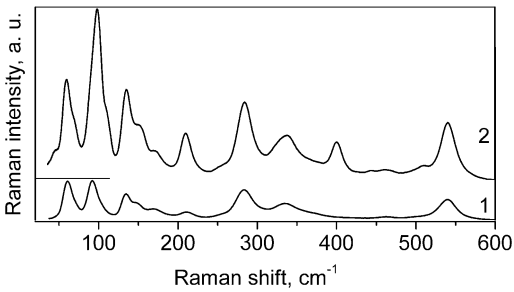

Fig. 22.9 Raman spectra of $Bi_{12}SiO_{20}$ powder (1) and opal-$Bi_{12}SiO_{20}$ sample (2)

22.4.2 Raman Spectra of Opal-$Bi_{12}SiO_{20}$

The Raman spectra of $Bi_{12}SiO_{20}$ powder (Fig. 22.9, curve 1) and SO filled by $Bi_{12}SiO_{20}$ (Fig. 22.9, curve 2) were measured. Comparative analysis, besides some redistribution in Raman intensity lines and the arising of new lines (that can be treated as a result of crystallization in opal pores), shows significant, more than three times, amplification of integral intensity of Raman lines.

The mismatch of Raman spectral range and spectral position of photonic stop-band in our samples allows to conclude that the amplification in this case is due to multiple scattering of exciting photons.

22.5 Conclusions

The classification of structural defect types in the SO samples was represented. All defects were divided into two classes: macroscopic defects whose dimensions are significantly larger than the light wavelength and microscopic defects whose size is comparable to the lattice constant of SO. The relative ordering parameter of SO structure was introduced. The reflection spectra by a transfer-matrix method and the DOS spectra by a plane wave expansion method were simulated. The comparison of the relative half-width of reflection band $\Delta\lambda/\lambda_0$ depending on η_{order} based on the calculated and experimental data was shown. The best agreement between experiment and simulation occurs if the effect of elastic multiple scattering is taken into account in the simulation. It was established that the small deviation up to 3 % of the quantities $d = 200 \div 220\,\text{nm}$ and $D = 250 \div 270\,\text{nm}$ leads to complete filling of photon states within photonic stop-band. The amplification of fluorescence spectra of R6G and Raman spectra of $Bi_{12}SiO_{20}$ in SO templates was observed.

Acknowledgments This work was supported by the project "Capture of electromagnetic emission in resonance structures and in resonance photonic crystals with luminescent centers".

References

1. Bechger L, Lodahl P, Vos W (2005) Directional fluorescence spectra of laser dye in opal and inverse opal photonic crystals. J Phys Chem B 109(5):9980–9988
2. Aliev G, Golubev V, Dukin A, Kurdyukov D et al (2002) Structural, photonic band-gap, and luminescence properties of the opal-erbium composite. Phys Solid State 44(12):2224–2231
3. Ambrozevich S, Gorelik V, Dirin D, Vasil'ev R et al (2009) Optical properties of 3D photonic crystals filled with CdSe/CdS quantum dots. J Russ Laser Res 30(4):384–391
4. López C (2003) Materials aspects of photonic crystals. Adv Mater 15(20):1679–1704
5. Qi M, Lidorikis E, Rakich PT et al (2004) A three-dimensional optical photonic crystal with designed point defects. Nature 429:538–542
6. Braun P, Rinne S, García-Santamaría F (2006) Introducing defects in 3D photonic crystals: state of the art. Adv Mater 18:2665–2678
7. Kaliteevskii M, Nikolayev V, Abram R (2005) Eigenstate statistics and optical properties of one-dimensional disordered photonic crystals. Phys Solid State 47(10):1948–1957
8. Zheltikov A, Magnitskii S, Tarasishin A (1999) Localization and channeling of light in defect modes of two-dimensional photonic crystals. JETP Lett 70(5):323–328
9. Lončar M, Nedeljković D, Pearsall T et al (2002) Experimental and theoretical confirmation of Bloch-mode light propagation in planar photonic crystal waveguides. Appl Phys Lett 80 (10):1689–1691
10. Inoue K, Ohtaka K (eds) (2004) Photonic crystals: physics, fabrication and application. Springer, Berlin
11. John S (1987) Strong localization of photons in certain disordered dielectric superlattices. Phys Rev Lett 58(23):2486–2489
12. John S (1991) Localization of light. Phys Today 44(5):32–40
13. Sinitskii A, Abramova V, Laptinskaya T et al (2007) Domain mapping of inverse photonic crystals by laser diffraction. Phys Lett A 366:516–522
14. Baryshev A, Kaplyanskii A, Kosobukin V et al (2003) Bragg diffraction of light in synthetic opals. Phys Solid State 45(3):459–471
15. Gottardo S, Sapienza R, Garcia P et al (2008) Resonance-driven random lasing. Nat Photonics 2:429–432
16. Stöber W, Fink A, Bohn E (1968) Controlled growth of monodisperse silica spheres in micron size range. J Colloid Interface Sci 26(2):62–68
17. Born M, Wolf E (1970) Principles of optics, 4th edn. Pergamon, Oxford
18. Yariv A, Yeh P (1984) Optical waves in crystals. Wiley, New York
19. Sakoda K (2005) Optical Properties of photonic crystals, 2nd edn. Springer, Heidelberg
20. Joannopoulos J, Johnson S, Winn J, Meade R (2008) Photonic crystals: molding the flow of light, 2nd edn. Princeton University Press, Princeton

Chapter 23
Correlation Processing of Speckle Pattern in Multimode Polymer Optical Fiber for Deformation Monitoring in Nanometer Range

V. Varyshchuk and Ya. Bobitski

23.1 Introduction

One of the mechanisms of optical fiber sensing is to convert the fiber strains caused by external parameters into changes of the phase of the light traveling inside the optical fiber. Hence, interferometric measuring systems should be employed to detect phase changes with high sensitivity. Conventional interferometers require two interacting waves with identical polarization state to ensure highly fringes visibility. Such a requirement is easily achievable when, for instance, the sensitive arm of the interferometer is a single mode fiber. However, in some practical cases using a multimode optical fiber (MMF) is much more convenient than using a single mode fiber.

Compared with a single mode fiber, the multimode type possesses higher numerical aperture and higher light power carrying capacity. Moreover, multimode optical fibers allow the easier implementation of efficient multiplexed fiber sensors. However, during operative conditions conventional interferometers do not perform well with MMF. Since an MMF has a bigger core than a single mode fiber, the light propagation in an MMF is characterized by more than one propagation mode. When highly coherent light travels through the MMF, the resulting wave at the fiber's output is characterized by a random distribution of the intensity and polarization state of the light due to the intermodal interference. Whenever external parameters such as strain, temperature, pressure, or even mechanical vibrations affect the MMF, they also affect the propagations of spatial modes in MMF, thus changing the distribution of the light field at its output. Based on this phenomenon, various schemes of sensors for measurement of strain [1], displacement [2, 3], temperature

V. Varyshchuk (✉) • Ya. Bobitski
Lviv Polytechnic National University, S. Bandery Str., 12, Lviv 79013, Ukraine
e-mail: vasya.v.v.9@gmail.com

O. Fesenko, L. Yatsenko (eds.), *Nanoplasmonics, Nano-Optics, Nanocomposites, and Surface Studies*, Springer Proceedings in Physics 167,
DOI 10.1007/978-3-319-18543-9_23

[4], and vibration [5, 6] were reported. Particularly, for strain measurement the great interest present using a polymer optical fibers (POF), because they have additional advantage compared with silica fiber, including high elastic strain limits, high fracture toughness, excellent flexibility, and high sensitivity to strain. In addition, POF can be easily surface mounted or embedded in engineering structures and composite materials to assess their reliability. Most of the reported applications based on multimode POF are not suitable for the precise deformation monitoring due to the limited dynamic range or the oversensitivity of the sensor principle. Nevertheless, a strain measurement scheme has been reported [7] by adhering MMF to a cantilever beam and measuring the speckle intensity variation that is proportional to the applied strain. The obtained results exhibit a good linearity, but dynamic range of scheme was fairly limited. This problem has been solved in [8] by analyzing the geometrical properties of the speckle pattern and employs the correlation value with the reference modal state of speckle pattern to determine the fine strain measurements. In other work, some photorefractive materials are employed to stabilize the processed speckle pattern [9]. This effect can be used to reduce the extra noise due to the typical oversensitivity of fiber speckle pattern. However, these systems were too complicated to implement in practice and is not suitable for low-cost applications.

The correlation methods of signal processing allow constructed fiber optic interferometer using only laser, multimode optical fiber, and digital camera. Even the small deformation of multimode fiber causes the change of propagation conditions of guided modes and, consequently, the change of speckle structure formed at the exit end of fiber [10]. These changes can be detected by comparing the resulting speckle pattern with a reference pattern. A good comparison of the speckle patterns can be accomplished by spatially correlating them [1]. The intensity distributions of speckle patterns before and after deformation action on the fiber are compared by measuring the correlation coefficient for these signals.

We considered POF as they are more sensitive to deformation compared to silica fibers [11]. The correlation method considered in the chapter allows one to measure an axial elongation of the fiber within 0–5,000 nm for typical multimode POF. The measuring range of such technique depends on properties of fiber and using wavelength.

23.2 Multimode Optical Fiber Speckle Metrology

It is well known that propagation modes with different phase velocities appear in a multimode optical fiber when coherent light travels through it. In this way, a speckle pattern is generated at the output end of the fiber due to the superposition of individual fields, each one with different phase delays. This phenomenon in multimode fibers has been studied by several authors [12–14]. Nevertheless, the problem of decoding this interference pattern is still not completely solved. However, we can already note some characteristics of speckle structures at the output of multimode fibers:

- The average speckle size decreases with increasing the number of excited modes, i.e., increases with decreasing of normalized frequency.
- With increasing of the fiber length contrast of speckle pattern decreases.
- Speckle-pattern is depolarized and at rotation of the analyzer change of a form and the position of individual speckle is observed.
- The distribution of the light in the far-field zone is determined by Fourier transformation of the field at the end of the fiber and is a statistical function.

In general, the number of speckles projected by a multimode optical fiber on a screen is approximately equal to the number of modes that supports the fiber. For a step-index fiber, the number of modes M is given by the expression:

$$M \approx \frac{V^2}{2}. \tag{23.1}$$

where V is the normalized propagation constant.

$$V = \frac{2\pi a}{\lambda}\sqrt{n_1^2 - n_2^2}, \tag{23.2}$$

where a is the radius of the fiber core, λ is the wavelength of the light source, n_1 is core refractive index and n_2 is cladding refractive index.

Of interest in speckle metrology is the average speckle size. The statistical average size of the speckle diameter of the light field formed by an optical fiber in the plane placed at the distance R from its output can be calculated as

$$S_\mathrm{d} = 2.44R\left(\frac{\lambda}{d}\right). \tag{23.3}$$

This equation demonstrates the relation between the speckle size and diameter of the fiber and distance from the fiber to observation plane [4]. As example, the speckle patterns at the end of the different fibers are shown in Fig. 23.1. The shown data demonstrate the relation between the speckle size and diameter of the multimode fiber.

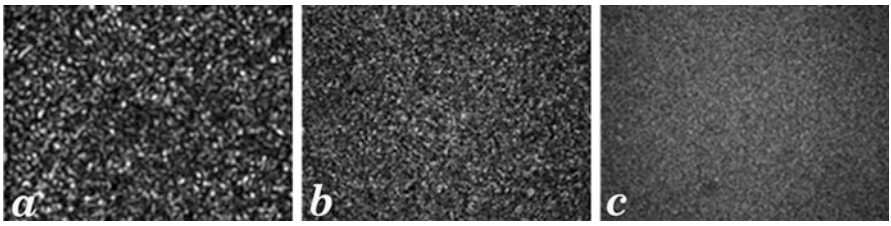

Fig. 23.1 Photography speckle patterns at the end of the 1 m multimode fiber, which were obtained with laser diode: (**a**) PCS fiber with diameter of 200 μm, (**b**) POF with diameter of 500 μm, (**c**) POF with diameter of 1,000 μm

Due to the number of speckles present in a pattern is approximately equal to M, a speckle pattern adaptable to the needs of the measured variable can be obtained just by choosing a fiber with a suitable diameter and consequently by determining the size of the speckles in the registration plane.

Fiber speckle patterns contain the information about propagation of coherence modes in fiber, which can be used in metrological applications. In multimode optical fibers, the speckle phenomenon can be explained by the coupled mode theory in terms of the relative phases of the optical propagation modes traveling throughout the fiber. Small perturbations on the multimode optical fiber will produce changes in the spatial distribution of the speckle pattern which can be detected by optical correlation techniques or by intensity changes. Sensing systems based on fiber speckle analysis are known as fiber specklegram sensors (FSS).

23.3 Correlation Processing Method Description

For speckle image analysis, both image differencing and image correlation features are widely used, and several different algorithms based on these two features are reported in the literature [15–18]. In this section, we show that strain sensing in nanometer range can be achieved by utilizing the intensity speckle fields in multimode fiber. In other words, by taking the intensity speckle patterns before and after the perturbation of the multimode fiber, the intensity inner product between the two speckle patterns can be calculated. Since the fiber speckle field is caused by the modal phasing of the fiber, the intensity inner product would be highly sensitive to the fiber status changes, which can be used for strain sensing.

When the multimode sensing fiber is subjected to perturbation, the optical path length of propagating modes undergoes changes. These changes can be detected by comparing the resulting output speckle pattern with a reference pattern. The correlation parameter is obtained between reference speckle image and varying perturbation speckle images. This correlation values represent the signal values of the perturbation. If $I_0(x,y)$ is the output pattern when there is no external effect to the fiber, which is also called the reference output pattern, and $I(x,y)$ is the corresponding output pattern when there is a perturbation, the correlation coefficient between the two images can be expressed as

$$C = \frac{\langle I_1(x,y) I_2(x,y)\rangle - \langle I_1(x,y)\rangle \langle I_2(x,y)\rangle}{\sqrt{\left(\langle I_1^2(x,y)\rangle - \langle I_1(x,y)\rangle^2\right)^2 \left(\langle I_2^2(x,y)\rangle - \langle I_2(x,y)\rangle^2\right)^2}}, \tag{23.4}$$

where the angle brackets mean averaging over spatial coordinates x and y. The correlation coefficient takes the value one if the intensity distribution of speckle pattern $I_2(x,y)$ correlated with $I_1(x,y)$ is identical to it and decreases gradually with the change of speckle pattern.

In [19, 20] it has been shown, theoretically and experimentally, that the correlation coefficient between two speckle patterns at the output of multimode fiber before and after deformation, respectively, is associated with maximal additional phase difference between guided modes by:

$$C = \frac{\sin^2(\Delta\phi_{\max}/2)}{(\Delta\phi_{\max}/2)^2}. \tag{23.5}$$

The value of an additional difference of phases between modes due to a change of fiber length can be estimated:

$$\Delta\phi_{\max} = \left(kn_m + kl\frac{dn_m}{dl}\right)\Delta l. \tag{23.6}$$

where

$$n_m = n_1 - \Delta n U_m^2/V^2 \tag{23.7}$$

is effective refractive index of mth guided mode; $\Delta n = n_1 - n_2$ is the difference of the refractive indices of the fiber core and cladding; U_m is phase mode parameter in fiber core, which can be calculated as:

$$U_m = a\sqrt{k^2 n_1^2 - \beta_m^2}, \tag{23.8}$$

where $k = 2\pi/\lambda$ is the wave number; β_m is the propagation constant of the mth guided mode. Equation (23.7) shows that the difference between the effective refractive indices is greatest for the lowest order modes and modes for which $U_m = V$. Maximum difference of the effective refractive indices of modes will be determined by the difference of the refractive indices of the fiber core and cladding. Accordingly, the phase shift of the mode caused by the axial deformation of fiber can be written in the form:

$$\Delta\phi_{\max} = \left(k\Delta n + kl\frac{d\Delta n}{dl}\right)\Delta l. \tag{23.9}$$

The change in the refractive index of the fiber due to its axial tension is given by expression [11]:

$$dn = 1 - \frac{n_1^2}{2}(p_{12} - v(p_{11} + p_{12}))\frac{dl}{l}, \tag{23.10}$$

where p_{11} and p_{12} are the Pockels coefficients, and v is the Poisson ratio of the fiber.

Combining the expressions (23.5), (23.9), and (23.10), we obtain

$$C = \frac{\sin^2(\pi \Delta n \Delta l(1+r))}{(\pi \Delta n \Delta l(1+r))^2}, \tag{23.11}$$

where

$$r = \frac{1}{\Delta n}\left(1 - \frac{n_1^2}{2}(p_{12} - v(p_{11} + p_{12}))\right). \tag{23.12}$$

In this model, it is assumed that the correlation coefficient of speckle patterns is determined by the fiber length change, and it is independent of the other factors. The dependence $C(\Delta l)$ calculated from (23.11) for conventional step-index POF with $\Delta n = 0.021$, the core diameter 980 μm, and wavelength $\lambda = 655$ nm is presented in Fig. 23.2.

As shown in Fig. 23.2, some characteristic elongation of the optical fiber exists above which a complete decorrelation of the speckle patterns is observed. In this case, the further correlation processing is impossible. If $\Delta l < \Delta l_0$ the correlation coefficient can be high enough for calculating from its measured value a change in the fiber length.

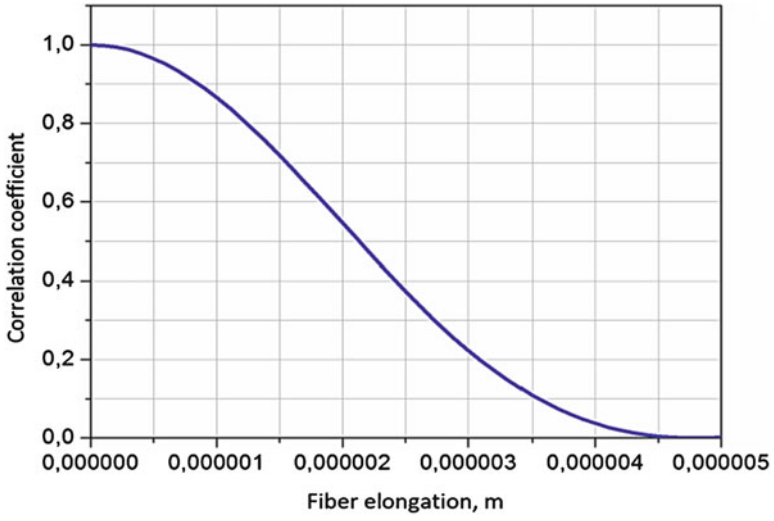

Fig. 23.2 Theoretical dependence of the correlation coefficient of speckle patterns on elongation of multimode polymer optical fiber

23.4 Experimental Results and Discussion

The experimental apparatus is shown in Fig. 23.3. A typical experimental setup employs a 655 nm diode laser source, section of multimode POF, used as sensitive element, and digital CCD camera.

The axial deformation of the sensitive part of fiber was produced by moving mount 4 along the axis of fiber. Notice that a small displacement of the translation stage would cause a small elongation of the sensing fiber. Thus, by capturing the fiber speckle intensity distributions with a CCD camera, the intensity speckle pattern evaluation can be performed by a computer. First digital camera records the reference image of speckle pattern, which corresponds to the initial state of the fiber waveguide. The deformation of the fiber due to external influence causes the changes in the spatial position of the speckles. The correlation coefficient between speckle patterns before and after deformation is calculated by using the developed software.

To provide the optimal condition of the CCD camera illumination need to average speckle size in registration plane is much larger than the cross size of the matrix pixel. On the other hand, the average speckle diameter must be much smaller than the light-sensitive area of the matrix. This is necessary that in the registered image is well-separated individual speckles. The distance D between the sensor and the fiber ends can be adjusted to obtain the desired speckle size.

The curves shown in Fig. 23.4 correspond to intensity diagrams recorded for fiber elongations ranging from 1 to 5 μm, in 1 μm steps. Each point represents the result obtained after applying the algorithm described in Sect. 23.3 to the initial diagram correlated with that associated to the corresponding displacement. The distance D between the fiber end and the CCD sensor was fixed to 4 cm. Accordingly with the above description, for this value of D the periodic modulation of the diagram can be resolved by the sensor. As a result, the expected decrease of the

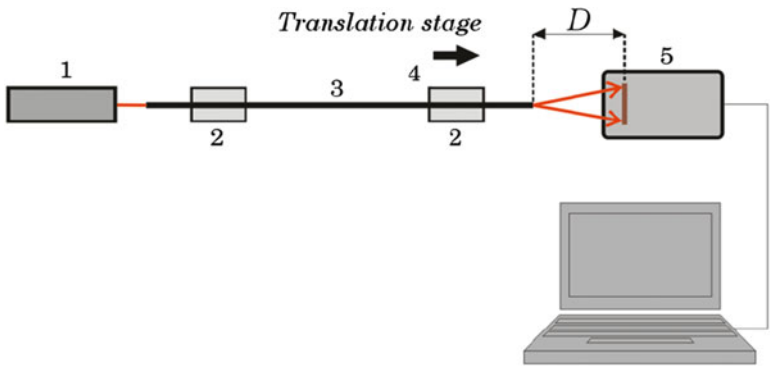

Fig. 23.3 Scheme of the experimental setup: 1—laser, 2—holder for fixing and tension of optical fiber, 3—multimode step-index POF, 4—moving mount for fiber deformation, 5—digital CCD camera

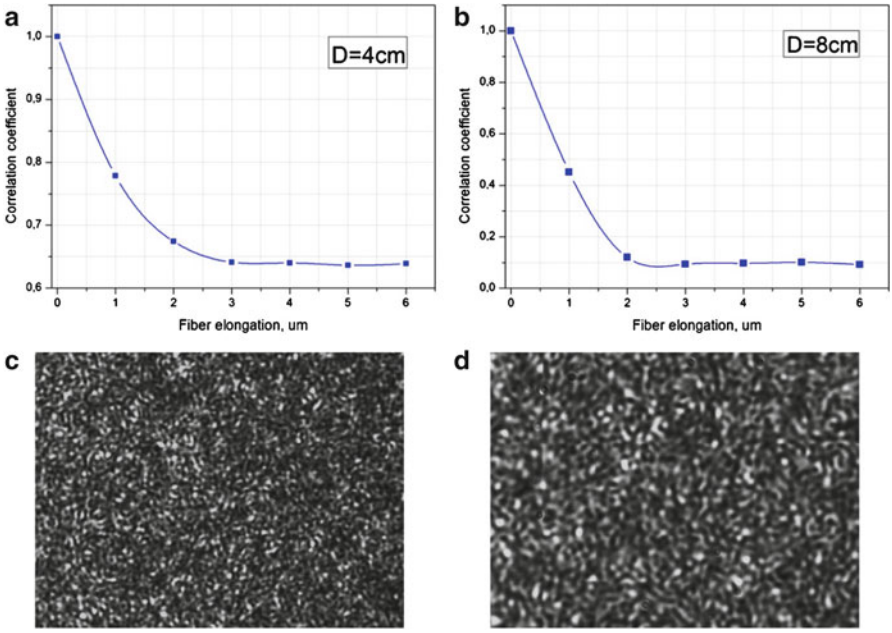

Fig. 23.4 Measured values of the correlation coefficient C for two different distances from fiber to CCD sensor (**a**, **b**) and corresponding images of speckle pattern (**c**, **d**)

correlation coefficient can be observed. Next, we changed the distance D to 8 cm in order to increase the speckle size to half of its previous value (Fig. 23.4b, d). Next, we changed the distance D between the fiber output and the CCD camera to a larger value, actually $D = 15$ cm, in such a way that the individual speckle can be resolved by the detector.

In order to better illustrate the effect of the speckle size on the deformation measuring, we present in Fig. 23.5 the corresponding curves for three values of the distance D. As can be expected, the best sensitivity (highest slope) is obtained for the shortest distance (smallest speckle size).

As can be observed, this system configuration of the fiber sensor allows to measure sub-micrometers deformations. As mentioned above, the quantitative measurements of the fiber elongation can be performed if the correlation coefficient is sufficiently high. For values of the correlation coefficient $C(\Delta l) < 0.6$, the decorrelation of speckle pattern was observed. This limits the measurement range of fiber deformation. However, this problem can be solved by rewriting the reference speckle pattern in computer memory with a decrease in the correlation coefficient to some specified value. This approach allows to use this technique for measuring in a much larger strain range. With increasing of distance from fiber exit face to CCD camera, and respectively increasing of speckle size, increases the probability of erroneous results.

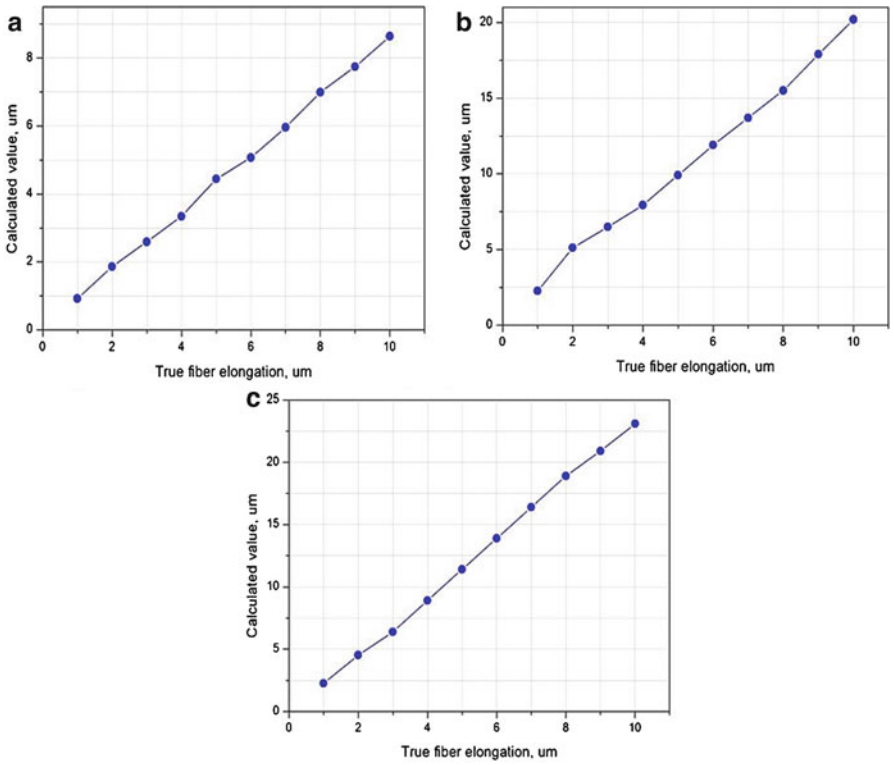

Fig. 23.5 Measured values of the fiber elongation for three different distances from fiber to CCD: $D = 4$ cm (**a**), $D = 8$ cm (**b**), and $D = 15$ cm (**c**)

23.5 Conclusions

In this work, we proposed an intrinsic polymer optical fiber sensor where the fiber elongation originates from a spatial change in a intensity speckle pattern which is measured through a correlation parameter. Our investigation shows that relative strain of conventional polymer optical fiber can be measured with high accuracy by correlation processing of speckle patterns formed at the exit face of fiber. The measuring range of such strain gauge depends on properties of fiber used as sensitive element of sensor and using wavelength. This method allows one to measure an axial elongation of the fiber within 0–5,000 nm for typical multimode POF with the length 1 m and core diameter 980 μm. As the correlation coefficient decreases to the value at which decorrelation of speckle pattern is observed, the rewriting of speckle image can be used for measuring strain in wide range. The sensitive of sensor is determined by the changes of refractive index and temperature variations due to fiber deformation. Device sensitivity may easily be modified to coincide with required measurement sensitivity through careful choice of the active

sensing fiber parameters. The device is simple, inexpensive, rugged, electrically passive, and compatible with existing multimode technology. The sensing technique presented in this chapter is simple, effective, and low-cost solutions to the problem of small deformation monitoring.

References

1. Pomarico A et al (1999) Optical fiber strain gauge based on speckle correlation. Opt Lasers Technol 31:219–224
2. Yu FTS et al (1993) Submicrometer displacement sensing using inner-product multimode fiber speckle fields. Appl Optics 32(25):4685–4689
3. Lomer M et al (2013) Measurement of displacement in the micrometer range using speckle pattern correlation in multimode fibers. In: Proceedings of SPIE 8794. Fifth European workshop on optical fibre sensors, Krakow
4. Gupta B et al (2008) Qualifying fibre optic temperature sensor using speckle metrology. Int J Inform Technol Knowl Manag 1:337–350
5. Spillman WB et al (1989) Statistical-mode sensor for fiber optic vibration sensing uses. Appl Optics 28(15):3166–3176
6. Rodriguez-Cobo L et al (2012) POF vibration sensor based on speckle pattern changes. In: Proceedings of SPIE 8421, OFS2012 22nd international conference on optical fiber sensors, Beijing, China
7. Zhang Z, Ansari F (2006) Fiber-optic laser speckle-intensity crack sensor for embedment in concrete. Sens Actuators A Phys 126(1):107–111
8. Rodriguez-Cobo L et al (2013) Optical fiber strain sensor with extended dynamic range based on specklegrams. Sens Actuators A Phys 203:341–345
9. Gomez J, Salazar A (2011) Self-correlation fiber specklegram sensor using volume characteristics of speckle patterns. Opt Lasers Eng 49(3):473–480
10. Redding B, Cao H (2012) Using a multimode fiber as a high-resolution, low-loss spectrometer. Opt Lett 37:3384–3386
11. Silva-Lopez M et al (2005) Strain and temperature sensitivity of a single-mode polymer optical fiber. Opt Lett 30:3129–3131
12. Crosignani B, Daino B, Porto P (1976) Speckle-pattern visibility of light transmitted through a multimode optical fiber. JOSA 66(11):1312–1313
13. Goodman J, Rawson E (1981) Statistics of modal noise in fibers: a case of constrained speckle. Opt Lett 6(7):324–326
14. Tremblay Y, Kawasaki B, Hill K (1981) Modal noise in optical fibers: open and closed speckle pattern regimes. Appl Optics 20(9):1652–1655
15. Lujo I et al (2008) Fiber-optic vibration sensor based on multimode fiber. Radioengineering 17 (2):93–97
16. Zhang Z, Ansari F (2005) Crack tip opening displacement in micro-cracked concrete by an embedded optical fiber sensor. Eng Fract Mech 72(16):2505–2518
17. Dhall A, Chhabra JK, Aulakh NS (2005) Intrusion detection system based on speckle pattern analysis. Exp Tech 29(1):25–31
18. Lim JH et al (2004) Car window antitrapping optical fiber system based on a fiber speckle pattern. Opt Eng 43(5):1148–1151
19. Kulchin YN et al (2008) Correlation processing of the signals of the single-fiber intermode interferometer with a small number of excited modes. Key Eng Mater 381–382:627–630
20. Kulchin YN et al (2009) Principles of correlation processing of the speckle fields. In: Adaptive methods of processing modulated optical speckle fields, Fizmatlit, Moscow, pp 37–55 (in Russian)

Chapter 24
Biosynthesis of Quantum Dots and Their Potential Applications in Biology and Biomedicine

M.N. Borovaya, O.M. Burlaka, A.I. Yemets, and Ya.B. Blume

24.1 Introduction

Quantum dots are nanometer-sized crystals composed of semiconductors and are one of the first high technological nanomaterials to be integrated with the biological sciences. A decade after their introduction to biology, quantum dots are proven powerful probes for fluorescence imaging and are being developed for a range of additional applications including the detection of diseases, fluorescent assays for drug discovery, single-protein tracking, and intracellular reporting. Quantum dots have some distinct properties that give them their unique capabilities. First, the dots themselves are small, ranging from 4 to 12 nm in diameter. Second, they have size-tunable, narrow, Gaussian emission spectra that can be excited at a single wavelength, enabling multiplexed experiments. Third, they have enormous absorption extinction coefficients and high fluorescent quantum yields, making them exceptionally bright. Indeed, the emission of a single quantum dot can be discerned by the eye with a fluorescent microscope. There is a growing interest in using semiconductor QDs as optical labels for biosensing events [1]. Among various nanoparticles, a great interest has been shown toward cadmium sulfide (CdS) nanoparticles because of availability of discrete energy levels, size-dependent optical properties, tunable band gap, and good chemical stability [2]. CdS nanoparticles are categorized under the group chalcogenides, and they are II–IV group semiconductor nanoparticles which show size-dependent optical and electrical properties due to their high surface area to volume ratio and quantum confinement. Due to their very high photosensitivity, they have usage in the detection of visible radiations and in light-emitting diodes, solar cells, photochemical catalysis,

M.N. Borovaya (✉) • O.M. Burlaka • A.I. Yemets • Ya.B. Blume
Department of Genomics and Molecular Biotechnology, Institute of Food Biotechnology and Genomics, National Academy of Sciences of Ukraine, Osypovskogo Str., 2a, Kiev 04123, Ukraine
e-mail: marie0589@gmail.com

O. Fesenko, L. Yatsenko (eds.), *Nanoplasmonics, Nano-Optics, Nanocomposites, and Surface Studies*, Springer Proceedings in Physics 167,
DOI 10.1007/978-3-319-18543-9_24

gas sensors, various luminescence devices, optoelectronic devices, and a range of biological applications [3]. Semiconducting optoelectronic materials play an important role in a variety of application due to their unique optical, electrical, magnetic, and piezoelectric properties. Modification of these properties of semiconductor materials depends upon the size, shape, morphology, and dimensions of material.

The important issue of nanotechnology is to develop available experimental protocols for the synthesis of nanocrystals (quantum dots) of different chemical compositions and sizes using nontoxic biological systems. Mainly for the biosynthesis of quantum dots, scientists predominantly use biological sources such as viruses, bacteria, actinomycetes, fungi, and algae that can catalyze specific reactions as a part of modern and realistic biosynthetic strategies. These nanocrystals exhibit high stability in the aqueous solution and resistance to photobleaching [4–6]. However, one thing important to mention is the eventual toxic effects of heavy metals, in particular, Cd on the cell viability.

This chapter reviews the basics of QDs, methods of their synthesis, mechanisms and advantages of biosynthetic process, potential biomedical applications, limitations, and future perspectives. In particular, the possibility of utilizing the QDs as fluorescent probes for cell biology purposes, DNA transformation, bioimaging, and cancer therapy is discussed here.

24.2 Characteristics and Synthesis of QDs

24.2.1 Basic Information and Optical Properties of QDs

QDs are fluorescent semiconductor nanocrystals that predominantly have a spherical morphology, composed of a semiconductor core including group II–VI or group III–V elements encased within a shell comprised of a second semiconductor material [7]. A typical QD has a diameter ranging from 2 to 10 nm containing roughly 200–10,000 atoms. For instance, semiconductor nanocrystals include ZnS, CdS, CdSe, CdTe, or InP and InAs [8]. Mentioned nanoparticles have been shown to possess unique optical, electrical, and optoelectronic properties for a wide range of applications [8]. It should be emphasized that QDs are highly photostable, with broad absorption, narrow and symmetric emission spectra, and slowly excited-state decay rates. Their emission color depends on their size, chemical composition, and surface chemistry and can be tuned from the ultraviolet to the visible and near-infrared (NIR) wavelengths [9]. It means that relatively large QDs have red luminescence spectrum and low-intensity radiation. At the same time, smaller nanocrystals observed green and blue fluorescence with appropriate higher level of radiation intensity. The dependence of the optical characteristics on the diameter of the nanocrystals is determined by the quantum confinement effect [10].

However, it was found that the specific drawback of QDs is instability of their fluorescence in time, the so-called blinking [11]. This phenomenon is a stochastic process that is caused by the temporary transfer of QDs in a charged state. Therefore, such lack of fluorescence can last for a few seconds. Blinking can be reduced by modifying the nanocrystals (cover them by a thicker shell) or by adding mercaptoethanol or other reducing agents to the solution with QDs [11]. Also an interesting property of QDs is their ability to form conjugates with biomolecules; this feature is essential for the detection of the localization of the nucleic acids, peptides, and proteins within the living cells [12].

It is commonly known that there are several classifications of QDs depending on their chemical composition, shape, and methods of synthesis. For example, there are epitaxial and colloidal QDs [13]. Basing on the composition the semiconductor material can be identified as wide-gap semiconductors (oxides ZnO, TiO_2)—ultraviolet radiation, transitional semiconductors (cadmium chalcogenides)—visible radiation, and narrow-gap semiconductors (e.g., lead chalcogenides)—near infrared radiation [9]. The shape of nanocrystals can also affect their properties. By the shape, nanocrystals are divided into spherical particles (QDs) that have wide practical applications; ellipsoid—a class of QDs—often is used as a source of polarized radiation; they are called nanowires and nanocrystals with complex geometry [13].

The most common structure of QDs is "core–shell" which consists of CdSe core, coated with ZnS inorganic shell [12]. This inorganic shell protects the CdSe core from oxidation. The shell is composed of two monolayers of ZnS that is optimal to ensure maximum quantum yield of the nanocrystals [14]. By varying the size of CdSe core, it is possible to obtain fluorescent label with the luminescent maximum at any part of the optical spectrum; such labels can be used in studies for tagging various objects in cell biology, for optical encoding, and as donors for energy transfer systems [14].

24.2.2 Chemical Methods of Synthesis of QDs

Basically, there are two approaches for nanoparticle synthesis, namely, the bottom-up approach and the top-down approach. In the top-down approach, scientists try to formulate nanoparticles using larger ones to direct their assembly. The bottom-up approach is a process that builds toward larger and more complex systems by starting at the molecular level and maintaining precise control of molecular structure [15]. The most effective method of chemical synthesis of QDs is a high-temperature organometallic method or method of the growth in nonpolar media [16]. During synthesis, process is necessary to maintain the stability of the QDs in an aqueous solution. It can be achieved through the direct ligand exchange or by steric stabilization, when the hydrophobic surface of the crystal is covered with amphiphilic molecules or polymers [17]. Ligands (thiol-containing components) should ensure the stability of the QDs and their solubility in biological buffers and

resistance to photobleaching, and they should contain specific functional groups that can form conjugates with biomolecules [15].

It should be noted that the organometallic approach has several advantages, namely, it allows to control the growth stages of QDs and provides narrow size distribution of the synthesized nanocrystals and further isolation and purification of QDs [15]. This method of the chemical synthesis consists of three stages: nucleation, growth of the crystal nuclei, and Ostwald ripening stage [18]. In that way, luminescent CdSe QDs have been produced. CdSe nanocrystal nuclei were grown at the temperature above 300 °C by varying the time period of their growth from minutes to hours depending on the desired size of nanoparticles [18]. Apart from the size indicated, technology allows you to control the shape of nanoparticles using high anisotropy of nanocrystals and a high concentration of monomers. Given the high growth rate of the nanocrystals, they started to stretch and form nanorods, the so-called quantum rods [14]. An important condition for the production of the spherical nanocrystals is a low growth rate. More complex shapes of the nanocrystals are obtained by selecting the conditions when the crystal structure of the nuclei differs from hexagonal, thereby providing crystal growth in four different directions [19].

Another method of chemical synthesis is the synthesis of the QDs in an aqueous phase using the stabilizing agents like thioglycerin and polyphosphate [20]. It was noticed that the growth rate and the surface charge of the nanocrystals are determined by the choice of specific stabilizing agents. For example, utilizing a glutathione, the component that eliminates heavy metals in plant cells, ensured successful coating and high levels of the photoluminescence during the synthesis of CdTe nanoparticles [21]. It is important that in order to obtain QDs with the high fluorescence efficiency, it is necessary to maintain a high pH level (11.2–11.8) during the synthesis in an aqueous phase [22].

The process of the CdTe synthesis can be represented as follows: inorganic cadmium Cd $(ClO_4)_2 \cdot 6H_2O$ or $CdCl_2$ is dissolved in water with intensive stirring, and then in solution thiol stabilizing agent is added. Depending on the origin of the stabilizer, the required pH level is selected. Then, oxygen is removed from the solution. After that the gas H_2Te is passed through the solution under stirring, with a weak stream of nitrogen, either the solution of NaHTe that is free of oxygen is supplied [18]. Eventually, synthesized CdTe precursors with the use of additional treatment are converted to QDs with desired sizes [22].

Significant improvement of the CdTe characteristics was achieved during additional treatment of the initial solution by combining selective deposition of the QDs and their UV irradiation [20]. Consequently, larger QDs precipitate primarily. Using this technique, the authors successfully separated the initial solution into 10–12 fractions containing the QDs with a narrow size distribution [20]. However, it should be mentioned that the synthesis of QDs in an aqueous medium usually occurs slowly, even over several days. Although this approach was commonly used

earlier, now new methods for rapid synthesis of high-quality QDs are developing fast, including hydrothermal synthesis under high pressure or under microwave irradiation [23, 24].

Hence, indicated methods are the basic techniques for the chemical synthesis of the biocompatible QDs. Many modifications of these approaches are known. Each protocol has certain advantages and disadvantages that are important for the subsequent applications of the synthesized nanoparticles [15].

24.2.3 Physical Methods of Synthesis of QDs

Apart from the described chemical methods for QD synthesis, some common physical methods are also known. For example, one of the several methods of depositing single crystals is molecular beam epitaxy [25]. Molecular beam epitaxy takes place in high vacuum or ultrahigh vacuum (10^{-8} Pa). The most important aspect of this method is the deposition rate (typically less than 3,000 nm per hour) which allows the films to grow epitaxially. During operation, reflection high-energy electron diffraction (RHEED) is often used for monitoring the growth of the crystal layers [26]. It is important that this method is successfully applied to III–V compounds. This class of semiconductors is effectively used to create high-speed devices. At first, such compounds as GaAs, GaP, and $GaAs_x$ Sb_{1-x} were synthesized [26]. The driving force for the creation of the QDs in this case is to reduce the strain energy. If on the substrate of GaAs the layer of InAs is increased, the elastic stresses will arise leading to the growth of InAs QDs on the surface of GaAs. Thus, the surface is covered by InAs pyramids with the size of several tens of angstroms [26].

Another physical approach to grow crystals is the method vapor phase epitaxy. It is a chemical vapor deposition method used to produce single or polycrystalline thin films. It is a highly complex process for growing crystalline layers to create complex semiconductor multilayer structures. In contrast to molecular beam epitaxy, the growth of crystals is by chemical reaction and not by physical deposition. As such, this technique is preferred for the formation of devices incorporating thermodynamically metastable alloys, and it has become a major process in the manufacture of optoelectronics. Using this method, you can get not only InAs QDs on the GaAs substrate but also such QDs as InAs on InP substrate, Ge on Si substrate, and CdSe on ZnS substrate [27].

It is also an interesting fact that there is a common method for the preparation of inorganic glasses colored by the nanocrystals that belong to II–VI groups. Such method is associated with the commercial production of optical filters [26]. The growth of semiconductor nanocrystals occurs by the decay of supersaturated ions in the glass. As a result, you can get a stable solid glass with inserted nanocrystals.

The growth of the crystals in a glass matrix occurs at the temperature 550–700 °C. The disadvantages of this method include a wide range of particle sizes and the inability to influence the parameters at the glass-nanocrystal border [26].

Summing up, it should be noted that ideal biocompatible QDs should have a high size homogeneity and colloidal stability in aqueous solutions, exhibit pH stability, and have a high fluorescence quantum yield [22]. These conditions are difficult to enforce simultaneously, but extreme relevance of QDs with such properties is stimulating for further investigations.

24.3 Features of the Biological Synthesis of Semiconductor QDs

The enormous interest in the biosynthesis of nanoparticles is due to their unusual optical, chemical, photochemical, electronic, and magnetic properties [28, 29]. It is important to understand the biosynthetic mechanism involved in the fabrication of metal nanomaterials mediated by a biological system in order to gain better control of the process and products. Biosynthesis of nanoparticles is a kind of bottom-up approach where the main reaction occurring is reduction/oxidation. The microbial enzymes or the plant phytochemicals with antioxidant or reducing properties are usually responsible for reduction of metal compounds into their respective nanoparticles.

24.3.1 Biosynthesis of QDs Using Bacteria

In the recent years, great attention was focused on the synthesis of the nanocrystals containing Cd and Zn using biological systems [30]. CdS nanocrystal is one typical type of sulfide nanoparticle which has been synthesized by microorganisms [31]. It was found that *Clostridium thermoaceticum* could precipitate CdS on the cell surface as well as in the medium from $CdCl_2$ in the presence of cysteine hydrochloride in the growth medium where cysteine most probably acts as the source of sulfide [32].

Besides, for the first time it was proved that *Escherichia coli* have the capacity to synthesize intracellular cadmium sulfide (CdS) nanocrystals, when incubated with cadmium chloride and sodium sulfide [33]. The nanocrystals are composed of a wurtzite crystal phase with a size distribution of 2–5 nm (see Table 24.1). Nanocrystal biosynthesis increased about 20-fold in *E. coli* cells grown to stationary phase compared to late logarithmic phase. These results highlight how different genetic and physiological parameters can enhance the formation of nanocrystals within bacterial cells [33]. The presence of cellular nanocrystals was strongly dependent on the strain used as well as the growth phase of the cells and occurred

Table 24.1 Semiconductor QDs synthesized by microorganisms [31]

Microorganisms	Products	Size (nm)	Shape	Location	References
Rhodopseudomonas palustris	CdS	8	Cubic	Intracellular	[34]
Escherichia coli	CdS	2–5	Wurtzite crystal	Intracellular	[33]
Schizosaccharomyces pombe and *Candida glabrata*	CdS	1–2	Hexagonal lattice	Intracellular	[4]
Rhodobacter sphaeroides	ZnS	8	Hexagonal lattice	Intracellular	[37]
Desulfobacteraceae	CdS	2–5	Hexagonal lattice	Intracellular	[31]
Fusarium oxysporum	CdS	5–20	Spherical	Extracellular	[48]
Fusarium oxysporum	CdSe	10	Spherical	Extracellular	[53]

predominantly in stationary phase. Attempts were made to correlate these observations with the amount of free thiols and the amount of glutathione present in the cells. Although these parameters may contribute, no trend emerged that adequately predicted nanocrystal formation. The bottom line is that cellular thiol content may play a role but does not determine nanocrystal formation ability in different *E. coli* strains and growth phase. Understanding the genetic and physiological factors that underlie nanocrystal formation in *E. coli* may ultimately enable manipulation of microbially derived nanocrystal production. For example, inorganic synthesis employs different ratios of multiple capping agents in order to synthesize nanocrystals of various shapes, such as rods or stars. By controlling the synthesis and relative amounts of small thiols, polyphosphates, and fatty acids in *E. coli*, it may someday be possible to control the crystallinity, shape, size distribution, and optical properties of nanocrystals in unprecedented ways [33].

It is worth noting that in the paper [5] authors confirmed the effectiveness of using culture supernatants of *E. coli* for successful biosynthesis of cadmium sulfide nanoparticles. It was shown that their maximum luminescence peak was at 443 nm, which is typical for cadmium sulfide nanoparticles synthesized using microorganisms. The stability of obtained QDs was investigated for the first time by spectral analysis. It was established that nanoparticles were aggregated; however, they retained the ability to luminescence for 10 days, 1 month, and 3 months after a sample preparation. By transmission electron microscopy, it was demonstrated that QDs are approximate to a spherical shape, do not have surface defects, and have a diameter from 2 to 6 nm [5].

Hence, *E. coli* represents a simple yet powerful prokaryotic genetic system with the potential to elucidate the key features of nanocrystal synthesis in living cells. By understanding parameters of nanocrystal synthesis in microbes, it might be possible to modulate the properties of biosynthesized nanocrystals, such as size, shape, and crystal structure [33].

A simple route for the synthesis of cadmium sulfide nanoparticles by photosynthetic bacteria *Rhodopseudomonas palustris* has been demonstrated in another study [34]. The cadmium sulfate solution incubated with *R. palustris* biomass changed to a yellow color from 48 h onward, indicating the formation of CdS nanoparticles. The purified solution yielded the maximum absorbance peak at 425 nm due to CdS particles in the quantum size regime. Also, X-ray analysis of the purified nanoparticles confirmed the formation of cadmium sulfide. Transmission electron microscopic analysis of the samples showed a uniform distribution of nanoparticles, having an average size of 8.01 ± 0.25 nm (see Table 24.1), and its corresponding electron diffraction pattern confirmed the face-centered cubic crystalline structure of cadmium sulfide [34].

Furthermore, it was observed that the cysteine desulfhydrase (C-S lyase) could control crystal growth, because cysteine-rich proteins can produce S^{2-} through the action of C-S lyase. It was suggested that the content of C-S lyase in *R. palustris* might be responsible for nanocrystal formation. CdS nanoparticles were not synthesized in the growth media alone in the absence of bacteria. The result is consistent with the fact that the C-S lyase is an intracellular enzyme and is located in the cytoplasm. Large amounts of CdS nanoparticles are present in the solution after S^{2-} production, indicating that *R. palustris* was able to efficiently transport CdS nanoparticles out of the cells. This conclusion is supported by the results of ultracentrifugation. This technology thus has important advantages over other biosynthetic methods [34].

Besides, nanoparticles of the semiconductor, zinc sulfide (ZnS), are the most attractive materials for applications in areas such as infrared optical devices and fast optical switching devices. ZnS nanoparticles can be prepared by different methods, such as colloidal aqueous and micellar solution synthesis [35]. It is necessary to obtain materials under simple and clean conditions. When ZnS nanoparticles are used as biological probes for medical purpose, the synthesis of zinc sulfide is expected to be clean [36].

Therefore, a novel, clean biological transformation reaction by immobilized *Rhodobacter sphaeroides* has been developed for the synthesis of ZnS nanoparticles with an average diameter of 8 nm (see Table 24.1). This average diameter of ZnS nanoparticles was found to be dependent on the culture time [37]. The nanoparticles were examined by X-ray diffraction, transmission electron microscopy, energy-dispersive analyses of X-rays, UV–Vis optical absorption, and photoluminescence spectra. The emission peaks at 335, 353, 376, and 450 nm each correspond to the samples obtained at 25, 30, and 35 h. These luminescence spectra show size-dependent quantum confinement effects [37].

In the biological synthetic process for ZnS nanoparticles, soluble sulfate acts as the source of sulfur. The formation mechanism of ZnS nanoparticles by biological transformation reaction of *R. sphaeroides* can be explained as follows. First, soluble sulfate enters into immobilized beads via diffusion and later is carried to the interior membrane of *R. sphaeroides* cell facilitated by sulfate permease. Then, the sulfate is reduced to sulfite by ATP sulfurylase and phosphoadenosine phosphosulfate reductase, and next sulfite is reduced to sulfide by sulfite reductase. The sulfide

reacts with *O*-acetylserine to synthesize cysteine via *O*-acetylserine thiolyase [38], and then cysteine produces S^{2-} by a cysteine desulfhydrase in the presence of zinc. Finally, ZnS nanoparticles are discharged from immobilized cells to the solution. Thus, it is expected that the high-grade ZnS will be useful as biological probe in medical testing [37].

24.3.2 Biosynthesis of QDs Using Yeasts

In early studies [4], scientists have used *Saccharomyces pombe* and *Candida glabrata* (yeasts) to produce intracellular CdS nanoparticles with cadmium salt solution (see Table 24.1). Short chelating peptides of general structure $(\gamma\text{-Glu/Cys})_n$-Gly control the nucleation and growth of CdS crystallites to peptide-capped intracellular particles of diameter 20 Å. The optical band gap of synthetic CdS crystallites increases with decreasing diameter of the particles. These CdS QDs were more monodisperse than CdS particles synthesized chemically. Moreover, such CdS nanoparticles had a luminescent peak at 460 nm and were stable at a physiological pH level [4].

In addition, a simple and efficient biosynthesis method to prepare easily harvested biocompatible cadmium telluride (CdTe) QDs with tunable fluorescence emission using yeast cells was suggested [39]. The CdTe QDs were synthesized by an extracellular growth approach by incubating cheap inorganic salts $CdCl_2$ and $NaTeO_3$ with yeast cells in a modified Czapek's medium at mild temperatures (25–35 °C). After incubation for 1 day, the CdTe QDs show an intense narrow absorption at ~440 nm from the first electronic transition and a strong emission centered at 492 nm with a narrow full width at half maximum (about 40 nm) in the PL spectra, indicating that the QDs have a narrow size distribution [39]. The morphology and crystallinity of the biosynthesized CdTe QDs were analyzed by TEM and XRD. TEM images reveal that the biosynthesized CdTe QDs incubated for 8 days at 35 °C are well-dispersed particles with a uniform diameter of ~3.6 nm. The biosynthesized CdTe QDs show intense fluorescence, and varying the particle size allows the emission to be tuned over the range from 490 to 560 nm. The protein-capped CdTe QDs show excellent biocompatibility and are well dispersed in the cells, and in situ bioimaging of the yeast cells is easily achieved [39].

24.3.3 Biosynthesis of QDs Using Earthworms

The earthworm *Lumbricus rubellus* can accumulate cadmium to levels in excess of one-thousandth of its total dry bodyweight [40]. This is achieved using an isolation strategy that relies on metallothioneins—a family of cysteine-rich proteins—to transport heavy metals to the chloragogenous tissues (cells that resemble the liver

in vertebrates) where toxins are neutralized [41, 42]. Although the cadmium detoxification system in earthworms is well established, little is known regarding the uptake, trafficking, and storage dynamics of tellurium. Authors suggested that the tellurite was reduced by glutathione reductase, reduced nicotinamide adenine dinucleotide phosphate (NADPH) and glutathione (GSH) via the GS–Te–SG complex, to H_2Te, a common Te precursor, and thus able to react with the available Cd^{2+} [42].

Earthworms exposed for 11 days to standard soil spiked with $CdCl_2$ and Na_2TeO_3 were shown to transport the precursors, via metallated metallothionein complexes, to the chloragogenous tissue located at the coelomic surfaces of the worm gut, where they reacted to form QDs before isolation. The particles demonstrated an absorption band edge of 450 nm with a slight excitonic feature at 360 nm, consistent with CdTe QDs. The observed green emission from the QDs was determined to be near the band edge, with Stokes shifted emission maxima at 520 nm and a second weaker component at 460 nm from residual autofluorescence [42]. High-resolution electron microscopy analyses confirmed the presence of crystalline nanoparticles with an average diameter of 2.33 + 0.59 nm (100 particles measured) and clear lattice fringes, while selective area electron diffraction (SAED) demonstrated diffuse rings consistent with CdTe nanoparticles. The resultant particles were easy to harvest, demonstrated optical characteristics typical of quantum-confined semiconductor materials, and were utilized for relevant cell imaging applications. These particles are comparable to thiol-capped CdTe prepared by typical benchtop methods, and, if extended to other technically important semiconducting materials, this method promises to be a convenient source of biologically compatible luminescent probes [42].

24.3.4 Biosynthesis of QDs Using Diatoms

A widespread detoxification mechanism developed by plants, algae, and fungi to avoid heavy metal poisoning involves intracellular sequestration of metal ions by means of glutathione-related peptides. These inducible peptides, named phytochelatins, are synthesized by the enzyme PC synthase, which is activated by the metal ions and uses glutathione as substrate. The structure of PC involves a repeating sequence of γ-glutamyl/cysteine pairs to give polypeptides of general formula $(\gamma\text{-Glu/Cys})_n\text{-Gly}$, with n values commonly ranging from 2 to 6. They bind metal ions such as Cd, Pb, Zn, and Cu [43] yielding stable metal/PC complexes, which effectively reduce the intracellular concentration of free metal ions. Most of the literature on phytochelatin synthesis in phytoplanktonic algae in response to Cd regards the induction of these chelating peptides [44], but only few papers deal with the characterization of the complexes formed with this metal ion [45].

The marine diatom *Phaeodactylum tricornutum* is able to incorporate Cd-induced sulfide ions in Cd/phytochelatin complexes, thus forming nanometer-sized

phytochelatin-coated CdS nanocrystallites. This process of biomineralization enhances the Cd-binding stoichiometry of the complexes [46].

P. tricornutum exposed to Cd forms Cd/phytochelatin complexes in which sulfide ions (S^{2+}) can be incorporated to stabilize phytochelatin-coated CdS nanocrystallites [46]. Native CdS particles exhibited differences in their particle size, sulfide content, and optical spectroscopic properties. The l_{max} of the UV transition ranged from 290 to 260 nm. Characterization of these complexes showed that CdS nanoparticles were mainly coated with γ-glutamyl peptides with n value from 3 to 5. The phytochelatin 2 oligopeptide was not found as a coating peptide. CdS particles were stable in the pH range from 8 to 6 and showed half-dissociation at pH 4.9. Native phytochelatin-coated CdS crystallites from *P. tricornutum* exhibit heterogeneity in the particle size. By using the reported relationship between l_{max} and the radius of nanocrystallites [47], the radii of phytochelatin-coated CdS nanocrystallites synthesized by this microalga were predicted to vary from 9 to 11 Å. The earliest eluting fractions produced optical spectra characterized by the lowest energy of the electronic transition and exhibited the highest sulfide/Cd ratio. The smallest-sized CdS particles, with low sulfide/Cd ratio, showed propensity to sulfide-mediated accretion in vitro. Thus, difference in size is due to different sulfide content, and a spectrum of complexes differing in their sulfide/Cd ratio exists in cells of *P. tricornutum* after exposure to Cd during their growth cycle [46]. The formation of phytochelatin-coated CdS crystallites in *P. tricornutum* could explain the low sensitivity to Cd of this alga, as compared with other marine diatoms.

24.3.5 Biosynthesis of QDs Using Fungi

While enzymatic processes in sulfate-reducing bacteria are relatively well understood and identified [48], the intracellular synthesis of CdS in yeast occurs by a process involving sequestering of the Cd^2 ions by glutathione-related peptides and a consequent production of CdS within the yeast cells [4]. Also it has been discovered that eukaryotic organisms such as fungi may be used to synthesize CdS and some other metal sulfide nanoparticles extracellularly by a purely enzymatic process [48]. The use of specific enzymes such as reductases secreted by fungi opens up the exciting possibility of designing a rational biosynthesis strategy for nanomaterials of different chemical compositions [48].

More specifically, *Fusarium oxysporum*, when exposed to aqueous Cd^{2+} and SO_4^{2+} ions, leads to the formation of extremely stable CdS nanoparticles in solution (see Table 24.1). The reaction solution with $CdSO_4$ at the beginning was colorless. The bright yellow color of the solution after reaction between inorganic components and the *Fusarium oxysporum* biomass indicates the presence of CdS nanoparticles in solution [48]. UV–visible spectra recorded from the *Fusarium oxysporum* $CdSO_4$ solution at different time intervals (in days) exhibit the

appearance of a weak absorption edge, which progressively increases in intensity as the reaction progresses. The presence of the absorption edge at 450 nm is characteristic of CdS particles in the quantum size regime [49]. The colloidal solution of CdS nanoparticles was extremely stable in time with no evidence for aggregation even after 1 month of storage [48]. The presence of an absorption at 280 nm attests to the presence of proteins in the reaction medium [50]. Authors believed that the long-term stability of the CdS nanoparticle solution is due to the presence of the proteins in the nanoparticle solution that bind to the surface of the nanoparticles and prevent aggregation [48].

The formation of extracellular CdS nanoparticles by enzymatic reduction of sulfate ions by *Fusarium oxysporum* was extended to the formation of PbS, ZnS, and MoS_2 nanoparticles starting with appropriate sulfate-containing salts. Preliminary investigations indicate that it is indeed possible to realize such chemical compositions by fungus-based extracellular biotransformations [48].

Another important potential benefit of the process described herein is the fact that the semiconductor nanoparticles, which are quite stable in solution, are synthesized extracellularly, and this is thus a very important advantage over other biosynthetic methods where the nanoparticles are entrapped within the cell matrix [51]. The extracellular synthesis of semiconductor nanoparticles makes it possible to harness and immobilize/deposit such nanoparticles onto desired solid surfaces for different practical purposes [48].

Moreover, in the paper [52] which is the first report on the successful biosynthesis of CdS QDs, authors used the mycelium of the basidiomycete fungus *Pleurotus ostreatus* during culturing with salts $CdSO_4$ and Na_2S. Using the spectral analysis of formed particles, it was established that the absorption peaks which were obtained are typical for CdS nanoparticles. They were at the range 440–524 nm. By the method of transmission electron microscopy, it was demonstrated that obtained QDs form dense clusters with a diameter from 40 to 70 nm. The size of individual nanoparticles within these clusters is from 5 to 8 nm [52]. Thus, the fungus *P. ostreatus* was found to be an effective biological capacity for nanotechnological transformations [52].

In addition, CdSe semiconductor nanocrystals are very promising luminescent probes. These crystalline clusters of semiconductors, also known as QDs, have a size of 1–10 nm and exhibit unique optical properties that arise due to their quantum confinement effect [53]. For the synthesis of highly luminescent CdSe QDs at room temperature, the fungus *Fusarium oxysporum* was incubated with a mixture of $CdCl_2$ and $SeCl_4$ salts [53]. The strong surface plasmon resonance centered at 370 nm is clearly visible indicating the formation of CdSe nanoparticles. Absorption band at 270–280 nm is also visible which is contributed by proteins present in the extracellular broth [54], suggesting a possible reducing enzyme-based process for the synthesis of CdSe nanoparticles. The solution was extremely stable, with no evidence of flocculation of the particles even a month after reaction. Luminescence characteristics were studied by fluorescence measurement of the CdSe nanoparticles by exciting the reaction mixture at 370 nm. An emission band centered at 440 nm [53].

24.3.6 Biosynthesis of QDs Using Plants

Employing plants toward synthesis of nanoparticles is emerging as advantageous compared to microbes with the presence of broad variability of biomolecules in plants that can act as capping and reducing agents and thus increases the rate of reduction and stabilization of nanoparticles [55].

In particular, researchers have reported a novel, eco-friendly route for rapid synthesis of ZnS nanoparticles by using 0.3 % latex solution prepared from *Jatropha curcas* L. [56]. It is interesting that *Jatropha* latex has some ethnomedical uses like wound healing and blood coagulation activities [57]. Particularly, the use of latex, proteins, and phytochemicals for the synthesis of metal nanoparticles has dual advantage that they not only act as a reducing agent but also act as a capping agent and deter the particle aggregation. Latex of *J. curcas* L. constitutes two cyclic peptides, curcacycline A (an octapeptide) and curcacycline B (a nonapeptide), and curcain (an enzyme) as possible reducing and stabilizing agents [56]. The average size of ZnS nanoparticles was found to be 10 nm. Latex of *J. curcas* L. itself acts as a source of sulfide (S^{-2}) ions that are donated to Zn ions under present experimental conditions. Source of sulfide (S^{-2}) ions is still unclear, but authors speculate that cysteine or thiol residues present in enzyme curcain may be donating these sulfide (S^{-2}) ions. It was found that 0.3 % latex solution prepared from *J. curcas* L. latex and 2.5 mM aqueous solution of zinc acetate were optimum to get maximum yield of ZnS nanoparticles [56].

But nowadays there is a little information about biosynthesis of semiconductor CdS QDs with plants. For instance, a novel approach to the biosynthesis of cadmium sulfide QDs using hairy root culture of flowering plant *Linaria maroccana* L. was suggested recently. By the method of transmission electron microscopy, it was revealed that obtained QDs have spherical shape and size in the range of 2–8 nm. Optical measurements showed clear absorption peaks at 362, 398, and 464 nm, whereas luminescent peaks corresponded to 425, 462, and 500 nm [58].

24.3.7 Advantages of the "Green" Synthesis of Nanoparticles

Summing up, "green" synthesis of nanomaterials is low-cost, eco-friendly, rapid, and nontoxic for medical applications. But, on the other hand, some studies have been carried out to evaluate the possible toxicity of these nanoparticles [59]. The toxicity of QDs is associated with their physicochemical properties. Due to the large diversity of semiconductor nanoparticles (CdTe, CdSe, CdS, CdS/Zn, PbSe, PbTe, and others) and different capping techniques (MAA, zinc sulfide, MAS) employed, it is not possible to elucidate all the toxicity mechanisms. Several attempts have been made to reduce toxic effects of nanoparticles by selecting the capping of the nanoparticles, using minimal concentrations, and modulating the

nanoparticle size [59, 60]. All these factors are important for cell toxicity response and consequently to the use of QDs as fluorescent marker.

The major QD toxicity is related to the induction of reactive oxygen species (ROS) formation or the direct release of metal ions (e.g., Cd^{2+}). In most cells, these reactions can cause cellular changes culminating in DNA damage. However, some biological questions remain open and need to be answered in order to optimize the use of QDs in the target cells [59].

24.4 Applications of Semiconductor QDs in Cell Biology, Biotechnology, and Biomedicine: Current Perspectives and Limitations

24.4.1 CdSe/ZnS QDs as Fluorescent Probes for Cytoskeleton Imaging

QDs have attracted enormous interest as labels for bioimaging because of their increased fluorescence intensity and bleaching resistance [9, 12]. A reliable and promising strategy for QD-mediated labeling of molecules and cell structures is based on the direct fluorescence detection. For instance, when QDs which are associated with streptavidin, are bound to the target molecules. For example, in [61], the observation of self-assembly process of tubulin molecules in microtubules was reported. QDs covered with inert silica shells were conjugated to tubulin. This resulted in good visualization of assembly process. QD-labeled antibodies were used then for direct immunofluorescence following the dynamic reorganization of microtubules during the cell cycle [61]. In this study, two strategies, through a biological surface (bovine serum albumin (BSA)) and through an inorganic surface (silica), were used to couple CdSe/ZnS QDs to monoclonal antibodies against tubulin. Both types of QD-based conjugates were used then for labeling microtubules in cells of tobacco cell line BY-2 (*Nicotiana tabacum* L. cv. Bright Yellow 2). Nanocrystals covered with BSA and conjugated to antitubulin antibodies were used to obtain the discontinuous signal from nanoparticles associated with microtubules [61]. To obtain a continuous microtubule signal, silica-shelled nanocrystals conjugated with antitubulin antibodies were used for imaging [62]. In premitotic interphase cells, the QD-based antitubulin conjugates visualized punctate signals in the cell periphery. During the prophase, when the DNA is condensed into chromosomes, nanocrystals were found to surround the forming spindle. Later on in metaphase, the nanocrystal signal was then attached to the chromosomes spread in the equatorial cell plane and redistributed to the newly reestablished nuclear envelopes of the daughter nuclei and at the newly forming cross wall in the final telophase. Thus, the localization, general appearance, and orientation of nanocrystal–antibody conjugate signals inside cells corresponded to microtubular redistributions during the cell cycle.

24.4.2 QDs as Labels for the Investigation of Intracellular Molecules

Understanding of the signal transmission mechanisms and sensitivity of cell compounds to the changes in extracellular environment is one of the most important problems in cell biology [63]. Most of these processes are mediated by the binding of extracellular ligands, such as growth factors, lipoproteins, and transferrins, to membrane-bound receptors at the plasma membrane. Subsequently, the receptor–ligand complexes are endocytosed and delivered to endosomal compartments [64]. The development of new QD-based bioimaging techniques is essential for improved understanding of the regulation of receptor-mediated endocytic pathways in cells and tissues [63].

Because of their brightness and photostability, QDs have been used to track many receptor-mediated endocytic trafficking events in living cells using fluorescence microscopy [17]. Labeled conjugates enter cells via endocytosis pathway or through the attachment to the cell membrane surface proteins [63]. For example, QDs conjugated to epidermal growth factor (EGF) molecules have been used to track the dimerization of the EGF receptor and its ability to elicit downstream signal transduction events [65]. QD–EFG conjugates were also used for the detection of early stages of tyrosine kinase-dependent signal pathway in cells [66]. This study revealed high specificity and high capacity of QDs to bind to and activate the EGF receptor erbB1. The investigation of this binding process is thought to be helpful for the understanding of intracellular retrograde transport mechanism. QDs conjugated to nerve growth factor (NGF) have been used to visualize the real-time endocytic behavior of NGF receptors at a nanoscale resolution [67]. Importantly, QDs are very effective for the long-term labeling of endosomes without significant negative effects [63]. Biotinylated α-bungarotoxin was bound to streptavidin-conjugated QDs to characterize the assembly dynamics of acetylcholine receptor clusters in the postsynaptic membrane [68]. Thus, QDs are promising tracking molecules for the investigation of membrane receptor surface dynamics [63].

In studies on living cells, QDs are used for nonspecific cell labeling as well as for targeted labeling of individual cell structures (membrane-binding proteins, for example) [9]. Experimental data show that QDs targeted to bind intracellular transport proteins are efficient for tracking molecules in cells of human bone marrow and embryonic blood [69]. It was shown that cells are labeled effectively by QDs during proliferation, and QD-derived signals are detectable after many cell division cycles [69]. Another study revealed that QD-RGD peptide (tripeptide composed of L-arginine, glycine, and L-aspartic acid) conjugates are useful for labeling of mesenchymal human stem cells during their differentiation into osteoblasts, chondrocytes, and adipocytes, without causing any detectable negative effects on normal cell function [70].

Another important field for QD exploitation is the detection of specific proteins and protein activity studies. QD-based labeling technology is viewed to be effective and suitable for investigation of protein in vivo dynamics, especially for

neurophysiology. Thus, specially designed QDs were used to study the presence and mobility of nicotine receptors in living tissues [71]. It is also possible to study translocation and redistributions of QD-labeled proteins in cells using luminescence microscopy [72]. In the study [73] QDs demonstrated the ability to bind amyloid protein and synuclein. It can be useful for the development of QD-based strategies for the detection of amyloid aggregates inside cells—an important issue for the diagnosis of neurodegenerative diseases.

24.4.3 QDs for the Fluorescent In Situ Hybridization

It should be underlined that QDs are thought to be suitable and promising biodetectors for cell biology. In particular, QDs can be designed for the DNA sensing. QDs demonstrated high imaging capacity in the luminescence microscopic studies of location and orientation of individual native DNA molecules inside the cells [74]. Besides, QDs can be exploited for the detection of mutations in DNA. In the study [75], the method for detecting DNA spot mutations based on CdS QD-mediated probing is reported. DNA methylation is also investigated using QDs during the PCR reaction [76].

As it was mentioned above, QDs can be efficiently designed for the DNA molecule detection [74, 75]. First, successful exploitation of QDs for fluorescence in situ hybridization (FISH) analysis was reported in [77]. The detailed hybridization protocol for the DNA analysis using comparatively short probes (150–600 nucleotides) tagged with digoxigenin was developed [78]. QDs with maximum emission in 655 nm wavelength were conjugated with antibodies targeted against digoxigenin and then used for detection. This method is viewed to be suitable for chromosome analysis and histological section examination. However, it is suitable for the only one DNA locus identification per one analysis [78].

Since QDs possess improved temperature stability in comparison with organic fluorochromes, they can easily undergo high hybridization temperature for the telomere labeling [79]. The vast majority of fluorochromes are damaged and lose their fluorescence after this procedure. In a study reported in [79], QD-based conjugates with luminescence emission maximums at 605, 655, and 705 nm wavelengths were used for labeling. Results obtained with the use of QDs were similar to results of conventional FISH and Southern blot analyses. Advantage of QD use in this case appears to be due to the possibility of combining immunophenotyping and telomere length definition analyses [79].

However, it is important to take into account the fact that an effective probe to nucleic acid binding depends on the presence of appropriate mediating molecules between the QD surface and hybridizing DNA sequence [80]. Besides, fluorescent hybridization using QDs has its limitations, in particular high noise and irregularity of staining when probes are used for the analysis of the whole of chromosome [81].

It should be underlined that QDs can be used for the detection of individual genes through the hybridization with short (100 times shorter than conventional) DNA probes due to the high intensity of QD signal [78]. QD–streptavidin-based probes are already designed for the detection of mRNA in tissue sections [80, 82].

24.4.4 QDs for Plant Genetic Transformation

It has been found that when certain DNA-coated nanoparticles are incubated with cells not having a cell wall, the cells take up the nanoparticles and begin expressing genes encoded on the DNA. Semiconductor nanoparticles (QDs) within the size range of 3–5 nm have also been used as carriers to deliver molecules into cells [83].

Delivery of foreign nucleic acid molecules to plants is challenging due to the presence of plant cell walls. Current methods rely on invasive delivery for genetic transformation of plants. In plant cells, the cell wall is a barrier against the delivery of exogenously applied molecules [83]. Many invasive cell delivery methods, for example, biolistic delivery (gene gun), microinjection, electroporation, and *Agrobacterium*-mediated transformation, have been employed to achieve gene and small molecule delivery into walled plant cells, but delivery of proteins has only been achieved by microinjection. Where nanoparticle delivery of nucleic acid molecules to plant cells is desired, the cell wall is removed before the addition of the particles to protoplasts of the plant. In some embodiments, the distinctive properties of linear nucleic acid molecules allow the delivery of specific gene sequences of interest without extraneous nucleic acid sequences that may have regulatory consequences for a transgenic target organism. In some embodiments, nanoparticles may be PEGylated with linear nucleic acid molecules. In particular embodiments, the nanoparticles may be semiconductor nanoparticles, such as QDs [83].

Authors of this patent have disclosed also methods for introducing a molecule of interest into a plant cell having a cell wall [83]. The methods may comprise providing the plant cell having a cell wall, coating the surface of nanoparticles with PEG to produce PEGylated nanoparticles, coating the PEGylated nanoparticles with at least one linear nucleic acid molecule of interest, placing the plant cell having a cell wall and the PEGylated nanoparticles coated with the linear nucleic acid molecule(s) of interest in contact with each other, and allowing uptake of the nanoparticle and the linear nucleic acid molecules of interest into the cell comprising a cell wall.

Further, these approaches open efficient ways for introgressing a trait into a plant. In some cases, the method may comprise providing a plant cell, coating the surface of nanoparticles with PEG to produce PEGylated nanoparticles, coating the PEGylated nanoparticles with a means for expressing the trait in the plant, placing the plant cell and the PEGylated nanoparticles coated with a means for expressing

the trait in the plant in contact with each other, allowing uptake of the nanoparticle and the means for expressing the trait in the plant into the plant cell to produce a transformed plant cell, regenerating a whole plant from the transformed plant cell, and propagating the plant.

Further, authors disclosed also the methods for generating stable plant lines comprising a desired trait or nucleic acid molecule of interest, wherein the desired trait or nucleic acid molecule of interest may be first introduced by uptake of a nanoparticle across a plant cell wall. Methods of generating stabilized plant lines are well known to biotechnologists and may include techniques such as selfing, backcrossing, hybrid production, and crosses to populations [83]. Finally, authors propose that plant cells comprising a desired trait or nucleic acid molecule of interest first introduced into the plant or cell (or its predecessors) by uptake of a nanoparticle across a cell wall can be used in crosses with other different plant cells to produce first-generation (F1) hybrid cells, seeds, or plants with desired characteristics [83].

24.4.5 QDs for Cancer Diagnosis: Bioimaging Applications

It is known that early cancer diagnosis is critical for successful treatment. Due to shortcomings of existing clinical diagnosis methods, new advanced solutions remain the issue of primary interest in this field. Semiconductor nanocrystals ZnS, CdS, ZnSe, CdSe, and CdTe and CdTe/CdS and CdS/ZnS structures possess high surface area, suitable for the attachment of functional groups responsible for binding to antibodies [84]. They are viewed to be suitable for the design of nanodevices for the cancer early diagnosis and therapy. Semiconductor nanoparticles demonstrate great efficiency when used as contrasting agents for the magnetic resonance imaging or fluorescent labels for the fluorescence tomography [85].

The critical stage for tumor growth and development is the vascularization or angiogenesis process. Its mechanisms are driven by signaling proteins—Basic fibroblast growth factor (FGFβ) and vascular endothelial growth factor (VEGF) produced by tumor cells. Thus, detection of FGFβ and VEGF using fluorescent tags can pose the basic step for early diagnosis of tumor [85]. Besides, in [85], the design of fluorescent nanoparticles with conjugated antibodies targeted against intercellular adhesion proteins E-cadherin, N-cadherin, vimentin, and factor 1-alpha is reported. In this work, two phenotypes of prostate tumor cells $ARCaP_E$ and $ARCaP_M$ were studied. Cells were stained with nanoparticle–antibody conjugates allowing the luminescence microscopic detection of tag distribution and their quantitative ratio evaluation [84]. Also, androgen receptors CD10, Ki-67, and p27, as well as insulin-like growth factor 1 receptor and MTA1 (metastasis-associated protein) receptor, are thought to be suitable specific markers for the development of QD-based approaches for the early diagnosis of prostate cancer [86].

Carbohydrate antigen 125 (CA 125) is an epithelial antigen and a useful tumor marker in the detection and therapy of ovarian cancer [87]. In [88], using QDs with maximum emission wavelength 605 nm to detect CA 125 in ovarian cancer specimens of different types (fixed cells, tissue sections, and tumor xenografts) with high specificity and sensitivity is reported. Several studies on the detection of human epidermal growth factor receptor (HER 2) for breast cancer diagnosis with QDs have been completed [89]. HER 2 on breast cancer cell membrane is found to be overexpressed in approximately 25–30 % breast cancer and plays an important role in breast cancer prognosis and treatment selection. CdSe/CdS/ZnS QDs with improved photoluminescence efficiency and stability were used as optical agent for imaging pancreatic cancer cells using transferrin and anti-claudin-4 [90]. Pancreatic cancer-specific uptake is also demonstrated using the monoclonal antibody anti-claudin-4. The mean survival of pancreatic cancer is around 6 months due to the fact that most patients are diagnosed at advanced stage, due to the lack of specific symptoms and limitations in diagnostics. QDs can target the purpose of early diagnosis of pancreatic cancer, even at an early stage of development, with the help of proteins/peptides directed against overexpressed surface receptors on the cancer cells/tissues such as the transferring receptor, the antigen claudin-4, etc. [7].

Intravital tumor imaging techniques rely on the accumulation of fluorescent substances (fluorophores) inside pathological cells [85]. Fluorescence of nanoparticles is more detectable and easy to distinguish from the autofluorescence of natural compounds occurring in tissues [91]. Sensitivity of photographical method allows imaging of tumors containing at least 10–100 pathological cells [91]. However, one of its main drawbacks is the difficulty of tumor deeper layer imaging. It is caused by low penetrating power of used UV irradiation and visible light for fluorescence excitation in biological tissues [83]. To overcome these limitations, efforts are implemented to develop fluorescent probes that are able to accumulate selectively in pathological tissues and having maximum fluorescence emission wavelengths in NIR range. Semiconductor nanocrystals having emission maximum within 700–800 nm wavelength range with high quantum yield of fluorescence are shown to be the most perspective materials for tumor imaging [85]. Radiation in wavelength range of 650–950 nm is able to penetrate deep inside biological tissue; therefore, it can be efficiently exploited for the intravital tumor imaging using florescent tomography techniques [92].

24.5 Conclusions

Due to their unique optical and chemical properties, QDs have significant advantages over organic fluorophores, which allows them to be used as fluorescent labels for a wide range of biological applications. At present, mechanisms of biological synthesis of QDs are extensively studied and still remain unclear. Conventionally, biological synthesis is divided into intracellular and extracellular, according to the location of the nanoparticles.

One of the major challenges of modern nanobiotechnology is the development of hypersensitive methods for rapid detection of proteins, genes, and cells, because application of semiconductor nanocrystals can provide higher sensitivity of many biological parameters. The use of nanocrystals can be the basis for new nondestructive imaging techniques for intracellular visualization of individual proteins, nucleic acids, or tracking molecules that allow to detect them, as well as to track their evolution and interaction in real time. The ability to determine a large number of biological parameters with sensitivity at the level of single molecules is necessary for the precise diagnosis and the development of new effective drugs.

Future prospects of QDs are associated with the development of new generations of particles that have small monodisperse dimensions with different optical characteristics. This is especially important for nanoparticles with long-wave infrared spectrum, because their large size has complicated their employment for intracellular labeling.

References

1. Rosenthal SJ, Chang JC, Kovtun O, McBride JR, Tomlinson ID (2011) Biocompatible quantum dots for biological applications. Chem Biol 18(1):10–24
2. Antolini F, Pentimalli M, Di Luccio T, Terzi R, Schioppa M, Re M, Tapfer L (2005) Structural characterization of CdS nanoparticles grown in polystyrene matrix by thermolytic synthesis. Mater Lett 59(24):3181–3187
3. Chen CC, Herhold AB, Johnson CS, Alivisatos AP (1997) Size dependence of structural metastability in semiconductor nanocrystals. Science 276:398–401
4. Dameron CT, Reese RN, Mehra RK (1989) Biosynthesis of cadmium sulphide quantum semiconductor crystallites. Nature 338(13):596–597
5. Borovaya MN, Naumenko AP, Yemets AI, Blume YB (2014) Stability of the CdS quantum dots, synthesized by the bacteria *Escherichia coli*. Proc Natl Acad Sci Ukraine 7:145–151 (In Ukranian)
6. Sastry M, Ahmad AM, Khan I, Kumar R (2003) Biosynthesis of metal nanoparticles using fungi and actinomycete. Curr Sci 85(2):162–170
7. Peng C-W, Li Y (2010) Application of quantum dots-based biotechnology in cancer diagnosis: current status and future perspectives. J Nanomater 2010:1–11
8. Singh S, Bozhilov K, Mulchandani A, Myung N, Chen W (2010) Biologically programmed synthesis of core-shell CdSe/ZnS nanocrystals. Chem Commun 46:1473–1475
9. Michalet X, Pinaud FF, Bentolila LA (2005) Quantum dots for live cells, in vivo imaging, and diagnostics. Science 307(5709):538–544
10. Rizvi SB, Ghaderi S, Keshtgar M, Seifalian AM (2010) Semiconductor quantum dots as fluorescent probes for in vitro and in vivo bio-molecular and cellular imaging. Nano Rev 1:1–15
11. Nirmal M, Dabbousi BO, Bawendi MG, Macklin JJ, Trautman JK, Harris TD, Brus LE (1996) Fluorescence intermittency in single cadmium selenide nanocrystals. Nature 383:802–804
12. Li J, Wu D, Miao Z, Zhang Y (2010) Preparation of quantum dot bioconjugates and their applications in bio-imaging. Curr Pharm Biotechnol 11:662–671
13. Drbohlavova J, Adam V, Kizek R, Hubalek J (2009) Quantum dots—characterization, preparation and usage in biological systems. Int J Mol Sci 10:656–673

14. Ghaderi S (2012) Development of fluorescent nanoparticles 'quantum dots' for biomedical application. UCL Center for Nanotechnology and Regenerative Medicine Division of Surgery & Interventional Sciences University College, London
15. Zhang Y, Clapp A (2011) Overview of stabilizing ligands for biocompatible quantum dot nanocrystals. Sensors 11:11036–11055
16. Murray CB, Norris DJ, Bawendi MG (1993) Synthesis and characterization of nearly monodisperse CdE (E=S, Se, Te) semiconductor nanocrystallites. J Am Chem Soc 115:8706–8715
17. Resch-Genger U, Grabolle M, Cavaliere-Jaricot S, Nitschke R, Nann T (2008) Quantum dots versus organic dyes as fluorescent labels. Nat Methods 5:763–775
18. Peng XG, Wickham J, Alivisatos AP (1998) Kinetics of II-VI and III-V colloidal semiconductor nanocrystal growth: "focusing" of size distributions. J Am Chem Soc 120:5343–5344
19. Ko WYL, Bagaria HG, Asokan S, Lin K-J, Wong MS (2010) CdSe tetrapod synthesis using cetyltrimethylammonium bromide and heat transfer fluids. J Mater Chem 20:2474–2478
20. Gaponik N, Talapin DV, Rogach AL, Hoppe K, Shevchenko EV, Kornowski A, Eychmüller A, Weller H (2002) Thiol-capping of CdTe nanocrystals: an alternative to organometallic synthetic routes. J Phys Chem 106:7177–7185
21. Qian H, Dong C, Weng J, Ren J (2006) Facile one-pot synthesis of luminescent, water-soluble, and biocompatible glutathione-coated CdTe nanocrystals. Small 2:747–751
22. Brichkin SB, Chernykh EV (2011) Hydrophilic semiconductor quantum dots. High Energy Chem 45(1):1–12
23. Zhang H, Wang L, Xiong H, Hu L, Yang B, Li W (2003) Hydrothermal synthesis for high quality CdTe QDs. Adv Mater 15(20):1712–1715
24. Li L, Qian H, Ren J (2005) Rapid synthesis of highly luminescent CdTe nanocrystals in the aqueous phase by microwave irradiation with controllable temperature. Chem Commun 8:528–530
25. Pfeiffer LN, West KW, Willett RL, Akiyama H, Rokhinso LP (2005) Nanostructures in GaAs fabricated by molecular beam epitaxy. Bell Labs Tech J 10(3):151–159
26. Nozik AJ, Beard MC, Luther JM, Law M, Ellingson RJ, Johnson JC (2010) Semiconductor quantum dots and quantum dot arrays and applications of multiple exciton generation to third-generation photovoltaic solar cells. Chem Rev 110(11):6873–6890
27. Winkler LD, Arceo JF, Hughes WC (2005) Quantum dots: an experiment for physical or materials chemistry. J Chem Educ 82(11):1700–1702
28. Krolikowska A, Kudelski A, Michota A, Bukowska J (2003) SERS studies on the structure of thioglycolic acid monolayers on silver and gold. Surf Sci 532:227–232
29. Watson JHP, Ellwood DC, Soper AK, Charnock J (1999) Nanosized strongly—magnetic bacterially-produced iron sulfide materials. J Magn Magn Mater 203:69–72
30. Sinha S, Pan I, Chanda P, Sen SK (2009) Nanoparticles fabrication using ambient biological resources. J Appl Biosci 19:1113–1130
31. Li X, Xu H, Chen Z-S, Chen G (2011) Biosynthesis of nanoparticles by microorganisms and their applications. J Nanomater 2011:1–16
32. Cunningham DP, Lundie LL (1993) Precipitation of cadmium by *Clostridium thermoaceticum*. Appl Environ Microbiol 59(1):7–14
33. Sweeney RY, Mao C, Gao X (2004) Bacterial biosynthesis of cadmium sulfide nanocrystals. Chem Biol 11(11):1553–1559
34. Bai HJ, Zhang ZM, Guo Y, Yang GE (2009) Biosynthesis of cadmium sulfide nanoparticles by photosynthetic bacteria *Rhodopseudomonas palustris*. Colloids Surf B 70:142–146
35. Kho R, Torres-Martinez CL, Mehra RK (2000) A simple colloidal synthesis for gram-quantity production of water-soluble ZnS nanocrystal powders. J Colloid Interface Sci 227:561–566
36. Dubertret B, Skourides P, Norris DJ, Noireaux V, Brivanlou AH, Libchaber A (2002) In vivo imaging of quantum dots encapsulated in phospholipid micelles. Science 298:1759–1762
37. Bai H-J, Zhang Z-M, Gong J (2006) Biological synthesis of semiconductor zinc sulfide nanoparticles by immobilized *Rhodobacter sphaeroides*. Biotechnol Lett 28:1135–1139

38. Bai HJ, Zhang ZM (2009) Microbial synthesis of semiconductor lead sulfide nanoparticles using immobilized *Rhodobacter sphaeroides*. Mater Lett 63(9–10):764–766
39. Bao H, Hao N, Yang Y, Zhao D (2010) Biosynthesis of biocompatible cadmium telluride quantum dots using yeast cells. Nano Res 3:481–489
40. Sturzenbaum SR, Winters C, Galay M, Morgan AJ, Kille P (2001) Metal ion trafficking in earthworms—identification of a cadmium specific metallothionein. J Biol Chem 276:34013
41. Sturzenbaum SR, Georgiev O, Morgan AJ, Kille P (2004) Cadmium detoxification in earthworms: from genes to cells. Environ Sci Technol 38:6283–6289
42. Sturzenbaum SR, Hockner M, Panneerselvam A, Levitt J, Bouillard J-S, Taniguchi S, Dailey L-A, Ahmad Khanbeigi R, Rosca EV, Thanou M, Suhling K, Zayats AV, Green M (2012) Biosynthesis of luminescent quantum dots in an earthworm. Nat Nanotechnol 8:57–60
43. Grill E, Winnacker EL, Zenk MH (1985) Phytochelatins: the principal heavy-metal complexing peptides of higher plants. Science 230:674–676
44. Ahner BA, Kong S, Morel FMM (1995) Phytochelatin production in marine algae. 1. An interspecies comparison. Limnol Oceanogr 40:649–657
45. Gekeler W, Grill E, Winnacker EL, Zenk MH (1988) Algae sequester heavy metals via synthesis of phytochelatin complexes. Arch Microbiol 150:197–202
46. Scarano G, Morelli E (2003) Properties of phytochelatin-coated CdS nanocrystallites formed in a marine phytoplanktonic alga (*Phaeodactylum tricornutum,* Bohlin) in response to Cd. Plant Sci 165:803–810
47. Bae W, Mehra RK (1998) Properties of glutathione- and phytochelatin-capped CdS bionanocrystallites. J Inorg Biochem 69:33–43
48. Ahmad A, Mukherjee P, Mandal D, Senapati S, Khan MI, Kumar R, Sastr M (2002) Enzyme-mediated extracellular synthesis of CdS nanoparticles by the fungus, *Fusarium oxysporum*. J Am Chem Soc 124:12108–12109
49. Henglein A (1989) Small-particle research: physicochemical properties of extremely small colloidal metal and semiconductor particles. Chem Rev 89(8):1861–1873
50. Cantor CR, Schimmel PR (1980) Biophysical chemistry, Part II: Techniques for the study of biological structure and function, W.H. Freeman and Co, San Francisco, 365p
51. Klaus T, Joerger R, Olsson E, Granqvist C-G (1999) Silver-based crystalline nanoparticles, microbially fabricated. Proc Natl Acad Sci 96:13611–13615
52. Borovaya MN, Naumenko AP, Pirko YV, Krupodorova TA, Yemets AI, Blume YB (2014) Production of CdS quantum dots with the use of the fungus *Pleurotus ostreatus*. Proc Natl Acad Sci Ukraine 2:153–159 (In Ukranian)
53. Kumar SA, Ansary AA, Ahmad A, Khan MI (2007) Extracellular biosynthesis of CdSe quantum dots by the fungus, *Fusarium Oxysporum*. J Biomed Nanotechnol 3:190–194
54. Eflink MR, Ghiron CA (1981) Fluorescence quenching studies with proteins. Anal Biochem 114:199
55. Kavitha KS, Baker S, Rakshith D, Kavitha HU, Yashwantha RHC, Harini BP, Satish S (2013) Plants as green source towards synthesis of nanoparticles. Int Res J Biol Sci 2(6):66–76
56. Hudlikar M, Joglekar S, Dhaygude M, Kodam K (2012) Latex-mediated synthesis of ZnS nanoparticles: green synthesis approach. J Nanoparticle Res 14(5):1–5
57. Osoniyi O, Onajobi F (2003) Coagulant and anticoagulant activities in *Jatropha curcas* latex. J Ethnopharmacol 89:101–105
58. Borovaya MN, Naumenko AP, Matvieieva NA, Blume YB, Yemets AI (2014) Biosynthesis of luminescent CdS quantum dots using plant hairy root culture. Nanoscale Res. Lett. 9(1):1–7
59. Gomes SAO, Vieira CS, Almeida DB, Santos-Mallet JR, Menna-Barreto RFS, Cesar CL, Feder D (2011) CdTe and CdSe quantum dots cytotoxicity: a comparative study on microorganisms. Sensors 11:11664–11678
60. Bruchez M, Moronne M, Gin P, Weiss S, Alivisatos AP (1998) Semiconductor nanocrystals as fluorescent biological labels. Science 281:2013–2016
61. Eggenberger K, Merkulov A, Darbandi M, Nann T, Nick P (2007) Direct immunofluorescence of plant microtubules based on semiconductor nanocrystals. Bioconjug Chem 30(20):1–7

62. Riegler J, Nick P, Kielmann U, Nann T (2003) Visualize the self-assembly of tubulin with luminescent nanorods. J Nanosci Nanotechnol 3:380–385
63. Barroso MM (2011) Quantum dots in cell biology. J Histochem Cytochem 59:237–251
64. Sorkin A, von Zastrow M (2009) Endocytosis and signalling: intertwining molecular networks. Nat Rev Mol Cell Biol 10:609–622
65. Danglot L, Chaineau M, Dahan M, Gendron MC, Boggetto N, Perez F, Galli T (2010) Role of TI-VAMP and CD82 in EGFR cell-surface dynamics and signaling. J Cell Sci 123:723–735
66. Lidke DS, Nagy P, Heintzmann R, Arndt-Jovin DJ, Post JN, Grecco HE, Jares-Erijman EA, Jovin TM (2004) Quantum dot ligands provide new insights into erbB/HER receptor-mediated signal transduction. Nat Biotechnol 22(2):198–203
67. Rajan SS, Liu HY, Vu TQ (2008) Ligand-bound quantum dot probes for studying the molecular scale dynamics of receptor endocytic trafficking in live cells. ACS Nano 2:1153–1166
68. Geng L, Zhang HL, Peng HB (2009) The formation of acetylcholine receptor clusters visualized with quantum dots. BMC Neurosci 10:80
69. Garon EB, Marcu L, Luong Q, Tcherniantchouk O, Crooks GM, Koeffler HP (2007) Quantum dot labeling and tracking of human leukemic, bone marrow and cord blood cells. Leuk Res 31 (5):643–651
70. Shah BS, Clark PA, Moioli EK, Stroscio MA, Mao JJ (2007) Labeling of mesenchymal stem cells by bioconjugated quantum dots. Nano Lett 7(10):3071–3079
71. Orndorff RL, Warnement MR, Mason JN, Blakely RD, Rosenthal SJ (2008) Quantum dot ex vivo labeling of neuromuscular synapses. Nano Lett 8(3):780–785
72. Bannai H, Levi S, Schweizer C, Dahan M, Triller A (2006) Imaging the lateral diffusion of membrane molecules with quantum dots. Nat Protoc 1(6):2628–2634
73. Roberti MJ, Morgan M, Menendez G, Pietrasanta LI, Jovin TM, Jares-Erijman EA (2009) Quantum dots as ultrasensitive nanoactuators and sensors of amyloid aggregation in live cells. J Am Chem Soc 131(23):8102–8107
74. Crut A, Geron-Landre B, Bonnet I, Bonneau S, Desbiolles P, Escude C (2005) Detection of single DNA molecules by multicolor quantum dot end-labeling. Nucleic Acids Res 33(11):98/1–98/9
75. Ye M, Zhang Y, Li H, Zhang Y, Tan P, Tang H, Yao S (2009) A novel method for the detection of point mutation in DNA using single-base-coded CdS nanoprobes. Biosens Bioelectron 24 (8):2339–2345
76. Bailey VJ, Easwaran H, Zhang Y, Griffiths E, Belinsky SA, Herman JG, Baylin SB, Carraway HE, Wang TH (2009) MS-qFRET: a quantum dot-based method for analysis of DNA methylation. Genome Res 19(8):1455–1461
77. Pathak S, Choi SK, Arnheim N, Thompson ME (2001) Hydroxylated quantum dots as luminescent probes for *in situ* hybridization. J Am Chem Soc 123:4103–4104
78. Knoll JHM (2007) Human metaphase chromosome FISH using quantum dot conjugates. Methods Mol Biol 374:55–66
79. Kapoor V, Hakim FT, Rehman N, Gress RE, Telford WG (2009) Quantum dots thermal stability improves simultaneous phenotype-specific telomere length measurement by FISH-flow cytometry. J Immunol Methods 344:6–14
80. Chan P, Yen T, Frederique R, Gonzalez-Maeso J, Seal-fon SC (2005) Method for multiplex cellular detection of mRNAs using quantum dot fluorescence *in situ* hybridization. Nucleic Acids Res 33:161–166
81. Ioannou D, Tempest HC, Skinner BM, Thornhill AR, Ellis M, Griffin DK (2009) Quantum dots as new-generation fluorochromes for FISH. Chromosome Res 17:519–530
82. Tholouli E, Hoyland JA, Di Vizio D, O'Connell F, Macdermott SA, Twomey D, Levenson R, Yin JA, Golub TR, Loda MK, Byers R (2006) Imaging of multiple mRNA targets using quantum dot based in situ hybridization and spectral deconvolution in clinical biopsies. Biochem Biophys Res Commun 348:628–636

83. Burroughs FG, Samboju NC, Samuel JP, Webb SR, Yau KY (2011) Linear DNA molecule delivery using PEGylated quantum dots for stable transformation in plants. US Patent 8653327 B2, 7 Jul 2011
84. Nie S, Xing Y, Kim GJ, Simons JW (2007) Nanotechnology applications in cancer. Annu Rev Biomed Eng 9:12.1–12.32
85. Riggio C, Pagni E, Raffa V, Cuschieri A (2011) Nano-oncology: clinical application for cancer therapy and future perspectives. J Nanomater 2011:1–10
86. True LD, Gao X (2007) Quantum dots for molecular pathology. J Mol Diagn 9:7–11
87. Høgdall EVS, Christensen L, Kjaer SK (2007) CA125 expression pattern, prognosis and correlation with serum CA125 in ovarian tumor patients. From The Danish "MAL-OVA" Ovarian Cancer Study. Gynecol Oncol 104(3):508–515
88. Wang Z, Wang H-Y, Liang R-Q, Ruan K-C (2004) Detection of tumor marker CA125 in ovarian carcinoma using quantum dots. Acta Biochim Biophys Sin 36(10):681–686
89. Xiao Y, Gao X, Gannot G (2008) Quantitation of HER2 and telomerase biomarkers in solid tumors with IgY antibodies and nanocrystal detection. Int J Cancer 122(10):2178–2186
90. Qian J, Yong K-T, Roy I (2007) Imaging pancreatic cancer using surface-functionalized quantum dots. J Phys Chem B 111(25):6969–6972
91. Gao X (2007) Multifunctional quantum dots for cellular and molecular imaging. In: Proceedings of 29th annual international conference on IEEE EMBS, Lyon, France, 23–28 Aug, pp 524–525
92. Kim SW, Zimmer JP, Ohnishi S (2005) Engineering InAsxP1-x/InP/ZnSe III-V alloyed core/shell quantum dote for the near-infrared. J Am Chem Soc 127:10526–10532

Part III
Nanobiotechnology

Chapter 25
Computer Simulation Study of the Molecular Dynamics in Homocysteine Systems

P. Raczyński, A. Dawid, and Z. Gburski

25.1 Introduction

Homocysteine is an amino acid given by the formula $C_4H_9NO_2S$ [1–3]. The role homocysteine plays in a human body is not fully understood and is the subject of the current debate. For example, a high level of homocysteine (homocysteinemia) is considered as a risk factor for cardiovascular disease [4–9]. Elevated level of homocysteine has been linked to increased fractures in humans [10, 11]. Moreover, higher homocysteine and lower folate concentrations in early pregnancy are associated with lower placental weight and birth weight, and higher risk of adverse pregnancy outcomes [12, 13]. It is not clear yet whether high serum homocysteine is itself the problem or if it as merely an indicator of other existing problems [14, 15]. In this chapter, we applied the molecular dynamic simulations method (MD) to the study of the homocysteine systems. Computer simulations are used to examine interesting structural and dynamical properties of various nanosystems [16–31].

The molecular dynamics of homocysteine was studied in case of pure cluster and in the presence of water, for several temperatures (including physiological). Knowledge of the properties of homocysteine systems may help, when one would attempt to clarified the role it plays in the biological environment.

P. Raczyński (✉) • A. Dawid • Z. Gburski
Institute of Physics, University of Silesia, Uniwersytecka 4, Katowice 40-007, Poland
e-mail: przemyslaw.raczynski@us.edu.pl

O. Fesenko, L. Yatsenko (eds.), *Nanoplasmonics, Nano-Optics, Nanocomposites, and Surface Studies*, Springer Proceedings in Physics 167,
DOI 10.1007/978-3-319-18543-9_25

25.2 Simulation Details

Molecular dynamics simulations were performed with NAMD 2.8 for BlueGeneQ-MPI simulation code [32, 33] and visualized with VMD 1.8.7 [34, 35]. In the first part of our work, we studied clusters consisting the finite numbers $n = 30$, 65, 140, 860, 2,500 of homocysteine molecules, using MD technique. Next, we surrounded these clusters with water and repeated all MD simulations with periodic boundary conditions and Particle Mesh Evald (PME) long range, electrostatic interactions summation method [36–40]. The charge distribution in the homocysteine molecule was calculated using ab initio method with 6-31G** basis set. Water was described with TIP3P, CHARMM adapted model [41, 42]. Homocysteine molecule was modelled with CHARMM27 force field for nucleic acids [41].

All simulations were performed for four temperatures (including physiological), $T = 290$, 300, 310 and 320 K. The initial configurations of the systems were obtained from a series of NVT simulations. All the systems studied were equilibrated for 1×10^6 simulation time steps in NVT ensemble. Moreover, the systems with water were equilibrated in NPT ensemble before the equilibration in NVT. The 0.5 fs integration time step was applied in all performed simulations.

25.3 Results

First, we present the results for the homocysteine free clusters (without water). Five ensembles of homocysteine ($n = 30$, 65, 140, 860 and 2,500) at four temperatures ($T = 290$, 300, 310, 320 K) have been examined.

In Fig. 25.1, we show the configurations for all studied systems, after 1×10^6 equilibration time steps. In other words, it is the beginning of "production" phase, i.e. at this moment we start to collect the simulation data. In each sample (Fig. 25.1a–e), the homocysteine molecules are close to each other. Moreover, in all studied systems the equilibration process leads to spherical shape of the cluster—energetically most favourable structure.

The first quantity we discuss is the mean square displacement (MSD) $\left\langle \left|\Delta \vec{r}(t)\right|^2 \right\rangle$ of the centre of mass of homocysteine, where $\Delta \vec{r}(t) = \vec{r}(t) - \vec{r}(0)$ and $\vec{r}$ is the position of centre of mass of a single molecule. Figure 25.2 shows the MSD plot for all homocysteine clusters at several temperatures.

In all samples, the slope of $\left\langle \left|\Delta \vec{r}(t)\right|^2 \right\rangle$ increases with an increasing of the temperature. The greater slope of $\left\langle \left|\Delta \vec{r}(t)\right|^2 \right\rangle$ reflects a higher mobility of molecule. Greater mobility of homocysteine molecules with heating of the cluster is natural. In MSD graph for $n = 65$ one can observe that at temperatures $T = 290$ K,

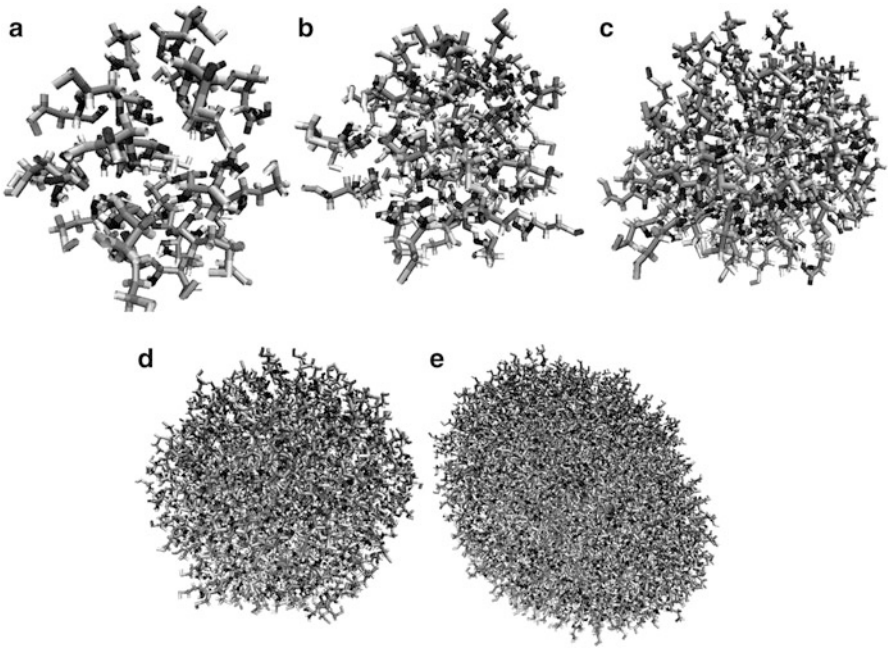

Fig. 25.1 The initial configurations for the clusters consisting of: (**a**) $n = 30$, (**b**) $n = 65$, (**c**) $n = 140$, (**d**) $n = 860$ and (**e**) $n = 2{,}500$ homocysteine molecules

$T = 300$ K and $T = 310$ K the plots of $\left\langle \left| \Delta \vec{r}(t) \right|^2 \right\rangle$ are similar. This may indicate that the similar processes occur in these temperatures for the cluster $n = 65$. For all studied systems, there are no drastic differences between the values/slopes of MSD function among particular clusters. This can be interpreted that the homocysteine systems do not vaporize and the phase transitions do not occur. It can be confirmed by plots of the radial distribution function $g(r)$ of the centre of mass of homocysteine, showed in Fig. 25.3.

As an example, we present the plots of $g(r)$ for two homocysteine clusters only, the smallest and the largest one ($n = 30$ and $n = 2{,}500$), since in all studied systems the shape of the $g(r)$ curves is similar. The radial distribution functions (Fig. 25.3) vary only very weakly with the changing of the temperature, for all considered systems. For all temperatures, the shapes of $g(r)$ and their maximal values are congruous. In case of the smallest cluster, the maximal $g(r)$ values for the highest peaks are 6.27×10^{-3}, 6.01×10^{-3}, 6.08×10^{-3} and 6.08×10^{-3}, for $T = 290$ K, $T = 300$ K, $T = 310$ K and $T = 320$ K, respectively. In case of the largest cluster ($n = 2{,}500$), the calculated maximal values of $g(r)$ are 8.5×10^{-3} ($T = 290$ K), 8.49×10^{-3} ($T = 300$ K), 8.41×10^{-3} ($T = 310$ K) and 8.36×10^{-3} ($T = 320$ K). The first two maxima of $g(r)$ are located at 6.1 and 10 Å and do not depend on the size of the cluster or temperature. Indicated similarities apply also to the plots of

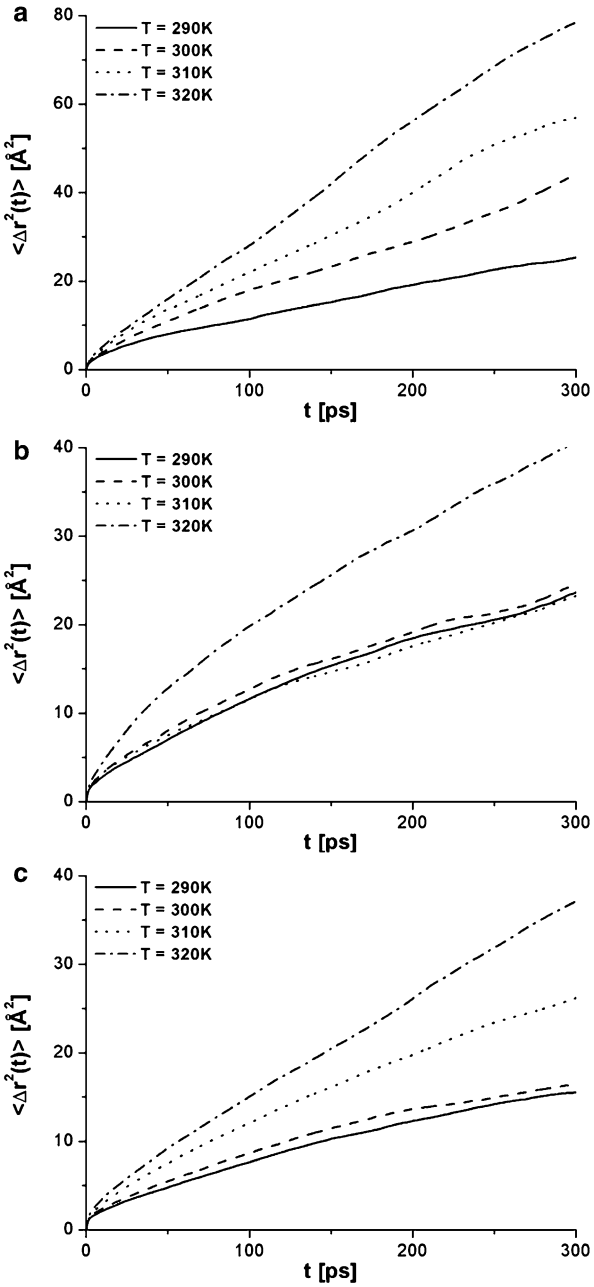

Fig. 25.2 The calculated mean square displacement of the centre of mass of homocysteine for the clusters consisting of: (**a**) $n = 30$, (**b**) $n = 65$, (**c**) $n = 140$, (**d**) $n = 860$ and (**e**) $n = 2{,}500$ molecules, for all temperatures studied

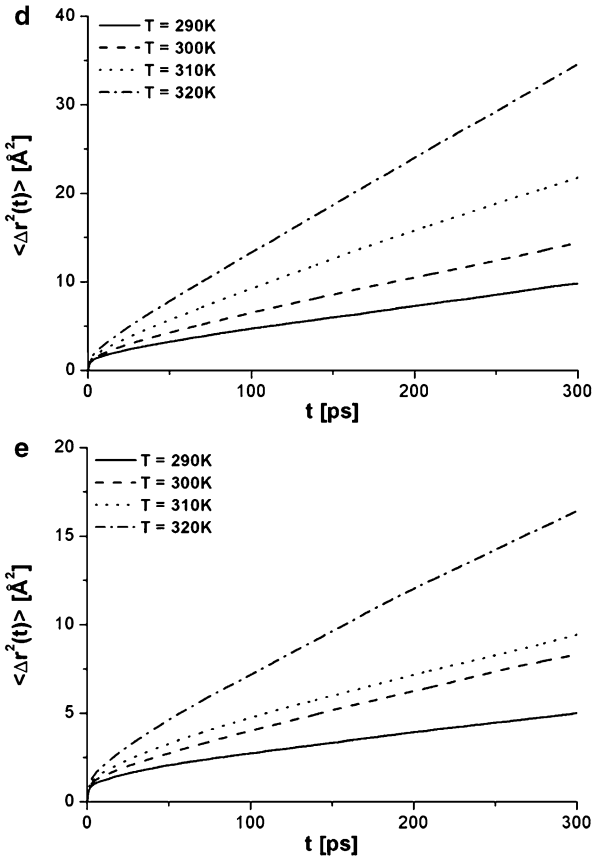

Fig. 25.2 (continued)

$g(r)$ (not presented here) for the remaining clusters. It confirms the previous conclusion about the absence of phase transitions in studied clusters at the investigated temperature range.

In $g(r)$ plots two distinct peaks appear. The first peak ($r \approx 6.1$ Å) can be connected with the distance to the nearest neighbours in the cluster, while the second peak ($r \approx 10$ Å) points to the second homocysteine neighbours. It is worth noting that the functions of $g(r)$ differ at the long distance part (for $r > 12$ Å). The radial distribution function in case of $n = 30$ cluster approaches zero at $r = 20$ Å while in the case of $n = 2{,}500$ the value of $g(r)$ is about 4.5×10^{-3} at the same distance $r = 20$ Å. Moreover, for the largest homocysteine cluster, the third peak ($r \approx 14.2$ Å) appears. These differences can be explained by the size of clusters. The smallest cluster contains only 30 homocysteine molecules, while the largest 2,500. This means that in case of $n = 30$ cluster the homocysteine molecules are surrounded by the smaller number of neighbours and the diameter d of the cluster

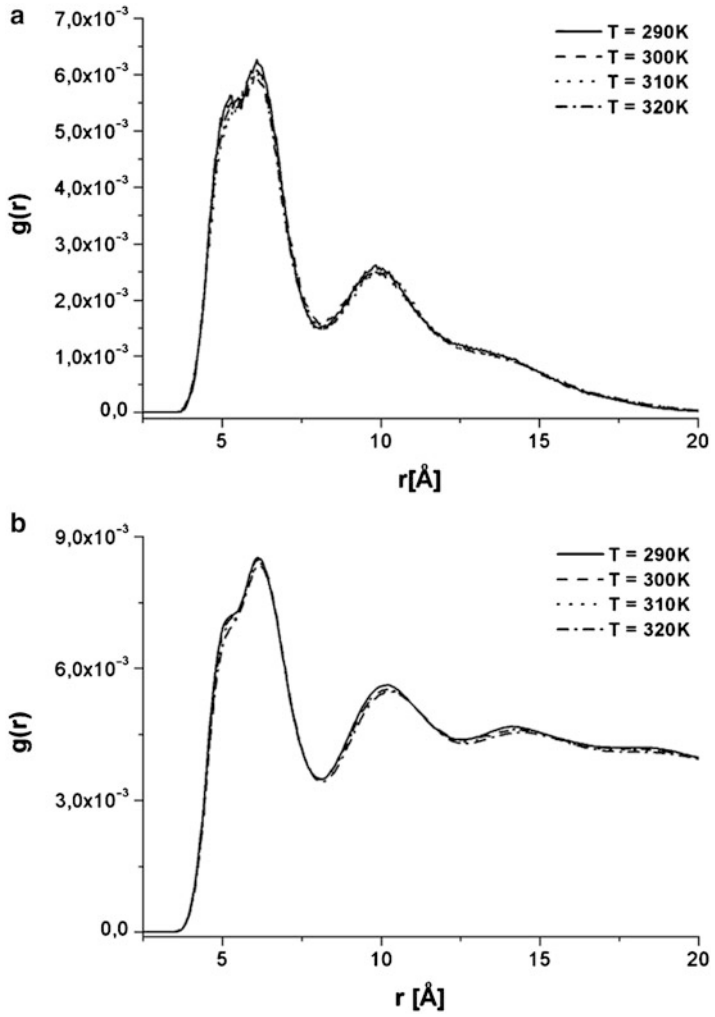

Fig. 25.3 The radial distribution function for the clusters containing: (**a**) $n = 30$ and (**b**) $n = 2{,}500$ homocysteine molecules, for all temperatures studied

is much smaller. We have found that the diameter of the smallest cluster is $d \approx 20$ Å whereas for the largest cluster $d \approx 90$ Å. The number of neighbours also explains the differences in the maximal values of the first and, particularly, second peak of $g(r)$ function (the second peak of $g(r)$ function is almost 2.2 times higher in case of $n = 2{,}500$).

Figure 25.4. shows the comparison of the MSD of the centre of mass of homocysteine for all temperatures and for all clusters studied.

At the lowest temperature ($T = 290$ K), the homocysteine molecules in clusters with $n = 30$ and $n = 65$ exhibit congruous mobility and their mobility is the highest. Larger size of the cluster means the lower mobility of homocysteine molecules. Inside the bigger cluster, the molecules are more crowded, hence their mobility decreases. In cluster with $n = 30$, the homocysteines have a greater mobility since in such a small cluster almost all molecules are located on a surface of the cluster. Only a few homocysteines form the less mobile, internal core (surrounded by majority of surface molecules). The surface molecules are loosely tied, have less number of neighbours, their mobility is higher.

Note, that the mobility of molecules with $n = 2{,}500$ is the lowest for all temperatures studied (Fig. 25.4a–d). It is connected with the large internal core of this big cluster. The core molecules are closely packed, they can move in a very limited volume.

Figure 25.5 shows the radial distribution function $g(r)$ for all studied clusters, at the temperature $T = 290$ K.

The graphs at the other temperatures are very similar and we do not present them. With an increasing number of homocysteine molecules included in the cluster, the height of the first and second peak of $g(r)$ also increases. This confirms that in larger clusters the number of neighbours increase, but the distance between the nearest and second neighbours does not change (the maxima of first and second peaks does not depend on the number of molecules inside the cluster). Only the positions of the third peaks are not overlap which may be associated with different orientations of small but elongated homocysteine molecules with respect to each other. Note that for the largest cluster the first peak of $g(r)$ is very sharp and distinct; hence, the homocysteine molecules inside this cluster move in a very small area and they are close surrounded by a large number of neighbours.

In Figs. 25.2 and 25.4, we show the plots of $\left\langle \left| \Delta \vec{r}(t) \right|^2 \right\rangle$. The MSD is connected with the diffusion coefficient via Einstein relation $\left\langle \left| \Delta \vec{r}(t)^2 \right| \right\rangle \approx 6Dt$, where D is translational diffusion coefficient. Figure 25.6 shows the calculated diffusion coefficient of the centre of mass of homocysteine for three largest clusters with $n = 140$, $n = 860$ and $n = 2{,}500$, as a function of temperature. The values of D[Å^2/ps] are given in Table 25.1.

In case of clusters with $n = 140$ and $n = 860$ molecules, there are no significant differences between the values of D, but for the cluster $n = 2{,}500$ the values of diffusion coefficient are lower. Comparing this result with the slope of the MSD (Fig. 25.4), one can notice that the molecules in the largest cluster are less mobile.

All observables presented ($\left\langle \left| \Delta \vec{r}(t) \right|^2 \right\rangle$, $g(r)$ and D) do not indicate the appearance of the phase transition in any cluster (at the temperature range studied). To confirm that conclusion, we have also calculated the Lindemann index δ_L [43]:

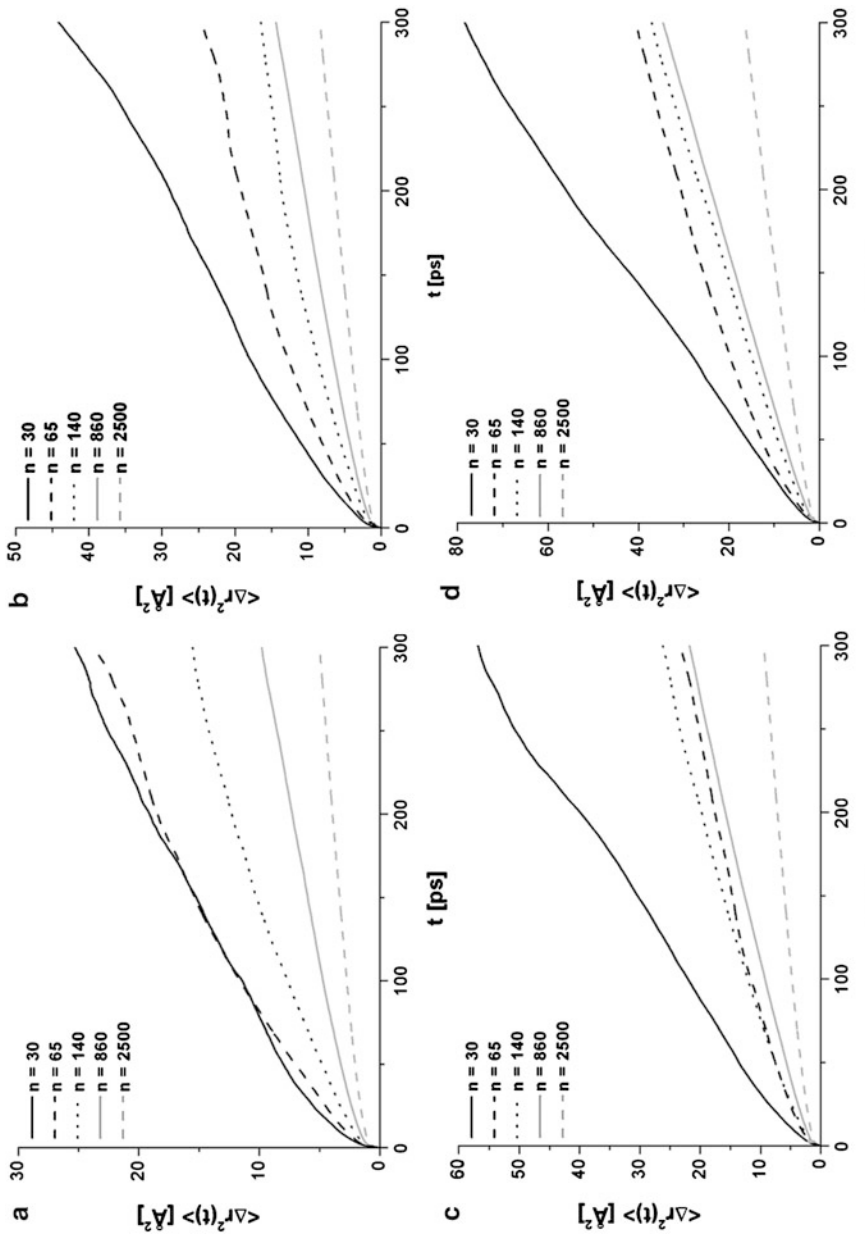

Fig. 25.4 The comparison of the mean square displacement of the centre of mass of homocysteine for all clusters studied, at: (**a**) $T = 290$ K, (**b**) $T = 300$ K, (**c**) $T = 310$ K and (**d**) $T = 320$ K

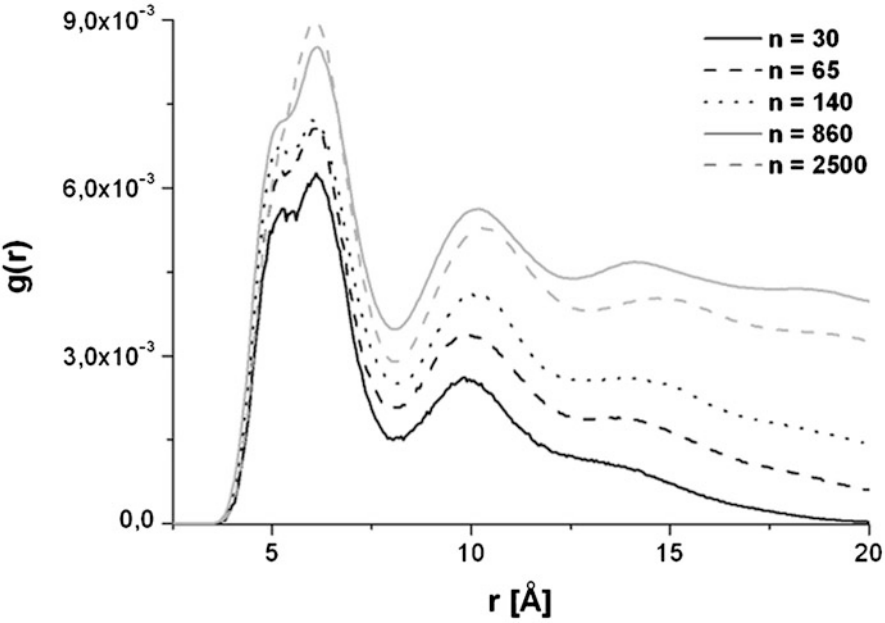

Fig. 25.5 The comparison of the radial distribution function of homocysteine for all studied systems, at $T = 290$ K

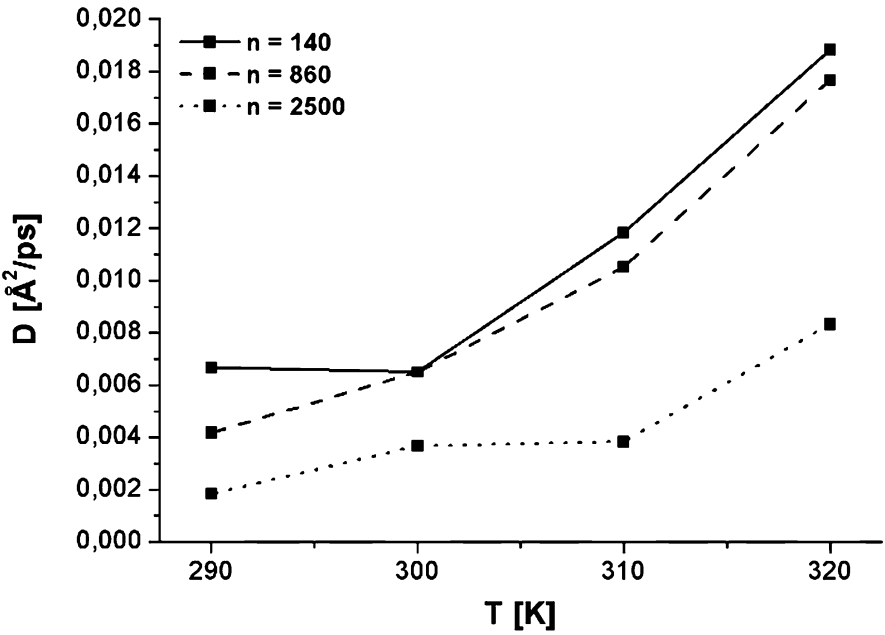

Fig. 25.6 The calculated diffusion coefficient of the centre of mass of homocysteine for the clusters containing: $n = 140$, $n = 860$ and $n = 2{,}500$ homocysteine molecules, as a function of temperature

Table 25.1 The values of diffusion coefficient D [Å^2/ps] for the three largest clusters and for all temperatures studied

	$n = 140$	$n = 860$	$n = 2{,}500$
$T = 290$ K	0.009	0.005	0.002
$T = 300$ K	0.010	0.008	0.0037
$T = 310$ K	0.015	0.012	0.0038
$T = 320$ K	0.020	0.018	0.008

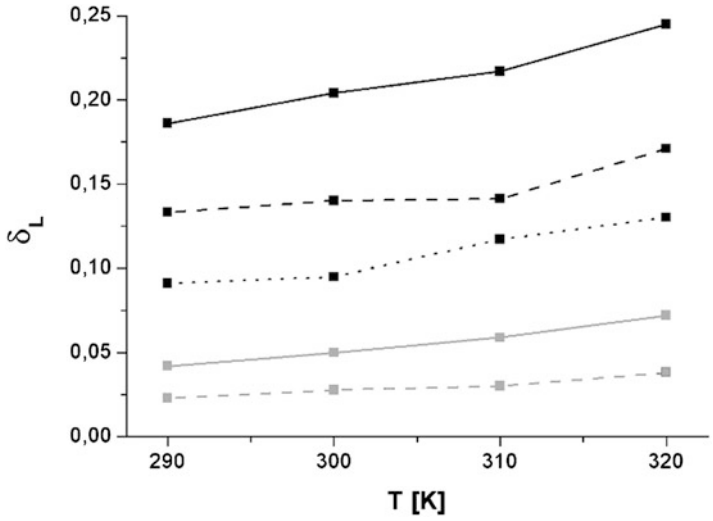

Fig. 25.7 The evolution of the Lindemann index for all studied clusters and for all temperatures

$$\delta_{\mathrm{L}} = \frac{2}{N(N-1)} \sum_{i<j}^{N} \frac{\left(\left\langle r_{ij}^2 \right\rangle - \left\langle r_{ij} \right\rangle^2 \right)^{1/2}}{\left\langle r_{ij} \right\rangle}$$

where r_{ij} is the distance between the centre of mass of ith and jth molecule. The evolution of δ_{L} for all studied clusters (for all temperatures) is showed in Fig. 25.7. There is no jump in the value of δ_{L}, which would be an indicator of the phase transition. Therefore, the phase transition does not appear [43–50].

Next, we surrounded the clusters (after equilibration process) by water and we repeated all simulations as a bulk samples with a determined/periodic boundary conditions.

First, we show an example of $\left\langle \left| \Delta \vec{r}(t) \right|^2 \right\rangle$, for the system containing 860 molecules of homocysteine, surrounded by water (Fig. 25.8).

One can observe that the slope of MSD increases with an increasing of the temperature. This means that the mobility of molecules grow up at higher temperatures. This observation is repeated for the other systems studied so we do not present them here. More conclusions can be drawn from the comparison of MSD function of the centre of mass of homocysteine, with water and without it (Figs. 25.9 and 25.10).

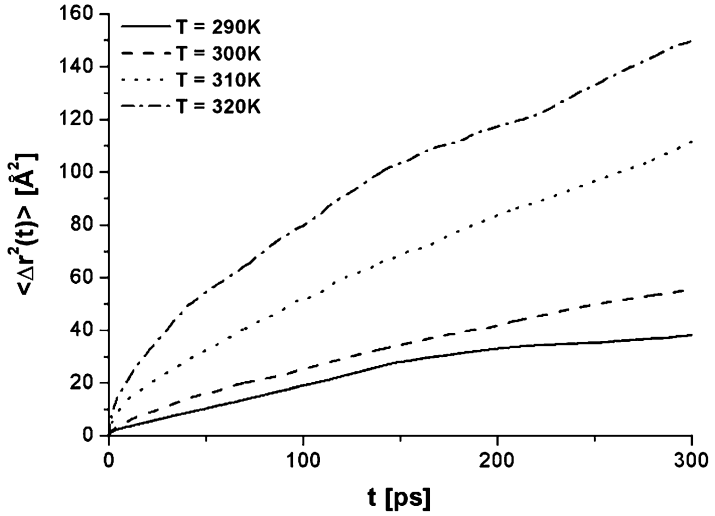

Fig. 25.8 The calculated mean square displacement of the centre of mass of homocysteine for the cluster consisting of $n = 860$ molecules, for four temperatures

Figure 25.9 shows the MSD for the system containing 140 homocysteine molecules (with water and without water) for all temperatures. Figure 25.10 shows the plots of $\left\langle \left| \Delta \vec{r}(t) \right|^2 \right\rangle$ for one temperature (physiological, $T = 310$ K) and for all systems studied (with water and without it). In Figs. 25.9 and 25.10 distinct differences are evident. These figures show that the mobility of homocysteine molecules is significantly higher when they are surrounded by water. Surrounding the cluster by water substantially affects the dynamics of homocysteine molecules, which further emphasizes the diffusion coefficient. The comparison of calculated D is presented in Table 25.2 and Fig. 25.11 (comparison of D for the system $n = 860$ with water and without it). The first value of D is given for the pure homocysteine cluster, the value after the slash is given for the system with water.

The values of the diffusion coefficient D are much lower for the clusters (without water). Therefore, the homocysteine molecules in pure clusters have much smaller mobility comparing to the mobility in the systems with water. The large differences between D indicate the process of dissolving of a group of homocysteine molecules by water.

To confirm this conjecture, we have also calculated the radial distribution function $g(r)$ for the systems with water (Fig. 25.12).

In small systems ($n = 30$ and $n = 65$), the maximum value of the radial distribution function significantly decreases with growing of the temperature. In the systems containing the largest number of homocysteine molecules ($n = 2{,}500$) $g(r)$ functions change only very slightly and they are quite similar to the $g(r)$ plots in Fig. 25.3. Moreover, in case of small systems the second peaks do not appear at the

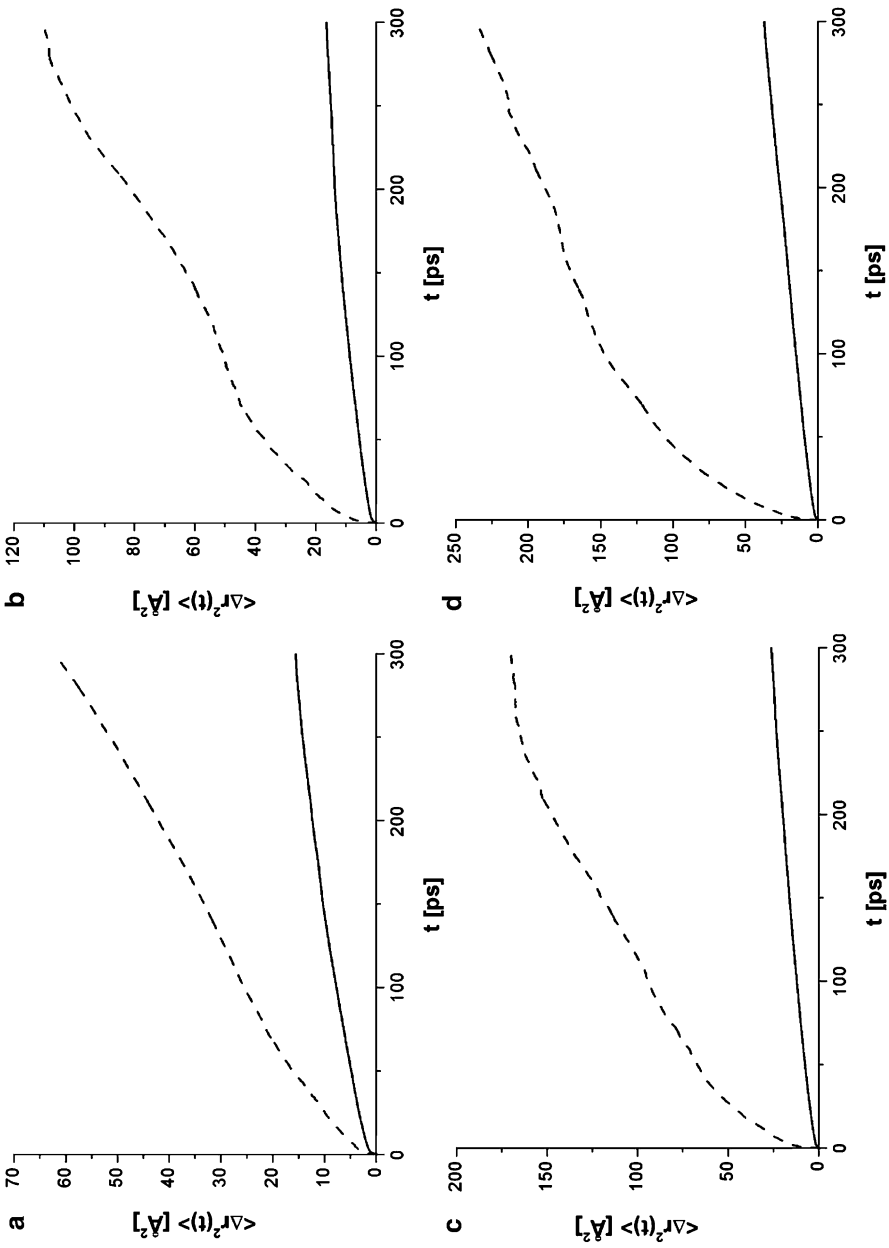

Fig. 25.9 The mean square displacement of the centre of mass of homocysteine for the system containing of $n = 140$ molecules, at: (**a**) $T = 290$ K, (**b**) $T = 300$ K, (**c**) $T = 310$ K, (**d**) $T = 320$ K. The *solid line* represents the pure cluster, the *dotted line* corresponds to the system with water

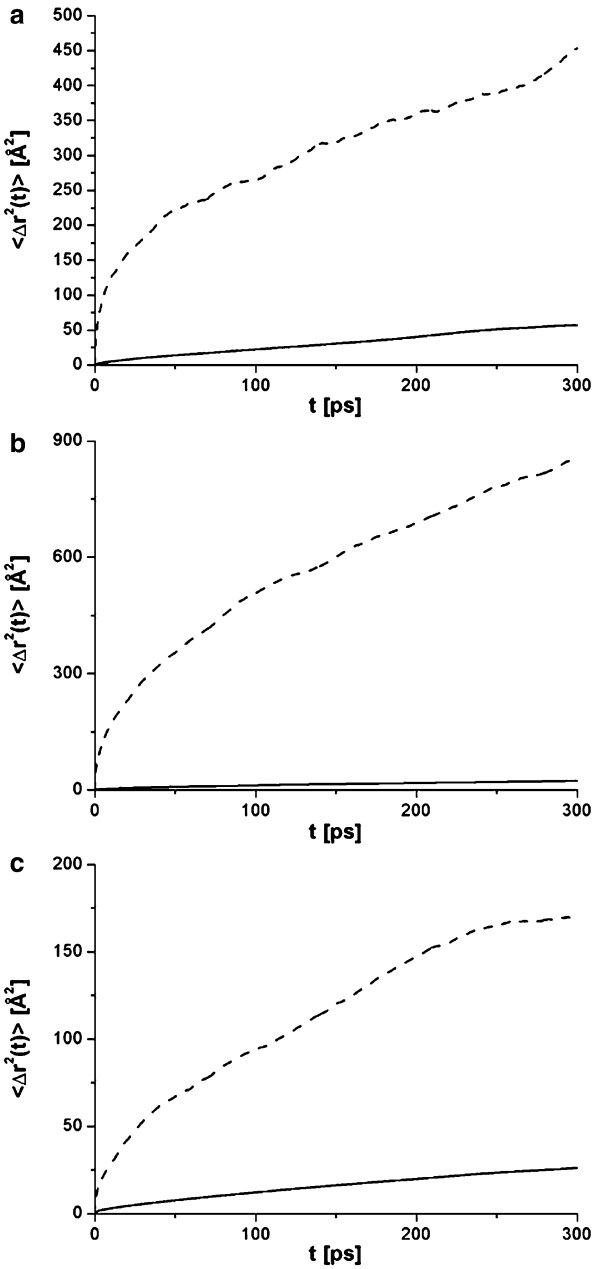

Fig. 25.10 The calculated mean square displacement of the centre of mass of homocysteine for the systems consisting of: (**a**) $n = 30$, (**b**) $n = 65$, (**c**) $n = 140$, (**d**) $n = 860$, (**e**) $n = 2{,}500$ molecules, at $T = 310$ K. The *solid line* represents the pure cluster, the *dotted line* corresponds to the system with water

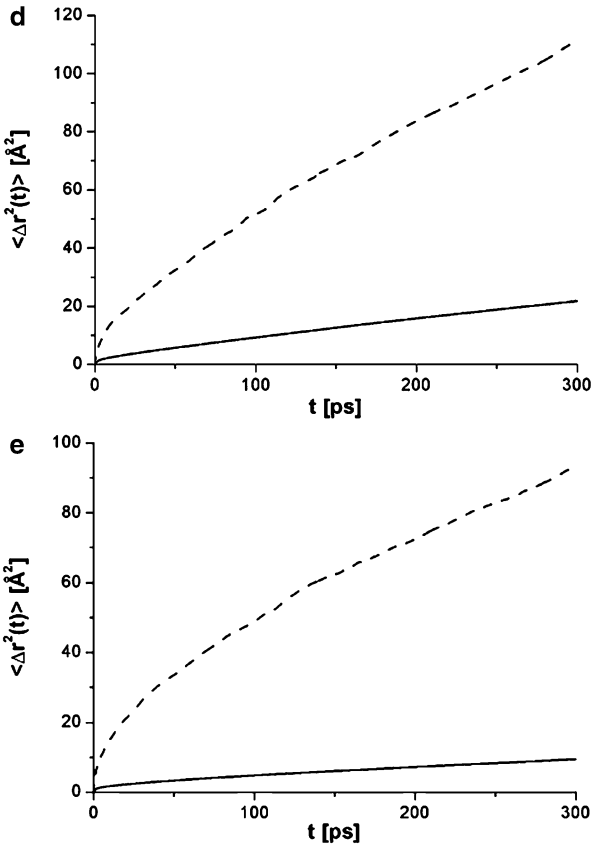

Fig. 25.10 (continued)

Table 25.2 The comparison of calculated D [Å^2/ps] between the clusters and systems with water, for all temperatures studied

	$n = 140$	$n = 860$	$n = 2{,}500$
$T = 290$ K	0.009/0.03	0.005/0.012	0.002/0.015
$T = 300$ K	0.010/0.059	0.008/0.026	0.0037/0.025
$T = 310$ K	0.015/0.086	0.012/0.048	0.0038/0.034
$T = 320$ K	0.020/0.072	0.018/0.054	0.008/0.042

high temperatures ($T = 310$ K and $T = 320$ K). The differences between the smallest system and the largest one are better visible in Fig. 25.13.

In case of the largest system (with water), the $g(r)$ function (at $T = 320$ K) is similar with the pure cluster. However, for the smallest system, the differences are distinct. In the smallest system with water, the peak associated with the second neighbours does not appear, homocysteine has only a few first neighbours. Figures 25.12 and 25.13 confirm that the water dissolve the groups of molecules. Moreover, water very easily dissolve small groups of homocysteine molecules

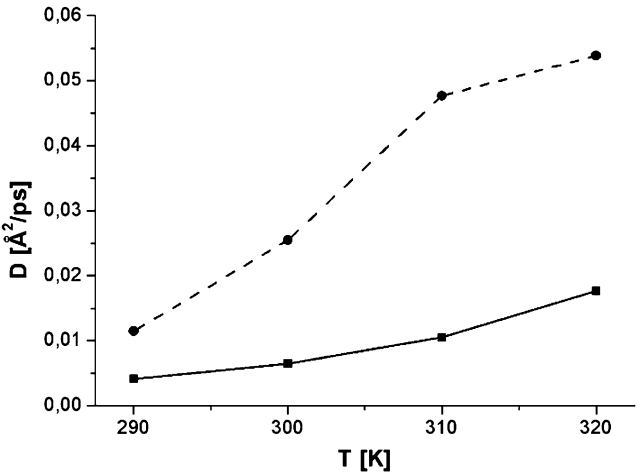

Fig. 25.11 The comparison of diffusion coefficient for the systems build of $n = 860$ homocysteine molecules, with water (*dotted line*) and without it (*solid line*), as a function of temperature

while the large groups of molecules keep together and water has no significant impact on them.

Figure 25.14 shows the snapshots of the final configuration of the systems surrounded by water in case of $n = 30$ and $n = 2{,}500$ (the smallest and the largest system), for $T = 290$ K and $T = 320$ K.

One can see, that in case of $n = 30$ the water molecules very easily smashed the group of homocysteine molecules. Moreover, the destructive impact of water on the group of homocysteine is clearly visible even at the lowest temperature $T = 290$ K. At the highest temperature ($T = 320$ K), the group of molecules practically does not exist, it reflects the plot of $g(r)$ (Fig. 25.13). In case of the largest system $n = 2{,}500$, the impact of water at the lowest temperature is negligible, while at the highest temperature $T = 320$ K is small. Comparing to the number of molecules in the largest system, a very few homocysteine molecules broke away from the group. It can be seen in the plot of $g(r)$ function (Fig. 25.13), the plots for pure cluster and system with water are similar. One have to keep in mind that in case of the largest system the dissolving process, although relatively slow, will be continued and it will finally leads to solvation dissolution of the cluster.

25.4 Conclusions

The homocysteine systems (with water and without it) were studied by MD technique. The systems consist of $n = 30$, 65, 140, 860 and 2,500 homocysteine molecules were taken into account. Each system was simulated for four

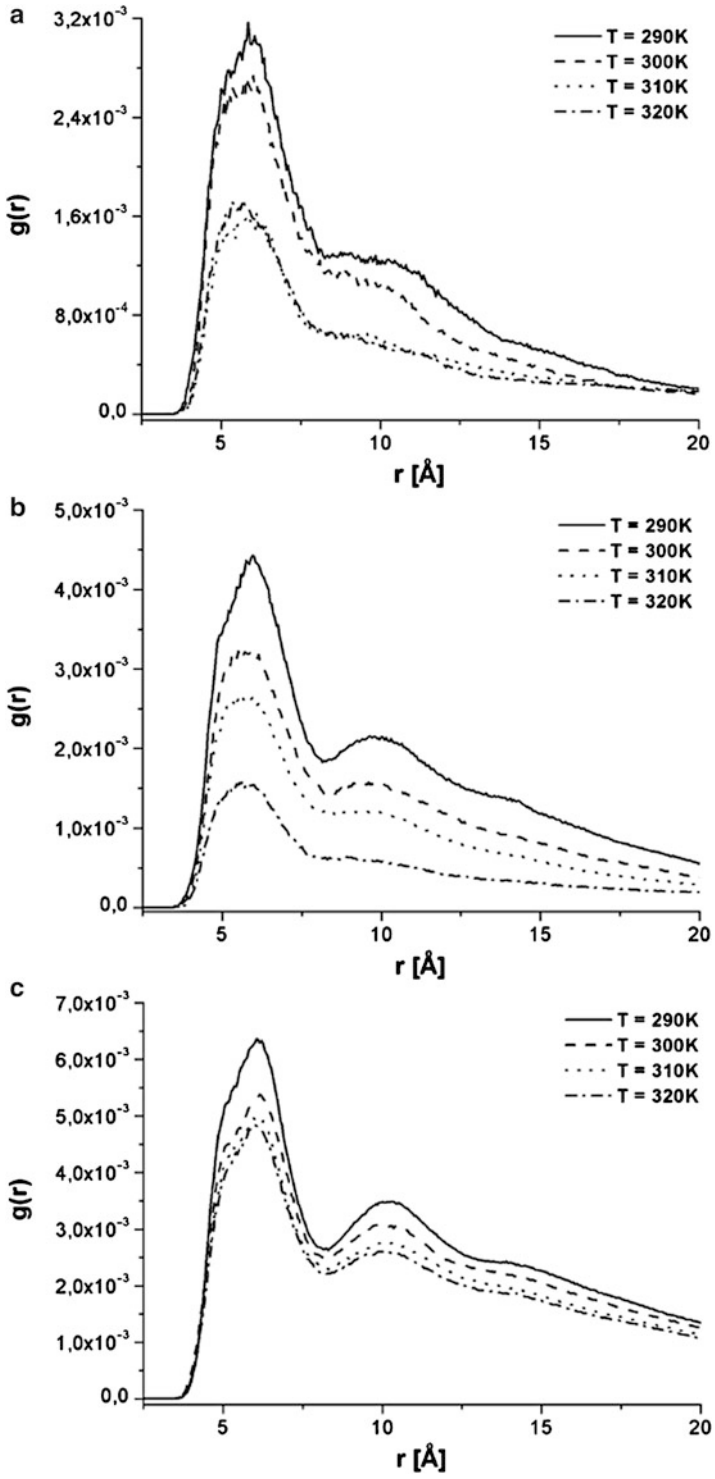

Fig. 25.12 The calculated radial distribution function of homocysteine for the systems with water and consisting of: (**a**) $n = 30$, (**b**) $n = 65$, (**c**) $n = 140$, (**d**) $n = 860$ and (**e**) $n = 2{,}500$ molecules and for all temperatures studied

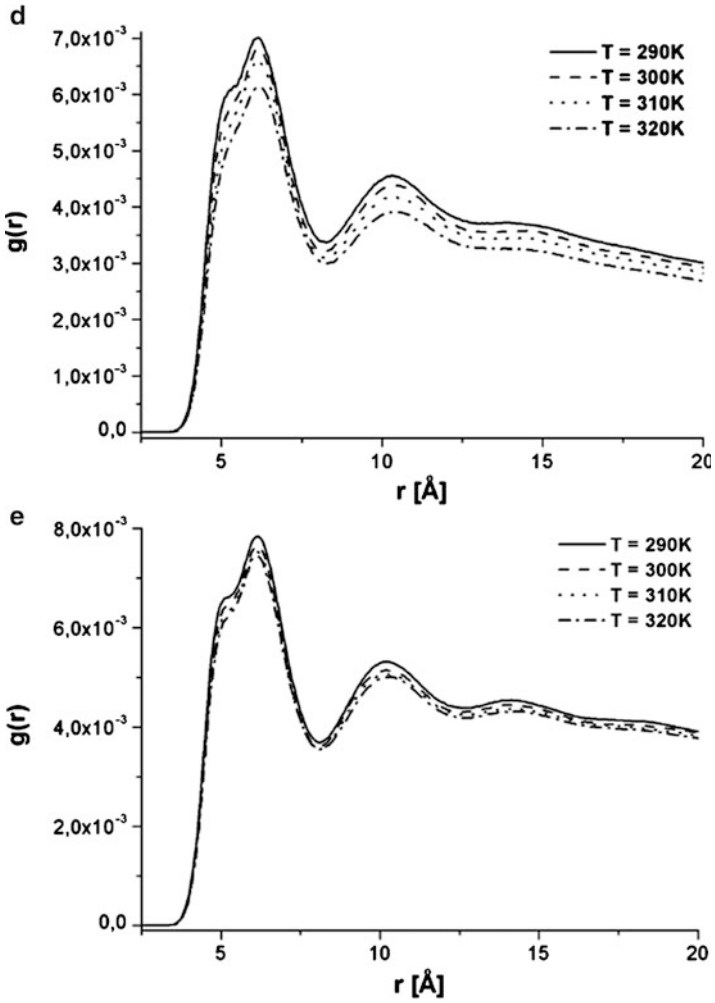

Fig. 25.12 (continued)

temperatures, including physiological ($T = 290$, 300, 310 and 320 K). Presented results show that homocysteine molecules in clusters keep together in all temperatures studied, the clusters do not disintegrate. The phase transition does not appear in the temperature range studied. The mobility of homocysteine molecules in clusters moderate increases with the raising of temperature. In case of homocysteine molecules surrounded by water, the process of dissolving homocysteine ensemble appears, even at the lowest temperature. This is particularly visible in the small systems ($n = 30$, 65 molecules).

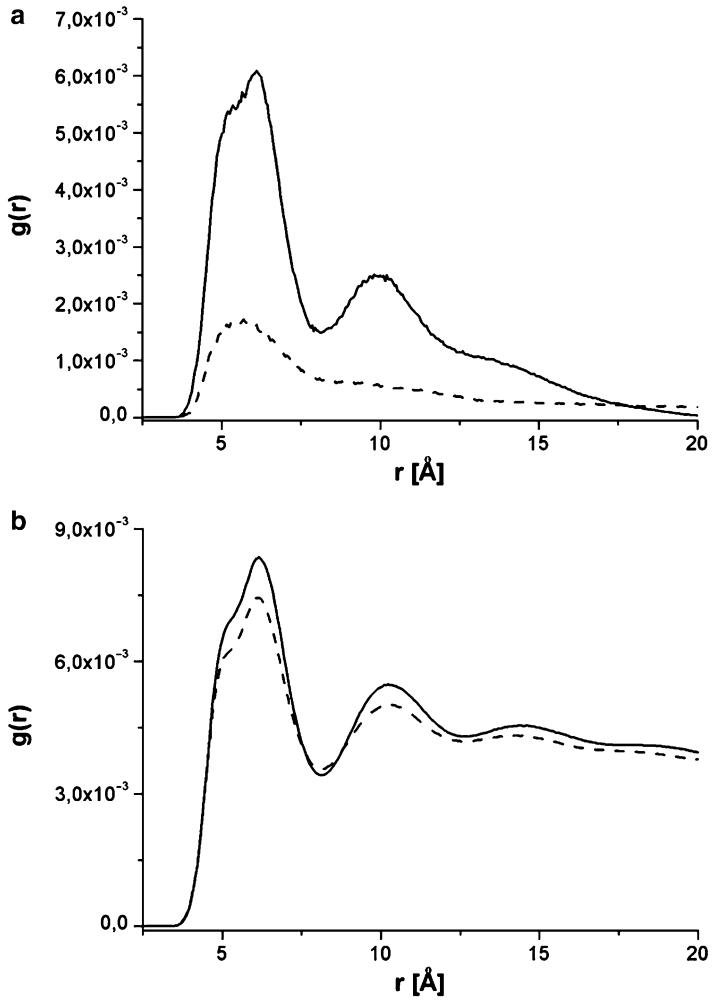

Fig. 25.13 The comparison of the radial distribution function of homocysteine for the systems build of: (**a**) $n = 30$ and (**b**) $n = 2{,}500$ molecules, at $T = 320$ K. The *solid line* represents the pure cluster, the *dotted line* corresponds to the system with water

Our simulations show that at the physiological temperature and in water environment the homocysteine cannot create the groups of molecules even at high concentration. Homocysteine is sometimes seen as one of the presumptive factors increasing the risk of cardiovascular disease. However, our simulations suggest that homocysteine's action, if contributes to the development of atherosclerosis, could be different from the formation of atherosclerotic plaques, triggered out by the settlement of cholesterol lodgment. That is because the homocysteine in water environment (water is substantial component of blood) cannot create the lodgment.

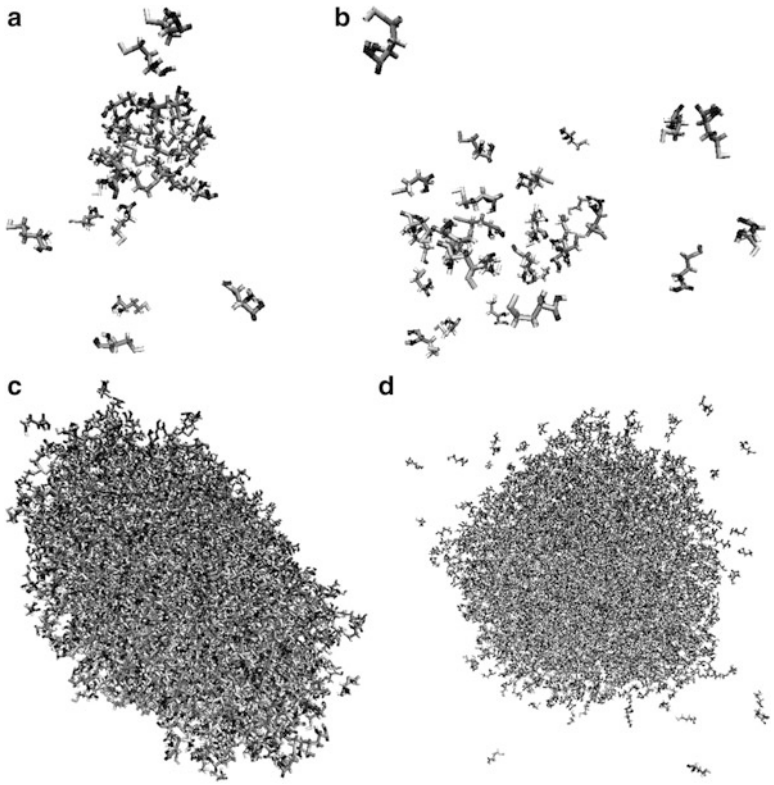

Fig. 25.14 The final configurations for the systems with water containing $n = 30$ (**a**, **b**) and $n = 2{,}500$ (**c**, **d**) homocysteine molecules, at $T = 290$ K (**a**, **c**) and at $T = 320$ K (**b**, **d**)

References

1. Graham I, Refsum H, Rosenberg IH, Ueland PM, Shuman JM (1997) Homocysteine metabolism: from basic science to clinical medicine. Springer, Boston
2. Carmel R, Jacobsen DW (2011) Homocysteine in health and disease. Cambridge University Press, Cambridge
3. McCully KS (1999) The homocysteine revolution: medicine for the new millennium. Keats Publications, Los Angeles
4. Fakhrzadeh H, Ghotbi S, Larijani B (2007) THE role of homocysteine in health and disease. Iran J Diabetes Lipid Disord 7:135–149
5. Houcher Z, Houcher B, Touabti A, Begag S, Egin Y, Akar N (2012) Nutritional factors, homocysteine and C677T polymorphism of the methylenetetrahydrofolate reductase gene in Algerian subjects with cardiovascular disease. Pteridines 23:14–21
6. Huang C, Zhang L, Wang Z, Pan H, Zhu J (2011) Endothelial progenitor cells are associated with plasma homocysteine in coronary artery disease. Acta Cardiol 66:773–777. doi:10.2143/AC.66.6.2136962
7. Robinson K (2000) Homocysteine and vascular disease. Springer, Dordrecht

8. Frayn KN, Stanner S, British Nutrition Foundation (2005) Cardiovascular disease: diet, nutrition and emerging risk factors□: the report of a British Nutrition Foundation task force. Published by Blackwell for the British Nutrition Foundation, Oxford, UK; Ames
9. Maitland-van der Zee A-H, Lynch A, Boerwinkle E, Arnett DK, Davis BR, Leiendecker-Foster C, Ford CE, Eckfeldt JH (2008) Interactions between the single nucleotide polymorphisms in the homocysteine pathway (MTHFR 677C > T, MTHFR 1298 A > C, and CBSins) and the efficacy of HMG-CoA reductase inhibitors in preventing cardiovascular disease in high-risk patients of hypertension: the GenHAT study. Pharmacogenet Genomics 18:651–656
10. Enneman AW, van der Velde N, de Jonge R, Heil SG, Stolk L, Hofman A, Rivadeneira F, Zillikens MC, Uitterlinden AG, van Meurs JBJ (2012) The association between plasma homocysteine levels, methylation capacity and incident osteoporotic fractures. Bone 50:1401–1405. doi:10.1016/j.bone.2012.03.013
11. Nagele P, Tallchief D, Blood J, Sharma A, Kharasch ED (2011) Nitrous oxide anesthesia and plasma homocysteine in adolescents. Anesth Analg 113:843–848. doi:10.1213/ANE.0b013e31822402f5
12. Bergen NE, Jaddoe VWV, Timmermans S, Hofman A, Lindemans J, Russcher H, Raat H, Steegers-Theunissen RPM, Steegers EAP (2012) Understanding health behaviours in a cohort of pregnant women at risk of gestational diabetes mellitus: an observational study. BJOG 119:739–751. doi:10.1111/j.1471-0528.2012.03321.x
13. Reyna-Villasmil E, Mejia-Montilla J, Torres-Cepeda D, Santos-Bolívar J, Aragon-Charrys J, Reyna-Villasmil N, Bravo-Henríquez A (2012) Efecto de las hormonas sexuales sobre las concentraciones de homocisteína en preeclámpticas y embarazadas normales. Prog Obstet Ginecol 55:226–231
14. Brozek W, Hassler N, Varga F, Klaushofer K, Paschalis EP (2012) Effect of bisphosphonates on gene expression of fibroblasts cultured in the presence of homocysteine. Bone 51:S8–S8. doi:10.1016/j.bone.2012.08.021
15. Zoungas S, McGrath BP, Branley P, Kerr PG, Muske C, Wolfe R, Atkins RC, Nicholls K, Fraenkel M, Hutchison BG, Walker R, McNeil JJ (2006) Cardiovascular morbidity and mortality in the atherosclerosis and folic acid supplementation trial (ASFAST) in chronic renal failure. J Am Coll Cardiol 47:1108–1116. doi:10.1016/j.jacc.2005.10.064
16. Grammatikopoulos P, Cassidy C, Singh V, Benelmekki M, Sowwan M (2014) Coalescence behaviour of amorphous and crystalline tantalum nanoparticles: a molecular dynamics study. J Mater Sci 49:3890–3897. doi:10.1007/s10853-013-7893-5
17. Kremer F (2002) Dielectric spectroscopy—yesterday, today and tomorrow. J Non-Cryst Solids 305:1–9. doi:10.1016/S0022-3093(02)01083-9
18. Dawid A, Gburski Z (1997) Dynamical properties of the argon-krypton clusters: molecular dynamics calculations. J Mol Struct 410–411:507–511. doi:10.1016/S0022-2860(96)09512-9
19. Grest G, Kremer K (1986) Molecular-dynamics simulation for polymers in the presence of a heat bath. Phys Rev A 33:3628–3631. doi:10.1103/PhysRevA.33.3628
20. Barker J, Fisher R, Watts R (1971) Liquid argon—Monte Carlo and molecular dynamics calculations. Mol Phys 21:657–673. doi:10.1080/00268977100101821
21. Kachel A, Gburski Z (1998) Chain formation in a model dipolar liquid: computer simulation study. J Phys Condens Matter 9:10095. doi:10.1088/0953-8984/9/46/007
22. Kosmider M, Dendzik Z, Palucha S, Gburski Z (2004) Computer simulation of argon cluster inside a single-walled carbon nanotube. J Mol Struct 704:197–201. doi:10.1016/j.molstruc.2004.02.050
23. Toukan K, Rahman A (1985) Molecular-dynamics study of atomic motions in water. Phys Rev B 31:2643–2648. doi:10.1103/PhysRevB.31.2643
24. Dawid A, Gburski Z (2003) Interaction-induced light scattering in a fullerene surrounded by an ultrathin argon atmosphere: molecular dynamics simulation. Phys Rev A 68:065202. doi:10.1103/PhysRevA.68.065202
25. Parrinello M, Rahman A (1981) Polymorphic transitions in single-crystals—a new molecular-dynamics method. J Appl Phys 52:7182–7190. doi:10.1063/1.328693

26. Gburski Z, Gray CG, Sullivan DE (1984) Lineshape in collision-induced absorption. Mori theory. Chem Phys Lett 106:55–59. doi:10.1016/0009-2614(84)87010-4
27. Pabis A, Geronimo I, York DM, Paneth P (2014) Molecular dynamics simulation of nitrobenzene dioxygenase using AMBER force field. J Chem Theory Comput 10:2246–2254. doi:10.1021/ct500205z
28. Smith L, Zimmerman JA, Hale LM, Farkas D (2014) Molecular dynamics study of deformation and fracture in a tantalum nano-crystalline thin film. Model Simul Mater Sci Eng 22:045010. doi:10.1088/0965-0393/22/4/045010
29. Raczynski P, Dawid A, Pietek A, Gburski Z (2006) Reorienatational dynamics of cholesterol molecules in thin film surrounded carbon nanotube: molecular dynamics simulations. J Mol Struct 792–793:216–220. doi:10.1016/j.molstruc.2006.01.064
30. Rahman A, Stillinger FH (1971) Molecular dynamics study of liquid water. J Chem Phys 55:3336–3359. doi:10.1063/1.1676585
31. Gwizdala W, Górny K, Gburski Z (2008) Molecular dynamics and dielectric loss in 4-cyano-4-n-pentylbiphenyl (5CB) mesogene film surrounding carbon nanotube—computer simulation. J Mol Struct 887:148–151. doi:10.1016/j.molstruc.2007.12.045
32. Kale L, Skeel R, Bhandarkar M, Brunner R, Gursoy A, Krawetz N, Phillips J, Shinozaki A, Varadarajan K, Schulten K (1999) NAMD2: greater scalability for parallel molecular dynamics. J Comput Phys 151:283–312. doi:10.1006/jcph.1999.6201
33. Phillips JC, Braun R, Wang W, Gumbart J, Tajkhorshid E, Villa E, Chipot C, Skeel RD, Kalé L, Schulten K (2005) Scalable molecular dynamics with NAMD. J Comput Chem 26:1781–1802. doi:10.1002/jcc.20289
34. Humphrey W, Dalke A, Schulten K (1996) VMD: visual molecular dynamics. J Mol Graph Model 14:33–38. doi:10.1016/0263-7855(96)00018-5
35. Price S (2011) Importing medicines: the VMD's special import and special treatment schemes. Vet Rec 168:445–446. doi:10.1136/vr.d2617
36. Allen MP, Tildesley DJ (1989) Computer simulation of liquids. Clarendon Press; Oxford University Press, Oxford
37. Frenkel D, Smit B (2001) Understanding molecular simulation, second edition: from algorithms to applications, 2nd edn. Academic, San Diego
38. Rapaport DC (2004) The art of molecular dynamics simulation. Cambridge University Press, New York
39. Raczynski P, Dawid A, Sakol M, Gburski Z (2007) The influence of the carbon nanotube on the structural and dynamical properties of cholesterol cluster. Biomol Eng 24:572–576. doi:10.1016/j.bioeng.2007.08.010
40. Dawid A, Gburski Z (2007) Dielectric relaxation of 4-cyano-4-n-pentylbiphenyl (5CB) thin layer adsorbed on carbon nanotube—MD simulation. J Non-Cryst Solids 353:4339–4343. doi:10.1016/j.jnoncrysol.2007.02.072
41. MacKerell AD Jr, Banavali N, Foloppe N (2000) Development and current status of the CHARMM force field for nucleic acids. Biopolymers 56:257–265. doi:10.1002/1097-0282(2000)56:4<257::AID-BIP10029>3.0.CO;2-W
42. Jorgensen WL, Chandrasekhar J, Madura JD, Impey RW, Klein ML (1983) Comparison of simple potential functions for simulating liquid water. J Chem Phys 79:926. doi:10.1063/1.445869
43. Jena P, Rao BK, Khanna SN (2013) Physics and chemistry of small clusters. Springer, New York
44. Stassen H, Gburski Z (1994) Instantaneous normal-mode analysis of binary-liquid Ar-Kr mixtures. Chem Phys Lett 217:325–332. doi:10.1016/0009-2614(93)E1390-3
45. Schneider T, Stoll E (1973) Molecular-dynamics investigation of structural phase-transitions. Phys Rev Lett 31:1254–1258. doi:10.1103/PhysRevLett.31.1254
46. Wentzcovitch R (1991) Invariant molecular-dynamics approach to structural phase-transitions. Phys Rev B 44:2358–2361. doi:10.1103/PhysRevB.44.2358

47. Gburski Z (1985) Convergence of memory functions for the vibrational dephasing process in liquids. Chem Phys Lett 115:236–240. doi:10.1016/0009-2614(85)80687-4
48. Fisher D, Fisher M, Huse D (1991) Thermal fluctuations, quenched disorder, phase-transitions, and transport in type-II superconductors. Phys Rev B 43:130–159. doi:10.1103/PhysRevB.43.130
49. Vicsek T, Czirok A, Benjacob E, Cohen I, Shochet O (1995) Novel type of phase-transition in a system of self-driven particles. Phys Rev Lett 75:1226–1229. doi:10.1103/PhysRevLett.75.1226
50. Dawid A, Dendzik Z, Gburski Z (2004) Molecular dynamics study of ultrathin argon layer covering fullerene molecule. J Mol Struct 704:173–176. doi:10.1016/j.molstruc.2004.01.065

Chapter 26
Nanocomposites in Technology of Cryopreservation of Sperm Boars

S.I. Kovtun, N.P. Galagan, O.V. Shcherbak, O.S. Osypchuk, and N.Yu. Klymenko

26.1 Introduction

Currently, in modern livestock, the method of deep-freezing of reproductive cells and animals embryos in so-called cryomedium is used, which provides for long-term preservation of genetic resources. Those media promote reduction of waste resulting in cold shock which causes damage of cell structure and decrease of cell viability. That is why the improvement of long-term preservation of gene pool essentially depends upon cryomedium which can promote increase of cell viability after thawing. Thus, the search of substances for cryomedium providing increase of undamaged cells during freezing is an important factor for optimization of cryotechnology.

Pig breeding is a traditional branch of livestock in Ukraine. But methods of cryoconservation of boar sperm are still complicated due to its physiological peculiarities. That is why obtaining of stable high results of artificial insemination is a complicated task. It is known [1] that preservation of vitality of boar spermatozoa during low-temperature treatment depends first of all upon methodical approach to the problem.

It is known also [2] that the addition of ultrafine silica (UFS) as an admixture to standard cryomedium in certain concentrations is able to stimulate viability of bull spermatozoa. Modification of UFS surface by some biomolecules, for example, mono- and oligosugars, allowed to synthesize on this basis promising

S.I. Kovtun • O.V. Shcherbak (✉) • O.S. Osypchuk
Biotechnology Laboratory, Institute of Animal Breeding and Genetics nd.a.
M.V. Zubets, National Academy of Agrarian Science of Ukraine, 1b Pogrebnyaka St.,
v. Chubinske, Borispol District, Kiev 08321, Ukraine
e-mail: ov19792006@yandex.ru

N.P. Galagan • N.Yu. Klymenko
O.O.Chuiko Institute of Surface Chemistry, National Academy of Science of Ukraine,
17 Gen. Naumova St., Kiev 03164, Ukraine

O. Fesenko, L. Yatsenko (eds.), *Nanoplasmonics, Nano-Optics, Nanocomposites, and Surface Studies*, Springer Proceedings in Physics 167,
DOI 10.1007/978-3-319-18543-9_26

nanocomposites (NC) which being admixed to various cryomedia containing spermatozoa of bulls, rams, and men provide for better mobility and survival [3].

The method of cryoconservation for spermatozoa, extracted from boar epididymis of the testicles using lactose-glycerol-yolk (LGY) medium [4] and some other NC synthesized in the O.O. Chuiko Institute of Surface Chemistry of NAS of Ukraine using bovine serum albumin (UFS/BSA) and carbohydrate sucrose (UFS/sucrose). It was found out that preliminary treatment of UFS surface by protein with next immobilization of sucrose on its surface decreased biological activity of such NC, opposite to NC UFS/BSA. As the result of those studies, it was proposed to use carbohydrates, serving as terminal fragments of cell receptors and a number of biopolymers.

Among them, it concerns so-called sialic acids (acylated neuraminic acids) including *N*-acetyl-neuraminic acid (NANA) [5]. They play the main role in reception of media signals and in contact mechanisms of the cells. It is known also [6, 7] that viability of cells depends essentially upon negative charge of its surface. It was also shown in [5] that value of electric charge of cell surface depends essentially upon NANA. Decialization of cell surface decreases functional activity of the cell due to decrease of its surface charge.

It is accepted [8] that formation of complexes on the cell membrane is based on the principle of complementarity of chemical structures. That is why in synthesis of NC, the aim was to use NANA to provide for essential affinity to cell surface. But previously [9] it was found out that non-covalent adsorption was not efficient in immobilization of NANA on the surface of UFS. That is why the pretreatment by BSA was used for fixation of the carbohydrate on the surface.

26.2 Materials and Methods

UFS (A-300, $S_{sp} = 285$ m^2/g, Ukraine, Kalush) was used as an adsorbent to obtain nanocomposites (NC) with protein and NANA. The surface was preliminary thermally treated at 400 °C for 2 h. NC was obtained by non-covalent adsorption in consequent order from water solution, firstly BSA ("Fluka," Swiss) and then NANA ("Sigma-Aldrich," USA).

Adsorption conditions are 2 h for protein and 1 h for NANA with permanent mixing at 22–23 °C. The adsorbate-to-adsorbent ratio was 1:10. The concentration of protein solution was 1–14 mg/mL and NANA solutions 16–60 μg/mL. The protein was adsorbed at pH 4.8. Solid phase was separated by centrifugation (4,000 fr/min, 10 min). Then residue was dried at 37 °C and mechanically crushed. Then the desorption of biomolecules to water was done and samples were dried once more and used in further experiments.

In the liquid layer concentrations of protein or NANA were measured by methods (according to [10, 11]) using spectrophotometer Lambda-35 (Perkin-Elmer, USA) and photoelectrocolorimeter KFK-2.

Adsorption parameters were calculated according to formula by [12]: $A - (C_{init} - C_{equil})\ V/m$, where C_{init} is the initial concentration in solution, mg/mL or

μg/mL; C_{equil}, equilibrium concentration, mg/mL or μg/mL; V, volume, mL; and m, mass, g.

Efficiency of adsorption interaction of biomolecules with UFS was estimated by isotherms of adsorption. The calculation of maximum adsorption value A_∞ was done according to [13].

The presence of immobilized protein on the surface of UFS nanoparticles was confirmed by mass spectrometry and infrared spectroscopy (IR spectroscopy). The surface of NC UFS/BSA/NANA was studied by IR spectroscopy.

Mass spectrometric measurements were conducted by temperature-programmed desorption mass spectrometry (TPD MS) method using MX-7304A equipment (Ukraine, Sumy). Specific details and features of TPD MS method are revealed in [14].

IR spectra were obtained using Thermo Nicolet Nexus FTIR in the range of 4,000–400 cm^{-1}. The probes were mixed with slightly dried KBr (Riedel-de Haen, France) in ratios of 1:19 (for protein) and 1:4 (for NANA). Spectra treatment was done using program "Omnic."

To assess the biological activity of NC, we used cryopreserved ejaculation boar sperm. The research was conducted in the Laboratory of Biotechnology, Institute of Animal Breeding and Genetics nd.a. M.V. Zubets of NAAS. NC after thawing sperm was added in three concentrations—0.1, 0.01, and 0.001 % (experimental group). The effect of adding UFS/BSA/NANA on the viability of thawed ejaculated Mirgorodska breed boar sperm was therefore investigated (Dnipro 641, Komush 853, Kohanyy 289). The effect on the viability of gametes in three concentrations (0.1, 0.01, 0.001 %) was assessed by motility percentage. It was expected that the use of this nanocomposite added after thawing the sperm eliminates existing complications and will increase the viability of the genetic material of endangered pig's breeds.

26.3 Results and Conclusions

It is known that adsorption isotherms depend upon the mechanism of adsorbent-adsorbate interaction. According to Fig. 26.1a, b, the isotherms of BSA and NANA may be attributed to Langmuir type [15]. It confirms the strong interaction of

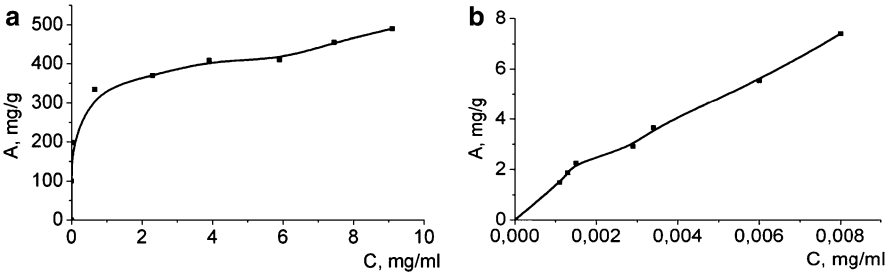

Fig. 26.1 Adsorption isotherms of BSA (**a**) and NANA (**b**) on UFS surface

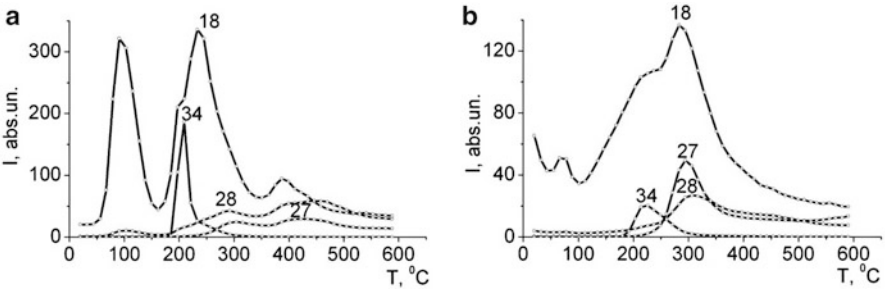

Fig. 26.2 Thermograms of decomposition of BSA in condensed (**a**) and adsorbed (**b**) states

protein and the surface of UFS. Maximum adsorption (A_∞) is 410 mg/mL and desorption does not exceed 11.3 %. The isotherm presented in Fig. 26.1b makes clear that preliminary immobilization of protein on the UFS surface promotes NANA adsorption. Desorption of NANA is insignificant (less than 0.015 %).

TPD MS and IR spectroscopy in accordance with adsorption results allow studying the specific features of surface layer formation of NC.

In Fig. 26.2 thermograms of BSA in condensed and adsorbed on UFS surface states are presented. The appearance of the peak at 34 a.u. during the UFS decomposition in condensed state was observed which was interpreted as molecular mass of hydrogen sulfide which appeared as the result of decomposition of sulfur-containing amino acids of protein. In accord with results in extension of maximum thermal liberation adsorption of 34 a.u. from 30 to 60 °C and more, process of thermal destruction loses its cooperative character as the result of becoming a possible interaction of BSA with the surface of ultrafine carrier. It is caused also by both decrease of number of OH groups on UFS surface and also by increase of adsorbed protein amount. Decrease of peak intensity is caused by the stabilization of protein molecule as the result of contact with the adsorbent.

During thermolysis three maxima of dehydration are observed. The first one is located about 100 °C and it is the most intense for condensed BSA. The second one is observed about 200 °C, which coincides with sulfur hydride by localization and kinetics. And the third one is located between 250 and 300 °C and correlates with temperature maxima of 27 and 28 a.u. Previously [16] we found out that the peak at 34 a.u. may serve as a test one for protein layer. Later [17] the presence of the same peak was confirmed also by other authors as the result of fixation of protein on carbon material.

In IR spectra of initial silica (Fig. 26.3, curve 2), the stripe of valent OH vibrations was detected in the 3,750 cm^{-1} region, which belongs to isolated OH groups. Decrease of adsorption stripe intensity at $\lambda = 3{,}750$ cm^{-1} which was observed after the contact of BSA or NANA with UFS/BSA (Fig. 26.3) testifies in favor of the possibility of formation of hydrogen links with surface layer of hydroxyl groups, thus confirming immobilization of biomolecules on adsorbent surface.

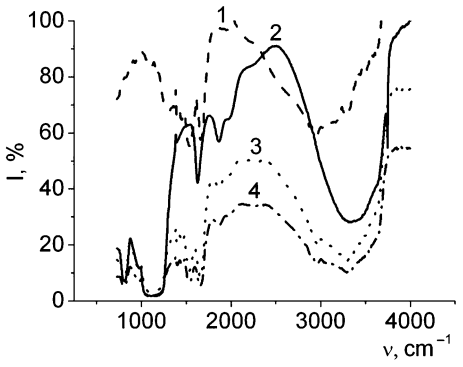

Fig. 26.3 IR spectra of biomolecules adsorbed on the surface of ultrafine silica: 1, BSA; 2, UFS; 3, UFS/BSA/NANA; 4, UFS/BSA

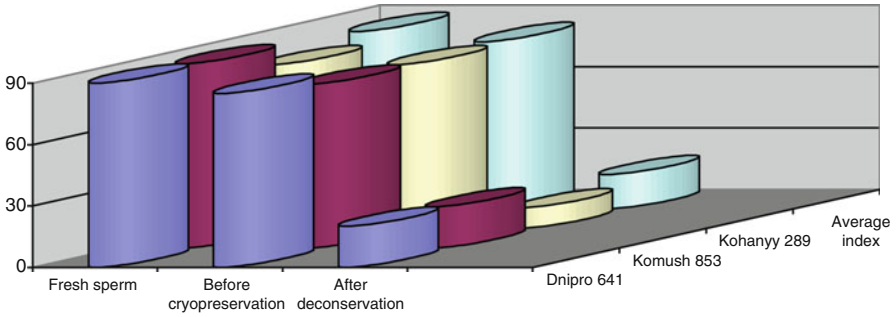

Fig. 26.4 Indicators of viability of ejaculated Mirgorodska breed boar's sperm

It testifies in favor of their connection with functional groups of adsorbed molecules [18]. In the case UFS/BSA the shift of absorption bands is observed for amid I, the valence oscillations of C=O and C–N– (from 1,650 to 1,657 cm^{-1}), and amid II, valence C–N and deformation vibrations N–H – (from 1,550 to 1,657 cm^{-1}), which are characteristic of IR spectroscopy of proteins [19]. So, there is reason to suppose formation of H-bond between N–H-groups of BSA molecule and hydroxyl groups of UFS [20].

In IR spectra NC UFS/BSA/NANA (Fig. 26.3, curve 3), disappearance or decrease of absorption bands in the region of $3{,}500 - 3{,}100$ cm^{-1}, characteristic for N–H-band in amino acids of carbohydrates, band 1,730 cm^{-1} and also a number of bands in the region of $1{,}241 - 1{,}015$ cm^{-1}, which are caused by deformation vibrations of CH_3^-, CH_2^- та CH^- groups [21]. Thus, the immobilization of NANA on the surface of the biocomposite UFS/BSA occurs with participation of hydroxyl, carbonyl, and amino groups both of protein and carbohydrate.

Through surface modification UFS by the protein BSA, made possible immobilization NANA, which allowed the production NC.

It is shown that sperm freshly obtained boars were active on average at 86.7 % (Fig. 26.4). After dilution and 3-h equilibration at +4 °C, sperm activity decreased by an average of 5 %. The process of cryopreservation has affected them so that,

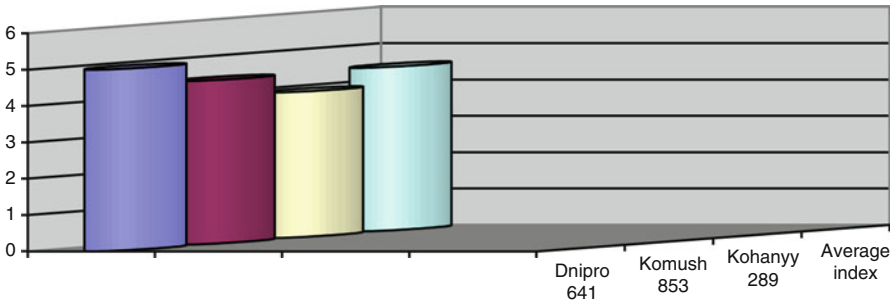

Fig. 26.5 Survival (in hours) of thawed ejaculated Mirgorodska breed boar's sperm

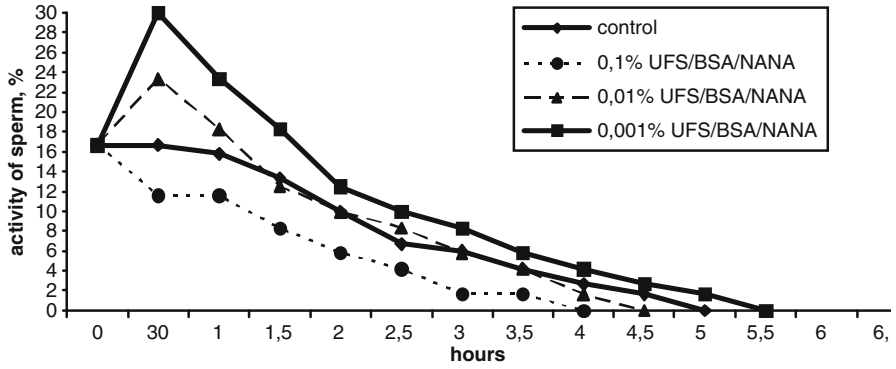

Fig. 26.6 Effect of nanocomposites UFS/BSA/NANA on the viability of thawed ejaculated boar's sperm

after thawing, boar sperm activity was 65 % lower compared to this indicator before freezing.

When analyzing the viability of sperm after thawing, it was found that their average survival rate is about 4.5 h (Fig. 26.5).

In experimental groups (Fig. 26.6) in 30 min, most active were the average sperm that were of 0.001 % concentration UFS/BSA/NANA (30 % ± 0.58), which is 13.3 % higher compared to the control (sperm with no added nanocomposites).

The lowest activity have spermatozoa that incubated in concentration 0.1 % UFS/BSA/NANA for 30 min, their activity decreased, compared with control at 5.1 %. In analyzing the activity of sperm, the remaining research groups with 0.1 % concentration nanocomposite UFS/BSA/NANA established that their activity decreased by 18 % compared to 0.001 % and 11.7 % compared to 0.01 % concentration UFS/BSA/NANA. Therefore, it is inappropriate to add 0.1 % UFS/BSA/NANA to thawed boar sperm, as significant decrease in its activity is observed. This indicates that high concentration nanocomposite, leads a rapid saturation of surface cell receptors spermatozoa this nanocomposite, which reduced their activity.

After 60 min of the start of the experiment, sperm from 0.001 % UFS/BSA/NANA (23.3 % ± 3.33) were the most active. As a control for this period, significantly lower activity of sperm (15.8 % ± 3.0), compared with the above experimental group and 0.01 % concentration UFS/BSA/NANA, was observed.

After 1.5 h from baseline, the control and experimental groups had a gradual decrease in activity. Absence of activity was observed in the control group at 5 h.

In the experimental group, with 0.1 % concentration UFS/BSA/NANA, absence of activity was noted at the fourth hour of the experiment. It should be noted that research groups containing 0.001 and 0.01 % UFS/BSA/NANA, as well as control, were similar period of survival that does not exceed 5 h. When we study the effect of different concentrations of nanocomposites, boar sperm viability proved most active sperm when adding 0.001 % concentration UFS/BSA/NANA. This concentration provided the initial increase in activity of sperm (Fig. 26.6) to the level of 30.0 %, but with more rapid declines at 5.5 h.

Thus, due to preliminary modification of UFS surface by protein, the immobilization of NANA on its surface was realized and NC on this basis was obtained. There is a reason to state that increase of gamete activity in the presence of NC is caused by high chemical affinity of synthesized NC to certain components of semen or to corresponding cell receptors. It is not excluded that this effect can accelerate metabolic transformations in energy supply system.

Have been worked out the conditions of synthesis the NC based on UFS, protein, and NANA by the method of their consecutive adsorption on the surface of the carrier. The NC samples as an admixture to cryomedium for thawed boar sperm.

It is shown that the most active proved to concentration 0.001 % UFS/BSA/NANA, this concentration NC in thawed ejaculation boar spermatozoa provide a positive impact on the viability of sperm.

In the present research we used the method of cryopreservation of ejaculation boars sperm Mirgorodskaya breeds and set efficiency UFS/BSA/NANA on improved viability sperm.

So, we proposed scheme of use nanocomposites in technology thawing of sperm boar's, that is essential for the implementation tasks of conservation and management of genetic resources of farm animals and reproduction of endangered breeds of pigs.

References

1. Eskin GV, Narizhnyj AG, Pochodnya GS (2007) Teoriya i praktika iskusstvennogo osemeneniya svinej svezhevzyatoj i zamorozhennoj spermoj [Theory and practice of artificial insemination of pigs taken fresh and frozen sperm]. Vezelica, Belgorod, p 253 (in Russian)
2. Nedava VE, Chujko AA, Begma LA, Begma AA (1990) Ispolzovanie aerosilov v praktike iskusstvennogo osemeneniya [Using aerosil in practice artificial insemination]. Zootechniya 8:63–65 (in Russian)
3. Galagan NP (2006) Nanomaterialy na osnove vysokodyspersnogo kremnezema i biomolekul v sredah s reproduktivnymy kletkami [Nanomaterials based on highly dispersed silica and

biomolecules in environments with reproductive cells]. In: Materialy II Vserosijskoj nauchnoj konferencii s megdunarodnym uchastiem “Sorbenty kak factor kachestva gyzni I zdorovja” [Materials of the II All-Russian Scientific Conference with International Participation “Sorbents as a factor in the quality of life and health”], Moscow, Belgorod, pp 55–59 (in Russian)
4. Galagan NP, Siora IV, Kovtun SI, Scherbak OV (2007) Nanocomposites in biotechnology for prolonged preservation of gene pool (synthesis and application). In: XI Polish—Ukrainian symposium “Theoretical and experimental studies of interfacial phenomena and their technological applications”, Krasnobrod, Zamosc, 22–26 Aug 2007, p 27
5. Meddy E (1979) Biochimicheskoe issledovanie membrane [Biochemistry investigation of membrane]. Mir, Moskow, 460p (in Russian)
6. Vasil’ev YuM, Malenkov AG (1963) Kletochnaja poverchnost’ i reakzii kletki [Cell surface and reaction of cell]. Medizina, Leningrad, 291p (in Russian)
7. Gennis R (1997) Biomembrany. Molekuljarnaja struktura I funkzii [Biomembranes. Molekular structure and function]. Mir, Moskwa, 624p (in Russian)
8. Vierula M, Rayamiemi H (1983) Effect of seminal plasma and calcium on the stability of the surface protein composition of ejaculated bull spermatozoa. Andrologia 15(5):436–445
9. Kulik TV, Paljanitsja BB, Galagan NP (2004) Molecular self-organizing in systems nanodimensional particles-carbohydrates. Nanosyst Nanomater Nanotechnol 1(2):681–690 (in Russian)
10. Kochetkov GA (1980) Prakticheskoe rukovodstvo po enzimologii [Practical guidance on enzymology]. Vysshaja shkola, Moskwa, pp 222–226 (in Russian)
11. Prochorova MI (1982) Metody biochimicheskich issledovaniy(lipidnyy i energeticheskiy obmen) [Methods of biochemical researches (lipid and energy exchange)]. Izdatel’stvo Leningratskogo universiteta, Leningrad, 272p (in Russian)
12. Chuiko AA (2003) Medizinskaja chimija i klinicheskoe primenenie dioksida kremnija [Medical chemistry and clinical application of silicon dioxyde]. Naukova dumka, 415p (in Russian)
13. Mitrophanov PP (1950) Praktikum po fizicheskoy i kolloidnoy chimii [Practical work for physical and colloidal chemistry]. Medgiz, 183p (in Russian)
14. Pokrovskiy VA (1995) Temperature-programmed mass-spectrometry of biomolecules in surface chemistry. Rapid Commun Mass Spectrom 9:588–591
15. Parfit G, Rochester C (1986) Adsorbzija iz rastvorov na poverchnosti tvjerdyh tel [Adsorption from solutions at the solid/liquid interface]. Mir, Moskwa, 488p (in Russian)
16. Klymenko NY, Galagan NP, Mischanchuk BG, Zarko VI, Pokrovskiy VO (2008) Temperaturno-programovana desorbziyna mass-spektrometrija bychachogo syrovatkovogo al’buminu v kondensovanomu stani i adsorbovanogo na poverchni vysokodyspersnyh oksydiv. Chimia, fizika I technologija poverchnosti 14:456–466 (in Ukrainian)
17. Gadiou R, Santos dos EA, Vijayaraj W, Anselme K, Dentzer J, Soares GA, Vix-Guter C (2009) Temperature-programmed desorption as a tool for quantification of protein adsorption capacity in micro- and nanoporous materials. Colloids Surf B Biointerfaces 73:168–174
18. Gun’ko VM, Turov VV, Gorbik PP (2009) Woda na mezhfaznoy granize [Water at the interface]. Naukova dumka, Kiew, 694p (in Russian)
19. Chirgadze YuN (1965) Infrakrasnye spektry I struktura polypeptidow I belkow [Infrared spectra and structure of polypeptides and proteins]. Nauka, Moscow, 134p (in Russian)
20. Tarasevich YuI, Monahova LI (2002) Wzaimodeystvie globuljarnogo al’bumina s poverchnost’ju kremnezjema [Interaction of globular albumins with silica surface]. Kolloidnyy zhurn [Coll J] 64(4):535–540 (in Russian)
21. Littls L (1969) Infrakrasnye spektry adsorbirovannyh molekul [IR spectres of adsorbed molecules]. Mir, Moskwa, 514p (in Russian)

Chapter 27
Plasmonic Nanochips for Application in Surface-Enhanced Fluorescence Spectroscopy: Factor of Dielectric Substrate

V.I. Chegel, O.M. Naum, A.M. Lopatynskyi, and V.K. Lytvyn

27.1 Introduction

The progress in modern nanotechnology, particularly nanoplasmonics, has initiated the development of a new class of optical sensor devices having sensing elements in the form of a nanochip with an array of high-conductive nanostructures, which is based on a localized surface plasmon resonance (LSPR) phenomenon. Such nanochip presents an optically transparent substrate, which the nanostructured surface of the noble metal, e.g. silver or gold, is somehow created on. If fluorophore molecules are placed at such a surface, then under certain conditions their emission intensity enhancement can be obtained compared to the case in the absence of nanostructures [1–3]. Sensors of this type make it possible to increase the sensitivity of measurements (e.g. detect the signal even from single molecules [4, 5]), and they are promising for applications in biochemistry and medicine.

To better understand the processes that affect the fluorescence intensity, we must examine in detail the interaction between the fluorophore molecule and the metal nanoparticle. The main characteristic of this interaction is the magnitude of the efficiency of energy exchange between the donor (fluorophore) and acceptor (nanoparticle). The energy exchange between the metal nanoparticle and fluorophore may occur involving the radiative and nonradiative processes that affect the enhancement and quenching of fluorescence. Which processes will dominate, depends on the characteristics of the system, such as the distance between donor and acceptor, the mutual orientation of their dipole moments, the fluorophore quantum yield, the size, and shape of metal nanoparticles. The possibility to change these characteristics allows regulating fluorescence response of fluorophore

V.I. Chegel (✉) • O.M. Naum • A.M. Lopatynskyi • V.K. Lytvyn
V.E. Lashkaryov Institute of Semiconductor Physics NAS of Ukraine,
41, Nauki Ave., Kyiv 03028, Ukraine
e-mail: vche111@yahoo.com

O. Fesenko, L. Yatsenko (eds.), *Nanoplasmonics, Nano-Optics, Nanocomposites, and Surface Studies*, Springer Proceedings in Physics 167,
DOI 10.1007/978-3-319-18543-9_27

molecules, adsorbed on the surface of metal nanostructures, and obtaining the enhancement or quenching of their radiation intensity.

Attention should be paid to the fact that during the nanochip fabrication metal nanoparticles in most cases are located on the surface of the dielectric substrate, which also makes its impact on the enhancement of the local electromagnetic field near metallic nanostructures and the enhancement of emission intensity of fluorescent molecules that are situated in this field. It should be noted that in the literature on the subject theoretical approaches are considered that do not account for the presence of a dielectric substrate, which the nanostructures are situated on [6–9]. Therefore, in this study the influence of the substrate dielectric permittivity on the behaviour of the local electromagnetic field intensity near the surface of spherical gold nanoparticle was theoretically demonstrated and the effect of the presence of a substrate on the quantum yield and emission of fluorophore molecules, located at the surface of such nanostructure, was determined.

27.2 Theory

Under the influence of external excitation, the metal nanoparticle in certain conditions induces the local electromagnetic field, which has a much higher strength than the field of external excitation. If a fluorophore molecule is placed at a certain distance from nanostructure, enhancement or quenching of molecule fluorescence can be observed. In order to mathematically simulate this problem, it is rational to divide it into two parts.

The first part of the problem is to find the local field strength near spherical gold nanoparticle on a dielectric substrate induced by external radiation, and hence the fluorophore molecule excitation rate. The second part involves finding the quantum yield and fluorescence rate of a fluorophore molecule.

Analysis of electromagnetic properties of nano-objects is closely related to the solution of Maxwell's equations [6]

$$\begin{aligned} &\nabla \times \mathbf{E}(\mathbf{r}) = i\omega \mathbf{B}(\mathbf{r}), \\ &\nabla \times \mathbf{H}(\mathbf{r}) = -i\omega \mathbf{D}(\mathbf{r}) + \mathbf{j}(\mathbf{r}), \\ &\nabla \mathbf{D}(\mathbf{r}) = \rho(\mathbf{r}), \\ &\nabla \mathbf{B}(\mathbf{r}) = 0, \end{aligned} \tag{27.1}$$

where

$$\begin{aligned} \mathbf{D} &= \varepsilon\varepsilon_0 \mathbf{E}, \\ \mathbf{B} &= \mu\mu_0 \mathbf{H}. \end{aligned}$$

The solution of the equations will be electric and magnetic fields as functions of the coordinates of a given distribution of currents $\mathbf{j}$ that create these fields. In nanophysics, unknown parameters of the electromagnetic field can be found using the analytical Green's function method [7]. This method reduces to integration over

the volume, which the currents are distributed in. For convenience, we write the fields **E** and **H** in terms of the vector potential **A** and scalar potential φ [6]:

$$\begin{aligned}\mathbf{E}(\mathbf{r}) &= i\omega\mathbf{A}(\mathbf{r}) - \nabla\varphi(\mathbf{r}),\\ \mathbf{H}(\mathbf{r}) &= \frac{1}{\mu\mu_0}\nabla\times\mathbf{A}(\mathbf{r}).\end{aligned} \tag{27.2}$$

Applying the Lorentz gauge to **A**

$$\nabla\mathbf{A}(\mathbf{r}) = i\omega\mu\mu_0\varepsilon\varepsilon_0\varphi(\mathbf{r})$$

and taking into account

$$\nabla\times\nabla\times = -\nabla^2 + \nabla\nabla,$$

we obtain inhomogeneous Helmholtz equations for the vector and scalar potentials, if we substitute these equations into the second equation of (27.1):

$$\begin{aligned}\left[\nabla^2 + k^2\right]\mathbf{A}(\mathbf{r}) &= -\mu\mu_0\mathbf{j}(\mathbf{r}),\\ \left[\nabla^2 + k^2\right]\varphi(\mathbf{r}) &= -\frac{\rho(\mathbf{r})}{\varepsilon\varepsilon_0}.\end{aligned} \tag{27.3}$$

Solution of equations (27.3) consists of a sum of homogeneous and particular solutions.

In many works [6–8], the dyadic Green's function defined by the environment is applied to calculate the electromagnetic field, which is created by a source of currents. The electric field **E** at a point **r**, which is created by a point dipole **μ** radiation at a point $\mathbf{r}'$ (Fig. 27.1) will be determined by the following equation:

$$\mathbf{E}(\mathbf{r}) = \omega^2\mu\mu_0\overleftrightarrow{\mathbf{G}}(\mathbf{r},\mathbf{r}')\boldsymbol{\mu}. \tag{27.4}$$

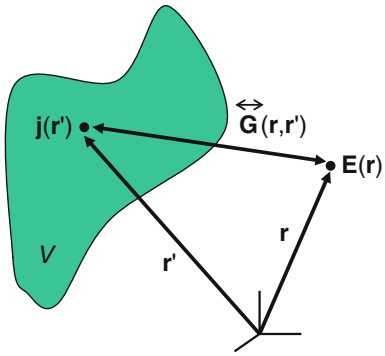

Fig. 27.1 Illustration for the determination of the electric field **E** at a point **r**, generated by the radiation of a current source **j** at a point $\mathbf{r}'$

For a point current source, Green's function is given by the inhomogeneous equation [6]

$$L\overleftrightarrow{\mathbf{G}}(\mathbf{r},\mathbf{r}') = \overleftrightarrow{\mathbf{I}}\,\delta(\mathbf{r}-\mathbf{r}'), \tag{27.5}$$

where L is an arbitrary linear operator, $\overleftrightarrow{\mathbf{I}}$ is the unit dyad, $\delta(\mathbf{r}-\mathbf{r}')$ is the delta function. In deriving the scalar Green's function for the Helmholtz equation, we replace the current source in (27.3) by the point current source, which is defined by the delta function, and get the following equation:

$$\left[\nabla^2 + k^2\right]G_0(\mathbf{r},\mathbf{r}') = -\delta(\mathbf{r}-\mathbf{r}'). \tag{27.6}$$

If a definition for the scalar Green's function is found, one can get a partial solution of (27.3). For vacuum, the only solution of (27.6) is

$$G_0(\mathbf{r},\mathbf{r}') = \frac{e^{-ik|\mathbf{r}-\mathbf{r}'|}}{4\pi|\mathbf{r}-\mathbf{r}'|}. \tag{27.7}$$

To determine the dyadic Green's function, we consider the wave equation for the electric field in a homogeneous medium:

$$\nabla\times\nabla\times\mathbf{E}(\mathbf{r}) - k^2\mathbf{E}(\mathbf{r}) = i\omega\mu_0\mu\,\mathbf{j}(\mathbf{r}). \tag{27.8}$$

Taking into account Eq. (27.4), we obtain

$$\nabla\times\nabla\times\overleftrightarrow{\mathbf{G}}(\mathbf{r},\mathbf{r}') - k^2\overleftrightarrow{\mathbf{G}}(\mathbf{r},\mathbf{r}') = \overleftrightarrow{\mathbf{I}}\,\delta(\mathbf{r}-\mathbf{r}'). \tag{27.9}$$

Within this approach, the general expressions for the strength of the electromagnetic fields generated by arbitrary-shaped nanoscale objects when irradiated with electromagnetic waves are called volumetric Lippmann-Schwinger equations and are as follows:

$$\begin{aligned}
\mathbf{E}(\mathbf{r}) &= \mathbf{E}_0(\mathbf{r}) + i\omega\mu_0\mu\int_V \overleftrightarrow{\mathbf{G}}(\mathbf{r},\mathbf{r}')\,\mathbf{j}(\mathbf{r}')dV', \quad \mathbf{r}\notin V,\\
\mathbf{H}(\mathbf{r}) &= \mathbf{H}_0(\mathbf{r}) + \int_V \left[\nabla\times\overleftrightarrow{\mathbf{G}}(\mathbf{r},\mathbf{r}')\right]\mathbf{j}(\mathbf{r}')dV', \quad \mathbf{r}\notin V,
\end{aligned} \tag{27.10}$$

where $\mathbf{E}(\mathbf{r})$ and $\mathbf{H}(\mathbf{r})$ are electric and magnetic fields at a point $\mathbf{r}$, respectively, which are generated by a current source $\mathbf{j}$ at a point $\mathbf{r}'$ (Fig. 27.1), V is a nanostructure volume.

The local field $\mathbf{E}$ can be found from the Lippmann-Schwinger equation (27.10). It is known that the local electromagnetic field enhancement observed near the metallic nanoscale objects of given shape and size occurs due to the surface plasmon resonance phenomenon. Localized surface plasmons can exist only at fixed

frequencies for specific conditions, which are called plasmon resonance frequencies. Nanoparticles with defined shapes and sizes have specific resonance frequency values, which the plasmon resonance line is observed at. For the theoretical determination of the plasmon resonance frequency and distribution of the corresponding electromagnetic fields inside and outside the nanoparticle, the method of effective susceptibility [10] is used as one of the main approaches in recent years. For convenience, this method does not operate with the resonant frequencies, but uses the corresponding dielectric permittivities. In this method, the main characteristic of the nanoparticle is its polarizability, which contains information about the dielectric constant of the nanoparticle material and depends on the environment. To calculate the local field strength in the case of spherical nanoparticles, the quasistatic polarizability is used, which is determined by the formula [6]

$$\overleftrightarrow{\boldsymbol{\alpha}} = \frac{4\pi\varepsilon_0\varepsilon_1 R^3(\varepsilon - \varepsilon_1)}{\varepsilon + 2\varepsilon_1}\overleftrightarrow{\mathbf{I}}, \tag{27.11}$$

where R is a nanoparticle radius, ε is the relative dielectric permittivity of the nanoparticle material, ε_1 is the relative dielectric permittivity of the environment, $\overleftrightarrow{\mathbf{I}}$ is the unit dyad. Plasmon resonance in this case is observed when approaching the condition $\varepsilon = -2\varepsilon_1$.

The presence of the substrate will affect the polarizability of the nanosphere. According to [11], polarizability of a nanoparticle on a dielectric surface can be calculated by the formula

$$\overleftrightarrow{\boldsymbol{\alpha}}(\varphi) = \left(1 - \frac{\varepsilon_2 - \varepsilon_1}{\varepsilon_1 + \varepsilon_2}\right)\overleftrightarrow{\boldsymbol{\alpha}}\left[\overleftrightarrow{\mathbf{I}} - \frac{\overleftrightarrow{\boldsymbol{\alpha}}\frac{\varepsilon_2-\varepsilon_1}{\varepsilon_1+\varepsilon_2}}{32\pi\varepsilon_0\varepsilon_1(R+\varphi)^3}\right]^{-1}, \tag{27.12}$$

where ε_2 is the relative dielectric permittivity of the substrate, φ is the surface-to-surface distance between the nanoparticle and the substrate.

So, if the polarizability of high-conductive nanoparticle is known and when its size is much smaller than the light wavelength, replacing the spherical nanoparticle with a point dipole with dipole moment $\overleftrightarrow{\boldsymbol{\alpha}}(\varphi)\mathbf{E}_0(\mathbf{r}')$ leads to the electric field strength generated by the dipole radiation, which can be calculated by the formula [9, 10]

$$\mathbf{E}(\mathbf{r}) = \frac{k^2}{\varepsilon_0}\overleftrightarrow{\mathbf{G}}(\mathbf{r},\mathbf{r}')\overleftrightarrow{\boldsymbol{\alpha}}(\varphi)\mathbf{E}_0(\mathbf{r}'), \tag{27.13}$$

where in accordance with [6] Green's function for the electromagnetic field at a given point will look like

$$\overleftrightarrow{\mathbf{G}}(\mathbf{r},\mathbf{r}') = \left(\overleftrightarrow{\mathbf{I}} + \frac{1}{k^2}\nabla\otimes\nabla\right)G_0(\mathbf{r},\mathbf{r}'). \tag{27.14}$$

Taking into account (27.7), (27.14) transforms as follows:

$$\overleftrightarrow{\mathbf{G}}(\mathbf{r},\mathbf{r}') = \frac{e^{ikW}}{4\pi W}\left[\left(1+\frac{ikW-1}{k^2W^2}\right)\overleftrightarrow{\mathbf{I}} + \frac{3-3ikW-k^2W^2}{k^2W^2}\frac{\mathbf{W}\otimes\mathbf{W}}{W^2}\right], \quad (27.15)$$

where $\mathbf{W} = \mathbf{r} - \mathbf{r}'$, $W = |\mathbf{r} - \mathbf{r}'|$.

In the case of near field, when $W \ll \lambda$, Eq. (27.15) is dominated by near-field components. In this approximation, Green's function can be found by the following formula [6]:

$$\overleftrightarrow{\mathbf{G}}_{\mathrm{NF}}(\mathbf{r},\mathbf{r}') = \frac{1}{4\pi W}\frac{1}{k^2W^2}\left(-\overleftrightarrow{\mathbf{I}} + 3\frac{\mathbf{W}\otimes\mathbf{W}}{W^2}\right). \quad (27.16)$$

Changes in the studied system configuration due to the nanosphere being placed on a dielectric substrate influence the distribution of electromagnetic field. Green's function in the presence of heterogeneity (in this case, the dielectric substrate) consists of two parts:

$$\overleftrightarrow{\mathbf{G}}(\mathbf{r},\mathbf{r}') = \overleftrightarrow{\mathbf{G}}^{\mathrm{D}}(\mathbf{r},\mathbf{r}') + \overleftrightarrow{\mathbf{G}}^{\mathrm{I}}(\mathbf{r},\mathbf{r}'), \quad (27.17)$$

where $\overleftrightarrow{\mathbf{G}}^{\mathrm{D}}(\mathbf{r},\mathbf{r}')$ is the direct part, where the presence of field heterogeneities is ignored, $\overleftrightarrow{\mathbf{G}}^{\mathrm{I}}(\mathbf{r},\mathbf{r}')$ is the indirect part, which takes into account existing field heterogeneities and the boundaries between them. When the field source and the point, which the field is observed at, are located in the same half-space with dielectric permittivity ε_1, and the inhomogeneity dielectric permittivity is ε_2, the indirect part in (27.17) will be as follows:

$$\overleftrightarrow{\mathbf{G}}^{\mathrm{I}}(\mathbf{r},\mathbf{r}') = \frac{\varepsilon_1-\varepsilon_2}{\varepsilon_1+\varepsilon_2}\frac{1}{4\pi k^2W^3}\left(-\overleftrightarrow{\mathbf{I}} + 3\frac{\mathbf{W}\otimes\mathbf{W}}{W^2}\right), \quad (27.18)$$

where $\mathbf{r}'$ is the point, where the field source is situated:

$$\mathbf{r}' = \sqrt{(x-x')^2 + (y-y')^2 + (z+z')^2}.$$

Now the total electric field strength near the nanoparticle can be expressed as follows:

$$\mathbf{E}(\mathbf{r}) = \mathbf{E}_0(\mathbf{r}) + \frac{k^2}{\varepsilon_0}\overleftrightarrow{\mathbf{G}}(\mathbf{r},\mathbf{r}')\overleftrightarrow{\boldsymbol{\alpha}}(\varphi)\mathbf{E}_0(\mathbf{r}'). \quad (27.19)$$

The second part of the problem involves finding the quantum yield and the fluorescence rate of a dye molecule and shows the substrate effect for these values. For this, we consider a single molecule that emits light under the influence of

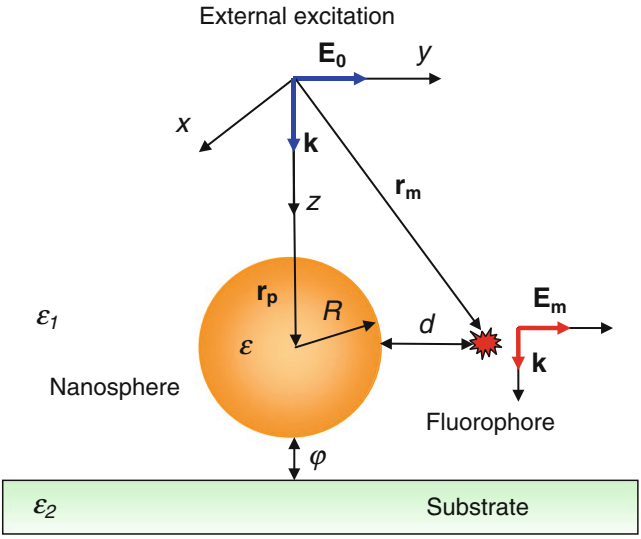

Fig. 27.2 Schematic drawing of the system under investigation. Spherical gold nanoparticle with a radius R is situated at a certain distance φ from the glass dielectric substrate. Fluorophore molecule is located at a distance d from the surface of the nanoparticle

external excitation. Let this molecule be located at a point $\mathbf{r_m}$ and have a dipole moment $\mathbf{p}$ and transition frequency ω (Fig. 27.2). The centre of the spherical nanoparticle with a radius of R is at a point $\mathbf{r_p}$. In the case of weak excitation, molecule fluorescence rate γ_{em} depends on the molecule excitation rate γ_{exc} and quantum yield q [9]. Let us consider the excitation rate in more detail. Excitation rate is proportional to the local field strength and dipole moment $\mathbf{p}$ [9]:

$$\gamma_{\text{exc}} \infty \left| \mathbf{p} \cdot \mathbf{E} \right|^2. \tag{27.20}$$

In the absence of nanoparticle, external radiation $\mathbf{E_0}$ excites the molecule with an excitation rate γ^0_{exc}. As mentioned earlier, the presence of nanoparticle leads to the occurrence of an additional local electromagnetic field. To assess the impact of the local electromagnetic field intensity near the surface of the metal nanoparticle on the molecule fluorescence rate, we will operate the normalized excitation rate [9]

$$\frac{\gamma_{\text{exc}}}{\gamma^0_{\text{exc}}} = \left| \frac{\left[\mathbf{n_p} \cdot \mathbf{E}(\mathbf{r_m})\right]}{\left[\mathbf{n_p} \cdot \mathbf{E_0}(\mathbf{r_m})\right]} \right|^2, \tag{27.21}$$

where $\mathbf{n_p}$ is a unit vector pointing in the direction of $\mathbf{p}$.

Knowing the electric field strength near the nanoparticle surface (27.19), we have everything needed to calculate the normalized excitation rate of a dye molecule (27.21), which is located near the surface of a spherical gold nanoparticle.

Taking into account (27.11–27.12, 27.16–27.19), we can write an explicit expression for the normalized excitation rate:

$$\frac{\gamma_{\text{exc}}}{\gamma_{\text{exc}}^0} = \left| 1 + \frac{k^2}{\varepsilon_0} \overleftrightarrow{\mathbf{G}} \left(\mathbf{r_m}, \mathbf{r_p} \right) \overleftrightarrow{\boldsymbol{\alpha}} \left(\varphi \right) \right|^2. \tag{27.22}$$

Fluorescence signal is proportional to the emission probability of molecule (fluorescence rate) γ_{em}:

$$\gamma_{\text{em}} = \gamma_{\text{exc}} \cdot q. \tag{27.23}$$

If γ_{r} is the radiative decay rate and γ is the total decay rate, then quantum yield is

$$q = \gamma_{\text{r}} / \gamma. \tag{27.24}$$

Then, the normalized molecule fluorescence rate near a spherical gold nanoparticle can be written in the following form [9]:

$$\frac{\gamma_{\text{em}}}{\gamma_{\text{em}}^0} = \frac{\gamma_{\text{exc}}}{\gamma^0{}_{\text{exc}}} \frac{q}{q^0}. \tag{27.25}$$

Here, variables with superscript "0" correspond to the molecule in the absence of nanoparticle and without superscript in its presence. Let us denote the total decay rate of the molecule in the absence of nanoparticle as

$$\gamma^0 = \gamma_{\text{r}}^0 + \gamma_{\text{nr}}^0, \tag{27.26}$$

where γ_{r}^0 and γ_{nr}^0 are the molecule radiative and nonradiative decay rates in the absence of nanoparticle, respectively. The presence of nanoparticle introduces additional losses into the system, such as ohmic losses in the nanoparticle γ_{abs} [9]. Then, in the presence of a nanosphere quantum yield of the molecule can be written in the modified form:

$$\begin{aligned} \gamma &= \gamma_{\text{r}} + \gamma_{\text{nr}} + \gamma_{\text{abs}}, \\ q &= \frac{\gamma_{\text{r}}}{\gamma_{\text{r}} + \gamma_{\text{nr}} + \gamma_{\text{abs}}}. \end{aligned} \tag{27.27}$$

If $\gamma_{\text{nr}}^0 = \gamma_{\text{nr}}$, then expression for the quantum yield can be presented as

$$q = \frac{\gamma_{\text{r}} / \gamma_{\text{r}}^0}{\gamma_{\text{r}} / \gamma_{\text{r}}^0 + \gamma_{\text{abs}} / \gamma_{\text{r}}^0 + (1 - q^0)/q^0}. \tag{27.28}$$

The rate of energy transfer from the molecule to the nanoparticle γ_{abs} can be calculated via the molecule emission power P_{abs} in the presence of the nanoparticle [6, 9]:

$$\frac{\gamma_{\text{abs}}}{\gamma_{\text{r}}^0} = \frac{P_{\text{abs}}}{P^0}. \tag{27.29}$$

In general, the emission power of the classical dipole in free space

$$P^0 = \frac{\omega^4 \mathbf{p}^2}{12\pi\varepsilon_0 c^3},$$

and, according to [6, 9]

$$P_{\text{abs}} = \frac{1}{2}\int_V \text{Re}(\mathbf{j}\times\mathbf{E}^*)d\mathbf{r}^3, \tag{27.30}$$

where the integration is performed over the volume of a nanoparticle, **j** is the current density, which is created by the molecule field in the volume of a nanoparticle, **E** is the electric field strength.

Further, given that γ_r is proportional to the emission power of the classical dipole, we can find the normalized radiative decay rate [6]:

$$\frac{\gamma_{\text{r}}}{\gamma_{\text{r}}^0} = \left|\mathbf{n}_{\mathbf{p}} + \overleftrightarrow{\boldsymbol{\alpha}}(\varphi)\frac{k^2}{\varepsilon_0} G_0(\mathbf{r}_{\mathbf{p}}, \mathbf{r}_{\mathbf{m}})\mathbf{n}_{\mathbf{p}}\right|^2. \tag{27.31}$$

The above-stated Eqs. (27.25, 27.28, 27.29, 27.31) allow calculating the molecule quantum yield and fluorescence rate near the surface of a spherical metal nanoparticle. The presence of the substrate is taken into account similarly to the approach used to determine the field strength in the vicinity of the nanoparticle. That is, the Green's function contains the term, which depends on the optical characteristics of the substrate, and polarizability of a nanosphere on a substrate is calculated by the formula (27.12).

27.3 Results and Discussion

Simulation shows a significant influence of the dielectric substrate on the local electric field strength in the vicinity of gold nanoparticles and, consequently, on the fluorophore molecule excitation rate. The field strength and, therefore, the excitation rate fall with increasing dielectric permittivity of the substrate material and, conversely, grow with the increasing size of the nanoparticle. Such multi-vector behaviour is explained, in the first case, by the increasing energy losses upon the interaction of the nanoparticle field with the substrate material while its dielectric permittivity increases. In the second case, the increase in the excitation rate as a result of increasing size of the nanoparticle prevails over the dielectric losses with a significant decrease of the excitation rate in general. It should be noted that in both cases the

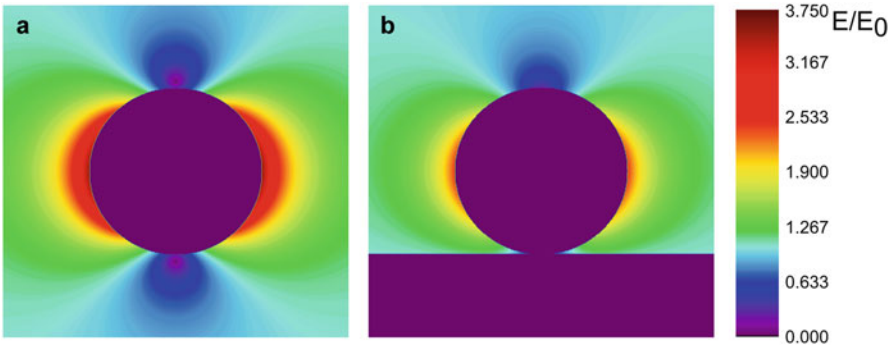

Fig. 27.3 Distribution of the electric field strength near the surface of a spherical gold nanoparticle with a radius of 20 nm at an external excitation wavelength of 650 nm (**a**) without and (**b**) in the presence of the glass substrate ($\varepsilon_2 = 2.59$). The maximum E/E_0 value in the case (**a**) is 3.75, and in the case (**b**) is 2.41

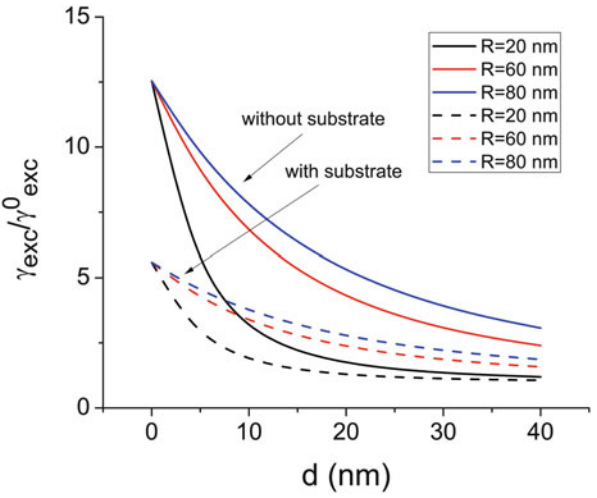

Fig. 27.4 Fluorophore molecule excitation rate change near spherical gold nanoparticles of different sizes in the absence and presence of the dielectric glass substrate ($\varepsilon_2 = 2.59$). R is the spherical nanoparticle radius, d is the distance from nanoparticle surface to the point of fluorophore molecule location

significant dependence of the excitation rate on the distance between the fluorophore molecule and nanoparticle was observed, which exhibits a nonlinear behaviour.

In Fig. 27.3, the distribution of electric field strength near the surface of a spherical gold nanoparticle with a radius of 20 nm in the absence of the glass substrate and in the case of its presence ($\varepsilon_2 = 2.59$) is depicted. The maximum field strength for these cases is 3.75 and 2.41, respectively; therefore, in this case the presence of a dielectric environment inhomogeneity reduces the maximum strength of the local electric field generated by a gold nanosphere under the influence of an external excitation. Obviously, the nanoparticle behaves as a classical dipole that emits light, which is consistent with the dipole approximation used in this approach.

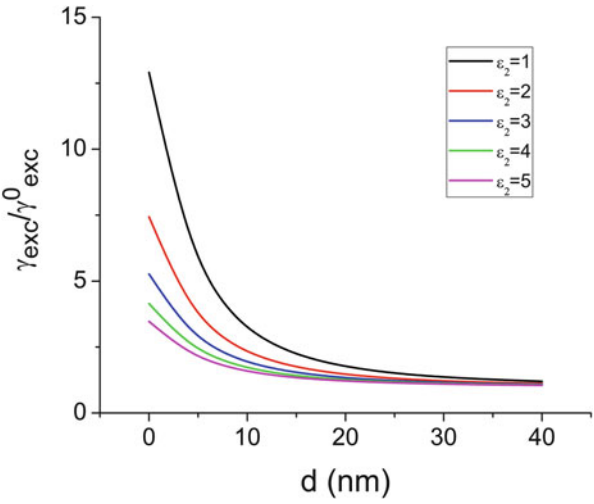

Fig. 27.5 Fluorophore molecule excitation rate change near the spherical gold nanoparticle with a radius of 20 nm for different values of the substrate dielectric permittivity. ε_2 is the substrate dielectric permittivity, d is the distance from nanoparticle surface to the point of fluorophore molecule location

Figure 27.4 shows the dependence of the fluorophore molecule excitation rate near spherical gold nanoparticles of different sizes on the distance to the surface of the nanoparticle. It should be noted that with increasing gold nanoparticle size and distance from the surface of the nanoparticle, the excitation rate derivative decreases due to the exponential nature of the field distribution.

Effect of substrate on the nanostructure's local electromagnetic field is determined by the dielectric permittivity of the material from which it is made, and, like in the previous case, there is an obvious dependence of excitation rate on the distance from nanoparticle surface to the point of fluorophore molecule location. The nature of this effect is shown in Fig. 27.5, which shows that in the presence of the glass substrate fluorophore excitation rate value is reduced by almost half compared with the case when the substrate is absent. Thus, the best way to obtain the fluorophore excitation rate enhancement is to use the substrate material with the least possible value of the dielectric permittivity.

The decrease in the fluorophore quantum yield, when it approaches the surface of a nanoparticle being in the resonant plasmon oscillations generation mode, is well known. Reduction of the quantum yield shows a gradual nonlinear decline to zero in contact of fluorophore with the surface of the nanoparticle. Usually, to enhance the fluorescence, a separating layer of dielectric material between the nanoparticle and fluorophore is used [12]. In this study, for modelling generalized system properties we first use the vacuum as an environment. Subsequently, to agree with experiment, simulation results for a particular case of a dielectric material that was used in the experiment will be presented. Figure 27.6 shows the typical behaviour of the molecule quantum yield dependence on the distance to the surface of a gold nanoparticle. It is noticeable that the presence of the substrate generally somewhat reduces the quantum yield. The figure shows the results for a gold nanoparticle with a radius of 40 nm and a model fluorophore with the maximum initial quantum yield q^0 (without the presence of a nanoparticle),

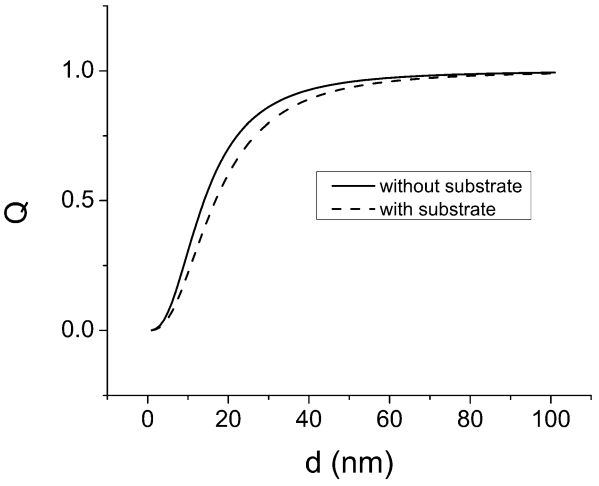

Fig. 27.6 Fluorophore molecule ($q^0 = 1$) quantum yield Q depending on the distance to the surface of the spherical gold nanoparticle with a radius of 40 nm in the absence (*solid line*) and in the presence (*dashed line*) of the glass substrate with $\varepsilon_2 = 2.59$. d is the distance from the molecule to the nanoparticle surface

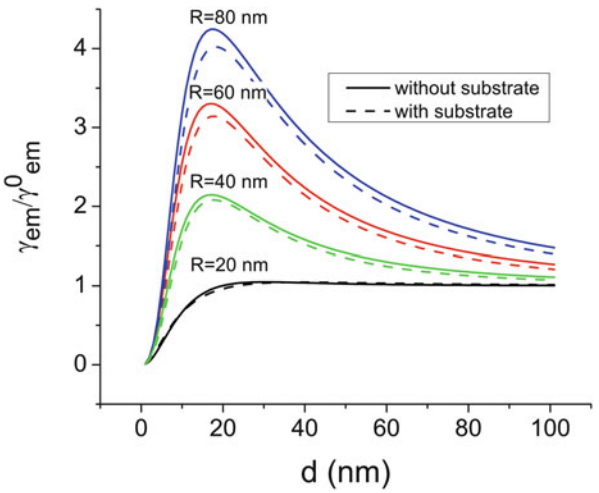

Fig. 27.7 Dependence of the fluorescence rate enhancement factor for a fluorophore molecule ($q^0 = 1$) on the distance from the surface of the spherical gold nanoparticle of different radii. d is the distance from the molecule to the nanoparticle surface

which equals to 1. Thus, we can conclude that the resulting reduction of the electric field strength near the nanoparticle in the presence of the dielectric substrate will subsequently reduce the fluorophore molecule quantum yield.

Theoretical approach using the Green's function, which is applied in this study, for the first time allowed us to estimate the fluorescence rate enhancement for fluorophores with different quantum yield in the presence of a spherical gold nanoparticle located on a dielectric substrate (Fig. 27.7). In confirmation of the results of [9], dependence of fluorescence rate enhancement factor on the distance between the fluorophore and surface of the nanoparticle exhibits a non-monotonic character and expresses a maximum depending on several factors. Known nonlinear dependence on the initial fluorophore quantum yield, nanoparticle size and the

distance between the fluorophore and nanoparticle is supplemented in our case with the influence of the presence of the dielectric substrate. It is evident from Fig. 27.7 that the presence of the dielectric substrate slightly reduces the amount of fluorescence rate enhancement in equidistant point, which increases in proportion to the size of the gold nanoparticle.

It is known that the value of the molecule initial quantum yield significantly affects their emission enhancement factor [13, 14]. Since the enhancement factor is inversely proportional to q^0, then the smaller the q^0 value, the more significant enhancement of emission can be obtained (Fig. 27.8). Simulation results show that the dependence of the fluorescence rate enhancement factor on the value of the initial quantum yield is pronouncedly nonlinear. In particular, in the case of the fluorophore molecule with $q^0 = 0.1$, located near the gold nanoparticle with a radius of 80 nm, simulation revealed that the maximum $\gamma_{em}/\gamma_{em}^0$ value is 22.5 in the absence of substrate and 16.1 in the presence of the glass substrate ($\varepsilon_2 = 2.59$). An important result of the simulation obtained is to find the existence of an optimal distance between the fluorophore and nanoparticle depending on the size of the initial quantum yield. As shown in Fig. 27.8 (inset), the optimal distance for a maximum fluorescence rate enhancement factor is markedly different in the case of low and high values of the fluorophore quantum yield. For example, for $q^0 = 0.1$ the optimal distance is 12 nm, and for $q^0 = 1$ it is 18 nm. Significant differences in enhancement values, which are introduced by the presence of the dielectric substrate, indicate the need to consider the impact of this factor in the design of plasmonic nanochips and optimization of dimensional parameters of nanostructures depending on the dielectric characteristics of the substrate. Factor of the substrate becomes even more important in the further consideration of the fluorescence enhancement mechanism depending on the wavelength resonance positions of the fluorophore molecule and nanoparticle.

Performed simulations identified common approaches in the development of nanochips for the fluorescence signal enhancement. Based on the experimental study conditions, we conducted simulation and experiment to determine the fluorescence signal level of Rhodamine 6G (R6G) organic dye in a polymer matrix near the gold nanostructures depending on the distance of the fluorophore molecules to the nanoparticles. As the plasmon-generating elements, random arrays of gold nanostructures were used with an average base diameter of 97 nm and an average height of 54 nm and a dielectric coating (SiO_2) of varying thickness on the surface of the glass substrate (Fig. 27.9). Gold nanostructures were fabricated by thermal annealing (450 °C, 2 h) of gold island films with a mass thickness of 10 nm. Gold island films and dielectric coatings were produced by evaporation in vacuum (10^{-5} Pa) with the film thickness control using a quartz balance. Samples with the thickness of the separating dielectric layer of about 10, 15, 20, and 25 nm were investigated. A layer of polymer composite with a thickness of about 2 μm (based on atomic force microscopy (AFM) data), consisting of an aqueous solution of polyacrylic acid and R6G, was deposited on each of the samples using the vertical dipping method, followed by a gradual (5 mm/min) withdrawal and drying. R6G concentration in a polymer matrix was equal to 10^{-5} mol/L. The measurements

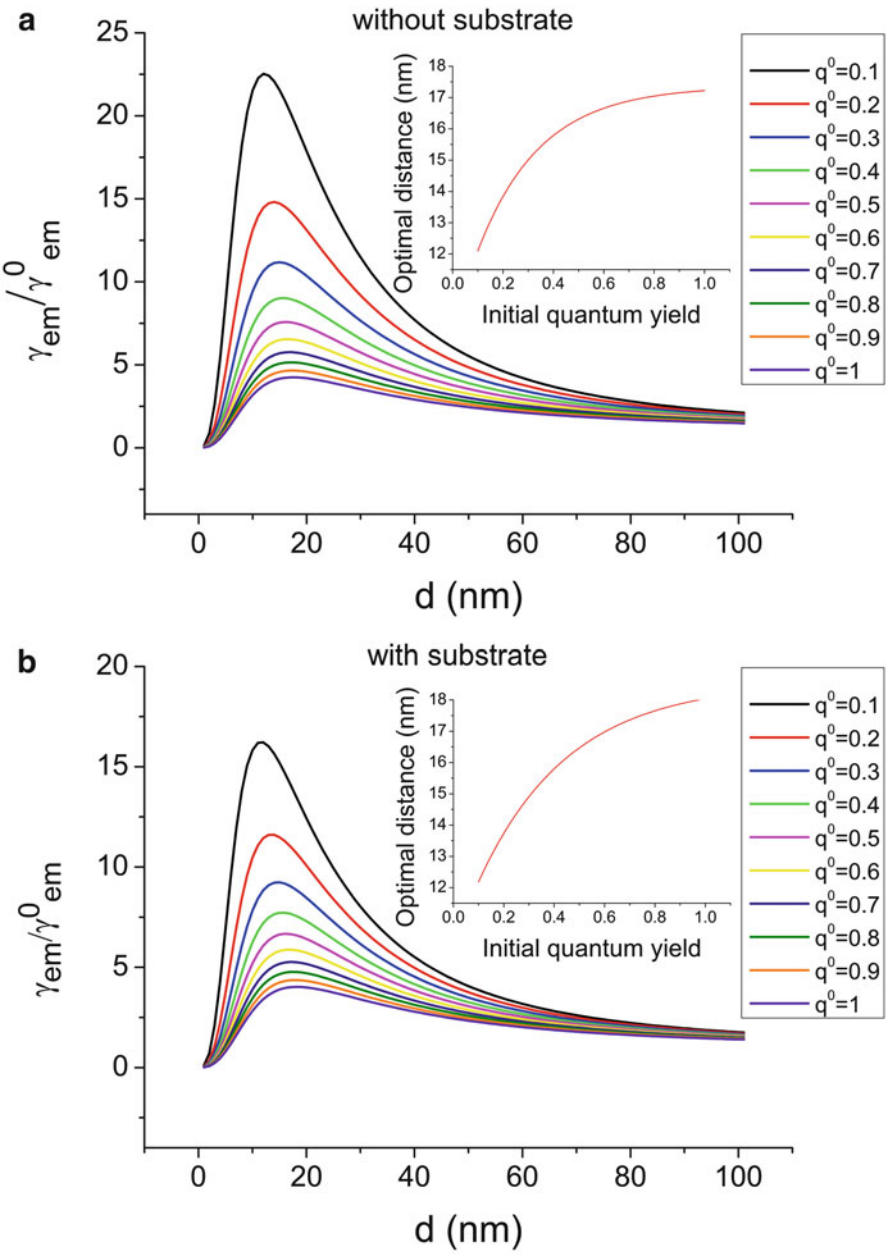

Fig. 27.8 Fluorescence rate enhancement factor for fluorophores with different initial quantum yield near the surface of a spherical gold nanoparticle with a radius 80 nm (**a**) in the absence and (**b**) in the presence of the glass substrate with $\epsilon_2 = 2.59$. d is the distance from the molecule to the nanoparticle surface. *Insets*: dependences of the optimal distance between the fluorophore and nanoparticle on the initial quantum yield value

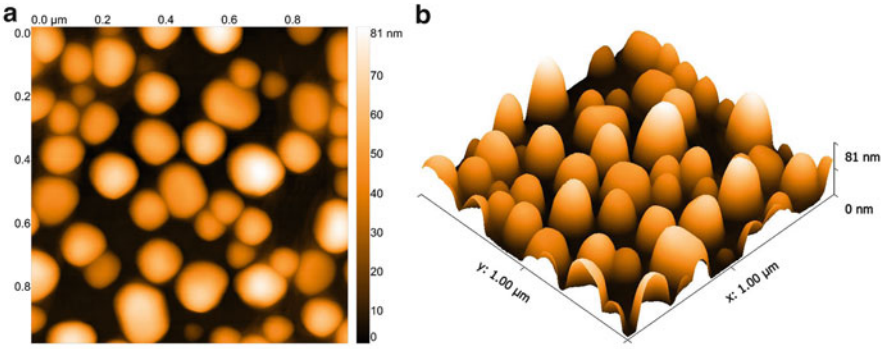

Fig. 27.9 AFM images of the random array of gold nanostructures: (**a**) top view and (**b**) 3D view

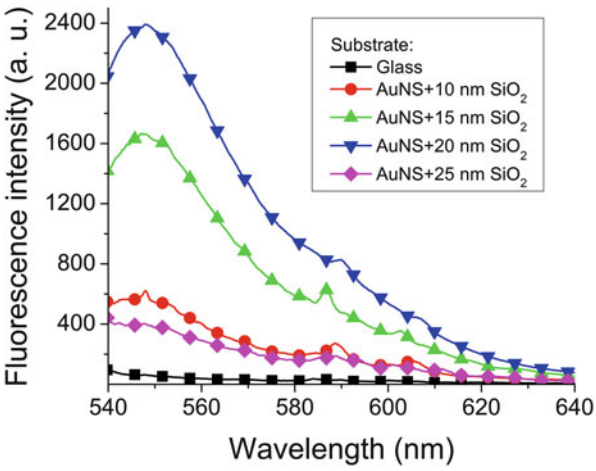

Fig. 27.10 Spectral dependences of the R6G dye fluorescence intensity for the different thickness of SiO_2 dielectric coating on the gold nanostructures

were performed using the method of fluorescence spectroscopy on the laser fluorimeter "FluoroTest^{Nano}-2S".

Prepared samples with different dielectric coating thickness were irradiated using a laser source with a wavelength of 532 nm and R6G fluorescence spectra were measured. The measurement results have shown (Fig. 27.10) that for all samples fluorescence enhancement of the dye near the gold nanostructures was observed in comparison with the signal obtained at similar samples without metal nanoparticles. Maximum fluorescence enhancement was obtained for samples with a thickness of the dielectric layer of about 20 nm, and the dependence of the fluorescence signal intensity on the dielectric thickness was nonlinear (Fig. 27.11).

For the simulation of the experimental results, the above-stated theoretical approach with point-dipole approximation was used. Known dimensional ratio of light wavelength and size of nanostructures used allows applying this approach. In the model, a spherical gold nanoparticle with a radius of 40 nm having the volume

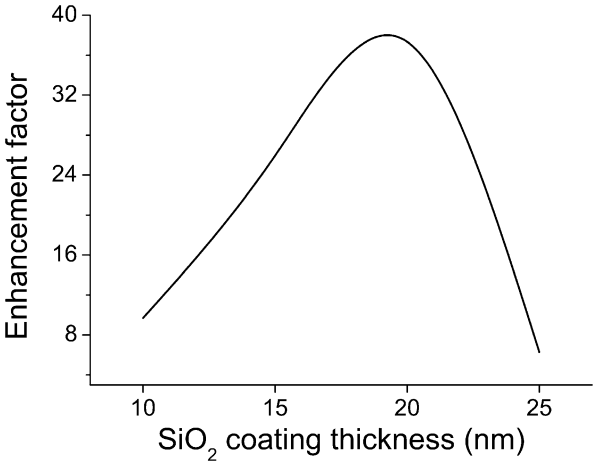

Fig. 27.11 Dependence of the fluorescence enhancement factor of R6G dye on the thickness of the SiO_2 dielectric coating on the gold nanostructures

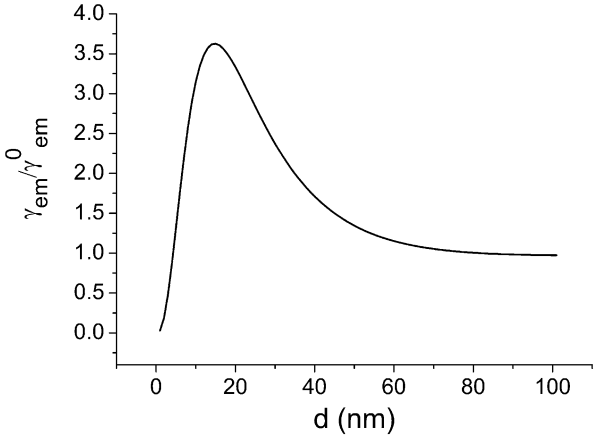

Fig. 27.12 Fluorescence rate enhancement factor for a fluorophore with initial quantum yield $q^0 = 0.95$ near the surface of a spherical gold nanoparticle with a radius of 40 nm, located on a glass substrate ($\varepsilon_2 = 2.59$) in a homogeneous medium ($\varepsilon_1 = 2.22$), upon the excitation with light wavelength of 532 nm. d is the distance from the molecule to the nanoparticle surface

equal to the average volume of nanostructures, which the nanochip consisted of, was located on a glass substrate ($\varepsilon_2 = 2.59$). Due to the close values of the refractive indices of SiO_2 (1.45) and polyacrylic acid (1.53), separating dielectric layer and polymer matrix were treated as a homogeneous environment with a refractive index 1.49 that surrounded the gold nanoparticle. Excitation wavelength (532 nm) and fluorophore quantum yield (0.95) conformed to the experimental values.

The simulation resulted in a dependence of fluorescence rate enhancement factor on the distance between the molecule and the nanoparticle surface shown in Fig. 27.12. As it can be seen from Figs. 27.11 and 27.12, applied theoretical approach can qualitatively describe non-monotonic dependence of experimental fluorescence enhancement factor on the distance between the fluorophore and nanoparticle and gives close to experimental values of the optimal distance between the fluorophore and nanoparticle providing maximum fluorescence enhancement (19–20 and 15 nm for the experiment and simulation, respectively).

27.4 Conclusions

Using the dyadic Green's function and volumetric Lippmann-Schwinger equations, computer simulation of fluorescence excitation rate enhancement in the vicinity of nanostructures, which are spherical gold nanoparticles, was conducted in order to study its dependence on the size of the gold nanoparticles and distance from their surface to a fluorophore molecule, as well as on the dielectric permittivity of the substrate, which the nanoparticle is located on. Calculations have shown that the local electric field strength values and the fluorophore quantum yield decrease with increasing value of the dielectric permittivity of the substrate. Simulation of the fluorophore molecule fluorescence rate enhancement $\gamma_{em}/\gamma^0_{em}$ revealed that $\gamma_{em}/\gamma^0_{em}$ value increases with the size of the spherical gold nanoparticle and the presence of the substrate slightly reduces its value. Special attention should be given to the discovered fact of existence of an optimal distance between the fluorophore and nanoparticle depending on the value of the initial quantum yield. Through experimental studies we have shown the possibility of up to 38-fold fluorescence enhancement for Rhodamine 6G dye near gold nanostructures with separating dielectric layer, located on the surface of the glass substrate, and have demonstrated the applicability of the developed theoretical approach for such systems. Developed theoretical approach and obtained results are important for the improvement of the fluorescence analysis method using the surface enhancement effect on nanoparticles and are useful for the development of novel nanochips based on gold and silver nanostructures for exploitation as sensitive elements of fluorescence sensors for registration of low-intensity fluorescence signals in biochemical applications.

References

1. Chumanov G, Sokolov K, Gregory BW, Cotton TM (1995) Colloidal metal films as a substrate for surface-enhanced spectroscopy. J Phys Chem 99:9466
2. Tam F, Goodrich GP, Johnson BR, Halas NJ (2007) Plasmonic enhancement of molecular fluorescence. Nano Lett 7:496
3. Xu S, Cao Y, Zhou J, Wang X, Wang X, Xu W (2011) Plasmonic enhancement of fluorescence on silver nanoparticle films. Nanotechnology 22:275715
4. Kühn S, Håkanson U, Rogobete L, Sandoghdar V (2006) Enhancement of single-molecule fluorescence using a gold nanoparticle as an optical nanoantenna. Phys Rev Lett 97:017402
5. Zhang J, Fu Y, Chowdhury MH, Lakowicz JR (2007) Metal-enhanced single-molecule fluorescence on silver particle monomer and dimer. Nano Lett 7:2101
6. Novotny L, Hecht B (2006) Principles of nano-optics. Cambridge University Press, New York
7. Jackson JD (1998) Classical electrodynamics, 3rd edn. Wiley, New York
8. Carminati R, Greffet J-J, Henkel C, Vigoureux JM (2006) Radiative and non-radiative decay of a single molecule close to a metallic nanoparticle. Opt Commun 261:368
9. Anger P, Bharadwaj P, Novotny L (2006) Enhancement and quenching of single-molecule fluorescence. Phys Rev Lett 96:113002
10. Lozovski V (2010) The effective susceptibility concept in the electrodynamics of nanosystems. J Comput Theor Nanosci 7:2077

11. Myroshnychenko V, Rodríguez-Fernández J, Pastoriza-Santos I, Funston AM, Novo C, Mulvaney P, Liz-Marzán LM, García de Abajo FJ (2008) Modelling the optical response of gold nanoparticles. Chem Soc Rev 37:1792
12. Bardhan R, Grady NK, Cole JR, Joshi A, Halas NJ (2009) Fluorescence enhancement by Au nanostructures: nanoshells and nanorods. ACS Nano 3:744
13. Kim J, Dantelle G, Revaux A, Bérard M, Huignard A, Gacoin T, Boilot J-P (2010) Plasmon-induced modification of fluorescent thin film emission nearby gold nanoparticle monolayers. Langmuir 26:8842
14. Derom S, Berthelot A, Pillonnet A, Benamara O, Jurdyc AM, Girard C, Colas des Francs G (2013) Metal enhanced fluorescence in rare earth doped plasmonic core-shell nanoparticles. Nanotechnology 24:495704

Chapter 28
Influence of Gold Nanoparticles on Human Fibroblast Before and After Cryopreservation

E.V. Pavlovich and N.A. Volkova

28.1 Introduction

Nowadays a colloidal gold as a chemically inert metal is used in clinical practice for the treatment of autoimmune diseases such as rheumatoid arthritis, as well as in medical diagnostics as a contrast agent. The use of gold nanoparticles as structural basis of nanocomposites, which are used for the delivery of molecules into cells with a therapeutic effect, is a new promising direction. In all these cases, the gold nanoparticles enter inside a human body and contact the cells. Nanocompounds in high concentrations can have a toxic effect on the body and cell culture, therefore the examining of a dose-dependent toxic effect of nanoparticles is an actual task for the researchers. Unfortunately, there are no clear conclusions on this issue as for the variability of parameters such as physical and chemical properties of the particles and the type of cell study parameters [1]. Results of application of gold nanoparticles during culturing both monolayer and suspension cell lines are of contradictory nature [2–4]. To elucidate the effect of metal nanoparticles on cells of different types of the cultures, it is necessary to assess morphological and functional parameters, namely, the viability (membrane integrity) and ability to adhere and proliferate.

For the development of current trends of biotechnology and medicine it's necessary to design optimal methods of long-term storage of cell lines of different etiology. To ensure the maximum preservation rate of cell cultures, a large number of protocols for cryopreservation, taking into account the individual characteristics of different cell types, have been developed. However, even under optimal

E.V. Pavlovich • N.A. Volkova (✉)
Department for Cryobiology of Reproduction System, Institute for Problems of Cryobiology and Cryomedicine, National Academy of Sciences of Ukraine, Pereyaslavskaya str., 23, Kharkiv 61015, Ukraine
e-mail: lenapavlovich@gmail.com; volkovanatali2006@yandex.ua

O. Fesenko, L. Yatsenko (eds.), *Nanoplasmonics, Nano-Optics, Nanocomposites, and Surface Studies*, Springer Proceedings in Physics 167,
DOI 10.1007/978-3-319-18543-9_28

conditions after freeze-thawing in the cells, the injuries, significantly reducing biological properties of cell cultures, are detected. The search for methods capable of activating the regenerative processes in the post-thaw cells is actual as well. Due to their unique structure and properties, the gold nanoparticles can be applied in a wide range of biological and biomedical researches [5, 6]. One among perspective areas is the use of gold nanoparticles as a stimulator of proliferation of cell cultures. The research aim was to study the morpho-functional state, changes in proliferative potential, and apoptotic processes of human fibroblast cell culture (HFCC) prior to and after cryopreservation in the presence of gold nanoparticles.

28.2 Materials and Methods

HFC were cultured in plastic flasks in Dulbecco's modified eagle medium (DMEM) (Sigma, USA) with 5 % fetal bovine serum (FBS) (v/v) (HyClone, USA) supplemented with penicillin/streptomycin (PAA, Austria) and amphotericin B (5 μg/mL) as reported [7]. Total number of the cultured cells was calculated by traditional method in Goryaev's chamber. Seeding concentration was 1.2×10^4 cells on petri dish. The cells were cultured in Sanyo incubator under 37 °C with 5 % CO_2 in humid atmosphere [8]. Cells were passaged at 100 % confluence. Culture medium was replaced every 3 days. HFC had expressed growth properties and during serial passage preserved initial morphological structure of monolayer without evidences of cell degeneration in the culture [9, 10]. In order to determine the number of cells in the control and in the presence of AuNPs there were counted the cells at 3, 5 and 7 days by enzymatic removal from plastic dish.

AuNPs were prepared by citrate synthesis [11] with the initial metal concentration of 45 μg/mL. The average size of nanoparticles was 15 nm. AuNPs were introduced in cells by passive diffusion at 37 °C.

Cryopreservation was performed under protection of 10 % DMSO and 20 % FBS on the base of nutritive medium in the presence of AuNPs in concentrations of 1.5, 3, and 6 μg/mL. The samples were cooled in cryostorage conditions with the rate of 1°/min down to −70 °C in liquid nitrogen vapors with following plunging into liquid nitrogen. The cryoampules were thawed on water bath at 40 °C up to the appearance of liquid phase.

Apoptotic and necrotic processes in HFC were investigated with FACSCalibur using Annexin V (BD, USA) and 7-amino-actinomycin (BD, USA) dyes. The group of comparison (control) was HFC cryopreserved under the same conditions without AuNPs. The results were analyzed with WinMDI v.2.8 program. The results were statistically processed using Excel software and Student *t*-test.

28.3 Results and Discussion

We have previously studied the effect of AuNPs on adhesive and proliferative properties of SPEV cells related to inoculated lines [8]. Change of cell state of HFC with AuNPs was investigated to obtain a comparative pattern of nanoparticles on different types of cultured cells. In previous studies, it has been found when culturing the cells with AuNPs, most of the particles concentrate on a cell membrane, but some of them penetrate into the cells and adsorb on membrane of cell nucleus. Experimental data testify to the fact that the nanoparticles penetrate into the cell passively, along with other substances [8].

There is endocytosis in the cells at 37 °C, i.e., capturing substances with a cell by retraction of plasma membrane site with the following formation of vesicles within the cell with extracellular content [1, 9].

We studied the effect of AuNPs within the concentration range of 1.5–6 μg/mL on proliferative processes in HFC.

At observation term of 1–7 days, the growth dynamics of adhered cells was studied, and a number of proliferating cells were calculated. In the studied cell culture of fibroblasts in the control and in the groups with AuNPs at concentrations of 1.5, 3, and 6 μg/mL, the cells that adhered to the culture plastic were of fibroblast-like morphology.

After a day of observation of cell culture with AuNPs of 1.5, 3, and 6 μg/mL, a cell number did not significantly differ from the control (Fig. 28.1).

Stimulating effect of AuNPs of 6 μg/mL was manifested to the third, fifth, and seventh days of observation. The number of cells in the samples cultured with NPs increases if compared with the control in 1.16 times (the fifth day) and 1.13 ones (the seventh day), respectively. Culturing fibroblasts with AuNPs of 3 μg/mL

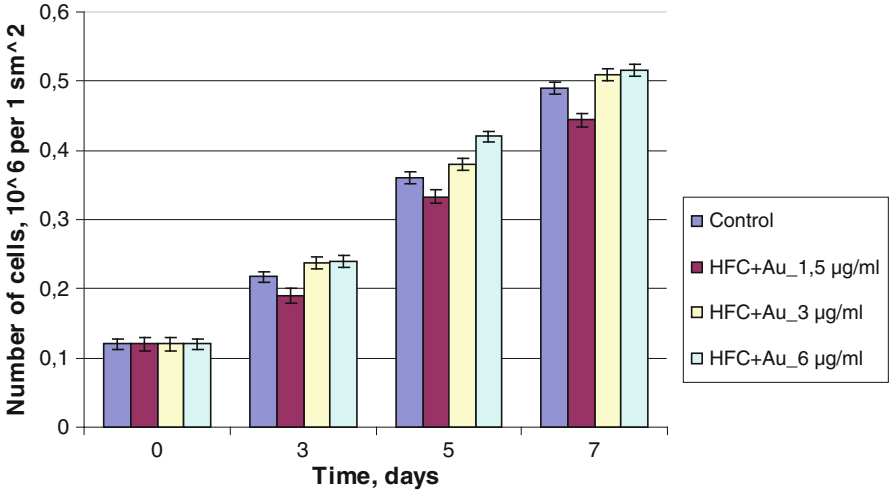

Fig. 28.1 Proliferation dynamics of HFC after exposure of AuNPs

resulted in a faster growth of fibroblast culture from the third to seventh days, but changes were statistically insignificant when compared with the effect of AuNPs of 6 μg/mL from the fifth to seventh days. Tendency to decrease in a cell number compared with the control at all the stages of culturing from third day was observed with AuNPs of 1.5 μg/mL in HFC.

Human fibroblasts are elongated and spindle shaped due to the uneven distribution of pseudopodia over the cell and oval nuclei. The cell morphology at the studied concentrations of NPs did not differ from the control during observation period. After 2 h, there occurs a radial spreading of fibroblasts. After 1 day of culturing, most cells have well-defined and stable edges. To the seventh day of HFC culturing in the control samples, a 90 % confluent was found; in the samples with AuNPs of 6 μg/mL, the monolayer density reached 95 %. The dynamics of culture growth in the control and groups with AuNPs of 1.5, 3, and 6 μg/mL was similar, but it differed in a rate.

Thus, AuNPs of 6 μg/mL stimulate the proliferative capacity of cells. Gold nanoparticles in other concentrations do not significantly affect adhesion and proliferation and do not change morphological picture of cells.

It is known [10–12] that metal nanoparticles can induce apoptosis of different origin in cells. Thus, NPs of titanium dioxide and iron oxide result in cell death due to generation of oxidative stress and the following apoptosis on activation of caspase-3 [13–19].

Simultaneous staining with Annexin V and 7-AAD enables to reveal both necrotic and apoptotic cells. At early stages of apoptosis, the cell membrane integrity is preserved, but there is rearrangement of its phospholipid components, and phosphatidylserine appears on cell surface. Annexin V is a protein, which has a high affinity for phosphatidylserine and binds with the cells expressing it only on external surface of membrane.

To clarify the appearance of apoptosis in HFC as a response to introduction of AuNPs, HFC suspended cells were incubated with NPs for 1 h.

The number of living cells in cell suspension containing AuNPs of 1.5, 3, and 6 μg/mL differed from the control at 1.3, 1.6, and 2 %, respectively (Table 28.1). The number of Annexin $V^+/7\text{-}AAD^-$ cells at the early apoptosis stages increased in the presence of NPs in all the studied concentrations. An increase in the percentage of necrotic cells during incubation with NPs of 6 μg/mL for 1 h ($p \leq 0.05$) was observed.

Table 28.1 Cytofluorimetric analysis of HFC after incubation with AuNPs for 1 h, staining with Annexin V and 7-AAD

Sample/region	Annexin $V^+/7\text{-}AAD^-$	Annexin $V^-/7\text{-}AAD^-$	Annexin $V^+/7\text{-}AAD^+$+Annexin $V^-/7\text{-}AAD^+$
Control	3.0 ± 0.9	92.1 ± 1.6	4.9 ± 1.2
HFC + Au_NPs _1.5 μg/mL	3.2 ± 0.9	90.8 ± 1.5	6.0 ± 1.1
HFC + Au_NPs _3 μg/mL	3.4 ± 0.8	90.5 ± 1.4	6.1 ± 1.1
HFC + Au_NPs _6 μg/mL	3.1 ± 0.9	90.1 ± 1.5	6.8 ± 1.2*

Note: *$p \leq 0.05$ is significant if compared with the control

Percentage of Annexin V^+/7-AAD^+ and Annexin V^-/7-AAD^+ cells (late stages of apoptosis, necrosis) during incubation with NPs for 1 h at concentrations of 1.5 and 3 μg/mL did not differ significantly from the indices of the control samples. When further culturing fibroblasts, a reduction in the number at apoptosis and necrosis in all the investigated samples both in the control and in HFC with AuNPs was observed.

HFC were cultured with AuNPs under standard conditions for 3 days, whereat the cells were suspended and the number of living, necrotic cells and the ones at early stages of apoptosis was evaluated. The number of living cells (Annexin V^-/7-AAD^-) in suspensions of the cells with NPs of 1.5, 3, and 6 μg/mL did not differ from the control (Table 28.2).

Culturing with AuNPs in 1.5, 3 and 6 μg/mL concentrations did not lead to a significant reduction in a viable cell percentage in respect to the control.

Cell state during samples' culturing with AuNPs within 7 days was also under study; the data obtained were presented in Table 28.3.

The AuNPs in 1.5 and 3 μg/mL concentrations during fibroblasts culturing with them within 7 days resulted in some increase in a viable cell percentage against a decreased percentage of the cells, being at a late stage of apoptosis and necrotic ones.

Thus, we have established the fact that the AuNPs' presence in the studied concentrations does not result in the enhancement of apoptosis and necrosis in cells during culturing and may result from a reparative effect of gold nanoparticles on cells when cultured.

Table 28.2 Cytofluorimetric analysis of HFC after 3-day culturing with AuNPs for 3 days, staining with Annexin V and 7-AAD

Sample/region	Annexin V^+/7-AAD^-	Annexin V^-/7-AAD^-	Annexin V^+/7-AAD^++Annexin V^-/7-AAD^+
Control	2.3 ± 0.3	92.0 ± 1.1	5.7 ± 0.5
HFC + Au_NPs _1.5 μg/mL	2.6 ± 0.5	91.6 ± 1.1	5.8 ± 0.6
HFC + Au_NPs _3 μg/mL	2.3 ± 0.6	92.5 ± 1.0	5.2 ± 0.8
HFC + Au_NPs _6 μg/mL	2.6 ± 0.5	91.7 ± 1.0	5.7 ± 0.7

Table 28.3 Cytofluorimetric analysis of HFC after 3-day culturing with AuNPs for 7 days, staining with Annexin V and 7-AAD

Sample/region	Annexin V^+/7-AAD^-	Annexin V^-/7-AAD^-	Annexin V^+/7-AAD^++Annexin V^-/7-AAD^+
Control	1.4 ± 0.7	93.0 ± 1.0	5.6 ± 0.2
HFC + Au_NPs _1.5 μg/mL	1.2 ± 0.4	95.0 ± 1.0	3.8 ± 0.1*
HFC + Au_NPs _3 μg/mL	1.6 ± 0.6	96.4 ± 1.1*	2.0 ± 0.2*
HFC + Au_NPs _6 μg/mL	2.0 ± 0.7	92.1 ± 1.2	5.9 ± 0.3

Note: $*p \leq 0.05$ is significant if compared with the control

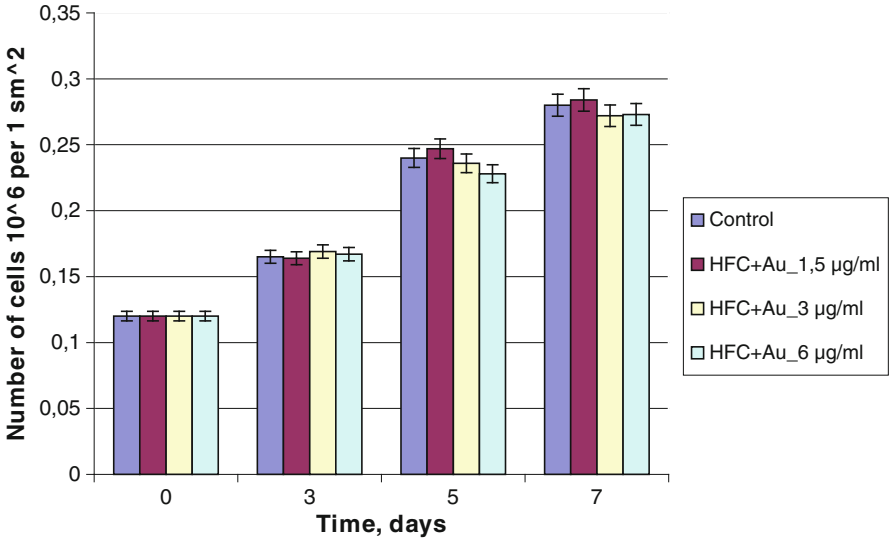

Fig. 28.2 Proliferation dynamics of HFC after cryopreservation with AuNPs

The index of HFC proliferative activity after cryopreservation in the presence of nanoparticles was studied. Our findings testify to the fact that after HFC cryopreservation, the capability to proliferate within culturing terms up to 7 days decreased in 1.8 times (comparison of the control samples prior to and after cryopreservation). The dynamics of HFC growth in the presence of nanoparticles of all the studied concentrations was similar (Fig. 28.2). The AuNPs presence in 1.5 μg/mL concentration in cryopreservation medium resulted in a slight stimulation (the tendency to growth) of proliferative activity in further culturing. Generally the index of proliferative activity of HFC, cryopreserved with AuNPs, did not differ from the control at all the terms of observation.

When culturing HFC, cryopreserved with AuNPs in 1.5 and 3 μg/mL concentrations within 7 days, no significant changes in a cell distribution in respect to the control were noted.

This research tasks included the tracing of appeared apoptotic and necrotic processes in HFC under AuNPs effect. In order to solve the task of apoptosis/necrosis presence after cryopreservation with AuNPs, we assessed the state of cells cryopreserved with AuNPs during further 7-day culturing (Table 28.4).

When culturing HFC, cryopreserved with AuNPs in 1.5 and 3 μg/mL concentrations for 7 days, no significant changes in cell distribution in respect to the control were observed.

After 7-day fibroblast culturing in the presence of gold nanoparticles (6 μg/mL concentration), there occurred a decrease in viable cell percentage by 4.7 % and an increase in cell number at an early stage of apoptosis by 4.1 % relative to the control samples.

Table 28.4 Cytofluorimetric analysis of cryopreserved HFC after 7-day culturing with AuNPs for 3 days, staining with Annexin V and 7-AAD

Sample/region	Annexin $V^+/7\text{-}AAD^-$	Annexin $V^-/7\text{-}AAD^-$	Annexin $V^+/7\text{-}AAD^+$+Annexin $V^-/7\text{-}AAD^+$
Control	2.2 ± 0.5	92.5 ± 1.0	5.3 ± 0.2
HFC + Au_NPs _1.5 μg/mL	1.5 ± 0.6	92.6 ± 1.1	5.9 ± 0.1
HFC + Au_NPs _3 μg/mL	2.3 ± 0.7	92.1 ± 1.3	5.6 ± 0.1
HFC + Au_NPs _6 μg/mL	6.3 ± 0.6*	87.8 ± 1.2*	5.9 ± 0.2

Note: $*p \leq 0.05$ is significant if compared with the control

Thus, the AuNPs presence in 6 μg/mL concentration in culturing medium was established to cause an increased proliferative activity of HFC. Using the flow cytometry, we revealed the fact that the cryopreservation and subsequent 7-day culturing of fibroblasts with AuNPs in 1.5 and 3 μg/mL concentrations caused no strengthening of apoptosis and necrosis processes in cells, which might be due to a reparative effect of gold nanoparticles on cells during culturing. The AuNPs presence in 1.5 μg/mL concentration in cryoprotective medium during cryopreservation causes a slight increase (the tendency to growth) of proliferative activity of cells during their further cultivation.

Fibroblast cryopreservation with 1.5 μg/mL gold nanoparticles did not result in the development of necrosis and apoptosis in cells during further culturing. When applying AuNPs in 6 μg/mL concentration, a decrease in the percentage of viable cells and a growth of cell number at an early stage of apoptosis occurred. In apoptotic cell, the phosphatidylserine moves from the cytoplasm to an external part of bilayer, resulting in activation of caspase cascade, chromatin condensation, disorder in electron-transport chain in mitochondria, and eventually the cessation of ATP synthesis. Therefore we do not recommend using gold nanoparticles in the concentration higher than 3 μg/mL for cryopreservation of cells of stromal origin.

28.4 Conclusions

1. AuNPs in 6 mg/mL concentration render a stimulating effect on proliferative ability of HFCC cells.
2. The flow cytometry results suggest that AuNPs in the studied concentrations during culturing with the cells for 7 days do not cause the development of apoptosis/necrosis in HFCC cells.
3. Cryopreservation of fibroblasts with gold nanoparticles in 1.5–3 mg/mL concentrations does not lead to the development of necrosis and apoptosis processes in cells at further culturing. At 6 μg/mL concentration of AuNPs in cryopreservation medium, a decrease in the percentage of viable cells and during culturing the growth of cells at the early stage of apoptosis occur.

Acknowledgment The work was carried out within the research project of targeted complex program of basic research of the National Academy Sciences of Ukraine "Fundamental problems of nanostructured systems, nanomaterials and nanotechnology."

References

1. Fëischer HC, Chan WCW (2007) Nanotoxicity: the growing need for in vivo study. Curr Opin Biotechnol 18(6):565–571
2. Bystrzejewska-Piotrowska G, Golimowski J, Urban PL (2009) Nanoparticles: their potential toxicity, waste and environmental management. Waste Manag 29:2587–2595
3. Mironava T, Hadjiargyrou M, Simon M et al (2010) Gold nanoparticles cellular toxicity and recovery: effect of size, concentration and exposure time. Nanotoxicology 4(1):120–137
4. Lewinski N, Colvin V, Drezek R (2008) Cytotoxicity of nanoparticles. Small 4(1):26–49
5. Dykman L, Khlebtsov N (2012) Gold nanoparticles in biomedical applications: recent advances and perspectives. Chem Soc Rev 41:2256–2282
6. BarathManiKanth S, Kalishwaralal K, Sriram M et al (2010) Antioxidant effect of gold nanoparticles restrains hyperglycemic conditions in diabetic mice. J Nanobiotechnol 8(16). doi:10.1186/1477-3155-8-16
7. Van Sprang PA, Janssen CR (2001) Toxicity identification of metals: development of toxicity identification fingerprints. Environ Toxicol Chem 20(11):2604–2610
8. Freshni R (1989) Culture of animal cells. Methods. Mir, Moscow
9. Volkova NA (2012) Study of morphological characteristics of cryopreserved cell cultures of stromal origin. Probl Cryobiol 22(2):118–125
10. Hayflick L, Moorhead PS (1961) The serial cultivation of human diploid cell strains. Exp Cell Res 25(12):585–621
11. Dykman LA, Bogatyrev VA, Schyogolev SY, Khlebtsov NG (2008) Gold nanoparticles. Synthesis, properties, biomedical applications. Nauka, Moscow, p 319 (in Russian)
12. Pavlovich EV, Volkova NA (2013) Research of gold nanoparticle influence on proliferate properties SPEV cell culture. Abstract book. In: International research and practice conference: nanotechology and nanomaterials (NANO-2013), pp 380–381
13. Chithrani DB (2011) Optimization of bio-nano interface using gold nanostructures as a model nanoparticle system. Insciences J 1(3):115–135
14. Gopinath P, Gogoi SK, Chattopadhyay A (2008) Implications of silver nanoparticle induced cell apoptosis for in vitro gene therapy. Nanotechnology 19(7). doi:10.1088/0957-4484/19/7/075104
15. Kim K, Lee M, Park H (2006) Cell-permeable and biocompatible polymeric nanoparticles for apoptosis imaging. J Am Chem Soc 22(11):3490–3491
16. Maynard AD, Aitken RJ, Butz T et al (2006) Safe handling of nanotechnology. Nature 444 (7117):267–279
17. Mukherjee P, Bhattacharya R, Bone N (2007) Potential therapeutic application of gold nanoparticles in B-chronic lymphocytic leukemia (BCLL): enhancing apoptosis. J Nanobiotechnol 5:4. doi:10.1186/1477-3155-5-4
18. Park E, Yi J, Chung K (2008) Oxidative stress and apoptosis induced by titanium dioxide nanoparticles in cultured BEAS-2B cells. FASEB J 22:3358–3369
19. Zhu MT, Wang Y, Feng WY (2010) Oxidative stress and apoptosis induced by iron oxide nanoparticles in cultured human umbilical endothelial cells. J Nanosci Nanotechnol 10 (12):8584–8590

Part IV
Applications

Chapter 29
Anodic Alumina-Based Nanoporous Coatings for Sensory Applications

I. Voitovich, T. Lebyedyeva, A. Rachkov, O. Gorbatiuk, and P. Shpylovyy

29.1 Introduction

Over the last few years, the research on nanoporous coatings for sensors intended for medical diagnostics, environmental monitoring, study of biomolecular interactions, etc. has been growing in popularity. A wide range of impedance, capacitive, acoustic, optical, and other sensors and biosensors are being developed. The devices on the surface plasmon resonance (SPR) [1] and waveguide sensors, including sensors on a metal-clad waveguide (MCWG) [2–4], where the remaining unanodized Al (near 15 nm) acted as the metal layer to excite the plasmon for waveguide coupling, are among the most sensitive optical sensors. SPR and MCWG sensors can be implemented by observation of shift of the resonance angle of incidence light or the wavelength. The shift corresponds to the changes in dielectric properties of the layer of molecules near the surface of the sensor (Fig. 29.1).

Coatings for sensors of porous anodic oxides generated by electrochemical oxidation on metal surfaces, such as porous anodic alumina (PAA), are being intensively developed [5, 6]. Highly porous surface provides the larger area of interaction of receptor and analyte and thus enables increase in the sensitivity of sensors. The unique structure of the vertical self-ordering pores and possibility to form into them the nanowires and nanodots can also serve as a basis for the development of new sensors, involving not previously used physical phenomena [7].

I. Voitovich • T. Lebyedyeva (✉) • P. Shpylovyy
V.M. Glushkov Institute of Cybernetics, National Academy of Sciences of Ukraine,
Glushkova Ave., 40, Kyiv 03680, Ukraine
e-mail: tetyana_leb@mail.ru

A. Rachkov • O. Gorbatiuk
Institute of Molecular Biology and Genetics, National Academy of Sciences of Ukraine,
Zabolotnoho Str., 150, Kyiv 03143, Ukraine

O. Fesenko, L. Yatsenko (eds.), *Nanoplasmonics, Nano-Optics, Nanocomposites, and Surface Studies*, Springer Proceedings in Physics 167,
DOI 10.1007/978-3-319-18543-9_29

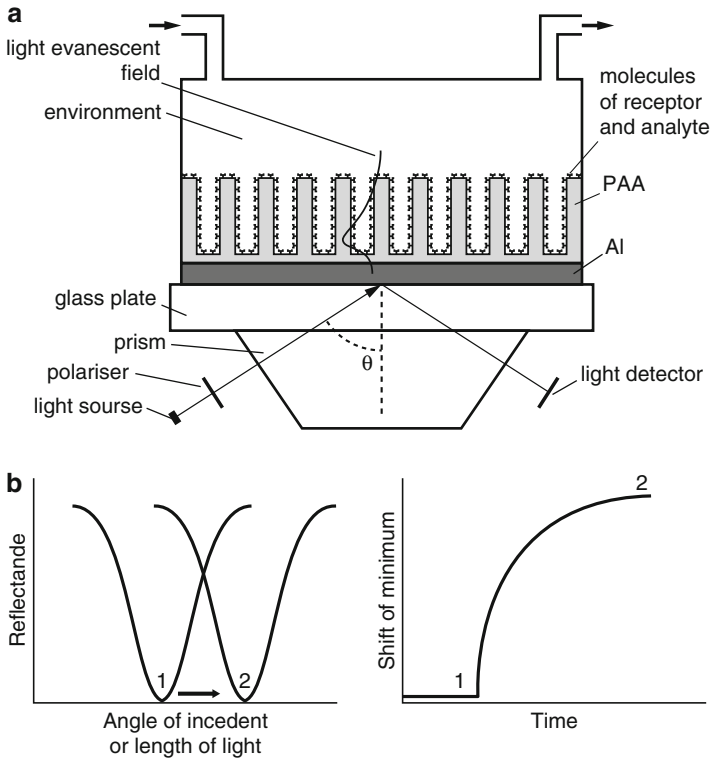

Fig. 29.1 MCWG with nanoporous coating as the waveguide layer. (**a**) Optical setup of sensor device, (**b**) principle of detection

An advantage of PAA for practical application is the simplicity and the cheapness of its production, the possibility of forming arrays of homogeneous pore diameters ranging from a few to hundreds of nanometers. Moreover, PAA has a number of chemical, mechanical, electrical, and optical characteristics, including high hardness and thermal and chemical stability that are important for sensor applications. Biocompatibility of PAA is especially important for biosensors. Sensor devices with PAA can be used as chemical sensors and biosensors in a wide range of tests for the presence of gas molecules, organic molecules, biomolecules (DNA or proteins), microorganisms (viruses, bacteria), and cancer cells. These devices can be used in gaseous and aqueous environments [6].

Most of the works on PAA were conducted at sufficiently thick layers of aluminum (thin plate or foil). Formation of porous anodic oxides on Al films is much less studied, though the thin-film structures with PAA can be efficiently used for coating of biosensor, in particular for SPR sensors and MCWG. It is the thickness and structure of the PAA film that determine the sensitivity of the sensors, as well as the shape of the resonance curve and design features of sensor devices [5, 6]. Special types of sensors and biosensors are developed on the PAA coating

with an additional layer of nanoparticles or ultrathin metal film [7, 8]. The use of gold enables implementation of well-developed bioimmobilization techniques for SPR sensors [1] and in the case of MCWG improves the sensitivity of the sensors due to the redistribution of the intensity of the light wave field. Due to relative simplicity, cheapness of production, and good compatibility with modern thin-film technologies, PAA has strong potential for routine use in sensors for environment, food control, and medical diagnostics.

We should remark that while PAA have the potential for numerous applications in sensor technology, it can also be used in other fields such as separation of molecules, catalysis, photonics, tissue engineering, controlled drug delivery, etc. [9].

The ultimate aim of our current studies is to develop nanoporous coating on PAA for optical waveguide sensors on a metal-clad waveguide (MCWG).

29.2 Development of the Technology of Nanostructured PAA as a Part of MCWG Sensors

We developed the technology of MCWG sensors with nanostructured PAA coating that includes the following steps (Fig. 29.2):

1. Magnetron deposition of aluminum films on optical glass plates
2. One-step anodic oxidation to form PAA and a semitransparent aluminum film with in situ control of the optical parameters of nanostructured coatings
3. Chemical etching for widening of pores with in situ control of the optical parameters of nanostructured coatings
4. Thermal deposition of nanometer-thick gold for the formation of covering with metal nanoparticles or nanofilms

Formation of aluminum films was carried out by magnetron sputtering at constant current. We used the round-shape magnetron with Al (purity 99.99) target of a diameter 140 mm. As an adhesive layer, we used thin (1–2 nm) layer of niobium. Thickness of deposited aluminum was preliminary calculated so that thickness of anodic oxide for the first waveguide mode has been formed and the aluminum layer 15 nm thick remains on glass.

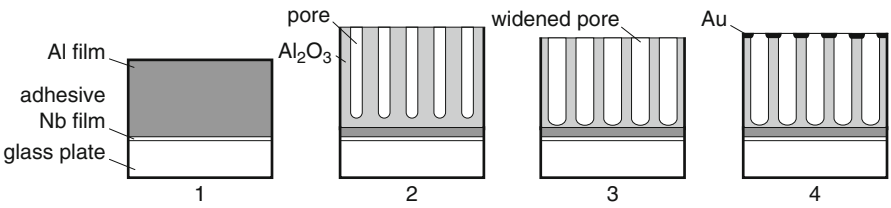

Fig. 29.2 Steps of MCWG sensors formation with nanostructured covering

The study of anodic oxidation of Al films was carried out on a specially designed computer-controlled stand, providing various regimes of forming and continuous time control of electrical parameters of the process of anodic oxidation and temperature stabilization [8]. Anodization was carried out in an aqueous solution of $H_2C_2O_4$ 0.3 M as electrolyte. The test areas were limited by photoresist mask. For potentiostatic oxidation, we used two-electrode cell with a flow of electrolyte and thermal stabilization. The oxidation was carried out at the temperature of 10 °C. In the galvanostatic mode, we used a capillary cell without any temperature control. Kinetic curves of the anodization of aluminum films of 250 nm thickness on glass are shown in Fig. 29.3.

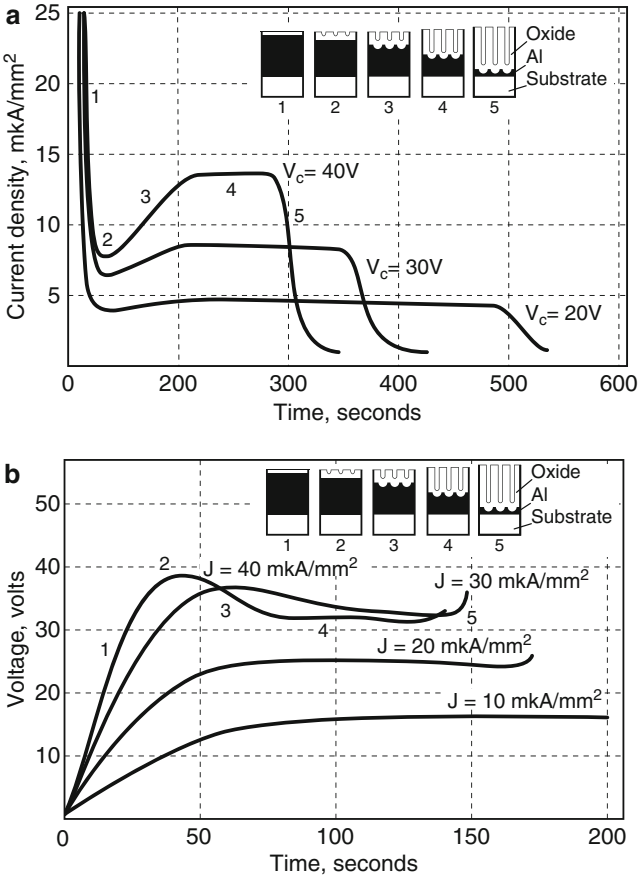

Fig. 29.3 Kinetic curves of the PAA formation: (**a**) potentiostatic mode, (**b**) galvanostatic mode

29.3 Formation of Nanostructured MCWG Sensor with Monitoring of Reflective Curves In Situ

In order to control the optical characteristics of MCWG sensors, we developed an original technique of PAA formation with simultaneous monitoring of the reflection curves. A specially designed clamping cell for anodic oxidation and etching was put on the sample and placed on the prism of the Plasmontest device [4]. Optical setup of the device corresponds to Fig. 29.1a. Refractive index of prism and sensor plate is 1.61. As the light source, the Hamamatsu LED L7868 with wavelength 670 nm is used. The Plasmontest device provided monitoring of reflective curves for the waveguide mode after reaching the front of the oxidation the thickness of aluminum that provides for the penetration of light into the waveguide layer. Sensogram (change of the angle of the reflection curve minimum) was recorded simultaneously with the above process.

Glass plates with initial thickness of deposited Al films in the range of 270–400 nm were used. The thickness of final Al films was 15–25 nm, the thickness of PAA was 300–450 nm, and the porosity of PAA constituted 0.1–0.5 depending on the regimes of oxidation and etching.

Reflective curves received under oxidation at a constant voltage 40 V are shown in Fig. 29.4a. The waveguide minimum on the reflective curve appeared when aluminum layer was thinning down to about 45 nm. In the processes of porous layer growth and Al layer thinning, the minimum on the reflective curves becomes deeper and the angle of the minimum increases. After formation of PAA by anodic oxidation, the etching was carried out in a 5 % aqueous solution of H_3PO_4 at room temperature. Sequence of the reflective curves reveals decreasing of the angle of the minimum in the process of pore widening by etching (see Fig. 29.4b). The sensogram of the process of MCWG formation is shown in Fig. 29.4c. Anodizing and etching were stopped once the reflective curve achieved the desired shape.

29.4 Study of Coatings by SEM

Samples of PAA on glass and Si produced by anodizing and etching as it was described above have been investigated by SEM. Studies have shown that traces of the polishing on glass substrates make the surface of aluminum film wavy. It leads to disordering of pore position in PAA film (Fig. 29.5a). Two-step anodization resulted in significantly smaller pore size distribution; however we have not received the self-ordering in the structure of PAA on glass.

SEM images of the samples PAA/Au on Si formed by anodic oxidation of aluminum film in 3 % oxalic acid at 30 V and then etched during 30 min at room temperature in 5 % phosphoric acid solution with subsequent thermal deposition of

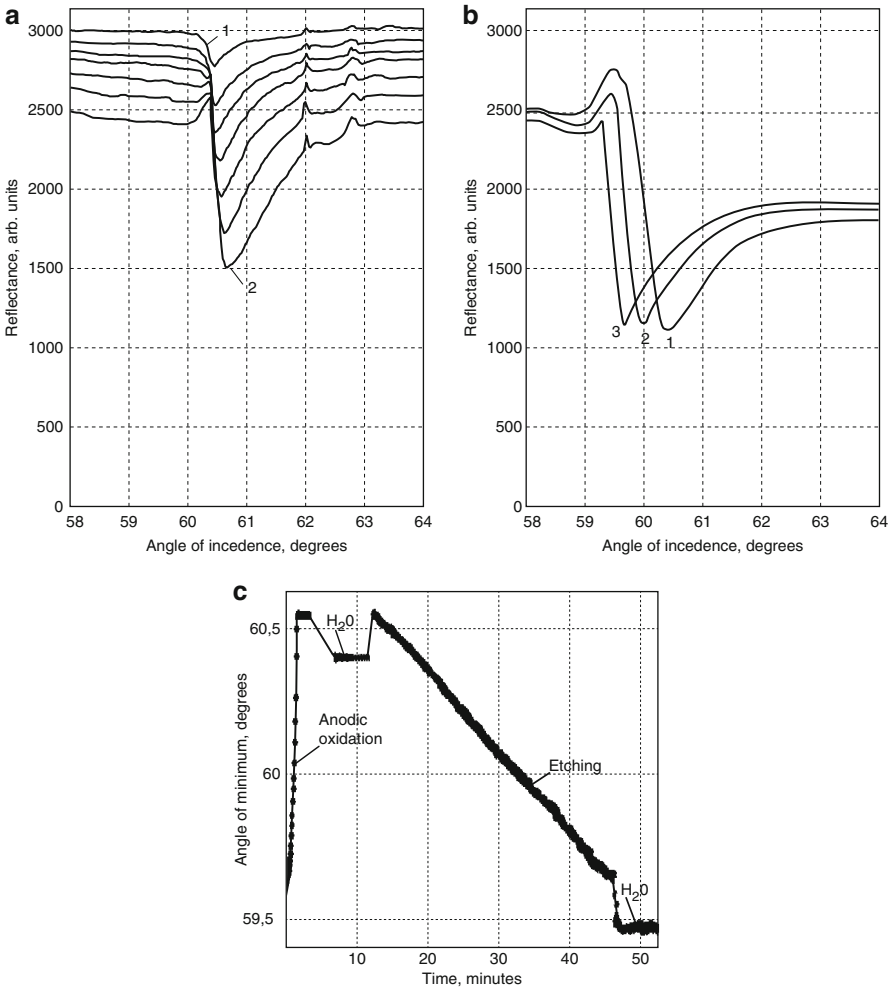

Fig. 29.4 Monitoring of formation of sensor structures Al/porous Al_2O_3 by the Plasmontest device. (**a**) Change in the shape of the reflection curve in the process of anodic oxidation of aluminum film on glass for MCWG Al/porous Al_2O_3 fabrication: 1, appearance of waveguide mode; 2, final of anodic oxidation. (**b**) Change in the shape of the reflection curve in the etching process: 1, beginning of the etching; 3, final structure. (**c**) Sensogram received during the process of formation of MCWG structure Al/porous Al_2O_3

12 nm thick gold film are shown in Fig. 29.5b, c. The cross-sectional SEM image shows vertically aligned pore structures of PAA. Figure 29.5c shows that the film of gold that was exfoliated from the PAA surface at cracking of sample is perforated at places of pore location.

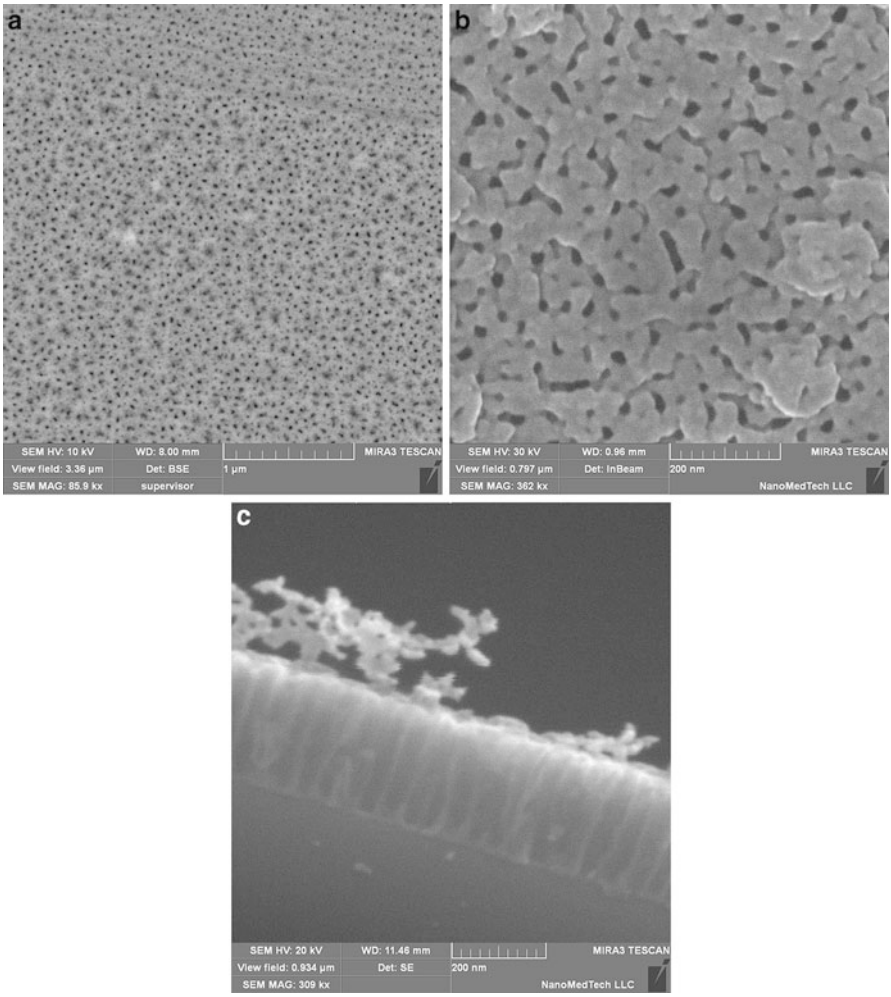

Fig. 29.5 SEM images of the samples PAA and PAA/Au. (**a**) Image of the surface of PAA on glass, (**b**) surface of PAA/Au on Si, (**c**) cross-sectional image showing vertically aligned pore structures of PAA and perforated Au film

29.5 Biosensory Experiments

We conducted preliminary experiments on the MCWG sensor substrates Al/porous Al_2O_3/Au employing a couple of immunoreagents—Staphylococcal protein A (SPA) and immunoglobulins (IgG). SPA can bind immunoglobulins mostly for their Fc fragments exposing their antigen-binding sites into solution. Preparation of recombinant analogue of PA modified by an additional cysteine residue (SPA-Cys), which due to the exposed *SH*-group strongly interacts with the gold sensor surface, can increase the reliability of its immobilization. Genetically engineered

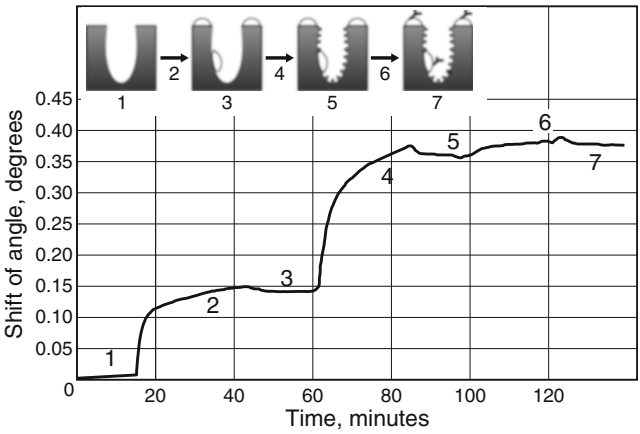

Fig. 29.6 Sensogram of investigations of immunoreagent interactions on MCWG sensors with nanoporous coating: 1, PBS; 2, 1 мкМ SPA-Cys; 3, PBS; 4, 0.5 mg/mL milk proteins; 5, PBS; 6, 20 μg/mL IgG_{hum}; 7, PBS

protein SPA-Cys contains five immunoglobulin-binding domains—*His-tag* for chromatographic purification and C-terminal cysteine residue. SPA-Cys was received in a soluble form at its expression in *Escherichia coli*. The immunoreagents were dissolved in phosphate buffer (PBS, pH 7.4); the same buffer was used for washing. The sensogram of test immunochemical experiments of SPA-Cys-IgG on MCWG with nanostructured coating Al/PAA/Au is shown in Fig. 29.6.

The experiment showed that SPA-Cys efficiently immobilized on gold surface of SPR sensors and nanostructured coating PAA with thin gold layer retaining its ability to bind human IgG. The data proved high sensitivity of immunosensors with nanoporous coatings and their potential for further use in biosensorics. To increase the sensitivity of biosensors with nanoporous coatings, it is necessary to develop the procedures of surface modification and structural engineering of PAA.

29.6 Conclusion

As the result of the research, the technology of optical metal-clad waveguide sensors with nanoporous anodic alumina covering was developed. It includes processes of magnetron deposition of Al films on optical glass plates, anodic oxidation, and chemical etching. Original technique of PAA formation with simultaneous monitoring of the reflection curves gives the opportunity of timely stop of the anodization and etching for fabrication of sensor substrates with optimal characteristics. Samples of PAA and PAA/Au have been tested by SEM. Preliminary investigations on the MCWG Al/porous Al_2O_3 and Al/porous Al_2O_3/Au

biosensors were successfully carried out. We came to the opinion that with the aim to increase the sensitivity of biosensors based on PAA, it is necessary to thoroughly develop surface modification methods and testing of modes of sensory analysis.

References

1. Voitovich I, Korsunsky V (2011) Sensory na osnove plazmonnogo rezonansa: printsipy, tekhnologii, primeneniya. (Сенсоры на основе плазмонного резонанса: принципы, технологии, применения. SPR sensors: principles, technologies, applications). Stal', Kiev
2. Skivesen N, Horvath R (2005) Optimization of metal-clad waveguide sensors. Sens Actuators B 106:668–676
3. Hotta K, Yamaguchi A, Teramae N (2010) Properties of a metal clad waveguide sensor based on a nanoporous-metal-oxide/metal multilayer film. Anal Chem 82(14):6066–6073
4. Budnyk M, Lebyedyeva T, Kurlov S, Minov Y, Sutkoviy P, Frolov Y, Shpylovyy P (2011) Modeling and data processing for thin-film optical sensors. In: Proceedings of sixth IEEE international conference on intelligent data acquisition and advance computing system: technology and application, Prague, 15–17 Sept, vol 1, pp 119–124
5. Hotta K, Yamaguchi A, Teramae N (2012) Nanoporous waveguide sensor with optimized nanoarchitectures for highly sensitive label-free biosensing. ACS Nano 6(2):1541–1547
6. Santos A, Kumeria T, Losic D (2013) Nanoporous anodic aluminum oxide for chemical sensing and biosensors. Trends Anal Chem 44:25–38
7. Hernández-Eguía L, Ferré-Borrull J, Macias G, Pallarès J, Marsal LF (2014) Engineering optical properties of gold-coated nanoporous anodic alumina for biosensing. Nanoscale Res Lett 9:414
8. Sulka GD (2008) Highly ordered anodic porous alumina formation by self-organized anodizing. In: Nanostructured materials in electrochemistry. Wiley, Weinheim
9. Ingham CJ, ter Maat J, de Vos WM (2012) Where bio meets nano: the many uses for nanoporous aluminum oxide in biotechnology. Biotechnol Adv 30:1089–1099

Chapter 30
New Nanosized Systems of Polymer Metal Complexes Based β-Diketones and Lanthanides for Electroluminescent Devices

I.A. Savchenko, A.S. Berezhnytska, and A. Mishchenko

30.1 Introduction

Since the invention of organic light-emitting devices (OLEDs) several decades ago, research has focused to a large extent on the engineering of their device structure for both high efficiency and reliable lifetime.

There has been increasing recent interest in light-emitting devices based on thin organic films of electroluminescent polymers or small molecules (OLEDs). Such systems offer several potential advantages over the more traditional in OLEDs, including relative ease of production and processing [1–5]. While many different systems have been examined, all are essentially variations on a theme. Typically, these devices consist of one or more organic layers situated between a low work function metal cathode such as calcium and a higher work function anode, often transparent indium-tin oxide (ITO). When a sufficient potential bias is applied across the electrodes, electrons are injected from the cathode into the conduction band of the luminescent layer, and holes are injected from the anode into the valence band. Under the influence of the applied potential, electrons and holes migrate to a plane within the organic film, where they meet. In an electroluminescent film, there is a reasonably high probability of photon emission due to electronhole recombination. When this occurs, photons of an energy determined by the band gap (or HOMO/LUMO gap, as the case may be) are produced.

The trivalent lanthanide ions are well known for their unique optical properties such as line-like emission band and high quantum efficiency owing to the special 4f

I.A. Savchenko (✉)
National Taras Shevchenko University of Kyiv, 60, Volodymyrska str., Kyiv 01601, Ukraine
e-mail: iras@univ.kiev.ua

A.S. Berezhnytska • A. Mishchenko
V.I.Vernadsky Institute of General and Inorganic Chemistry NASU,
32/34 Palladina prosp., Kiev 03680, Ukraine

O. Fesenko, L. Yatsenko (eds.), *Nanoplasmonics, Nano-Optics, Nanocomposites, and Surface Studies*, Springer Proceedings in Physics 167,
DOI 10.1007/978-3-319-18543-9_30

electron configuration [6–9]. Nevertheless, the f–f electron transition belongs to the forbidden transition, which results in the relatively low-absorption coefficient. Thereby, researchers construct the complexes of lanthanide ions with organic ligands, which can not only strongly absorb the energy and transfer the energy to central lanthanide ions but also expel water molecule from the first coordination sphere and protect lanthanide ions from vibrational coupling through "antenna effect" [10, 11].

Due to their unique photophysical properties that aid in shielding 4f electrons from interactions with their surroundings by the filled $5s^2$ and $5p^6$ orbital, lanthanide ions have been well known as important components in phosphors, lasers, and optical amplifiers [12, 13]. However, the direct Ln^{3+} photoexcitation is not very efficient, with the low molar absorption coefficients limiting the light output. Some organic ligands such as aromatic carboxylic acids are well known to be efficient sensitizers for the luminescence of lanthanide ions, whose organic chromophores typically present effective absorption and a much broader spectral range than the corresponding Ln^{3+} ions can absorb energy to be transferred to nearby Ln^{3+} ions by an effective intramolecular energy transfer process. This process is called lanthanide luminescence sensitization or antenna effect [14–16]. These chelates possessing the effective emission in the near-UV, visible, and NIR spectral regions are of great interest for a wide range of optical applications, such as tunable lasers, amplifiers for optical communications, components of the emitter layers in multilayer organic light-emitting diodes, light concentrators for photovoltaic devices, and so on [17–20].

The aim of this work were synthesis of Pr complexes with 2-methyl-5-phenylpentene-1-3,5-dione and allyl-3-oxo-butanoate as well as (co)polymers based on them and investigations of properties of metal-containing polymeric systems (Fig. 30.1).

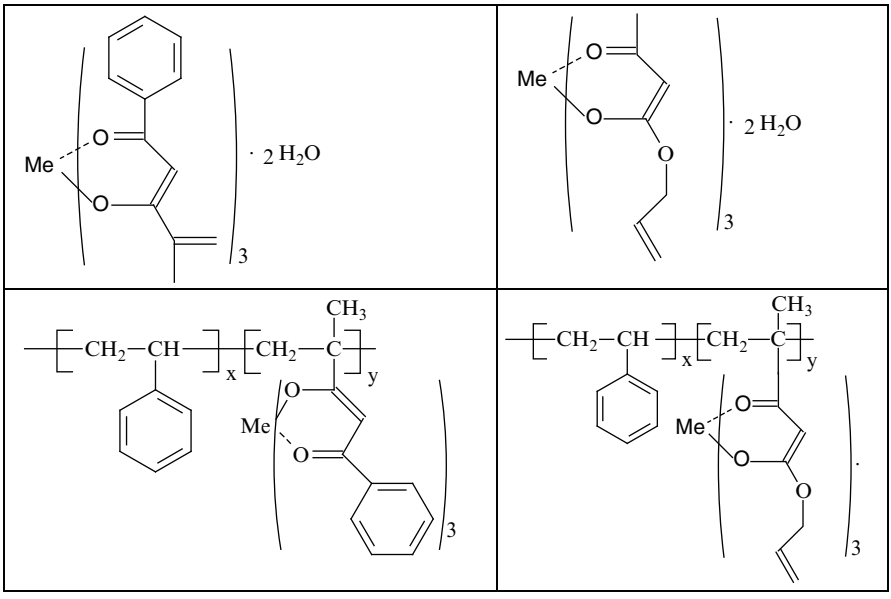

Fig. 30.1 Structures of investigated monomers and copolymers (Me = Pr)

30.2 Experimental

30.2.1 Samples

Complexes obtained by an exchange reaction between equimolar amounts of lanthanide acetate and sodium 2-methyl-5-phenylpentene-1-3,5-dione salt or allyl-3-oxo-butanoate in a water-alcohol solution at pH 9–9.5 with a slight excess of the ligand.

The polymerization was carried out at 80 °C in the thermostat in dimethylformamide solution with monomer concentration 0.03 mol/L and initiator 2,2-′-azobisisobutyronitrile concentration 0.003 mol/L. Thus, obtained metal polymers precipitate out from propanol-2 solution.

30.2.2 Observation and Measurements

The synthesized compounds have been studied by NMR, IR-, electronic absorption, diffuse reflectance spectroscopy, and thermal analysis. The infrared spectra were recorded in KBr tablets at a range of 4,000–400 cm^{-1} with Spectrum BX II FT—IR manufactured by Perkin Elmer, Nicolet Nexus 670 FTIR spectrometer. Thermograms were recorded on a TA instruments Q-1500 D apparatus by system of Setsys evolution-1750 at a heating rate of 5 °C/min from room temperature up to 500 °C in platinum capsule in the presence of carrier Al_2O_3 (anhydrous).

The electronic absorption spectra were recorded using spectrophotometer Shimadzu "UV-VIS-NIR Shimadzu UV-3600" and the diffuse reflectance spectra were obtained using the Specord M-40 spectrophotometer in the range of 30,000–12,000 cm^{-1}. The excitation and luminescence spectra of solid samples were recorded on a spectrofluorometer "Fluorolog FL 3-22," "Horiba Jobin Yvon" (Xe-lamp 450 W) with the filter OS11. The InGaAs photoresistor (DSS-IGA020L, Electro-Optical Systems, Inc, USA) cooled to the temperature of liquid nitrogen was used as a radiation detector for infrared region. The excitation and luminescence spectra were adjusted to a distribution of a xenon lamp reflection and the photomultiplier sensitivity. The particle size studying was performed at 25 °C using the equipment from "Zeta Sizer Nano by Malvern." Photomicrographs were obtained by a scanning electron microscope "Hitachi H-800" (SEM).

30.3 Results and Discussion

The monomeric complexes of $Pr(mphpd)_3 \cdot 2H_2O$ and $Pr(allyl)_3 \cdot 2H_2O$ were prepared in an aqueous alcohol solution at pH 8–10.

$$Pr(NO_3)_3 + 3Na(mphpd) \rightarrow Pr(mphpd)_3 + 3NaNO_3$$

The monomeric and polymeric complexes of Pr with 2-methyl-5-phenylpentene-1-3,5-dione (mphpd), $Pr(mphpd)_3{\cdot}2H_2O$, allyl-3-oxo-butanoate (allyl) $Pr(allyl)_3{\cdot}2H_2O$ were synthesized at the first time. The metallopolymers on their basis $[Pr(mphpd)_3]_n$ and $[Pr(allyl)_3]_n$, copolymers $Pr(mphd)_3$-co-styrene $Pr(allyl)_3$-co-styrene were obtained by free-radical polymerization with the initiator AIBN and the kinetics of polymerization was studied by dilatometric method.

Kinetic parameters of radical polymerization of complexes $Pr(mphpd)_3$ were calculated: the rate of polymerization is 1.18×10^{-4} mol/L s, the reduced rate of polymerization is 8.80×10^{-1}s, the total rate constant is 11.27×10^{-3} $dm^{1.5}/(mol^{0.5}\ s)^1$, respectively.

With the aim of the identification of ligand functional groups coordination method to metal ions were studied the IR spectra of synthesized compounds (Fig. 30.2, Table 30.1).

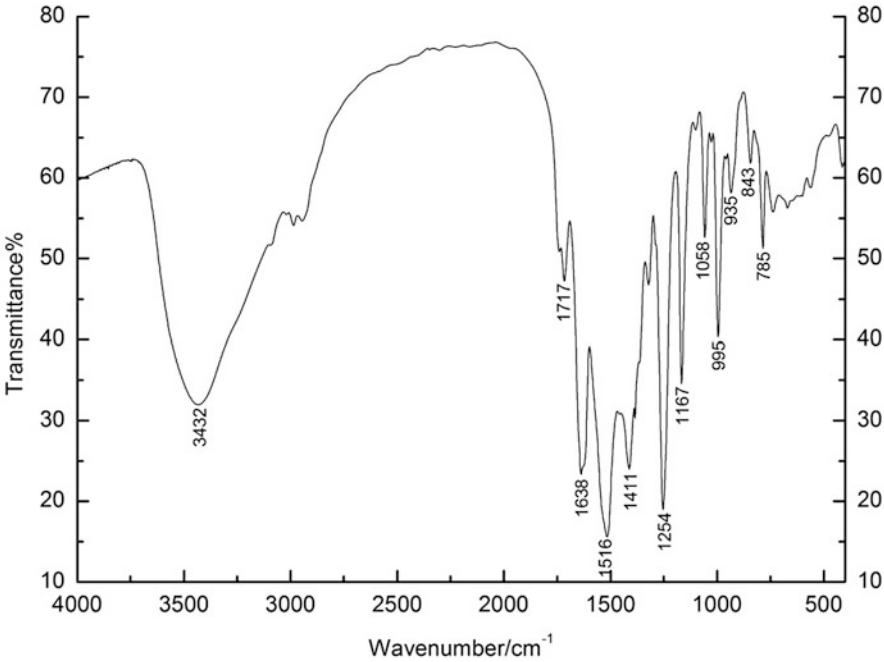

Fig. 30.2 IR spectrum of $Pr(allyl)_3{\cdot}2H_2O$

Table 30.1 Some distinctive absorption band of metallic complexes and metallopolymers

Complex	ν(M–O)	ν_{as}(C–O)	ν_{as}(C–C)	ν_s(C–O)	ν_s(C=C)
$Pr(mphpd)_3{\cdot}2H_2O$	412	1,461	1,543	1,590	1,680
$[Pr(mphpd)_3]_n$	413	1,467	1,552	1,600	1,666
$Pr(allyl)_3{\cdot}2H_2O$	415	1,411	1,516	1,638	1,717
$[Pr(allyl)_3]_n$	412	1,410	1,516	1,638	–

In the IR spectra of the synthesized complexes and polymetallocomplexes in 1,500–1,600 cm^{-1}, there are bands corresponding to stretching vibrations of the ν (C–O) and ν (C–C), which confirms the bidentate cyclic coordination of the ligand to the metal ions (Table 30.1). At the same time, a higher frequency band should be attributed to the stretching vibrations ν (CC) and a lower frequency to the stretching vibrations of the ν (CO). The region of 1,680–1,710 cm^{-1} contains stretching vibrations ν (C=C). In the case of polycomplexes, this band disappears or is significantly reduced in intensity, indicating the presence of only the terminal unsaturated groups. Fairly broad band of coordinated water molecules is observed in the region 3,300–3,500 cm^{-1}.

In IR spectra of the polycomplexes $[Pr(mphpd)_3]_n$ and $[Pr(allyl)_3]_n$ comparatively with monomeric complexes the location of main absorption bands are shifted in short-wave spectrum region, their intensity is lower significantly, the intensity is decreased especially which corresponds to vibration of the double bond. Presented results are confirmed of the polymer complex formation.

A band pattern of the Pr^{3+} ion transition with the $^3H_4$ main (quantum) state is observed (Table 30.2, Figs. 30.3 and 30.4).

The shift of the main absorption bands in the long-wavelength region, compared with the spectrum of aqua-ion, and an increase in their intensity indicates the formation of a complex.

In diffuse reflectance spectra of complexes, four major transitions from the main level $^3H_4$ are observed.

Table 30.2 Energy of the f–f transitions in the complexes under study (cm^{-1})

$^3H_4 \rightarrow {}^{2S+1}L_J$	$Pr(NO_3)_3$	$Pr(mphpd)_3$	$Pr(allyl)_3$
$^3P_2$	22,504	22,492	22,376
$^3P_1$	21,340	21,322	21,238
$^3P_0$	20,738	20,670	20,517
$^1D_2$	16,956	16,906	16,800

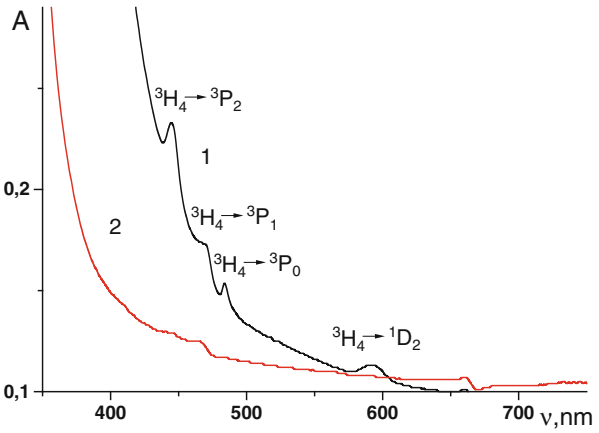

Fig. 30.3 Electronic absorption spectra. 1—$Pr(mphpd)_3$, 2—$[Pr(mphpd)_3]_n$

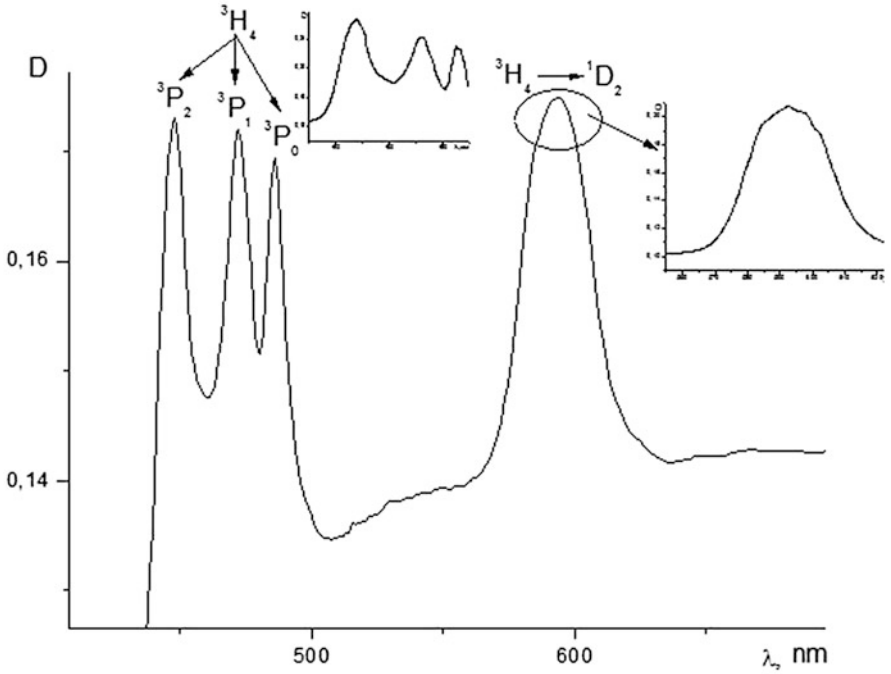

Fig. 30.4 Diffuse reflection spectrum of $Pr(allyl)_3 \cdot 2H_2O$

In complexes with organic ligands, these bands may be shifted under the influence of crystal field ligands, and the amount of deflection can be seen on the deviation value from ionic band of praseodymium—ligand.

As seen from the detailed spectra, lines (Fig. 30.4) corresponding to transitions $^3H_4 \rightarrow {}^3P_1$ include shoulder, transition $^3H_4 \rightarrow {}^3P_0$ laminates into two components, and the transition $^3H_4 \rightarrow {}^1D_2$ laminates into four components. This is due to the possible existence of two forms of complexes or dimeric structure.

However, the shift of the maximum of this band is 112 and 128 cm^{-1} mphpd and allyl, respectively, which is typical for complexes with high coordination number, which in turn the existence of multiple forms complexes is inhibited.

In the absorption spectrum of the given set of half-width for highly sensitive transition $^3H_4 \rightarrow {}^1D_2$ is (+439 cm^{-1}) and (−443 cm^{-1}), the band is laminated, which is characteristic for compounds with relatively high symmetry.

Based on the shape of the spectra and the splitting of spectral lines can assume C_{3v} or D_3 symmetry of the nearest coordination environment. Unfortunately, the structure of the coordination polyhedron according to electronic absorption spectra and diffuse reflection spectrum is not possible. We can assume that the most likely structure of the coordination polyhedron is a square antiprism.

Based on the electronic spectra nephelauxetic parameter and covalency were calculated (Table 30.3).

Table 30.3 Slater integrals and bonding parameters for the complexes under study

	$Pr(mphpd)_3$	$Pr(allyl)_3$
F_2, cm^{-1}	305.0	302.8
β	0.997	0.990
δ, %	0.30	1.01
$b^{½}$	0.039	0.071
η	1.5×10^{-3}	5.04×10^{-3}

The nephelauxetic effect is commonly quantified by a nephelauxetic ratio β and a number of parameters derived from it, namely, Sinha's parameter δ, bonding parameter $b^{½}$ and angular overlap parameter η. The β values for the complexes under study were calculated as a ratio of the second-order Slater integrals F_2 for the Pr^{3+} ion in a complex and in praseodymium nitrate ($F_2 = 306.0$ cm^{-1}). The Slater integrals were computed using a simple energy-level fitting procedure according to [21]. All other parameters were calculated using appropriative equations [21, 22].

The results (Table 30.3) indicate the metal-ligand bond is more covalent for the allyl acetoacetate complex.

Diffuse reflection spectra (Fig. 30.4) and electronic absorption spectra (Fig. 30.3) of all samples do not differ much, suggesting a similar structure in solution and polycrystalline state.

The results of DTA confirm the presence of two coordinated molecules of water in both complexes.

In the case of praseodymium complex with endothermic and weight loss 5.1 % ($\Delta m_{theor.} = 4.9$ %), corresponds to two water molecules, respectively. Weak endothermic at 215 °C caused by melting complex mass loss observed in this case, a small (2.5 %). The process of decomposition of the complex starts with the cleavage of one molecule of ligand corresponding exothermic at 257 °C and 26 % weight loss ($\Delta m_{theor.} = 25.3$). The following heating is attended by exoeffects at temperature 337, 384, 419, 460, 484 °C, and results in the total complex decomposition $\Delta m = 29$ %. The total weight is 72 % loss for praseodymium complex.

Based on the mass loss curve and DTA for complex $Pr(allyl)_3 \cdot 2H_2O$ at 106 °C detached one uncoordinated water molecule corresponding endoeffect and weight loss while 3 % approximately, $\Delta m_{theor.} = 2.91$ %. Further heating to 126 °C endothermic and accompanied by mass loss 6.7 %, which corresponds to two molecules of water ($\Delta m_{theor.} = 6.0$ %). Decomposition of complexes begins with cleavage of two allyl (C_2H_3O) substituents at the temperature range 180–270 °C exothermic and mass loss 14.7 % ($\Delta m_{theor.} = 14.3$ %). Further heating in the range 267–847 °C accompanied by a set of exothermic 333, 390, 425, 650, 780 °C and endothermic 567, 720 °C. This is due to the destruction of organic molecules. Weight loss is 23.5 % in this temperature range.

The presented results allow to assume that the complexes composition corresponds to the formula, $Pr(mphpd)_3 \cdot 2H_2O$, $Pr(allyl)_3 \cdot 2H_2O$.

The praseodymium complex $Pr(mphpd)_3 \cdot 2H_2O$ emit the visible luminescence (Fig. 30.5) from two excited states $^3P_0$ and $^1D_2$ in solid state at room temperature, like β-diketonate and carbochelates [23].

Investigations of a particle size were performed at 25 °C on the Zeta Sizer Malvern instrument. The results showed (Fig. 30.6) that the systems obtained are polydisperse with a predominance of particles 6–10 nm for $Pr(mphpd)_3 \cdot 2H_2O$, and 4–9 nm for metal complex $[Pr(mphpd)_3]_n$.

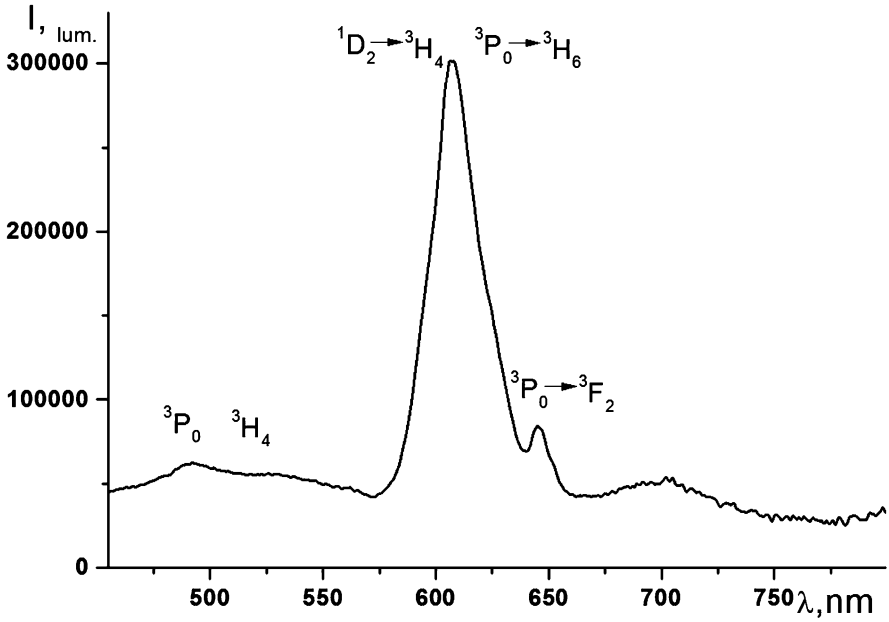

Fig. 30.5 Luminescence spectrum of $Pr(mphpd)_3 \cdot 2H_2O$ in solid state ($\lambda_{ex} = 364$ nm, 298K)

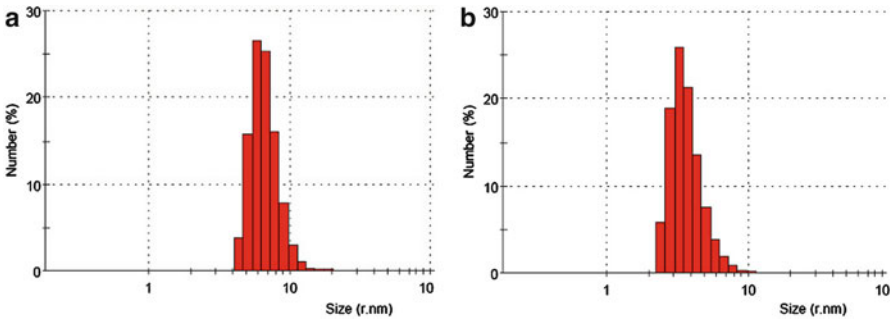

Fig. 30.6 The polydisperse assignment of particles in system. (**a**) $Pr(mphpd)_3$, (**b**) $[Pr(mphpd)_3]_n$

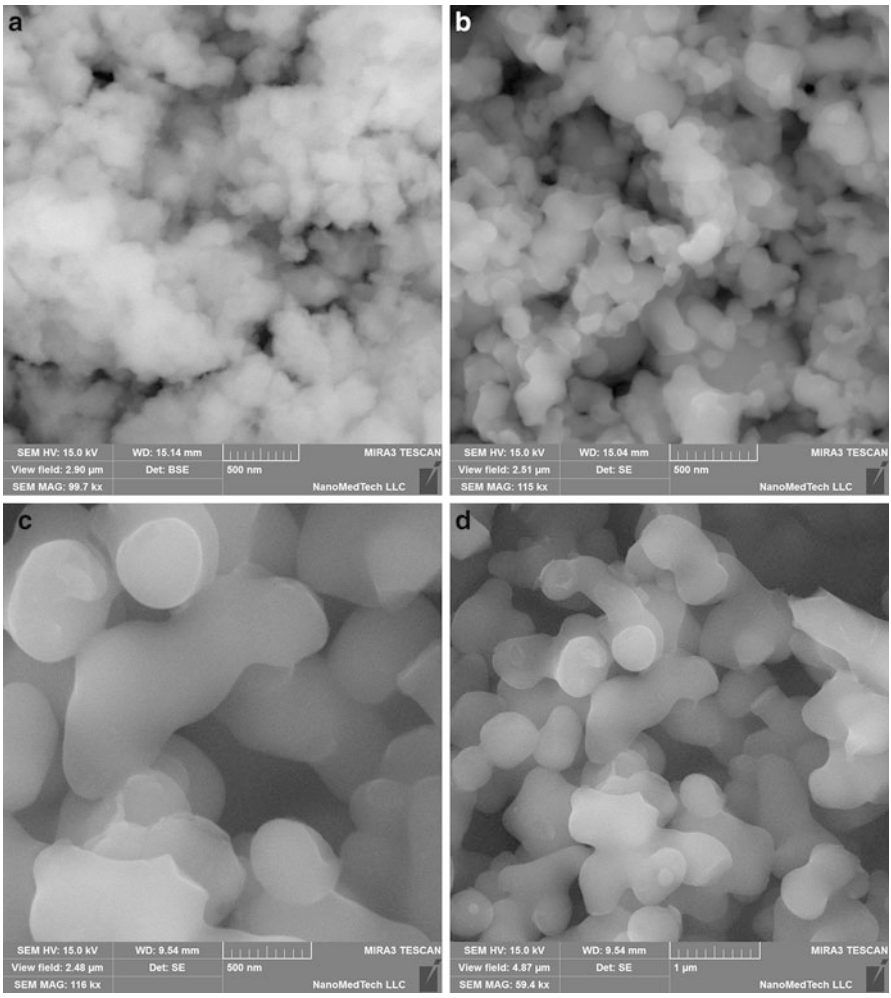

Fig. 30.7 SEM microphoto of powders. (**a**) $Pr(mphpd)_3 \cdot 2H_2O$, (**b**) $[Pr(mphpd)_3]_n$, (**c**) $Pr(mphd)_3$-co-styrene, scale 500 nm (**a–c**), 1 µm (**d**)

The systems of $Pr(mphpd)_3 \cdot 2H_2O$, $[Pr(mphpd)_3]_n$, $Pr(mphd)_3$-co-styrene are homogeneous in terms of uniform distribution of metal throughout the polymer matrix as seen from the micrographs of powdered samples (Fig. 30.7).

The method of dynamic light scattering and the results of electronic microscopy showed that the obtained polymer systems are nanoscale (the copolymer excepted).

30.4 Conclusions

The investigations conducted in the present work allowed to determine the composition, structure, and symmetry of coordination polyhedron of the monomeric complexes and polycomplexes on their basis obtained for the first time. The results of the above study showed that the configuration of the chelate unit is unchanged during the polymerization.

It was shown that all synthesized compounds are nano systems. The similarity of monomers electronic absorption spectra with polymers spectra confirms of identical coordinative environment of lanthanide ions in both cases.

The obtained polycomplexes can be used as materials for OLEDs and other optical applications.

References

1. Kuo Y, Chi-Chou L (2013) A light emitting device made from thin zirconium-doped hafnium oxide high-k dielectric film with or without an embedded nanocrystal layer. Appl Phys Lett 102(031117):1–7
2. Li Y, Chian W, Wang X et al (2011) Coordination assembly and characterization of red-emitting europium (III) organic⁄inorganic polymeric hybrids. Photochem Photobiol 87:618–625
3. Yan B, Guo M, Qiao X-F (2011) Luminescent lanthanide (Eu3+, Tb3+) hybrids with 4-vinylbenzeneboronic acid functionalized Si-O bridges and beta-diketones. Photochem Photobiol 87:786–794
4. Pekka H, Harri H (2011) Lanthanide luminescence: photophysical, analytical and biological aspects. Springer, Berlin, p 385
5. Quirino W, Legnani C, Dos Santos R, Teixeira K, Cremona M, Guedes M, Brito H (2008) Electroluminescent devices based on rareearth tetrakis beta-diketonate complexes. Thin Solid Films 517:1096–1100
6. Silva C, Li F, Huang C, Zheng Z (2008) Europium b-diketonates for red-emitting electroluminescent devices. Thin Solid Films 517:957–962
7. Guedes M, Paolini T, Felinto M et al (2011) Synthesis, characterization and spectroscopic investigation of new tetrakis(acetylacetonato)thulate (III) complexes containing alkaline metals as counteractions. J Lumin 131:99–103
8. Chen Z, Ding F, Hao F et al (2009) A highly efficient OLED based on terbium complexes. Org Electron 10:939–947
9. Mishchenko A, Berezhnytska O, Trunova O, Savchenko I (2014) Novel ytterbium(III) β-diketonates as a precursors of nir-emitting materials. Mol Cryst Liq Cryst 590:49–57
10. Bekiari V, Lianos P (1998) Strongly luminescent poly(ethylene glycol)-2,2′-bipyridine lanthanide ion complexes. Adv Mater 10:1455–1458
11. Driesen K, Van Deun R, Walrand C et al (2004) Near-infrared luminescence of lanthanide calcein and lanthanide dipicolinate complexes doped into a silica–PEG hybrid material. Chem Mater 16:1531–1535
12. Savchenko I, Bereznitskaya A, Smola S et al (2012) Novel electroluminescent materials on polymer metal complexes. Funct Mater 19(4):541–547
13. Savchenko I, Bereznitskaya A, Fedorov Y et al (2013) Structural organization of polymer metal complexes with water or phenanthroline and their influence on luminescence properties. Chem Chem Technol 7(4):423–428

14. Parker D, Dickins S, Puschmann H, Crossland C, Howard JAK (2002) Being excited by lanthanide coordination complexes: aqua species, chirality, excited-state chemistry, and exchange dynamics. Chem Rev 102:1977–2010
15. Eliseeva S, Bunzli JCG (2010) Lanthanide luminescence for functional materials and bio-sciences. Chem Soc Rev 39:189–227
16. Mech A, Monguzzi A, Meinardi F (2010) Sensitized NIR erbium(III) emission in confined geometries: a new strategy for light emitters in telecom applications. J Am Chem Soc 132:4574–4576
17. Chen Z, Ding F, Hao F, Guan M, Bian ZQ, Ding B, Huang CH (2010) Synthesis and electroluminescent property of novel europium complexes with oxadiazole substituted 1,10-phenanthroline and 2,2′-bipyridine ligands. New J Chem 34:487–494
18. Terai T, Kikuchi K, Iwasawa S, Kawabe T, Hirata Y, Urano Y, Nagano T (2006) Modulation of luminescence intensity of lanthanide complexes by photoinduced electron transfer and its application to a long-lived protease probe. J Am Chem Soc 128:6938–6946
19. Savchenko I, Berezhnytska A, Fedorov Y, Trunova E (2014) Copolymers of rare earth elements complexes with unsaturated β-diketones and N-vinylcarbazole for OLEDs. Mol Cryst Liq Cryst 590:66–72
20. Berezhnytska O, Savchenko I, Denysova Z et al (2014) The new nanosized system basis Eu (III) complexes as precursors for organic electroluminescent diodes. Mol Cryst Liq Cryst 590:58–65
21. Sastri V, Bünzli J, Ramachandra Rao V et al (2003) Modern aspects of rare earths and their complexes. Elsevier, North-Holland
22. Vyas M, Chawla G, Pandey H (2010) Electronic spectral characterization of Tm (III) systems involving N, S & O environment in DMSO Medium. Int J Chem Sci 8:2756
23. Voloshyn A, Shavaleev N, Kazakov V (2001) Luminescence of praseodymium (III) chelates from two existed states ($^3P_0$ and $^1D_2$) and its dependence on ligand triplet state energy. J Lumin 93:199–204

Chapter 31
Nanomaterials for Ink-Jet Printed Electronics

R. Lesyuk, H. Petrowska, O. Kravchuk, Ya. Bobitski, and B. Kotlyarchuk

31.1 Colloidal Metal Solutions: Synthesis Methods

The conventional technology of conductive coating fabrication for PCBs is based on the photolithography—multistep wet process accompanied by wastes up to 90 %, masks fabrication, chemical deposition, and electroplating. For the other widely used technology of thick film screen printing, the stencils and high temperatures for pastes sintering (above 800 °C) are required. Although these approaches are capable to ensure high stability and reliability, the search for alternative methods of microfabrication in the recent two decades was very active with the aim of technology simplification and lowering of the process temperatures and adaptation to the roll-to-roll technology. Application of the metal nanoparticle as the primary electroconductivity unit has opened new possibilities—essential drop of processing temperature compared to Ag-Pd pastes and noncontact dispensing through various techniques like ink-jet printing and many others (Fig. 31.1).

R. Lesyuk • B. Kotlyarchuk
Pistryhach Institute for Applied Problems of Mechanics and Mathematics of NAS of Ukraine, Naukowa 3b, Lviv 79060, Ukraine

H. Petrowska (✉)
Lviv Polytechnic National University, S. Bandery 13, Lviv 79012, Ukraine
e-mail: galina_petrovska@mail.ru

O. Kravchuk
Lviv Polytechnic National University, S. Bandery 13, Lviv 79012, Ukraine

Department EFI, G.-S. Ohm University of Applied Sciences, Nuremberg 90489, Germany

Ya. Bobitski
Lviv Polytechnic National University, S. Bandery 13, Lviv 79012, Ukraine

Institute of Technology, University of Rzeszow, Rzeszow 35-959, Poland

O. Fesenko, L. Yatsenko (eds.), *Nanoplasmonics, Nano-Optics, Nanocomposites, and Surface Studies*, Springer Proceedings in Physics 167,
DOI 10.1007/978-3-319-18543-9_31

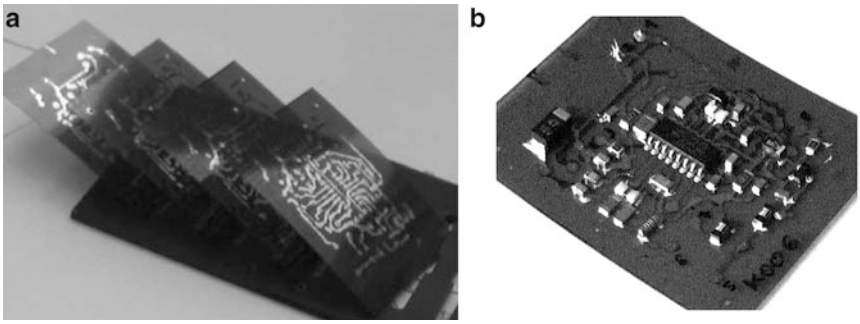

Fig. 31.1 (**a**) Polyimide substrates (40×50 mm) with printed silver conductive tracks after thermal sintering by 250 °C for 60 min. Specific conductivity of patterns $\approx 2 \times 10^7$ S/m. (**b**) VHF radio after surface mounting of components with conductive glue [1]

To the present time, more than 100 papers are published in this field that keeps on developing. The mostly used are inks based on noble metals (silver and rarely gold). Beside this, papers about application of copper, nickel, aluminum nanoparticles, as well as core-shell copper-silver and copper-graphene particles are published. Copper is a promising material due to its low price (0.24$/oz vs. 29 $/oz for silver) and the lowest resistivity among non-noble metals. However, its application in the ink-jet technology is restricted due to spontaneous oxidation property in air—as a result, the produced patterns can be nonconductive at all. This issue can be solved by the photonic sintering [2].

In general, the synthesis methods for obtaining any metal colloids can be divided into several groups: physical, chemical, electrochemical, and other methods. The group of chemical methods is very well suited for the ink-jet inks production since it provides colloids with high metal load (10 % wt and more). In the first place, the reactions of metal reduction in the presence of surfactants are used, e.g., the reduction of silver salts of fatty acids during their thermal decomposition under inert atmosphere allows synthesis of particles with several nanometers in diameter. Felba et al. have shown the influence of process parameters—reaction rate and fatty acid residue—onto mean diameter and size distribution of produced stabilized nanoparticles [3].

In 2002, Fuller et al. [4] pioneered in the fabrication of active microelectronic systems by ink-jet technology with the use of gold and silver nanoparticles (size 5–7 nm, 10 % wt), dispersed in α-terpineol. Redinger et al. [5, 6] as well as Kamushny et al. [7] were likely the first to use stabilized particles for that purpose. In [7], two concepts of ink were proposed: (a) the water solution of 40–60 nm silver particles in the presence of polymer stabilizer and (b) the solution based on the oil microemulsion (oil-water). However, the metal content was not high (8 % wt).

Similarly, the polyol method can be applied for metal nanoparticles production [8, 9] that was approved by Kim et al. with production of silver and copper inks. The main idea lies in dispersing of protecting agent or stabilizer in polyol with further addition of silver precursor. Although the general concept of the polyol

method was known, Kim et al. studied some detailed mechanisms like influence of the precursor injection rate on particle size and option between precursor preheating to the reaction temperature and injection of metal salt water solution in the preheated ethylene glycol. It was found that the determinative influence on the particle size has the precursor temperature and injection rate, and the optimal conditions (the injection rate 2.5 mL/s, $T = 100$ °C) allow obtaining of spherical monodisperse particles with the size 17 ± 2 nm. We briefly describe some options of chemical reaction for the synthesis of silver nanoparticles:

- According to [5], the $NaBH_4$ in 2-propanol was added to the silver nitrate and alkanethiol in 2-propanol solution. The silver particle size can be controlled by alkanethiol content. The duration of reaction is 2 h.
- In [10], the silver nitrate in ethylene glycol was used as the precursor. For the particle stabilization, the polyvinylpyrrolidone was used. The solution was stirred in reactor with refluxer by the temperature 120 °C for 30 min. Two fractions of 21 ± 3 and 47 ± 15 nm were obtained. As the dispersing medium, the mixture of ethylene glycol with ethanol and polyvinylpyrrolidone (3 %) was used.
- Lee et al. proposed reduction of silver from its nitrate by formaldehyde in the presence of polyvinylpyrrolidone with addition of NaOH. The main fraction of 50 nm particles was dispersed in diethylene glycol and water.

It should be noted that the frequently used α-terpineol is a volatile compound, and therefore, its industrial application is complicated, similarly to toluene that is in addition as a toxic agent classified. An attempt to use nontoxic solvents is described by Lee et al. [12]. They explored the sintering of ink based on water and ethylene glycol. However, the resistivity of patterns produced was one order of magnitude higher than by bulk silver.

31.1.1 Copper Inks Synthesis

Copper colloids are of high interest for the ink-jet technology since the replacement of silver by copper will essentially lower the costs of the ink with slight conductivity reduction after the sintering stage ($\rho_{Cu} = 1.7$ μΩ × cm vs. $\rho_{Ag} = 1.59$ μΩ × cm). From the view of electron work function (4.5 eV), copper is an appropriate candidate as a contact material for a variety of organic conductive materials (PEDOT, pentacene, etc.). Beside this, copper is less predisposed to electromigration than silver and other metals [13]. In 1999–2000, the fabrication of copper contacts from organometallic ink was shown [14] and gave challenge for the development of copper colloidal systems for electronics. Thus, Park et al. [11] fabricated printable copper colloid by abovementioned polyol method with particle size 45 ± 8 nm and achieved the resistivity of printed traces after sintering in the range of 17 μΩ × cm. Lee et al. [15] modified the polyol method and were able to make a high metal content ink (30 % wt), however, with bigger size

dispersity (30–65 nm). Prepared solutions were printed with a commercial printer and thermally cured by 200 °C in the reducing atmosphere. The minimal achieved resistivity of patterns averaged to 3.6 μΩ × cm and until today remains as one of the best results in the field (48 % of copper bulk conductivity). As the precursor, the copper sulfate ($CuSO_4 \cdot 5H_2O$) was used, reducer, sodium hypophosphite monohydrate ($NaH_2PO_2 \cdot H_2O$) and stabilizing agent, polyvinylpyrrolidone. Copper reduction passes according to the following summarized reaction:

$$Cu^{2+} + H_2PO_2^- + H_2O \rightarrow Cu^0 + H_2PO_3^- + 2H^+$$

Authors showed the influence of technological parameters on the size distribution and stability of resulting solution, proposed new technique of hot addition, and, in general, raised the shelf storage time to 3 weeks without special conditions. Also, the high throughput of the method—*5l*—is remarkable.

The classical and simple is the method used by Volkman et al. for the synthesis of copper nanoparticles in organic matrix for ink-jet printing [5]. The sodium borhydrate in 2-propanol was added to the mix of copper nitrate water solution and hexylamine in 2-propanol. After 2 h of reaction and further filtering, the stabilized copper colloid has been obtained.

Kim et al. [2] and Kang et al. [15] explored photonic and thermal sintering of commercial copper ink (Samsung Electro-Mechanics, South Korea) with the following basic parameters: particle size 5 nm, solvent (ethylene glycol and 2-methoxy ethanol), and metal content (40 % wt), but the synthesis method itself is not reported. Kim et al. achieved 5 μΩ × cm by the pulsed light treatment, and Kang et al. achieved 3.67 μΩ × cm with thermal curing by 200 °C in the reducing atmosphere of nitrogen. The colloid from Harima Inc. (Japan) with similar physical properties ($d < 10$ nm) was applied by Saito et al. [33] through the thermal sintering in a reducing atmosphere as well. After 15-min sintering by 300 °C, the structure with 5 μΩ × cm has been obtained. The different approach was proposed by Yung and Plura [17], who explored both copper and copper-tin (core-shell) colloids. The mixing of nanopowders in different dispersing media was used (where the metal load was very high—around 37 % wt). After printing, structures were sintered with YAG:Nd laser (third harmonic), but the practical outlook for this approach is restricted by prompt sedimentation (30 min) of particles in the ink. The presence of electroconductivity in resulted patterns was not reported.

The high metal content ink (40 % wt, $d = 20$ nm) was also used in the electrohydrodynamic ink-jet printing process by Khan et al. [18]. Details of ink preparation were not reported again, but through this technique, unique structures can be produced—patterns with 1 μm width and 30 μm thickness on the glass substrate. After thermal curing by 230 °C in the inert atmosphere, the 9.2 μΩ × cm resistivity was achieved, which is a nice indicator for the future outlook of this approach.

Remarkable progress has shown the Novacentrix company (Austin, TX, USA), who has developed and moved to the market innovative ink Metalon® ICI-003 and photonic curing machine for conductive track production on flexible and rigid

substrates. The ICI-003 was developed on the basis of copper oxide [19] and contains specific reducing additive. During the light pulse of powerful Xe lamp (duration of the impulse 1–10 ms), the reaction of copper reduction passes, and the mesoporous conductive coating with the sheet resistance less than 20 mΩ/sq is formed. According to Marjanovic et al. [20], this can correspond to 50 μΩ × cm, which is 30 times higher than that of bulk copper and has to be improved for industrial application.

31.1.2 Gold Inks

An essential push for the development of gold particle synthesis technology has been made among others by groups of Murray and Badia [21–25], who elaborated an effective method of gold particle synthesis with small and precisely predictable cluster diameter. This was later used by Redinger et al. [6] for the ink-jet printing technology. The main idea lies in the reduction of gold ions and formation of clusters, protected by the self-assembled layers (SAMs) of chemisorbed ligands of alkanethiol, dodecanethiol, etc. For the reaction, the tetrachloroaurate of hydrogen as precursor can be used in reducing agent—sodium borohydride. During 2003–2007, Grigoropoulos et al. [26–32] extensively used gold inks for the formation of different conductive patterns and coatings, in particular for the field-effect transistor fabrication. They obtained gold nanoparticles ($d = 1$–3 nm), protected with hexanethiol and dispersed in toluene [26], α-terpineol [32], using the abovementioned method of two-phase reduction with formation of SAM on the particle surface [22].

31.2 Vapor-Phase Synthesis of Nanoparticles

Parallel to chemical methods, some laboratories successfully used the gas evaporation techniques for the printable inks production with high metal (Cu, Ag, Au) content (up to 58 %). To our best knowledge based on published results of [33–36], we can designate Harima (Japan) and Advanced Nano Products (South Korea), who were able to move their products to the conductive ink market.

For the formation of nanoobjects from the vapor, one condition is needed—the transition of atoms and molecules into condensed state should be thermodynamically advantageous. This can be achieved by supersaturation of vapors to the certain limit where the homogeneous nucleation takes place as well as the aggregation of formations. Residual oversaturation is realized through condensation or chemisorption on the formed particles, and thus, growth of particles advances generation of new centers of condensation [37]. In general, for this kind of process, the high velocity and low controllability are specific. Evaporation of material results from violent local heating, and coagulation and coalescence of particles are very

intensive here. These conditions determine the wide size distribution of obtained particles compared to chemical reduction methods. It is known that for the small particles formation, the in-time abrupt cooling down is very important [38]. Frequently, the chemical oversaturation is used, similar to CVD method. Mentioned approaches are realized in the following methods: laser evaporation and ablation (massive samples [39–41], particles in aerosol [42]), condensation in an inert gas [43], CVD [44], generation in spark discharge [45], gas flame evaporation [46, 47], and others. The main advantage of these methods lies in their simplicity and not in the big amount of agents compared to chemical wet methods. However, the most important details of high metal content inks production for the printing of electronic components by the gas-phase method are not reported as a rule by the producers (Harima, ANP, Novacentrix).

31.3 Metal-Organic Compositions

Historically, the first materials used not for the pictures printing but for printing of electronic components were metal-organic decomposition inks. Pioneers K. Teng and R. Vest explored the ink-jet printing for solar cell metallization [48, 49] and used both silver- and gold-containing inks. In spite of high resistive losses in fabricated solar cells, fundamentals for the further technology development have been laid. Metal-organic compositions (MOC) used in mentioned works contained the central metal atom connected to hydrocarbon radical (ligand) through a hetero-atom (S, O, N) in contrast to the organometallic complexes, where the central metal atom is directly bonded to the carbon atom. Authors used silver neodecanoate, for example, that provided better solubility in xylene or toluene in comparison to primary or secondary ligands [48]. The metal load was high—over 20 % wt—and the ink was stable. The decomposition start temperature for this ink was found by 175 °C, and by 230 °C, the peak of the process was reached. TGA showed the whole carbon quits the structure by 250 °C. Similar processes were elaborated for gold amine 2-ethylhexoate with addition of ruthenium, bismuth and copper 2-ethylhexoates for the film formation and adhesion enhancement [49]. After these efforts, the MOC were for a long time (more than decade) not used for printing of electronics until the early 2000s, when copper and gold MOC were again applied for ink-jet technique. Wagner et al. [14] fabricated the source and drain electrodes using copper hexanoate $\{Cu_2(OH_2)_2(O_2CR)_4$, $R=(CH_2)_4CH_3\}$ in isopropanol/ chloroform. This application was patented [50]. The golden contacts were fabricated through solution of mercaptopropionyl-glycine powder in methanol; the decomposition took place under 200 °C.

A unique water-based MOC ink was presented by Jahn et al. [51] who elaborated printing technology of conductive tracks. Silver atoms were bonded in the complex $\{AgO_2C(CH_2OCH_2)_3H\}$ directly to the oxygen atoms without additives. This condition defined the purity of fabricated coatings. To obtain necessary rheological properties, the complex was mixed with water (the silver

content became less than 10 %). As a result, it was possible to fabricate very thin smooth layers (150 nm). By the temperature 250 °C, 43 % of bulk silver conductivity was reached (2.7×10^7S/m).

An attempt to minimize the decomposition temperature was presented by Dearden et al. [52] and Valeton et al. [53]. Authors used silver neodecanoate for the ink-jet printing with subsequent thermal treatment by 125–200 °C in the air with similar to [51] result of conductivity. In [53], the method was extended to room temperatures through UV exposure (365 nm) in the presence of reducing agent in the ink. This approach allowed getting 10 % of bulk silver conductivity, which is relatively a good result taking into account a large variety of substrates that can be used in this method.

There are also reports about using silver carboxylate MOCs [57] in printing technology. Having a low decomposition temperature (110–170 °C), this material produces relatively high-resistive structures (90 μΩ × cm after 30 min, 0.2 % of silver bulk conductivity). Under 30 °C, the ink is transparent and starting from 80 °C clusters, ~10 nm are observable. With the temperature, the grain grows and reaches ~30 nm by 150 °C. Detailed study on synthesis methods, parameters, and mechanisms of MOC decomposition can be found in review [54] devoted to carboxylate complexes. Many of the abovementioned MOCs are commercially available today.

Another type of ink for conductive components printing can be the mixture of two agents—metal precursor and reducing agent. By some certain temperature, the metal precipitation takes place. This scheme was explored by Chen et al. [55]. Authors used silver-ammonia complex $\{Ag(HN_3)_2\}^+$ with diethanolamine—self-oxidizing component. Thus, by the temperature >50 °C, diethanolamine generates formaldehyde that spontaneously reacts with silver complex, and classical "silver mirror reaction" occurs. Through such approach, the treatment temperature can be essentially reduced. Chen et al. obtained 26 % of bulk silver conductivity merely by 75 °C after 20-min treatment. Wu et al. [56] obtained by 100 °C smooth silver layers with conductivity of 13.7 μΩ × cm (11 % of silver bulk conductivity) using $AgNO_3$ and 1-dimethylamino-2-propanol.

In conclusion, we would like to point out that intensification of research in this field in the first place is related to aiming of treatment temperature reduction in comparison to nanoparticle-based inks and thus extending the choice of substrates to cheap polymer materials (PET, FR4, polycarbonate, and others vs. frequently used expensive polyimide). This could open the mass production possibility. Additionally, the safety of nanoparticles is permanently discussed. MOC don't contain any particles and this reduces the probability of nozzle clogging. However, MOC have drawbacks as well. They are very volatile, sensitive to atmosphere and humidity, and have low temperature stability. Some important results of MOC applications are summarized in the Table 31.1.

Table 31.1 Application of molecular and ionic inks for functional printing (brief review)

Metal	MOC (molecular solution)	Precursor (ionic solution)	Metal content, wt%	T, °C	ρ, μΩ × cm	Authors
Cu	CuHex + isopropanol, chloroform	–	–	200	10	Hong et al. [15]
Au	Mercaptopropionyl-glycine + methanol	–	31	400÷500	24	Nur et al. [58]
Ag	Silver carboxylate	–	30–50	110÷170	90	Kawazome et al. [59]
Ag	$\{AgO_2C(CH_2OCH_2)_3H\}$	–	9.1	130÷250	12.5÷3.7	Jahn et al. [51]
Ag	–	$Ag(NO)_3$		100	13.7	Wu et al. [56]
Ag	–	$\{Ag(HN_3)_2\}OH$	–	75	6.15	Chen et al. [55]

31.3.1 Electronics from Vitamin C

To enhance the thermal stability of MOC inks, the precursor and reducing agent can be separated into different solutions and printed independently onto the substrate. This idea was described among others in the patent [60], where the alternate printing of metal salt and reducing agent for the conductive patterns fabrication was proposed. For the precursor, all noble metals as well as copper, cobalt, and nickel salts were considered for the reducing agent—hydrophosphites, boranes/aminoboranes, glucose, aldehydes, tartrates, etc. Many of these agents are toxic and dangerous for the environment, and some of proposed reactions cannot be carried out by ambient conditions. In spite of this, the usability of described idea was demonstrated by Bidoki et al. [61] who used the ascorbic acid (vitamin C) for the reduction of silver from silver nitrate. Water-based solutions of these compounds were printed with an office printer sequentially, and the reaction passed on the substrate. The low conductivity of obtained tracks and contacts (0.3 % from bulk silver conductivity) can be partially compensated by ecological compatibility and simplicity of method and non-toxicity of inks. Similar process with copper sulfide led to forming of metal phase and its prompt oxidation, and as a result, it led to the lack of conductivity.

31.4 Conclusion

Progress in the field of materials development for printed electronics was remarkable during the last two decades. Huge motivation laid in reduction of treatment temperatures from over 800 °C for Ag-Pd pastes in thick film technology to 200 °C

with application of metal nanoparticles and under 100 °C for metal-organic inks. A variety of applications were elaborated with ink-jet printing technology—antennas, MEMS, FET contacts, electrodes for batteries, and many others on different substrates—from ceramics and polyimide to paper and textile. It is remarkable that silver was during this period and still the main material for printing of conductive tracks, contacts, and coatings due to the well-elaborated synthesis technology, highest conductivity, and relatively good stability. The main drawback—price—stimulates the search for new materials, and many interesting ideas to develop copper-based ink were presented in literature. The main challenge appears the stability of inks for ink-jet technology, as well as stability of structures fabricated from nanomaterials.

References

1. Lesyuk R, Bobitski Y, Jillek W (2008) Fabrication of VHF-radio receiver with ink-jet printed circuit board using silver nano particles. In: Proceedings of IV international conference "electronics and applied physics", Kyiv, 23–25 Oct 2008, pp 46–47
2. Kim H-S et al (2009) Intense pulsed light sintering of copper nanoink for printed electronics. Appl Phys A 97(4):791–798
3. Moscicki A et al (2005) Electrically conductive formulations filled nano size silver filler for ink-jet technology. In IEEE fifth international conference on polymers and adhesives in microelectronics and photonics, polytronic, 2005
4. Fuller SB, Wilhelm EJ, Jacobson JM (2002) Ink-jet printed nanoparticle microelectromechanical systems. J Microelectromech Syst 11(1):54–60
5. Volkman SK et al (2004) Ink-jetted silver/copper conductors for printed RFID applications. In: Materials research society symposium proceedings. Cambridge University Press, Cambridge
6. Redinger D et al (2004) An ink-jet-deposited passive component process for RFID. IEEE Trans Electron Devices 51(12):1978–1983
7. Kamyshny A et al (2005) Ink-Jet printing of metallic nanoparticles and microemulsions. Macromol Rapid Commun 26(4):281–288
8. Kurihara L, Chow G, Schoen P (1995) Nanocrystalline metallic powders and films produced by the polyol method. Nanostruct Mater 5(6):607–613
9. Wiley B et al (2004) Polyol synthesis of silver nanoparticles: use of chloride and oxygen to promote the formation of single-crystal, truncated cubes and tetrahedrons. Nano Lett 4 (9):1733–1739
10. Kim D, Moon J (2005) Highly conductive ink jet printed films of nanosilver particles for printable electronics. Electrochem Solid-State Lett 8(11):J30–J33
11. Park BK et al (2007) Direct writing of copper conductive patterns by ink-jet printing. Thin Solid Films 515(19):7706–7711
12. Lee H-H, Chou K-S, Huang K-C (2005) Inkjet printing of nanosized silver colloids. Nanotechnology 16(10):2436
13. Yi S-M et al (2008) Effect of microstructure on electrical and mechanical properties: impurities of inkjet-printed Ag and Cu interconnects. In IEEE 58th electronic components and technology conference, 2008. ECTC 2008
14. Hong CM, Wagner S (2000) Inkjet printed copper source/drain metallization for amorphous silicon thin-film transistors. IEEE Electron Device Letters 21(8):384–386
15. Lee Y et al (2008) Large-scale synthesis of copper nanoparticles by chemically controlled reduction for applications of inkjet-printed electronics. Nanotechnology 19(41):415604

16. Kang JS et al (2010) Inkjet printed electronics using copper nanoparticle ink. J Mater Sci Mater Electron 21(11):1213–1220
17. Yung K, Plura T (2010) Selective laser processing of ink-jet printed nano-scaled tin-clad copper particles. Appl Phys A 101(2):393–397
18. Khan A et al (2012) Direct printing of copper conductive micro-tracks by multi-nozzle electrohydrodynamic inkjet printing process. J Mater Process Technol 212(3):700–706
19. http://www.novacentrix.com/products/metalon-inks/copper
20. Marjanovic N et al (2011) Inkjet printing and low temperature sintering of CuO and CdS as functional electronic layers and Schottky diodes. J Mater Chem 21(35):13634–13639
21. Wuelfing WP et al (1998) Nanometer gold clusters protected by surface-bound monolayers of thiolated poly (ethylene glycol) polymer electrolyte. J Am Chem Soc 120(48):12696–12697
22. Hostetler MJ, Green SJ, Stokes JJ, Murray RW (1996) Monolayers in three dimensions: synthesis and electrochemistry of omega-functionalized alkanethiolate-stabilized gold cluster compounds. J Am Chem Soc 118:4212–4213
23. Badia A et al (1996) Structure and chain dynamics of alkanethiol-capped gold colloids. Langmuir 12(5):1262–1269
24. Hostetler MJ et al (1998) Alkanethiolate gold cluster molecules with core diameters from 1.5 to 5.2 nm: core and monolayer properties as a function of core size. Langmuir 14(1):17–30
25. Leff DV et al (1995) Thermodynamic control of gold nanocrystal size: experiment and theory. J Phys Chem 99(18):7036–7041
26. Bieri N et al (2003) Microstructuring by printing and laser curing of nanoparticle solutions. Appl Phys Lett 82(20):3529–3531
27. Chung J et al (2004) Conductor microstructures by laser curing of printed gold nanoparticle ink. Appl Phys Lett 84(5):801–803
28. Chung J et al (2004) In-tandem deposition and sintering of printed gold nanoparticle inks induced by continuous Gaussian laser irradiation. Appl Phys A 79(4-6):1259–1261
29. Choi TY, Poulikakos D, Grigoropoulos CP (2004) Fountain-pen-based laser microstructuring with gold nanoparticle inks. Appl Phys Lett 85(1):13–15
30. Chung J et al (2005) Damage-free low temperature pulsed laser printing of gold nanoinks on polymers. J Heat Transf 127(7):724–732
31. Ko S et al (2005) Fabrication of inkjet printed flexible electronics by low temperature subtractive laser processing. In: Proceedings of the IMECE, Orlando, FL, Nov 2005, pp 5–10
32. Ko SH et al (2007) All-inkjet-printed flexible electronics fabrication on a polymer substrate by low-temperature high-resolution selective laser sintering of metal nanoparticles. Nanotechnology 18(34):345202
33. Saito H, Matsuba Y (2006) Liquid wiring technology by ink-jet printing using NanoPaste. In: 35th international symposium on microelectronics IMAPS, San Diego
34. Radivojevic Z et al (2007) Optimised curing of silver ink jet based printed traces. arXiv preprint arXiv:0709.1842
35. Murata K et al (2005) Super-fine ink-jet printing: toward the minimal manufacturing system. Microsyst Technol 12(1-2):2–7
36. Felba J, Schaefer H (2009) Materials and technology for conductive microstructures. In: Nanopackaging. Springer, New York, pp 239-263
37. Swihart MT (2003) Vapor-phase synthesis of nanoparticles. Curr Opin Colloid Interface Sci 8 (1):127–133
38. Kruis FE, Fissan H, Peled A (1998) Synthesis of nanoparticles in the gas phase for electronic, optical and magnetic applications—a review. J Aerosol Sci 29(5):511–535
39. Mafune F et al (2000) Formation and size control of silver nanoparticles by laser ablation in aqueous solution. J Phys Chem B 104(39):9111–9117
40. Mafuné F et al (2000) Structure and stability of silver nanoparticles in aqueous solution produced by laser ablation. J Phys Chem B 104(35):8333–8337
41. Tsuji T et al (2002) Preparation of silver nanoparticles by laser ablation in solution: influence of laser wavelength on particle size. Appl Surf Sci 202(1):80–85

42. Nichols W et al (2001) Large-scale production of nanocrystals by laser ablation of microparticles in a flowing aerosol. Appl Phys Lett 78(8):1128–1130
43. Maisels A et al (2000) Synthesis of tailored composite nanoparticles in the gas phase. Appl Phys Lett 77(26):4431–4433
44. Nasibulin AG et al (2002) Nanoparticle synthesis by copper (II) acetylacetonate vapor decomposition in the presence of oxygen. Aerosol Sci Technol 36(8):899–911
45. Weber AP, Seipenbusch M, Kasper G (2001) Application of aerosol techniques to study the catalytic formation of methane on gasborne nickel nanoparticles. J Phys Chem A 105 (39):8958–8963
46. Keskinen H et al (2004) Generation of silver/palladium nanoparticles by liquid flame spray. J Mater Res 19(5):1544–1550
47. Mädler L et al (2002) Controlled synthesis of nanostructured particles by flame spray pyrolysis. J Aerosol Sci 33(2):369–389
48. Teng K, Vest R (1987) Liquid ink jet printing with MOD inks for hybrid microcircuits. IEEE Trans Components Hybrids Manufacturing Technol 10(4):545–549
49. Teng K, Vest RW (1988) Metallization of solar cells with ink jet printing and silver metalloorganic inks. IEEE Trans Components Hybrids Manufacturing Technol 11(3):291–297
50. Kydd PH, Wagner S, Gleskova H (2001) Material and method for printing high conductivity electrical conductors and other components on thin film transistor arrays. Google Patents
51. Jahn SF et al (2010) Inkjet printing of conductive silver patterns by using the first aqueous particle-free MOD ink without additional stabilizing ligands. Chem Mater 22(10):3067–3071
52. Dearden AL et al (2005) A low curing temperature silver ink for use in ink-jet printing and subsequent production of conductive tracks. Macromol Rapid Commun 26(4):315–318
53. Valeton JJ et al (2010) Room temperature preparation of conductive silver features using spin-coating and inkjet printing. J Mater Chem 20(3):543–546
54. Grodzicki A et al (2005) Copper (I), silver (I) and gold (I) carboxylate complexes as precursors in chemical vapour deposition of thin metallic films. Coord Chem Rev 249(21):2232–2258
55. Chen S-P et al (2012) Silver conductive features on flexible substrates from a thermally accelerated chain reaction at low sintering temperatures. ACS Appl Mater Interfaces 4 (12):7064–7068
56. Wu J-T et al (2011) Inkjet printing of low-temperature cured silver patterns by using AgNO3/1-dimethylamino-2-propanol inks on polymer substrates. J Phys Chem C 115 (22):10940–10945
57. Suganuma K et al (2006) Low temperature printing wiring with Ag salt pastes. In: 39th International symposium on microelectronics IMAPS, San Diego, pp 1050–1054
58. Nur H et al (2002) Ink-jet printing of gold conductive tracks. J Mater Sci Mater Electron 13 (4):213–219
59. Kawazome M et al (2006) Nano particles fine pitch wiring for printed electronics. Micromeritics 50:27–31
60. Johnson DR, Damarell WN, Kynaston-Pearson AW (2003) Depositing solid materials. World Patent WO2003049515 A1
61. Bidoki S et al (2007) Ink-jet fabrication of electronic components. J Micromech Microeng 17 (5):967

Chapter 32
Influence of Hydrogen on the Mechanical Properties of Steels with the Surface Nanostructure

H. Nykyforchyn, E. Lunarska, V. Kyryliv, and O. Maksymiv

Nanocrystalline structure (NCS) in engineering steels allows combining the high strength and good plasticity in comparison with the ordinary steels [1, 2]. As an effect, the higher plasticity of material provides the higher brittle fracture resistance, as well as the crack growth resistance [3, 4]. In general, the high brittle fracture resistance of steel assumes its low sensitiveness to an aggressive action of the hydrogen containing environments. However, it is not clear whether such regularity can be also observed in the case of the nanocrystalline materials. The specific feature of those materials is the high total length of the grain boundaries which may serve as the strong accumulator of hydrogen and thus may promote the hydrogen embrittlement.

The technology has been developed [5, 6] to form the NCS surface by the severe plastic deformation (SPD) produced by the high speed friction of the metal tool pressed against the treated material. During this so-called mechanical-pulse treatment (MPT), the shear deformation rate reaches 10^2–10^3/s and a temperature in the friction zone reaches about 1,000 °C [5, 6]. The special technological medium has been supplied into the friction zone to play two roles: (1) alloying the surface layer with chemical elements present in medium due to its thermal destruction within the contact zone and intensive mass transfer; (2) the structural-phase transformations in material during its rapid cooling. The MPT nanodispersion leads to the formation of the surface layer with modified chemical and phase composition and consisting of grains, about 15 nm in size.

The NCS surface layer, about 100–800 μm thick, produced by MPT exhibits the improved mechanical properties [5, 6], in the first turn the strength and hardness

H. Nykyforchyn (✉) • V. Kyryliv • O. Maksymiv
Karpenko Physico-Mechanical Institute of the NASU, 5 Naukova Str., Lviv 79060, Ukraine
e-mail: nykyfor@ipm.lviv.ua

E. Lunarska
Institute of Physical Chemistry of PAN, Warsaw, Poland

O. Fesenko, L. Yatsenko (eds.), *Nanoplasmonics, Nano-Optics, Nanocomposites, and Surface Studies*, Springer Proceedings in Physics 167,
DOI 10.1007/978-3-319-18543-9_32

(microhardness of strengthened layer reaches 8–12 GPa) which unambiguously rises the wear resistance of the surface.

Our previous investigations of hydrogen embrittlement of nanostructurized engineering steels [2, 4] have shown some promising results. Since MPT may provide the simultaneous increase in strength and in plasticity in comparison with the usual thermal treatment (quenching and tempering), it may lead to the lower susceptibility to the hydrogen action. Indeed, in some cases the NCS steels do not reveal the hydrogen embrittlement. The present investigation has been directed to achieve the nanostructured engineering steels exhibiting the combination of the high strength and the hydrogen embrittlement resistance, as well.

32.1 Materials and Experimental Methods

MPT has been performed on the flat polishing machine. As schematically shown in Fig. 32.1, the rotating cylindrical tool (*1*) assembled on the axis of the machine spindle has been pressed to the flat surface of specimen (*2*) fixed on the machine table and moving against the tool (*1*). Technological medium (*3*) has been injected into the friction zone between the tool and specimen using the system of cooling liquid supply of the polishing machine. The tools of two geometries have been used: ordinary narrow cylinder with straight generatrix (Fig. 32.2a) and of the special chevron geometry one (Fig. 32.2b). In the later case, the tool has provided the shear deformation in different directions.

The following regimes of MPT have been used: rotating speed of the strengthened tool $V_1 = 50$ m/s, linear speed of moving machine table with fixed specimen $V_2 = 1$ m/min, tool transversal feed $S = 0.5$ mm for double motion of the table, depth of tool incut 0.3 mm. The industrial oil has been used as the technological medium.

Effects of MPT of the 45 (0.45C) and 40Kh (0.45C-1Cr) steels on the structure, strength, microhardness, hydrogen permeation, and hydrogen embrittlement resistance have been studied. Flat specimens 1.6 mm thick (Fig. 32.3) with both A and B sides subjected to MPT have been tensile tested. It should be taking into account that the tensile properties of such a composite "surface layer–base material–surface layer" specimens can only partially reflect the properties of the strengthened surface layer.

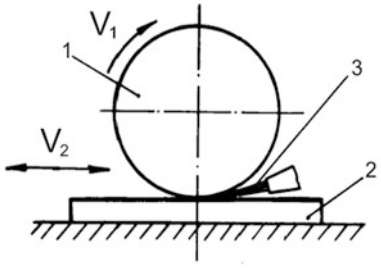

Fig. 32.1 The scheme of MPT of plane surfaces: 1—strengthening tool; 2—treated metal; 3—technological medium

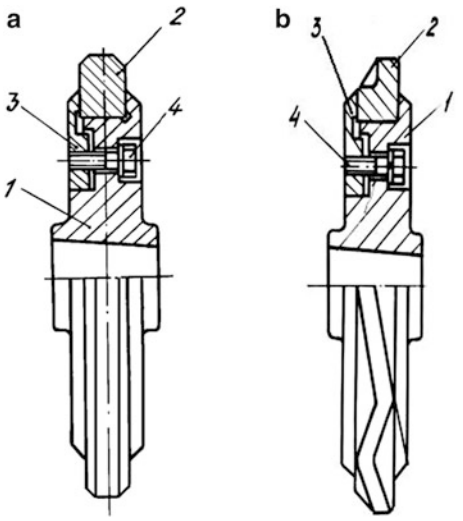

Fig. 32.2 Tools for MPT of straight (**a**) and chevron (**b**) geometry: 1—body; 2—variable working insertion; 3—flange; 4—bolt

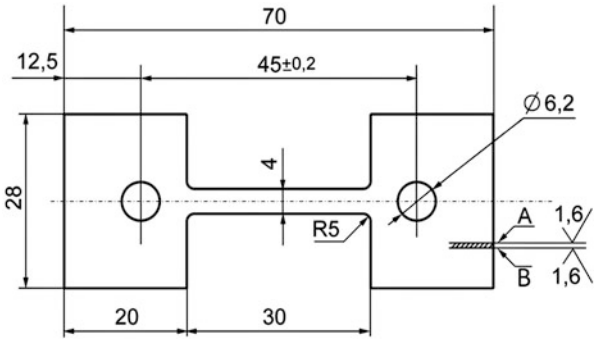

Fig. 32.3 Scheme of the tensile test specimen

Therefore, to decrease the gradient of hardness along the cross-section, specimens have been preliminary quenched and tempered at 200, 300, 400, and 500 °C, polished, subjected to MPT and again tempered the second time at the same temperature.

For hydrogen permeation studies, flat specimens (18 × 30 mm) 0.6 and 0.8 mm thick have been used in as-received and MPT states, respectively. Only one side of those specimens has been subjected to MPT.

The X-ray diffraction spectra have been recorded on DRON-3 diffractometer at $Cu_{k\alpha}$ radiation ($U = 30$ kV, $I = 20$ mA) with the 0.05° step and the point exposition of 4 s. The phase composition of the surface layers, dislocation density (ρ), and the grain size of the steel have been estimated from obtained spectra using the JCPDS-ASTM database [7] and taking into account the half-breadth of the XRD peaks [8].

Surface microhardness has been measured on microhardener PMT-3 at a load of 50 g. The tensile tests have been carried out at the grip rate of 0.5 mm/min.

A susceptibility of the mechanical-pulse treated metal to hydrogen embrittlement has been established by comparison the mechanical properties (plasticity) of specimens before and after electrolytic hydrogenation. Specimens have been hydrogen charged for 60 min in 1 N solution $H_2SO_4 + 2.5$ g/L of thiourea at cathodic current density of 0.1 mA/cm^2.

Hydrogen permeation measurements have been done by the Devanathan-Stachurski [9] electrochemical method using the double cell divided by the studied membrane. The egress side of a membrane, coated with Pd has been exposed to 0.1 N NaOH and polarized at +150 mV (all potentials are given vs. Hg/HgO reference electrode). Anodic current, being the measure of the hydrogen permeation rate through the membrane has been recorded in the egress cell. At the step-by-step application of cathodic current of 2, 5, and 10 mA/cm^2 to the ingress side of membrane exposed to the 3 % NaCl test solution, the build-up hydrogen permeation transients have been recorded for each step in the egress cell until the steady state has been achieved. At switching off the polarization of the ingress side, the decay permeation transients have been recorded in the egress cell. Mechanical-pulse treated surface served as the ingress side of the membrane. From the hydrogen permeation tests, the following parameters have been estimated [9, 10]: (1) steady state hydrogen permeation current at given cathodic polarization ($-J_i^{\infty}$); (2) hydrogen diffusion coefficient (D_i) calculated from each build-up transient; (3) hydrogen diffusion coefficient (D_o) calculated from the decay transient. It should be noted that determined from those experiments coefficient D_o characterizes diffusion of hydrogen in crystal lattice, whereas the effective diffusion coefficient D_i—characterizes the hydrogen transport through the metal with defects served as the hydrogen traps.

32.2 Test Results and Discussion

According to X-ray and mass-spectrum [5] analyses, the MPT changes the chemical composition of the surface layer of 45 steel, increases (up to two orders of magnitude) the dislocation density (ρ) and forms the ferrite-austenite NCS with the average grain size (d) 19 nm (Table 32.1). Surface has been enriched in hydrogen, nitrogen, and carbon. The 2.3 times increase in carbon content means that the treated surface contains about 1 % C, which should affect the metal

Table 32.1 Analysis of the surface of 45 steel in as received condition and after MPT by the tool with straight profile

State of surface	$\rho \cdot 10^{11}$, cm^{-2}	d, nm	Quantity of the chemical element on surface, relative unit				
			H_2	N_2	O_2	C	Si
Without MPT	0.08	–	1.0	1.0	1.0	1.0	1.0
After MPT	9.8	19	3.0	1.7	1.2	2.3	1.1

strength. The increased content of hydrogen might lead to the hydrogen embrittlement of the strengthened layer.

Since the treated metal is not susceptible to etching, the depth of the MPT effect has been evaluated by the thickness of unetched white layer being about 150 μm thick (Fig. 32.4a). Treated layer exhibits the high microhardness which gradually decreases from the surface to the core (Fig. 32.4b).

The SPD as the method to obtain the NCS has been considered in [11–14], and it has been shown that the microlocalization of dislocation structure during the SPD strongly depends on the mode of the shear deformation. Quantitative characterization of the deformation mode has been determined by the distribution of the deformation velocity between the main directions of continual shear and corresponds to the limited states of the pure and simple shear. It has been shown that the mode of simple shear corresponds to the development of the polyangle boundaries and fragmentation of the structure. One of the technological ways to achieve the simple shear is deformation in different directions, which can be realized during MPT using the special tool with the chevron profile [15].

The parameters of surface structure and the tensile mechanical properties of 40Kh steel strengthened by tools of different geometry are presented in Table 32.2. MPT by the chevron tool enlarges a level of the structure nanodispersion,

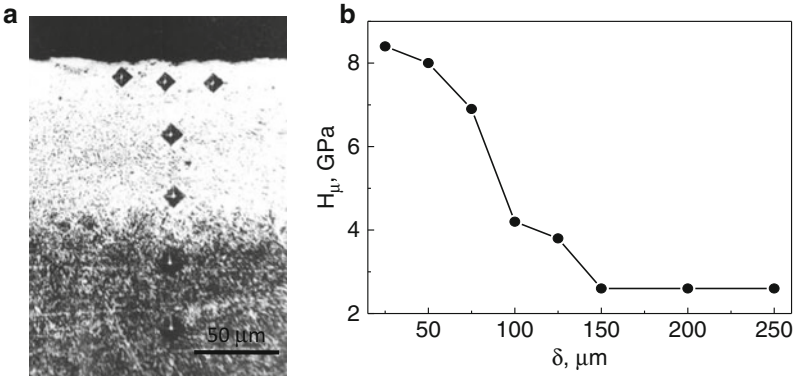

Fig. 32.4 Microstructure with the microhardness marks (**a**) and distribution of microhardness H_μ (**b**) along the distance from surface (δ) for 40Kh steel after MPT by the tool with straight profile

Table 32.2 Parameters of the 40Kh steel surface strengthened by MPT, depending on the tool profile

Profile of tool	d, nm	P, % α (γ)-phase	$\rho*10^{12}$, cm^{-2}	R_a, μm	H_μ, GPa	σ_{UTS}, MPa	σ_{YS}, MPa	ε, %	RA, %
Without MPT	–	–		–	2.4	550	290	25.0	43.0
Straight	16	60 (40)	1.51	2,2	10.0	580	515	12.5	33.4
Chevron	12	63 (37)	2.02	1,2	10.5	620	550	9.0	52.0

dislocation density, slightly increases the microhardness and a percentage of α-phase (P) at corresponding decrease in a γ-phase and decreases the roughness (R) of strengthened surface. Those effects have been accompanied by an increase in the strength of the both side strengthened flat specimens. MPT, increasing strength, especially the yield stress (σ_{YS}), essentially decreases elongation (ε), being more pronounced at the application the chevron tool. Concerning the data of reduction of area (RA), the MPT effect occurs to be ambiguous. The use of the straight profile tool diminishes RA from 43.0 to 33.4 %, although much less pronounce than the decrease in ε (from 25.0 to 12.5 %). On the other hand, MPT by the chevron tool significantly raises RA to the values even higher than those measured for the not treated metal. These revealed opposite direction of a change of the different characteristic of plasticity demands the special study. It is possible to be an effect of the complexity of the "surface layer–matrix–surface layer" composite tested specimens, or to be the effect of testing not cylindrical but flat specimens. Thus, it is not possible to explain unambiguously how decrease of d from 16 to 12 nm affects the plasticity of composite specimen.

The positive effect of nanostructurization of steel on its mechanical properties arises the problem of NCS stability at the tempering of the specimen subjected to MPT. Since the maximum tempering temperature after MPT has been 500 °C, the study has been limited to this temperature. As it has been revealed earlier [16], the tempering after MPT of 65G (0.65C-1 Mn) steel at that temperature did not cause the enlargement of NCS. Apparently, the similar phenomena should also occur in the case of studied 40Kh steel. Therefore, the observed drop of microhardness due to the tempering at 500 °C after MPT, from 8.1 to 4.2 GPa (Table 32.3) has not been supposedly caused by the change of grain size within the range of nanolevel, but the other reason should be involved.

The results of the tensile mechanical properties of the 40Kh steel specimens strengthened by MPT using different tools, tested without and after hydrogenation, are presented in Fig. 32.5. Hydrogen charging mainly increases the yield stress of specimens (Fig. 32.5a), variant *4* of the treatment (preliminary quenching and tempering) being an exception. Hydrogen also decreases σ_{UTS} for this variant and for as-received state (without MPT) but increases strength after only MPT independently of the type of the tool (variants *2* and *3* in Fig. 32.5b).

The more pronounced effect produces the hydrogen charging on plasticity parameters. It decreases elongation ε (with the exception of MPT by the chevron tool, variant *3* in Fig. 32.5c). Reduction of area decreases for as-received state and for all variants of MPT as well (Fig. 32.5d). However, if to consider the absolute values of RA of hydrogenated specimens, then MPT by the chevron tool allows improving

Table 32.3 Effect of MPT produced by the tool with straight profile and the following tempering on surface microhardness H_μ (GPa) of 40Kh steel

		Tempering temperature after MPT, °C			
Without MPT	MPT without tempering	200	300	400	500
2.4	8.1	8.0	5.5	5.2	4.2

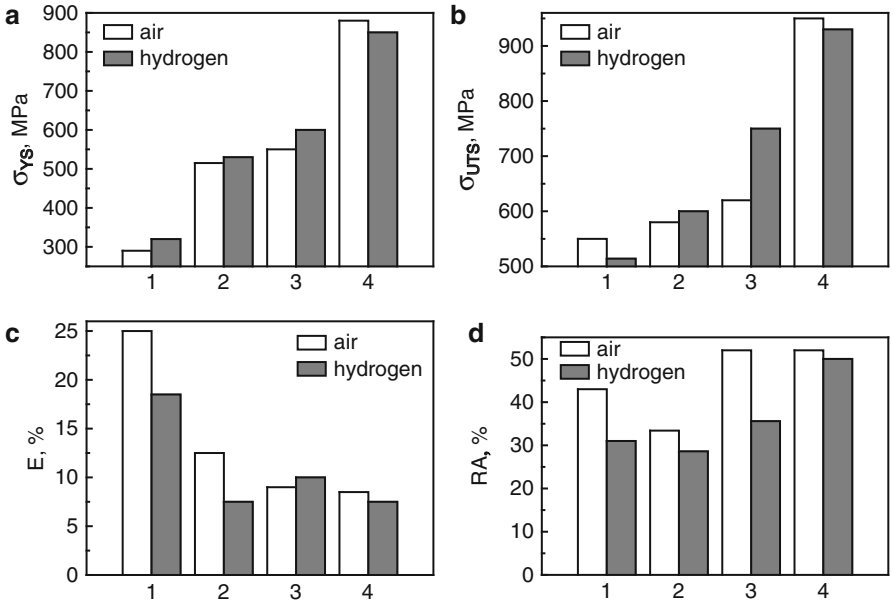

Fig. 32.5 The change of tensile mechanical properties of 40Kh steel specimens strengthening by MPT, depending on the tool type: 1—without MPT; 2—MPT by the tool with the straight profile; 3—MPT by the tool with the chevron profile; 4—quenching + tempering at 500°C + MPT by the chevron tool + tempering at 500°C

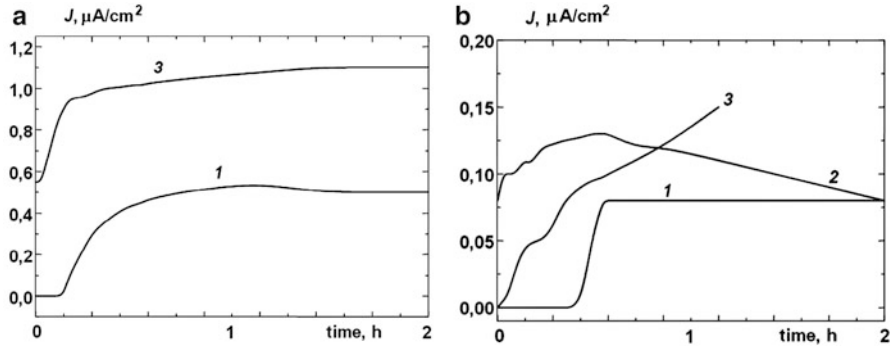

Fig. 32.6 The build-up permeation transients recorded for untreated (a) and subjected to MPT (**b**) specimens of 45 steel at application of consequently increased cathodic polarization to the ingress side: *1*—2 mA/cm^2; *2*—5; *3*—10 mA/cm^2

their strength and RA. Besides in spite of the generally decrease in elongation by MPT, a using of the chevron tool provides higher ε levels than that measured for the specimens treated with the ordinary tool (variant *3* against *2* in Fig. 32.5c).

The results of hydrogen permeation are presented in Fig. 32.6 and Table 32.4. The character of time dependencies of permeation current density and the determined

Table 32.4 The parameters of hydrogen permeation in 45 steel

State of metal	Current density of cathodic charging, mA/cm^2						
	2		5		10		Switching off
	J_∞, μ/cm^2	D_i, cm^2/s	J_∞, μ/cm^2	D_i, cm^2/s	J_∞, μ/cm^2	D_i, cm^2/s	D_0, cm^2/s
Without MPT	0.48	$6.1{\cdot}10^{-7}$	–	–	1.1	$2.85{\cdot}10^{-6}$	$2.86{\cdot}10^{-6}$
After MPT	0.08	$6.2{\cdot}10^{-7}$	0.13	$5.9{\cdot}10^{-7}$	0.15	$7.35{\cdot}10^{-7}$	$6.94{\cdot}10^{-7}$

parameters are principally different for the unstrengthened and strengthened specimens. For MPT-treated materials, a maximum on the curves of permeation current has been registered at the cathodic current density already 5 mA/cm^2 (Fig. 32.6b), although such a maximum has not been revealed on the permeation curve recorded for the metal in as-received condition (Fig. 32.6a). It has been considered that a drop of permeation current after a receiving of maximum level is caused a development of microdamages due to electrolytic charging which makes hydrogen more difficult to permeate through the membrane. Thus, MPT facilitates the creation of defects during hydrogen charging of metal. In addition, such an observation might be supported by the data shown in Table 32.3: (1) the steady state current of hydrogen permeation J_i^∞ has been considerably higher for as-received metal than for that subjected to MPT what indicates the easer conditions for hydrogen transport in the first case; (2) effective diffusion coefficient D_i is lower than the lattice one D_o, which is an evidence of more difficult transport of hydrogen in the real defected material.

Thus NCS, generated by MPT using the ordinary tool with the straight profile has been characterized by the lower resistance to the creation of defects caused by hydrogen. At the same time, one should expect that a using of chevron tool, which increases plasticity of hydrogenated metal (see Fig. 32.5c, d) would also decrease the sensitivity of metal to hydrogen embrittlement. From the other hand, it should be noted that MPT forms the surface layer which serves as hydrogen accumulator and correspondingly the barrier layer which reduces penetration of hydrogen in the core of the metal.

32.3 Conclusions

1. Mechanical-pulse treatment by high speed friction of middle carbon steel produces the surface layer of the nanocrystalline structure with the grain size lower than 20 nm.
2. By using the special chevron tool, which forms the thermal-plastic deformation in different directions, the better values of mechanical properties can be achieved than in the case of tool with the straight profile.
3. Hydrogen permeation experiments indicate a hampering of hydrogen transport within the strengthened surface layer which can be accounted for the intensive hydrogen trapping due to created defects. Hence, surface layer serving as an

accumulator of hydrogen may affect its susceptibility to hydrogen embrittlement but from the other hand—that barrier layer hampers the penetration of hydrogen into the metal core.

4. Hydrogen decreases the plasticity of the composite specimens with the surface nanocrystalline structure. However, by the selection of preliminary thermal treatment and tempering temperature after mechanical-pulse treatment it is possible to combine the high strength, plasticity, and resistance to hydrogen embrittlement.

References

1. Kyryliv VI, Nykyforchyn HM, Maksymiv OV (2013) Physic-mechanical properties of the surface nanocrystalline structure formed by mechanical-pulse treatment. Abstrakt book. In: International conference: HighMatTech, 7-11 Oct, Kiev, Ukraine, p 176
2. Maksymiv OV, Kyryliv VI, Nykyforchyn HM (2014) Influence of hydrogen on the mechanical properties of steels with surface nanostructures. Abstract book. In: Nanotechnology and nanomaterials, 23-30 Aug, Yaremche-Lviv, Ukraine, p 373
3. Andrievski RA (2007) Hydrogen in nanostructures. PHYS-USP 50(7):691–704
4. Maksymiv OV, Nykyforchyn HM (2011) Effect of hydrogen on mechanical behaviour of surface nanocrystalline steel structure. In: E-MRS 2011 fall meeting—symposium C: mechanical properties of nanomaterials—experiments and modeling (CD). University of Technology, Warsaw
5. Nykyforchyn H, Kyryliv V, Maksymiv O (2014) Chapter 2: physical and mechanical properties of surface nanocrystalline structures, generated by severe thermal-plastic deformation. Nanocomposites, nanophotonics, nanobiotechnology, and applications. av Olena Fesenko, Leonid Yatsenko. Inbunden, Springer, Berlin, pp 31-41
6. Nykyforchyn HM, Kyryliv VI, Slobodjan DV et al (1998) Structural steels surface modification by mechanical pulse treatment for corrosion protection and wear resistance. Surf Coat Technol 100–101:125–127
7. Akselrud LG, Gryn' YM, Zavaliy PY et al (1993) Use of the CSD program package for structure determination from data. In: Abstract of the European powder diffraction Conference, Enshede, Netherlands, 1992. Material Science Forum, vol 41 (133–136), pp 335–342
8. Powder Diffraction File 1973 (1974) Search manual alphabetical listing and search section of frequently encountered phases. Inorganic, Philadelphia
9. Devanathan MAV, Stachurski ZJ (1964) The mechanism of hydrogen evolution on iron in acid solutions by determination of permeation rates. J Electrochem Soc 111:619–623
10. Pressouyre GM, Bernstein IM (1978) A quantitative analysis of hydrogen trapping. Metall Trans A 9:1571–1576
11. Gutkin M, Ovid'ko IA (2003) Declination and rotation deformation in nanocrystalline materials. Rev Adv Mater Sci 4:79–113
12. Hansen N (1990) Cold deformation structures. Mater Sci Technol 6:1039–1047
13. Segal VM (2002) Severe plastic deformation: simple shear versus pure shear. Mater Sci Eng A 338:331–344
14. Segal VM (2005) Deformation mode and plastic flow in ultra fine grained material. Mater Sci Eng A 406:205–216
15. Kyryliv VI, Nykyforchin HM, Maksymiv OV et al (2012) Tools for surface nanocrystalline structures multidirectional thermoplastic deformation [in Ukrainian]. Patent of the Ukraine No 70431, MPK B24B 39/00. Publ. 11.06.2012, Bull. No. 11
16. Nykyforchin HM, Kyryliv VI, Maksymiv OV (2015) Effect of nanostructurisation for structural steels on their wear hydrogen embrittlement resistance. Solid State Phenomena 225:65–70

Chapter 33
Optimization of Graphene Oxide Synthesis and Its Reduction

I. Kondratowicz, K. Żelechowska, and W. Sadowski

33.1 Introduction

Graphene and its preparation methods have attracted intense interest all over the world. This two-dimensional carbon material possesses excellent properties: good electrical conductivity and fast mobility of charges (200,000 $cm^2\ V^{-1}\ s^{-1}$) and high value of Young modulus (1.1 TPa) [1–3]. Nowadays, there are a lot of methods of graphene synthesis such as bottom-up methods: chemical vapor deposition or epitaxial growth from SiC, and top-down methods such as mechanical, physical, and chemical exfoliation of graphite. Geim and Novosielov isolated single graphene layers using a scotch tape that was glued to the surface of graphite [3]. This method however produces small amounts of graphene. Chemical exfoliation introduced by Hummers [4] allows to obtain graphite oxide whose layers are subsequently separated to produce graphene oxide which is reduced in the next step. This derivative of graphene is often called a reduced graphene oxide (rGO) as it still has some residual oxygen-containing groups introduced during the oxidation process. The history of graphite oxidation researches is dated to the nineteenth century when Brodie [5] proposed the method in which one portion of graphite was mixed with three portions of $KClO_3$ in H_2SO_4 solution at 60 °C for 4 days. Staudenmaier [6] improved this method by replacing a part of HNO_3 with H_2SO_4 and adding $KClO_3$ solution drop by drop. The most efficient and used to these days method was introduced by William Hummers and Richard Offeman [4]. In this method, a graphite powder is mixed with $NaNO_3$ and H_2SO_4, and then $KMnO_4$ is added as an oxidizer. The advantages of the reaction include completion within few hours and no emission of explosive ClO_3. However, the toxic gases such as NO_2

I. Kondratowicz (✉) • K. Żelechowska • W. Sadowski
Department of Solid State Physics, Faculty of Applied Physics and Mathematics, Gdansk University of Technology, Narutowicza 11/12, 80-233, Gdansk, Poland
e-mail: ikondratowicz@mif.pg.gda.pl

O. Fesenko, L. Yatsenko (eds.), *Nanoplasmonics, Nano-Optics, Nanocomposites, and Surface Studies*, Springer Proceedings in Physics 167,
DOI 10.1007/978-3-319-18543-9_33

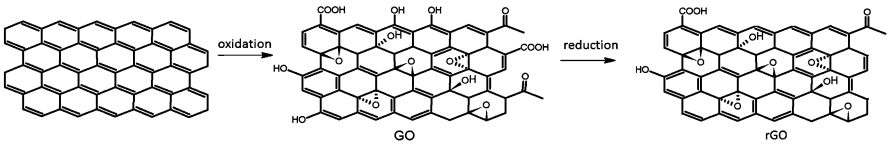

Fig. 33.1 Synthesis of the reduced graphene oxide from graphite

and N_2O_4 are produced in this process, and the Na^+ and NO_3^- ions are hard to remove from the reaction mixture after synthesis [7]. Graphite oxide obtained during the oxidation possesses carboxyl and carbonyl groups at the edges and epoxy and hydroxyl groups in the basal plane. Therefore, graphite oxide is considered to be amphiphilic with hydrophilic edges and more hydrophobic basal plane, unlike graphite which is hydrophobic and insoluble in water. Sulfuric acid acts as an intercalator between graphite layers separating them to produce expanded graphite. The layer distance in graphite is 3.35 Å, and after dissolving it in sulfuric acid, this value can be increased even twofold [8]. Figure 33.1 depicts the general idea of the synthesis of the rGO.

33.1.1 Traditional Hummers Method

As mentioned above, in the traditional Hummers method, one portion of graphite powder is mixed with 0.5 portion of $NaNO_3$, followed by dropwise addition of concentrated H_2SO_4 (1:42 graphite to acid mass ratio). The solution is cooled down to 0 °C. Then, the three portions of $KMnO_4$ are added slowly to the suspension keeping the temperature below 20 °C. The solution is stirred magnetically and it warms up to 35 °C. $NaNO_3$ is used to pre-oxidize graphite. Sulfate anions from sulfuric acid intercalate between the graphene layers, allowing oxidation of graphite layers in an acid environment. Afterward, distilled water is added into the suspension, causing strong exothermic reaction and increasing the temperature to 90 °C. The formed paste is kept in this temperature for 15 min and then cooled down to rt. The next step consists in slow pouring of 30 % solution of hydrogen peroxide with the distilled water which stops the reaction and changes the color of suspension from dark brown to yellow [9–11]. As a result, the suspension is centrifuged, and the solid is washed three times with a solution of 3 % HCl, followed by drying at room temperature. As a result, the powder of graphite oxide (GrO) is obtained. Finally, in order to produce graphene oxide (GO), ultrasonication of GrO in water for 12 h is performed. The Lerf–Klinowski model [12] of a graphene oxide layer with oxygen-containing groups such as hydroxyl, epoxy, carboxyl, or carbonyl groups is depicted in Fig. 33.2.

After the development of the Hummers method, the scientists started to work on its improvement that can lower the cost and enhance the efficacy and safety of the reaction. Wang et al. [9] increased twice the amount of $KMnO_4$ which allowed to shorten the mixing and sonication time during and after oxidation. In the process of

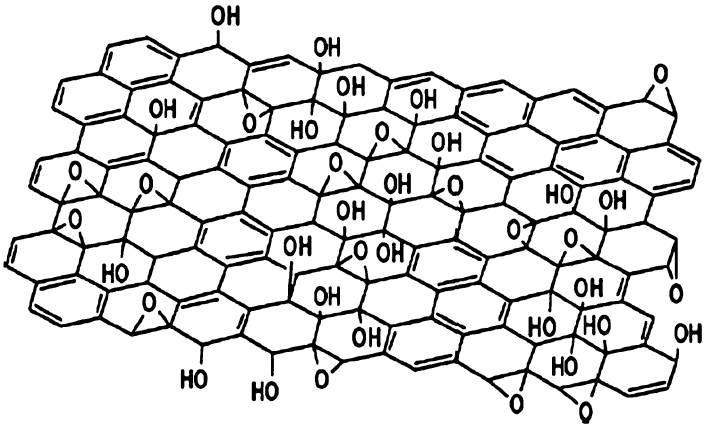

Fig. 33.2 Lerf–Klinowski model of a graphene oxide layer (Reprinted with permission from [12]. Copyright 1998, American Chemical Society)

GO synthesis, toxic gases are emitted. Moreover, this process is strongly exothermic (temperature increases to 100 °C) which may cause an explosion. Because of this inconveniences, new more benign methods are required to provide the environmental safety and the possibility to apply this material in biomedical sciences. Beak's group examined the etching process of highly ordered pyrolytic graphite (HOPG) using the mixture of H_2SO_4 and HNO_3 after many hours of sonication [10]. The results confirmed that graphene oxide layers were obtained. Marcano and Huang [11, 13] showed that the use of $NaNO_3$ is unnecessary, replacing it with the mixture of H_2SO_4 with H_3PO_4 in different proportions. This eco-friendly method allowed to obtain graphene oxide without the emission of hazardous gases.

The next step in the chemical synthesis of graphene is the reduction of graphene oxide. The oxidation of graphite causes the deterioration in electrical properties due to disrupted sp^2 bonding networks; thus, the removal of the oxygen functional groups from the graphene oxide layers is crucial to obtain a material that can be used in the electronic applications. Experiments as well as computer simulations confirmed that the complete removal of functional groups is not possible, so the layers still have some residual oxygen groups [12]. Therefore, this material as a derivative of graphene is often called a reduced graphene oxide (rGO). The effects of the reduction can be observed in three ways. Firstly, rGO acquires the hydrophobicity which can be seen after its dispersion in water. Secondly, the color of the material changes to black because of the removal of oxygen groups. Thirdly, one can also measure the electrical conductivity that increases after the reduction. Often, the carbon to oxygen atomic ratio measurements are also performed [14]. Graphene oxide has C/O atomic ratio of approximately 2, whereas this value increases after the reduction to is equal to 20–30 which depends on the reducing agent used. Reduction can be conducted using different methods. Among them, the chemical one is the most cost-effective and the easiest. The chemical methods do not need the use of any complicated setup and may be conducted in mild conditions

and room temperature. One of the most promising methods is the reaction in the solution [8]. The reducing agents used most frequently are hydrazine monohydrate, sodium borohydrate, hydroquinone, *p*-phenethylamine, and sodium hydrosulfide. However, these compounds are harmful to the environment and human health. Some of them are strongly explosive and poisonous; thus, the safety precautions have to be taken while using them. Taking into account the possibility of the biomedical application of the rGO, it is important to provide the least toxic and harmful reagents. In the literature, there are examples of the use of ascorbic acid [14], different alcohols [15], and triethylamine [16] that have equally good reducing properties.

33.1.2 Methods of Characterization of Graphene and Graphene Oxide

Graphene oxide and rGO can be characterized using different spectroscopic and microscopic methods. X-ray diffraction (XRD) analysis can provide the information about the structure of the crystalline materials. The incident X-ray radiation interacts with the sample and produces constructive interference according to Bragg's law: $n\lambda = 2d\sin\theta$, where λ, d, and θ refer to the wavelength of the radiation, the lattice spacing, and the diffraction angle, respectively. The unique X-ray diffraction pattern allows to identify the crystalline structure—for instance, the spacing between layers and the orientation of a single crystal.

Figure 33.3 (left) shows the XRD patterns of pure graphite, GO, and rGO [17]. In the pure graphite, a sharp peak at around 26° is observed that corresponds to (002) plane of graphite. In graphene oxide, a new peak appears at 11° that corresponds to (001) plane. The interlayer spacing of the rGO was calculated to be 3.76 Å. This value is lower than that of GO (6.94 Å) while slightly higher than that of natural graphite (3.36 Å). These results suggest the existence of π–π stacking between graphene sheets in the rGO and also the presence of residual functional groups on reduced GO sheets.

Kuila et al. [18] reported the UV–Vis spectroscopic analysis of graphene oxide and rGO. It uses light in visible and near-UV ranges that is absorbed by the sample in use. The photons are absorbed by the π electrons (bonding orbitals) in a molecule and are excited to higher antibonding orbitals. The spectra show the maximum absorption of light depending on the energy band gap in the investigated material.

The spectrum of graphene oxide exhibits an absorption band at around 230 nm, while the spectrum for reduced graphene oxide shows maximum absorption at around 260 nm. This is due to the π–π* transitions of electrons in C–C double bonds. Decrease in absorbance of rGO is mainly caused by the recovery of sp^2 carbons which indicates the restoration of electronic conjugation in rGO. As the light transmittance for graphene depends on whether it is monolayer or bilayer, UV–Vis spectroscopy also provides information of the number of layers (Fig. 33.3, middle).

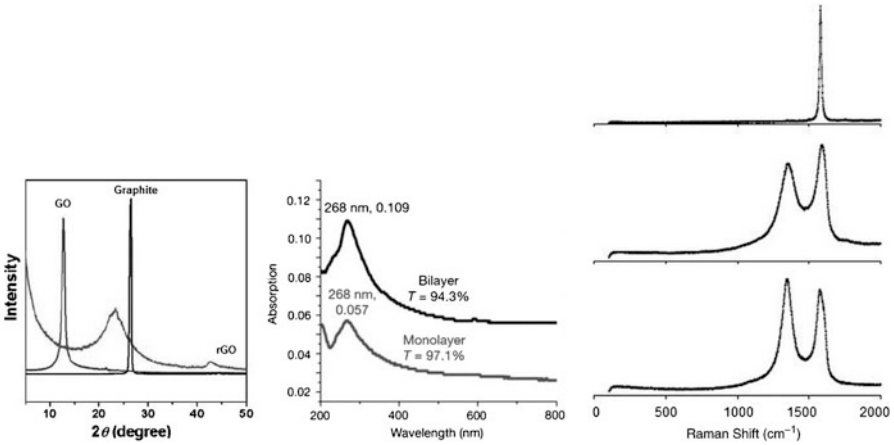

Fig. 33.3 *Left*: XRD patterns of graphene oxide, reduced graphene oxide, and pure graphite (Reprinted with permission from [17]. Copyright 2012, American Chemical Society). *Middle*: UV–Vis spectroscopy of bilayer and monolayer of reduced graphene oxide (Reprinted with permission from [18]. Copyright 2010, Rights Managed by Nature Publishing Group). *Right*: Raman spectroscopy of graphite (*top*), graphene oxide (*middle*), and reduced graphene oxide (*bottom*) (Reprinted with permission from [19]. Copyright 2007, Elsevier)

Raman spectroscopy is another tool to characterize graphene-type materials [19]. This method gives both structural and electronic information about the samples and is fast and nondestructive, which makes it one of the most popular techniques for the investigation of different carbonaceous materials such as fullerenes, carbon nanotubes, or amorphous carbons. The incident radiation coming from a laser interacts with phonons in the material. The photons are mainly reemitted with the same frequency (Rayleigh scattering) but can also be scattered inelastically (Raman scattering) which causes the energy shift up or down. The latter gives information about the vibrational, rotational, and other transitions in molecules, and it is a fingerprint for the investigated materials.

Figure 33.3 (right) shows the Raman spectra of graphite (top), graphene oxide (middle), and rGO (bottom). The pure graphene and graphite exhibit three characteristic bands: G (1,560 cm^{-1}), D (1,320 cm^{-1}), and 2D (2,700 cm^{-1}) bands that are related to the vibrations of sp^2-bonded carbon atoms, the presence of defects, and the interactions between graphene layers (due to the second-order zone boundary phonons), respectively. Spectrum of GO shows high D band due to the disruption of hexagonal network of carbon atoms. Chemically, rGO shows more intensive D band due to the ultrasonication processes which introduced defects and not full restoration of sp^2 carbon bonds in graphene plane. By the analysis of the relative intensities of peaks, their shape, and shift, it is possible to determine the number of graphene layers, strains in materials, and doping concentration. Therefore, it is common to analyze I_G/I_{2D} ratio as well as the FWHM (full width at half-maximum)

of peaks and their splitting into more components. For example, with more graphene layers, 2D peak is blueshifted, and G peak is redshifted with more tensile strain in the planes [3].

Another powerful tool to characterize carbonaceous materials is the XPS (X-ray photoelectron spectroscopy) analysis. It is used to investigate the chemical composition at the surface of a specimen. X-ray radiation causes the photoemission of electrons from the atoms below the surface which can be described by the well-known photoelectric equation. In principle, by the analysis of the kinetic and binding energies of the photoelectrons, it is possible to determine the atoms the electrons were ejected from. The resulting energy spectra show the resonance peaks allowing the identification of the chemical structure of the samples. The C1s XPS spectrum of graphene oxide (Fig. 33.4, left) exhibits characteristic peaks that can be attributed to carbon atoms in different oxygen-containing groups: the non-oxygenated C (284.8 eV), the C in C–O bonds (286.2 eV), the carbonyl C (287.8 eV), and the carbon in a carboxyl group (289.0 eV) [20]. The C1s XPS spectrum of the rGO (Fig. 33.2b) also exhibits some oxygen functionalities which confirms an incomplete reduction of graphene oxide.

To investigate the thermal properties of graphene oxide, the thermogravimetry analysis (TGA) is commonly used [21]. Due to the hydroxyl, epoxy, and carboxyl groups, graphene oxide remains thermally unstable. Thus, the first observation of a mass loss starts at the temperature around 150–200 °C (Fig. 33.4, right). The loss at around 500 °C is attributable to the pyrolysis of a carbon frame similarly to the drops on rGO and graphite curves. rGO curve differs from the one for graphite, and the first loss is observed at around 200 °C. This indicates that oxygen-containing

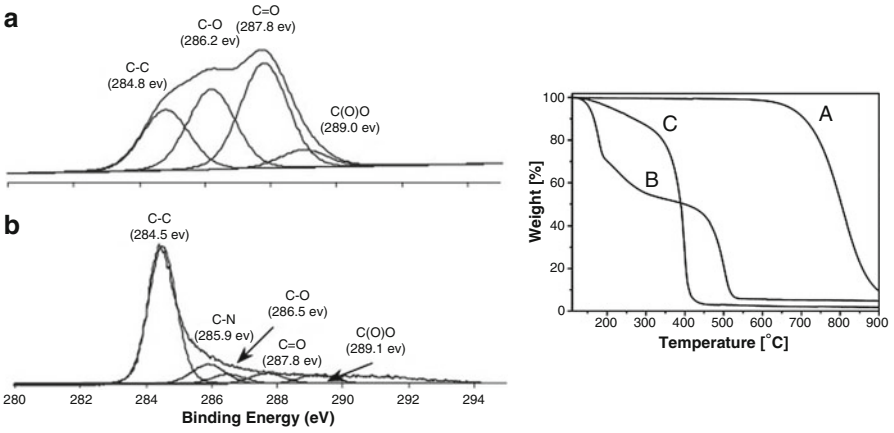

Fig. 33.4 *Left*: XPS spectra of (**a**) graphene oxide and (**b**) reduced graphene oxide (Reprinted with permission from [20]. Copyright 2006, The Royal Society of Chemistry). *Right*: TGA curves of (**a**) graphite, (**b**) graphene oxide, and (**c**) reduced graphene oxide (Reprinted with permission from [21] Copyright 2011, Elsevier)

groups were not fully removed. During the heating, the rapid thermal expansion of GO is observed which is accompanied by the release of several gases such as CO and CO_2. Therefore, the thermal reduction of GO can be also applied in order to obtain the graphene-like material.

33.1.3 Modifications and Applications

Due to its excellent properties, graphene has attracted much attention all over the world. Its applications are numerous ranging from nanoelectronics, biomedicine, energy storage and conversion, etc. Graphene is insoluble in water, is chemically inert, and has no energy band gap. Therefore, often a proper modification of graphene sheets is required in order to obtain a functionalized material for a new generation of biosensors, batteries, coatings, or composites. We do not attempt to review it here, but to give an overall picture of the topic, interested readers are referred to [22, 23]. The surface modification of graphene can be realized through covalent or noncovalent bonding of different species to the surface of graphene, and the latter usually dominates as a pure graphene has an ordered carbon network and no functional groups exist [24]. The noncovalent bonds are preferred when one needs to retain the high electrical conductivity of graphene, whereas by covalent bonding it is able to receive a material with good stability and mechanical properties. The examples of the noncovalent modifications include a role of the van der Waals forces, electrostatic interactions, π–π stacking, or hydrogen bonding. For the covalent bonding, graphene oxide is commonly used as this approach takes advantage of the oxygen-containing functionalities (epoxy, hydroxyl, carboxyl groups) on the hexagonal carbon sheet. Fan et al. [25] functionalized graphene oxide with ethylenediamine, and the amine groups were used to attach ferrocene derivatives to enhance the electron transfer for the hydrogen peroxide sensing. For optoelectronic application, the opening of the band gap is required, and it is usually performed by atom doping. Graphene has also found application in catalysis, and the immobilization of metal catalysts (such as platinum) is a key challenge. It should be noted here that graphene planes usually have defects which can be also used as active centers for the covalent modification of graphene.

33.2 Experimental

33.2.1 Materials and Methods

As sources of a graphite, natural graphite rocks and carbon electrodes from zinc–carbon batteries were used. Potassium permanganate ($KMnO_4$), L-ascorbic acid, citric acid, 98 % sulfuric acid (H_2SO_4), 85 % phosphoric acid (H_3PO_4), 30 %

hydrogen peroxide (H_2O_2), 35 % hydrochloric acid (HCl), and ethanol were purchased from POCh (Gliwice, Poland). Sodium dodecyl sulfate, hydrazine monohydrate, and triethylamine were purchased from Sigma-Aldrich. They were used without further purification.

UV–Vis spectra were measured using Lambda 10, PerkinElmer. Fourier transform infrared (FTIR) spectrophotometer used was Frontier FTIR/FIR PerkinElmer. SEM images of the samples were prepared using the ESEM Quanta FEG 250 FEI scanning electron microscope (SEM). The samples were prepared using the KBr pellet method with a weight concentration of a sample of 1 %. During the experiments, the magnetic stirrer Heidolph MR Hei-Standard with hot plate was used, and the centrifugation for all samples was done using Chemland model P3032 centrifugator with the speed 15,000 rpm for 10 min.

33.2.2 Traditional Hummers Method

Prior to the synthesis, a piece of graphite was crushed using a sandpaper, and the obtained powder was ground thoroughly in a mortar. Five portions of graphite powder were weighted—0.1, 0.1, 0.2, 0.2, and 0.8 g—and they were used for the synthesis of five different samples (GO1, GO1′, GO2, GO3, and GO4, respectively). The first sample was prepared using the traditional Hummers method according to [4]. Briefly, 0.05 g of $NaNO_3$ was added to graphite, and 2.25 mL of 95 % H_2SO_4 was slowly poured to the flask under magnetic stirring in an ice bath (5 °C). After this, 0.3 g of $KMnO_4$ was slowly added to the suspension keeping the temperature below 20 °C. The ice bath was removed, and the suspension was warmed up to 35 °C, while the stirring was continued for 1 h. During this time, the oxidation of graphite occurred. Afterward, 14 mL of deionized water was added that caused a strong exothermic reaction and an increase of temperature to 95 °C. The brown paste was kept in this temperature for 15 min under vigorous stirring. Then, 30 % H_2O_2 was added to stop the reaction, and the color of the suspension turned from brown to yellow (see Fig. 33.3). The mixture was filtered and washed with 1:10 HCl solution to remove any impurities. Figure 33.5 shows the graphite powder and the graphene oxide suspension after ultrasonication for 4 h.

The sample denoted as GO1′ was prepared using the same recipe, but the time of oxidation (before adding H_2O_2) was elongated to 24 h. This synthesis aimed to determine the correlation between the time of oxidation and the level of oxidation of graphite. In order to obtain graphene oxide, the suspension was diluted and then ultrasonicated for several hours. The next sample (GO2) was obtained in the same manner as GO1, except that the graphite powder was sonicated before the oxidation for 2 h. The third sample (GO3) was sonicated for 2 h with the addition of sodium dodecyl sulfate which is a surfactant and facilitates the separation of graphite planes. The aim of this was to determine the influence of surfactant and ultrasonication on the properties of graphite oxide. The last sample (GO4) was prepared in the same way as GO1, but $KMnO_4$ was added slowly in small portions

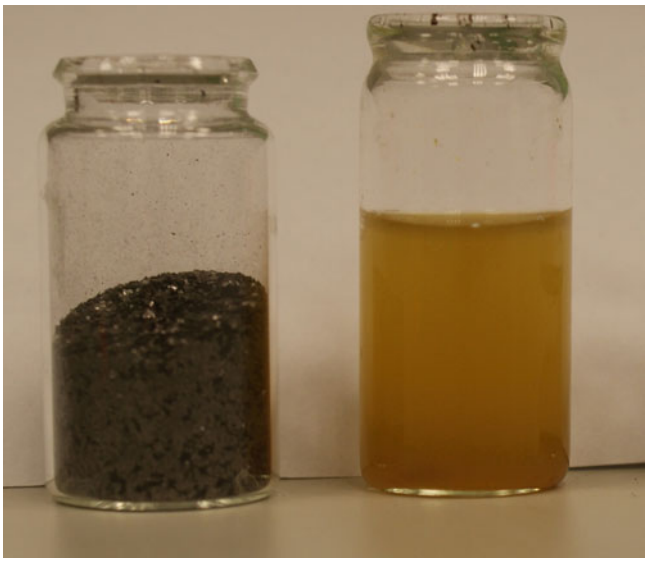

Fig. 33.5 Graphite powder (*left*) and graphene oxide suspension (*right*)

and was stirred magnetically after each portion. In this way, the reaction could occur more precisely. All samples were purified in the same manner and dried in 60 °C.

33.2.3 Modified Hummers Methods

For the next synthesis, a graphite rod from zinc–carbon batteries was isolated. This material has smaller particles than a natural graphite which can make an oxidation easier. Prior to the synthesis, graphite rods were washed thoroughly in deionized water and H_2SO_4 and crashed with the use of a mortar. GO5 sample was prepared using the traditional Hummers methods alike GO1 sample described earlier. The next three samples were prepared using the method described in [26]. This method is more environmentally friendly. $NaNO_3$ was excluded, and the mix of phosphoric and sulfuric acid in different ratios was used. The sixth sample GO6 was prepared by adding 1.2 g of $KMnO_4$ to 0.2 g of graphite. Then, 9:1 H_2SO_4/H_3PO_4 (18 mL:2 mL) was added dropwise, and the suspension was stirred magnetically for 24 h. Afterward, the solution of 3 % of hydrogen peroxide was added until the color changed to yellow. The suspension was centrifuged with a subsequent washing with water and HCl. Then, it was dried and the powder of graphene oxide was obtained. In order to separate the graphene flakes and obtain graphene oxide, the ultrasonication of water dispersion of graphite oxide (0.1 % w) was conducted for 4 h.

33.2.4 Reduction of Graphene Oxide

For the graphene oxide reduction, four different reducing agents were used, namely, ascorbic acid (vitamin C), citric acid, triethylamine (TEA), and hydrazine. The aim of this experiment was to compare the efficiency of each reductant. Samples GO1, GO1′, GO2, GO3, and GO4 were reduced using vitamin C using the recipe from [7]. Firstly, the water suspensions of each oxide were prepared by adding 6 mg of graphene oxide to 3 mL of water, and the solution was ultrasonicated for 1 h. Secondly, 24 mg of ascorbic acid was added and sonicated for the next 5 min. The required amount of reducing agent was found in [7] where authors analyzed the stoichiometry of the reaction and estimated that the mass ratio of 4:1 (reducing agent/carbon material) should be sufficient. In the next step, the solution was warmed to 95 °C and kept in this temperature for 4 h. Obtained product was centrifuged and dried at room temperature. The samples were denoted as rGO1, rGO1′, rGO2, rGO3, and rGO4. Samples GO6, GO7, and GO8 were reduced by hydrazine. Two mg of each graphene oxide was mixed with 1 mL of distilled water, and the whole was sonicated for 30 min. Then, 0.5 mL of hydrazine was added; the samples were heated to 100 °C and kept at this temperature for 12 h. Figure 33.6 shows the suspension of graphene oxide immediately after addition of hydrazine on the left and the rGO (after a few hours with hydrazine) on the right.

These samples were denoted as rGO6, rGO7, and rGO8. Sample GO5 was divided into four portions of 6 mg GO in 3 mL of water. Then, four different reducing agents were used to reduce graphene oxide. The first sample was obtained by adding 24 mg of citric acid, and the flask was heated to 90 °C. The second reduction was performed by pouring 1 mL of TEA according to [16]. One mL of hydrazine was added to the third vial, and the last one was prepared by adding 24 mg of vitamin C to GO5. The vials were put into the ultrasonication bath for 3 h,

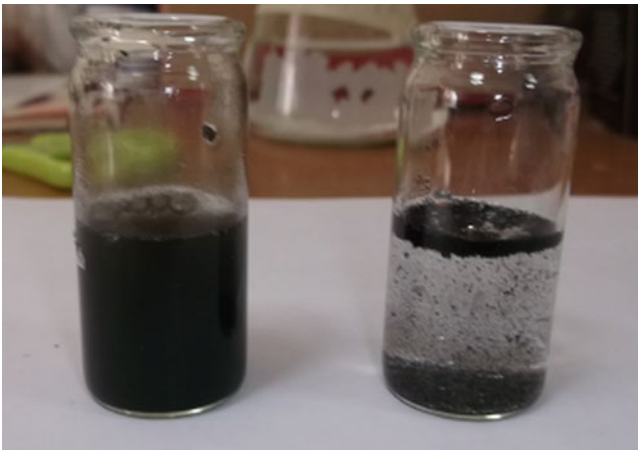

Fig. 33.6 Graphene oxide with hydrazine (*left*) and reduced graphene oxide (*right*)

and then they were washed five times with water and ethanol and were dried at room temperature. They were denoted as rGO5-K, rGO5-T, rGO5-H, and rGO5-W, respectively.

33.3 Results and Discussion

For clarity, the conditions of the synthesis of each sample were presented in Table 33.1. It shows the sample symbol; the amount of graphite (indicating the source of graphite, natural or battery); additional sonication and/or addition of surfactant; the amount of sodium nitrate, sulfuric acid, phosphoric acid, and potassium permanganate; and time of oxidation, respectively.

All samples were analyzed using FTIR and UV–Vis spectroscopy. Figure 33.7a shows the spectra of GO1 and GO1′ samples. As we can see, characteristic bands appear: C=O bonds (1,650–1,700 cm^{-1}) and C=C bonds (1,590 cm^{-1}). The relative intensity of these bands is higher for GO1′, so this may indicate that more carbonyl groups are attached to this sample. The broad peak at 1,200 cm^{-1} in GO1 can be assigned to C–O–C, C–O, and C–OH bonds jointly. It may indicate that due to the longer oxidation time (1 vs. 24 h), GO1′ is more oxidized. The spectra of GO1 and GO4 are compared in Fig. 33.7b. Both oxides were prepared using the same method, but in the case of GO4, permanganate was added slowly in small portions with a successive rigorous stirring. It should be noted that the volume of sulfuric acid was reduced and it was two times lower for GO4 as compared to GO1. The FTIR spectrum analysis revealed that the ratio intensity of C=O to C=C band is higher in sample G4 than in sample GO1, which indicates higher oxidation level of the former one. In the next step, we compare GO1, GO2, and GO3 (Fig. 33.7c). During the synthesis of GO2 and GO3, additional sonication was conducted, and the surfactant was added to GO3 suspension to facilitate the exfoliation and dispersion of graphite. All samples exhibit characteristic bands

Table 33.1 Conditions of the oxidation reaction of nine different samples

GO symbol	Graphite [g] (nat/bat)	$NaNO_3$ [g]	H_2SO_4 [mL]	H_3PO_4 [mL]	$KMnO_4$ [mL]	Oxidation time [h]
GO1	0.1 (nat)	0.05	2.25	–	0.3	1
GO1′	0.1 (nat)	0.05	2.25	–	0.3	24
GO2	0.2 (nat) + surf	0.1	4.5	–	0.6	1
GO3	0.2 (nat) + son + surf	0.1	4.5	–	0.6	1
GO4	0.8	0.4	9	–	2.4	1
GO5	0.2	0.1	2.25	–	0.6	1
GO6	0.2	–	18	2	1.2	24
GO7	0.2	–	18	2	0.6	24
GO8	0.2	–	12	3	0.6	24

nat natural graphite, *bat* graphite from a battery, *son* additional sonication, *surf* addiction of a surfactant

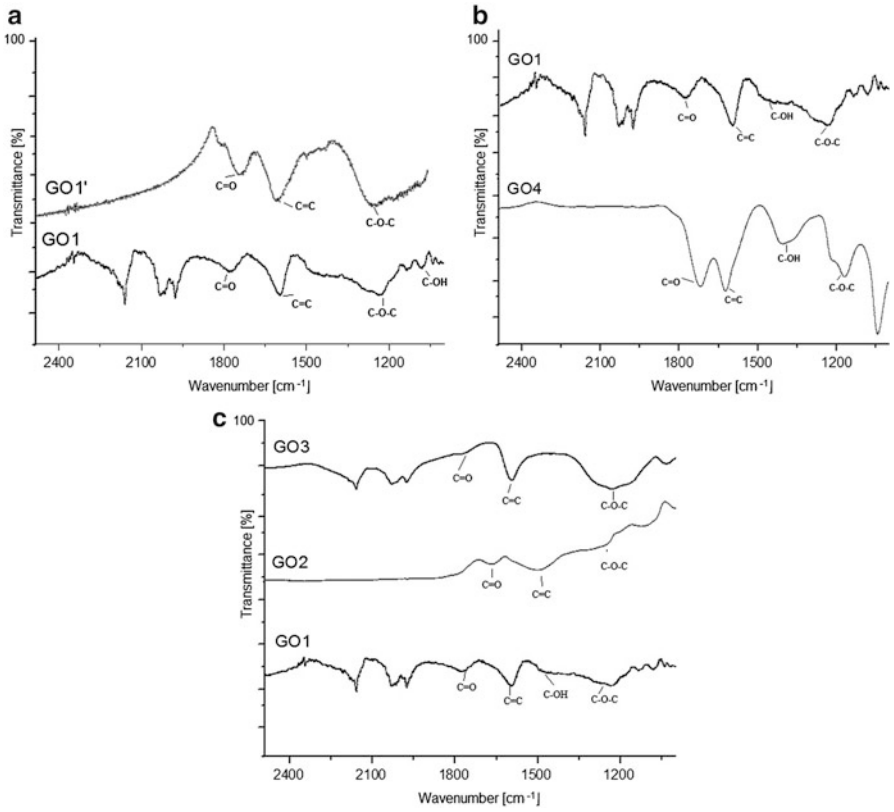

Fig. 33.7 FTIR spectra of (**a**) GO1 and GO1′, (**b**) GO1 and GO4, and (**c**) GO1, GO2, and GO3

mentioned earlier. Moreover, there is no significant difference in spectra of GO3 and GO2, and the intensity ratio between C=O and C=C is greater for GO2.

Marcano et al. [12] showed that increasing the amount of $KMnO_4$ and performing the reaction in a 9:1 mixture of H_2SO_4/H_3PO_4 within 3 days improved the efficiency of the oxidation process. Our findings confirmed the effectiveness of the proposed method, and its optimization was undertaken. Time of the reaction was shortened to 24 h, and the total volume of acids was decreased (see Table 33.1). Figure 33.8 shows the spectra of GO6, GO7, and GO8. GO spectrum exhibits more distinct band corresponding to the C=O bond (1,650 cm^{-1}) which results from the higher amount of potassium permanganate used. All of the spectra show sharp peaks that correspond to the bonds from other oxygen-containing groups mentioned above. There is no significant difference in the relative intensities of these peaks between all three samples. Thus, the higher amount of oxidant is important mainly for the introduction of epoxy groups. We did not observe any considerable influence of the amount and the concentration of acids on the intensity of peaks in the spectra of GO7 and GO8.

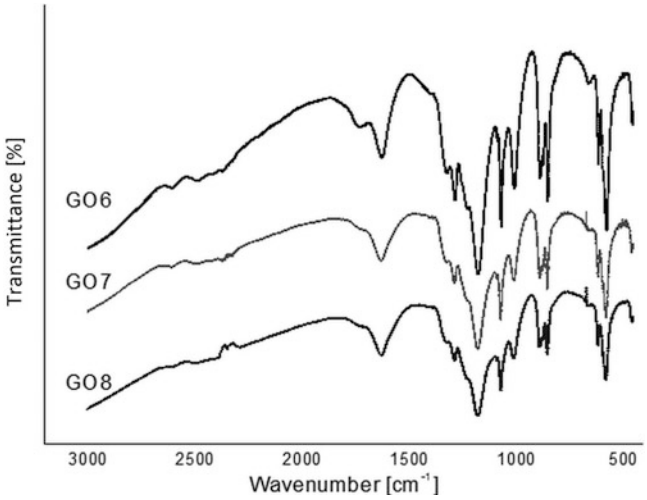

Fig. 33.8 FTIR spectra of GO6, GO7, and GO8

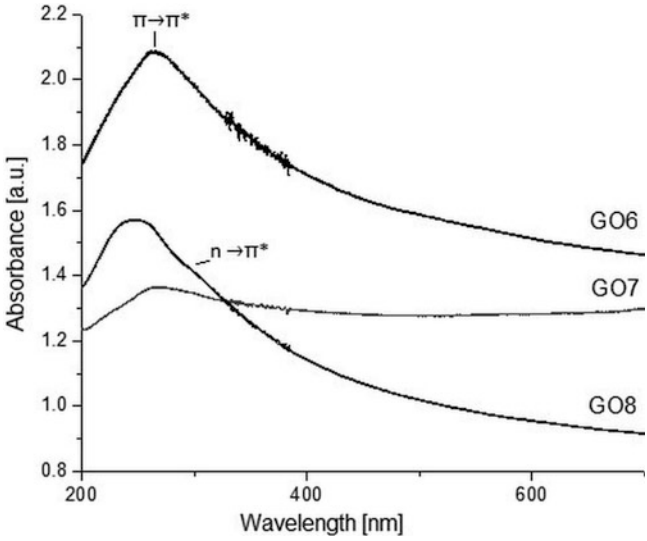

Fig. 33.9 UV–Vis spectra of GO6, GO7, and GO8

The UV–Vis spectra of GO6, GO7, and GO8 samples are presented in Fig. 33.9. Sample GO6 exhibits a sharp peak at around 270 nm. There is no significant band corresponding to n–π* transitions of electrons in C=O groups. For GO7, the maximum absorption band is blueshifted (250 nm); however, the intensity is low. GO8 spectrum shows a sharp band at 230 nm and a small peak that is attributed to n–π* transitions within C=O groups.

Table 33.2 Conditions of the reduction reaction for nine prepared samples

rGO symbol	Reducing agent
rGO1	V
rGO1′	V
rGO2	V
rGO3	V
rGO4	V
rGO5-H, rGO5-V, rGO5-T, rGO5-C	H,V,T,C
rGO6	H
rGO7	H
rGO8	H

V vitamin C, *C* citric acid, *H* hydrazine, *T* triethylamine

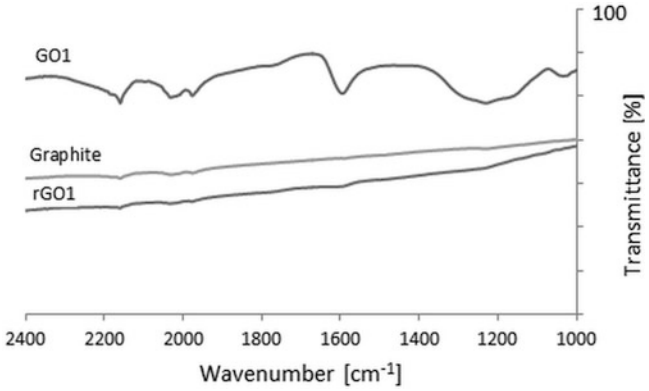

Fig. 33.10 FTIR spectra of graphite, GO1, and rGO1

Graphene oxide reduction was performed using different reductants. The table for the reduction reactions is presented below (Table 33.2).

Infrared, UV–Vis, and Raman spectroscopy measurements of obtained samples were carried out. Figure 33.10 shows the FTIR spectra of graphite, GO1, and rGO1 reduced by ascorbic acid. Spectrum for GO1 contains characteristic bands that correspond to oxygen functional groups: epoxy groups, C–O–C (1,230 cm^{-1}), C–O (1,050 cm^{-1}), C=C (1,600 cm^{-1}), and a signal from C=O (1,720 cm^{-1}) stretching bonds. A peak at 1,385 cm^{-1} corresponds to the vibrations of C–OH bonds. Bands present in the range of 2,000–2,200 cm^{-1} can correspond to the adsorbed carbon dioxide.

In the case of rGO1, a disappearance of almost all peaks can be observed, except of those referring to C–O–C bonds at 1,250 cm^{-1} that indicates only the partial reduction of GO. Carbon–carbon double bonds at 1,620 cm^{-1} are also visible. This is in agreement with the literature data [12] as the epoxy groups are considered to be the most difficult to reduce.

Figure 33.11a shows the FTIR spectra of GO5 and rGO5 reduced by hydrazine. It can be seen that after the reduction the intensity of bands corresponding to oxygen

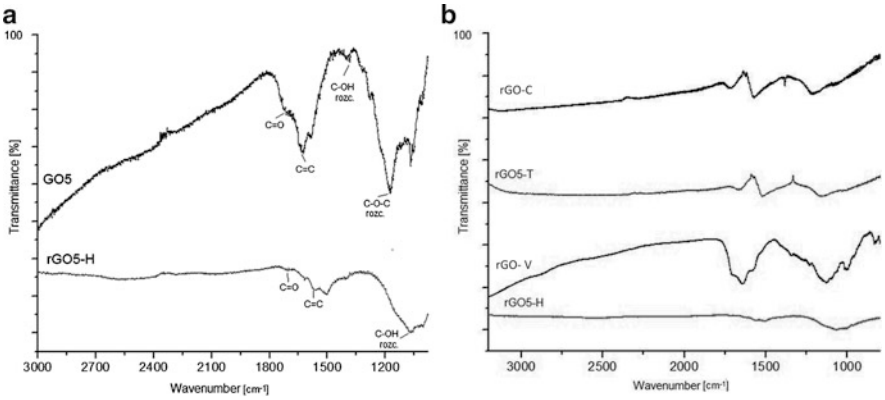

Fig. 33.11 FTIR spectra of (**a**) GO5 and rGO5 reduced by hydrazine and (**b**) comparison of rGO5 spectra after the reduction with four different reducing agents

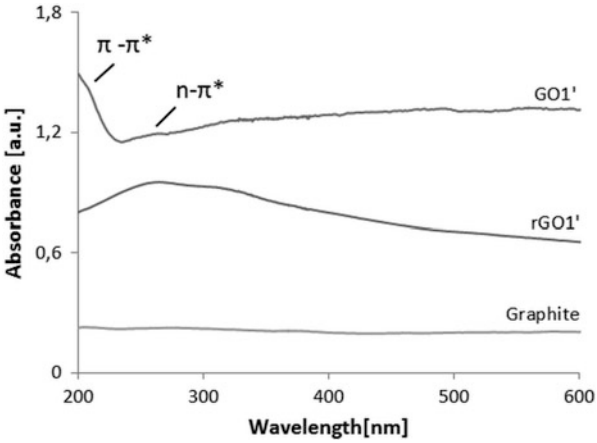

Fig. 33.12 UV–Vis spectra of graphite, GO1′, and rGO1′

functional groups is smaller in comparison to C=C bonds. It can testify the successful reduction. By comparing four spectra of rGO5 (Fig. 33.11b) reduced by four different reducing agents (citric acid, triethylamine, vitamin C, and hydrazine, respectively), we can estimate the efficiency of the used reductant. The spectrum of the sample reduced by hydrazine shows the smallest band intensities, while in the spectrum of sample reduced using ascorbic acid, there are still some bands that can be assigned to oxygen-containing groups. Thus, among all used reducing agents, ascorbic acid can be considered as the least effective one.

UV–Vis spectra of chosen samples are shown in Fig. 33.12. Spectra were collected for suspensions of the same material concentration (0.05 mg/mL). Spectrum of GO1′ exhibits an absorption band at ~200 nm attributable to π–π* transition of electrons in C–C bonds and additional band at ~280 nm due to n–π* transitions within C–O bonds. rGO shows a maximum absorption band that is shifted toward

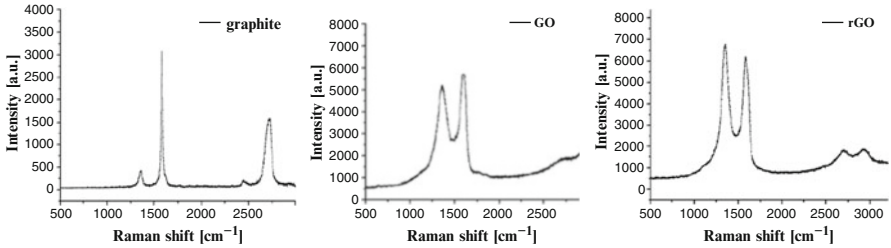

Fig. 33.13 Raman spectroscopy of graphite, graphene oxide (GO), and reduced graphene oxide (rGO)

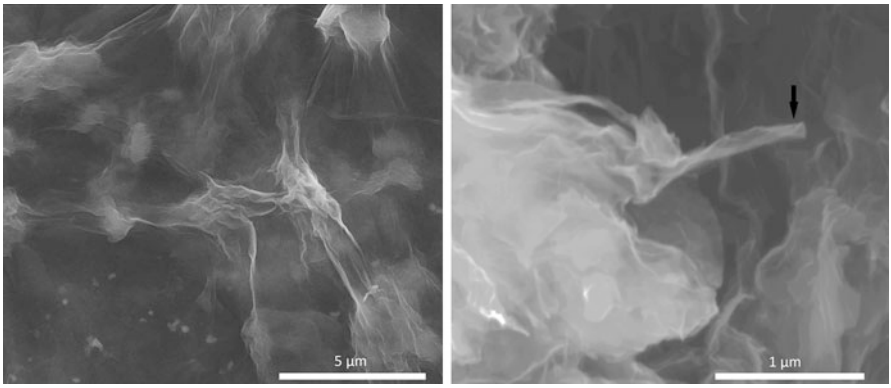

Fig. 33.14 SEM images of graphene oxide (*left*) and reduced graphene oxide (*right*)

higher wavelengths (~280 nm) which confirmed the reduction of graphene oxide. However, the peak that is due to n–π* transitions is also present and indicates not full reduction.

Raman spectroscopy measurements of graphite, graphene oxide, and rGO were performed (Fig. 33.13). Raman spectra of different samples did not exhibit any significant differences; therefore, we denoted the spectra GO and rGO generally. The spectra are in accordance with the literature data for graphene oxide and rGO [19]. Graphite spectrum exhibits three characteristic bands: D (1,355 cm^{-1}), G (1,579 cm^{-1}), and 2D (2,720 cm^{-1}). For graphene oxide, we observe an increase in D band intensity due to the defects introduced on a graphene sheet. In the spectrum of GO, 2D band is substantially lower and wider than G band, suggesting the presence of multilayered graphene derivatives. For the pure graphene layer, the D band is smaller than for rGO. rGO spectrum has D band which is more intense than G band. This may be due to the longer sonication time that cut graphene flakes into smaller ones and thus produced more edges.

SEM images of graphene oxide and rGO are shown in Fig. 33.14. We can distinguish few-layer flakes which are pointed by arrows. There is no significant

difference in a surface area of flakes although those for rGO are slightly smaller with more graphene edges. The reason is also the longer time of ultrasonication of rGO sample.

33.4 Conclusions

Nine different samples were prepared in order to optimize the synthesis of rGO. We used different methods found in the literature that base on the traditional Hummers method of oxidizing a graphite. Several modifications were applied. We investigated the influence of the concentration of reagents, time of oxidation, ultrasonication, and the addition of surfactant. The GO2, GO4, and GO6 samples exhibited the highest peak intensities referring to oxygen functional groups, as analyzed by FTIR spectroscopy. It can be concluded that oxidation in the presence of phosphoric acid and without sodium nitrate is very efficient and such method can be used to obtain GO replacing the traditional Hummers method. Moreover, the high level of oxidation was obtained with the higher amount of potassium permanganate; thus, to achieve the best performance, the amount of this substance should not be reduced. Also the influence of acid concentration on the level of oxidation was negligible. No significant difference in the oxidation level was observed when the surfactant was added. In order to obtain rGO, hydrazine seems to be the most suitable agent as it reduces the greatest amount of oxygen-containing groups. Thus, these three methods of graphene oxide synthesis with the following reduction by hydrazine are proposed to be the most efficient for the production of rGO.

Acknowledgment The authors would like to gratefully thank Jakub Karczewski for performing the SEM images and Mirosław Sawczak from the IMP PAN, Gdańsk, for the help with the Raman spectroscopy measurements.

References

1. Novoselov K, Geim AK (2009) The electronic properties of graphene. Rev Mod Phys 81:109–162
2. Novoselov K, Geim AK et al (2004) Electric field effect in atomically thin carbon films. Science 306:666
3. Singh V et al (2011) Graphene based materials: Past, present and future. Prog Mater Sci 56:1178–1271
4. Hummers W, Offeman R (1958) Preparation of graphitic oxide. J Am Chem Soc 80:1339
5. Brodie B (1859) On the atomic weight of graphite. Philos Trans R Soc Lond 149:249–259
6. Staudenmaier L (1898) Verfahren zur Darstellung der Graphitsaure. Ber Deut Chem Ges 31:1481–1499
7. Dreyer D et al (2010) The chemistry of graphene oxide. Chem Soc Rev 39:228–240
8. Park S, Ruoff R (2009) Chemical methods for the production of graphenes. Nat Nano 4:217–224

9. Wang K et al (2011) Biocompatibility of graphene oxide. Res Lett 6:8
10. Chen J, Yao B, Li C (2013) An improved Hummers method for eco-friendly synthesis of graphene oxide. Carbon 64:225–229
11. Marcano D et al (2010) Improved synthesis of graphene oxide. ACS Nano 4:4806–4814
12. Lerf A, He H, Klinowski J, Phys J (1998) Structure of graphite oxide revisited. Chem B 102:4477–4482
13. Pei S, Cheng H (2012) The reduction of graphene oxide. Carbon 50:3210–3228
14. Zhang J et al (2010) Reduction of graphene oxide via L-ascorbic acid. Chem Commun 46:1112–1114
15. Chao X et al (2014) Selective reduction of graphene oxide. New Carbon Mater 29:61–66
16. Gurunathan S et al (2013) Green chemistry approach for the synthesis of biocompatible graphene. Int J Nanomedicine 8:2719–2732
17. Xu Y, Sheng K (2010) Self-Assembled Graphene Hydrogel via a One-Step Hydrothermal Process. ACS Nano 4:4324–4330
18. Sun Z, Yan Z, Yao J (2010) Growth of graphene from solid carbon sources. Nature 468:549–552
19. Stankovich S, Ruoff R (2007) Synthesis of graphene-based nanosheets via chemical reduction of exfoliated graphite oxide. Carbon 45:1558–1565
20. Stankovich S et al (2006) Stable aqueous dispersions of graphitic nanoplatelets via the reduction of exfoliated graphite oxide in the presence of poly (sodium 4-styrenesulfonate). J Mater Chem 16:155–158
21. Wojtoniszak (2012) Synthesis, dispersion, and cytocompatibility of graphene oxide and reduced graphene oxide. Colloids Surf B Biointerfaces 89:79–85
22. Boukhvalov DW, Katsnelson MI (2009) Chemical functionalization of graphene. J Phys Condens Matter 21:344205
23. Georgakilas V (2012) Functionalization of Graphene: Covalent and Non-Covalent Approaches, Derivatives and Applications. Chem Rev 112:6156–6214
24. Liu J et al (2012) Strategies for chemical modification of graphene and applications of chemically modified graphene. J Mater Chem 22:12435
25. Fan L (2012) Ferrocene functionalized graphene: preparation, characterization and efficient electron transfer toward sensors of H_2O_2. J Mater Chem 22:6165–6170
26. Huang H et al (2011) Simple room-temperature preparation of high-yield large-area graphene oxide. Int J Nanomed 6:3443–3448

Index

O. Fesenko, L. Yatsenko (eds.), *Nanoplasmonics, Nano-Optics, Nanocomposites and Surface Studies*, Springer Proceedings in Physics 167,
DOI 10.1007/978-3-319-18543-9